ARO 30380.33-EG-URI

PROCEEDINGS OF SPIE

SPIE—The International Society for Optical Engineering

Smart Structures and Materials 1997

Passive Damping and Isolation

L. Porter Davis
Chair/Editor

3–4 March 1997
San Diego, California

Sponsored by
SPIE—The International Society for Optical Engineering

Cosponsored by
SEM—Society for Experimental Mechanics, Inc.
ASME—American Society of Mechanical Engineers

19970528 093

DTIC QUALITY INSPECTED 3

SPIE P PROCEEDINGS SERIES

Volume 3045

DISTRIBUTION STATEMENT A
Approved for public release;
Distribution Unlimited

REPORT DOCUMENTATION PAGE

Form Approved
OMB NO. 0704-0188

Public reporting burden for this collection of information is estimated to average 1 hour per response, including the time for reviewing instructions, searching existing data sources, gathering and maintaining the data needed, and completing and reviewing the collection of information. Send comment regarding this burden estimates or any other aspect of this collection of information, including suggestions for reducing this burden, to Washington Headquarters Services, Directorate for information Operations and Reports, 1215 Jefferson Davis Highway, Suite 1204, Arlington, VA 22202-4302, and to the Office of Management and Budget, Paperwork Reduction Project (0704-0188), Washington, DC 20503.

1. AGENCY USE ONLY *(Leave blank)*	2. REPORT DATE	3. REPORT TYPE AND DATES COVERED Reprint

4. TITLE AND SUBTITLE	5. FUNDING NUMBERS
Smart Structures and Materials 1997, Passive Damping and Isolation	DAAL03-92-G-0121
6. AUTHOR(S) L. Porter Davis	
7. PERFORMING ORGANIZATION NAMES(S) AND ADDRESS(ES) University of Maryland College Park, MD 20742	8. PERFORMING ORGANIZATION REPORT NUMBER
9. SPONSORING / MONITORING AGENCY NAME(S) AND ADDRESS(ES) U.S. Army Research Office P.O. Box 12211 Research Triangle Park,, NC 27709-2211	10. SPONSORING / MONITORING AGENCY REPORT NUMBER ARO 30380.33-EG-URI

11. SUPPLEMENTARY NOTES

The views, opinions and/or findings contained in this report are those of the author(s) and should not be construed as an official Department of the Army position, policy or decision, unless so designated by other documentation.

12a. DISTRIBUTION / AVAILABILITY STATEMENT	12 b. DISTRIBUTION CODE
Approved for public release; distribution unlimited.	

13. ABSTRACT *(Maximum 200 words)*

14. SUBJECT TERMS	15. NUMBER IF PAGES
	16. PRICE CODE

17. SECURITY CLASSIFICATION OR REPORT	18. SECURITY CLASSIFICATION OF THIS PAGE	19. SECURITY CLASSIFICATION OF ABSTRACT	20. LIMITATION OF ABSTRACT
UNCLASSIFIED	UNCLASSIFIED	UNCLASSIFIED	UL

NSN 7540-01-280-5500

Standard Form 298 (Rev. 2-89)
Prescribed by ANSI Std. 239-18
298-102

PROCEEDINGS OF SPIE

SPIE—The International Society for Optical Engineering

Smart Structures and Materials 1997

Passive Damping and Isolation

L. Porter Davis
Chair/Editor

3–4 March 1997
San Diego, California

Sponsored by
SPIE—The International Society for Optical Engineering

Cosponsored by
SEM—Society for Experimental Mechanics, Inc.
ASME—American Society of Mechanical Engineers

Cooperating Organizations
Air Force Wright Laboratory
DARPA—Defense Advanced Research Projects Agency
The American Institute of Chemical Engineers
The American Physical Society—Division of Materials Physics
The Ceramic Society of Japan
U.S. Army Research Laboratory
Intelligent Materials Forum (Japan)

Published by
SPIE—The International Society for Optical Engineering

SPIE P PROCEEDINGS SERIES

Volume 3045

DTIC QUALITY INSPECTED 3

SPIE is an international technical society dedicated to advancing engineering and scientific applications of optical, photonic, imaging, electronic, and optoelectronic technologies.

The papers appearing in this book comprise the proceedings of the meeting mentioned on the cover and title page. They reflect the authors' opinions and are published as presented and without change, in the interests of timely dissemination. Their inclusion in this publication does not necessarily constitute endorsement by the editors or by SPIE.

Please use the following format to cite material from this book:
Author(s), "Title of paper," in *Smart Structures and Materials 1997: Passive Damping and Isolation,* L. Porter Davis, Editor, Proceedings of SPIE Vol. 3045, page numbers (1997).

ISSN 0277-786X
ISBN 0-8194-2458-7

Published by
SPIE—The International Society for Optical Engineering
P.O. Box 10, Bellingham, Washington 98227-0010 USA
Telephone 360/676-3290 (Pacific Time) • Fax 360/647-1445

Copyright ©1997, The Society of Photo-Optical Instrumentation Engineers.

Copying of material in this book for internal or personal use, or for the internal or personal use of specific clients, beyond the fair use provisions granted by the U.S. Copyright Law is authorized by SPIE subject to payment of copying fees. The Transactional Reporting Service base fee for this volume is $10.00 per article (or portion thereof), which should be paid directly to the Copyright Clearance Center (CCC), 222 Rosewood Drive, Danvers, MA 01923. Payment may also be made electronically through CCC Online at http://www.directory.net/copyright/. Other copying for republication, resale, advertising or promotion, or any form of systematic or multiple reproduction of any material in this book is prohibited except with permission in writing from the publisher. The CCC fee code is 0277-786X/97/$10.00.

Printed in the United States of America.

Contents

vii *Conference Committee*

SESSION 1 PARTICLE AND HYSTERETIC DAMPING

2 **Hydrodynamic fluctuations and averaging problems in dense granular flows** [3045-03]
C. Salueñya, Univ. of Chicago and Univ. de Barcelona (Spain); S. E. Esipov, Univ. of Chicago; T. Pöschel, Humboldt-Univ. zu Berlin (FRG)

SESSION 2 LAUNCH VIBRATION ISOLATION

14 **Need for and benefits of launch vibration isolation** [3045-06]
A. S. Bicos, McDonnell Douglas Aerospace; C. D. Johnson, CSA Engineering, Inc.; L. P. Davis, Honeywell Satellite Systems

20 **Payload isolation system for launch vehicles** [3045-07]
P. S. Wilke, C. D. Johnson, CSA Engineering, Inc.; E. R. Fosness, Air Force Phillips Lab.

31 **Development of a launch vibration isolation system** [3045-08]
D. L. Edberg, McDonnell Douglas Aerospace; C. D. Johnson, CSA Engineering Inc.; L. P. Davis, Honeywell Satellite Systems Operation; E. R. Fosness, Air Force Phillips Lab.

SESSION 3 EMBEDDED PIEZO AND ACTIVE CLD

40 **Structural vibration damping experiments using improved piezoelectric shunts** [3045-09]
S. Wu, A. S. Bicos, McDonnell Douglas Aerospace

51 **Tunable electrically shunted piezoceramic vibration absorber** [3045-10]
C. L. Davis, G. A. Lesieutre, The Pennsylvania State Univ.; J. Dosch, PCB Piezotronics, Inc.

60 **Vibration control through passive constrained layer damping and active control** [3045-11]
M. J. Lam, D. J. Inman, W. R. Saunders, Virginia Polytechnic Institute and State Univ.

70 **Analysis of edge elements for a new active constrained layer treatment** [3045-12]
W. H. Liao, K. W. Wang, The Pennsylvania State Univ.

82 **Some insights on active-passive hybrid piezoelectric networks for structural controls** [3045-13]
M. S. Tsai, K. W. Wang, The Pennsylvania State Univ.

SESSION 4 ELECTRORHEOLOGICAL FLUID (ERF) DAMPING

96 **Experimental study of an ER long-stroke vibration damper** [3045-14]
D. J. Peel, R. Stanway, W. A. Bullough, Univ. of Sheffield (UK)

108 **Nonlinear modeling and performance prediction of electrorheological fluid dampers** [3045-15]
G. M. Kamath, N. M. Wereley, Univ. of Maryland/College Park

119 **Experimental study of a multi-electrode cylindrical ER fluid damper for in-plane motions** [3045-16]
F. Gordaninejad, M. S. Saiidi, S. Uthiram, Univ. of Nevada/Reno

130 **Experimental testing of a semi-active control scheme for vibration suppression** [3045-17]
W. Taniwangsa, Santa Clara Univ.; J. M. Kelly, Univ. of California/Berkeley

140 **Large-scale ER-damper for seismic protection** [3045-18]
S. McMahon, Univ. of Notre Dame; N. Makris, Univ. of California/Berkeley

148 **Design rules for MR fluid actuators in different working modes** [3045-19]
R. Bölter, H. Janocha, Univ. of Saarland (FRG)

SESSION 5 PASSIVE CONSTRAINED LAYER DAMPING (CLD)

162 **Fluid surface damping versus constrained layer damping for vibration suppression of simply supported beams** [3045-20]
H. Ghoneim, Rochester Institute of Technology

173 **Kinematic assumptions for sandwich beams** [3045-21]
E. M. Austin, D. J. Inman, Virginia Polytechnic Institute and State Univ.

184 **Passive damping of beams with constrained viscoelastic material** [3045-22]
A. Fasana, L. Garibaldi, E. Giorcelli, M. Ruzzene, Politecnico di Torino (Italy)

190 **Multilaminated plates with thin compliant adhesive layers** [3045-24]
S. W. Hansen, Iowa State Univ.

SESSION 6 CHARACTERIZATION OF DAMPING MATERIALS

204 **Time domain characterization of the dynamic properties of viscoelastic materials** [3045-25]
S. O. Oyadiji, L. Chu, Univ. of Manchester (UK)

SESSION 7 SYSTEM APPLICATIONS OF PASSIVE DAMPING AND ISOLATION

214 **Durability patch: application of passive damping to high-cycle fatigue cracking on aircraft** [3045-28]
L. C. Rogers, CSA Engineering, Inc.; I. R. Searle, R. Ikegami, Boeing Defense & Space Group; R. W. Gordon, D. Conley, Air Force Wright Lab.

224 **Compensation for passive damping in a large-amplitude microgravity suspension system** [3045-29]
M. C. Anderson, T. K. Hasselman, ACTA Inc.; T. C. Pollock, Texas A&M Univ.

236 **Performance prediction of D-Strut isolation systems** [3045-31]
G. W. Wilson, P. J. Wolke, Honeywell Inc.

251 **Trade study on damping curved airfoil-shaped plates** [3045-32]
M. L. Drake, G. J. Frank, D. M. Hopkins, Univ. of Dayton Research Institute

259 **Passive damper exhibiting the ideal dashpot characteristic: F=CV** [3045-39]
S. Bennett, T. Davis, Honeywell Satellite Systems Operation; P. S. Wilke, CSA Engineering Inc.; E. R. Fosness, Air Force Phillips Lab.

268 **Passive damping in optical tables using highly distributed inertial dampers** [3045-41]
J. A. Zapfe, Kinetic Systems, Inc.

SESSION 8 ACTIVE CLD

282 **Passive and active constrained layer damping of ring-type structures** [3045-33]
J. A. Rongong, G. R. Tomlinson, Univ. of Sheffield (UK)

293 **Vibration control of cylindrical shells using active constrained layer damping** [3045-35]
M. Ray, T. Chen, A. M. Baz, Catholic Univ. of America

315 **Finite element for beams having segmented active constrained layers with frequency-dependent viscoelastic material properties** [3045-36]
G. A. Lesieutre, The Pennsylvania State Univ.; U. Lee, Inha Univ. (Korea)

329 **Modeling and experimental validation of a sandwich plate with isotropic face plates and viscoelestic core** [3045-37]
S. Veermani, N. M. Werely, Univ. of Maryland/College Park

341 *Addendum*
342 *Author Index*

Conference Committee

Conference Chair

L. Porter Davis, Honeywell Satellite Systems Operation

Cochair

Daniel J. Inman, Virginia Polytechnic Institute and State University

Program Committee

Andrew S. Bicos, McDonnell Douglas Aerospace
Kimberly Balkema J. Demoret, Air Force Wright Laboratory
Michael L. Drake, University of Dayton Research Institute
Eugene R. Fosness, Air Force Phillips Laboratory
Ephrahim Garcia, Vanderbilt University
Roy Ikegami, Boeing Defense & Space Group
Conor D. Johnson, CSA Engineering, Inc.
George A. Lesieutre, The Pennsylvania State University
Ronald N. Miles, SUNY/Binghamton
Daniel J. Segalman, Sandia National Laboratories
Geoffrey R. Tomlinson, University of Sheffield (UK)

Session Chairs

1 Particle and Hysteretic Damping
Michael L. Drake, University of Dayton Research Institute

2 Launch Vibration Isolation
Eugene R. Fosness, Air Force Phillips Laboratory

3 Embedded Piezo and Active CLD
Andrew S. Bicos, McDonnell Douglas Aerospace

4 Electrorheological Fluid (ERF) Damping
Roger Stanway, University of Sheffield (UK)

5 Passive Constrained Layer Damping (CLD)
Daniel J. Inman, Virginia Polytechnic Institute and State University

6 Characterization of Damping Materials
Conor D. Johnson, CSA Engineering, Inc.

7 System Applications of Passive Damping and Isolation
Roy Ikegami, Boeing Defense & Space Group

8 Active CLD
George A. Lesieutre, The Pennsylvania State University

SESSION 1

Particle and Hysteretic Damping

Hydrodynamic fluctuations and averaging problems in dense granular flows

C. Salueña[a,b], S. E. Esipov[a] and T. Pöschel[c]

[a]James Franck Institute and the Department of Physics,
University of Chicago, 5640 S. Ellis Ave., Chicago, IL 60637 USA

[b] Departament de Física Fonamental, Universitat de Barcelona,
Diagonal 647, Barcelona 08028 Spain

[c] Institut für Physik, Humboldt-Universität zu Berlin,
Invalidenstraße 110 Berlin D-10115, Germany

ABSTRACT

The properties of dense granular systems are analyzed from a hydrodynamical point of view, based on conservation laws for the particle number density and linear momentum. We discuss averaging problems associated with the nature of such systems and the peculiarities of the sources of noise. We perform a quantitative study by combining analytical methods and numerical results obtained by ensemble-averaging of data on creep during compaction and molecular dynamics simulations of convective flow. We show that numerical integration of the hydrodynamic equations gives the expected evolution for the time-dependent fields.

Keywords: Granular viscosity, Glasses, Hydrodynamic equations

1. INTRODUCTION

The interest in granular materials goes back to the early sixties, when industries needing to process powders required more and more control over the quality of their products. One may imagine a variety of shapes for mixers and many different ways to drive the grains inside into motion; a down-to-earth approach would consist of an answer for the question: in which of these mixers should I spend money? This can be done if one can compare their performances by means of realistic models that reproduce true flow patterns.

In order to answer aspects of this problem, and based on the gas-like appearance of the compounding particles, attempts were made to apply a hydrodynamical description to granular systems. It has been more than a decade since the pioneering contributions to the understanding of granular materials from a hydrodynamical point of view.[1,2] This understanding, however, is still far from being complete. We will address here several questions of theoretical and practical interest, namely fluctuations and averaging problems intrinsic to granular nature, modelling of dense granular flows by means of hydrodynamic equations and boundary conditions, comparisons with experimental data and results from molecular dynamics simulations, and fluctuations and mixing problems.

2. THE SOURCES OF FLUCTUATIONS

The behavior of a granular mass is fundamentally different from that of typical fluids. For instance, consider ordinary hydrodynamic fluctuations: the lack of an intermediate length scale –much larger than the typical diameter of the grains but much smaller than the size of the system, makes the thermodynamic limit unnatainable and therefore hydrodynamic fluctuations may subsist in the continuum limit. In addition, the fact that solid grains in a dense arrangement can't be regarded as points in any length scale leads to a second source of fluctuations; it operates at distances much larger than the typical diameter of the particles and is related to the appearance of extensive arrangements inside the system. Given a mean density not far away from the close-packing limit, there is a fraction

Further author information:
C.S (correspondence): Email: clara@hermes.ffn.ub.es; Telephone: 34-3-4021150; Fax: 34-3-4021149; S.E.E: Email: esipov@franck.uchicago.edu; T.P: Email:thorsten@sp10.physik.hu-berlin.de; Telephone:49-(0)30-2093-7896; Fax: 49-(0)30-2093-7638.

of the free volume which is still available and can be distributed in many ways. Some of these configurations will flow, some will not allow net motion, so different actual realizations in the configuration space of the particles may lead to departing dynamic properties and, ultimately, in generating completely different time-sequences. This contribution is what we call non-local noise. Both, local and non-local noise, are always present but their relative importance strongly depends on the forcing applied to the system, measured by the parameter $\mathcal{F}g = f/\rho g$, f being the volume density of the forcing and g the acceleration of gravity.

Therefore, one can distinguish two sources of fluctuations and two types of averaging, one over local noise and the other over different configurations or realizations.

We propose the existence of two regimes; in the weak-forcing limit, $\mathcal{F}g \lesssim 1$, the non-local component of the noise dominates, and consequently one expects very long relaxation rates and non-self-averaging quantities. In this limit, only ensemble averaging is meaningful, as in every possible realization the system explores a small region of the configurational space. The glass-like behavior is most apparent. In the opposite limit, $\mathcal{F}g \gg 1$, the system is not easily trapped in an immobile arrangement, and one can safely assume that in a sufficiently long time it explores the representative part of the configuration space. Time averaging can substitute ensemble averaging only in this limit. Consistently with this picture, the critical density, ρ_c, is not unique in general, but is a distributed quantity depending on the configurational state, Γ. Actually, we shall see that experimental data on compaction at weak forcing display quenched behavior, and the final density may vary over more than 10%. Instead, our numerical study of granular convection under strong forcing indicates a much narrower histogram of maximal achieved densities, ρ_c, despite the fact that the number of particles and the used number of samples for averaging were much smaller. Consider that for high forcing, the mean density evolves within a comparatively wide margin and the system very rarely, if ever, visits any of the corresponding trapping configurations. In the mean-field limit, one can consider ρ_c as an unique constant, which would correspond to the strict close-packing limit.

In spite of the complexity of this picture, we show that it is possible to understand both weak and strong forcing limits within the frame of hydrodynamic equations, which are in general stochastic equations including both local and non-local noise. It is beyond of the scope of this paper a detailed analysis of the properties of such equations, which is extensively done elsewhere. Our aim is to present some results of our study of the evolution of the mean hydrodynamic fields, comparing them with their observed behavior in a sample of cases.

3. HYDRODYNAMIC EQUATIONS

By hydrodynamic equations we mean balance equations for mean mesoscopic hydrodynamic fields. We will focus on the equations for the conservation of mass and linear momentum, leaving the energy balance for a later discussion. As said in the previous section, the lack of an intermediate length scale –contrary to what happens in simple fluids for instance, containing a sufficiently large number of particles such that local fluctuations fade away, adds on the above exposed problem of non-local fluctuations due to the intrinsic granular nature of the system, operating at length scales where hydrodynamic fields can already be defined. The former can be modelled as the usual additive stochastic contribution to the dissipative flows and comes related to the existence of some kind of "temperature", the latter enters via distributed kinetic coefficients (depending on the configurational state Γ). In the continuum approach, conservation of mass and linear momentum read, in the Stokes approximation,

$$\partial_t \rho + \nabla \cdot \rho \mathbf{v} = 0, \tag{1}$$

$$\rho \partial_t v_i = \frac{\partial \sigma_{ij}}{\partial x_j} + f_i, \tag{2}$$

where f_i are the components of the volume density of forcing. Note that these equations express very basic laws. However, they are valid in the usual form when the averages decouple, that is, when the average of the "microscopic" linear momentum equals the product of the averages of ρ and $\mathbf{v}$. However, due to the mesoscopic nature of the averaging procedure, this is not guaranteed. It will work if the local fluctuations are small enough. We shall discuss the fact that local fluctuations of the velocity field are very small in dense granular flows, except the very few moments when the granular mass undergoes dramatic changes, and close to the boundaries of the system.

As for the terms constituting the stress tensor σ_{ij} a few comments are in order. Provided that the granular particles may be modelled as sufficiently hard spheres, we neglect any elastic contribution other than that introduced

by pressure effects, and assume that the non-equilibrium part of σ_{ij} is a local functional of the derivatives of the local velocity,

$$\sigma_{ij} = -p\delta_{ij} + \eta(\rho,\Gamma)\Big(\frac{\partial v_i}{\partial x_j} + \frac{\partial v_j}{\partial x_i} - \frac{2}{3}\delta_{ij}\nabla\cdot\mathbf{v}\Big) + \zeta(\rho,\Gamma)\delta_{ij}\nabla\cdot\mathbf{v} + \xi_{ij}. \tag{3}$$

where p is the pressure and η and ζ the shear and volume viscosities, respectively.

3.1. The role of temperature and the pressure term

Our molecular dynamic simulations indicate that the evolution of the velocity field in dense granular flow is nearly independent from the granular temperature, defined as the mean fluctuational part of the velocity. Effectively, well inside the bulk, the quantity $\delta v/v$, measuring such fluctuational deviations from the mean velocity v, is typically about six orders of magnitude smaller than close to the boundary. This and other evidences allow us to suppose that granular flows in dense systems can't be sustained by a temperature-based mechanism alone –unlike Rayleigh-Bénard convection in simple fluids, for instance. Note that the equation for the energy balance has been omitted; consistently with the observation that the granular temperature plays no significant role, its evolution appears decoupled from the previous system of equations*. Similarly, one cannot account for elastic contributions in the high density limit only by using a thermal pressure. Therefore, one has to model such terms by means of an artificial equation of state which must help to resolve the delicate limit $\rho \to \rho_c$. We assumed the most simple dependence, $p = p_0/(1-\rho/\rho_c)$, where p_0 represents a certain constant, in our numerical integration of the hydrodynamic equations in the strong forcing regime.

3.2. The viscosity

.

Accordingly, the model that we adopt for the viscosity is not thermal, but glass-like. In dense clusters, in order to move, a complex rearrangement of particles has to occur making use of voids. Similar properties are exhibited by glasses. Available experimental data and our numerical results indicate the presence of a factor $\exp[c/(1-\rho/\rho_c))]$ in the mean flow rates, where c is a dimensionless number. This formula is related to the Vögel-Fultcher law for glasses[3]; it measures the number of attempts needed for one step in the direction of average flow in a dense granular system. Sufficiently close to ρ_c, we then expect a shear viscosity of the form

$$\eta(\rho,\Gamma) = \eta_0(\rho,\Gamma)\exp\Big(\frac{c}{1-\rho/\rho_c(\Gamma)}\Big). \tag{4}$$

and a similar dependence for the bulk viscosity, $\zeta(\rho,\Gamma)$.

4. TEST OF THE HYDRODYNAMIC EQUATIONS

We discuss some representative examples of each regime. For the weak forcing limit, available experimental data on compaction of sand during tapping experiments[4] provide the necessary reference. For the strong forcing limit we perform extensive ensemble averaging of samples generated by molecular dynamic (MD) simulations of vertical and horizontal shaking, comparing the resulting hydrodynamic fields with those generated integrating numerically the hydrodynamic equations. We shall also show analytical results on the cycle-averaged velocity profiles in vertical shaking that fit experimental profiles.[5]

*Actually, we observed that the rate of energy release, coming from inellastic collisions, was clearly correlated with the viscous heating (see next subsection for the model for the viscosity). These terms are therefore responsible for the evolution of the temperature field, since the energy loss is proportional to some power of the granular temperature, T. We checked the functional dependency, resulting in the expected $T^{3/2}$.

4.1. Weak forcing limit. Application to compaction experiments.

These results provide additional support for the existence of non-local noise, and evidence that the mean flows are of hydrodynamic nature even in very dense limits. Beginning with a loosely packed sand at volume fraction $\rho_0 = 0.57$ the authors report a logarithmic density growth,

$$\rho_c - \rho(t) = \frac{A}{1 + B\ln(1 + t/\tau)}, \tag{5}$$

where A, B, τ, ρ_c are four fitting parameters. It can be shown that it is possible to retrieve such a dependence by integration of hydrodynamic equations. Omitting further details about calculations and average over non-local noise, one finds after integration of the 1-dimensional version of (1,2) at late times

$$\bar{\rho}_c - \rho(t) = \frac{c}{\ln[(\int_0^t dtF)/c\bar{\eta}_0]}, \tag{6}$$

$\bar{\rho}_c$ and $\bar{c}$, already averaged over non-local noise, are constants which depend on, say, the amplitude of forcing, but do not change over time. The quantity F is related to the integral of the density of forcing and is left unspecified. Equation (6) can be compared with experimental fit, (see Fig. 1a) assuming $\int_0^t dtF = t\langle F\rangle$, where the average is taken over a period of repeated tapping. We find $A/B = \bar{c}$, $\tau = c\bar{\eta}_0/\langle F\rangle$. This is a three parameter fit. It demonstrates that hydrodynamics may be used for analyzing experimental data. Different fitting values of $\bar{\rho}_c$, $\bar{c}$ support the assumption that granular configurations with different ρ_c, c (different states Γ) do not communicate at weak forcing. Now we can be more specific in what we mean by "weak" forcing. Note that the fit is satisfactory at late times. At early times that situation is different: the higher is the value of $\mathcal{F}g$ the longer it takes before the fit is any good. If we plot the density when the deviation from the fit is a few percent versus the forcing parameter we get Fig. 1b. It suggests that the fits are good when the assumption of quenched values of ρ_c and c is fulfilled. Therefore, one may expect that the non-local noise is quenched above a certain line in the $(\rho, \mathcal{F}g)$ plane.

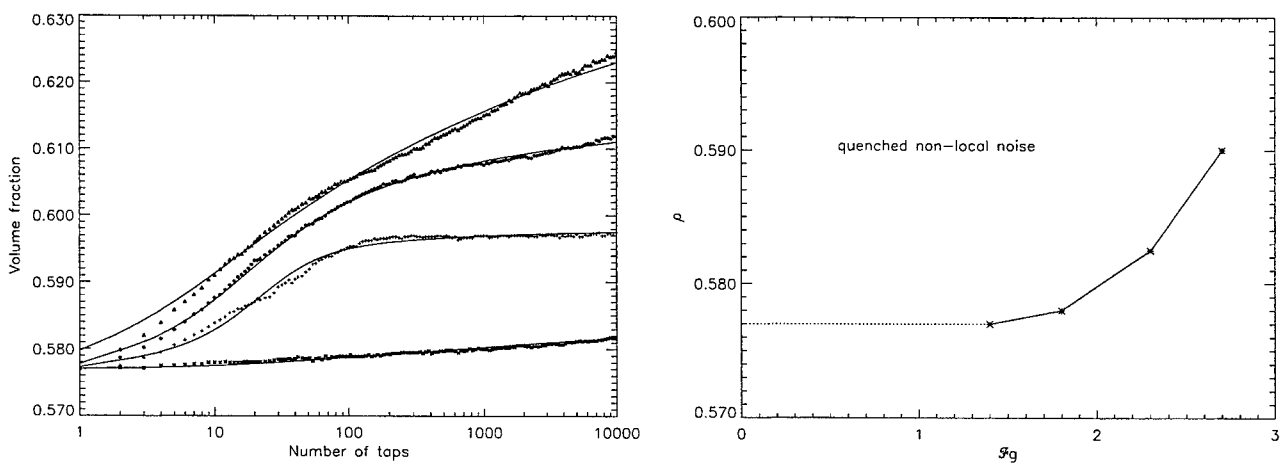

Figure 1. a) Fits of the experimental curves of the density dependence on the number of taps, from Ref. 4. $\mathcal{F}g = 1.4, 1.8, 2.3, 2.7$ from the bottom to top. The following parameter values were used to fit the curves in the same order: $\langle F\rangle/\eta_0 = (6.9 \cdot 10^{-8}, 4.1 \cdot 10^2, 3.1 \cdot 10^1, 1.1 \cdot 10^{-2})$, $c = (0.92, 0.029, 0.18, 1.35)$, $\rho_c = (0.5985, 0.599, 0.62, 0.67)$. b) Region of quenched non-local noise as a function of the density and the forcing parameter Fg.

4.2. Strong forcing limit. Results from MD simulations.

This case is object of a more complete study. Consider for example periodic vertical shaking of sand under gravity. It is well known that sand in such conditions develops typical convective rolls, with particles going upwards inside, and downwards along the vertical walls. The motion is evidenced, for example, by the bulging colored stripes resulting

from Magnetic Resonance Imaging experiments,[5] which represent cycle-averaged displacements. Again, it is possible to show that the system of equations (1,2) can be integrated to give a good fit of the experimental data. We will omit here the detailed derivation, which can be found in Ref. 6. Imposing the geometry of a tall container of width L in which the density slightly decreases with height, assuming Eq. (4) for the viscosity and the incompressibility condition (see step 4, below, for the reasons of such approximation), one finds

$$v_z(x,z) = v_0 e^{k^2 z l_z} \left[1 - kL \frac{\cosh(kx)}{\sinh(kL)} \right]. \tag{7}$$

which is solution of Eq. (2) for the cycle-averaged vertical velocity, in a two dimensional geometry. Here l_z represents the scale of variation of the viscosity in the linear approximation, k an arbitrary inverse length scale and v_0 a characteristic amplitude of the velocity, unspecified. See Ref. 5 for experimental evidence of Eq. (7).

A major understanding of the motion requires, however, a time-resolved analysis, and we show how this can be done via molecular dynamics simulations. We will not discuss details about the simulations here, it suffices to say that we used a polydisperse sample of 2000 soft spheres in a rectangular container, and the chosen values for the friction parameters reproduce correctly the experimental MRI images mentioned above. $\mathcal{F}g$ was about 2 in the study of vertical shaking, and 9 in the case of horizontal shaking. We choose the first for presentation, although the results can be extended to the horizontal shaking, leaving aside some peculiarities which are not worth to comment here. The following steps summarize the procedure we used, which is schematized in the chart of Fig. 2:

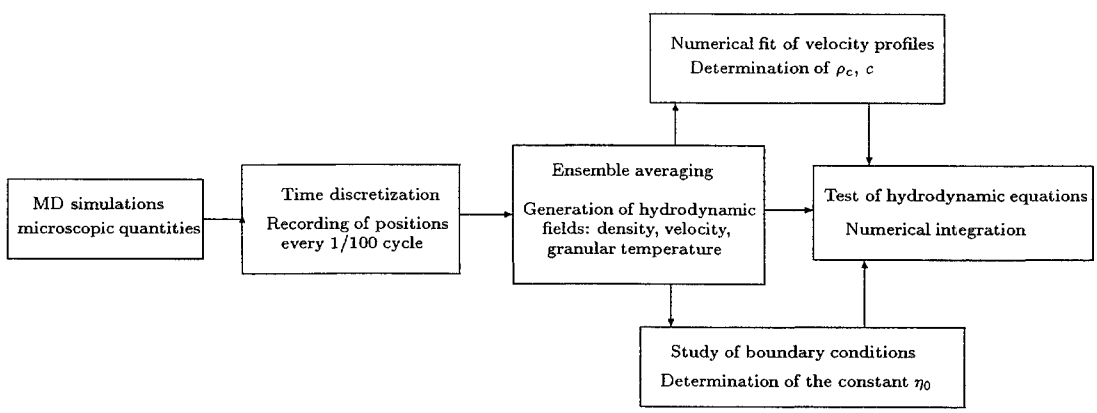

Figure 2. Scheme of the procedure followed for the test of the hydrodynamic equations.

1. Time discretization. Each period of shaking was divided in an equal number of frames, where positions of particles were recorded.

2. Spatial discretization and averaging. Using a high resolution grid, the container was divided in cells of the size of the order of one particle. Time averaging –which can replace ensemble averaging in this case, was performed with data of the corresponding frames of more of 100 periods of shaking.

3. Mean density, velocity and temperature (mean fluctuational velocity) were obtained and displayed. Visualization was done by means of IDL movies, showing smooth, well behaved fields. The sequences revealed unsuspected details about the motion that the granular mass experiences during a cycle, totally hidden when a cycle-average is performed (which leads to the typical convective rolls and has confused the sand community for long time). As an example, we reproduce in Fig. 3a the horizontal component of the velocity, v_x. Observe

that the motion is complex and unexpected, in the sense that one cannot infer from the sequence of pictures of v_x (neither from v_y, not shown) the direction of the global motion. The evolution of the granular temperature is shown in Fig. 4. Since the darkest regions represent the lowest values, it is obvious that its importance is restricted to the region close to the free surface, and in the bulk, to a limited number of frames.

4. Test of the hydrodynamic equations. By using the mean hydrodynamic fields obtained in 3., the system of equations (1,2) was checked. Selected frames provided fitting values for c and ρ_c (see Fig. 5a). η_0 was found to be about 300 cpoise by comparing histograms of the tangential force and the velocity gradient close to the walls (Fig. 5b), whereas the observation that the flow was mostly divergence-free allowed us to neglect the effects of ζ.

5. Study of boundary conditions. We obtained effective boundary conditions for the flow that reproduce to some extent the assumptions of microscopic friction during collisions, but we also found that the motion of sand along the vertical walls comes accompanied by dramatic periodic changes in the density and the stress (Fig. 6).

6. The previous results were used to integrate numerically the system of hydrodynamic equations. In Fig. 3b we show comparatively the sequence obtained for v_x. Observe that, apart from a qualitative agreement (including the order of magnitude of the velocity fields) there is room for improvement.

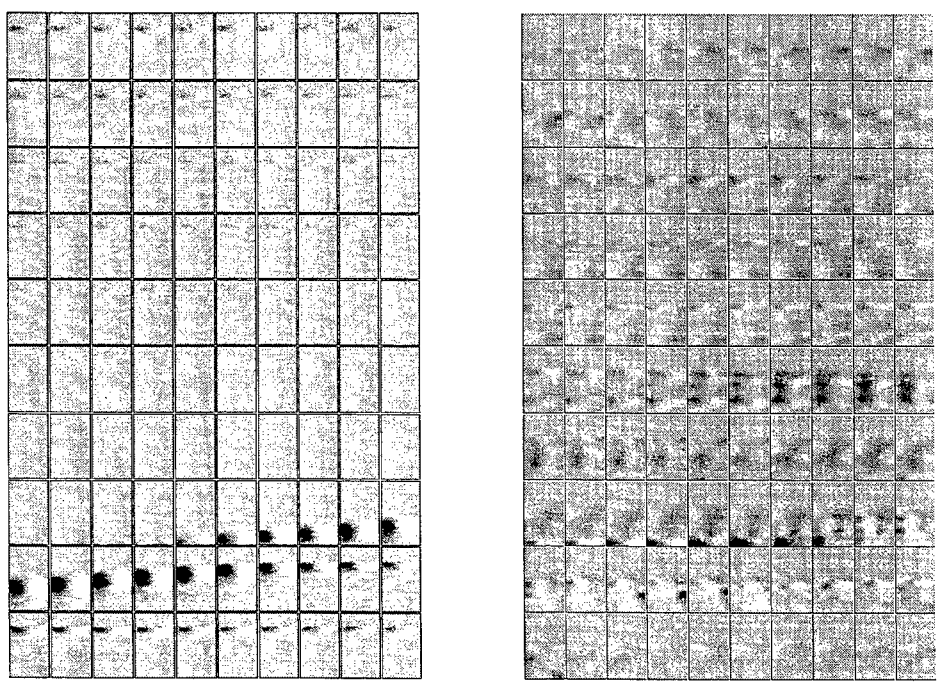

Figure 3. a) (left) Ensemble-averaged horizontal velocity, v_x of granular material in the course of vertical shaking. 10×10 frames taken during one cycle of oscillation are positioned from left to right and from top to the bottom. The frames of highest contrast indicate the collision of the granular system with the bottom wall, with compression of the material propagating upwards. b) (right) Evolution obtained by numerical integration of the mean-field hydrodynamical equations (1,2) with the boundary conditions obtained in step 5. In both pictures dark areas represent negative values and white ones positive values of the velocity.

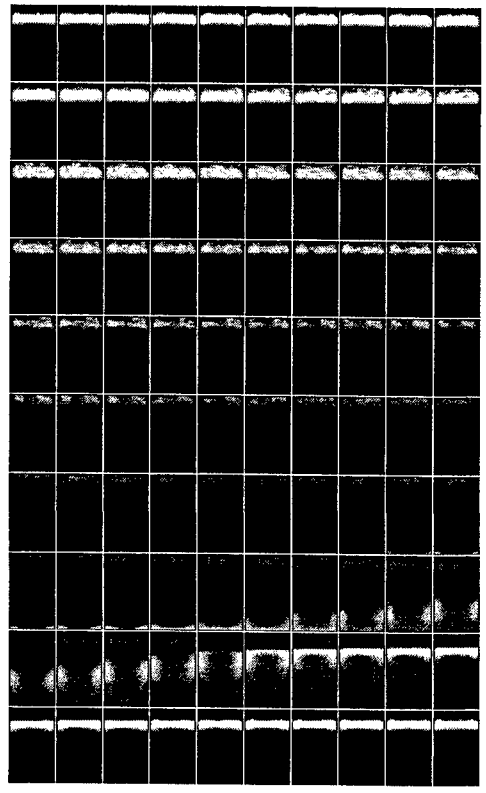

Figure 4. 10×10 sequence for the granular temperature (ensemble-averaged fluctuational velocity) in one cycle of horizontal shaking. The positioning of frames is the same as in Fig. 3. White areas indicate high temperature regions. By comparing with Fig. 3, observe that the granular mass moves in the opposite direction of the temperature gradient.

5. FLUCTUATIONS AND MIXING

Consider the motion of a test granular particle in any averaged velocity field generated by the procedure exposed above (different container shapes, various types of shaking). This is of practical interest in order to determine, for example, the effectiveness of a mixing device. In the absence of granular temperature, the motion of the test particle would follow the flux lines. Starting from a given position, $\mathbf{x}_n$, after one period a new location $\mathbf{x}_{n+1}$ will be reached, which is the result of the integration of elementary displacements (here equating the number of frames per cycle). Fig. 7 shows the results for vertical and horizontal shaking in the same way as the Magnetic Resonance Imaging.[5] In this case computer imaging simulates the horizontal and vertical motion of colored bands initially parallel, which become distorted in the course of one period. The cycle-averaged motion is then reducible to iterative maps, leading to mixing. Such mixing is incomplete since there may exist regions undergoing periodic motion, which are not mixed at all. It happens, for example, in the center of convection rolls accompanying horizontal shaking, potentially making the horizontal shaking of thick layers ineffective for mixing particles.

The second origin of mixing is due to noise, leading to diffussion which superimposes to the iterative map discussed above. The distance to diffuse in order to achieve complete mixing is determined by the largest region containing limiting cycles and/or fixed points. Non-local noise at a length scale l_n and time scale t_n leads to nested displacements correlated in space and time and helps to mix particles at distances exceeding l_n and times exceeding t_n. This subject has to be postponed until the properties of non-local noise are specified.

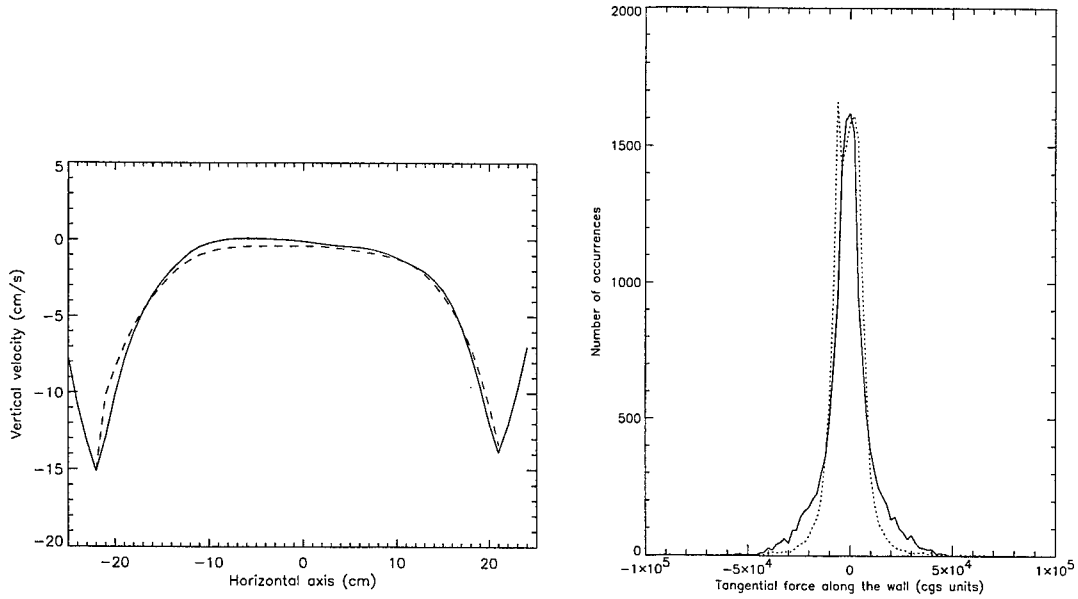

Figure 5. a) (left) Fit of the ensemble-averaged profiles of vertical velocity, $v_y(x)$, in frames 55-70 (numbered in the same way as in Fig. 3). In the fitting procedure the values for the constants c=0.15 and ρ_c= 1.01 max(ρ) were found. Dramatic changes at the boundaries are due to density discontinuities accompanying downward sliding of sand along the side walls. b) (right) Comparative histograms of the distribution of tangential force density acting at a wall (solid line) and the non-diagonal component of the hydrodynamic stress tensor, $\sigma_{\tau n} = \eta(\rho)(\partial v_\tau/\partial n)$, where n and τ stand for normal and tangential directions, respectively.

6. CONCLUSIONS

1. Hydrodynamic equations provide an adequate theoretical frame for the study of dense granular systems.
2. Non-local or configurational noise adds on the ordinary hydrodynamic noise, leading to non-selfaveraging properties in the limit of dense flows.
3. Temperature-based mechanisms can be practically dismissed in the description of dense granular flows.
4. Averaging of data from molecular dynamic simulations is an useful tool to reveal the details of the evolution of hydrodynamic fields.
5. Results of numerical integration of the system of hydrodynamic equations show a qualitative agreement with the evolution of hydrodynamic fields.
6. Study of fluctuations and cycle-averaged motion concern practical applications such as mixing.

ACKNOWLEDGEMENTS

We wish to thank A. Malagoli, A. Patashinski and S. Nagel for useful conversations, and H. Jaeger for providing the file with the experimental data published in Ref. 4. S.E.E. is grateful to T. Shinbrot for discussing practical aspects of granular mixing. C. S. acknowledges support by the Spanish Ministerio de Educacion y Cultura, grant number EX95-35065343. At the initial stage the work of S.E.E. and T.P. was supported by MRSEC Program of the NSF under the Grant Number DMR-9400379.

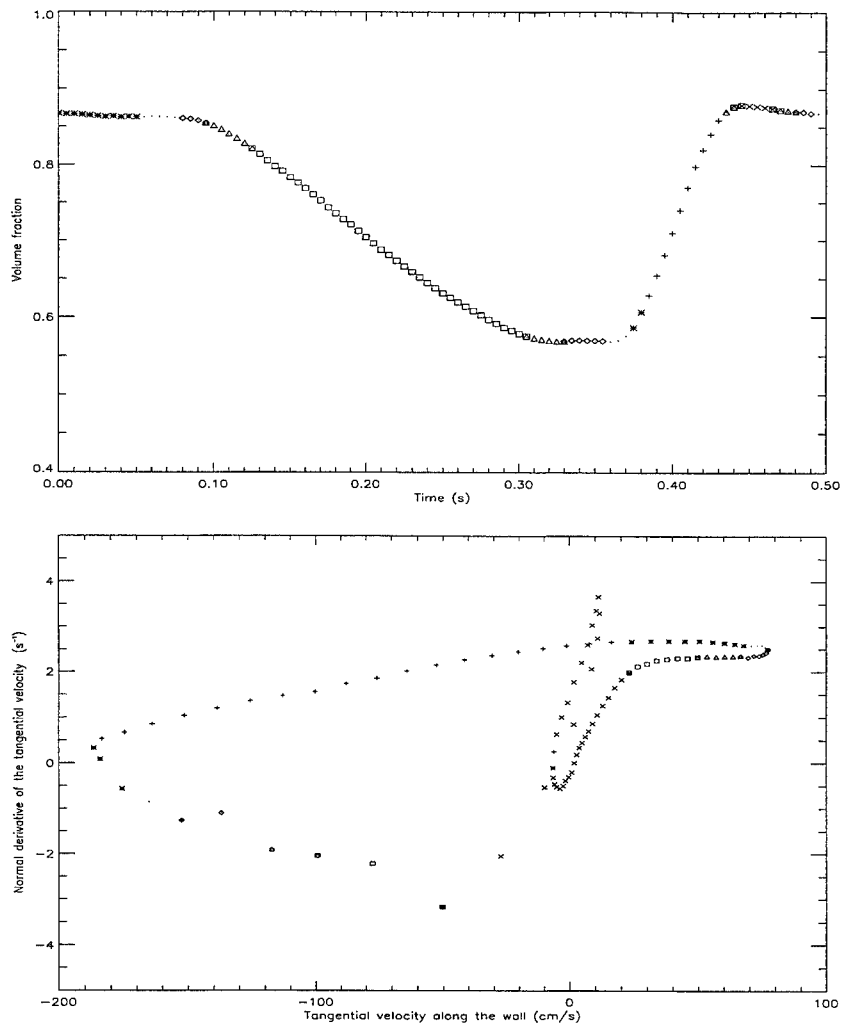

Figure 6. a) (above) Averaged dependence of granular density close to the vertical walls during one period of vertical shaking. The decrease in boundary density starts with the take-off of the granular material from the bottom of the container and reaches its maximum just before its landing (maximum acceleration downwards). Different symbols indicate the value of the off-diagonal component of the stress tensor, $\sigma_{\tau n}$. There are seven symbols used in linear proportion to the increasing value of $\sigma_{\tau n}$: (+, *, ·, ◇, △, □, ×). b) (below) The same data plotted in a different representation ($\partial v_\tau / \partial n$ vs v_τ). Plotting symbols now account for the value of granular density, in the same ascending order in the density range $0.55 \leq \rho \leq 0.9$.

REFERENCES

1. P. K. Haff, "Grain flow as a fluid mechanical problem," *J. Fluid Mech.* **134**, pp. 401–430, 1983.
2. P. K. Haff, "A physical picture of kinetic granular flows," *J. Rheology* **30**, pp. 931–948, 1986.
3. N. F. Mott and E. A. Davis, *Electronic Properties of Non-Crystalline Materials*, Oxford U. Press, New York, 1979.
4. J. B. Knight, C. G. Fandrich, C. N. Lau, H. M. Jaeger, and S. R. Nagel, "Density relaxation in a vibrated granular material," *Phys. Rev. E* **51**, pp. 3957–3963, 1995.
5. E. E. Ehrichs, H. M. Jaeger, G. S. Karczmar, V. Y. Kuperman, and S. R. Nagel, "Granular convection observed by magnetic resonance imaging," *Science* **267**, pp. 1632–1634, 1995.

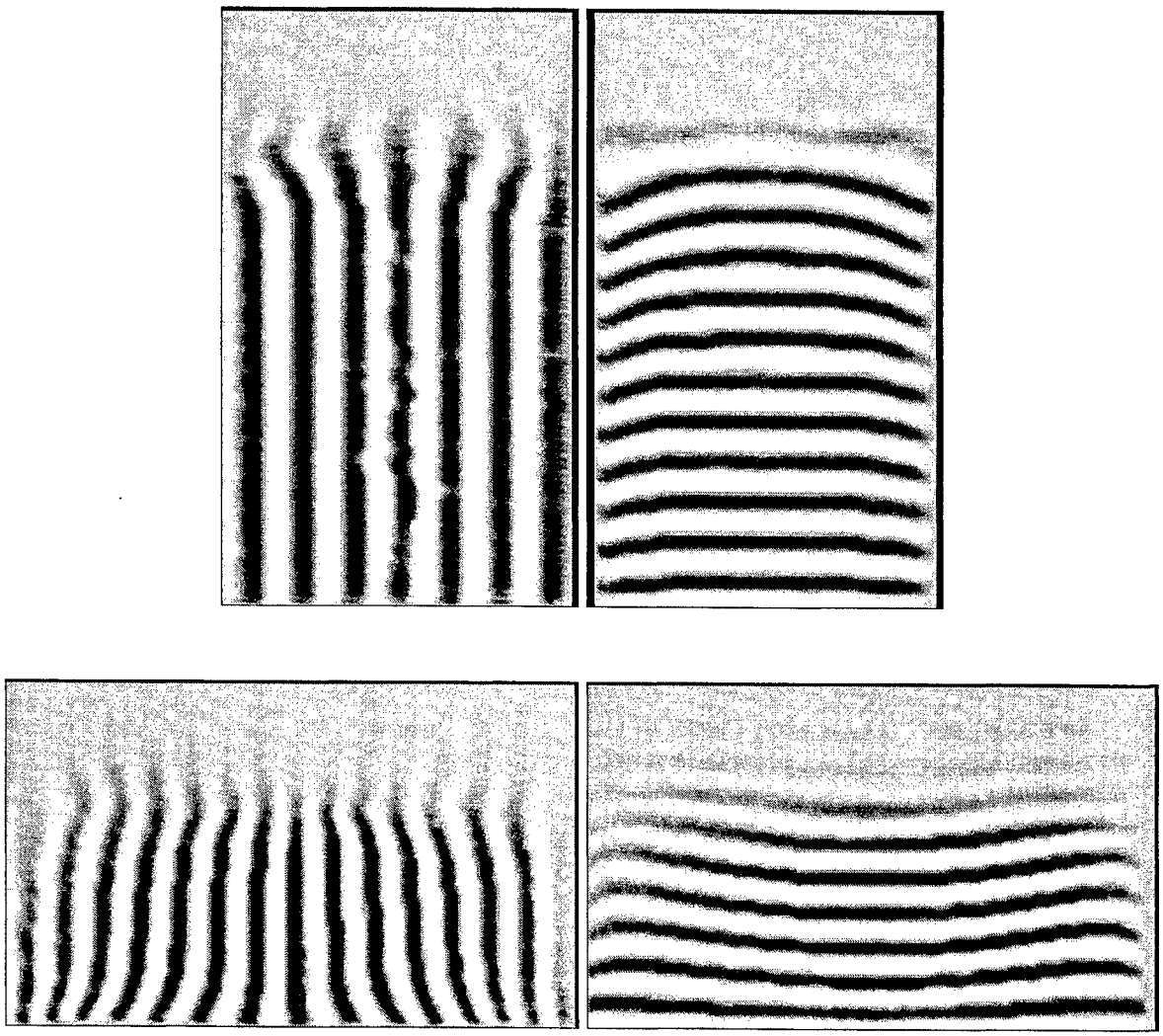

Figure 7. (above) Computer images simulating the motion of vertical (left) and horizontal (right) layers of granular material in the course of vertical shaking; (below) the same for horizontal shaking.

6. S. E. Esipov, C. Saluena and T. Poschel, "Granular glasses and fluctuational hydrodynamics." Preprint.

SESSION 2

Launch Vibration Isolation

Need for and benefits of launch vibration isolation

Andrew S. Bicos[a], Conor Johnson[b], L. Porter Davis[c]

[a]McDonnell Douglas Aerospace, 5301 Bolsa Ave, Huntington Beach, CA 92647
[b]CSA Engineering, Inc., 2850 West Bayshore Road, Palo Alto, CA 94303-3843
[c]Honeywell Satellite Systems, 19019 N. 59th Ave, Glendale AZ 85308

ABSTRACT

Spacecraft designs are driven by the necessity of the spacecraft to survive being launched into orbit. This launch environment consists of structure-borne vibrations transmitted to the payload through the payload attach fitting (PAF) and acoustic excitation. Here we present a discussion on the need for and benefit of isolating the structure-borne vibrations. If the PAF were replaced with an isolator with the correct characteristics the potential benefits would be significant. These benefits include reduced spacecraft structural weight and cost, as well as increased life and reliability. This paper will present an overview of the problem of vibration on a launch vehicle payload and the benefits that an isolating PAF would provide. The structure-borne vibrations experienced by a spacecraft during launch are made up of transient, shock, and periodic oscillations originating in the engines, pyrotechnic separation systems, and from aerodynamic loading. Any isolation system used by the launch vehicle must satisfy critical launch vehicle constraints on weight, cost, and rattle space. A discussion of these points is presented from the perspective of both a launch vehicle manufacturer and a spacecraft manufacturer/user.

Keywords: isolation, launch vehicle, spacecraft, vibration, attenuation, damping, active control

1. INTRODUCTION

Current spacecraft designs are driven in part by the necessity of the spacecraft to survive the launch environment. This environment consists of structure-borne vibrations transmitted to the payload through the payload attach fitting (PAF) and acoustic excitation. Here we concentrate on isolating the structure-borne vibrations through the PAF. If the PAF were replaced with an isolator the potential benefits would be significant. These include reduced spacecraft weight and cost, as well as increased life and reliability. The structure-borne vibrations experienced by a spacecraft during launch are made up of transient, shock, and periodic oscillations originating in the engines and pyrotechnic separation systems and also due to aerodynamic loading. While these vibrations are broadband, the need is to provide isolation above 10kHz for shock loading and below 1000 Hz and usually most critical below 100 Hz for the other loading conditions. Any isolation system used by the launch vehicle must satisfy critical launch vehicle constraints on weight, cost, and payload rattle space. The cost benefits of an isolation system are due to the reduced environments requiring less qualification testing and at lower levels, as well as fewer analysis cycles being required. The weight benefits include reduced structural mass of secondary (and to a lesser extent primary) structures. Even though this may be a relatively small percentage of total spacecraft mass, even a few pounds of mass savings can be turned into increased attitude control fuel, which is usually the item that sets the life of a large number of communication satellites. The benefits of reduced vibration loads will also increase the reliability of spacecraft components and/or allow more use of commercial off-the-shelf (COTS) components, which are significantly less expensive.

The following discussion does not focus on any one launch vehicle but on launch vehicles in general, with loading environments usually given as a range that envelopes the typical launch vehicles used today. The spacecraft flown on these launch vehicles have several different mission classes. These include scientific missions where only one or a small number of spacecraft are built, geosynchronous communications missions where a standard, relatively large, spacecraft is used, and low-earth-orbit (LEO) and medium-earth-orbit (MEO) communication constellations that can encompass ten to hundreds of relatively small spacecraft launched either singlely or several grouped together for launch. The benefits of isolation will depend in part on the spacecraft mission and this will be addressed.

We will first discuss the problems that the launch environment creates for a spacecraft and where the needs for reduced vibration exist. This will be followed by some examples of currently used solutions for overcoming these problems. Finally,

SPIE Vol. 3045 • 0277-786X/97/$10.00

we will discuss what the potential benefits of whole-spacecraft vibration isolation are for the different categories of spacecraft flown today or planned to fly in the near future.

2. PROBLEM and NEED

The launch environment, which typically only lasts a few minutes, is the most severe dynamic environment the spacecraft will experience during its normal mission life. This environment is composed of acoustic excitation due to very high sound pressure levels coming through the launch vehicle payload shroud and structural excitation due to vibrations and shock transmitted through the payload attach fitting (Figure 1). It has been shown[1,2] that nearly half of the spacecraft failures that occur soon after launch are attributable to vibration and acoustic loading during launch.

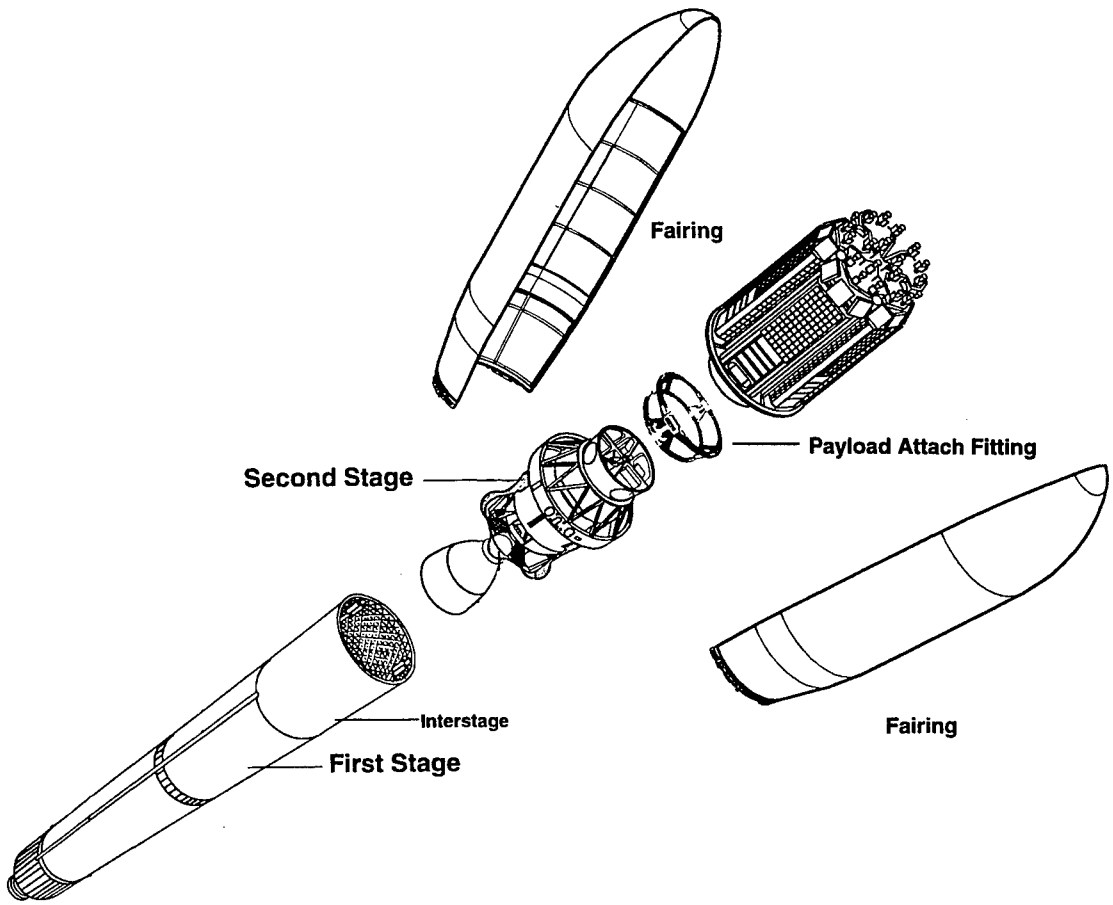

Figure 1. Typical launch vehicle and satellite with payload attach fitting (PAF).

These loadings drive the design of the spacecraft. The loading on the spacecraft during launch is due to various combinations of the following dynamic load cases: acoustics and random vibrations, sinusoidal vibrations from motor oscillations, shock from separation systems, liftoff loads, buffet and gust loads during transonic and maximum dynamic pressure regimes, and pre-engine-shutdown and engine-shutdown loads. A typical launch vehicle acceleration time history is shown in Figure 2. As can be inferred by this figure, there are relatively high dynamic loads right at lift-off and during transonic flight, also high shock loads occur at solid rocket motor and payload fairing separation. Other large transient loads are induced during stage engine shutdowns.

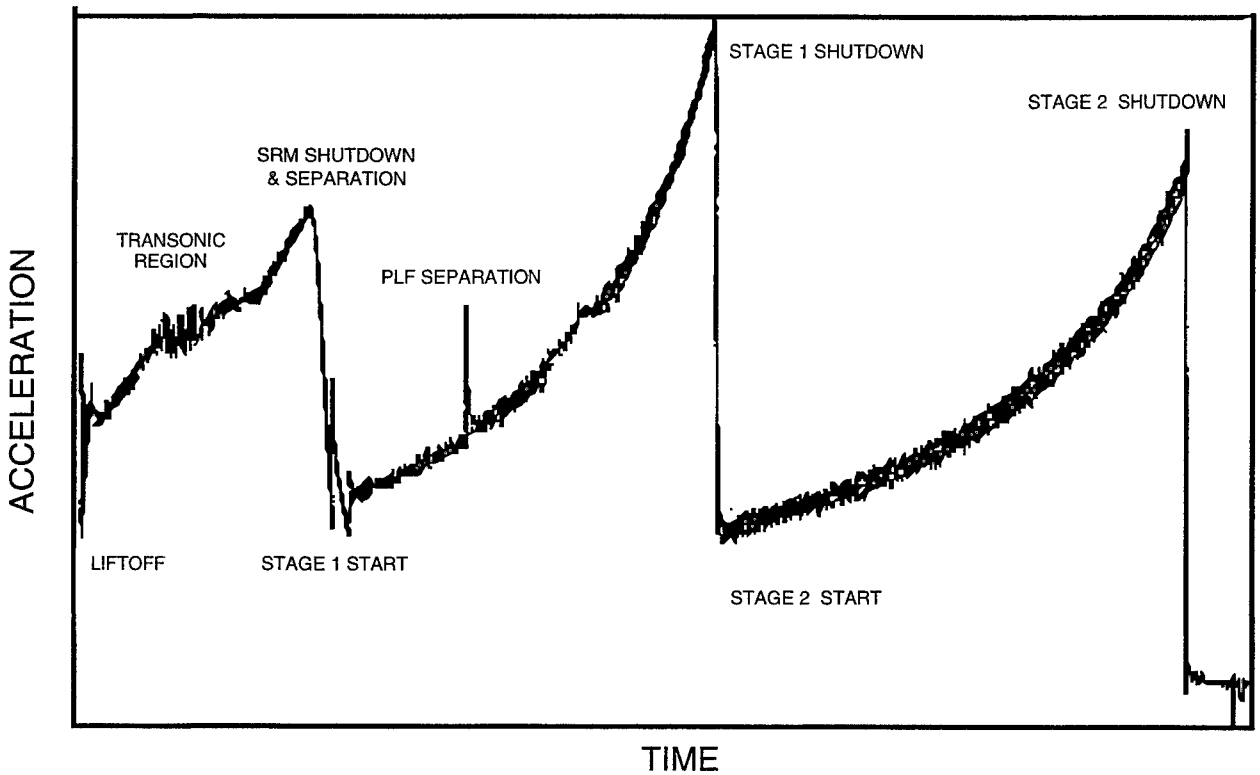

Figure 2. Typical launch vehicle axial acceleration flight profile.

The spacecraft primary structure is designed to meet the minimum frequency requirements imposed by the launch vehicle dynamics. These frequency requirements are specific to the launch vehicle and for typical ELVs these are 10 to 15 Hz in the lateral direction and 25 to 35 Hz in the axial direction. These requirements translate into structural stiffness requirements for the spacecraft, which tends to make the spacecraft primary structure, depending on the mission, be about 20% of the total spacecraft mass. This is significant for structural mass, which, to a great extent, once the spacecraft is in orbit is no longer really useful. The cost of putting each pound into orbit is about $10,000, therefore, each unnecessary pound put into orbit uses resources better spent elsewhere.

The spacecraft secondary structure is designed to meet a higher minimum frequency requirement of approximately 50 Hz or higher. However, once built some secondary structural elements have frequencies well below this design value. This is sometimes as low as the 30 Hz to 40 Hz range. These elements can then be excited by the launch vehicle loads in that frequency range to acceleration levels exceeding that to which they were designed for. This then usually requires some effort to mitigate this condition, which adds additional cost and weight to the spacecraft, and may even cause schedule slips depending on how far along the program is when the problem is discovered.

In these times of reduced spacecraft budgets, existing components and instruments, such as from previous spacecraft in the form of "flight spares," and other "off-the-shelf" elements, are being used to meet limited mission budgets. However, if the components have been qualified to fly on a mission using a launch vehicle that is different from that of the new mission then an expensive and time consuming process to determine if the old component must be requalified and if so, how and to what levels. Also, in applying the "faster, better, cheaper" paradigm, some testing and analysis that in the past had been done before the launch of a spacecraft is now not done. This allows, in theory, a faster and thus cheaper program. This gives some spacecraft designers and manufacturers concerns usually resulting in a more conservative design, i.e., higher margins being designed into the spacecraft, which can translate into more weight and potentially more cost. These higher design margins can also use up the traditional weight reserve used by the program manager to accommodate weight growth as the design matures and hardware is built. If significant weight growth occurs such that a larger launch vehicle may be required (a very

expensive proposition) then the mission can be jeopardized by this or by having to reduce total weight by removing important instruments or components.

Program delays and overruns can result from components failing during qualification testing and having to be redesigned, rebuilt, and retested. One of the reasons that this happens is that to qualify components to survive the launch environment, the components are tested to even more severe levels than expected in flight. This conservative approach to ensuring component reliability, while very successful in the past, may become an expensive luxury for some future missions.

3. SOLUTIONS IN CURRENT PRACTICE

On existing launch vehicles there is currently no general provision made for isolating vibration from the launch vehicle coming through the PAF to the spacecraft. Because the spacecraft is designed to survive the launch environment with plenty of margin there is usually no need for isolation. This is the primary solution for overcoming most vibration problems. However, if during preflight coupled loads analysis (CLA) a dynamic excursion is encountered a refinement of the CLA is usually done to make sure the potential problem is real. If this confirms the earlier concern, then some mitigating measures are developed. Usually in the early part of the program a design fix is possible but this becomes more expensive and less likely as the program moves into the hardware phase. It will also add cost and usually more weight to the spacecraft design. If a problem is discovered during hardware testing then there are fewer options available. Usually, it is a component of the spacecraft, such as an instrument or appendage (solar array or antenna) that is discovered to be experiencing loads above those that it was designed for. A stiffening of the structure that supports the component or isolation of the component is considered. In some cases when it will be too difficult to do this or too expensive there is an option to use whole-spacecraft isolation. This is usually done when it is determined that it is more expensive to modify and requalify the spacecraft than to modify and requalify the PAF. In the past, whole-spacecraft isolation has been done by modifying the PAF to provide the required destiffening and/or damping and each design is tailored to the specific spacecraft/launch vehicle configuration. For example, this has been done in the past for a solid rocket motor burn resonance that was adversely exciting some spacecraft components. In this case all that was required was a destiffening of the PAF to provide the proper isolation. However, there is currently no standard isolating PAF for providing whole-spacecraft isolation.

4. POTENTIAL BENEFITS OF A WHOLE-SPACECRAFT ISOLATOR SOLUTION

Whole-spacecraft isolation has many benefits depending on how it is implemented. For the purposes of this discussion, we consider an isolation system that will replace the relatively "rigid" PAF that attaches the spacecraft to the launch vehicle. An isolation system can be either passive or active or a combination of both. It can isolate in either the lateral or axial directions, or both. Its break frequencies can occur below the structural system's modes or within them. Depending on this is the degree and sort of complexity of the system. If the break frequency is below the structural modes will be a very soft system with large strokes required. This then results in potential violation of rattle space constraints and a possible interaction with the launch vehicle controller. If, on the other hand, the break frequency occurs among the structural modes then keeping modal interaction to a minimum is required. This may require the addition of more damping and/or adjustability or tuning of the isolator characteristics. Each case has its associated technical challenges. These are covered in other papers[3,4]. The focus here is, assuming these technical issues can be successfully overcome, what are the benefits that can address the needs discussed above. In this section, we discuss the benefits from several, increasingly more capable, isolation systems. We will consider passive lateral isolation, passive lateral and axial isolation, and passive/active lateral/axial isolation. The first two systems are passive and as such are best suited for systems that have break frequencies above 10 Hz to 15 Hz. This keeps strokes and rattle space requirements at reasonable levels (on the order of an inch or less for both) and makes for a relatively simple and low-cost system[3]. The third system, being active and passive, can have lower break frequencies (below 10 Hz) and still maintain reasonable levels of stroke and rattle space, but is more complex[4]. The following discusses some of the potential benefits for each case by giving examples based on past history.

Passive lateral isolation. In some spacecraft the most severe environment occurs from the dynamics during launch that is due to lateral loads in the 25 Hz to 40 Hz range. The components of the spacecraft and its secondary structures are the items most affected in this frequency range. Passive isolation in the lateral direction can provide significant relief for these elements. These components can be subsystem electronics boxes (though usually these are more susceptible to higher frequency acoustic loads) and sensitive instruments such as cameras and telescopes. Secondary structures include solar array panels and supports, antennae and their supports, and other similar structures that do not make up the primary bus structure. Primary structure can also have some benefit from the reduced loads.

Reductions on the order of 25% to 50% in dynamic loading to these types of spacecraft elements resulting from lower loads imparted by the launch vehicle would provide the following benefits.

- **Reduced cost in use of "flight spares."** Spacecraft designed to use instruments that are "flight spares" from other spacecraft, which may have been qualified for launch on another launch vehicle and may have had a softer ride, can be used without an extensive and expensive re-evaluation and possible requalification. The process to evaluate if a "flight spare" should be requalified and how can take from one to three man-months of effort per instrument. For five to 10 instruments this is on the order of one man-year of effort that could be saved if an isolator was used to reduce the loads. Spacecraft that would benefit from this are typically scientific spacecraft that will only have one or two units built.

- **Piece part reduction and quality control cost reduction.** Designing spacecraft to higher loads results in secondary structures, such as supports and brackets, being more complicated, with more pieces and more weight than would be required for lower loads. It has been estimated that the number of parts could be reduced by 25% if the loads could be reduced by using whole-spacecraft isolation. This 25% reduction in the number of parts would lead to a concomitant reduction in costs associated with designing, tracking, and assuring part quality for each simplified structure.

- **Increased margins and reliability.** Spacecraft that have already been designed and built can still benefit. Even if no changes in the spacecraft occurs because an isolator is used, the benefit from the reduced loads is realized through an effective increase in design margins and reliability. The reason for this is that a spacecraft is designed and built with certain margins based on the anticipated loads that it will experience during its lifetime. If after it is built the loads are reduced, the spacecraft now has effectively more design margin. The reliability of components is based, in part, on the vibration environment experienced. Again, if this vibration is reduced, the reliability and lifetime of the components can be increased. This effectively increases the life of a spacecraft, which for a large number of missions then decreases overall mission costs because the fixed mission costs are spread out over a longer operational lifetime.

- **Primary structure weight reduction.** Even primary structure can benefit. Because some spacecraft bus structures are of a standard design (usually used for communication satellites), they must be built to survive all launch vehicles that could launch a spacecraft based on that bus. This causes the design loads to be an envelope of worst cases for all launch vehicles. There have been cases where a spacecraft bus structure was designed for only one launch vehicle instead of the standard design to be flown on several launch vehicles. In one case, the primary advantage of this was a reduction in the lateral launch load from 2.0g to 1.5g below 50 Hz (a 25% decrease). This resulted in an approximately 10% mass reduction in the bus primary load path structure. If an isolating PAF were used to give the same load reduction of 25% the mass savings would be the same but could now be applied to the standard bus as well, giving an overall mass reduction.

Passive axial/lateral isolation. In addition to lateral loads, there are cases where the axial loading is a problem above 25 Hz to 30 Hz. The spacecraft elements affected are the same as for the lateral passive case discussed above but because of their composition or orientation on a specific spacecraft they may be more susceptible to axial loading. Passive isolation of these can provide significant relief. Overall reductions on the order of 25% to 50% in dynamic loading in all axes gives benefits as discussed above but with reductions in all directions, the benefits will be more likely to be realized in individual cases. As an example to illustrate this point, a coupled loads analysis on a spacecraft gave a response higher than the design load for an antenna support module in the 25 Hz to 30 Hz frequency range. This resulted in a redesign of the antenna support structure (a secondary structure) to handle the higher loads. This redesign resulted in approximately a 5% increase in the mass of this structure and increased the cost on the order of $100,000. An isolating PAF, providing whole-spacecraft isolation, would have eliminated the need for a redesign and the associated cost and weight impact.

Active/passive isolation. In some spacecraft the low frequency lift-off environment causes problems, typically below 20 Hz. This typically is a primary structure design driver. If the loading could be reduced 50% or more then it is possible that the primary structure could be reduced by up to 10%. This seems like a small amount but is really quite significant. Consider a communication satellite weighing 7000 lbs with primary structure being about 20% of this or 1400 lbs. A 10% reduction would save 140 lbs. This type of comsat uses about 70 lbs/yr of attitude control fuel for stationkeeping. It is the amount of stationkeeping fuel that determines the satellite's useful life, thus, any increase in the amount of stationkeeping fuel would increase the revenue-producing life of the satellite. Therefore, 140 lbs of weight savings can be translated into approximately

two years of added stationkeeping fuel. When you consider that each comsat can carry between 24 and 48 transponders and each transponder generates between $1M and $2M per year in revenue, this means between $48M and $192M in added revenue from the two years of additional operation of this satellite.

This discussion is by no means meant to be all inclusive, but rather to give some insight into the different, yet significant, benefits to spacecraft that can result from the use of whole-spacecraft isolation.

5. CONCLUSION

It has been shown that, based on past experience, a reduction in launch loads can result in significant cost and weight savings for space missions. A way to reduce the loads is to provide an isolation system for the whole spacecraft by inserting the appropriate isolation system between the spacecraft and the launch vehicle, i.e., replacing the PAF with an isolator.

6. REFERENCES

1. A. R. Timmins and R. E. Heuser, "A Study of First Day Spacecraft Malfunctions," NASA TN-D-6474, September 1971.

2. A. R. Timmins, "A Study of First Month Space Malfunctions," NASA TN-D-7750, October 1974.

3. P. S. Wilke, C. D. Johnson, and E. R. Fosness, "Payload isolation system for launch vehicles," to be published in Proceedings of SPIE Smart Structures and Materials - Passive Damping and Isolation, 1997.

4. E. L. Edberg, P. S. Wilke, and T. Davis, "Development of a launch vibration isolation system," to be published in Proceedings of SPIE Smart Structures and Materials - Passive Damping and Isolation, 1997.

Payload isolation system for launch vehicles

Paul S. Wilke, Conor D. Johnson
CSA Engineering, Inc.
2850 West Bayshore Road, Palo Alto, CA 94303-3843 USA
Eugene R. Fosness
Air Force Phillips Laboratory, PL/VTVD
3550 Aberdeen Ave, SE, Kirtland AFB, NM 87117-5776 USA

ABSTRACT

A spacecraft is subjected to very large dynamic forces from its launch vehicle during its ascent into orbit. These large forces place stringent design requirements on the spacecraft and its components to assure that the trip to orbit will be survived. The severe launch environment accounts for much of the expense of designing, qualifying, and testing satellite components. Reduction of launch loads would allow more sensitive equipment to be included in missions, reduce risk of equipment or component failure, and possibly allow the mass of the spacecraft bus to be reduced. These benefits apply to military as well as commercial satellites. This paper reports the design and testing of a prototype whole-spacecraft isolation system which will replace current payload attach fittings, is passive-only in nature, and provides lateral isolation to a spacecraft which is mounted on it. This isolation system is being designed for a medium launch vehicle and a 6500 lb spacecraft, but the isolation technology is applicable to practically all launch vehicles and spacecraft, small and large. The feasibility of such a system on a small launch vehicle has been demonstrated with a system-level analysis which shows great improvements. The isolator significantly reduces the launch loads seen by the spacecraft. Follow-on contracts will produce isolating payload attach fittings for commercial and government launches.

Keywords: launch vehicle, vibration, isolation, attenuation, spacecraft, spacecraft isolation, payload isolation, launch loads

1. Introduction

One of the most severe environments that a spacecraft will be subjected to during its lifetime will occur during launch. This paper summarizes the results and status of a research effort in the area of spacecraft isolation from the launch vibration environment. The object of this effort was to reduce the launch-induced structure-borne dynamic acceleration of the spacecraft by insertion of a vibration isolation device. The term launch loads refers to all loads from liftoff through final engine shutdown at orbit insertion. Isolation issues involving the use of passive elements and launch vehicle system-level requirements will be discussed.

Phillips Laboratory (PL) Space Vehicle Technologies Division of the Space Technology Directorate has been monitoring the development of whole-spacecraft isolation. The result of this effort has been an isolation design methodology developed from a system-level point of view. This methodology, along with models and simulations will be used to develop new spacecraft payload attach fitting (PAF) designs which incorporate vibration isolation capability. PL is developing the technology for whole-spacecraft isolation in two phases. The first phase, discussed in this paper, is the development of passive isolation designs.[1,2] The second phase will add active control elements to develop a hybrid passive/active vibration isolation system.[3] These whole-spacecraft isolation technologies could be used to great advantage in many future launches of both government and commercial spacecraft such as the proposed constellation of satellites necessary to form global telecommunication networks.

Other author information:
P.S.W.: Email: wilke@csaengr.com; Telephone: 415-494-7351; http://www.csaengineering.com
C.D.J.: Email: cjohnson@csaengr.com; Telephone: 415-494-7351; http://www.csaengineering.com
G.R.F.: Email: fosnesse@smtpgw1.plk.af.mil; Telephone: (505) 846-7883

SPIE Vol. 3045 • 0277-786X/97/$10.00

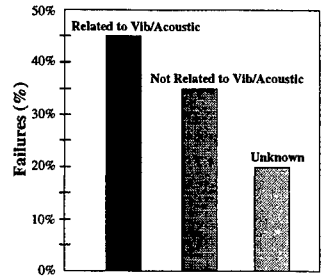

Figure 1. Causes of space flight malfunctions

2. The Need For Isolation

The deployment of a spacecraft into its final orbit configuration is a highly-complex operation. During the ascent of the launch vehicle, the spacecraft is subjected to many different quasi-static and dynamic loads which vary throughout the launch. These loads change due to environmental effects such as wind gusts and buffeting, discrete events such as motor ignitions and cutoffs, and also due to changing structural dynamics caused by fuel depletion and stage jettisons. These transient loads can have a detrimental impact on the launch survival and life cycle performance of the spacecraft. Undeniably, the load environment that spacecraft endures during launch far exceeds that encountered during on-orbit operations.

Launch dynamics are a major design driver in the structural design of a spacecraft. The vibrations that occur in a spacecraft during launch are both structure-borne and acoustic in nature. It is well established that a significant number of spacecraft malfunctions occur during launch, and that they are often due to vibro-acoustic loads. A NASA study,[4] shown in Figure 1, estimates that 45 percent of all first-day spacecraft failures and malfunctions are known to be attributed to damage caused by vibrations. While the study is over twenty years old, the problem has changed little.

Payload attach fittings are used to provide an interface between the launch vehicle (LV) and spacecraft. Typical PAFs are designed to be very stiff and subsequently they provide an efficient transmission path for both dynamic and quasi-static launch loads. The traditional approach to spacecraft design against launch vibration has been through structural stiffening or component isolation. However, this approach is costly, time consuming, adds weight, and can lead to other liabilities once the spacecraft is in orbit. Current PAFs do not provide isolation from launch loads except on a case-by-case basis. Implementing an isolation system into the PAF is the logical place for a payload isolator. However, whole-spacecraft isolation is a substantial change in the dynamic properties of the combined system and is bound to have side effects which must be addressed. Critical to the acceptance for flight is that an isolation system must not introduce intractable new problems into either the product or process. First flight of any whole-spacecraft isolator will occur only when both the LV and spacecraft contractors are satisfied that, at worst, a failure of the isolator will impose vibration on the spacecraft no worse than that which would occur with a standard PAF.

Reduced vibration environments for future spacecraft can have a direct impact on the overall cost of spacecraft design, testing, and operation. Several subsystems, such as solar arrays and other flexible structures, can be made lighter and use less expensive materials, resulting in both a mass and production cost savings. This also allows a larger percentage of the payload weight to be dedicated to scientific equipment. A whole-spacecraft isolation system is envisioned to replace the traditional PAFs used to physically attach a spacecraft to a LV as shown in Figure 2. The implementation of this technology will directly effect the following: 1) greater survivability at launch; 2) a reduction of loads seen by the spacecraft; 3) a minimization of dynamic-related spacecraft failures; 4) a reduction of cost, size, and weight of some spacecraft; 5) a lowering of certain test requirements; 6) the allowance for tuning of the isolator instead of spacecraft requalification; and 7) a reduction of the number of analysis load cycles.

In the course of a spacecraft development program, updated coupled-loads analyses often result in increased launch loads which necessitate unforeseen spacecraft design changes. Consequently, the spacecraft design organization is faced with unplanned hardware redesigns, schedule slips, and cost over-runs. Reduction of dynamic launch loads seen by the spacecraft will minimize spacecraft redesign, reduce risk, reduce spacecraft development time, reduce costs, eliminate many vibration-related failures, and increase reliability.

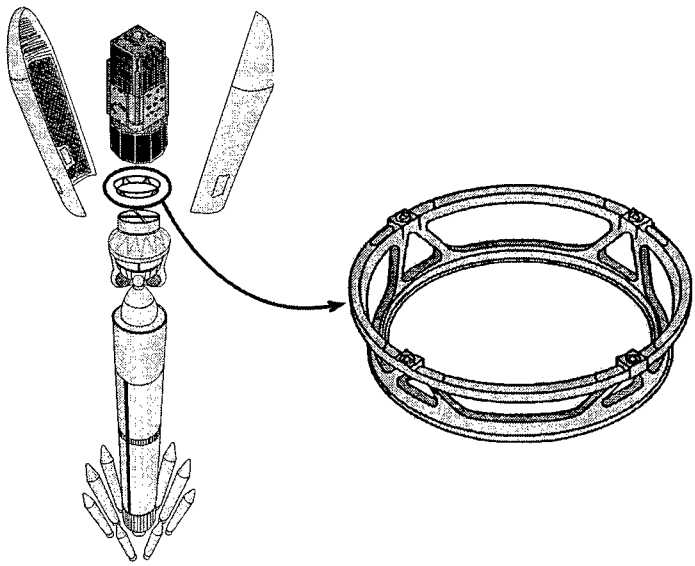

Figure 2. Medium launch vehicle and payload attach fitting

3. Isolation Design Methodology

Vibration isolation is a technique used to reduce vibration of a structure by altering the frequency content of the forces that act on that structure. Isolation of a whole spacecraft from a launch vehicle requires a unique design methodology. Figure 3 shows two connected structures being acted upon by external forces. Classic isolation design assumes that structure 2 is rigid with respect to structure 1 and only the dynamics of structure 1 must be considered in the design process. This is not at all true for whole-spacecraft isolation design. The spacecraft (structure 1) and the launch vehicle (structure 2) are both considered to be very flexible structures and the dynamics of one has significant influence on the other.

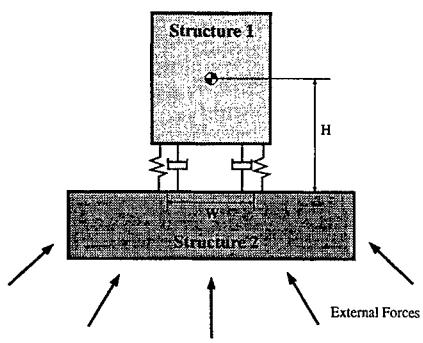

Figure 3. Two connected structures

Historically, the connection between the spacecraft and the launch vehicle has been made with a very stiff payload attach fitting. This is generally considered to be a "hard mount" and is extremely efficient at transmitting all structure-borne forces from the launch vehicle to the spacecraft over a very wide frequency band. A whole-spacecraft isolation system replaces this hard mount with a soft mount which filters out a great deal of the frequency spectrum of the forces from the LV.

Most spacecraft are cantilevered to their launch vehicle, being attached only at their base. Whole-spacecraft isolation is a challenging problem because spacecraft typically have a very large ratio of center-of-gravity height, H, to attachment width, W (Figure 3). Reduction of the axial attachment stiffness will introduce low-frequency

spacecraft rocking (pitch & yaw) modes and large lateral displacements at the upper end of the spacecraft. This is generally undesirable because it may cause guidance control system instabilities or the spacecraft may hit the fairing. However, these problems may be avoided through innovative isolator hardware design.

Launch vehicles often have closely-spaced flexible modes with frequencies starting as low as 1 Hz and spacecraft may have modes with frequencies starting as low as 6 Hz. Isolation of a 6 Hz spacecraft from a 1 Hz LV necessitates a unique design methodology which deviates from classic isolation system design. More than ever, it is necessary to have a clear understanding of the isolation objectives and the design constraints present. Whole spacecraft isolation systems must be designed from a system-level point of view, accounting for the coupled dynamics of two very flexible bodies which will now be connected with a flexible interface as opposed to a hard mount. Indeed, the challenge is to determine exactly where to insert the new dynamics introduced by the isolation system within the sea of structural dynamics already present. The following sections discuss the methodology which was used to develop a whole-spacecraft isolation system for a medium launch vehicle.

3.1. Isolation objectives

The specific objectives for the design of this isolation system were the following:

- Isolate the spacecraft, as a whole, from the launch vehicle. Individual components of spacecraft have been isolated and flown, but a whole spacecraft has never been isolated.
- Provide lateral isolation only. It was decided to only reduce lateral accelerations in this program. Axial isolation, while feasible, was deemed beyond the scope of this program. This objective is tied closely to the design constraints, discussed later.
- Provide a 2:1 broadband RMS reduction in accelerations in the 25 Hz to 35 Hz range. Many spacecraft have secondary structures such as solar arrays, antennas, etc. with modes in this range; these modes will not be excited as much if isolation is designed in this range.
- Reduce accelerations on spacecraft secondary structure. Primary structure of spacecraft is usually designed to meet quasi-static loads and does not, in itself, generally require dynamic load reduction.

3.2. Design constraints

There are many design constraints which pertain to whole-spacecraft isolation. Some of the typical constraints are weight, volume, and strength. However, the two most critical design constraints are:

1. Must not introduce structural modes below 6 Hz. This constraint is related to the vehicle guidance, navigation, and control systems. Structural modes below 6 Hz encroach on the controller bandwidth and may cause flight instabilities.
2. Must not increase the rattle displacement (payload-to-fairing displacement) by more than one inch. Insertion of a whole-spacecraft isolator will introduce compliance between the LV and the spacecraft. This compliance must not significantly increase the rattle displacements which could cause the spacecraft to hit the fairing during launch.

3.3. System-level analysis

Realistic and thorough system-level mathematical models are required to properly design and analyze the system-level benefits of whole-spacecraft isolation. The correct approach to designing isolation for a launch vehicle and spacecraft system is to use finite element models of all parts of the system. This allows accurate simulation of the structural dynamics of the non-isolated system and subsequently provides a tool for simulation of various isolation hardware designs.

The launch vehicle changes significantly during its ascent, due to fuel depletion and stage jettisons. Therefore, many LV models and associated loads would be required to fully analyze any isolator design. For the purpose of designing this isolation system, two flight events were selected: liftoff and pre main-engine cutoff (preMECO). Separate finite element models were obtained for a generic medium launch vehicle, representing these two distinct

periods of launch. The first is a liftoff model, matching the vehicle as it sits on the launch pad. This model was obtained in matrix form only, with 185 physical degrees of freedom (DOF) and 49 modal DOF, for a total of 234 DOF. The second finite element launch vehicle model represents the preMECO period of flight. It was also obtained in matrix form only, with 12 physical DOF and 139 modal DOF, for a total of 151 DOF.

A realistic model was obtained of a NASA spacecraft which weighs 6500 lb and is 16 feet in height. This model originally consisted of a bus structure and 14 substructured equipment items totaling more than 20,000 DOF. This was all combined into one modal-reduced spacecraft substructure having 138 physical DOFs and 148 modal DOFs for a total of 286 DOF. This model is representative of the complicated high-modal-density dynamics present in a typical spacecraft, and was therefore very useful in the isolation design.

The substructuring facility of UAI/NASTRAN was used to simplify the system-level analyses. The launch vehicle models were each stored in the database as separate substructures, as was the spacecraft. The only changing component in each analysis was the PAF, which was also substructured. The assembly of a system-level model involved combining the spacecraft substructure, the current PAF iteration substructure, and the desired launch vehicle substructure into a single system. Then this system was analyzed using either frequency response or transient response solutions. This process is illustrated in Figure 4. Direct solutions were quite feasible, as opposed to modal solutions, because the substructuring significantly reduced the solution matrix sizes.

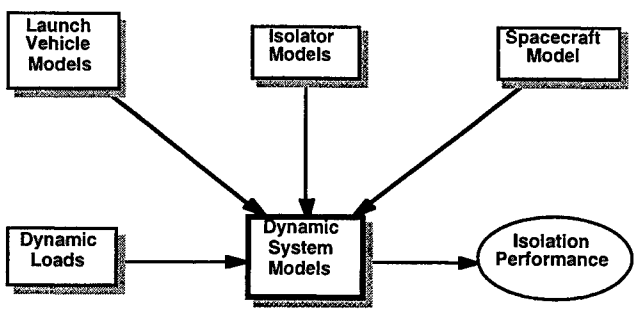

Figure 4. System-level dynamic analysis

Selection of an isolation system design was an iterative procedure, in which each concept was analyzed in a dynamic system model to assess its performance characteristics. Since the main isolation target was the preMECO stage of flight, this model and preMECO loads were used for preliminary evaluation of isolation designs. Initially, the isolation system was modeled as a set of springs and dampers between the launch vehicle and the spacecraft. This allowed rapid trade studies to be performed with several variables such as lateral stiffness, axial stiffness, and damping. Full finite element models of the isolating PAF (IPAF) were used once the design progressed.

The most useful analysis method for the isolation trade studies was frequency response analysis. Using this method, transfer functions were generated between main-engine force inputs and spacecraft acceleration outputs. Comparison of these transfer functions between non-isolating and isolating PAFs provided considerable insight into the isolation performance. Figure 5 shows the isolation performance for the final isolating PAF design in this program. This figure shows that the acceleration response will be greatly reduced in the 25 Hz to 35 Hz frequency range. The amount of broadband attenuation may be indicated by a single number called the "RMS ratio". This is simply the ratio of the RMS of the isolated acceleration PSD to the RMS of the non-isolated acceleration PSD when subjected to uniform white noise input. For the final design, the RMS ratio is 0.39 over the 0 Hz to 40 Hz frequency band, and it is 0.17 over the 20 Hz to 40 Hz frequency band. This exceeds the program goal of an RMS ratio of 0.50.

A thorough coupled-loads analysis was done to evaluate the final design for many other load cases. Table 1 shows the reductions in accelerations due to the isolator and the RMS ratios. These acceleration values were the peak values from all load cases analyzed. The IPAF has reduced the peak lateral accelerations by as much as 46%. The system-level analysis shows that the isolating payload attach fitting provides excellent lateral vibration isolation for the spacecraft.

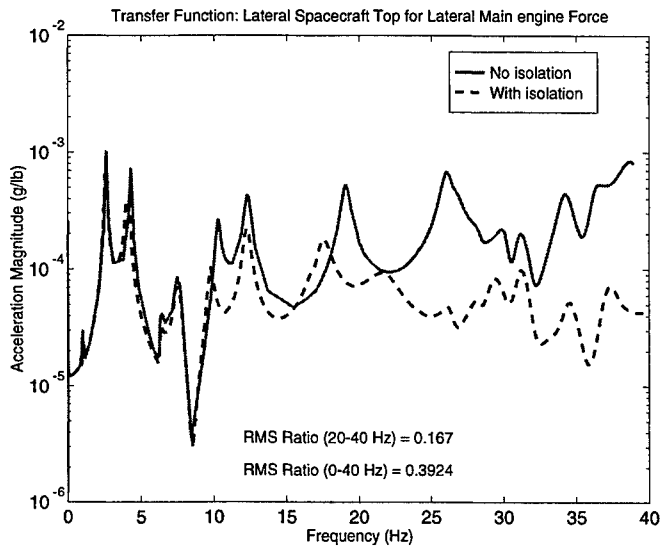

Figure 5. Transfer function showing lateral isolation

Location	Dir*	Max Overall† Acceleration Change	PreMECO Acceleration Change	RMS Ratio§
Top of spacecraft	X	-30%	-33%	0.39
	Y	-31%	-33%	0.37
	Z	-9%	-69%	0.77
Component on top of spacecraft	X	-41%	-46%	0.37
	Y	-29%	-30%	0.38
	Z	-14%	-70%	0.42

* X and Y are lateral directions; Z is axial
† "Max Overall" is the max of liftoff, transonic, and max Q
§ "RMS Ratio" is the isolated RMS acceleration divided by the non-isolated RMS acceleration (0-40 Hz)

Table 1. Summary of isolation performance

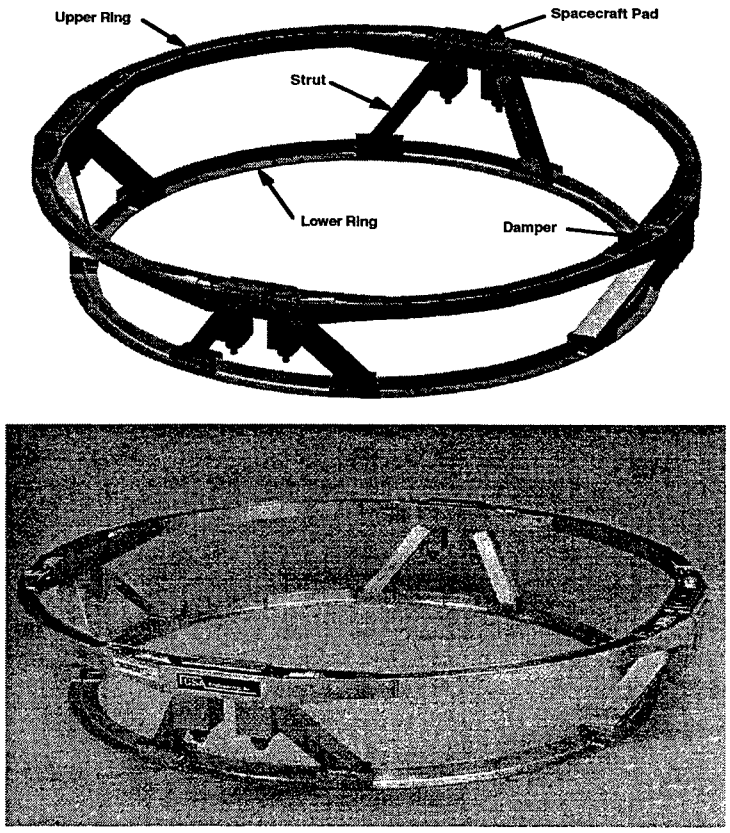

Figure 6. PIP isolating payload attach fitting: solid model and full-scale hardware (69" diameter)

3.4. Component-level analysis

The isolation system consists of both stiffness components and damping components. The system-level analysis was used to arrive at the optimum values for stiffness and damping of this isolator. Then, using these requirements, the isolator stiffness and damping elements were designed. This process consisted of both hardware design and component-level analyses, using detailed finite element models, to size and verify the design.

4. Hardware Design & Fabrication

One purpose for building hardware on this program was so that it could be tested and the resulting data be used for tuning the mathematical models. High confidence in the isolating PAF mathematical model gives high confidence in the full system-level coupled-loads analysis results.

The final design for the isolating PAF structure and its full-scale hardware implementation are shown in Figure 6. This design is intended to be a "slip-in" replacement for the existing hard-mount PAF. Care was taken to match the same basic dimensions and bolt patterns. The lower ring bolts to the upper stage of the launch vehicle. The spacecraft bolts at four locations to the spacecraft pads. The load path from the spacecraft to the launch vehicle goes through the spacecraft pads into a flexure system (not shown), then into the upper end of the struts, then down to the lower ring, and finally into the launch vehicle. Space is left between the upper ends of the strut pairs to accommodate a pyrotechnic nut at each spacecraft mounting location.

The original hard-mount PAF, which has flown many times, is fabricated from a monolithic piece of aluminum. The resulting structure has no welds and is extremely costly to manufacture. To avoid prohibitive costs in this program, the full-scale hardware for the isolating PAF was made from several pieces welded together. Both the lower ring and the upper ring were made from eight machined pieces welded together. The struts were bolted to the upper and lower rings. This was a perfectly reasonable approach for building a non-flight version of this isolating PAF. A flight version of the isolating PAF would not have any welds or bolted strut joints.

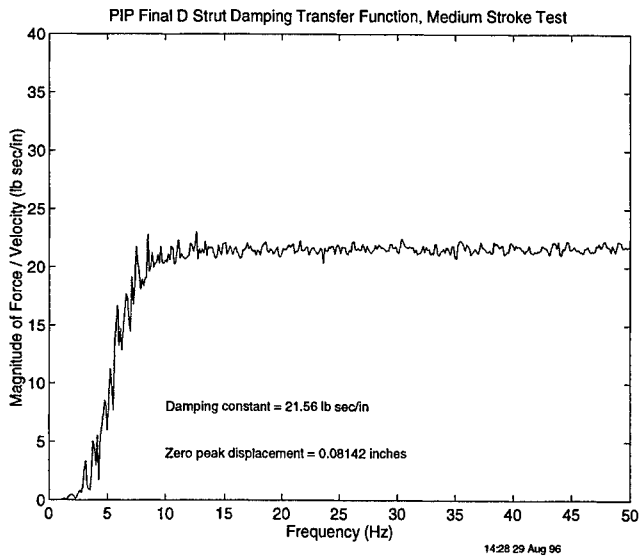

Figure 7. Results from medium-stroke test of PIP D-strut

5. Hardware Tests

Several tests were performed to measure the stiffness and damping of the hardware for the purpose of test-verifying the mathematical models.

The damping element, which is a version of Honeywell's D-strut, behaves like a viscous dashpot and was tested to measure its damping constant. Direct complex stiffness testing resulted in force/velocity transfer functions such as that shown in Figure 7. This shows the magnitude of the force/velocity transfer function for a damping strut which was subjected to a medium-stroke and 50 Hz bandwidth test. The measured damping constant is independent of frequency, for all practical purposes, and meets the requirements for the system.

The isolator stiffness elements, which consist of a system of flexures, were tested for both their axial and lateral stiffness values. The isolation performance, at the system level, is crucially dependent on the stiffness of these flexures. Table 2 shows a comparison of the stiffnesses from both the test and the finite element model of the flexures. This shows excellent correlation between the model and the test data, indicating that the flexures behave in test exactly as they were designed to.

Stiffness Direction	**Test Stiffness** (lb/in)	**Model Stiffness** (lb/in)	**Difference**
Lateral	15,540	15,580	+0.3%
Axial, Tension	1,670,000	1,660,000	-0.6%
Axial, Compression	2,018,000	2,011,000	-0.3%

Table 2. Comparison of the stiffnesses of the flexure system

A modal test was performed on the complete assembled structure to verify that the finite element model is accurate and correctly predicts the behavior of the isolating payload attach fitting. This test was designed to simply extract the first few modes of the structure for use in tuning and validating the model. The measures of comparison between the test and analysis results were a frequency comparison and a mode shape cross-orthogonality matrix. The frequency comparison is shown in Table 3. It can be seen that the frequencies for the first several modes match within about 5%, indicating good correlation.

Frequency (Hz)		Difference
Test	Analysis	
20.65	19.56	-5.3%
33.75	32.21	-4.6%
37.38	37.78	1.1%
77.06	81.78	6.1%
83.50	75.70	-9.3%

Table 3. Frequency comparison between test and analysis

The mode shapes were compared by calculating the cross-orthogonality matrix between test and analysis mode shapes. An analytical reduced mass matrix was calculated, using Guyan reduction in NASTRAN, and was used in the cross-orthogonality calculation. All data were imported into MATLAB for this process. The cross-orthogonality matrix is shown in Table 4. This matrix indicates that there is excellent correlation between the finite element model and the hardware.

		Analysis				
	Freq (Hz)	19.56	32.21	37.78	81.78	75.70
Test	20.65	**0.993**	0.012	0.085	0.000	0.023
	33.75	0.006	**0.995**	0.030	0.078	0.003
	37.38	0.083	0.046	**0.991**	0.002	0.073
	77.06	0.015	0.048	0.014	**0.970**	0.020
	83.50	0.107	0.007	0.202	0.003	**0.844**

Table 4. Modal test & analysis cross-orthogonality matrix

6. Small Spacecraft / Small Launch Vehicle Isolation

While the preceding places emphasis on isolation of a large 6500 lb spacecraft from a medium launch vehicle, it must be clarified that similar isolation methods may also be applied to a smaller class of problems. Whole-spacecraft isolation of a small spacecraft (less than 1500 lb) from the launch environment of a small launch vehicle is an extremely feasible task. Indeed, the isolation problem becomes easier because the ratio of center-of-gravity height to attachment width (discussed previously) is generally smaller. This minimizes collateral problems of low-frequency rocking and payload-to-fairing clearance reduction. A study was performed on a 600 lb spacecraft and a small launch vehicle to assess the feasibility of launch isolation. Figures 8 and 9 show the significant reductions in spacecraft acceleration loads that may be achieved in the lateral and axial directions, respectively. Isolation designs are currently in progress for this class of problem and are considered very promising.

7. Summary

There is a need to reduce launch loads on spacecraft so that spacecraft and their instruments can be designed with more concentration on orbital performance rather than launch survival. A softer ride to orbit will allow more sensitive equipment to be included in missions, reduce risk of equipment or component failure, and possibly allow the mass of the spacecraft bus to be reduced. These benefits apply to military as well as commercial satellites.

The approach taken in this work was to incorporate an isolation system into the payload attach fitting, which is the structure that connects the spacecraft to the launch vehicle. The isolation system was to provide lateral isolation in the 25 - 35 Hz range, an important dynamic range for secondary equipment.

Whole-spacecraft isolation is a challenging problem requiring a great deal of system-level and detail design engineering. Using realistic models of a launch vehicle and spacecraft, coupled-loads analyses were performed for several

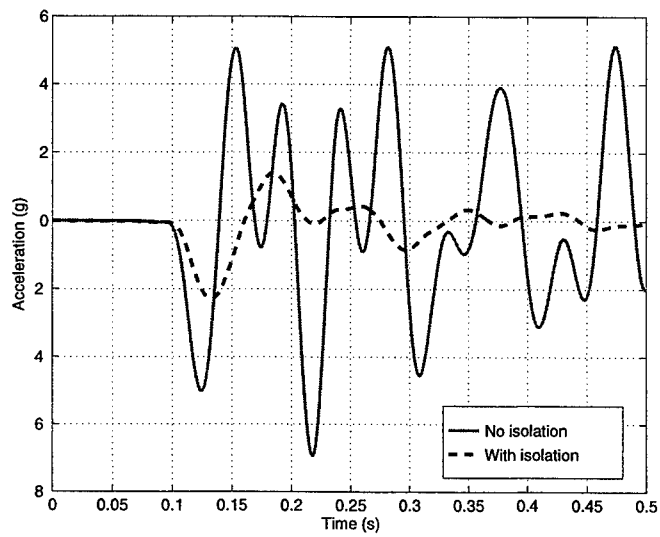

Figure 8. Lateral isolation performance for small spacecraft / small launch vehicle

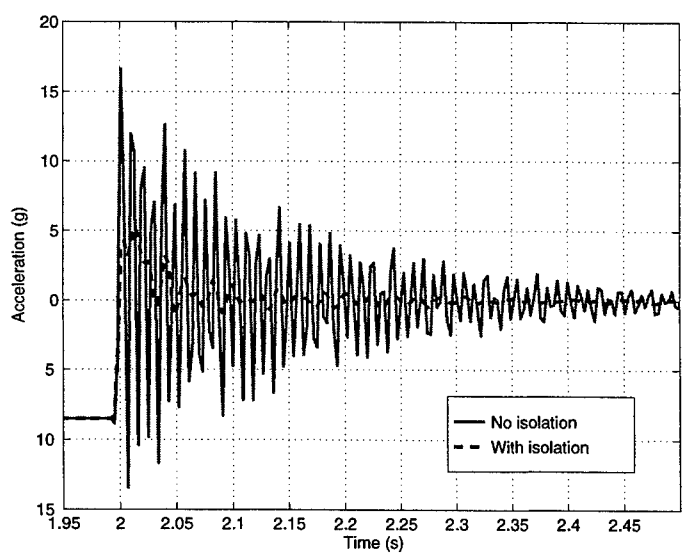

Figure 9. Axial isolation performance for small spacecraft / small launch vehicle

flight events to determine the optimum isolation parameters. Once these parameters were determined, detailed design analysis was used to develop hardware that would produce the desired results. Full-scale prototype hardware (69 inches in diameter) was fabricated and tested to verify the analytical models. The isolating payload attach fitting was a one-for-one replacement for the original. At the conclusion of the design phase, complete (all cases) coupled-loads analyses were also performed to verify the performance of the isolation system.

Additionally, isolation of small spacecraft from small launch vehicles is seen as a very tractable problem which may provide significantly softer rides on these vehicles, which typically have solid rocket motors.

This work brings technology to the launch community which may significantly reduce launch vibration problems and reduce risk of spacecraft component failure.

8. Acknowledgments

This work was performed under a SBIR (Small Business Innovation Research) Phase II with the Air Force Phillips Laboratory. The contract number was F29601-94-C-0127. The authors are grateful for the financial support of the SBIR program that allowed the development of this innovative technology. The authors wish to express their thanks to the engineers at McDonnell Douglas Aerospace and Honeywell Satellite Systems Operation for their technical assistance and encouragement on this effort.

REFERENCES

1. Fosness, Eugene R., Wilke, Paul S., and Johnson, Conor D., "Passive Isolation Systems for Launch Vehicles," *Proceedings of the Fifth International Conference on Space '96,* Albuquerque, New Mexico, June 1-6, 1996, Volume 2, pp. 1176.
2. Fosness, Eugene R., Ninneman, Rory R., Wilke, Paul S., and Johnson, Conor D., "Launch Vibration Isolation System," *Engineering Mechanics, Proceedings of the 11th Conference,* Fort Lauderdale, Florida, May 19-22, 1996, Volume 1, pp. 228.
3. Edberg, D.L., Wilke, P., Davis, T., and Fosness, E., "On the Design and Testing of a Spacecraft Launch Vibration Isolation System (LVIS)," *38th Structures, Structural Dynamics, and Materials Conference and Exhibit, Adaptive Structures Forum,* Kissimmee, Florida, April 7-10, 1997.
4. Timmins, A.R., and Heuser, R.E., "A Study of First-Day Space Malfunctions," *NASA TN D-6474,* September, 1971.

On the development of a launch vibration isolation system

Donald L. Edberg[a] , Conor D. Johnson[b], L. Porter Davis[c], Eugene R. Fosness[d]

[a]McDonnell Douglas, Mail Code H011-C124, Huntington Beach, CA 92647
[b]CSA Engineering Inc., Palo Alto, CA
[c]Honeywell Satellite Systems Operation, Phoenix, AZ
[d]U.S.A.F. Phillips Laboratory, Albuquerque, NM

ABSTRACT

The U. S. Air Force's Phillips Laboratory has sponsored several programs to isolate payloads from mechanical vibrations during launch. This paper details a program called LVIS (for Launch Vibration Isolation System). LVIS' goals are to reduce the RMS accelerations felt by an isolated payload by a factor of 5 compared to an unisolated payload while using minimal launch vehicle services, fitting within existing payload attach fittings' dimension and mass envelopes, and providing fail-safe operation.

The LVIS system must provide axial isolation while at the same time not allowing its host spacecraft to "rattle" too much and make contact with the launch vehicle's external payload fairing, which is present to protect against heat, aerodynamic, and acoustic loads. This challenging set of goals will be accomplished using an innovative suspension system specially designed to be relatively soft in the vertical and lateral directions and stiff in the rotational directions to prevent payload fairing contact. An overview of the LVIS design and predicted performance is given.

Keywords: vibration isolation, attenuation, launch vehicle, payload attach fitting.

2. LVIS CONCEPT DESCRIPTION

Figure 1 depicts a typical spacecraft on its payload adaptor fitting (PAF). The PAF is rigidly connected to both the spacecraft and the launch vehicle and provides minimal attenuation of vibrations being applied at its base. In most cases, all loads are transmitted directly to the payload; in a handful of cases special modifications have been made to provide attenuation for solid rocket motor resonances in specific frequency bands. LVIS' goal is to provide axial and lateral attenuation for a wide band in the low frequency (5-50 Hz) regime.

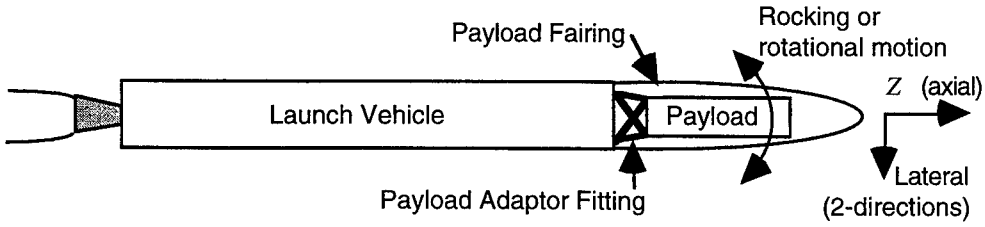

Figure 1. Arrangement of launch vehicle, PAF, and spacecraft, with coordinate systems definition.

The quasi-static axial acceleration during boost tends to cause compression within the spacecraft's long (*Z*) axis. The resulting axial deformations are typically small, since most spacecraft are built to withstand the axial loading created by the quasi-static and transient accelerations. Attenuation of the axial excitation may be attained by softening the PAF in the axial direction so that it behaves as a vibration isolator.

Further author information —
D.L.E. (correspondence): Email: edberg@netsun.mdc.com; telephone 1-714-896-5210; FAX 1-714-896-6930.
C.D.J: email: cjohnson@csaengr.com. L.P.D.: email: pdavis@space.honeywell.com. E.R.F.: email: fosnesse@plk.af.mil

Although the axial loading caused by the launch vehicle's steady axial acceleration provides the largest magnitude of loading during flight, there are also lateral loads which occur primarily due to maneuvers initiated by the vehicle's guidance system and encounters with wind shear situations. This lateral loading tends to excite the launch vehicle's body bending modes and in turn drives the payload's lateral displacements ("rocking" motion) of the spacecraft.

The lateral displacements created by launch vehicle bending modes translates into a horizontal excitation at the location of the payload. Since the payload's mass center is generally axally far in front of the PAF, this tends to excite strong rocking motion of the payload. This means that clearance requirements at the inside of the payload fairing forces the PAF to have very high rocking stiffness.

The conflicting requirements of low axial stiffness to attenuate axial vibrations along with high rocking stiffness to achieve payload fairing clearance requirements make the design of a launch vibration isolation system particularly challenging. The unique design of the LVIS isolator shows good promise in meeting both of these design challenges. The analysis leading to the desired LVIS mechanical and performance parameters is described in detail in the following section.

3. LVIS ANALYTICAL MODELLING

Passive system modelling. Although LVIS is not intended to be a "point design," its sizing and design requires realistic inputs of loading conditions. For this reason, the LVIS system simulations combined several finite-element models: a liftoff-configuration Delta II launch vehicle model, several payload attach fitting models, and a spacecraft model.

During the course of the LVIS effort, several PAF models were generated; a typical one is shown in Figure 2. In this figure, the upper and lower rings are modeled in great detail and to represent the actual structure of a Delta PAF. The isolating LVIS strut elements connecting the two rings are modeled as bar elements. This modeling scheme allowed us to easily modify the dynamics of the struts (stiffness, damping, and active control if desired) to represent various PAF configurations.

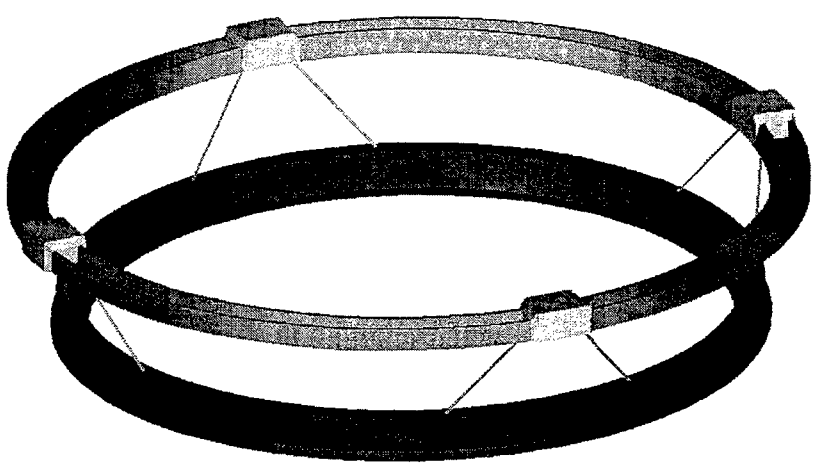

Figure 2. Finite element model of payload attach fitting

For comparison purposes, a baseline configuration mimicking the standard Delta PAF machined from a solid aluminum block was utilized. A second configuration modelled the LVIS dynamics, including the effects of incorporating hydraulically cross-linked struts of various stiffnesses to provide flexibility in some axes and stiffness in rocking directions. The cross-linking is incorporated into the finite element model and provides enhanced rocking stiffness. Its implementation into hardware is described in detail in a later section. The detailed design could not proceed with first carrying out some simulations whose results would be used to assess the LVIS' isolation performance.

PERFORMANCE ESTIMATION

A transfer function approach was used to assess the performance and isolation benefits of candidate LVIS systems. We carried out a number of simulations computing the response at the satellite top due to axial forcing applied at the main engine location. These simulations were run in order to generate a family of RMS ratio curves as a function of the axial isolation frequencies (whole spacecraft fixed-base axial frequencies), as depicted in Figure 3. A 5 Hz axial frequency is seen to provide good isolation, and it may be seen that no isolation benefit is achieved for axial frequencies above 10 Hz. This figure shows that there is definitely a response reduction over the broad band due to the LVIS — the axial isolator attenuates the acceleration seen by the spacecraft for most frequencies.

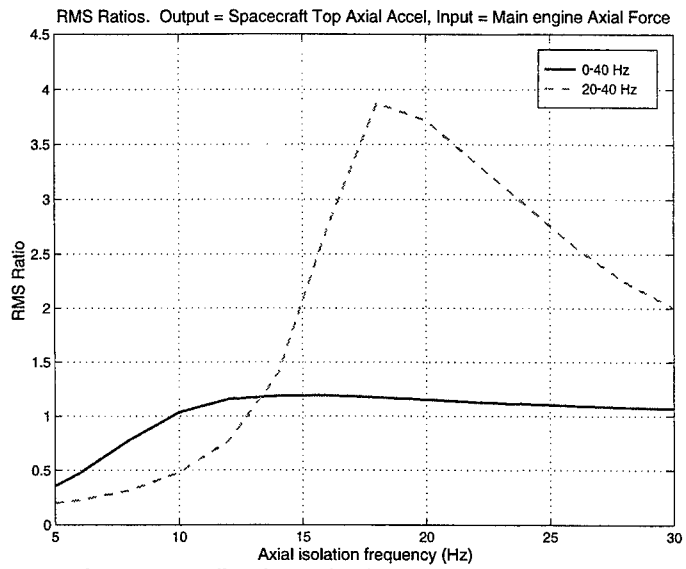

Figure 3 Spacecraft top RMS vibration reduction as a function of LVIS vertical stiffness.

The result of selecting a 5 Hz axial isolation frequency is indicated in the peak transient acceleration due to liftoff loads shown in Figure 4. Note that there are benefits at nearly all frequencies. The 5 Hz axial frequency became the basis of the LVIS hardware design effort detailed below.

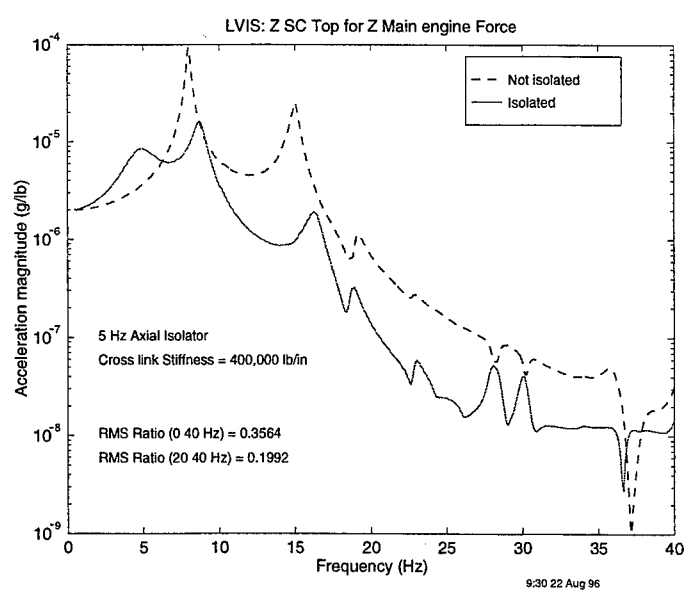

Figure 4. Comparison of spacecraft top RMS vibration levels with and without 5 Hz LVIS system.

4. LVIS HARDWARE IMPLEMENTATION

The design effort's goal was to generate hardware providing a 5 Hz plunge frequency (fixed-base frequency) for the LVIS 8-strut design. These struts are the special elements connecting the top and bottom rings of the PAF shown in Figure 2. Based on a conservative assessment of the loads produced by a 3000 kg (6600 lb_f) satellite exposed to loads ranging from –1.0 to +6.5 g), these strut elements were sized at 87.6 MN/m (500 klb_f/in) and provide up to 3.8 cm (1.5 in) allowable axial displacement. A normal system with this low axial stiffness would also have relatively low rocking stiffness. However, in the LVIS system the rotational or rocking degrees of freedom are stiffened significantly by a unique hydraulic cross-linking system, which is described below.

Our mechanical design effort occurred in parallel with the performance analysis in the previous section and yielded two potential LVIS strut concepts. Both of these concepts utilize a means of "offloading" the static weight of the payload, so that potential future implementations of active control methods would not be burdened with generating the large forces necessary to provide the static loading. One of the LVIS strut concepts utilizes combined pneumatic and hydraulic elements, and the second utilizes mechanical-spring and hydraulic elements. Implementations of these two potential LVIS systems are shown schematically in Figures 5 and 6. Both passive isolator concepts have a proprietary hermetically-sealed hydraulic "cross-link" technology which provides mechanical stiffness for rotation while permitting axial deformations.

Concept 1 (left-hand side of Fig. 5) is a mechanically-offloaded hydraulically cross-linked passive system. A spring is used to support the forces produced by the quasi-static acceleration, allowing the payload to respond to transient accelerations induced by the launch vehicle. Concept 2 (right-hand side of Fig. 5) is essentially the same as Concept 1 except the offloading is provided by a pneumatic support system. One benefit of using a pneumatic support is that the element forces needed to support the payload may be supplied by the internal air cylinder pressure. In addition, the pneumatic offloading system may be easily adapted to payloads of widely varying mass, or accommodate varying acceleration levels, simply by adjusting the internal air pressure. For this reason, we adopted the pneumatic design as our baseline for the LVIS system.

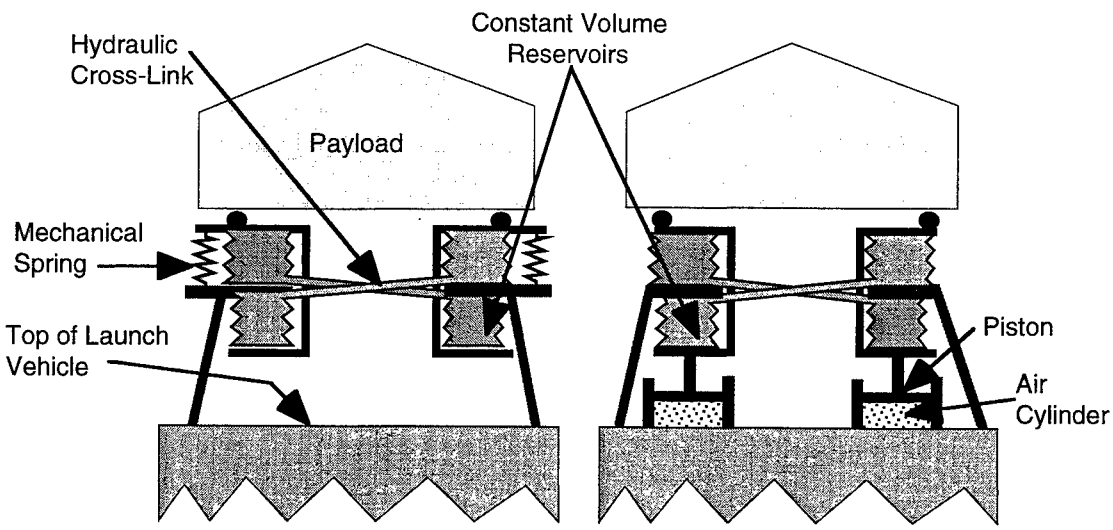

Figure 5. Our two isolation concepts provide low axial stiffness, high rocking stiffness, and static offloading by either mechanical or pneumatic means.

A primary goal of this program is to design, build, and operate LVIS struts which demonstrate that the unique cross-linking technology provides both axial flexibility and lateral stiffness while meeting the upper bound requirements specified in preliminary design and analysis. Details of the mechanical spring strut and the pneumatic spring strut are shown in Figures 6 and 7.

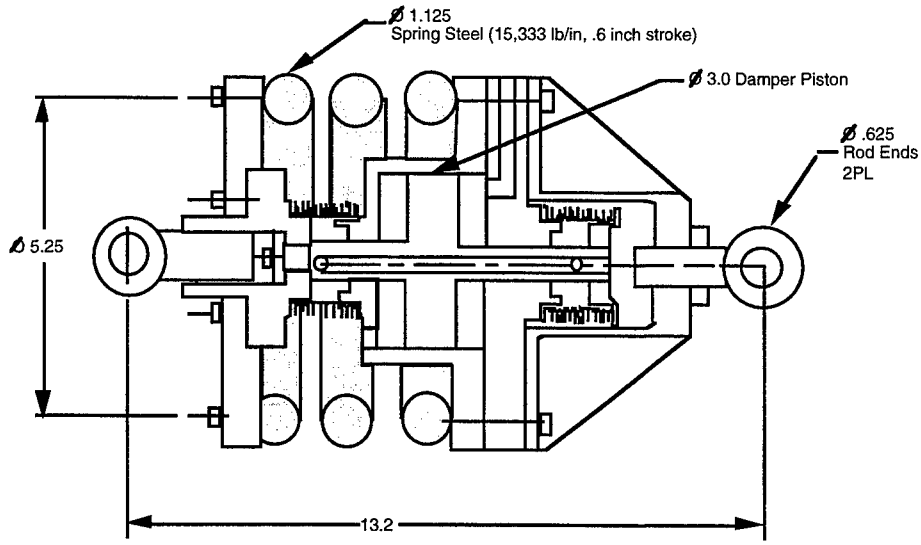

Figure 6. LVIS Mechanical Spring/Hydraulic Cross-Link Isolator Member

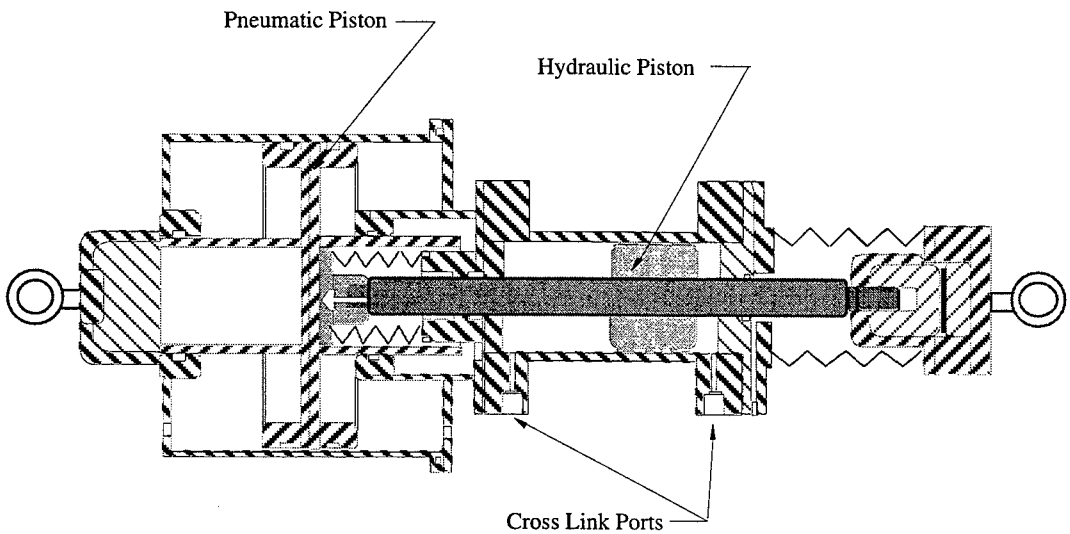

Figure 7. LVIS Pneumatic Spring/Hydraulic Cross-Link Isolator Member

5. ACTIVE SYSTEM MODELLING

Another of the objectives of the LVIS effort was to simulate the effects of an active control system and carry out a trade study to obtain a quantitative evaluation of potential increased payload isolation performance. Our efforts focused on determining how actuator performance requirements (including force magnitude, direction, and the rate of application) affect various spacecraft displacements and accelerations induced by disturbances such as liftoff, transonic and upper atmosphere winds, main engine cut off, etc.

Figure 8 shows the Multiple-Input Multiple-Output (MIMO) control system design topology evaluated. There were 13 inputs: five disturbance inputs u_d and eight active control inputs u_c from actuators located within the PAF. Three outputs y were used for the preliminary evaluation which included the X, Y, and Z spacecraft bus positions (on top).

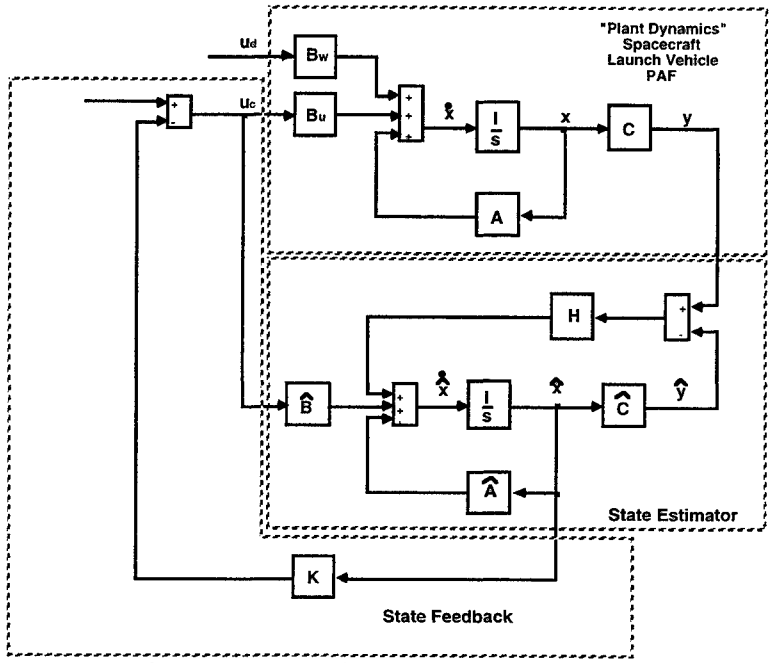

Figure 8: LVIS Active Control Design Topology

The state estimator shown in Figure 8 is used to estimate the states associated with the most important structural modes from a limited number of measurement outputs y. The estimator is required because the direct measurement of all modes of interest isn't cost-effective or operationally efficient. We found that 44 states (22 modes) between 1 and 40 Hz were significant based on frequency response comparisons between the plant model and the reduced-order state estimator. Several different algorithms were utilized to reduce the estimator size because of the impact to real-time processing throughput and memory requirements. Estimator size is one variable in the control system trade study. The state estimator is defined by the $\hat{A}$, $\hat{B}$, and $\hat{C}$ matrices shown in Fig. 8.

Current efforts are focused on evaluating two different methods of calculating the state feed back gain matrix$K$ and the quantitative trade with actuator requirements and isolation performance. These methods include eigenstructure assignment/ pole placement and Linear Quadratic Regulator (LQR)/optimal control approaches. These tasks will provide the information necessary for trade studies considering force magnitude and rate vs. control system cost and mass requirements.

6. GROUND TESTING

The LVIS program includes measurements of the isolator system performance. The testing will include component-level testing of a single LVIS strut, as well as a measurement of the "rocking" stiffness of a pair of LVIS struts.

The component-level tests will measure the strut's direct complex stiffness, which will provide the tangent stiffness and loss as a function of DC preload. This testing will also determine the magnitude of any friction in each strut due to sliding seals, and demonstrate the structural integrity of each strut under under the equivalent of a 6 g static preload.

The system-level testing will verify the high rotational stiffness of a pair of hydraulically cross-linked LVIS struts. A potential configuration for the dual-strut testing is shown in Figure 9. The configuration simulates a pure rotation by applying a compressive load to one strut and a tensile load to the other strut simultaneously.

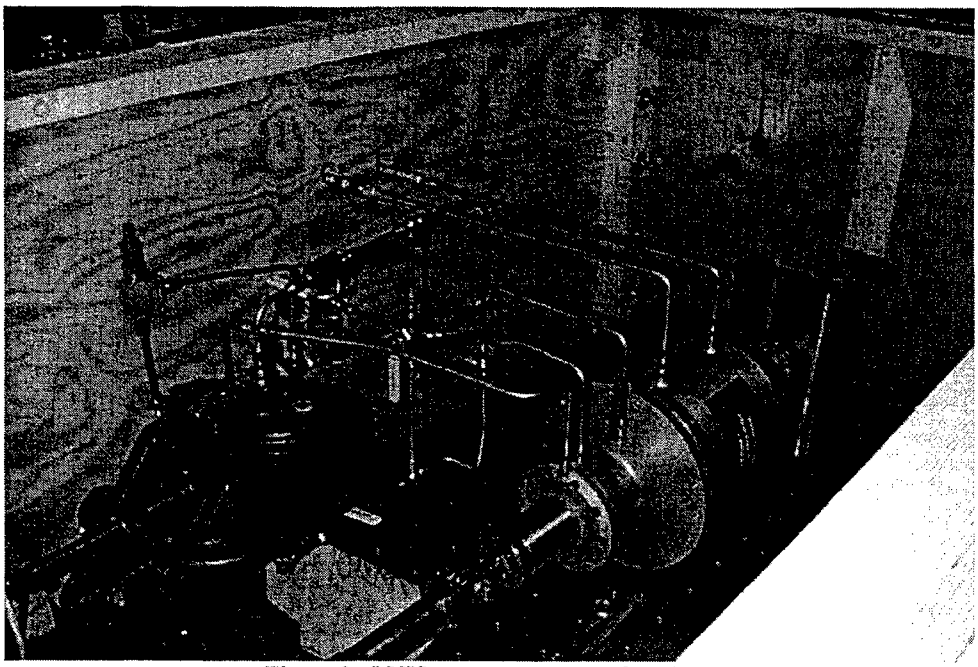

Figure 9. LVIS component ground testing.

As described earlier, the high rotational stiffness created by the struts arises as a result of the hydraulic cross-linking between the struts. Under a pure rotation, the hydraulic load generated by a compressive load in one of the struts is equal in magnitude to the tensile load experienced by its mate. While the near-incompressibility of the fluid linking the adjacent struts implies that the system is theoretically infinitely stiff in rotation, the reality is that stray compliances may arise through the elasticity of the hydraulic lines as well as compressibility of any residual gas contained within the hydraulic lines. The system-level testing will determine the actual rotational stiffness and will be input to the simulations for improved fidelity.

7. CONCLUSIONS

The LVIS program has carried out analytical simulations which indicate significant benefits to the payload, include reduced vibration and shock levels. This reduction can in turn provide some real benefits, including

- relaxed coupled loads analysis requirements
- reduced analysis load cycles and test criteria
- reduced cost, weight, & size of spacecraft components
- better performance & reliability of components
- lessened power and fuel requirements or increased on-orbit service time with larger propellant loads
- reduced LV loads or increased launch survivability
- improved compatibility of payloads & launchers.

The LVIS effort has built a foundation of launch-isolation understanding and real hardware. It will advance the state of the practice with the goal of producing a system that provides isolation with negligible increase in risk, so that it will be accepted by the conservative launch vehicle and spacecraft industry.

ACKNOWLEDGEMENTS

This work was supported by the U.S. Air Force Phillips Laboratory under contract F29601-95-C-0192.

SESSION 3

Embedded Piezo and Active CLD

Structural vibration damping experiments using improved piezoelectric shunts

Shu-yau Wu and Andrew S. Bicos

McDonnell Douglas Aerospace Company
5301 Bolsa Avenue, Huntington Beach, CA 92647

ABSTRACT

The theoretical analysis of an improved piezoelectric shunt using a piezoelectric PZT element shunted with a parallel resistor and inductor circuit for passive structural damping and vibration control was studied[1]. In this paper, we will report results of the experiments of the improved shunting technique which were performed and demonstrated successfully for passive vibration control in the ARPA consortium SPICES program on several structures including thermoset fiberglass/epoxy composite plates with embedded PZT patches and cantilever beams with surface bonded patches. Vibration reductions on resonant response of more than 17 dB using the single mode shunting have been obtained on an 18" x 18" x 0.5" composite plate with eight embedded PZT patches. When we excite another composite plate with a commercial compressor mounted on top of it and turn on the shunt circuits, the transmitted vibration level measured with a force gauge at a plate mounting post is reduced about 15 dB. The improved piezoelectric shunting technique has been studied further to shunt-damp multiple vibration modes using only a single PZT patch. The experimental result of the multiple mode shunting will also be presented.

Keywords: vibration control, piezoelectric shunting, passive damping, multiple mode shunting, resonant frequency, structural mode, piezoelectric PZT, composite plate, embedded actuator.

1. INTRODUCTION

In an earlier paper[1] we reported the theoretical analysis of a piezoelectric shunt on a cantilever beam structure using a surface-bonded piezoelectric PZT element for passive structural damping and vibration control. The PZT element is electrically shunted at its external terminals with a resistor and an inductor in parallel. The piezoelectric shunt is a simple and low-cost vibration control technique. Because of its light weight and ease of implementation on a vibrating structure, the technique is especially suited for space applications. If properly implemented, such as in the inner-loop damping augmentation, it can provide additional stability and robustness to marginally stable active control systems[2].

In the passive vibration damping control employing the piezoelectric shunt, the PZT piezoelectric element is used to convert the mechanical energy of a vibrating system to electrical energy. The electrical energy is forced to flow as an electric current in the external circuit and be dissipated by joule heating through the shunt resistor. To dissipate the electrical energy more efficiently, the current in the external circuit should be limited in the resistor. This is done by tuning the inductor such that the total reactive impedance of the shunt circuit becomes infinite or anti-resonant. This leaves the shunt circuit with the resistive component only. A method well known as impedance matching[3] is then employed to adjust the resistance to extract and transfer the maximum amount of energy to the external circuit for dissipation.

As we have mentioned in the earlier paper[1], the piezoelectric shunt can be operated by shunting the external terminals of the PZT element, either with a resistor and an inductor in series[4,5,6,7,8], or a resistor and an inductor in parallel[1]. We have found, however, that it is more difficult and time consuming to tune and to reduce the structural vibration when the resistor and the inductor are connected in series. This is because in the series connection, the factor Q ($Q = \omega L / R$ in electrical engineering terminology) of the inductor branch is affected by the existence of the resistor. When the resistance R needed for damping becomes large or Q becomes small, the electrical resonant frequency of the series shunt circuit, ω_e, is not equal to $1 / (LC)^{1/2}$, as used by Hagood[4,5]. The correct ω_e becomes $[(L - R^2C) / L^2C]^{1/2}$. Also the correct inductor L needed for tuning the shunt circuit to ω_e should be $L = [1 + (1 - 4\omega_e^2R^2C)^{1/2}] / (2\omega_e^2C)$ and not be $L = 1 / (\omega_e^2C)$.

For an ideal shunt-damping, the frequency tuning and the vibration reduction should be done independently with the inductor and the resistor. The inductor is used to tune the shunt circuit to a resonant frequency of a structural mode of interest. The resistor is used to reduce the peak amplitude of the vibration mode. For the series arrangement, however, because ω_e depends both on the R and L, when the resistance is varied for getting better peak amplitude reduction after the

SPIE Vol. 3045 • 0277-786X/97/$10.00

inductance L is tuned, the L has to be readjusted again. Otherwise the pretuned frequency of the shunt circuit will be off-tuned from the resonant frequency and, consequently, the optimum reduction of the peak amplitude can not be obtained. To reach the optimum vibration reduction, this would require several iterative operations between the L and R, which is a tedious and time consuming operation. To overcome this difficulty, we have reexamined the piezoelectric shunt with the parallel connection. Since in the parallel arrangement ω_e is always equal to $1 / (LC)^{1/2}$, the frequency tuning and vibration reduction can be obtained independently with the inductor and the resistor. Therefore it is a better circuit arrangement.

The detailed theoretical analysis, computer simulation and testing of the piezoelectric shunt using the parallel resistor-inductor arrangement on a cantilever beam has been reported[1]. In this paper we will present results of our piezoelectric shunt-damping experiments performed under the SPICES consortium program sponsored by ARPA. We will first describe the experimental methods in the first section with two subsections: (1) determination of the optimum tuning inductance and the optimum shunt resistance, and (2) the simulated inductor circuit. This will be followed with the experimental results. Two interesting experimental results will be reported. One is the piezoelectric single mode shunting experiment performed on composite plates with embedded actuators, and the other, the multiple mode shunting performed on a two-wing aluminum cantilever beam using only a single PZT patch. The summary will be given in the last section.

2. EXPERIMENTAL METHODS

2.1 Determination of optimum tuning inductance and shunt resistance

We will describe the experimental method using a cantilever beam as an example. Figure 1 shows the sketch of a thin cantilever beam. A PZT piezoelectric ceramic patch is bonded on the upper surface near the high strain energy area. Both the major surfaces of the PZT patch are coated with silver electrodes. Wires are bonded to the electrodes for external connection to the shunt circuit. Two collocated patches may be used which are bonded on the upper and lower surfaces of the beam for more efficient damping control. The cantilever beam is excited with random white noise from an external vibration source, which can be a piezoelectric PZT driver, as shown in the figure, or a shaker. The vibration signal is monitored with a sensor which can be a strain gauge, another piezoelectric PZT element, or an accelerometer. The output from the sensor is amplified by a signal conditioner and then fed to a spectrum analyzer

The structural vibration modes to be shunt-damped are first determined from the frequency response curve. The optimum tuning inductance and the shunt resistor to be used in the shunt circuit for each mode are then determined from the experiment as described below.

1. Obtain f_o and f_s from the frequency response curve, where f_o and f_s are the peak frequencies of the structural mode of interest when the PZT terminals are open- and short-circuited, respectively. Use a narrow frequency band centered around the frequency of the structural mode and also use more analyzer lines for accuracy.

2. Calculate the generalized transverse electro-mechanical coupling coefficient of the mode, $\mathcal{K}_{31}$, using $\mathcal{K}_{31} = [(f_o)^2 - (f_s)^2]^{1/2} / f_s$.

3. Determine the PZT capacitance at constant strain, C^S, from the equation $C^S = (1 - k_{31}^2) C^T$. k_{31} is the PZT material transverse coupling constant, which can be obtained from the PZT manufacturer. C^T is the PZT patch capacitance before it is bonded to the beam. If the PZT is already bonded to the beam, the measured capacitance is close to C^S.

4. Calculate the optimum normalized tuning frequency, α^*, using $\alpha^* = (1 - \mathcal{K}_{31}^2 / 2)^{1/2}$.

5. Calculate the optimum tuning inductance, L^*, using $L^* = 1 / [C^S (2 \pi f_s \alpha^*)^2]$.

6. Calculate the optimum shunt resistance, R^*, using $R^* = 1 / (2.828 \pi f_s C^S \mathcal{K}_{31})$.

2.2 Simulated inductor circuit

As described in the previous section, the piezoelectric shunting for passive damping of structural vibration needs an inductor for tuning the shunt circuit to the natural frequency of the mode of interest. The optimum tuning inductance, L^*, may be very high, in some cases, on the order of several ten to hundred henries. The use of a normal inductance coil with such a high inductance value would be impractical and therefore is not recommended for some applications due to its heavy weight and

bulky volume. The high resistance associated with the high inductance coil could also impose problems because it reduces the Q factor of the inductor branch in the shunt circuit.

Use of an inductor simulator with operational amplifier circuits for high inductance has been reported, such as using a gyrator[9], an integrator in conjunction with a voltage-to-current converter[10], or a differentiator in conjunction with a current-to-voltage converter[5]. The input impedance of these simulated inductor circuits, however, are not of pure inductance, i.e., there is always a resistive component in series with the inductor. The simulated inductor circuit we have selected to use is the Riordan gyrator[11], which was employed for the piezoelectric shunting by Edberg et al[6] and is shown in Figure 2. The equivalent circuit of the Riordan gyrator is a pure inductor with the inductance value of $L = C R_1 R_3 R_4 / R_2$ provided that the capacitor C has a very low dissipation factor. The inductance therefore can be varied by changing either the resistance R_3 or R_4 using a variable resistor.

3. EXPERIMENTAL RESULTS

3.1 Single mode shunting on thermoset fiberglass/epoxy composite plates

During the SPICES program we have performed the single mode piezoelectric shunting on several plate and rail structures made from different materials embedded with piezoelectric actuators, sensors and accelerometers, fiber optic sensors, and shape memory alloys[12]. For the plate structures made from thermoset fiberglass/epoxy composite materials, the piezoelectric transducers (or patches) were embedded in the plates using the resin transfer molding (RTM) technique[13] by FMI Inc. In this subsection we will present results of the single mode shunting experiments on 18" x 18" x 0.5" composite plates. Each plate with a commercial compressor mounted on top of it in the center was bolted at the four corners on a seismic mass plate. A proof mass shaker used to excite vibration was also attached vertically to the top of the compressor. Figure 3 shows the arrangement of the piezoelectric shunting experiment.

The first composite plate was embedded with four pairs of ACX PZT QuickPack patches. Each pair consisted of two 3" x 4" patches which were embedded symmetrically with respect to the neutral axis of the plate and approximately 0.07" below the surface. The four pairs were located each on one side of the plate in the middle and about 1" in from the edge. For the convenience of identification, they were designated as 0026 and 0031 transducer pair at the position N. The 0027 and 0032 pair were at the position E. The 0028 and 0033 pair were at the position S and the 0030 and 0034 pair were at the position W. We first performed simulated shaker input tests on the plate and examined the vibration modes and the transducer characteristics. After measuring the transfer functions between the shaker and each PZT transducer pair we measured the open-circuit frequency, f_o, and the short-circuit frequency, f_s, for the structural mode at 41 Hz. An accelerometer sensor was collocated with the transducer pair being tested. The measured data were used to calculate the generalized transverse electro-mechanical coupling coefficients of these transducer pairs at this mode frequency. The coupling coefficients of the four pairs were about 5%, as illustrated in Table 1, which indicated that the bonds between the embedded transducers and the composite plate were good.

The piezoelectric shunt was performed next to damp the 41 Hz structural mode using four shunt circuits. We first used one shunt circuit for each transducer pair. The optimum tuning inductance and the shunt resistance of each shunt circuit were determined from the equations, as described in Section 2. The result of the shunt-damping experiment using one shunt circuit is given in Table 1. The 41 Hz peak amplitude reductions with each shunt circuit were about 12 dB. The critical damping factors of the mode after shunting were increased from about 0.47 ~ 0.53% to 2.82 ~ 3.51%.

The shunt-damping experiment was next repeated using two and four shunt circuits simultaneously. During this experiment the accelerometer sensor was positioned over the transducer pair W. Table 2 summarizes the test results of the 41 Hz mode amplitude reductions and the final critical damping factors when the plate was shunted with one, two and four shunt circuits. It indicates that when the four shunt circuits were all activated together, the 41 Hz mode amplitude reduction went up to 17.78 dB and the critical damping factor increased from the initial 0.512 to 6.795%. Figures 4a and 4b display the frequency response curves near the 41 Hz mode before and after shunt-damping with four shunt circuits. We also tried to shunt-damp the composite plate with one shunt circuit by connecting the four transducer pairs in parallel and terminating them to a shunt circuit with proper inductor and resistor. We obtained an amplitude reduction of 17.75 dB for the 41 Hz mode and the final critical damping factor of 6.80%. These data were close to that obtained earlier when the shunt-damping was performed with four separate shunt circuits. But the plateau of the frequency response curve near the 41 Hz mode after the shunt-damping was very noisy.

Figures 5a and 5b illustrate the time response of the same composite plate before and after shunt-damping with four shunt circuits. In each figure the upper curve is the input signal to the shaker and the lower curve is the output from the

accelerometer sensor. The sinusoidal frequency used was 41 Hz. The critical damping factor determined from the decay of the response curve before and after the shunt-damping were 0.65% and 6.89%, respectively.

Another fiberglass/epoxy composite plate processed with the RTM technique and embedded with twenty four (twelve-pair) different-size ACX PZT QuickPack patches was also tested. Figure 6 shows a photograph of the plate with its test fixture. The piezoelectric shunt-damping test was performed on the four large transducer pairs which were the same size as those embedded in the previous plate. For this plate the frequency of the structural mode of interest was at around 46.5 Hz. The sensor used was a PCB uniaxial force transducer which was mounted below the plate at one of the supporting posts. We first obtained the frequency response curve by exciting the plate with a shaker and measuring the transmitted force with the force transducer. Figures 7a and 7b show the force transmission frequency response curves before and after shunting four transducer pairs with four shunt circuits. An amplitude reduction of 14.38 dB was observed for the 46.5 Hz mode. We next turned off the shaker, excited the plate with the compressor, and measured the transmitted force power spectra before and after shunting. Figure 8 illustrates the force transmission power spectra before and after shunting. An amplitude reduction of 14.20 dB for the peak at around 46.18 Hz was obtained.

3.2 Multiple mode shunting using a single PZT patch

In our earlier paper[1] we described a simple, practical and cost effective method for passive structural vibration reduction and damping using a parallel resistor-inductor (R-L) shunt circuit shunted across the external two terminals of a PZT transducer. The circuit is intended to reduce and damp vibration of one structural mode. To reduce and damp two or several modes simultaneously, two or more PZT transducers bonded or embedded in the structure have to be used. But the use of several PZT transducers on or in the structure may create some problems. First, the structure may not have enough room to accommodate these transducers in one area. Second, if there is enough room, the structural property may be altered or weakened when these transducers are embedded in or bonded on it. Third, the addition of a large number of PZT transducers will increase the weight of the structure, which is not recommended for space applications requiring light weight.

In this subsection we will describe a method of shunt-damping two or multiple vibration modes simultaneously using a single piezoelectric PZT transducer. Although there have been two reports[6,7] of the multiple mode piezoelectric shunting, the circuits and the approaches employed by these authors were not practical. This was due to the fact that tuning of the inductor in one shunt branch for one mode would cause detuning of other modes or the entire shunt circuit. The analysis and the computation used to determine the shunt circuit components were very complex and tedious. There are always two questions to ask when one wants to design a shunt circuit to simultaneously shunt-damp multiple modes with the use of a single PZT patch terminated by several series R-L or parallel R-L shunt circuits, each designed to control one structural mode. They are: (1) how to avoid interference among the shunt circuits after they are all connected to the same PZT terminals, and (2) how easily and reliably one can do the fine-tuning with the inductors or the resistors to optimize the shunting performance.

To solve these questions we have conceived and developed a new method, which has been successfully demonstrated experimentally. Our approach is to insert a "blocking" circuit in series with the parallel R-L shunt circuit designed for each mode. The "blocking" circuit consists of one parallel capacitor and inductor (C-L) anti-resonant circuit or a series of them. The number of the C-L anti-resonant circuits in each branch circuit depends on the number of the structural modes to be shunt-damped simultaneously. The blocking circuit of each R-L shunt circuit is designed to produce infinite electrical impedance, or anti-resonance, at the natural frequencies of all other R-L shunt circuits. The individual branch circuits with its "blocking" circuit inserted are then connected to the two common terminals of the PZT transducer to form the multiple mode shunt-damping circuit. The tuning inductance of the original R-L parallel circuit, of course, has to be recalculated and corrected after the "blocking" circuit is connected to it. The capacitor used for the C-L anti-resonant circuit should be a low dissipation factor one and the inductor should have a very high Q factor, which can be obtained from the simulated inductor circuit described earlier in section 2.2.

Two multiple mode shunt-damping circuits designed to attenuate two structural vibration modes simultaneously have been fabricated. Both circuits have been tested experimentally to reduce the vibration amplitudes of the first and the second modes of a two-wing aluminum cantilever beam whose sketch is given in Figure 9. This beam was also used earlier for the preliminary single mode shunting experiment reported in ref. 1. Figures 10a and 10b show the frequency response curves of the two-wing cantilever beam before and after the PZT transducer was shunted with the multiple mode shunt circuit. We have obtained amplitude reductions of about 10 dB for both the first mode at 122 Hz and the second mode at 205 Hz. The critical damping factor for the first mode was increased from 0.35 to 2.61% and from 0.353 to 2.96% for the second mode. A more detailed theoretical and experimental paper on the multiple mode shunt-damping will be reported in the future.

4. SUMMARY

We have reported experimental results of the improved piezoelectric shunting technique following the presentation of the theoretical paper[1] at the last year's SPIE conference. The experiments were performed under the Synthesis and Processing of Intelligent Cost Effective Structures (SPICES) consortium program sponsored by the Advanced Research Projects Agency (ARPA) on several composite structures, in particular, on thermoset fiberglass/epoxy composite plates with embedded PZT patches and cantilever beams with surface bonded patches. We first described the experimental methods in two parts.. First we reported the method of how to determine the optimum tuning inductance and the optimum shunt resistance of the parallel resistor and inductor shunt circuit. It was followed by the second part in which we described how to obtain the high value inductance for the shunt circuit utilizing the Riordan simulated inductor circuit.

During the SPICES program several successful piezoelectric shunting experiments were performed. We have presented in the "Experimental Results" section the test results from two thermoset fiberglass/epoxy composite plates manufactured by the resin transfer molding technique embedded with ACX PZT QuickPack actuators. Excellent vibration reductions on resonant response of more than 17 dB have been obtained on an 18" x 18" x 0.5" composite plate using shaker excitation. On another composite plate we excited it with a commercial compressor which was mounted on top of it. The transmitted vibration level measured with a force gauge at one of the plate mounting posts was reduced about 15 dB after shunting.

The improved piezoelectric shunting technique was extended further to shunt-damp multiple structural vibration modes using only a single PZT patch. The approach was to employ a "blocking" circuit in series with the parallel resistor and inductor R-L shunt circuit designed for each mode. The "blocking" circuit consists of one parallel capacitor and inductor (C-L) anti-resonant circuit or a series of them. The number of the C-L anti-resonant circuits in each branch circuit depends on the number of the structural modes to be shunt-damped simultaneously. The blocking circuit of each R-L shunt circuit is designed to produce infinite electrical impedance, or anti-resonance, at the natural frequencies of all other R-L shunt circuits. The individual branch circuits with its "blocking" circuit inserted are then connected to the two common terminals of the PZT transducer to form the multiple mode shunt-damping circuit. Experimentally we have tested this technique with a two-wing aluminum cantilever beam. We have demonstrated successfully shunt-damping of the first and the second modes of more than 10 dB. The critical damping factors for the first mode was increased from 0.35 to 2.61% and from 0.353 to 2.96% for the second mode.

ACKNOWLEDGMENTS

The authors would like to thank Dr. Robert Crowe of ARPA/DSO and Dr. Janet Sater of IDA for their support and interest on this passive shunting study. This research was sponsored in part by the Advanced Research Projects Agency (ARPA) under the SPICES consortium program under contract no. MDA 972-93-2-0010.

REFERENCES

1. S. Y. Wu, "Piezoelectric Shunts with a Parallel R-L Circuit for Structural Damping and Vibration Control," *Proceedings of the International Society for Optical Engineering*, vol. 2720, pp. 259-269, 1996.
2. H. Ashley and D. L. Edberg, "On the Virtues and Prospects for Passive Damping in Large Space Structures," *Proceedings of the Damping, 1986 Conference*, Rept. AFWAL-TR-86-3059, March 1986.
3. C. Belove, ed., *"Handbook of Modern Electronics and Electrical Engineering*," John Wiley & Sons, New York, 1986, p. 622.
4. N. W. Hagood and A. von Flotow, "Damping of Structural Vibrations with Piezoelectric Materials and Passive Electrical Networks," J. Sound and Vibration, 146, 2, 243 (1991).
5. N. W. Hagood and E. F Crawley, "Experimental Investigation of Passive Enhancement of Damping for Space Structures," J. Guidance, Control and Dynamics, 14, 6, 1100 (1991).
6. D. L. Edberg, A. S. Bicos, C. M. Fuller, J. J. Tracy and J. S. Fechter, "Theoretical and Experimental Studies of a Truss Incorporating Active Members," J. Intell. Mater. Syst. and Struct., 3, 333 (1992).
7. J. J. Hollkamp, "Multimode Passive Vibration Suppression with Piezoelectric Materials and Resonant Shunts," J. Intell. Mater. Syst. and Struct., 5, 4 (1994).
8. S. P. Kahn and K. W. Wang, "Structural Vibration Control via Piezoelectric Materials with Active-Passive Hybrid Networks," ASME/Active Control of Vibration and Noise, DE-75 (1994).
9. *"Linear Applications Handbook,"* National Semiconductor Application Note 31, Op Amp Circuit Collection, 1986, p.96.
10. D. F. Stout, "*Handbook of Operational Amplifier Circuit Design*," ed. by Milton Kaufman, McGraw-Hill Book Company, New York, 1976, Chapter 22.2.

11. R. H. S. Riordan, "Simulated Inductors Using Differential Amplifiers," Electron. Lett., vol. 3, 1967, pp. 50-51.
12. J. H. Jacobs, "Synthesis and Processing of Intelligent Cost Effective Structures: A Final Review of the ARPA SPICES Program," *Proceedings of the International Society for Optical Engineering*, vol. 2721, pp. 167-188, 1966.
13. M. Thomas and M. Trottier, "Industrial Fabrication of Smart Structures for Vibration Control," 1995 International Mechanical Engineering Congress & Exposition, San Francisco, CA, November 1995.

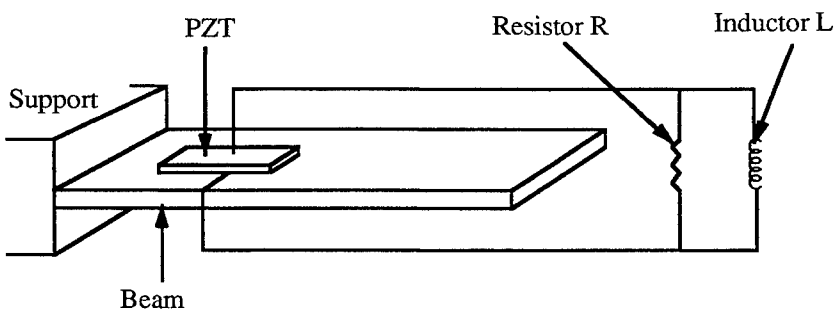

Figure 1. Sketch of a thin cantilever beam shunted with a parallel resistor-inductor circuit.

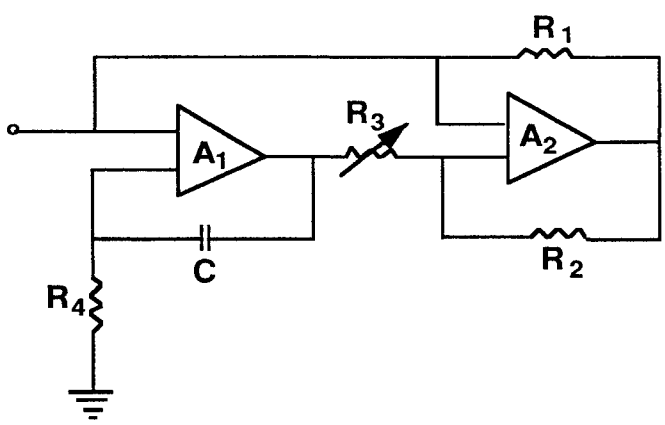

Figure 2. Simulated inductor circuit employing two operational amplifiers.

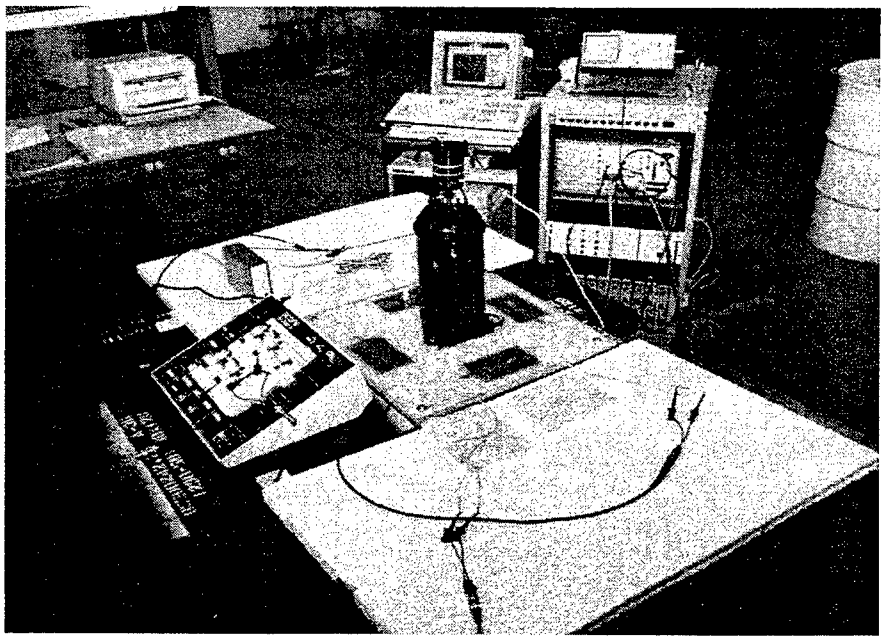

Figure 3. Arrangement of piezoelectric shunt experiment on a thermoset composite plate.

PZT Patch ID & Location	Measured Capacitance (μF)	Generalized Electro-Mechanical Coupling Coefficient (%)	41 Hz Mode Amplitude reduction (dB)	Damping Factor Initial, Final (%)
0026 & 0031 Position N	1.372	4.982	11.97	0.534 3.377
0027 & 0032 Position E	1.241	4.368	11.60	0.489 2.877
0028 & 0033 Position S	1.112	4.792	11.66	0.473 2.825
0030 & 0034 Position W	1.281	5.178	12.64	0.495 3.512

(Accelerometer sensor collocated with PZT patch being tested)

Table 1. Shunt test data before and after activating one PZT pair to its shunting circuit.

PZT Patch(es) Shunted	41 Hz Mode Amplitdue Reduction (dB)	Final Damping Factor (%)
0026 & 0031 (N)	12.32	3.506
0027 & 0032 (E)	11.08	3.049
0028 & 0033 (S)	10.98	2.973
0030 & 0034 (W)	12.81	3.512
0026 & 0031 (N), 0030 & 0034 (W)	15.17	5.035
0027 & 0032 (E), 0028 & 0033 (S)	13.59	4.355
0026 & 0031 (N), 0027 & 0032 (E), 0028 & 0033 (S), 0030 & 0034 (W)	17.78	6.795

When four PZT groups are connected to one shunt circuit, the amplitude reduction is 17.75 and final damping factor is 6.80%. But FTF is noiser

Table 2. Shunt test data after activating one, two and four PZT pairs to their shunting circuits. (measured with accelerometer sensor at position W).

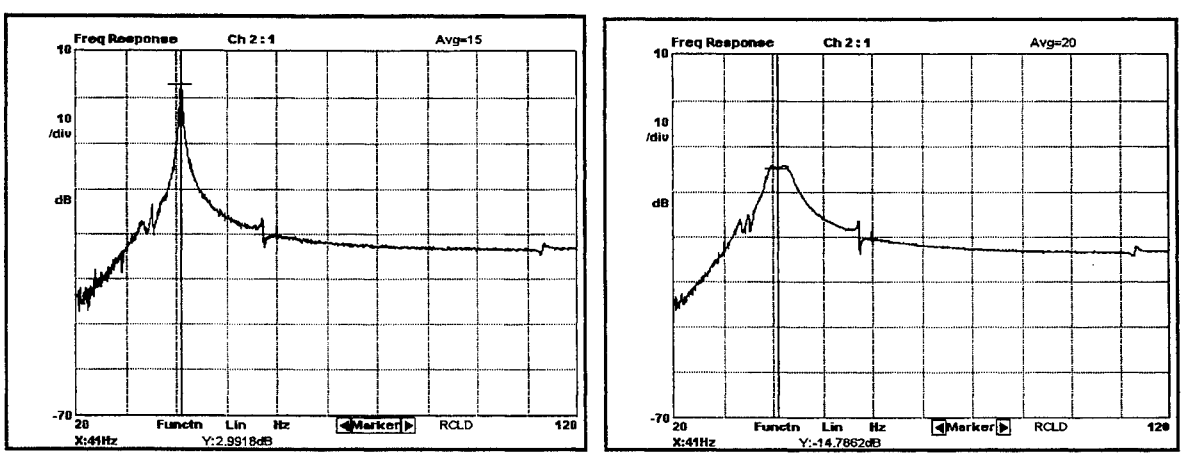

(a) (b)

Figure 4. Frequency response curves near 41 Hz mode before (a) and after (b) shunt-damping with four shunt circuits.

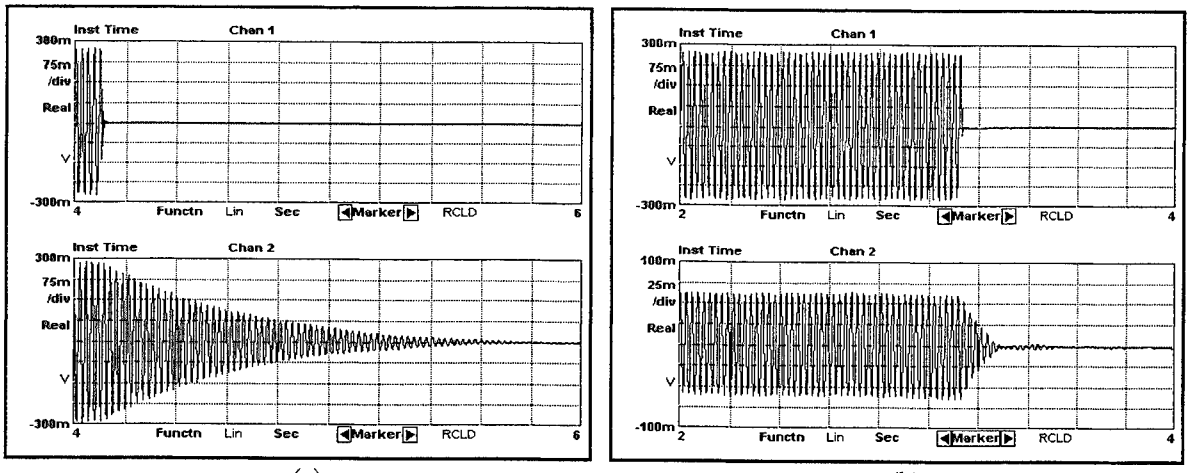

(a) (b)

Figure 5. Time response curves at 41 Hz before (a) and after (b) shunt-damping with four shunt circuits. The upper curve of each figure is the input signal to the shaker and the lower one is the plate time response.

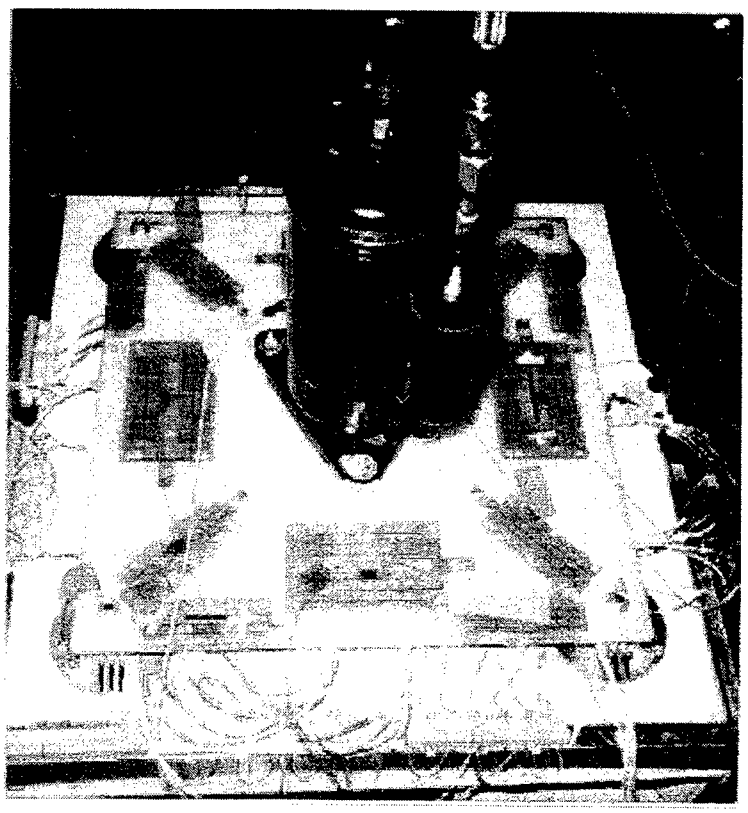

Figure 6. Photograph of a fiberglass/epoxy composite plate and its test setup.

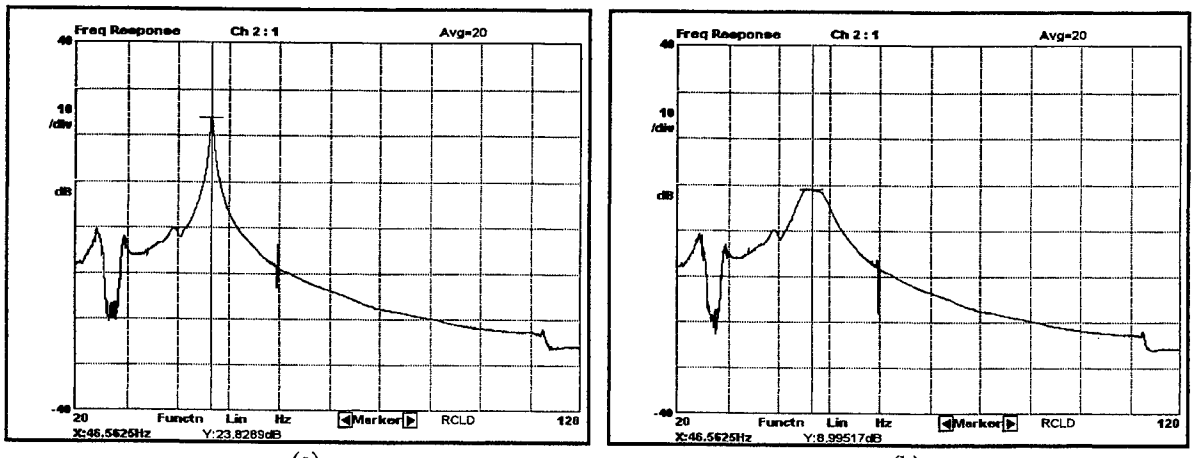

(a) (b)

Figure 7. Force transmission frequency response curve near 46 Hz mode before (a) and after (b) shunt-damping with four shunt circuits. (using shaker excitation).

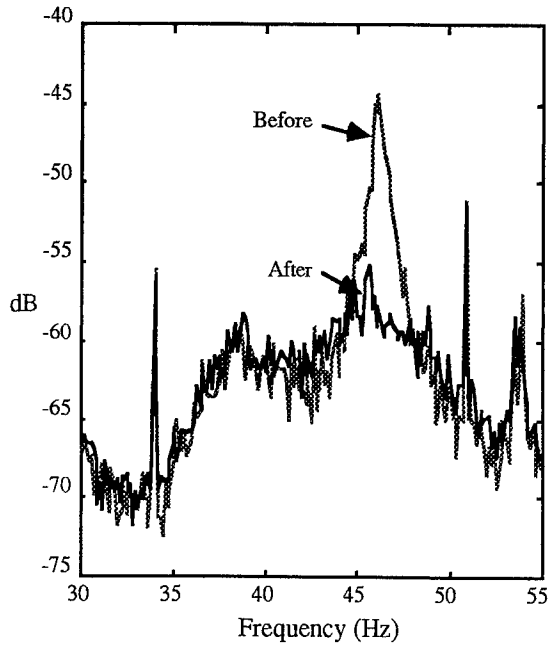

Figure 8. Force transmission power spectra near 46 Hz before and after shunt-damping. (using compressor excitation).

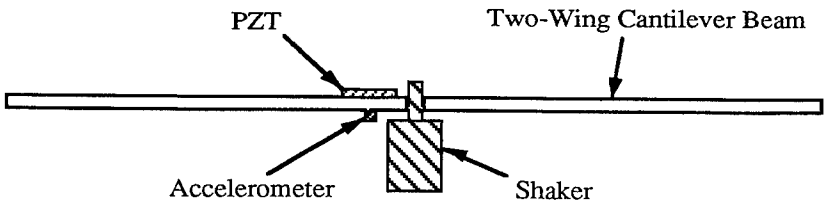

Figure 9. Sketch of two-wing cantilever beam using a single PZT patch for shunt-damping experiments.

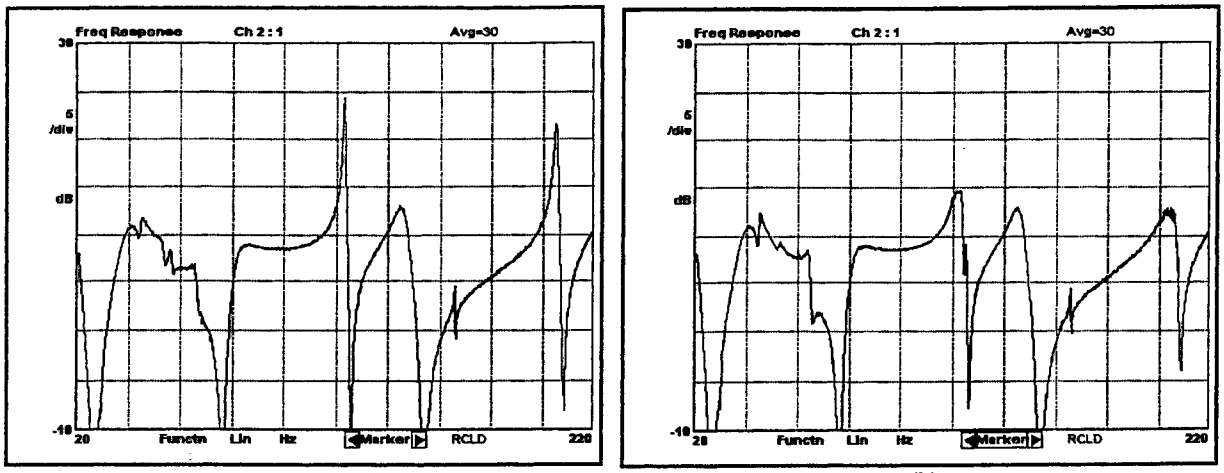

(a) (b)

Figure 10. Frequency response curves showing vibration reductions of two modes, around 122 and 205 Hz, before (a) and after (b) multiple mode shunt-damping using a single PZT patch.

A tunable electrically shunted piezoceramic vibration absorber

Christopher L. Davis[a], George A. Lesieutre[a], and Jeffrey Dosch[b]

[a]Department of Aerospace Engineering, The Pennsylvania State University, University Park, PA 16802
[b]AVC Instrumentation Division; PCB Piezotronics, Inc., Depew, NY 14043

ABSTRACT

A shunting method has been developed and experimentally verified for tuning the natural frequency and damping of a piezoceramic inertial actuator (PIA). Without power, a PIA behaves much like a passive vibration absorber (PVA). PVAs typically minimize vibration at a specific frequency often associated with a lightly damped structural mode. Large response reductions, however, may only be achieved if the PVA is accurately tuned to the frequency of concern. Thus, an important feature of a PVA is the ability to be accurately tuned to the possibly varying frequency of a target vibration mode. Tuning an absorber requires a change in either the mass or stiffness of the device. The electromechanical properties of the piezoceramic forcing element within a PIA in conjunction with an external passive electrical shunt circuit can be used to alter the natural frequency and damping of the device. An analytical model of a PIA was created to predict changes in natural frequency and damping due to passive electrical shunting. Capacitive shunting alters the natural frequency of the actuator only, while resistive shunting alters both the natural frequency and damping of the actuator. Experiments using both passive capacitive and passive resistive shunt circuits verified the ability to predictably shift the natural frequencies of the piezoceramic inertial actuator by more than 5%.

Keywords: vibration absorber, tuning, piezoelectric ceramic, shunting, inertial actuator

1. INTRODUCTION

Vibrations in aerospace structures create many important and difficult engineering problems. In certain aircraft and rotorcraft applications, structural vibrations may increase interior cabin noise levels and/or accelerate material fatigue. Identifying the sources of troublesome vibrations and subsequently developing strategies for reducing these vibrations has been and continues to be the focus of a large body of research.

Interior noise levels in certain propeller driven aircraft, rotorcraft, and the more advanced high-speed turboprop aircraft are, in general, higher than desirable. In these vehicles, noise is generated from both airborne and structure-bore sources. Airborne noise arises from acoustic sources such as the interaction of the propeller wake/vortex with the aircraft fuselage or the impingement of jet exhaust directed at the fuselage.[1,2] Structure-borne noise is a result of vibrations from the engine or vibrations from the interaction of the propeller wake/vortex with the wing surface being transmitted via the aircraft structure to the main cabin.[3,4] In addition, the flexible attachment of the rotor blades to the rotor hub and gear meshing in the main rotor gearbox of rotorcraft may also generate extremely high cabin noise levels. Thus with many of the sources of interior noise identified, the problem becomes that of reducing the resulting noise/vibration levels within the aircraft or rotorcraft cabin.

Structural acoustic control is a method for reducing the interior cabin acoustic field by reducing vibrations due to external excitation sources before they propagate to and excite the coupled interior structural acoustic modes of the aircraft fuselage. Direct airborne induced disturbances may be inhibited from propagating to the fuselage by altering the stiffness of the wing and fuselage,[5] by adding surface damping treatments to the wing and fuselage,[3,5] by adding blocking masses to the aircraft structure,[3] by using passive and active vibration abosorbers,[3,5,6] by using resistively shunted[7,8] and resonantly shunted[7,9] piezoceramics, or by using active vibration control. Vibrations that propagate from the engine may be reduced by passive and active isolation, by active control, and by passive[4] and active vibration absorbers. Of particular interest to this research is the use of passive vibration absorbers for structure-borne noise/vibration control.

Further author information -
C.L.D. (correspondence): Email: cld103@psu.edu; Telephone: 814-865-9072. Ph.D. Candidate.
G.A.L.: Email: gal4@cac.psu.edu; Telephone: 814-863-0103. Associate Professor.

Passive vibration absorbers are conceptually simple devices consisting of a mass attached to a structure via a complex spring. The primary function of these devices is to increase the dynamic stiffness of the airframe and/or engine mounts of an aircraft. PVAs are typically used to minimize vibration at a specific frequency often associated with a lightly damped structural mode. For the device to operate at the correct frequency, the mass and stiffness must be chosen correctly so as to tune the actuator to the frequency of the offending mode or disturbance. The fact that a PVA may only be used at a specific frequency, however, can sometimes be the largest drawback of using these devices.

Passive vibration absorbers have been used in the aviation industry for quite some time. For example, the DC-9 uses a set of four PVAs attached to each engine pylon[4] to reduce the aft cabin noise associated with the operating spool frequency of the engines. Similarly, both the Fokker F27[10] and the Saab 340[11] aircraft use PVAs attached directly to the fuselage frame to lower interior cabin noise levels. In these applications, the absorbers provide adequate vibration attenuation at specific frequencies. Performance can be seriously degraded, however, if the disturbance source changes frequency. If this occurs, the PVA(s) must be physically re-tuned. Re-tuning the absorber(s) may often be either impractical or impossible, hence there is a need for a vibration absorber with properties that are easy to alter.

The purpose of this research was to develop a straightforward method for tuning a vibration absorber. This was accomplished by electrically shunting a piezoceramic inertial actuator. In the passive sense, an inertial actuator behaves much like a PVA. This work exploits the frequency dependent properties of shunted piezoceramic forcing elements within the PIA by using them (*i.e.*, the piezo elements) as variable stiffness complex springs.

2. BACKGROUND

A model was created to gain insight into the effects of shunting a piezoceramic inertial actuator. First, a single degree-of-freedom (DOF) structure and absorber model were created. Next, the absorber model was altered to incorporate the effects of the piezoceramic forcing element of the inertial actuator. Finally, the electro-mechanical dynamics of the passively shunted piezoceramic were added to the model to create the desired frequency dependent effects.

Consider a damped vibration absorber attached to a single DOF system, as shown in Figure 1(a). Let m_s and k_s^* represent the effective mass and complex stiffness of the structure respectively and m_a and k_a^* represent the mass and complex stiffness of the absorber respectively.

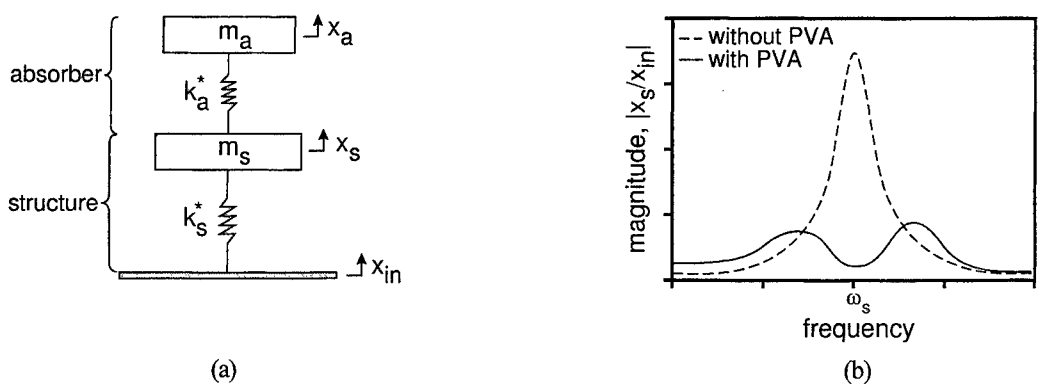

Figure 1. (a) PVA attached to single DOF system, (b) Sample frequency response function for the combined system

Equation (1) represents the ratio of the structural displacement, X_s, to the base disturbance displacement, X_{in}, in the Laplace domain (Note: the stiffness terms k_a and k_s are the real parts of the complex stiffnesses, k_a^* and k_s^* respectively; damping was assumed to be small and was removed to simplify the analysis).

$$\frac{X_s(s)}{X_{in}(s)} = \frac{k_s}{m_s s^2 + k_s} \tag{1}$$

The magnitude of the ratio of the structural displacement to the base disturbance displacement is shown by the dashed line in Figure 1(b). The natural frequency of the structure, ω_s, is directly proportional to the square root of the quantity k_s/m_s. Equation 2 represents the dynamics of combined absorber/structure system in the Laplace domain. If k_a is chosen in such a way that the natural frequency of the absorber is equal to the natural frequency of the structure and the damping is adjusted appropriately, then it is possible to obtain a system response similar to the solid line shown in Figure 1(b). Notice that it is possible to have an increase in response when the absorber is attached to the system and the input disturbance frequency deviates from ω_s.

$$\frac{X_s(s)}{X_{in}(s)} = \frac{m_a k_s s^2 + k_a k_s}{m_a m_s s^4 + \left(m_a\left(k_a + k_s\right) + m_s k_a\right)s^2 + k_a k_s} \tag{2}$$

Next consider a simple model of a piezoceramic inertial actuator, as shown in Figure 2. Like PVAs, inertial actuators consist of passive mass and complex stiffness elements. The difference between the two devices is the inclusion of a forcing element, F_p, in parallel with the complex spring of the inertial actuator. The most common form of inertial actuator, the voice-coil actuator, utilizes a coil and moving magnet for a forcing element. Recently, however, a new class of inertial actuator has been developed based on dual-unimorph displacement amplification of a piezoceramic forcing element.[12,13]

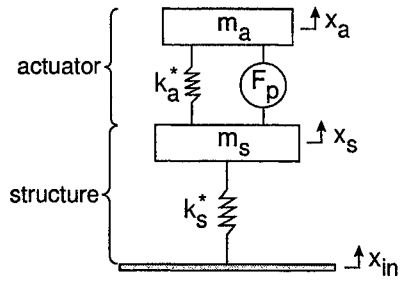

Figure 2. Inertial actuator attached to a single DOF structure model

Piezoceramic materials are capable of producing large forces but relatively small displacements (strains). The practical implementation of piezoceramics for actuation usually requires some form of piezoceramic strain amplification. Unimorph amplification is achieved by attaching one side of a piezoceramic plate or disk to a stiff cap (Figure 3(a)). The in-plane displacement of the piezoceramic causes the cap to displace in the transverse direction. The resulting transverse cap displacement is comparatively larger than the in-plane piezo displacement. Dual-unimorph amplification refers to placing two unimorphs in series in order to double the displacement amplification effect, as shown in Figure 3(b).

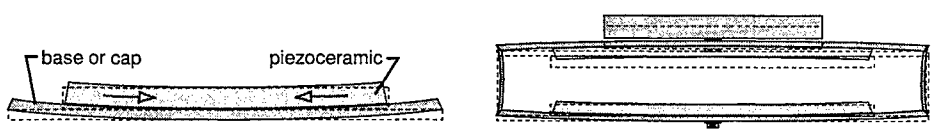

(a) unimorph (b) dual-unimorph inertial actuator

Figure 3. Unimorph actuation and the dual-unimorph inertial actuator

At this point, it is desirable to couple the electro-mechanical dynamics of the piezo elements to the mechanical dynamics of the PIA. To do this, the following forms of the piezoceramic constitutive equations were used:

$$F_p = k_{sc}\left(X_a - X_s\right) + d_{31}k_{sc}V \tag{3}$$

$$I = d_{31}k_{sc}s\left(X_a - X_s\right) - C_p^T sV \tag{4}$$

where F_p, V, and I are the force, voltage, and current respectively in the piezoceramic material, X_a and X_s are the displacements of masses m_a and m_b respectively, s is the Laplace parameter (s=iω), k_{sc} is the short circuit stiffness of the piezoceramic, d_{31} is the piezoceramic charge coefficient, and C_p^T is the capacitance of the piezoceramic measured under constant stress conditions. Equations (3) and (4) were coupled with the equation of motion for the PIA model shown in Figure 2, namely:

$$m_a s^2 X_a = -k_a\left(X_a - X_s\right) - F_p \tag{5}$$

The result is an expression for the ratio of the absorber mass displacement, X_a, to the structural displacement, X_s, in the Laplace domain:

$$\frac{X_a(s)}{X_s(s)} = \frac{k_a + k_{sc}^*}{m_a s^2 + k_a + k_{sc}^*} \tag{6}$$

In Equation (7), k_{sc}^* is a frequency dependent (and potentially complex) stiffness of the form:

$$k_{sc}^* = k_{sc}\left[1 + k_p^2 \frac{1}{1+\alpha(s)}\right] \tag{7}$$

where the piezo coupling coefficient is $k_p^2 = d_{31}^2\, k_{sc}/C_p^T$ and $\alpha(s)$ is the ratio of the electrical impedance of the open circuit piezo capacitance, $Z_{oc}(s)$, to the electrical impedance of the external shunt circuit, $Z_{sh}(s)$. The electrical impedance of the open circuit piezo measured under constant stress mechanical conditions, $Z_{oc}(s)$, can be expressed as:

$$Z_{oc}(s) = \frac{1}{sC_p^T} \tag{8}$$

The $\alpha(s)$ term in Equation (7) allows the effective piezoceramic stiffness, k_{sc}^*, to be tuned by changing the electrical impedance of the external shunt circuit. In the next section, two types of shunting will be examined analytically: capacitive and resistive. In each case, the goal is to determine the effect of varying the electrical shunt condition on the natural frequency and modal damping of the passive PIA model.

3. ANALYTICAL SHUNTING ANALYSIS

Equation (6) describes the response of a single DOF piezoceramic inertial actuator due to an input structural displacement disturbance as a function of the variable piezo stiffness, k_{sc}^*. By varying the impedance of an external shunt circuit, the natural frequency and, in some cases, the modal damping of the piezoceramic inertial actuator will vary. The objective of the investigation described in this section was to gain insight into the effects of capacitive and resistive shunting on natural the frequency and modal damping of a hypothetical PIA.

First, consider capacitively shunting the piezoceramic element of the PIA. Recall the expression for the ratio of open circuit electrical impedance of the piezoceramic to the electrical shunt impedance ($\alpha(s)=Z_{oc}(s)/Z_{sh}(s)$) in Equation (7). The electrical impedance of the shunt capacitor is:

$$Z_{sh}(s) = \frac{1}{sC_{sh}} \tag{9}$$

Thus, $\alpha(s)$ is equal to:

$$\alpha(s) = \frac{C_{sh}}{C_p^T} \tag{10}$$

Equation (7) is now a purely real stiffness that varies with a change in shunt capacitance. Notice that for a very large shunt capacitance (*i.e.*, approximately a short circuit electrical shunt condition), k_{sc}* approaches the nominal short circuit stiffness of the piezoceramic, k_{sc}. Conversely, as the shunt capacitance becomes much smaller than the capacitance of the piezoceramic (*i.e.*, approximately an open circuit electrical shunt condition), k_{sc}* approaches a value of $k_{sc}(1+k_p^2)$. For a planar piezo coupling coefficient of 0.6, the open circuit (*i.e.*, small shunt capacitance) piezo stiffness will be approximately 36% stiffer than the short circuit case.

Figure 4 illustrates the effect of varying the shunt capacitance on the natural frequency of a representative PIA. When C_{sh} is very small compared to C_p^T (*i.e.*, approaching open circuit) the natural frequency of the device is approximately 4.5% larger than the short circuit natural frequency (i.e., when C_{sh} is very large compared to C_p^T). Because the shunt capacitor is a purely reactive element, there are no loss terms and thus no change in damping.

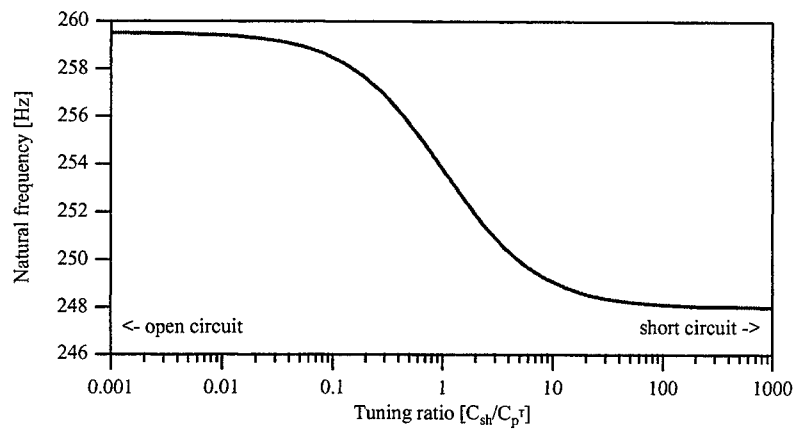

Figure 4. Capacitive shunting effect on the natural frequency of the PIA model

Next, consider resistive shunting of the piezo element of the PIA. In this case, the electrical impedance of the shunt resistor is simply:

$$Z_{sh}(s) = R_{sh} \tag{11}$$

Thus, $\alpha(s)$ is equal to:

$$\alpha(s) = \frac{1}{sR_{sh}C_p^T} \tag{12}$$

Define the natural frequency, ω_{rc}, of the RC-circuit corresponding to the combination of the shunt resistance and the piezo capacitance as:

$$\omega_{rc} = \frac{1}{R_{sh}C_p^T} \tag{13}$$

The effective piezo stiffness, k_{sc}* may then be expressed in a complex form in terms of the ratio of shunt circuit natural frequency to input frequency (ω_{rc}/ω) as follows:

$$k_{sc}^{*} = k_{sc}\left[\left\{1 + k_p^2 \frac{1}{1+\left(\frac{\omega_{rc}}{\omega}\right)^2}\right\} - i\left\{k_p^2 \frac{\left(\frac{\omega_{rc}}{\omega}\right)}{1+\left(\frac{\omega_{rc}}{\omega}\right)^2}\right\}\right] \tag{14}$$

The real part of k_{sc}* (*i.e.*, the storage modulus) has the same dependence on the tuning ratio as k_{sc}* has on the capacitance ratio in the capacitive shunting case. Furthermore, resistive elements also increase energy dissipation. Thus, for the resistive shunting case, additional damping may be introduced.

Figure 5 illustrates the effect of resistive shunting on the natural frequency and modal damping ratio of the PIA model. Notice that a tuning ratio of 1 corresponds to maximum system modal damping. Thus, both the natural frequency and damping of the passive PIA can be tuned using the shunt resistance.

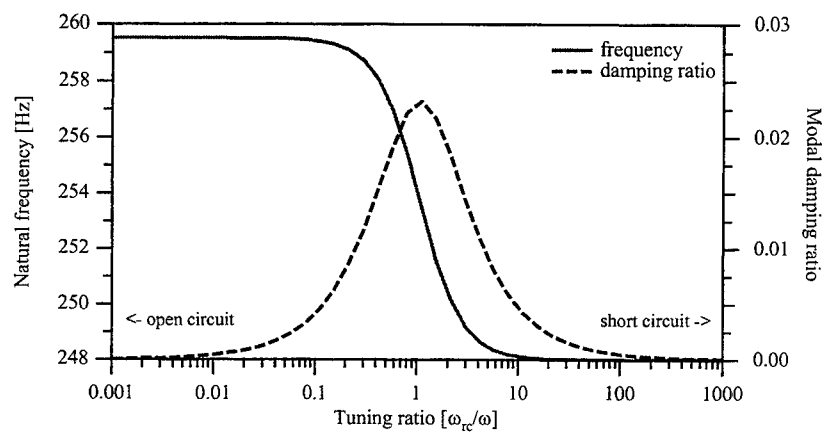

Figure 5. Resistive shunting effects on natural frequency and modal damping ratio of the PIA model

In the next section, experimental results are presented that show the effects of capacitive and resistive shunting on the natural frequency and modal damping ratios of a prototype piezoceramic inertial actuator.

4. EXPERIMENTAL SHUNTING RESULTS

A series of tests were performed to measure the natural frequency and modal damping ratio of a passive PIA. The tests conducted involved measuring the ratio of the acceleration of the actuator's reaction mass to the acceleration of the actuator's base for a variety of passive resistive and passive capacitive shunt circuits.

Figure 6 illustrates the experimental setup. A shaker was used to excite the actuator and two accelerometers were used to measure the actuator base (input) and reaction mass (output) accelerations. The acceleration of the base of the actuator could not be measured directly, but a reference accelerometer was mounted very close to the base of the actuator on a short aluminum bar also attached to the shaker. The flexibility of the aluminum bar limited the frequency range of the experiments because above approximately 2.0 kHz, the reference acceleration began to lag the mounting base acceleration.

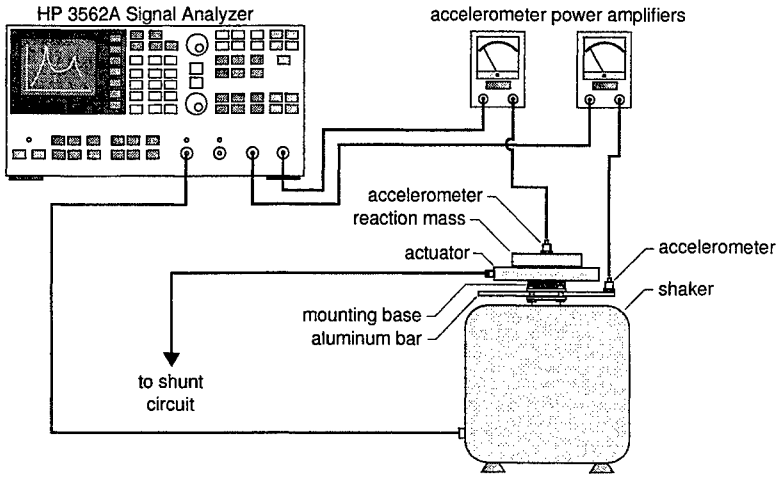

Figure 6. Experimental setup

Frequency response measurements were taken in the frequency range from 0 to 2000 Hz and averaged 30 times. Figure 7 illustrates a typical passive PIA frequency response function (FRF). The actuator was connected to a solderless breadboard where variable resistors or individual capacitors were used as shunt circuit elements. Resonant frequencies and modal damping ratios for the first mode of the actuator were calculated from *s*-domain curve fit estimates of the experimental FRFs.

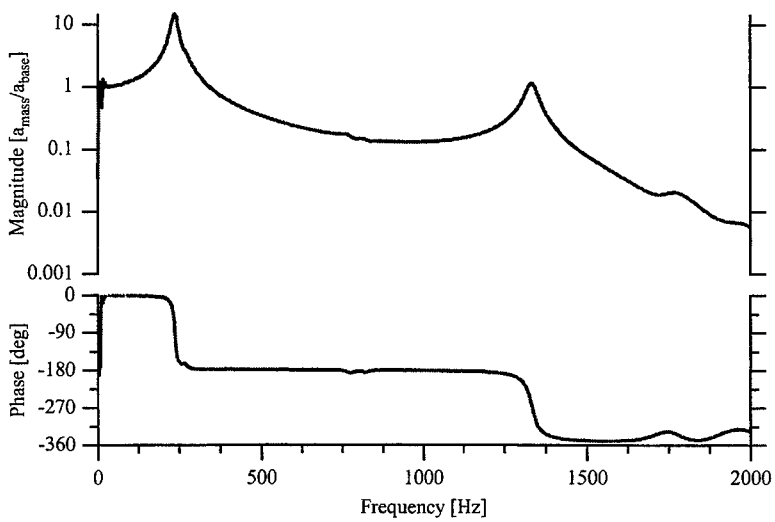

Figure 7. Sample experimental acceleration ratio frequency response function

Figure 8 illustrates the effects of capacitive shunting on both the actuator's fundamental natural frequency and the actuator's fundamental modal damping ratio. Note that the abscissa of the capacitive shunting plots represents the ratio of shunt capacitance to actuator capacitance (the actuator capacitance, C_p^T, was approximately 58 nF). In Figure 8, at very low values of capacitive shunt ratio (*i.e.*, close to open circuit electrical conditions) the fundamental natural frequency is approximately 258 Hz. As the shunt ratio increases, the fundamental natural frequency decreases, and as C_{sh}/C_p^T approaches infinity, the natural frequency asymptotically approaches a value of approximately 244 Hz (over a 5% change in natural frequency from short circuit to open circuit condition). Figure 8 also illustrates the effect of varying the shunt capacitance on the fundamental modal damping ratio. From the data, it appears that as the piezo becomes less stiff, there is a corresponding increase in modal damping ratio. Thus, the fundamental modal damping ratio ranges from roughly 3.2% for the open circuit case (C_{sh}/C_p^T very small) to approximately 4.0% for the short circuit case (C_{sh}/C_p^T very large). One explanation for the

increase in the fundamental mode's modal damping ratio from open circuit to short circuit is that as the piezo becomes less stiff with increasing shunt capacitance, a larger fraction of strain energy is imparted to the lossy material included in the actuator, thus raising the modal damping ratio.

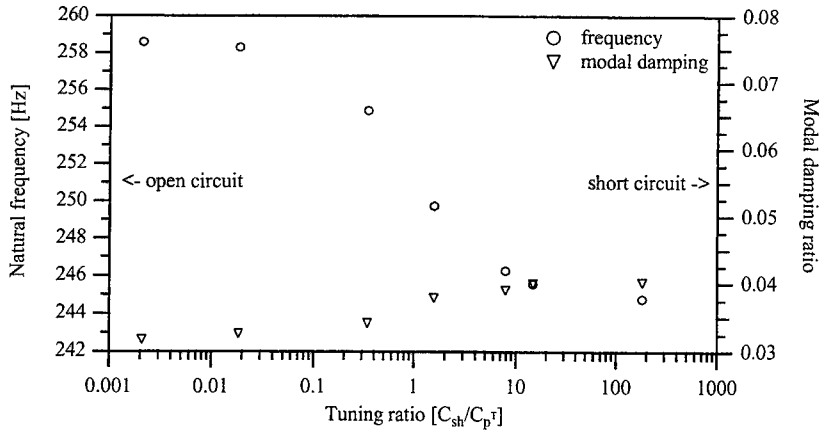

Figure 8. Experimental capacitive shunting results

Figure 9 illustrates the effects of resistive shunting on both the fundamental natural frequency and the modal damping ratio of the PIA. Note that the abscissa of the resistive shunting plots represents the ratio of the shunt circuit electrical natural frequency to the fundamental dynamic short circuit resonance frequency of the actuator. For very small tuning ratios (*i.e.*, approximately open circuit electrical conditions) the natural frequency of the fundamental mode of the actuator is approximately 257 Hz. For very large tuning ratios (*i.e.*, approximately short circuit electrical conditions) the natural frequency of the fundamental mode of the actuator is approximately 243 Hz (over a 5% change in natural frequency from short circuit to open circuit condition). A transition region exists between the open and short circuit limits. The mid-range of this transition occurs for a tuning ratio of approximately 1.0. As in the capacitive shunting case, there is a transition from the open circuit (small tuning ratio) modal damping ratio of approximately 3.2% to the short circuit (large tuning ratio) modal damping ratio of approximately 4.0%. However, for a tuning ratio of slightly greater than one, the modal damping ratio peaks at about 7%.

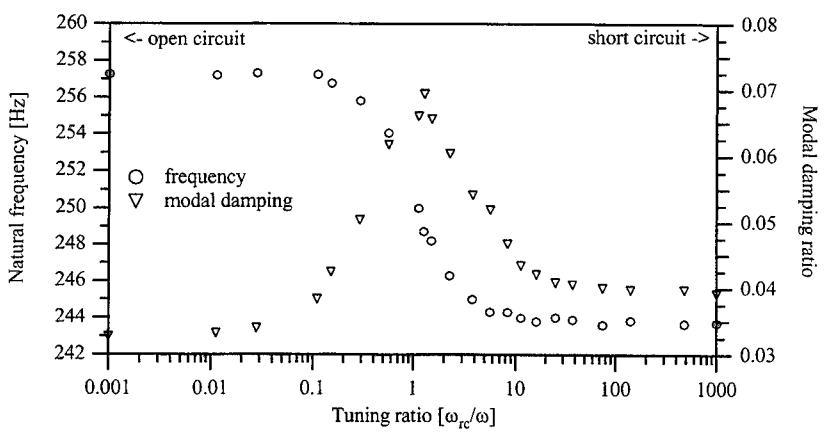

Figure 9. Experimental resistive shunting results

5. CONCLUSIONS

A shunting method for tuning the natural frequency and modal damping ratio of a piezoceramic inertial actuator has been developed. Shunting the actuator with a capacitor alters the stiffness of the piezoceramic forcing element, thus changing the

natural frequency of the device. Very large values of shunt capacitances (compared to the clamped capacitance of the piezoceramic forcing elements) correspond to a short circuit electrical boundary condition, while very small shunt capacitances correspond to an open circuit condition and have the effect of stiffening the piezo elements, in some cases, by more than a factor of 1/3. Large shunt resistances have the same effect on piezo stiffness as small shunt capacitances and, conversely, small shunt resistances have the same effect as large shunt capacitances. In addition, if the shunt resistance is chosen properly, such that the resonance frequency of the RC-circuit matches the mechanical vibration frequency of the PIA, damping may be significantly increased.

With the knowledge of the effects of capacitive and resistive shunting on both natural frequency and modal damping ratio of the passive PIA, it is conceivable to "coarse- tune" the actuator to a troublesome frequency by choosing an appropriate reaction mass and then "fine-tune" the actuator via capacitive or resistive shunting. In doing so, it may be possible to maintain a high degree of narrow-band vibration attenuation by keeping the PIA accurately tuned to the proper frequency. Because this approach is based on the use of passive electrical elements, it could also be readily used for on-line adjustment of an actuator to track a changing problem frequency.

ACKNOWLEDGEMENTS

This work was supported by the NASA Langley Research Center under a Phase II SBIR program (NAS1-20205).

REFERENCES

1. L. Pope, C. Willis, and W. Mayes, "Propeller aircraft interior noise model, part II: scale-model and flight-test comparisons," *Journal of Sound and Vibration* **118(3)**, pp. 469-493, 1987.
2. H. Kuntz and R. Prydz, "Interior noise in the untreated Gulfstream II propfan test assessment aircraft," *AIAA Journal of Aircraft* **27(7)**, pp. 647-652, 1990.
3. J. Unruh, "Structure-borne noise control for propeller aircraft," *AIAA Journal of Aircraft* **25(8)**, pp. 752-757, 1988.
4. A. von Flotow and M. Mercadal, "The measurement of noise and vibration transmitted into aircraft," *Sound and Vibration*, pp. 16-19, November 1995.
5. M. Simpson, "Cabin noise control ground tests for ultra high bypass aircraft," *AIAA Journal of Aircraft* **27(10)**, pp. 893-900, 1990.
6. J. Unruh, "Simulation of control of propeller induced structure-borne noise," *Noise Control Engineering Journal* **36(2)**, pp. 91-96, 1991.
7. N. Hagood and A. von Flotow, "Damping of structural vibrations with piezoelectric materials and passive electrical networks," *Journal of Sound and Vibration* **146(2)**, pp. 243-268, 1991.
8. C. Davis and G. Lesieutre, "A modal strain energy approach to the prediction of resistively shunted piezoceramic damping," *Journal of Sound and Vibration* **184(1)**, pp. 129-139, 1995.
9. J. Lai and K. Wang, "Parametric control of structural vibrations via adaptable stiffness dynamic absorbers," *Journal of Vibration and Acoustics* **118**, pp. 41-47, 1996
10. E. Waterman, D. Kaptein, and S. Sarin, "Fokker's activities in cabin noise control for propeller aircraft," *Proc. of the SAE Business Aircraft Meeting & Exposition*, SAE Paper No. 830736, 1983.
11. W. Halvosen and U. Emborg, "Interior noise control of the Saab 340 aircraft," *Proc. of the SAE General Aviation Aircraft Meeting & Exposition*, SAE Paper No. 891080, 1989.
12. G. Lesieutre, R. Rusovici, G. Koopmann, and J. Dosch, "Modeling and characterization of a piezoceramic inertial actuator," *Proc. of the 36th AIAA/ASME/ASCE/AHS Structures, Structural Dynamics & Materials Conference* **5**, pp. 3440-3449, 1995.
13. J. Dosch, G. Lesieutre, G. Koopmann, and C. Davis, "Inertial Piezoceramic Actuators for Smart Structures," *Proc. of the Smart Structures and Materials 1995 Industrial and Commercial Applications of Smart Structures Technologies Conference* **2447**, pp. 14-25, 1995.

Vibration control through passive constrained layer damping and active control

Margaretha J. Lam[a], Daniel J. Inman[b], and William R. Saunders[a]

[a]Department of Mechanical Engineering
[b]Department of Engineering Science
Virginia Polytechnic Institute and State University

ABSTRACT

To add damping to systems, viscoelastic materials (VEM) are added to structures. In order to enhance the damping effects of the VEM, a constraining layer is attached. When this constraining layer is an active element, the treatment is called active constrained layer damping (ACLD). Recently, the investigation of ACLD treatments has shown it to be an effective method of vibration suppression. In this paper, the treatment of a beam with a separate active element and passive constrained layer (PCLD) element will be investigated. A Ritz-Galerkin approach is used to obtain discretized equations of motion. The damping is modeled using the GHM method and the system is analyzed in the time domain. By optimizing on the performance and control effort for both the active and passive case, it will be shown that this treatment is capable of lower control effort with more inherent damping, and is therefore a better approach to damp vibration.

Keywords: passive constrained layer damping, active constrained layer damping, active control, viscoelastic material, optimal placement and size

1. INTRODUCTION

In the last few years, the area of active constrained layer damping (ACLD) has been shown to be an effective method of vibration suppression in structures.[1] It is advantageous to use ACLD as opposed to pure active control, due to the inherent damping present in the treatment. The control effort required is less than for the purely active case, and in some instances does give better performance.[2] The main advantage for using ACLD is in the event that the active element fails, the VEM will still damp vibration. This paper proposes the use of an active element (PZT) along with a passive constrained layer damping (PCLD) element to damp vibration. The active element is separate from the PCLD, so that the active element can actuate effectively. The PCLD treatment will improve robustness and reliability of the system and reduce vibration at the higher modes. It is shown through optimization of performance and control effort that the separate application of the PZT and PCLD give better performance than either then active, PCLD, or ACLD treatment. The damping will be modeled using the Golla-Hughes-McTavish (GHM) method.[3] The use of GHM to model damping of ACLD treatments was first developed by Lam, et al.[4] While the active model proposed in this paper has not be experimentally verified, a fully covered free-free beam was tested to verify the GHM modeling.

2. FORMULATION OF THE EQUATIONS

In this section, the equations of motion for a clamped-free beam with an active element as well as PCLD will be derived (see figure 1).

The kinetic, **E**, and potential, **T**, energy equations for a beam with a PZT, assumed to be perfectly bonded, and a PCLD patch are

Further Author Correspondence:
M.J.L.: Email: mjlam@cooper.edu; WWW: http://rio.esm.vt.edu/group/mjlam/mjlam.html; Telephone: (212)-353-4307
D.J.I.: Email: dinman@vt.edu; WWW: http://www.esm.vt.edu/chals/faclist/inman.html; Telephone: (540)-231-4709
W.R.S.: Email: saunders@stnick.me.vt.edu; WWW: http://www.me.vt.edu/ME/people/faculty/saunders.html; Telephone: (540)-231-7295

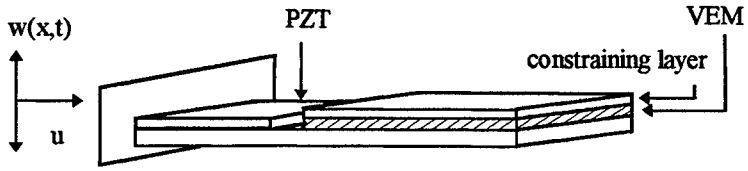

Figure (1). Beam with separate active and PCLD treatment.

$$\mathbf{T}_b = \frac{1}{2}\int_0^L \rho_b A_b \left[\left(\frac{\partial u_b}{\partial t}\right)^2 + \left(\frac{\partial w}{\partial t}\right)^2\right] dx \tag{1}$$

$$\mathbf{T}_p = \frac{1}{2}\int_0^L \rho_p A_p \left[\left(\frac{\partial u_p}{\partial t}\right)^2 + \left(\frac{\partial w}{\partial t}\right)^2\right]\left[\mathrm{H}(x-x_1) - \mathrm{H}(x-x_2)\right] dx \tag{2}$$

$$\mathbf{T}_s = \frac{1}{2}\int_0^L \rho_s A_s \left[\left(\frac{\partial u_s}{\partial t}\right)^2 + \left(\frac{\partial w}{\partial t}\right)^2\right]\left[\mathrm{H}(x-x_3) - \mathrm{H}(x-x_4)\right] dx \tag{3}$$

$$\mathbf{T}_c = \frac{1}{2}\int_0^L \rho_c A_c \left[\left(\frac{\partial u_c}{\partial t}\right)^2 + \left(\frac{\partial w}{\partial t}\right)^2\right]\left[\mathrm{H}(x-x_3) - \mathrm{H}(x-x_4)\right] dx \tag{4}$$

$$\mathbf{E}_b = \frac{1}{2}\int_0^L \left[E_b A_b \left(\frac{\partial u_b}{\partial x}\right)^2 + E_b I_b \left(\frac{\partial^2 w}{\partial x^2}\right)^2\right] dx \tag{5}$$

$$\mathbf{E}_p = \frac{1}{2}\int_0^L \left[C_{11}^D A_p \left(\frac{\partial u_p}{\partial x}\right)^2 + C_{11}^D I_p \left(\frac{\partial^2 w}{\partial x^2}\right)^2 - 2A_p h_{31} D \frac{\partial u_p}{\partial x} + A_p \beta_{33}^S D^2\right]\left[\mathrm{H}(x-x_1) - \mathrm{H}(x-x_2)\right] dx \tag{6}$$

$$\mathbf{E}_s = \frac{1}{2}\int_0^L \left[E_s A_s \left(\frac{\partial u_s}{\partial x}\right)^2 + E_s I_s \left(\frac{\partial^2 \psi}{\partial x^2}\right)^2\right]\left[\mathrm{H}(x-x_3) - \mathrm{H}(x-x_4)\right] dx \tag{7}$$

$$\mathbf{E}_c = \frac{1}{2}\int_0^L \left[E_c A_c \left(\frac{\partial u_c}{\partial x}\right)^2 + E_c I_c \left(\frac{\partial^2 w}{\partial x^2}\right)^2\right]\left[\mathrm{H}(x-x_3) - \mathrm{H}(x-x_4)\right] dx \tag{8}$$

where the subscript b denotes the beam, p the active layer, s the shear layer, and c the cover plate. The transverse displacement is denoted by w, the longitudinal displacement by u, and the shear angle of the VEM by Ψ. The equations for the virtual work done by the viscoelastic layer (subscript g), applied voltage of the piezoelectric element and externally applied forces are

$$\mathbf{E}_g = \frac{1}{2}\int_0^L \left[G A_s \left(\frac{\partial w}{\partial x} - \psi\right)^2\right]\left[\mathrm{H}(x-x_3) - \mathrm{H}(x-x_4)\right] dx \tag{9}$$

$$\delta \mathbf{W}_p = \int_0^L b V(t) \delta D \left[H(x-x_1) - H(x-x_2)\right] dx \tag{10}$$

$$\delta \mathbf{W}_f = \int_0^L f(x,t) \delta w(x,t) dx \tag{11}$$

respectively. G is the complex modulus which will be modeled using GHM. Using Hamilton's Principle and equations (1)-(11), three equations of motion can be derived.

$$\rho_b A_b \frac{\partial^2 w}{\partial t^2} + E_b I_b \frac{\partial^4 w}{\partial x^4} + \left[\rho_p A_p \frac{t_b + t_p}{2}\left(\frac{\partial^3 u_b}{\partial x \partial t^2} - \frac{t_b + t_p}{2}\frac{\partial^4 w}{\partial x^2 \partial t^2}\right) + \rho_p A_p \frac{\partial^2 w}{\partial t^2} - C_{11}^D A_p \frac{t_b + t_p}{2}\left(\frac{\partial^3 u_b}{\partial x^3} - \frac{t_b + t_p}{2}\frac{\partial^4 w}{\partial x^4}\right) + C_{11}^D I_p \frac{\partial^4 w}{\partial x^4}\right]$$

$$
\begin{aligned}
&[\mathrm{H}(x-x_1)-\mathrm{H}(x-x_2)]+\Bigg[(\rho_s A_s+\rho_c A_c)\frac{\partial^2 w}{\partial t^2}+\rho_s A_s\frac{t_b}{2}\left(\frac{\partial^3 u_b}{\partial x\partial t^2}-\frac{t_b}{2}\frac{\partial^4 w}{\partial x^2\partial t^2}-\frac{t_s}{2}\frac{\partial^3\psi}{\partial x\partial t^2}\right)\\
&+\rho_c A_c\frac{t_b+t_c}{2}\left(\frac{\partial^3 u_b}{\partial x\partial t^2}-\frac{t_b+t_c}{2}\frac{\partial^4 w}{\partial x^2\partial t^2}-t_s\frac{\partial^3\psi}{\partial x\partial t^2}\right)-E_s A_s\frac{t_b}{2}\left(\frac{\partial^3 u_b}{\partial x^3}-\frac{t_b}{2}\frac{\partial^4 w}{\partial x^4}-\frac{t_s}{2}\frac{\partial^3\psi}{\partial x^3}\right)\\
&-E_c A_c\frac{t_b+t_c}{2}\left(\frac{\partial^3 u_b}{\partial x^3}-\frac{t_b+t_c}{2}\frac{\partial^4 w}{\partial x^4}-t_s\frac{\partial^3\psi}{\partial x^3}\right)+E_c I_c\frac{\partial^4 w}{\partial x^4}+GA_s\left(-\frac{\partial^2 w}{\partial x^2}+\frac{\partial\psi}{\partial x}\right)\Bigg][\mathrm{H}(x-x_3)-\mathrm{H}(x-x_4)]\\
&+\Bigg[-\rho_p A_p\frac{t_b+t_p}{2}\left(\frac{\partial^2 u_b}{\partial t^2}-\frac{t_b+t_p}{2}\frac{\partial^3 w}{\partial x\partial t^2}\right)+2C_{11}^D A_p\frac{t_b+t_p}{2}\left(\frac{\partial^2 u_b}{\partial x^2}-\frac{t_b+t_p}{2}\frac{\partial^3 w}{\partial x^3}\right)-2C_{11}^D I_p\frac{\partial^3 w}{\partial x^3}+C_{11}^D I_p\frac{\partial^2 w}{\partial x^2}\\
&-C_{11}^D A_p\frac{t_b+t_p}{2}\left(\frac{\partial u_b}{\partial x}-\frac{t_b+t_p}{2}\frac{\partial^2 w}{\partial x^2}\right)\Bigg][\delta(x-x_2)-\delta(x-x_1)]+\Bigg[-\rho_s A_s\frac{t_b}{2}\left(\frac{\partial^2 u_b}{\partial t^2}-\frac{t_b}{2}\frac{\partial^3 w}{\partial x\partial t^2}-\frac{t_s}{2}\frac{\partial^2\psi}{\partial t^2}\right)\\
&-\rho_c A_c\frac{t_b+t_c}{2}\left(\frac{\partial^2 u_b}{\partial t^2}-\frac{t_b+t_c}{2}\frac{\partial^3 w}{\partial x\partial t^2}-t_s\frac{\partial^2\psi}{\partial t^2}\right)+E_s A_s\frac{t_b}{2}\left(2\left(\frac{\partial^2 u_b}{\partial x^2}-\frac{t_b}{2}\frac{\partial^3 w}{\partial x^3}-\frac{t_s}{2}\frac{\partial^2\psi}{\partial x^2}\right)-\left(\frac{\partial u_b}{\partial x}-\frac{t_b}{2}\frac{\partial^2 w}{\partial x^2}-\frac{t_s}{2}\frac{\partial\psi}{\partial x}\right)\right)\\
&+E_c A_c\frac{t_b+t_c}{2}\left(2\left(\frac{\partial^2 u_b}{\partial x^2}-\frac{t_b+t_c}{2}\frac{\partial^3 w}{\partial x^3}-t_s\frac{\partial^2\psi}{\partial x^2}\right)-\left(\frac{\partial u_b}{\partial x}-\frac{t_b+t_c}{2}\frac{\partial^2 w}{\partial x^2}-t_s\frac{\partial\psi}{\partial x}\right)\right)-2E_c I_c\frac{\partial^3 w}{\partial x^3}+E_c I_c\frac{\partial^2 w}{\partial x^2}\\
&+GA_s\left(\frac{\partial w}{\partial x}-\psi\right)\Bigg][\delta(x-x_4)-\delta(x-x_3)]+\left[C_{11}^D A_p\frac{t_b+t_p}{2}\left(\frac{\partial u_b}{\partial x}-\frac{t_b+t_p}{2}\frac{\partial^2 w}{\partial x^2}\right)-C_{11}^D I_p\frac{\partial^2 w}{\partial x^2}-bd_{31}C_{11}^D\frac{t_b+t_p}{2}V(t)\right]\\
&[\delta'(x-x_2)-\delta'(x-x_1)]+\Bigg[E_s A_s\frac{t_b}{2}\left(\frac{\partial u_b}{\partial x}-\frac{t_b}{2}\frac{\partial^2 w}{\partial x^2}-\frac{t_s}{2}\frac{\partial\psi}{\partial x}\right)+E_c A_c\frac{t_b+t_p}{2}\left(\frac{\partial u_b}{\partial x}-\frac{t_b+t_p}{2}\frac{\partial^2 w}{\partial x^2}-t_s\frac{\partial\psi}{\partial x}\right)\\
&-E_c I_c\frac{\partial^2 w}{\partial x^2}\Bigg][\delta'(x-x_4)-\delta'(x-x_3)]=f(x,t)
\end{aligned}
\tag{12}
$$

$$
\begin{aligned}
&\rho_b A_b\frac{\partial^2 u_b}{\partial t^2}-E_b A_b\frac{\partial^2 u_b}{\partial x^2}+\left[\rho_p A_p\left(\frac{\partial^2 u_b}{\partial t^2}-\frac{t_b+t_p}{2}\frac{\partial^3 w}{\partial x\partial t^2}\right)-C_{11}^D A_p\left(\frac{\partial^2 u_b}{\partial x^2}-\frac{t_b+t_p}{2}\frac{\partial^3 w}{\partial x^3}\right)\right][\mathrm{H}(x-x_1)-\mathrm{H}(x-x_2)]\\
&+\Bigg[\rho_s A_s\left(\frac{\partial^2 u_b}{\partial t^2}-\frac{t_b}{2}\frac{\partial^3 w}{\partial x\partial t^2}-\frac{t_s}{2}\frac{\partial^2\psi}{\partial t^2}\right)+\rho_c A_c\left(\frac{\partial^2 u_b}{\partial t^2}-\frac{t_b+t_c}{2}\frac{\partial^3 w}{\partial x\partial t^2}-t_s\frac{\partial^2\psi}{\partial t^2}\right)-E_s A_s\left(\frac{\partial^2 u_b}{\partial x^2}-\frac{t_b}{2}\frac{\partial^3 w}{\partial x^3}-\frac{t_s}{2}\frac{\partial^2\psi}{\partial x^2}\right)\\
&-E_c A_c\left(\frac{\partial^2 u_b}{\partial x^2}-\frac{t_b+t_c}{2}\frac{\partial^3 w}{\partial x^3}-t_s\frac{\partial^2\psi}{\partial x^2}\right)\Bigg][\mathrm{H}(x-x_3)-\mathrm{H}(x-x_4)]+\left[C_{11}^D A_p\left(\frac{\partial u_b}{\partial x}-\frac{t_b+t_c}{2}\frac{\partial^2 w}{\partial x^2}\right)-bd_{31}C_{11}^D\frac{t_b+t_c}{2}V(t)\right]\\
&[\delta(x-x_2)-\delta(x-x_1)]+\left[E_s A_s\left(\frac{\partial u_b}{\partial x}-\frac{t_b}{2}\frac{\partial^2 w}{\partial x^2}-\frac{t_s}{2}\frac{\partial\psi}{\partial x}\right)+E_c A_c\left(\frac{\partial u_b}{\partial x}-\frac{t_b+t_c}{2}\frac{\partial^2 w}{\partial x^2}-t_s\frac{\partial\psi}{\partial x}\right)\right][\delta(x-x_4)-\delta(x-x_3)]=0
\end{aligned}
\tag{13}
$$

$$
\begin{aligned}
&\Bigg[\rho_s A_s\frac{t_s}{2}\left(\frac{\partial^2 u_b}{\partial t^2}-\frac{t_b}{2}\frac{\partial^3 w}{\partial x\partial t^2}-\frac{t_s}{2}\frac{\partial^2\psi}{\partial t^2}\right)+\rho_c A_c t_s\left(\frac{\partial^2 u_b}{\partial t^2}-\frac{t_b+t_c}{2}\frac{\partial^3 w}{\partial x\partial t^2}-t_s\frac{\partial^2\psi}{\partial t^2}\right)+E_s I_s\frac{\partial^2\psi}{\partial x^2}\\
&-E_s A_s\frac{t_s}{2}\left(\frac{\partial^2 u_b}{\partial x^2}-\frac{t_b}{2}\frac{\partial^3 w}{\partial x^3}-\frac{t_s}{2}\frac{\partial^2\psi}{\partial x^2}\right)-E_c A_c t_s\left(\frac{\partial^2 u_b}{\partial x^2}-\frac{t_b+t_c}{2}\frac{\partial^3 w}{\partial x^3}-t_s\frac{\partial^2\psi}{\partial x^2}\right)-GA_s\left(\psi-\frac{\partial w}{\partial x}\right)\Bigg][\mathrm{H}(x-x_4)-\mathrm{H}(x-x_3)]\\
&+\left[E_s A_s\frac{t_s}{2}\left(\frac{\partial u_b}{\partial x}-\frac{t_b}{2}\frac{\partial^2 w}{\partial x^2}-\frac{t_s}{2}\frac{\partial\psi}{\partial x}\right)-E_s I_s\frac{\partial\psi}{\partial x}+E_c A_c t_s\left(\frac{\partial u_b}{\partial x}-\frac{t_b+t_c}{2}\frac{\partial^2 w}{\partial x^2}-t_s\frac{\partial\psi}{\partial x}\right)\right][\delta(x-x_4)-\delta(x-x_3)]=0
\end{aligned}
\tag{14}
$$

with boundary conditions

$$
x=0;\quad w=0;\quad \frac{\partial w}{\partial x}=0;\quad u_b=0 \tag{15}
$$

$$
x=L;\quad \frac{\partial^2 w}{\partial x^2}=0;\quad \frac{\partial^3 w}{\partial x^3}=0;\quad \frac{\partial u_b}{\partial x}=0 \tag{16}
$$

For more detail on the derivation, see Liao and Wang.[2] A Ritz-Galerkin approach is used to discretize the equations into a set of ordinary differential equations. Three spatially dependent functions were chosen that satisfied the boundary conditions: clamped-free beam (transverse motion of beam), clamped-free bar (longitudinal motion of beam) and a free-free bar (longitudinal motion of constraining layer).[5]

3. GOLLA-HUGHES-McTAVISH METHOD

The Golla-Hughes-McTavish (GHM) modeling approach models hysteretic damping.[3] This is achieved by adding additional "dissipation coordinates" to the system to achieve a linear non hysteretic model providing the same damping properties. The dissipation coordinates are used with the discretized equations of motion (equations (12) and (13)). Linear matrix-second-order form is maintained as well as symmetry and definiteness of the augmented system matrices. The time domain stress relaxation is modeled by a modulus function in the Laplace domain.

A system which has viscoelastic damping is often modeled as having a complex modulus. However, use of the complex modulus directly in the equation of motion leads to a dynamic model useful only at single-frequency steady-state excitations. The GHM approach provides an alternative method which includes viscoelastic damping effects without the restriction of steady-state motion by providing extra coordinates. This complex modulus can be written in Laplace domain as

$$G^*(s) = G_0(1+h(s)) = G_0\left(1+\sum_{n=1}^{k}\hat{\alpha}_n \frac{s^2+2\hat{\zeta}_n\hat{\omega}_n s}{s^2+2\hat{\zeta}_n\hat{\omega}_n s+\hat{\omega}_n^2}\right) \tag{17}$$

where G_0 is the equilibrium value of the modulus, i.e. the final value of the relaxation function $G(t)$, and s is the Laplace domain operator. The hatted terms are obtained from the curve fit to the complex modulus data for a particular VEM. The expansion of $h(s)$ represents the material modulus as a series of mini-oscillator (second order equation) terms (McTavish and Hughes, 1987). The number of terms kept in the expansion will be determined by the high or low frequency dependence of the complex modulus. In many cases only two to four terms are necessary.

The equation of motion in the Laplace domain is

$$\mathbf{M}\left(s^2\mathrm{x}(s) - s\mathrm{x}_0 - \dot{\mathrm{x}}_0\right) + \mathbf{K}(s)\mathrm{x}(s) = \mathrm{F}(s) \tag{18}$$

where $\mathbf{M}$ is the mass matrix, $\mathbf{K}$ the complex stiffness matrix, $\boldsymbol{F}$ the forcing function, and $\boldsymbol{x}_0$ and $\dot{\boldsymbol{x}}_0$ the initial conditions. The complex stiffness matrix can be written as the summation of the contributions of the n complex moduli to the stiffness matrix such that

$$\mathbf{K}(s) = \left(G_1^*(s)\overline{\mathbf{K}}_1 + G_2^*(s)\overline{\mathbf{K}}_2 + \cdots + G_n^*(s)\overline{\mathbf{K}}_n\right) \tag{19}$$

where G_n^* refers to the nth complex modulus and $\overline{\mathbf{K}}_n$ to the contribution of the nth modulus to the stiffness matrix. For simplicity, assume a complex modulus model with a single expansion term and zero initial conditions, so equation (19) can be written as

$$\mathbf{M}s^2\mathrm{x}(s) + G_0\left(1+\hat{\alpha}\frac{s^2+2\hat{\zeta}\hat{\omega}s}{s^2+2\hat{\zeta}\hat{\omega}s+\hat{\omega}^2}\right)\overline{\mathbf{K}}\mathrm{x}(s) = \boldsymbol{F}(s) \tag{20}$$

In this formulation all of the eigenvalues have dissipation modes associated with them. After some manipulation, equation (20) can be written as

$$\begin{bmatrix} \mathbf{M} & \mathbf{0} \\ \mathbf{0} & \frac{\hat{\alpha}}{\hat{\omega}^2} G_0 \mathbf{I} \end{bmatrix} \begin{bmatrix} \mathrm{x}(s) \\ \mathrm{z}(s) \end{bmatrix} s^2 + \begin{bmatrix} \mathbf{0} & \mathbf{0} \\ \mathbf{0} & \frac{2\hat{\alpha}\hat{\zeta}}{\hat{\omega}} G_0 \mathbf{I} \end{bmatrix} \begin{bmatrix} \mathrm{x}(s) \\ \mathrm{z}(s) \end{bmatrix} s + \begin{bmatrix} (1+\hat{\alpha}) G_0 \overline{\mathbf{K}} & -\hat{\alpha} G_0 \overline{\mathbf{K}} \\ -\hat{\alpha} G_0 \mathbf{I} & \hat{\alpha} G_0 \mathbf{I} \end{bmatrix} \begin{bmatrix} \mathrm{x}(s) \\ \mathrm{z}(s) \end{bmatrix} = \begin{bmatrix} \mathrm{F}(s) \\ \mathbf{0} \end{bmatrix}. \quad (21)$$

This is the final form of the Golla-Hughes-McTavish model as described by McTavish and Hughes.[3]

In order to model the behavior of the VEM which partially covers a beam, the stiffness and mass matrices for the covered area are first assembled, in this case just the terms relating to the PCLD. The effects of the dissipation modes on the system are calculated as described above. The full mass and stiffness matrices for the whole beam are assembled, using the mass and stiffness matrices obtained from equation (21) to model the effects of the VEM on the whole structure. The order of the system increases as the number of terms in the expansion are kept, which increases the accuracy for modeling the damping effects.

4. EXPERIMENTAL VERIFICATION OF GHM METHOD

In order to verify the accuracy of the GHM model, an experiment was performed on a fully covered, free-free aluminum beam. The dimension of the beam were 15 in. long, 1.5 in. wide and 0.125 in. thick. It was suspended from the ceiling with fish wire which was attached 1 in. from either end. The beam was excited using an impact hammer, applied at the center of the beam. The accelerometer was placed on the other side of the beam also in the center. The placement of the impact and sensor was chosen to minimize excitation of the torsional modes. The constraining layer was a beam of the same dimensions as the base beam, thus creating a sandwich beam. The beam was tested with 5 mil and 10 mil thick 3M ISD 112 VEM.[6] This was done to insure that the GHM model accounted for the increase in damping with the increase in thickness.

Figure (2) shows the acceleration bode plots for the experimental (dashed) and the analytical (solid) transfer functions. The units of the magnitude curve are g/N. As can be seen, there is good correlation in both the magnitude and phase for the first and third mode for both thicknesses. The correlation starts to break down for the fifth mode. This is due to the fact that the accelerometer was attached to the beam using wax. The accurate data range for wax is about 0 - 2000 Hz.[7] The GHM model included three summations in the expansion of the material properties. The constants were found to be $G_0 = 5\text{x}10^4$, $\hat{\alpha} = [9.6 \;\; 99.1 \;\; 26.2]$, $\hat{\zeta} = [73.4 \;\; 1.1 \;\; 3.28]$, and $\hat{\omega} = [1 \;\; 2 \;\; 0.5]\text{x}10^4$. It was necessary to include three terms to assure that the damping was modeled over the full frequency range of interest.

5. OPTIMAL PLACEMENT AND SIZING OF PZT AND PCLD

The placing and size of the passive constrained layer and the piezoelectric patch were determined using two optimization routines. For the passive case, the energy of the states was minimized. The optimal placement and size for the active case

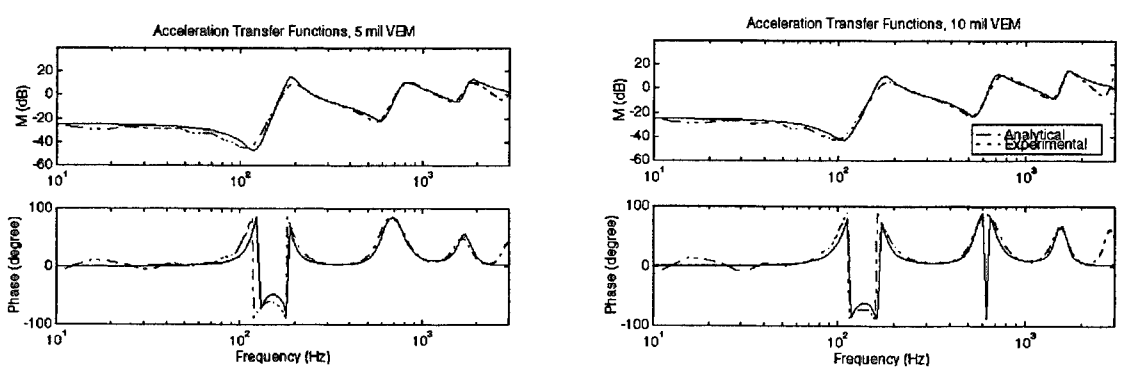

Figure (2). Analytical and Experimental Transfer Functions using 5 and 10 mil ISD 112

was determined using LQR.[8] The cost function for the passive case is

$$J_p = \int_0^\infty \left(\underline{x}^T Q_1 \underline{x} \right) dt \tag{22}$$

where $\underline{x}$ is the state vector, and Q_1 is a semi positive-definite (SPD) weighting matrix. Equation (22) is minimized as the length and placement of the PCLD treatment is varied such that

$$J_{\min,p} = \underline{x}_0^T P_1 \underline{x}_0 . \tag{23}$$

where $\underline{x}_0^T$ is a vector of initial states and P_1 is the unique positive definite solution to the Ricatti type equation

$$P_1 A + A^T P_1 = -Q_1 . \tag{24}$$

The cost function for the active case is

$$J_a = \int_0^\infty \left(\underline{y}^T Q \underline{y} + \underline{u}^T R \underline{u} \right) dt \tag{25}$$

where $\underline{y}$ is the output vector, and Q and R are SPD and positive definite weighting functions respectively. A higher value on Q means more vibration suppression, while a higher value on R signifies greater limit on the control effort. The minimum of this cost function, equation (25), is defined as

$$J_{\min,a} = \underline{x}_0^T P \underline{x}_0 \tag{26}$$

where the length and placement of the PZT patch is varied. P is satisfies the Ricatti equation

$$PA + A^T P - PBR^{-1} B^T P = -Q . \tag{27}$$

The corresponding control law is given as

$$\underline{u} = -K_c \underline{x} \tag{28}$$

where $K_c = R^{-1} B^T P$.

6. NUMERICAL EXAMPLE

In this example, a cantilevered aluminum beam with different treatments was considered. The beam was 15 in. long, 1.5 in. wide, 0.125 in. thick, (0.381 x 0.0381 x 0.003175 m), and had a density of 2710 kg/m^3. Young's modulus for the beam was assumed to be 70x10^9 Pa. The PZT had a density of 7600 kg/m^3 and was 0.02 in (0.5 mm) thick. This thickness is one of the standard thicknesses available. The elastic modulus was 6.3x10^{10} Pa and the electromechanical coupling coefficient, d_{31}, was -109x10^{-12}. The VEM was assumed to be 5 mil thick ISD 112, and was modeled using the same GHM parameters as delineated in section 4 with three terms in the summation. The density was set at 1000 kg/m^3 and the thickness was 5 mil (0.127 mm). The constraining layer was assumed to be aluminum with the same thickness of the beam. The minimal length for any treatment was set at 1 cm. Since neither the PCLD nor PZT can be clamped, the constraint on its placement was 1 mm from the base. In the hybrid case, there was assumed to be at least a 1 mm space between treatments. The equations of motion (equations (12)-(14)) were discretized using a five term expansion. The excitation force was assumed to be a unit impulse function, applied at 0.9L. The transverse displacement was measured at the tip. For either optimization

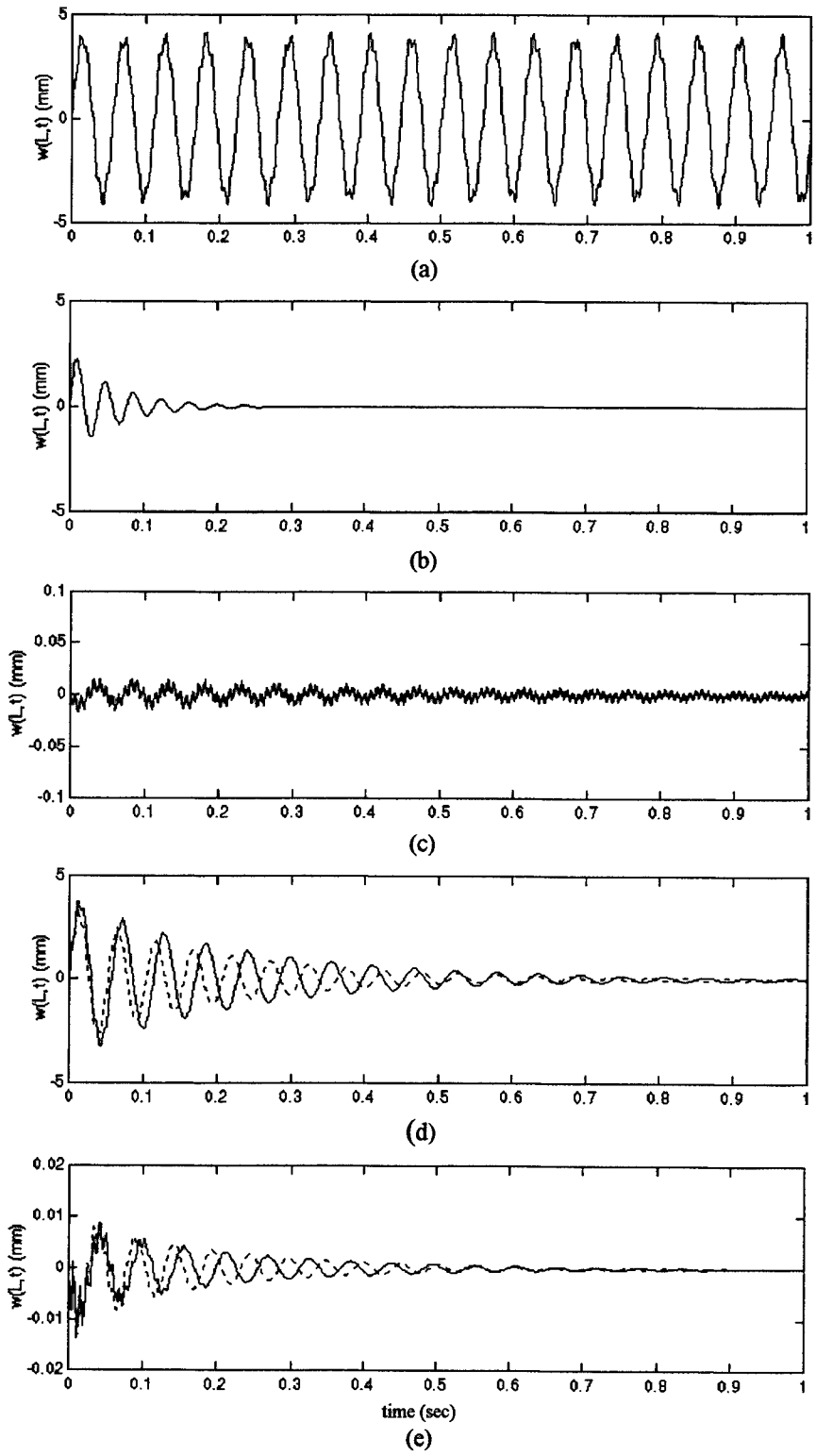

Figure 3. Time responses for optimal configuration of (a) plain beam, (b) beam with PCLD, (c) beam with active PZT, (d) beam with passive ACLD, (e) beam with active ACLD. (for (d) and (e), solid line: passive optimization, dashed: active optimization)

	L_{pcld} (m)	start PCLD (m)	L_{pzt} (m)	start PZT (m)	$J_{min,p}$	$J_{min,a}$
PCLD	0.35	0.011			1313	
active			0.277	0.001		3.543e5
ACLD - passive	0.36	0.001	0.36	0.001	2686	
ACLD - active	0.27	0.001	0.27	0.001		8.157e4
hybrid -passive	0.357	0.001	0.01	0.001	1510	
hybrid - active	0.262	0.001	0.01	0.001		2.413e4

Table 1. Optimal lengths and placements for different treatments and the minimum cost functions (start refers to the starting point of the treatment from clamped end).

scheme, only the transverse modes were weighted. To find the minimum passive cost function, $J_{min,p}$, equations (22) - (24) were used, where the weighting matrix, Q_1, was 0.1I for the transverse modes (I is the identity matrix), and zeros elsewhere. Equations (25) - (28) were used to find the minimum cost function, $J_{min,a}$, for the active case. In this case, the weighting matrix, Q, was 10^9I for the transverse modes, and zeros for all others.

The time responses for tip displacement in the transverse direction of a clamped aluminum beam with different treatments are shown in figures 3 and 4. The optimal lengths and placements of those treatments, as well as the minimal cost functions can be found in table 1. The time response of a clamped aluminum beam without any treatment is shown in figure 3(a). The optimal placement and size of a PCLD patch was investigated and its response is given in figure 3(b). The time response of the purely active case is shown in figure 3(c). The beam with ACLD performs better than a PZT patch. The time response for the passive case is shown in figure 3(d) where the solid line represents the length of the ACLD by minimizing the passive cost function, while the dashed line represents the minimum active cost function. In figure 3(e), the time response for an active ACLD is given. Note that there is little response to an impulse function. The main advantage of using ACLD over a PZT is that the active cost function is an order of magnitude lower and in case of failure, there still is passive damping available. For a purely passive response, just applying a PCLD is more effective in this example, however, the benefit of the active element is clearly shown in figure 3(e).

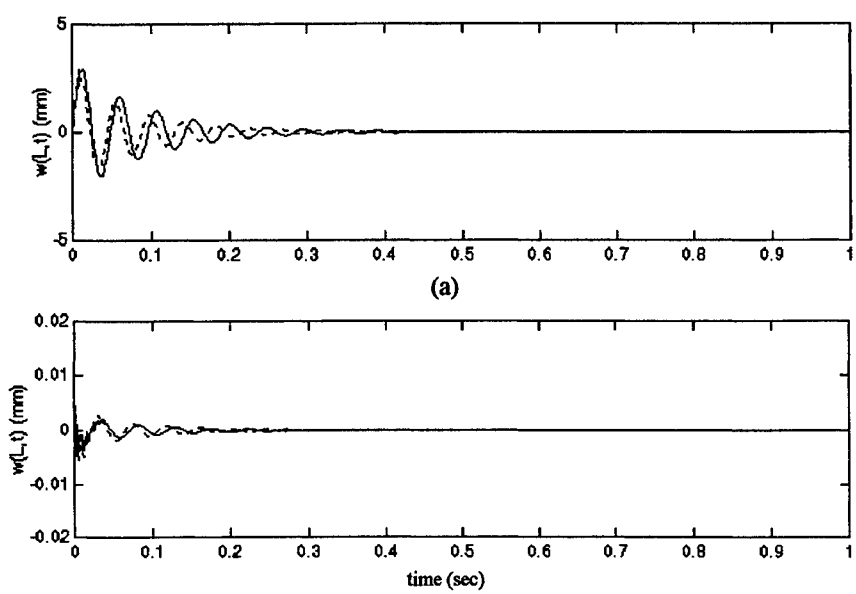

Figure 4. Time response for the optimal configuration of a hybrid PZT and PCLD treatment (a) without control, (b) with control

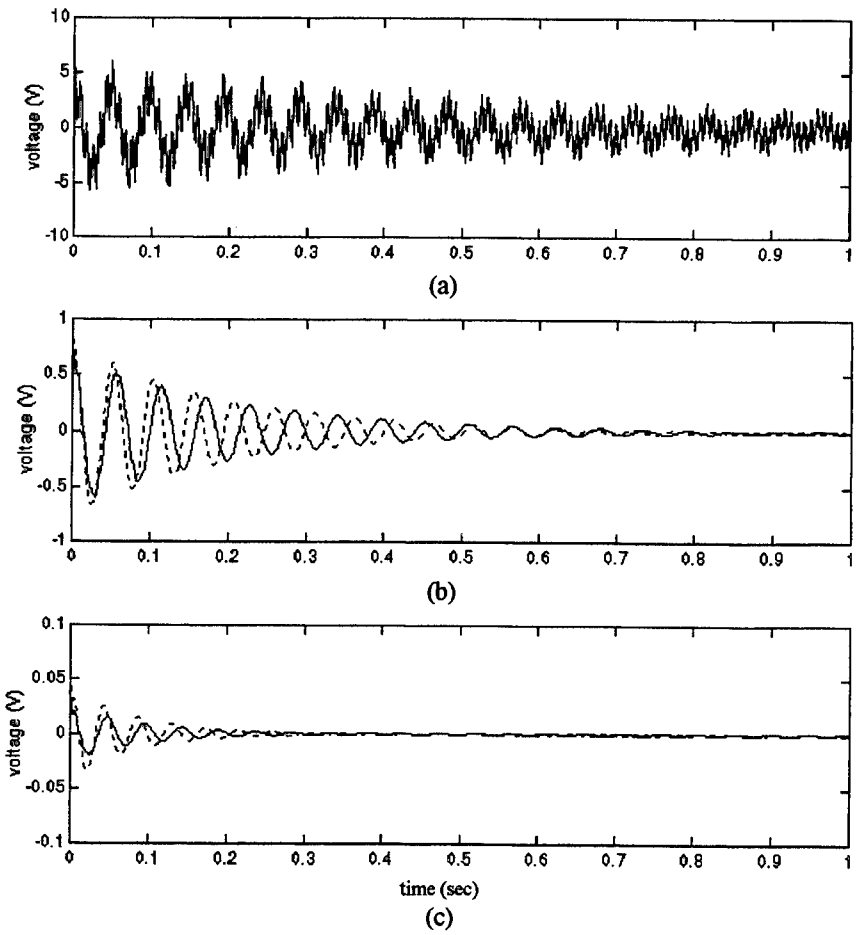

Figure 5. Required control effort for (a) PZT, (b) ACLD, (c) hybrid
(solid line: passive optimization, dashed: active optimization)

The time responses of the new hybrid combination of an active element separate from a passive element is shown in figure 4. In figure 4(a), the passive responses are given for the passive (solid) and active (dashed) optimizations. For both the active and passive case, the length of the PZT was 1 cm, placed at the root and the PCLD started 1 mm from the PZT. In other words, the minimum constraints on the length of the PZT, its placement, and the placement of the PCLD were enforced. Note in figure 4(b) that there is hardly any response. In other words, the active element in conjunction with the passive element is able to damp the vibration almost immediately. When looking at the passive cost functions, the optimal case is for PCLD on the beam. There is only a slight rise in the cost function for the hybrid case, but the advantage is the added effect of the active element. The cost function for the active optimization for the hybrid is the lowest, since it takes advantage of the inherent damping available with the PCLD.

The required control effort for the PZT, ACLD and hybrid treatment is given in figure 5. The required control effort for the PZT only is given in figure 5(a). When this is compared to the effort required for the ACLD, it is easily seen that it is more advantageous to use ACLD treatment. However, when comparing both results to the new hybrid treatment, it is seen in figure 5(c) that requires about an order of magnitude of control effort less than the ACLD. It is therefore more advantageous to use the new hybrid treatment than PCLD, PZT, or ACLD. The passive hybrid response is slightly slower than the PCLD response, but the advantage is the ability to use the active element as necessary.

7. CONCLUSIONS

This paper proposes a new hybrid treatment to damp vibration. This treatment of applying PZT and PCLD separately incorporates both the passive damping capabilities of the VEM and the active damping capabilities of the PZT. The power consumption is reduced, since the active control is turned on as needed.

The vibration of the beam with partial coverage is modeled using Hamilton's Principle and the constitutive equations of the beam, VEM and PZT. GHM modeling is applied to take into effect the dynamics of the VEM. It is shown through an experiment that GHM effectively models the damping of a system. The effects of PCLD, PZT, ACLD, and the new hybrid treatment are analyzed using both a passive and an active (LQR) optimal control formulation. It is shown that using the new hybrid treatment is advantageous, due to the combination of passive and active damping. The control effort required is much less than that for PZT or ACLD.

8. REFERENCES

1. A. Baz and J. Ro, "Optimum Design and Control of Active Constrained Layer Damping," *ASME Special 50th Anniversary Design Issue*, **117**, pp. 135-144 , 1995.

2. W. H. Liao and K. W. Wang, "On the Active-Passive Vibration Control Actions of Structures with Active Constrained Layer Treatments," *ASME Design Engineering Technical Conferences*, **84-3**, pp. 125-141, 1995.

3. D. J. McTavish and P. C. Hughes, "Modeling of Linear Viscoelastic Space Structures," *Journal of Vibration and Acoustics*, **115**, pp. 103-110, 1993.

4. M. J. Lam, W. R. Saunders, and D. J. Inman, "Modeling Active Constrained Layer Damping Using Golla-Hughes-McTavish Approach," *Passive Damping*, 1995 North American Conference on Smart Structures and Materials, Ed. C. D. Johnson and L. C. Rogers, **2445**, pp. 86-97, 1995.

5. D. J. Inman, *Engineering Vibration*, Chapter 6, Prentice Hall, Englewood Cliffs, 1994.

6. 3M: Scotchdamp™ Vibration Control Systems, *Product Information and Performance Data*, St. Paul, 1993.

7. R. J. Allemang, D. L. Brown, and R. W. Rost, *Experimental Modal Analysis and Dynamic Component Synthesis*, **2**, AFWAL-TR-87-3069, 1987.

8. D. E. Kirk, *Optimal Control Theory, an Introduction*, Prentice Hall, Englewood Cliffs, 1970.

Analysis of edge elements for a new active constrained layer treatment

W. H. Liao and K. W. Wang

Structural Dynamics and Controls Laboratory
Mechanical Engineering Department
The Pennsylvania State University
University Park, PA 16802

ABSTRACT

This paper is concerned with the investigations of edge elements' effects on a new class of active constrained layer (ACL) treatment, the so-called enhanced active constrained layer (EACL) configurations. Specific interests are on understanding how the edge elements will influence the passive damping ability, the active action transmissibility, and their combined effects in EACL. Analysis results indicate that the edge elements can significantly improve the active action transmissibility of the current ACL treatment. Although the edge elements will slightly reduce the viscoelastic material (VEM) passive damping effect, the EACL will still have significant damping from the VEM. Combining the overall active and passive actions, the new EACL with sufficiently stiff edge elements can achieve better performance with less control effort as compared to systems with purely active or current ACL treatments.

Keywords: edge elements, active constrained layer, active-passive hybrid control, piezoelectric, viscoelastic, vibration control

1. BACKGROUND

The active constrained layer (ACL) system generally consists of a piece of passive viscoelastic damping material (VEM) sandwiched between an active piezoelectric cover sheet and the host structure. Such a configuration has been studied by various researchers.[1-19] It has been shown that the ACL treatments can enhance the system damping when compared to a traditional passive constrained layer (PCL) system. However, it is also recognized that the viscoelastic layer will reduce the direct control authorities from the active source to the host structure, due to the reduction of transmissibility. [10,14-15] The significance of this effect depends very much on the viscoelastic layer configuration and material properties.[14-15] Therefore, with some combinations of parameters, the ACL configuration could require more control effort while achieving less vibration reductions when compared to a purely active system (zero VEM thickness). Liao and Wang[15] have identified the VEM parameter regions that will provide satisfactory transmissibility of the active actions, and have overall results outperforming both purely passive and active systems. While this study is helpful in setting up guidelines for ACL designers, it is recognized that the VEM design space is much more limited for ACL than PCL. Also, since VEM properties vary significantly with temperature and age, an original effective design with sufficient transmissibility can become ineffective as operating condition changes.

To reduce the negative effects of VEM on active action transmissibility and enhance the actuator authority, Liao and Wang[20] recently created a new and enhanced ACL (EACL) configuration by adding edge elements to connect the boundaries of the piezoelectric coversheet and the host structure (Figure 1). Such elements create a path for the active piezoelectric action to be transferred to the structure more directly. They will thus increase the active action transmissibility of the ACL, and enhance the system performance and robustness.

SPIE Vol. 3045 • 0277-786X/97/$10.00

2. PROBLEM STATEMENT AND OBJECTIVE

While feasibility studies on EACL structures have illustrated promising results, a thorough analysis on how the edge elements will influence the passive damping and active action transmissibility is still needed. This effort will provide more understanding and physical insight to the problem, and further provide design guidelines for synthesizing the edge elements. The goal of this research is to perform such an analysis and identify the edge elements' effects on the system's passive damping ability, active authority, and the active-passive combined structural control ability. Comparisons between the EACL, the current ACL, and the purely active systems will also be discussed.

3. SYSTEM MODEL

For the purpose of discussion and without loss of generality, a cantilever beam with a partially covered active constrained layer and edge elements is used to illustrate the concept (Figure 2). The edge elements are modeled as equivalent springs (stiffness k_{eq}) mounted at the boundaries of the piezoelectric layer. The piezoelectric cover sheet is connected to an external voltage source which is used as the control input.

A finite element model is developed for the system based on the following assumptions:

(a) The rotational inertia is negligible. The shear deformations in the piezoelectric layer and the beam are negligible.
(b) The transverse displacement $w(x,t)$ is assumed to be the same for all layers.
(c) Linear theories of elasticity, viscoelasticity, and piezoelectricity are used.
(d) There is perfect continuity at the interfaces, and no slip occurs between the layers.
(e) The applied voltage is uniform along the beam.

3.1. Kinematics relationships

The geometry and deformation of the sandwich beam is shown in Figure 3. Let the axial displacements of the neutral axis of the piezoelectric layer, the VEM, and the beam be u_c , u_s , and u_b , respectively. The subscripts *c, s,* and *b* refer to the piezoelectric constraining layer, the viscoelastic shear layer (VEM), and the beam, respectively. Here, *w* denotes the transverse displacement. From Figure 3, the shear strain β of the VEM is

$$\beta = \frac{\partial w}{\partial x} - \psi \tag{1}$$

where ψ is the rotational angle of the VEM layer. For perfect bonding conditions, we can further derive the following kinematics relations

$$u_s = u_b - \frac{t_b}{2}\frac{\partial w}{\partial x} - \frac{t_s}{2}\psi \tag{2}$$

$$u_c = u_b - \frac{t_b + t_c}{2}\frac{\partial w}{\partial x} - t_s\psi \tag{3}$$

3.2. Energy of beam with new ACL treatments

For one-dimensional structures with uni-axial loading, the constitutive equation of the piezoelectric materials[21] can be written as

$$\begin{bmatrix} \tau \\ E \end{bmatrix} = \begin{bmatrix} C_{11}^D & -h_{31} \\ -h_{31} & \beta_{33}^S \end{bmatrix} \begin{bmatrix} \varepsilon \\ D \end{bmatrix} \tag{4}$$

where D is the electrical displacement (charge/area in the beam vertical direction), E is the electrical field (voltage/length along the vertical direction), ε is the mechanical strain in the x-direction, and τ is the mechanical stress in the x-direction. C_{11}^D is the elastic stiffness, β_{33}^S is the dielectric constant, and h_{31} is the piezoelectric

constant. Based on the above constitutive equation, and assuming D is constant along the piezoelectric layer thickness for thin materials, one can derive the potential energies of the piezoelectric layer, the VEM, the beam, and the edge spring elements, to be:

$$E_P^c = \frac{1}{2}\int_{V_c} (\tau\varepsilon + ED)dV$$

$$= \frac{1}{2}\int_0^L [C_{11}^D A_c(\frac{\partial u_c}{\partial x})^2 + C_{11}^D I_c(\frac{\partial^2 w}{\partial x^2})^2 - 2A_c h_{31} D(\frac{\partial u_c}{\partial x}) + A_c \beta_{33}^S D^2][H(x-x_1) - H(x-x_2)]dx \tag{5}$$

$$E_P^s = \frac{1}{2}\int_0^L [E_s A_s(\frac{\partial u_s}{\partial x})^2 + E_s I_s(\frac{\partial \psi}{\partial x})^2][H(x-x_1) - H(x-x_2)]dx \tag{6}$$

$$E_P^b = \frac{1}{2}\int_0^L [E_b A_b(\frac{\partial u_b}{\partial x})^2 + E_b I_b(\frac{\partial^2 w}{\partial x^2})^2]dx \tag{7}$$

$$E_P^k = \frac{1}{2}k_{eq}[u_c(x_1,t) + a\frac{\partial w}{\partial x}(x_{1L},t) - u_b(x_{1L},t)]^2 + \frac{1}{2}k_{eq}[u_c(x_2,t) + a\frac{\partial w}{\partial x}(x_{2R},t) - u_b(x_{2R},t)]^2 \tag{8}$$

where

$$a \equiv t_s + \frac{t_b + t_c}{2} \tag{9}$$

I_c, I_s, and I_b are the moments of inertia about the neutral axis of the piezoelectric layer, the VEM, and the beam, respectively. H is the Heaviside's function. The other parameters are defined in the nomenclature.

The kinetic energies of the beam, the VEM layer, and the cover sheet (T_b, T_s, T_c respectively) are represented as:

$$T_b = \frac{1}{2}\int_0^L \rho_b A_b[(\frac{\partial u_b}{\partial t})^2 + (\frac{\partial w}{\partial t})^2]dx \tag{10}$$

$$T_s = \frac{1}{2}\int_0^L [\rho_s A_s[(\frac{\partial u_s}{\partial t})^2 + (\frac{\partial w}{\partial t})^2]][H(x-x_1) - H(x-x_2)]dx \tag{11}$$

$$T_c = \frac{1}{2}\int_0^L \rho_c A_c[(\frac{\partial u_c}{\partial t})^2 + (\frac{\partial w}{\partial t})^2][H(x-x_1) - H(x-x_2)]dx \tag{12}$$

All parameters used in the above equations are defined in the nomenclature.

3.3. Virtual work

Using the theory of linear viscoelasticity[22], the constitutive relation for one-dimensional stress-strain system can be written as the following Stieltjes integral

$$\tau(x,t) = G \circ \beta \equiv \int_{-\infty}^{t} G(t-\tau)\frac{\partial \beta}{\partial \tau}(x,\tau)d\tau \tag{13}$$

where $G(t)$ is the relaxation function of VEM - the stress response to a unit-step strain input. This stress relaxation represents energy loss from the material, hence damping.

The virtual work done by the viscoelastic layer is therefore

$$\delta W_s = -\int_0^L A_s(G \circ \beta)\delta\beta[H(x-x_1) - H(x-x_2)]dx \tag{14}$$

The virtual work done by the applied voltage is

$$\delta W_c = \int_0^L bV(t)\delta D[H(x-x_1) - H(x-x_2)]dx \tag{15}$$

The virtual work done by the external disturbance force is

$$\delta W_d = \int_0^L f(x,t)\delta w(x,t)dx \tag{16}$$

3.4. Finite element model

The finite element method[23] is used to express energy and work equations (5)-(16) into forms in terms of the global nodal displacements through matrix assembly of elements. The local shape functions are chosen to be cubic polynomial in x (for transverse displacement w) and linear polynomial in x (for axial displacement u_b and shear β). During the discretization process, the Golla-Hughes-McTavish[24-25] (GHM) method is employed to analyze the Stieltjes integral in time domain.[14-16]

Using Hamilton's Principle, one can construct

$$\int_{t_1}^{t_2} [\delta T_b + \delta T_s + \delta T_c - \delta E_P^b - \delta E_P^s - \delta E_P^c - \delta E_P^k + \delta W_s + \delta W_c + \delta W_d]dt = 0 \tag{17}$$

With the kinematics relations (1)-(3), and assuming the Young's modulus of the VEM is negligible compared to those of the beam and the piezoelectric material, one can derive the discretized *time-domain* model:

$$M\underline{\ddot{q}} + C\underline{\dot{q}} + K\underline{q} = \underline{f}_c + \underline{f}_d \tag{18}$$

where, $\underline{q}$, $\underline{\dot{q}}$, and $\underline{\ddot{q}}$ are the generalized displacement, velocity, and acceleration vectors. M, C, and K are the mass, damping, and stiffness matrices. In addition, $\underline{f}_c$ and $\underline{f}_d$ are vectors representing the control and disturbance forces, respectively. In the above formulation, the internal structural damping is also included via Rayleigh damping, which is of the form $C_b = \hat{a}M_b + \hat{b}K_b$. Here, M_b and K_b are submatrices of M and K, respectively, from which the parts corresponding to the GHM dissipation coordinates are excluded.

The discretized equation can be placed in standard state-space form:

$$\underline{\dot{x}} = A\underline{x} + B\underline{u} + \hat{B}\underline{u}_d \tag{19}$$

$$\underline{y} = C_o\underline{x} \tag{20}$$

where A is the system matrix, B is the control matrix, $\hat{B}$ is the disturbance matrix, C_o is the output matrix, and $\underline{u}_d$ is the disturbance input vector. The state vector $\underline{x}$ and control input $\underline{u}$ are defined by

$$\underline{x} = [\underline{q}^T \quad \underline{\dot{q}}^T] \tag{21}$$

$$\underline{u} = V(t) \tag{22}$$

4. CONTROL LAW DEVELOPMENT

For the purpose of fair comparison among different cases, the optimal control theory[26] is used to determine the active control gains. To examine the system response under broadband excitation, a stochastic regulator problem is formulated. The cost function is given as

$$J = \lim_{t\to\infty} E[\underline{y}^T Q\underline{y} + \underline{u}^T R\underline{u}] \tag{23}$$

Here, $E[\ ]$ is the expectation operator, Q and R are the semi-positive-definite and positive-definite weighting matrices on the outputs and control inputs, respectively. Assume full-state feedback, the control law is given by

$$\underline{u} = -K_c \underline{x} \tag{24}$$

with control gain $K_c = R^{-1}B^T P$. Here, P satisfies the Ricatti equation

$$A^T P + PA - PBR^{-1}B^T P + C_o{}^T Q C_o = 0 \tag{25}$$

The closed-loop system thus becomes

$$\dot{\underline{x}} = (A - BK_c)\underline{x} + \hat{B}\underline{u}_d = A_{cl}\underline{x} + \hat{B}\underline{u}_d \tag{26}$$

For broadband excitation considerations, one can assume the external disturbance to be a zero-mean white noise process.

$$E[\underline{u}_d(t)]=0 \tag{27}$$

$$E[\underline{u}_d(t)\underline{u}_d{}^T(\tau)]=U_d(t)\delta(t-\tau) \tag{28}$$

The system response will consist of a state vector with zero mean and a variance given by the solution (P_l) to the Lyapunov equation

$$A_{cl}P_l + P_l A_{cl}^T + \hat{B}U_d\hat{B}^T = 0 \tag{29}$$

where

$$P_l = E[\underline{x}(t)\underline{x}^T(t+\tau)] \tag{30}$$

The output co-variance matrix can be written as:

$$W = E[\underline{y}\underline{y}^T] = E\{[C_o\underline{x}][C_o\underline{x}]^T\} = E\{C_o\underline{x}\,\underline{x}^T C_o{}^T\} = C_o E[\underline{x}\,\underline{x}^T]C_o{}^T = C_o P_l C_o{}^T \tag{31}$$

5. ANALYSIS AND DISCUSSIONS

To evaluate the system performance, numerical analyses are carried out on the beam structure. In this research, covariance response to white noise is observed. A random disturbance with variance (2.5×10^{-5}) is applied to the beam at the free end and the output $\underline{y}$ is chosen to reflect the beam tip displacement. The state-space equations form a single-input-single-output (SISO) system. That is, the weighting matrices Q and R are scalars. The piezoelectric cover sheet is assumed to be made of PZT ceramics. The system parameter values used are given in Table 1 unless stated otherwise.

5.1. Active action transmissibility

To examine the active action transmissibility of various configurations, the structure is statically deformed by the actuator with DC voltage input. The beam deflection at the free end is further transferred to an equivalent point load (transmitted force) by multiplying it by the equivalent beam stiffness at the tip. Given the same input voltage, higher transmitted force indicates larger transmissibility of the active action. The transmitted force per input voltage is then normalized with respect to that of the purely active system, which is defined as I_a. Here, I_a is an index to quantify the active action transmissibility.

The I_a values versus k_{eq} are shown in Figure 4. It should be noted that the current ACL is the case with $k_{eq} = 0$. The purely active case (corresponding to a straight dashed line since no k_{eq} is involved) is also plotted for the purpose of comparison. It is illustrated that the I_a of the current ACL ($k_{eq} = 0$) is much lower than that of the purely active structure (without the VEM and edge elements). This again shows that the active action is degraded due to

transmissibility reduction caused by the VEM. With the edge elements ($k_{eq} > 0$), I_a increases with increasing k_{eq}. Note that through increasing k_{eq}, the EACL's active action transmissibility can become even higher than that of the purely active configuration.

5.2. Performance (J_1) and control effort (J_2) indexes

To obtain further insight, we define the standard deviations of the output vibration amplitude and required voltage as J_1 and J_2, respectively. Here, J_1 is an index representing the vibration suppression performance (the less J_1, the better the performance) and J_2 is an index representing the required control effort.

5.3. Passive damping ability

For the purely passive case ($V(t) = 0$), define $J_1 = J_{1P}$. We then define J_{1P0} to be the J_{1P} value for a case without VEM damping (by removing the GHM dissipation coordinates, but still keeping the VEM stiffness modulus) and J_{1Pd} to be the J_{1P} value with VEM damping. That is, J_{1P0} and J_{1Pd} are obtained with the same system stiffness for given k_{eq}. The J_{1P} values versus k_{eq} are shown in Figure 5. Observing J_{1P0}, we see that the vibration amplitude reduces with increasing k_{eq} due to the increase of stiffness. It is shown that J_{1Pd} first increases with k_{eq}. This indicates that the edge elements are reducing the VEM damping ability. However, as k_{eq} gets even lager, J_{1Pd} reduces again. This is due to the combined effects of system stiffness increment and VEM damping variation.

We define an index to quantify the VEM passive damping ability:

$$I_p = \frac{J_{1P0} - J_{1pd}}{J_{1P0}} \times 100 \tag{32}$$

Here, ($J_{1P0} - J_{1pd}$) can be viewed as vibration amplitude reduction due to contributions from the VEM damping. The I_p values versus k_{eq} for the ACL systems are shown in Figure 6. Observing the changes of I_p in the figure, we see that the VEM passive damping effect on the EACL is reduced compared to that of the current ACL ($k_{eq} = 0$). However, comparing with a purely active case (of which I_p is zero), we see that the new EACL system still maintains a significant amount of VEM damping ability.

5.4. Active-passive hybrid actions

From the above discussions, we see that the new EACL can greatly enhance the active action transmissibility while retaining a significant level of passive damping ability, when compared to the current ACL. The major interest now is to study the overall system performance combining the active and passive actions. Under control action ($Q = 10^{10}$, $R = 1$), the structure response J_1 and corresponding required control voltage J_2 are shown in Figures 7 and 8. It is shown that the current ACL configuration ($k_{eq} = 0$) requires more control effort while achieving less vibration reduction when compared to a purely active system. With the edge elements, both vibration amplitude and required voltage are reduced as k_{eq} increases. Furthermore, the new EACL with sufficiently large k_{eq} not only can outperform the current ACL significantly (more vibration reduction with less control effort), but also shows improvement over the purely active system. To further investigate this, we define an index I_{ap}:

$$I_{ap} = \frac{J_{1P0} - J_1}{J_2} \tag{33}$$

Here, $(J_{1P0} - J_1)$ can be viewed as the vibration amplitude reduction due to contributions from the combined active-passive hybrid actions. I_{ap} thus represents the vibration suppression ability per control effort, which indicates the effectiveness or efficiency of the active-passive hybrid system.

The I_{ap} values versus k_{eq} are plotted in Figure 9. The region in which the I_{ap} value of the new EACL is larger than that of the purely active system will give us a design that can outperform both the purely active and passive approaches. On the other hand, the k_{eq} region in which the I_{ap} value is lower than the dashed line (purely active results) is not desirable.

6. CONCLUSIONS

From this research, it is recognized that the edge elements can significantly improve the active action transmissibility of the current ACL treatment, and the EACL can even achieve more active action authority than a purely active configuration. On the other hand, the edge elements will slightly reduce the VEM passive damping effect. However, the EACL system will still have significant passive damping from the VEM. Combining the overall active and passive actions, the new EACL with sufficiently stiff edge elements not only can outperform the current ACL (more vibration reduction with less control effort), but also shows improvement over the purely active system. Based on this study, design guidelines can be set up to effectively integrate the edge elements with ACL structures, such that an overall optimal active-passive hybrid system can be achieved.

7. ACKNOWLEDGMENT

This research is supported by the US Army Research Office.

8. REFERENCES

1. Bailey, T., A. Gruzen, P. Madden, "RCS/Piezoelectric Distributed Actuator Study", AFAL-TR-88-038, 1988.
2. Agnes, G. and K. Napolitano, "Active Constrained Layer Viscoelastic Damping," *Proc. 34th AIAA SDM Conf.*, pp. 3499-3506, 1993
3. Baz, A., "Active Constrained Layer Damping," *Proc. of Damping 93*, San Francisco, CA., pp. IBB 1-23, 1993.
4. Baz, A. and J. Ro, "Partial Treatment of Flexible Beams with Active Constrained Layer Damping," *Recent Developments in Stability, Vibration, and Control of Structural Systems*, ASME, AMD-167, pp. 61-80, 1993.
5. Baz, A. and J. Ro, "The Concept and Performance of Active Constrained Layer Damping Treatments," *Sound and Vibration*, March issue, pp. 18-21, 1994.
6. Baz, A. and J. Ro, "Optimum Design and Control of Active Constrained Layer Damping," *ASME Special 50th Anniversary Design Issue*, Vol. 117, pp. 135-144, 1995.
7. Shen, I. Y., "Hybrid Damping Through Intelligent Constrained Layer Treatments," *ASME Journal of Vibration and Acoustics*, Vol. 116, pp. 341-349, 1994.
8. Shen, I. Y., "Variational Formulation, Work-Energy Relation and Damping Mechanism of Active Constrained Layer Treatments," *Proceedings of the 1995 Design Engineering Technical Conferences*, ASME DE-Vol. 84-3, pp. 149-160, 1995.
9. Shen, I. Y., "Stability and Controllability of Euler-Bernoulli Beams With Intelligent Constrained Layer Treatments," *Journal of Vibration and Acoustics*, Vol. 118, pp. 70-77, 1996.
10. Van Nostrand, W. C., *Active Constrained Layer Damping Using PZT Actuators*, Ph.D. Dissertation, State University of New York at Buffalo, 1994.
11. Van Nostrand, W. C., G. J. Knowles, and D. J. Inman, "Finite Element Model for Active Constrained Layer Damping," *Proceedings of Conference on Smart Structures and Materials*, SPIE Vol. 2193, pp. 126-137, 1994.
12. Azvine, B., G. R. Tomlinson, and R. J. Wynne, "Use of Active Constrained Layer Damping for Controlling Resonant Vibration", *Journal of Smart Materials and Structures*, Vol. 4, No. 1, pp. 1-6, 1995.
13. Lam, M. J., W. R. Saunders, and D. J. Inman, "Modeling Active Constrained Layer Damping Using Golla-Hughes-McTavish Approach," *Proceedings of Conference on Smart Structures and Materials*, SPIE Vol. 2445, pp. 86-97, 1995.

14. Liao, W. H. and K. W. Wang, "On the Active-Passive Hybrid Vibration Control Actions of Structures with Active Constrained Layer Treatments", *Proceedings of the 1995 Design Engineering Technical Conferences*, ASME DE-Vol. 84-3, pp. 125-141, 1995.
15. Liao, W. H. and K. W. Wang, "Analysis and Design of Viscoelastic Materials for Active Constrained Layer Damping Treatments," *Proceedings of Conference on Smart Structures and Materials*, SPIE Vol. 2720, pp. 212-223, 1996.
16. Huang, S. C., D. J. Inman, and E. M. Austin, "Some Design Considerations for Active and Passive Constrained Layer Damping Treatments," *Journal of Smart Materials and Structures*, Vol. 5, pp. 301-313, 1996.
17. Lesieutre, G. A. and U. Lee, "A Finite Element for Beams Having Segmented Active Constrained Layers with Frequency-Dependent Viscoelastics," *Journal of Smart Materials and Structures*, Vol. 5, pp. 615-627, 1996.
18. Veley, D. E. and S. S. Rao, "A Comparison of Active, Passive and Hybrid Damping in Structural Design," *Journal of Smart Materials and Structures*, Vol. 5, pp. 660-671, 1996.
19. Yellin, J. M. and I. Y. Shen, "A Self-Sensing Active Constrained Layer Damping Treatment for a Euler-Bernoulli Beam," *Journal of Smart Materials and Structures*, Vol. 5, pp. 628-637, 1996.
20. Liao, W. H. and K. W. Wang, "A New Active Constrained Layer Configuration with Enhanced Boundary Actions", *Journal of Smart Materials and Structures*, Vol. 5, pp. 638-648, 1996.
21. *IEEE Standard on Piezoelectricity*, ANSI-IEEE Std 176-1987, 1987.
22. Christensen, R.M., *Theory of Viscoelasticity: An Introduction*, 2nd Ed., Academic Press, Inc., New York, 1982.
23. Bathe, K. J., *Finite Element Procedures*, Prentice Hall, Englewood Cliffs, New Jersey, 1996.
24. Golla, D. F. and P. C. Hughes, "Dynamics of Viscoelastic Structures - A Time Domain, Finite Element Formulation," *Journal of Applied Mechanics*, Vol. 52, pp. 897-906, 1985.
25. McTavish, D. J. and P. C. Hughes, "Modeling of Linear Viscoelastic Space Structures," *ASME Journal of Vibration and Acoustics*, Vol. 115, pp. 103-110, 1993.
26. Kwakernaak, H. and R. Sivan, *Linear Optimal Control Systems*, John Wiley and Sons, Inc., 1972.

9. NOMENCLATURE

A	=	Open-loop system matrix
A_{cl}	=	Closed-loop system matrix
A_b, A_c, A_s	=	Cross sectional area of beam, piezoelectric layer, and VEM, respectively
B	=	Control matrix
$\hat{B}$	=	Disturbance matrix
b	=	Width for beam, piezoelectric layer, and VEM
C	=	Damping matrix
C_o	=	Output matrix
C_{11}^D	=	Young's modulus of piezoelectric materials with open circuit
D	=	Electrical displacement
d_{31}	=	Piezoelectric constant
E	=	Electric field
E_b, E_s, E_c	=	Young's modulus of beam, VEM, and piezoelectric materials (short circuit)
G	=	Relaxation function of VEM
h_{31}	=	Piezoelectric constant
I_a	=	Index of active action transmissibility
I_{ap}	=	Effectiveness index of active-passive hybrid actions
I_b, I_c, I_s	=	Moment of inertia of beam, piezoelectric layer, and VEM, respectively
I_a	=	Index for passive damping ability
J	=	Cost function
J_1	=	Index of vibration control performance
J_2	=	Index of required control effort
K	=	Stiffness matrix
k_{eq}	=	Equivalent stiffness of edge element
L	=	Beam length

M	=	Mass matrix
Q	=	Weighting matrix on output
$\underline{q}$	=	Generalized displacement vector
R	=	Weighting matrix on control input
t	=	Time
t_b, t_c, t_s	=	Thickness of beam, piezoelectric layer, and VEM, respectively
$\underline{u}$	=	Control input
$\underline{u}_d$	=	Disturbance input vector
u_b, u_c, u_s	=	Axial displacement of beam, piezoelectric layer, and VEM, respectively
V	=	Applied voltage
w	=	Beam transverse displacement
x	=	Position coordinate along beam length
$\underline{x}$	=	State vector
x_1	=	Left end of ACL
x_{1L}	=	Left end of edge element
x_2	=	Right end of ACL
x_{2R}	=	Right end of edge element
$\underline{y}$	=	Output vector
α	=	Weighting on GHM dissipation coordinate
β	=	Shear strain of VEM
β_{33}^s	=	Dielectric constant of piezoelectric materials
ε	=	Mechanical strain of piezoelectric materials
κ	=	Final value of *G(t)*
$\hat{\zeta}$	=	Damping factor in GHM dissipation coordinate
ρ_b, ρ_c, ρ_s	=	Mass density of beam, piezoelectric layer, and VEM, respectively
τ	=	Mechanical stress
ψ	=	Rotational angle in VEM
$\hat{\omega}$	=	Natural frequency in GHM dissipation coordinate

Table 1. System Parameters

$\hat{a}$	0.64	b	12 mm
$\hat{b}$	1.2×10^{-6}	C_{11}^D	$7.40\times10^{10}\ N/m^2$
d_{31}	$-175\times10^{-12}\ m/v$	E_b	$7.1\times10^{10}\ N/m^2$
E_c	$6.49\times10^{10}\ N/m^2$	L	258 mm
t_b	2 mm	t_c	0.5 mm
t_s	0.25 mm	x_1	28 mm
x_{1L}	20 mm	x_2	128 mm
x_{2R}	136 mm	α	1.0
κ	$10^6\ Pa$	ρ_b	2700 kg/m^3
ρ_c	7600 kg/m^3	ρ_s	1250 kg/m^3
$\hat{\omega}$	10000 rad/sec	$\hat{\zeta}$	4.0

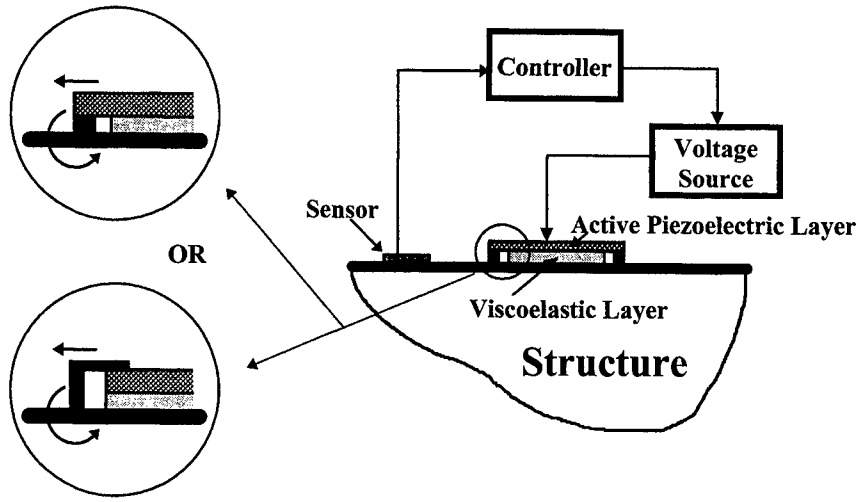

Figure 1. Structure with new EACL treatments

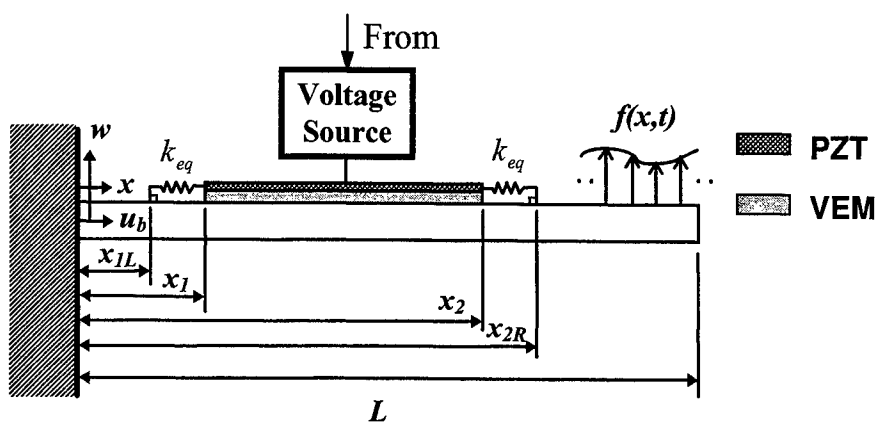

Figure 2. Cantilever beam with partially covered EACL

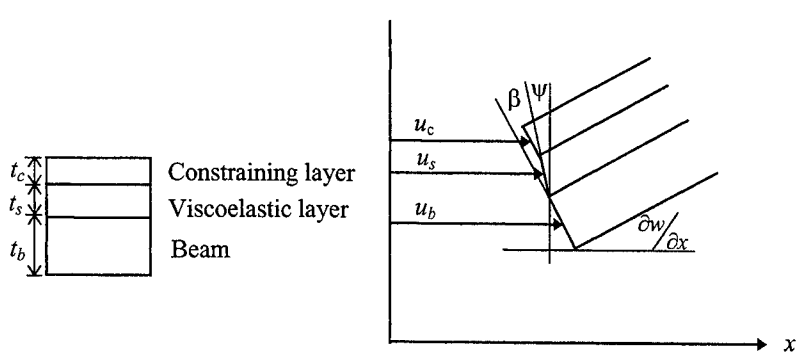

Figure 3. The geometry and deformation of a sandwich beam

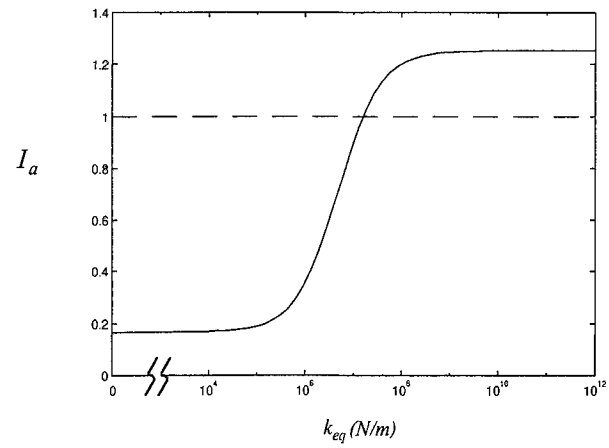

Figure 4. I_a versus k_{eq} , solid line: EACL, dashed line: purely active

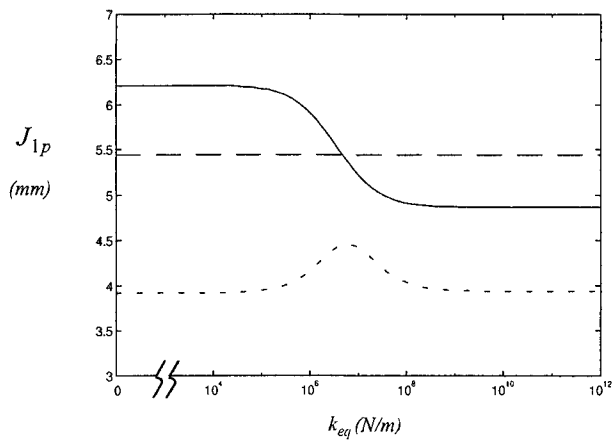

Figure 5. J_{1p} versus k_{eq} , solid line: J_{1p0} , dotted line: J_{1pd} , dashed line: purely active

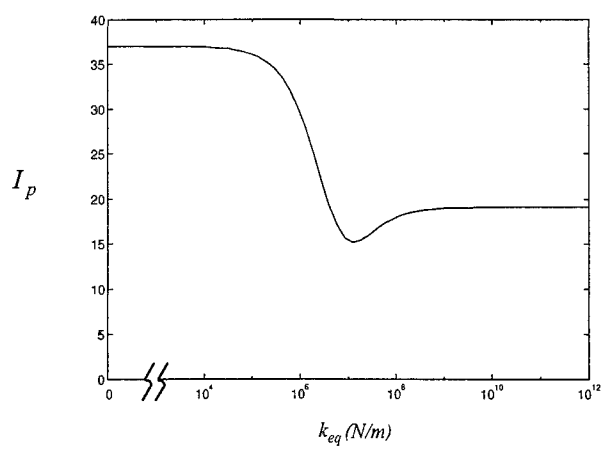

Figure 6. I_p versus k_{eq}

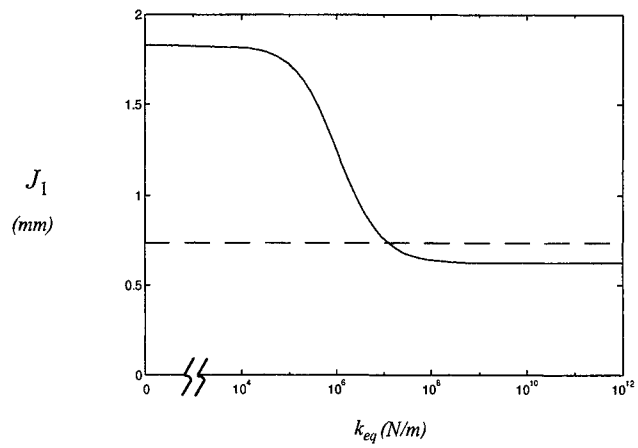

Figure 7. J_1 versus k_{eq} , solid line: EACL, dashed line: purely active

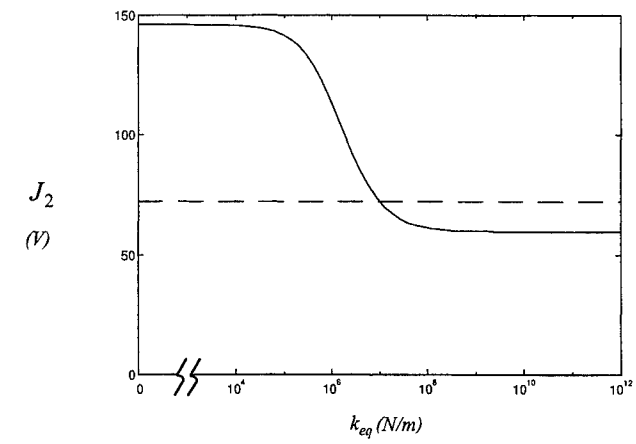

Figure 8. J_2 versus k_{eq} , solid line: EACL, dashed line: purely active

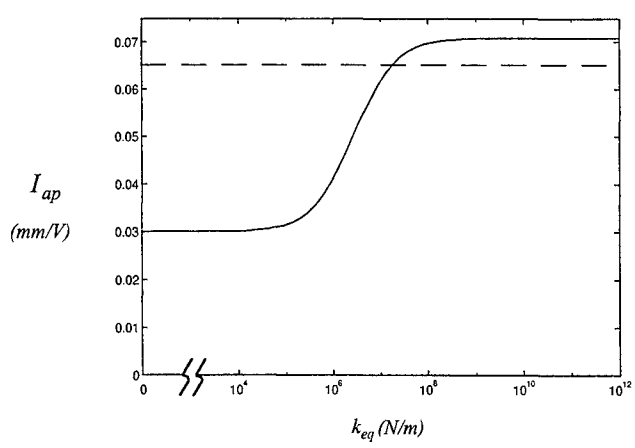

Figure 9. I_{ap} versus k_{eq} , solid line: EACL, dashed line: purely active

Some insights on active-passive hybrid piezoelectric networks for structural controls

M. S. Tsai and K. W. Wang

Structural Dynamics and Controls Lab
Mechanical Engineering Department
The Pennsylvania State University
University Park, PA 16802, USA

ABSTRACT

This paper presents new insights obtained from analyzing the active-passive hybrid piezoelectric network (APPN) concept. It is shown that the shunt circuit not only can provide passive damping, it can also enhance the active action authority if tuned correctly. Therefore, the integrated APPN design is more effective than a system with separated active and passive elements. However, it is also recognized that a systematic design/control method is needed to ensure that the passive and active actions are optimally synthesized. Such a method is presented. The bandwidth issue for the APPN configuration is also addressed.

Keywords: Active-passive hybrid control, piezoelectric materials, piezoelectric shunt, vibration control

1. INTRODUCTION

Because of their active and passive damping features, piezoelectric materials have been explored for their active-passive *hybrid* control abilities, which could have the advantages of both the passive (stable, fail-safe, low power requirement) and active (high performance, feedback or feedforward actions) systems. An active-passive hybrid piezoelectric network (APPN) concept has been proposed[1-4] for this purpose. This actuator configuration integrates piezoelectric materials with an active voltage source and a passive R (resistance) L (inductance) shunting circuit (Figure 1). On one hand, structural vibration energy can be transferred to and dissipated in the tuned shunting circuit passively. On the other hand, the control voltage will drive the piezo-layer, through the circuit, and actively suppress vibration of the host structure. Feasibility studies have demonstrated[1-4] that such an APPN-based adaptive structure could suppress vibration and noise radiation effectively, and could achieve better performance with less control effort as compared to a purely active (without shunt circuit) system.

2. PROBLEM STATEMENT AND OBJECTIVE

While previous investigations on APPN have illustrated promising results, there are still some fundamental and important issues need to be addressed. These items are summarized in the following paragraphs.

(a) While the APPN configuration includes both the active and passive elements, the interactions between these elements are not clear. Do the passive elements always complement the active actions ?

(b) If the active and passive elements do not always complement each other, should we separate them? In other words, if we separate the active and passive elements, will the active-passive hybrid actions be affected ? If they are, will they be enhanced or reduced ?

(c) It has been shown that the APPN can outperform a purely active system. However, since the APPN is conceptually an active-passive hybrid tuned damper, it should have a bandwidth limitation. Will its advantage over a purely active

SPIE Vol. 3045 • 0277-786X/97/$10.00

arrangement becomes insignificant as the demand on bandwidth increases ? Can this bandwidth factor be included in the design process ?

The objective of this investigation is to address the fundamental issues presented above. In other words, we want to provide more insight and basic understandings to the APPN configuration, and eventually achieve a truly beneficial active-passive hybrid structure for the purpose of vibration suppressions.

3. SYSTEM MODEL

For the purpose of discussion, a cantilever beam with a single pair of partially covered piezoelectric (PZT) layers is used to illustrate the active-passive hybrid system. The schematic of configuration (referred to as Configuration A in this paper) is shown in Figure 1. The actuator is connected to a external voltage source in series with an RL circuit. The sensor layer is mounted on the other side of the beam at the same axial location.

The system equation is derived based on the following assumptions:

(a) The poling direction of the PZTs is in the positive w-direction
(b) The rotational inertia is negligible
(c) Only uni-axial loading of the PZTs in the u-direction is considered
(d) The piezoelectric material layers are thin and short compared to the beam
(e) The applied voltage is uniform

Using Hamilton's Principle, one can construct

$$\int_{t_1}^{t_2} [\delta T_b - \delta U_b - \delta U_s + \delta W_v] dt = 0 \tag{1}$$

where T_b is the beam kinetic energy, U_b is the beam strain energy, U_s is the mechanical and electrical energy of the piezoelectric material, and δW_v is the virtual work term.

For one-dimensional structures with uni-axial loading, the constitutive equation of the piezoelectric materials can be written as

$$\begin{bmatrix} \tau \\ E_v \end{bmatrix} = \begin{bmatrix} E_s & -h_{31} \\ -h_{31} & \beta_{33} \end{bmatrix} \begin{bmatrix} \varepsilon \\ D \end{bmatrix} \tag{2}$$

where D is the electrical displacement (charge/area in the transverse direction), E_v is the electric field (volts/length along the transverse direction), ε is the mechanical strain in the x-direction, and τ is the material stress in the x-direction. E_s is the elastic stiffness, β_{33} is the dielectric constant, and h_{31} is the piezoelectric constant of the PZT. Based on the above constitutive equation, and assuming D is constant along the PZT thickness for thin materials, one can derive

$$U_s = \frac{1}{2}\int_V (\tau\varepsilon + E_{va}D_a)dV + \frac{1}{2}\int_V (\tau\varepsilon + E_{vs}D_s)dV = \frac{1}{2}\int_0^{L_b} [2E_s\, I_s(\frac{\partial^2 w}{\partial x^2})^2 + 2h_{31}J_s(\frac{\partial^2 w}{\partial x^2})D_a$$
$$+ A_s\beta_{33}D_a^2 + 2h_{31}J_s(\frac{\partial^2 w}{\partial x^2})D_s + A_s\beta_{33}D_s^2](H(x-x_1) - H(x-x_2))dx \tag{3}$$

The other functions are presented as follows

$$T_b = \frac{1}{2}\int_0^{L_b} \rho_b A_b (\frac{\partial w}{\partial t})^2 dx \tag{4}$$

$$U_b = \frac{1}{2}\int_0^{L_b} E_b I_b (\frac{\partial^2 w}{\partial x^2})^2 dx \tag{5}$$

$$\delta W_v = V_a(t)\int_0^{L_b} b_s \delta D_a (H(x-x_1)-H(x-x_2))dx + V_s(t)\int_0^{L_b} b_s \delta D_s (H(x-x_1)-H(x-x_2))dx$$
$$+\int_0^{L_b} (\hat{F}(x,t) - c_b \frac{\partial w(x,t)}{\partial t})\delta w(x,t)dx \tag{6}$$

Note that the voltage is related to the external circuit:

$$V_a = -L\frac{d^2 Q_a}{dt^2} - R\frac{dQ_a}{dt} - V_c \tag{7}$$

$$V_a = E_{va}(h_s - h_b), \quad V_s = E_{vs}(h_s - h_b) \tag{8}$$

$$Q_a = b_s(x_2 - x_1)D_a, \quad Q_s = b_s(x_2 - x_1)D_s \tag{9}$$

Here, $w(x,t)$ is the transverse displacement of the beam, E_b is the beam elastic modulus, E_s is the piezoelectric elastic modulus with an open circuit, L_b is the beam length, ρ_b is the beam density, b_s is the width of the beam and PZT, h_b is the distances from the beam neutral axis to the outside surface of the beam, h_s is the distance from beam neutral axis to the outside surface of the PZT, A_b, A_s are the cross sectional area of the beam and PZT, respectively. c_b is the uniform damping constant, and I_b and I_s are the beam and PZT layer moments of inertia, respectively. Also, $J_s = b_s(h_s^2-h_b^2)/2$, (x_2-x_1) is the length of the PZT, R is the resistance, L is the inductance, V_c is the external voltage for control, V_s is the sensor voltage, D_a, D_s are the electric displacement of the actuator and sensor, respectively. Q_a, Q_s are the electric charge of the actuator and sensor, E_{va}, E_{vs} are the electric field of actuator and sensor, respectively. $\hat{F}(x,t)$ is the external load distribution, and H is the Heavyside's function. The other parameters are defined in the nomenclature.

Substituting the above equations into Eq. (1) and further assuming that the field within and electrical displacement on the surface are uniform for the piezoelectric material, one can derive the system model. The structure equation is

$$\rho_b A_b \frac{\partial^2 w}{\partial t^2} + c_b \frac{\partial w}{\partial t} + E_b I_b \frac{\partial^4 w}{\partial x^4} + (2E_s I_s \frac{\partial^4 w}{\partial x^4} + h_{31} J_s \frac{\partial^2 D_a}{\partial x^2})(H(x-x_1) - H(x-x_2))$$
$$+(4E_s I_s \frac{\partial^3 w}{\partial x^3} + 2h_{31} J_s \frac{\partial D_a}{\partial x})(\delta(x-x_1) - \delta(x-x_2)) + (2E_s I_s \frac{\partial^2 w}{\partial x^2} + h_{31} J_s D_a)$$
$$(\delta'(x-x_1) - \delta'(x-x_2)) = \hat{F}(x,t) \tag{10}$$

where δ is the Dirac Delta function and $0 < x < L_b$. The boundary conditions are

$$w(0,t) = \frac{\partial w(0,t)}{\partial x} = \frac{\partial^2 w(L_b,t)}{\partial x^2} = \frac{\partial^3 w(L_b,t)}{\partial x^3} = 0 \tag{11}$$

The actuator circuit equation is

$$(V_c + L\frac{d^2 Q_a}{dt^2} + R\frac{dQ_a}{dt} + \frac{\beta_{33}(h_s - h_b)}{b_s(x_2 - x_1)}Q_a + \frac{h_{31} J_s}{b_s}\frac{\partial^2 w}{\partial x^2})((H(x-x_1) - H(x-x_2)) = 0 \tag{12}$$

Assume an open circuit ($D_s = 0$), the sensor equation is

$$(V_s + \frac{h_{31}J_s}{b_s}\frac{\partial^2 w}{\partial x^2})((H(x-x_1)-H(x-x_2)) = 0 \tag{13}$$

Galerkin's method[5] can be used to discretize Eqs. (10-13) into a set of ordinary differential equations. For the structure, one can obtain

$$M_b\ddot{\underline{q}} + C_b\dot{\underline{q}} + K_b\underline{q} + \frac{h_{31}(h_s^2 - h_b^2)}{2(x_2 - x_1)}[\underline{\phi}'(x_2) - \underline{\phi}'(x_1)]Q_a = \hat{\underline{f}} \tag{14}$$

and for the actuator and sensor circuits

$$L\ddot{Q}_a + R\dot{Q}_a + \frac{\beta_{33}(h_s - h_b)}{b_s(x_2 - x_1)}Q_a + \frac{h_{31}(h_s^2 - h_b^2)}{2(x_2 - x_1)}\left[\underline{\phi}'(x_2) - \underline{\phi}'(x_1)\right]^T \underline{q} = -V_a \tag{15}$$

$$\frac{h_{31}(h_s^2 - h_b^2)}{2(x_2 - x_1)}\left[\underline{\phi}'(x_2) - \underline{\phi}'(x_1)\right]^T \underline{q} = -V_s \tag{16}$$

where $\underline{q}, \dot{\underline{q}}$, and $\ddot{\underline{q}}$ are vectors of generalized displacement, velocity, and acceleration. $(\dot{})$ and $(')$ are derivatives with respective to time and x, respectively. $\hat{\underline{f}}$ is the external disturbance vector. The vector $\underline{\phi}$ contains the comparison functions, which are chosen to be the eigenfunctions of a uniform fixed-free beam. The matrices M_b and C_b are diagonal with constant elements $\rho_b A_b$ and c_b, respectively.

The discretized adaptive structure model, Eqs. (14) and (15), can be expressed in a standard state-space form:

$$\begin{aligned} \dot{\underline{y}} &= A(R,L)\underline{y} + B_1\underline{f} + B_2(R,L)\underline{u} \\ \underline{y} &= [\underline{q}^T \quad Q_a \quad \dot{\underline{q}}^T \quad \dot{Q}_a \quad]^T, \quad \underline{u} = V_c \end{aligned} \tag{17}$$

where $\underline{y}$ is the state vector, $\underline{u}$ is the control input, $\underline{f}$ is the external disturbance vector. The system matrix, A, and control matrix, B_2 are functions of the passive resistance and inductance.

The system described above has $(N+1)$ modes, where N is the number of terms in the Galerkin expansion. The $(N+1)^{th}$ mode is due to the passive circuit. Because the comparison functions in the expansion are chosen to be the eigenfunctions of a fixed-free beam, the ith generalized coordinate will closely resemble the ith structural modal coordinate $(i=1,2,3,....,N)$.

4. ANALYSIS OF THE OPEN LOOP SYSTEM

In this section, the system model will be used to investigate the effects of the passive circuit parameters (resistance and inductance) have on the active control authorities in the APPN. Also, the APPN will be compared to the configuration with separated active and passive elements. The system parameters used are shown in Table 1 unless stated otherwise.

4.1 Effects of Passive Circuit Elements on Active Authority

For a linear system described in the previous section, the overall structural response will be a sum of the response contributed from the excitation force $\underline{f}$ and the response contributed from the control voltage $\underline{u}$. We define Y_1 to be the magnitude of the transfer function w_1/f and Y_2 to be the magnitude of the transfer function w_2/u. Here, w_1 and

w_2 are the beam responses close to the tip ($x=0.92L_b$) caused by a point force at $x=0.95L_b$ and the control voltage, respectively. With $u=0$, Y_1 represents the structural vibration amplitude without active control. That is, Y_1 is an index of the system's passive damping ability (the smaller the better). On the other hand, Y_2 represents the structural vibration amplitude created by the active actuator. Larger Y_2 indicates that the actuator has more authority to excite the host structure for the given voltage input. Thus, Y_2 is used as an index for the system's active control authority (the larger the better).

To illustrate the basic concepts and observations, we are focusing on the first modal response in the analysis presented in this section, thus only an one-term Galerkin expansion is used. We first compare the APPN with the purely active system. The R and L values are chosen to be the optimal values for the passive system[6]. Figures 2 and 3 show the passive damping index Y_1 and the active authority index Y_2 for both systems. The Y_1 plot reconfirms that the passive shunt circuit behaves like a tuned resonant damper. In other words, the RL circuit will enhance the passive damping ability around the first resonant frequency. On the other hand, Figure 3 (Y_2 plot) illustrates that the shunt circuit is enhancing the active authority as well. Therefore, it is obvious that the active-passive hybrid system could outperform the purely active system as reported in the past.[2-4]

Since the R and L values are chosen to optimize the passive system, it is not clear that they will be the best for maximizing the active action. For example, while the resistor is designed to dissipate the structure vibration energy, it could be dissipating the control power from the active element as well. This can be observed in Figure 4, where Y_2 is shown to be decreasing with increasing R. In other words, the resistor is reducing the active action authority of the actuator.

4.2 Integrated Versus Separated Active and Passive Elements

One simple-minded approach to resolve the problem discussed above is to separate the passive shunt circuit from the active source (Figure 5). While this is still an active-passive hybrid configuration (referred to as configuration B), the active and passive elements do not interact directly anymore. That is, we are simply applying active control on an optimized (tuned circuit) passive system. The structure equation of motion for configuration B is

$$\rho_b A_b \frac{\partial^2 w}{\partial t^2} + c_b \frac{\partial w}{\partial t} + E_b I_b \frac{\partial^4 w}{\partial x^4} + (2E_s I_s \frac{\partial^4 w}{\partial x^4} + h_{31} J_s \frac{\partial^2 D_a}{\partial x^2} + h_{31} J_s \frac{\partial^2 D_s}{\partial x^2})(H(x-x_1) - H(x-x_2))$$
$$+ (4E_s I_s \frac{\partial^3 w}{\partial x^3} + 2h_{31} J_s \frac{\partial D_a}{\partial x} + 2h_{31} J_s \frac{\partial D_s}{\partial x})(\delta(x-x_1) - \delta(x-x_2)) + (2E_s I_s \frac{\partial^2 w}{\partial x^2} + h_{31} J_s D_a + h_{31} J_s D_s)$$
$$(\delta'(x-x_1) - \delta'(x-x_2)) = \hat{F}(x,t) \tag{18}$$

The shunt circuit and actuator equations are

$$(L\frac{d^2 Q_s}{dt^2} + R\frac{dQ_s}{dt} + \frac{\beta_{33}(h_s - h_b)}{b_s(x_2 - x_1)} Q_s + \frac{h_{31} J_s}{b_s} \frac{\partial^2 w}{\partial x^2})(H(x-x_1) - H(x-x_2)) = 0 \tag{19}$$

$$(V_a + \frac{\beta_{33}(h_s - h_b)}{b_s(x_2 - x_1)} Q_a + \frac{h_{31} J_s}{b_s} \frac{\partial^2 w}{\partial x^2})(H(x-x_1) - H(x-x_2)) = 0 \tag{20}$$

The sensor equation is

$$(V_s + \frac{\beta_{33}(h_s - h_b)}{b_s(x_2 - x_1)} Q_s + \frac{h_{31} J_s}{b_s} \frac{\partial^2 w}{\partial x^2})(H(x-x_1) - H(x-x_2)) = 0 \tag{21}$$

Here, the sensor voltage V_s is the voltage across the shunt circuit.

Since the A and B configurations are the same without the active source, the passive damping index Y_1 plot is the same for the two (Figure 6). This implies that the two configurations have the same passive damping ability. However, the active authority index Y_2 plot shows that configuration A can drive the host structure much more effectively than configuration B (Figure 7). This is because the circuit parameters are tuned to enhance the voltage output from the circuit (equal to the voltage input into the piezoelectric layer) around the resonant frequency. This fact illustrates the merit of the integrated configuration over the separated design. Therefore, a sensible thing to do is to use configuration A with better selected R and L values (instead of the R and L values optimized for the passive system). In order to achieve such a purpose, a systematic control/design method is presented in the next section.

5. ACTIVE-PASSIVE CONTROL LAW

A scheme is synthesized to *concurrently* design the passive elements and the active control law in a systematic and integrated manner. The strategy is to combine the optimal control theory with an optimization process and to determine the active control gains *together* with the values of the passive system parameters (the shunt circuit resistance and inductance). The method proposed in [4] is used as a starting point, but is modified in order to consider the bandwidth of external excitations. The procedure contains three major steps as outlined in the following paragraphs.

5.1 Determine Active Gains

The disturbance $\underline{f}$ is modeled as the result of passing a Gaussian, white noise process through a second order low pass Butterworth filter. The bandwidth of the filter is defined to be the radian cutoff frequency at which the filter output has a 3-dB attenuation of its value at zero frequency. The equations that describe such a process are:

$$\begin{aligned} \dot{\underline{s}} &= A_d \underline{s} + B_d \underline{d} \\ \underline{f} &= C_d \underline{s} \end{aligned} \tag{22}$$

The inputs in $\underline{d}$ are Gaussian and white. Here, the mean and spectral density of $\underline{d}$ is given by $E[\underline{d}(t)]=0$ and $E[\underline{d}(t)\underline{d}^T(\tau)]=D(t)\delta(t-\tau)$. Here, $E[\,]$ is the expectation operator.

By defining an augmented state vector as $\underline{x}=[\underline{y}\ \ \underline{s}]^T$, the overall system state equations become:

$$\dot{\underline{x}} = \begin{bmatrix} A & B_1 C_d \\ 0 & A_d \end{bmatrix} \underline{x} + \begin{bmatrix} B_2 \\ 0 \end{bmatrix} \underline{u} + \begin{bmatrix} 0 \\ B_d \end{bmatrix} \underline{d} = A_a \underline{x} + B_{2a}(R,L)\underline{u} + B_{1a}\underline{d} \tag{23}$$

With a given set of passive parameters (R and L), the optimal control theory[7] is used to determine the value of the active gains.

The cost function is

$$J_e = \lim_{t\to\infty} E[\underline{x}^T Q_e \underline{x} + \underline{u}^T S \underline{u}] \tag{24}$$

Q_e is a positive-semi-definite weighting matrix chosen to be

$$Q_e = \begin{bmatrix} K_b & & & & \\ & 0 & & 0 & \\ & & 0 & & \\ & & & M_b & \\ & 0 & & 0 & \\ & & & & 0 \end{bmatrix} \tag{25}$$

Here, $\underline{x}^T Q_e \underline{x}$ represents the overall structure energy. S is the positive-definite weighting matrices on the control inputs. Since the purpose of this paper is mainly on investigating the actuator characteristics, the sensor equation is not used here and full state feedback is assumed.

With this stochastic regulator control problem, the optimal control gain is given by

$$K_c = S^{-1} B_{2a}{}^T P_r \tag{26}$$

where P_r satisfies the Ricatti equation

$$A_a{}^T P_r + P_r A_a - P_r B_{2a} S^{-1} B_{2a}{}^T P_r + Q_e = 0 \tag{27}$$

The closed-loop system thus becomes

$$\frac{d}{dt}\underline{x} = (A_a - B_{2a} K_c)\underline{x} + B_{1a}\underline{d} = A_{cl}\underline{x} + \underline{v} \tag{28}$$

$\underline{v}$ is Gaussian and white. Here, the mean and spectral density of $\underline{v}$ is given by $E[v(t)]=0$ and $E[\underline{v}(t)\underline{v}^T(\tau)]=V(t)\delta(t-\tau)$.

5.2 Determine Objective Functions

For broadband excitation, the objective function is selected to be the minimized cost function of the stochastic regulator problem[7]

$$J = Min\, J_e = tr\,(P_r V) \tag{29}$$

The system response will consist of a state vector with zero mean and a variance given by the solution (P_l) to the Lyapunov equation :

$$A_{cl} P_l + P_l A_{cl}^T + V = 0 \tag{30}$$

where

$$P_l = E[\underline{x}(t)\underline{x}^T(t+\tau)] \tag{31}$$

Therefore, for any output vector (not necessary from sensor outputs), $\underline{z} = C\underline{x}$, the output co-variance matrix can be written as:

$$W = E[\underline{z}\underline{z}^T] = E\{[C\underline{x}][C\underline{x}]^T\} = E\{C\underline{x}\,\underline{x}^T C^T\} = CE[\underline{x}\,\underline{x}^T]C^T = CP_l C^T \tag{32}$$

5.3 Iteration on Active Gains and Passive Parameters to Minimize *J*

Note that for each set of the passive control parameters R and L, there exists an optimal control with the corresponding minimized cost function and control gains. That is, J is a function of R and L. Utilizing a nonlinear programming algorithm[8], one can determine the resistance and inductance which further minimize J. In other words, by varying the values of the active gains and passive parameters simultaneously, the "optimized" optimal control can be obtained.

6. ANALYSIS OF THE CLOSED-LOOP SYSTEM

With the concurrent design/control method, one can directly optimize the circuit parameters for the hybrid system. This also gives us the opportunity to examine the system performance for multi-mode and broadband excitation rejections. The system parameters used in the following analysis are shown in Table 1 unless stated otherwise.

6.1 The Effects of Excitation Bandwidth

In order to examine the APPN system under broadband excitations, a five-mode expansion is used which covers modal frequencies up to 1.67K Hz. The APPN system is designed based on the algorithm presented in the last section. To evaluate the effects of frequency bandwidth on the performance of APPN, the bandwidth of the Butterworth filter for filtering disturbances is used as a variable. A different set of APPN parameters is designed for each given filter bandwidth. Figure 8 shows the value of J versus filter bandwidth for the purely active and active-passive cases. It is clear that the hybrid system works very well around the first resonant frequency. However, as the bandwidth gets larger, the APPN starts to approach the purely active case. This is because the best way to utilize the shunt is to use it to enhance the active action around a certain resonant frequency of the structure, and thus the results will become less effective when the number of contributing modes greatly exceeds the number of actuators. Nevertheless, the APPN will always outperforms the purely active system, as illustrated in Figure 8.

6.2 Multiple APPNs for Broadband Applications

It is shown in the section 6.1 that the single patch APPN works very well for narrow band applications but becomes less effective when the excitation bandwidth increases. To enhance the system's broadband performance, two methods have been investigated. One is to integrate the APPN with an Enhanced Active Constrained Layer (EACL) treatment[9], which will be presented in a separate paper. The other method is to increase the number of actuators.

To evaluate the multi-actuators effect, the beam structure with three APPNs is used as an example. The three PZT pairs are located on the beam with their left edges at x = 2.38mm, 85mm, and 180mm, respectively. The length of the PZTs is 63.5mm. The equations of motion are modified to reflect this condition. A five-term expansion is used in the Galerkin's discretization process. Figure 9 shows the value of the objective function J versus filter bandwidth for the purely active and the APPN cases. Comparing with Figure 8, it is clear that with multiple actuators, the vibration reduction effect is much more significant under multi-mode excitations. Define ΔJ to be the difference between the objective function value (J_{pa}) of the purely active case and that of the APPN case, $\Delta J/J_{pa}$ is plotted in Figure 10. We see that for broadband applications, the multi-actuator system can outperform the purely active configuration with a much larger margin (percentage reduction) than the single-actuator system.

7. SUMMARY

This paper presents analysis results that provide more insights and understandings to the APPN system. It is shown that comparing to a purely active arrangement, the shunt circuit not only can provide passive damping, it can also enhance the active action authority around the tuned frequency. Therefore, the integrated APPN design is more effective than a system with separated active and passive elements. However, it is also clear that the active authority will be degraded if the inductance is mistuned or if the resistance is too high. Therefore, a systematic design/control method is developed to ensure that the passive and active actions are optimally synthesized. With this methodology, this paper also addresses the bandwidth issue for the APPN configuration. It is concluded that with a single actuator, the difference between the APPN and purely active cases becomes smaller when the excitation frequency bandwidth becomes larger. One possible method to enhance the system's broadband performance is to increase the number of actuators.

8. ACKNOWLEDGMENT

This research is supported by the Office of Naval Research Office.

9. REFERENCES

1. Agnes, G., "Active/Passive Piezoelectric Vibration Suppression," *SPIE Smart Structures and Materials*, vol. 2193, pp. 24-34, 1994.
2. Kahn, S. and K.W. Wang. "On the Simultaneous Design of Active-Passive Hybrid Piezoelectric Actions," *ASME IMCE* paper # 95-WA/AD5, 1995.
3. Wang, K.W. and S. Kahn. "Active-Passive Hybrid Structural Vibration Controls via Piezoelectric Networks," *Structronic Systems, Smart Structures, Devices and Systems,* invited book chapter, edited by H.S. Tzou et al., World Scientific Publishing Company, to appear in 1997.
4. Tsai, M.S. and K. W. Wang " Control of a Ring Structure with multiple active-passive hybrid piezoelectrical networks," *IOP Journal of Smart Materials and Structures*, vol. 5, pp. 695-703, 1996.
5. Inman, D.J., *Vibrations with Control, Measurement, and Stability*, Prentice Hall, 1989.
6. Hagood, N.W. and A. von Flotow, "Damping of Structural Vibrations with Piezoelectric Materials and Passive Electrical Networks," *Journal of Sound and Vibration*, vol. 146(2), pp. 243-268, 1991.
7. Kwakernaak, H. and R. Sivan, *Linear Optimal Control Systems*, John Wiley and Sons, Inc, 1972.
8. Arora, J.S., *Introduction to Optimum Design*, McGraw Hill Inc, 1989.
9. Liao, W.H. and K.W.Wang, "A New Active Constrained Layer Configuration with Enhanced Boundary Actions," *IOP Journal of Smart Materials and Structures* , vol. 5, pp. 638-648, 1996.

NOMENCLATURE

A	Open-loop system matrix	A_a	Augmented system matrix
A_{cl}	Closed-loop system matrix	A_d	Butterworth filter system matrix
B_1	Excitation matrix of open-loop system	B_{1a}	Excitation matrix of the augmented system
B_2	Control matrix of open-loop system	B_{2a}	Control matrix of the augmented system
B_d	Butterworth filter input matrix	C_d	Butterworth filter output matrix
K_c	Control gains	P_l	Solution of the Lyapunov
P_r	Solution of the Ricatti equation for Eq. (27)	Q_e	Weighting matrix on states
t	Time	V	Volume of PZT
W	Output covariance matrix	$\underline{z}$	System output

Table 1 - System Parameters

A_b	$= 8.0645\text{x}10^{-5}$ m^2	b_s	$= 0.0254$ m
c_b	$= 0.60$ N-s/m^2	E_b	$= 6.93 \times 10^{10}$ Pa
E_s	$= 7.1\text{x}10^{10}$ Pa	h_b	$= 0.001588$ m
h_s	$= 0.00207$ m	h_{31}	$=8.4147\text{x}10^{8}$ N/C
I_b	$= 6.774\text{x}10^{-11}$ m^4	I_s	$= 4.1192\text{x}10^{-11}$ m^4
L	$= 0.3$m	S	$= 2\text{x}10^{-7}$
x_1	$= 0.00238$m	x_2	$=0.06588$m
β_{33}	$= 7.9396\text{x}10^{7}$ volt-m/coulomb	ρ_b	$= 2700$ k$_g$/m^3

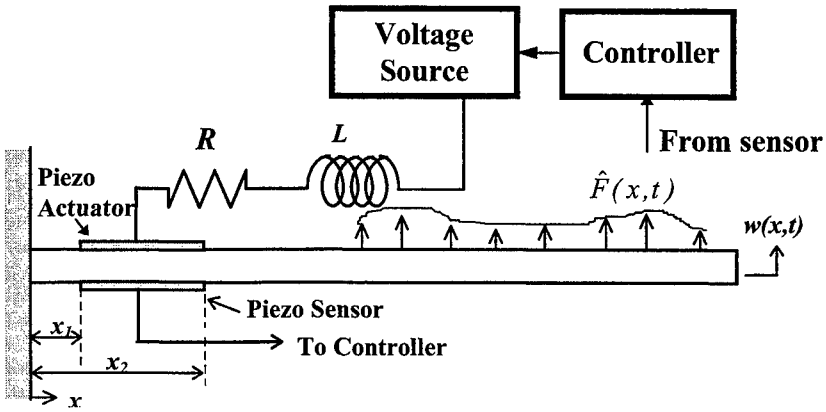

Figure 1. Schematic of a cantilever beam with APPN (Configuration A)

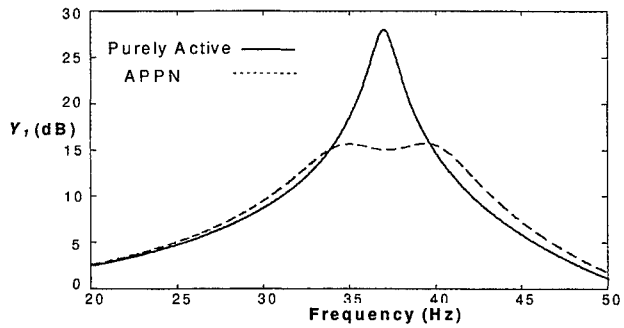

Figure 2. The passive damping index Y_1 for the purely active and APPN systems

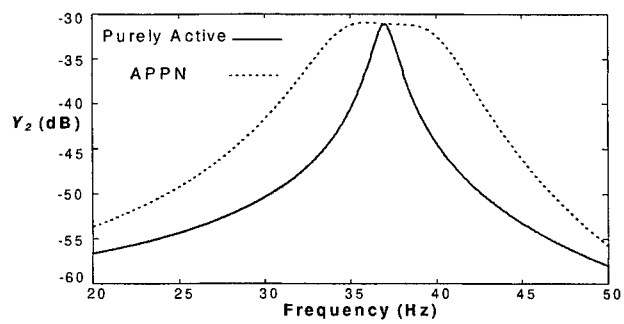

Figure 3. The active control authority index Y_2 for the purely active and APPN systems

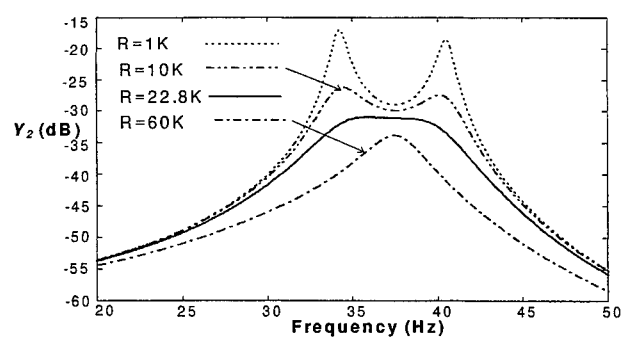

Figure 4. The active control authority index Y_2 with different resistors

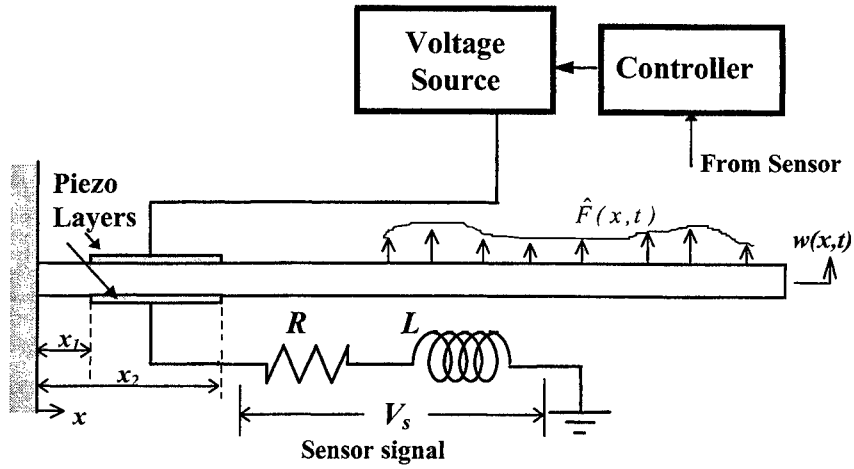

Figure 5. Schematic of a cantilever beam with separated active and passive elements (Configuration B)

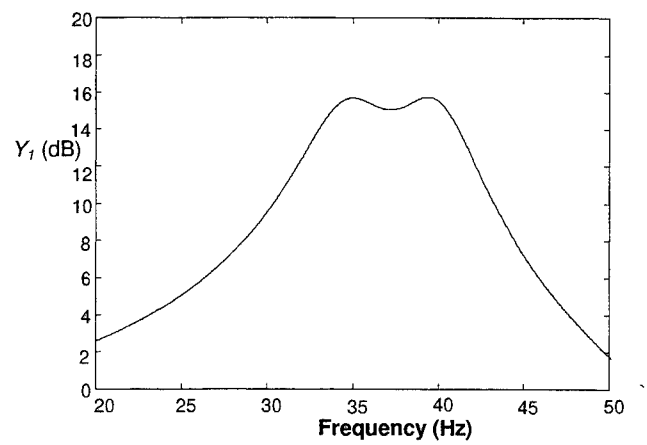

Figure 6. The passive damping index Y_1 for configurations A and B

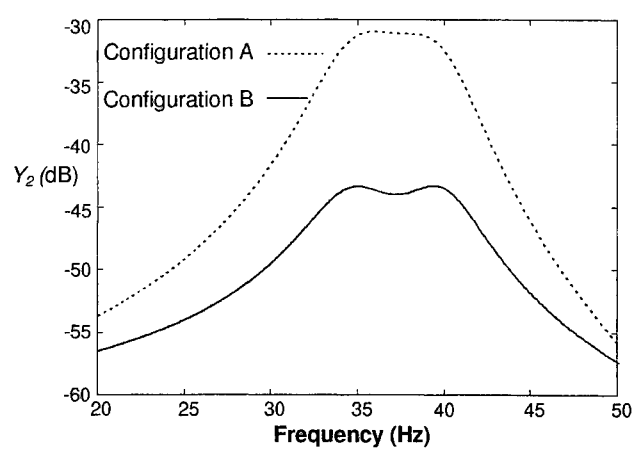

Figure 7. The active control authority index Y_2 For configurations A and B

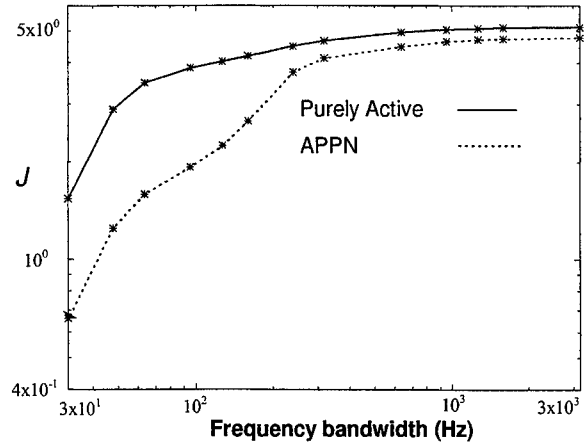

Figure 8. Value of objective function *J* versus excitation frequency bandwidth (Single actuator)

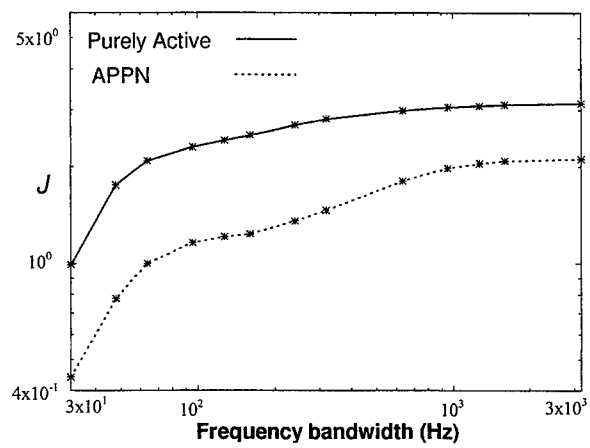

Figure 9. Value of objective function *J* versus excitation frequency bandwidth (Three actuators)

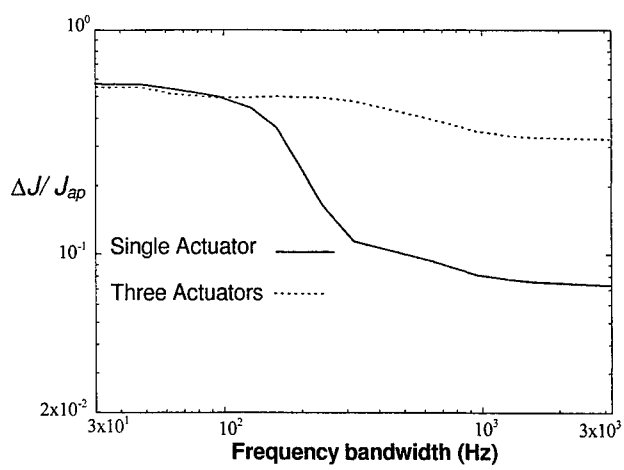

Figure 10. Comparison of multiple (three) actuators and single actuator actions

SESSION 4

Electrorheological Fluid (ERF) Damping

Experimental study of an ER long-stroke vibration damper

David J. Peel, Roger Stanway and
William A Bullough

Department of Mechanical Engineering
The University of Sheffield
Mappin Street
Sheffield
S1 3JD
United Kingdom

ABSTRACT

The development of controllable suspension dampers for ground vehicles is the subject of much current research. In this paper the authors describe aspects of a design methodology for controllable dampers which use electro-rheological (ER) fluid as the working medium. This methodology is based upon a non-dimensional characterisation of ER fluid data which allows measurements obtained from small-scale tests to be used to predict the behaviour of industrial-scale vibration dampers. The ER damper is represented via a Bingham plastic constitutive relationship, augmented by terms to account for fluid inertia and compressibility. An industrial-scale test facility is described and the first available set of experimental results are presented. A comparison is made between model predictions and observed behaviour.

Keywords: vibration isolation, vehicle dynamics, semi-active dampers, electro-rheological fluids.

1. INTRODUCTION

In the development of suspension systems for ground vehicles, the advantages available from the introduction of controllable damping elements are well-established[1] . So-called "semi-active" dampers[2] offer performance superior to that of conventional passive devices without the drawbacks (notably cost, weight and complexity) associated with fully active schemes. The exploitation of semi-active damping concepts, principally by manufacturers of road vehicles, has resulted in mass-produced vehicles fitted with suspension systems that can be controlled either manually or automatically.

Perhaps the most elegant solution to the problem of producing semi-active dampers is through the use of electrically-active fluids. Upon the application of an electrostatic or electromagnetic field of sufficient intensity, such special fluids exhibit a rapid and reversible increase in their resistance to flow. That this solution has not been developed commercially has been due to shortcomings in early developments of the fluids themselves, which could perform admirably under laboratory conditions[3] but failed to meet more stringent industrial specifications, particularly with regard to operating temperature range. However recent years have seen dramatic advances in the formulation of the two main classes of electrically-active fluids. Electro-rheological (ER) fluids[4], the subject of the present study, can now

SPIE Vol. 3045 • 0277-786X/97/$10.00

provide force levels consistent with industrial applications and over sufficiently wide temperature ranges. Magneto-rheological (MR) fluids will operate from a low-voltage source, thus avoiding the need to introduce high levels of electric field strength (typically up to 4 kV/mm or higher) which is required for the operation of ER devices, but at a penalty of slower response times.

In order to be able to examine the feasibility of introducing ER/MR dampers into a range of vehicle suspension applications, there is an urgent need to develop a reliable modelling package for performance prediction and use in device design studies. The development of a modelling package is not straightforward, for a number of reasons. The first problem involves characterisation of the fluid's behaviour. Traditionally, data available on ER fluids has been found to be heavily dependent on the measurement device. Thus data obtained from small samples of fluid could not be relied upon as a basis for predicting the performance of an industrial-scale device. Secondly the damping behaviour of an electrically-active fluid device is liable to be highly non-linear and significantly modified by the effects of fluid inertia and compressibility. Thus the formulation and solution of the equations of motion is non-trivial and requires care if numerical problems are to be avoided. Thirdly, in order to provide convincing validation of the characterisation and modelling procedures, the experimental facility used for testing must include a damper of industrial proportions but be capable of examining the dampers performance under tightly controlled laboratory conditions.

In what follows here, the authors describe the progress that has been made towards the development of a package for modelling semi-active dampers which use the ER fluid as the working medium. Using as an example a damper for controlling the lateral vibrations of a rail vehicle, the key requirements for such a device are summarised. A procedure for characterising the performance of an ER fluid is then presented in order that data from small samples of fluid can be used to predict the behaviour of industrial dampers. The modelling procedure is introduced with emphasis on the use of a Bingham plastic representation, modified to include fluid inertia and compressibility effects. Finally, the experimental facility is described and the first experimental results are presented. The influence of the electric field on damping levels is demonstrated and tentative comparisons are made between model predictions and observed behaviour.

2. CONTROLLING THE LATERAL VIBRATIONS OF A RAIL VEHICLE

In order to place subsequent sections into perspective, it is appropriate to begin by describing a typical vehicle suspension problem and summarising the requirements of the damper.

The problem concerns the control of the lateral vibrations of a rail vehicle[5]. In simplified form the vehicle is modelled as a rigid body which is assumed to have a moment of inertia of 10^6 kg m^2. It is further assumed that motions induced by track irregularities produce a harmonic angular displacement of amplitude ±0.005 rad about a central vertical axis at a natural frequency of 1 Hz. With a span of 14 m between the bogie centres, this angular oscillation results in a linear lateral motion of amplitude 35 mm at each bogie centre where the lateral damper acts.

In the current generation of (UK) rail vehicles the lateral damper is a conventional hydraulic unit with typically an initial rate of 50 kN s m^{-1} up to a piston velocity of 0.2 ms^{-1}. Above this velocity the

rate drops to approximately 7.5 kN s m^{-1}. A comparable damper based upon ER technology might provide a minimum rate of 25 kN s m^{-1}, equivalent to a fail-safe level equal to 50% of that available from the conventional damper. At minimum velocity it is assumed that the application of an electric field would cause the damper to develop a force of 5 kN. At a velocity of 0.2 ms^{-1} the damper would develop a force greater than 10 kN. Taking into account the factors mentioned above leads to the requirement for a force/velocity/displacement envelope of some ±11 kN / ±22 ms^{-1} / ±0.035 m. We will now summarise the modelling of the ER damper so that the appropriate force/state maps can be generated and compared with this requirement.

3. MODELLING THE ER DAMPER : A SUMMARY

3.1 The ER Flow-Mode Damper

It is now well-established that there are three modes of operation - flow, shear and squeeze-flow - through which an ER fluid can provide controllable damping forces. For vehicle suspension applications, such as the one described in the previous section, a flow-mode damper is the most appropriate for accommodating the relatively large force and displacement levels.

A flow-mode damper comprises an ER flow control valve connected in parallel with a hydraulic piston and cylinder arrangement. As we shall explain, the application of an electric field to an ER fluid results in a substantial increase in the fluid's resistance to motion and in the development of a yield stress which must be overcome before flow can occur. Thus the ER valve is effectively a device for modulating the relationship between pressure drop and linear flow rate. Placed in parallel with a piston and cylinder it becomes a device which can modulate the force/velocity characteristics associated with the piston. We will begin to explain the operation of the flow mode damper and then proceed to develop the modelling methodology by considering the control of steady flow in an ER valve.

3.2 Controlling Flow in an ER Valve

Consider an ER valve comprising an annular flow channel of length ℓ, total effective width b and radial channel gap size h. It is assumed that the ratio of channel diameter to electrode gap size is large enough to regard the flow as being between flat plates of infinite width. Also the ratio ℓ/h is assumed to be large enough for flow development effects to be negligible.

Start by considering a steady volume flow rate, Q, of a Newtonian fluid with viscosity coefficient μ and density ρ, through the valve. If the mean fluid velocity through the valve is defined as $\bar{u} = Q / bh$, then it is well known that the uniform shear stress τ_{wo} over the smooth channel walls is a function of four parameters, i.e.

$$\tau_{wo} = fn(\rho, \mu, \bar{u}, h) \tag{1}$$

Dimensional analysis now leads to characterisation of the fluid behaviour in terms of only two parameters : the flow condition Reynolds number $Re = \rho\bar{u}h / \mu$ and a friction coefficient

$Cf = \tau_{wo} / \rho\bar{u}^2$. A graphical plot of Cf versus Re from test data bears a strong similarity to the familiar Moody or Stanton diagram and is useful in that it distinguishes resistance and flow parameters: most importantly, by adding a third parameter to represent the influence of the applied electric field we can visualise the controlling influence of the electric field.

This third parameter follows by plotting Cf versus Re for steady flow of an ER fluid through different valves under various values of constant electric field E. Referring to Fig. 1 each Cf versus Re relationship corresponds to some constant value of the field control parameter. This family of relationships can be ordered in terms of a field-controlled yield stress which we will denote by τ_b.

With the electric field applied, the yield stress τ_b influences the wall shear stress τ_{weo} such that

$$\tau_{weo} = fn(\tau_b, \rho, \mu, \bar{u}, h) \tag{2}$$

Dimensionless groups can be formed from equation (2) such that

$$\left(\frac{\tau_{weo}}{\rho\bar{u}^2}\right) = fn\left[\left(\frac{\rho\bar{u}h}{\mu}\right), \left(\frac{\tau_b \rho h^2}{\mu^2}\right)\right] \quad \text{or} \quad Cf = fn[Re, He] \tag{3}$$

Hence the quasi-steady behaviour of the ER valve can be specified in terms of three non-dimensional groups. The third group, He, the so-called Hedström number, which accounts for the influence of the applied electric field, cannot be determined directly by measurement of valve flow conditions. However by assuming a Bingham plastic constitutive relationship it is possible to estimate a yield stress value corresponding to any valve flow condition. From the Bingham plastic assumption follows a well-known cubic equation which can be written in terms of the three non-dimensional groups defined in equation (3). This equation takes the form

$$Cf^3 - \left\{\frac{3}{2} + 6\left(\frac{Re}{He}\right)\right\}\left(\frac{He}{Re^2}\right)Cf^2 + \frac{1}{2}\left(\frac{He}{Re^2}\right) = 0 \tag{4}$$

Equation (4) can be solved (by any suitable numerical technique) over a range of values of Re: either to give the ER fluid characteristic from test data in the form of He versus Re at constant E; or vice versa when the fluid characteristic is known, to give the steady flow characteristic for any plane valve in the form of Cf versus Re at constant electric field E. Using equation (3) the plot can be interpreted for any control valve size as pressure drop versus volume flow rate at constant electric field excitation. By this means, from a single fluid characteristic plot, steady plane valve flow can be evaluated for a wide range of valve dimensions, flow rates and pressures. This approach to ER fluid characterisation has been validated in tests involving a variety of flow control valves[6], and with yield stress generated from ER clutch data[7,8], for ER fluids of more than one type[8,9].

3.3 Predicting the Performance of the ER Damper

Using a numerical procedure which is described in detail in reference[7], the non-dimensional approach summarised in 3.2 is used to predict the pressure drop versus volume flow rate characteristics of an ER valve. When an ER vibration damper is formed by placing such a valve in parallel with a hydraulic piston/cylinder arrangement this analysis needs to be extended in order to predict the force/velocity characteristics of the piston and to account for the influence of fluid inertia and compressibility on the performance of the damper[5].

The dynamic model is derived on the assumption that the mass of fluid in the cylinder is represented by a mass m and that compressibility effects in the fluid and ducts are accounted for by a spring constant k_1. Resistance to flow between the electrodes is represented by a function, generally non-linear, of the relative velocity, say $f(\dot{x}, \dot{x}_1)$ where $\dot{x}$ is the piston velocity and $\dot{x}_1$ is a velocity associated with the spring element. For this simple lumped arrangement, where F is the nett force on the piston, we can write down the equations of motion,

$$\left.\begin{aligned} m\ddot{x} + f(\dot{x}, \dot{x}_1) &= F \\ -f(\dot{x}, \dot{x}_1) + k_1 x_1 &= 0 \end{aligned}\right\} \tag{5}$$

Essentially, the need to obtain simultaneous estimates of the velocities $\dot{x}$ and $\dot{x}_1$ requires a special numerical procedure. The solution of equation (5) is discussed in detail in reference[6], where there is also a discussion of techniques for assigning numerical values to the fluid inertia term m and the stiffness term k_1.

In the following section, calculations with equation (5) for predicting the response of the damper will be demonstrated in parallel with the presentation of results from the experimental facility.

4. EXPERIMENTAL TESTS

4.1 Introduction

In extensive previous experimental programmes, the authors have investigated various aspects of the behaviour of ER fluids, and these have been reported in numerous publications. The scope of these studies has included electrical characteristics[10,11], thermal behaviour[12], control aspects[1,13], mechanical and physical properties[14,15], and engineering characteristics of the fluids[16].

The operating modes have included the valve flow mode[6], both static[7] and dynamic[17] clutch modes, and the squeeze mode[3]. The test programmes have encompassed steady flows in the valve mode, steady rotational speeds and also "latch" type operation in the clutch mode, and both steady and non-steady electric field excitation, with sinusoidal and step (switched) variation.

These wide-ranging test programmes, and those of other workers in the field, have demonstrated in particular : the useful levels of strength of the fluid response, which can be represented in terms of a static yield stress, related to field excitation strength, which may be of the order 10 kPa; the high speed response to excitation, with time constants of order 1 msec, and reversibility of the effect; the repeatability of the response to a given control signal; the long term reliability of the response; the possibilities for both continuous and switched forms of control; and the possibility for operation with standard items of equipment (e.g. filters, pumps, seals, bearings) without abrasion and without deterioration of fluid performance.

In the operation of any electrically-active fluid system, the variables which are of primary interest are those of force and displacement, the (direct) control signal, and time. The value of the dimensionless presentation of test data, which has been summarised in section 3 above, is that it greatly reduces the number of variables to be assimilated in characterising the system; further, the variables remaining are those of primary interest, viz. force, displacement and control parameters; and finally the performance of devices operating in different modes, or of devices of different sizes operating in one single mode, is related through what is identified essentially as a fluid characteristic.

Although this generalised characterisation technique has been developed for steady state test data - i.e. where the displacement (flow or rotational speed) and control parameters are constant in time - the high speed of fluid response to non-steady field excitation, coupled with the generally second-order significance of change of the force (pressure or surface shear stress) parameter with change of the displacement (flow or rotational speed) parameter, suggests that the generalised characterisation technique might be adaptable to the prediction of ER fluid device behaviour over a low-to-medium frequency range of cyclic mechanical excitation.

The principal outstanding step in the test programmes is that of time dependence of the displacement (i.e. flow or rational speed) parameter. A test rig providing a regulated non-steady (cyclic) flow serves both for investigation of this aspect of ER fluid behaviour, and for development of an application to large force/displacement controllable vibration damping, for which the recent developments of wider operational temperature range and increased available yield strength make ER fluids particularly attractive. For such a system operating at constant control field excitation, in addition to the introduction of inertia and elasticity effects, interest lies initially in two particular points. Firstly, there is the question of the effect of repeated reversal of the flow direction, and of acceleration of the flow from rest, through a period of relatively low flow. Here, hysteresis effects[17] and irregularities at low flow values[6,17] may be significant. Secondly, there is the question of the effect of long fluid residence time within the control valve which will occur, in comparison with the situation prevailing in steady flow; this might be expected to be reflected in the repeatability (or otherwise) of such a cyclic flow.

4.2 The Damper Rig

The force and displacement related data in particular will span wide ranges of value in different ER fluid devices. With this in mind, the non-steady flow test rig - which is called the Damper Rig - was

designed for industrial scale ER fluid device testing, and for realistic study of modelling and design questions. The Damper Rig is illustrated schematically in Fig. 2.

The rig comprises:

(i) a damper unit, with parallel piston-and-cylinder and ER control valve;
(ii) a drive system, having a speed-controlled DC motor driving a variable throw crankshaft via a four speed gearbox;
(iii) a temperature control and ER fluid circulation system;
(iv) a high voltage control signal unit; and
(v) an instrumentation and data-logging system.

4.2.1 The Damper Unit

The damper unit is designed, partly, to investigate practical aspects of operation of a damper in component form. The piston and cylinder and the ER control valve are in parallel, and component size or form can be relatively simply modified. The unit addresses the question of bearing and seal operation with the two-phase fluid. The high pressure fluid circuit is stiff and of low volume. The ER valve has a water cooling jacket. At present the nett piston area is $A = 1355\ mm^2$ (effective diameter 42 mm) and the ER control valve has a single annular channel of length $\ell = 70$ mm, breadth $b = 102$ mm, and inter-electrode gap $h = 0.5$ mm.

4.2.2 The Drive System

The variable speed drive is provided by a 7.5 kW DC motor with feedback speed control, which drives through a four speed gearbox with ratios from 1:1 to 10:1, so that a steep torque/speed slope can be maintained. The drive is transmitted to the piston via a variable throw crankshaft, and at present provides speed/displacement/force ranges of order 0 - 25 Hz / ±80 mm/ ± 10 kN respectively.

4.2.3 The Temperature Control Circuit

Although some settling of the solid phase of an ER fluid may be in some degree inevitable, fluids are generally easily dispersed by motion. In many, or most, working machines, no special provision should be necessary then to maintain fluid in dispersion. The Damper Rig however includes a large fluid reservoir - at present the capacity is some 10 litres - to assist with temperature control, and to provide a store of fluid with known characteristics after a test programme. The reservoir is immersed in a temperature controlled water bath, and ER fluid is circulated through the damper unit from the reservoir, using standard pump and filtration equipment. In an experimental programme, temperature control is necessary for separation of the many test variables. A small base pressure level (≈0.5 bar gauge) is applied at the ER fluid surface in the reservoir.

4.2.4 The High Voltage Control Circuit

The high voltage control power requirement varies with control valve size and ER fluid temperature, as well as with field excitation strength. The high voltage control signal is at present provided from a 300 watt, 0-5 kV capacity operational amplifier, driven by a low voltage (0-10 V) signal generator device. The actual control signal power requirement is frequently <1% of this available power, at a voltage of order 1 kV.

4.2.5 The Instrumentation and Data Logging System

The piston displacement is monitored using an inductive displacement transducer, with crank position indicated additionally by means of a photoelectric probe. The pressure at each side of the piston is measured by means of piezo-resistive type pressure transducers, which operate from dc to high frequency. The ER fluid temperature at each side of the control valve, well within the fluid volume displaced by the piston motion, is measured by means of platinum resistance thermometer probes. The voltage and current of the control signal to the ER valve are monitored directly from the high voltage amplifier. All eight data channels - viz. piston displacement and crank position, pressure, temperature, voltage and current, are coupled to a PC-controlled high speed, multi-channel digital recorder, with 1 Mhz, 12 bit, 16 K sampling per channel. Data record analysis is carried out on a university mainframe computer.

4.3 The Test Programme

The Damper Rig test programme falls into two parts. Firstly, extensive tests have been carried out using a standard hydraulic oil of known characteristics, pressure response being measured for a range of displacement amplitudes and frequencies, and over a range of oil temperatures/viscosities.

The second part of the test programme comprises pressure response measurements for the ER fluid for a range of displacement amplitudes and frequencies, control field values, and operating temperatures. This programme is in progress at the time of writing. The test fluid is Bayer AG Rheobay VP AI 3565.

4.4 Test Results and Discussion

Some preliminary test results from the ER fluid test programme in the Damper Rig are shown in Figs. 3a,b and 4a,b. The results are typical and are not selected for maximum or optimum performance.

In Fig. 3a, a pressure versus velocity plot is shown for constant field excitation at 2 kV/mm, and piston displacement amplitude ±8 mm and frequency 1 Hz. For comparison, a model prediction is shown based on a static yield stress of ≈1.5 kN and fluid bulk modulus of 1.0×10^9 N/m^2. The associated pressure versus displacement plots are shown in Fig. 3b. The same constant field excitation experimental plot is shown again in Fig. 4a, where it is compared with the pressure versus velocity plot for the same piston motion at zero field excitation.

With the exception of the pressure overshoot following the reversal of the piston motion, the piston pressure/velocity/displacement plots under excitation conditions follow qualitatively the expectations which arise from the model calculations, with a prominent loop around the zero velocity point associated with the yield stress and elasticity of the fluid. This loop is seen to be of little significance in the pressure/displacement work diagram.

The comparison of the constant field excitation with the zero field excitation characteristic in Fig. 4a,b shows a large damping gain even at this low field excitation value of 2 kV/mm. In the zero field excitation condition, for the test conditions of Fig. 4a,b, the present piston/cylinder/control valve device has a damping coefficient of $\approx$5 kN s m^{-1}, for a nett effective piston diameter of $\approx$40 mm. For constant field excitation at 2 kV/mm, the equivalent viscous damping coefficient is increased by a factor of $\approx$6.5 to $\approx$32 kN s m^{-1}, with a small phase shift of $\approx 1.5°$.

For constant field excitation at 2 kV/mm the characteristic of Fig. 4a,b represents hydraulic power dissipation at $\approx$40 watts.. This compares with a high voltage control signal power requirement under the prevailing conditions of < 0.4 watt.

Up to the present the test rig and ER fluid have operated reliably with no mechanical or practical problems, and the test data is repeatable. The data shown is at low control field strength, and tests are expected to extend to field strengths of order 6 - 8 kV/mm, to give more than proportionate increases in the equivalent viscous damping coefficient.

5. CONCLUSION

A methodology for the characterisation of ER fluid performance data, and its application to the modelling of a controllable ER vibration damper, have been described. An industrial scale ER damper test rig has been described, and some early experimental results presented, and compared satisfactorily with model predictions.

6. REFERENCES

1. A. S. Naem, R. Stanway, J. L. Sproston and W. A. Bullough, "A strategy for adaptive damping in vehicle primary suspension systems", Proc. ASME Winter Annual Meeting, Chicago, 1994, pp. 395-399.
2. D. Karnopp, M. J. Crosby and R. A. Harwood, "Vibration control using semi-active force generators", Trans, ASME, Journal of Engineering for Industry, Vol. 98, 1974, pp. 619-626.
3. R. Stanway, J. L. Sproston, M. J. Prendergast, J. R. Case and C. E. Wilne, "ER fluids in the squeeze-flow mode : an application to vibration isolation", J. Electrostatics, 28(1992), pp. 89-94.
4. R. Bloodworth and E. Wendt, "Materials for ER fluids", Proc. 5th Int. Conf. ER Fluids, MR Suspensions and Assoc. Technol. (Sheffield, 1995) (Singapore : World Scientific), pp. 118-131.
5. D. J. Peel, R. Stanway and W. A. Bullough, "Dynamic modelling of an ER vibration damper for vehicle suspension applications", Smart Mater. Struct., 5(1996), pp. 591-606.

6. D. J. Peel and W. A. Bullough, "Bingham plastic analysis of ER valve flow", Int. J. Mod. Phys. B., Vol. 8 (20,21), pp. 2967-2985, 1994.
7. D. J. Peel and W. A. Bullough, "Prediction of electro-rheological valve performance in steady flow", Proc. I.Mech.E., Pt. C, J. Mech. Eng. Sci., Vol. 208, pp. 253-266, 1994.
8. D. J. Peel and W. A. Bullough, "A technique for the normalisation of electro-rheological fluid performance data in cylindrical/shear and pressure/flow modes of steady operation", Proc. SPIE 96 Smart Structures Conference, Bangalore, Dec. 1996, to be published (SPIE).
9. D. J. Peel, R. Stanway and W. A. Bullough, "A generalised presentation of valve and clutch data for an ER fluid, and practical performance prediction methodology", Proc. 5th Int. Conf. ER Fluids, MR Suspensions and Assoc. Technol. (Sheffield, 1995) (Singapore : World Scientific), pp. 279-290.
10. M. Whittle, R. Firoozian, D. J. Peel and W. A. Bullough, "A model for the electrical characteristics of an ER valve", Int. J. Mod. Phys. B., 6(15), pp. 93-108, 1993.
11. A. H. Sianaki, W. A. Bullough, R. Tozer and M. Whittle, "Experimental investigation into electrical modelling of electro-rheological fluid shear mode", Proc. I.E.E., Sci. Mest. and Tech., Vol. 141, No. 6, pp. 531-537, 1994.
12. R. Smyth, W. A. Bullough, L. K. Lim and J. Makin, "Heat transfer considerations for Couette devices operating with electro-structured fluids", Proc. of Conf. on Adapt. Mats., Williamsburg Va, USA, June 1994 (Technomic Press), pp. 1164-1175.
13. R. Tozer, C. T. Orrell and W. A. Bullough, "On-off excitation switch for ER devices", Int. J. Mod. Phys. B, 8 (20,21), pp. 3005-3014, 1994.
14. M. Whittle, W. A. Bullough, D. J. Peel and R. Firoozian, "Electro-rheological dynamics derived from pressure response experiments in the flow mode", J. Non-Newtonian Fl. Mech., Vol. 57, No. 1, pp. 1-25, 1995.
15. M. Whittle, D. J. Peel, R. Firoozian and W. A. Bullough, "Dependence of ER response time on conductivity and polarisation time", Phys. Rev. E., Pt. 6A, Vol. 49, pp. 5249-5259, 1994.
16. D. J. Peel, D. Brooks and W. A. Bullough, "Experiences in the pumping of electro-rheological fluids", Proc. 9th Conf. on Fluid Machines, Budapest, 1991, pp. 362-369 (Acad. of Sci., Hungary).
17. W. A. Bullough, A. R. Johnson, A. H. Sianaki, J. Makin and R. Firoozian, "The electro-rheological clutch : design, performance characteristics and operation", Proc. I.Mech.E., Pt. I, J. of Syst. and Control Eng., Vol. 207, pp. 87-95, 1993.

ACKNOWLEDGEMENTS

The authors wish to thank Bayer AG for supply of the ER fluid for the test programme and the Advanced Rail Research Centre for financial support of the work. The assistance of Mrs L. A. Carter in preparing the manuscript is also gratefully acknowledged.

RS/PAPER16/LAC

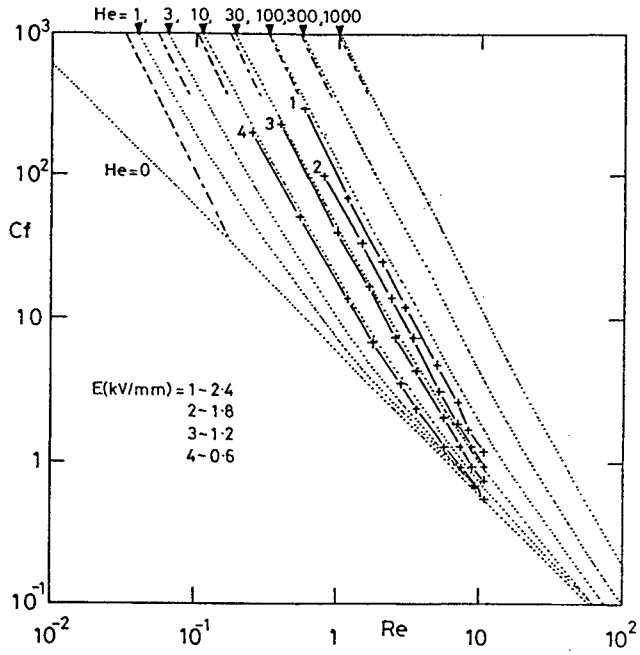

Fig. 1. Dimensionless characteristic of plane valve flow. Friction Coefficient Cf vs. Reynolds Number Re at constant field excitation E.

_____ experimental data

..... calculation at constant He from equation (4)

_ _ _ asymptote $Cf.Re^2/He = 1$ (static boundary)

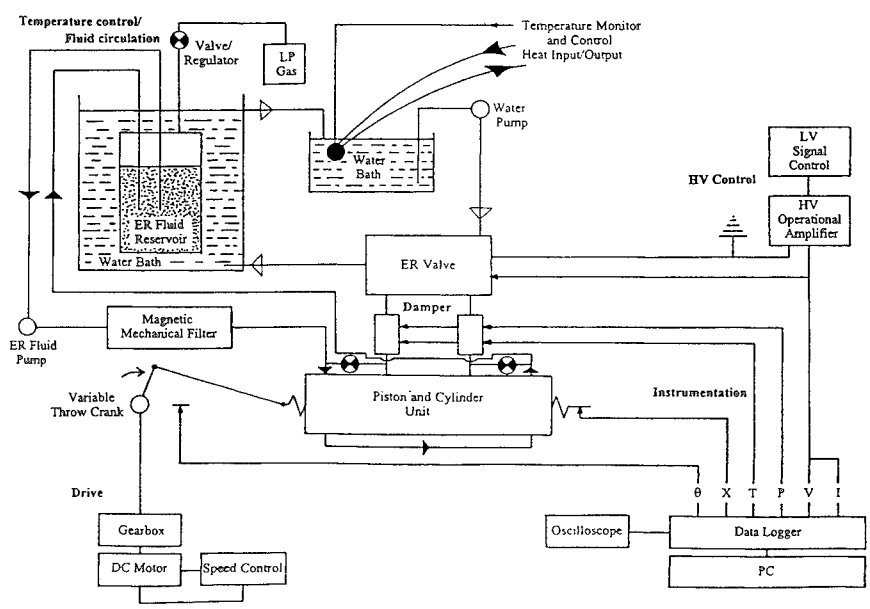

Fig. 2. General arrangement of the Damper Test Rig.

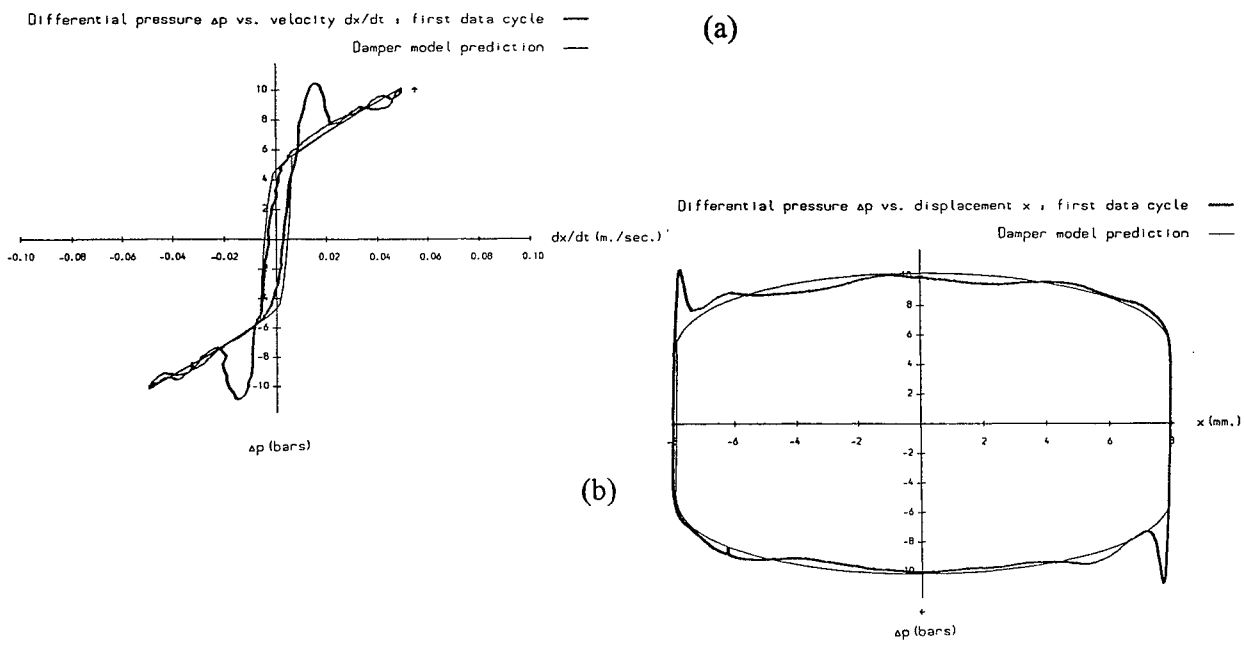

Fig. 3. Damper Rig test data : (a) pressure vs. velocity; (b) pressure vs. displacement. Constant field excitation E=2kV/mm, compared with model calculation, 1Hz, ±8mm:

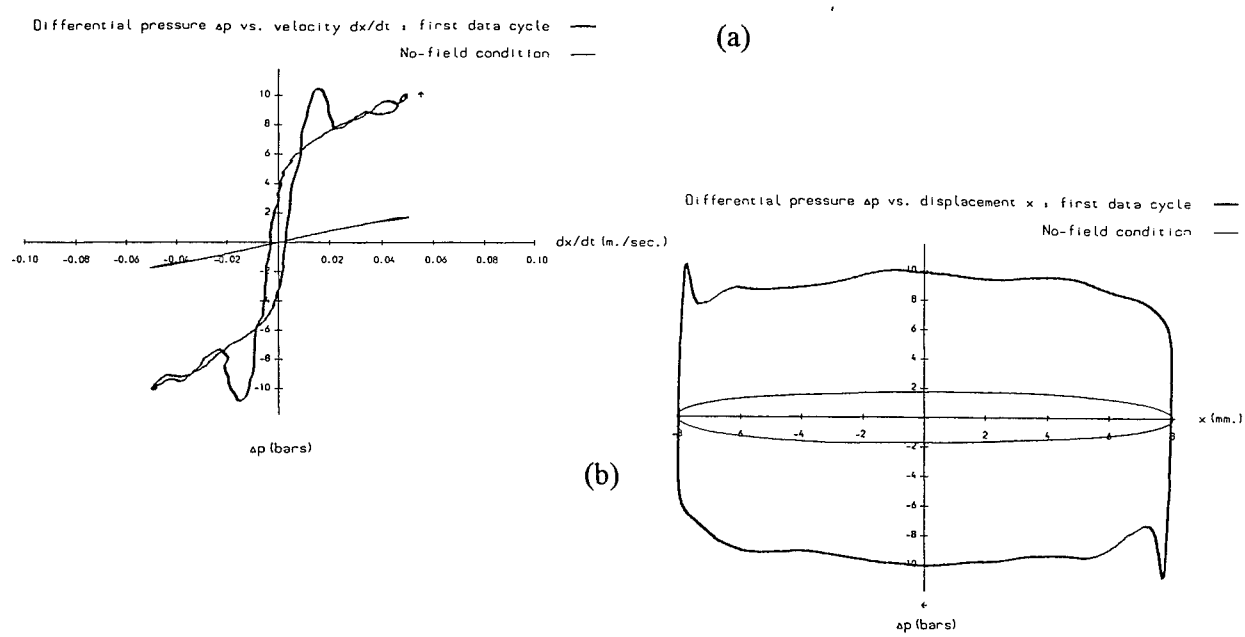

Fig. 4. Damper Rig test data : (a) pressure vs. velocity; (b) pressure vs. displacement. Constant field excitation E=2kV/mm, compared with zero field excitation, 1Hz,±8mm.

Nonlinear Modeling and Performance Prediction of Electrorheological Fluid Dampers *

Gopalakrishna M. Kamath †
Graduate Research Assistant

Norman M. Wereley ‡
Assistant Professor

Center for Rotorcraft Education and Research
Dept. of Aerospace Engineering
University of Maryland
College Park, MD 20742

Abstract

A combined theoretical and experimental study of electrorheological (ER) fluid dampers is presented here. A moving electrode ER damper was built and tested for its dynamic characteristics for different electric field strengths and varying displacement amplitudes. Based upon the phenomenology observed in the experimental results, an augmented nonlinear model is proposed to describe the dynamic characteristics of the damper. The six model parameters are estimated from the experimental hysteresis data. The force vs. displacement and force vs. velocity hysteresis cycles are then reconstructed using these estimated parameters. The results show that the model captures the nonlinear damper behavior quite accurately. The importance of the various components in the model is illustrated.

Introduction

There has been an increased emphasis on reducing the number of movable parts in helicopter rotor hubs to prolong life and reduce maintenance costs. This has lead to the development of advanced rotor systems such as hingeless and bearingless rotors. These soft in-plane rotor systems tend to suffer from aeromechanical instabilities such as air and ground resonances [1]. These instabilities can be mitigated by augmenting the lag mode damping in these rotors. Hydraulic dampers and elastomeric dampers which use viscoelastic materials, are currently being used for this purpose. However, elastomers are highly nonlinear materials whose properties are dependent on both frequency and temperature. Their nonlinear dual frequency behavior has been shown to reduce damping and thus cause limit cycle oscillations at low amplitudes [2]. In order to circumvent the problems associated with elastomers, Fluidlastic dampers have been proposed whose stiffness remains relatively constant with amplitude [3, 4]. But for accurate blade tracking, the damper for each blade has to be matched exactly. Moreover, damping augmentation is required only in certain flight regimes. These specifications can be met with a damper with adaptive properties. Controllable fluid dampers have thus proven to be an attractive choice for augmenting lag mode damping in advanced rotor systems. One of the impediments in the application of these dampers is the lack of a good model to predict their dynamic behavior. The dynamics of the helicopter rotor system is sensitive to the dynamic characteristics of the lag mode damper. Hence it is important to be able to model the the damper behavior with a fair amount of confidence. This paper presents a theoretical and experimental study of controllable fluid dampers that serves as a step towards this goal.

Controllable fluids such as electrorheological (ER) and magnetorheological (MR) fluids belong to the class of *smart* materials that have the unique ability to change properties when acted upon by an electric or magnetic field. This change is mainly manifested as a substantial increase in the dynamic yield stress of the fluid. ER fluid applications have so far outnumbered those of MR fluids primarily due to the wider commercial availability of

*Presented at the 1997 4th Annual Symposium on Smart Structures and Materials Symposium, Passive Damping and Isolation Conference, San Diego, CA, 2–6 March 1997.

†Student Member, AIAA, AHS

‡Member AIAA, AHS. Tel: (301) 405-1927, Fax: (301) 314-9001, E-mail: wereley@eng.umd.edu

ER fluids [5, 6, 7]. MR fluids have captured the attention of researchers only recently, on account of their superior properties [8]. Inspite of numerous applications, a definitive model to account for the dynamic behavior of controllable fluids is lacking. ER and MR fluids exhibit qualitatively similar characteristics [9]. This paper focusses primarily on the phenomenological model for ER fluid damper behavior which can be applied to MR fluid dampers as well. The model uses linear mechanisms in conjunction with nonlinear shape functions to model the various nonlinear effects, such as transition at yield and Coulomb friction effects at low amplitudes. This paper also describes the experiments that were conducted to support and validate the phenomenological ER damper model. The results show that the model captures the nonlinear effects quite accurately and thus would provide a valuable tool in the design and prediction of systems incorporating controllable fluids.

ER fluids behave like simple viscous fluids in the absence of an electric field and their behavior can be described by the Newtonian shear model. When an electric field is applied, the fluid exhibits the presence of a yield phenomenon wherein the material does not flow until the critical yield stress value is exceeded. This yield stress value increases as a quadratic function of the applied electric field. A simplified model to describe this yield phenomenon is the Bingham plastic model. This model is a good approximation for the post-yield behavior and can be used as a starting point for damper design [10]. But under dynamic conditions, the pre-yield behavior also plays an important role in determining the overall dynamic characteristics of the damper. In these cases, factors such as frequency and amplitude of excitation also need to be considered.

Various models have been proposed to describe the dynamic properties of ER fluids and ER fluid dampers. Gamota, *et al* [11] proposed a model based on the Fourier analysis of ER fluid stress response for different cases. The experimental studies upon which this model was based provided valuable insight into the dynamic behavior of these materials [12, 13]. We proposed a nonlinear viscoelastic-plastic model which described the pre-yield and the post-yield characteristics of an ER fluid using a nonlinear network of linear viscoelastic and viscous elements [14, 15]. The above discussed models are strictly for describing ER material behavior. These models depend only on the material properties.

There are also models that describe controllable fluid damper behavior. Apart from the fluid properties, the modeling of a damper involves geometry dependent properties such as the damper size and built-up effects due to rod seals and bearings. Stanway, *et al* [16] proposed using a Coulomb element in parallel with a dashpot element. The element parameters were estimated using a nonlinear filtering algorithm. Ehrgott and Masri [17] conducted experiments with a dynamic testing device incorporating an ER fluid. The device response was simulated using a non-parametric identification method based on Chebyshev polynomials. Lou, *et al* [18] used the Bingham plastic model with factors to account for the frequency effects and conducted a parametric study to evaluate the performance of different configurations. Spencer, *et al* [19] proposed the Bouc-Wen model to describe MR damper behavior. We extended the nonlinear viscoelastic-plastic fluid model to describe the behavior of a mixed mode type of damper [20, 21]. The frequency response of a mass-spring-ER damper system was shown to be very close to that of a proportional Coulomb and viscously damped system [21]. Makris, *et al* [22] developed a phenomenological elastic-plastic model to account for the pre-yield and post-yield behavior and used it in conjunction with a neural network.

This paper presents a combined experimental and theoretical study of an ER fluid damper. A mixed mode, moving electrode ER damper was built and tested for different field strengths and excitation amplitudes. An augmented nonlinear model is presented that simulates both the force-displacement and the force-velocity hysteresis cycles. The model accurately captures the nonlinear Coulomb effects and the effects of fluid inertia. The model uses linear mechanisms networked with smooth nonlinear functions that make it numerically more robust. The linear mechanisms contain only a few parameters (6 in number) that can be easily estimated.

ER Damper Experiments

A moving electrode ER damper was fabricated. In this damper configuration, one electrode moves relative to the other. The resisting force of the damper is then a sum of the viscous drag due to the relative motion and the pressure drag force created as a reaction to the liquid being forced through the electrode gap. A sketch of the ER damper is shown in Fig. 1. The outer shell and the piston head are made of aluminum so that it also serves as the two electrodes. In the damper used for this study, the electrode gap was chosen to be 0.1 inches. The other dimensions shown in Figure 1 were then determined using the quasi-steady Bingham plastic model equations for a moving electrode damper [10]. We allowed for a nominal stroke of 2 inches peak-to-peak. The ER fluid used was the VersaFlo ER-100 manufactured by Lord Corporation. O-ring seals were used to contain the fluid inside the damper and linear bearings were used to align the inner electrode with the outer shell. A steel frame was built to support

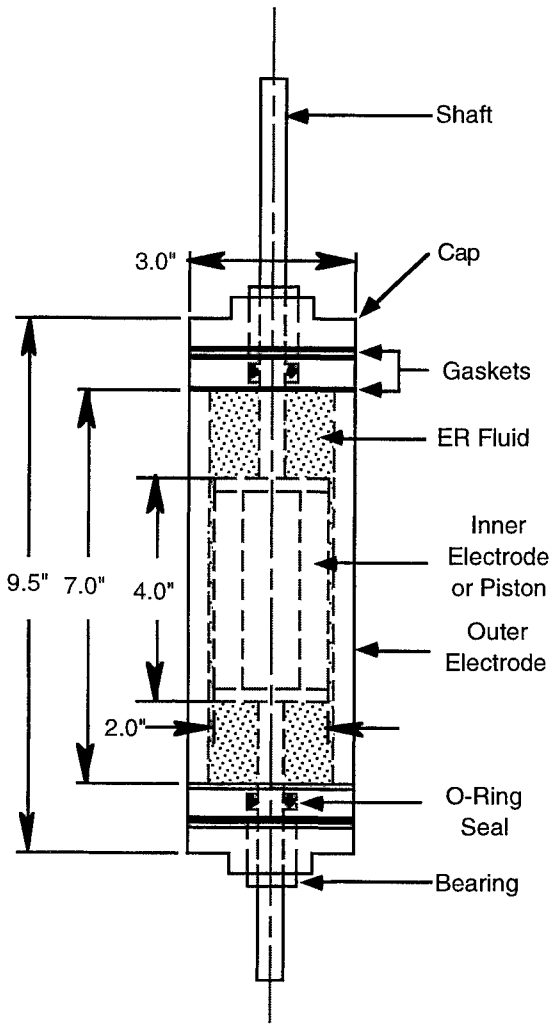

Figure 1: A sketch of the moving electrode ER fluid damper.

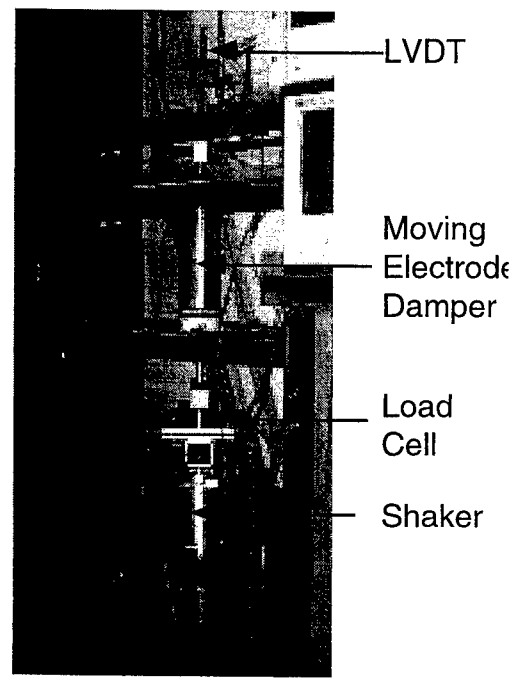

Figure 2: The experimental setup for dynamic testing of ER fluid dampers.

the outer shell and the shaft with the piston was free to be connected to the shaker. The experimental setup for the dynamic test measurements is shown in Fig. 2. A Brüel Kjær 4801T shaker was used to excite the shaft which is connected to the piston. The shaker had a maximum force output of 85 lbs with a displacement range of 0.5 inches peak-to-peak. A Sensotec load cell with 100 lbs range was mounted between the shaft and the shaker to measure the force input to the damper. A Schaevitz LVDT measured the shaft displacement. The time history signals from the load cell and the LVDT were recorded using a Hewlett Packard 35665A spectrum analyzer. A sinusoidal signal with a frequency of 10 Hz was used to drive the shaker. The force levels and hence the displacement levels were changed by varying the gain on the shaker amplifier. The measurements were made for various displacement amplitudes, and each of these measurements were repeated for varying electric field strengths. The readings from the load cell were plotted against the LVDT measurements to generate the force vs. displacement hysteresis cycles. The velocity time histories of the damper were calculated from the respective displacement data using a fourth order central difference scheme. The LVDT data was first filtered to remove the high frequency noise components using a simple Fourier decomposition.

Experimental Results

A representative set of experimental hysteresis data is plotted in Fig. 3. The plot shows the force vs. displacement

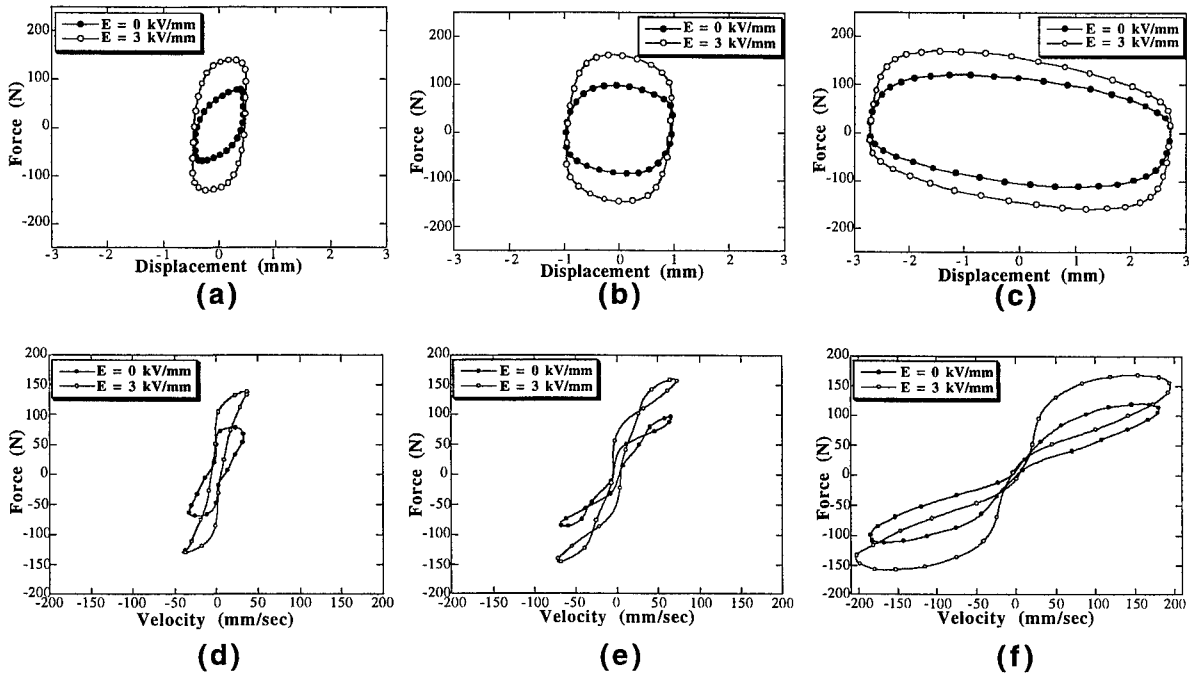

Figure 3: A sample set of experimental hysteresis data for different displacement amplitudes and field strengths: (a) F vs. X plots for 0.5 mm amplitude (b) F vs. X plots for 1.0 mm amplitude (c) F vs. X plots for 3.0 mm amplitude (d) F vs. V plots for 0.5 mm amplitude (e) F vs. V plots for 1.0 mm amplitude (f) F vs. V plots for 3.0 mm amplitude.

(F vs. X) and the force vs. velocity (F vs. V) hysteresis cycles for the two extreme values of electric field, 0 and 3 kV/mm, and for three displacement amplitudes, 0.5, 1.0, 3.0 mm.

Effect of Electric Field

It can be seen from Figs. 3(a),(b) and (c) that, as the applied electric field is increased, the amount of damping which is represented by the area enclosed by the force vs. displacement hysteresis cycle also increases. The Bingham plastic like behavior of ER materials can be seen in the force vs. velocity hysteresis cycles (Figs. 3(d), (e) and (f)). If a line is drawn approximately through the center of the F vs. V cycles, a curve is obtained that is reminiscent of the force vs. velocity (or shear stress vs. strain rate) curves for Bingham plastic materials (Fig. 4). It can also be seen that the yield force increases with the electric field.

Effect of Displacement Amplitude

The three amplitudes for which the hysteresis plots are shown in Fig. 3 were chosen to nominally represent the three rheological domains: the pre-yield, yield and post-yield regions of the ER fluid behavior. The differences in behavior through these three domains is manifested in a more obvious way in the F vs. V hysteresis cycles, and in a more subtle way in the F vs. X hysteresis cycles. For an amplitude of 0.5mm (Fig. 3(d)), which is the pre-yield phase, the F vs. V hysteresis cycles form a single loop traversing in an anti-clockwise direction (the directions discussed are not obvious from the hysteresis plots and were determined from the raw experimental data), which is indicative of a viscoelastic nature. As the amplitude is increased to 1.0 mm (Fig. 3(e)), two additional loops appear at the extremities in which the direction is clockwise. This is indicative of a viscous nature with fluid inertia effects. Thus this curve shows the transition at yield from a viscoelastic behavior to a viscous behavior. As the amplitude is increased further (Fig. 3(f)), the inner loop shrinks for E = 3 kV/mm and totally disappears for E = 0 kV/mm. This shows that the fluid as fully yielded and its viscous nature dominates the damper behavior. The elliptical nature of

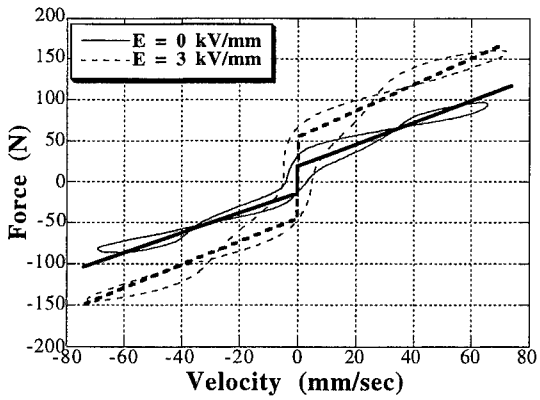

Figure 4: A comparison of force vs. velocity hysteresis cycles with the classical Bingham plastic model for a displacement amplitude of 1.0 mm.

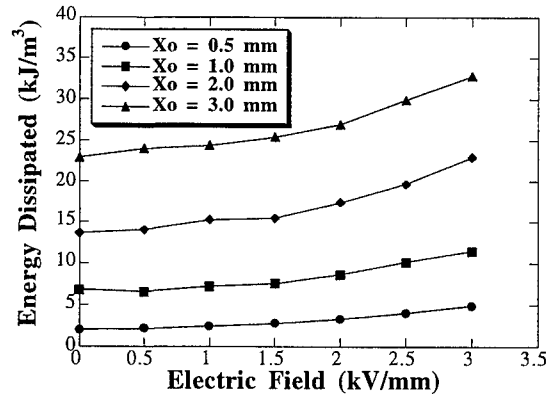

Figure 5: Variation of dissipated energy with electric field for different displacement amplitudes.

the F vs. X hysteresis cycles (Fig. 3(c)) also suggests this viscous behavior, and the slight negative inclination of the ellipses demonstrates the effects of fluid inertia.

Energy Dissipation and Equivalent Damping

The energy dissipated by a damper over one vibration cycle is a measure of its damping capacity. This is given by the area enlosed within the F vs. X hysteresis cycle, which is given by the integral

$$U = \oint F\,dx = \int_0^{\frac{2\pi}{\omega}} F.v\,dt \tag{1}$$

Using the experimental data and integrating it numerically, the dissipated energies were calculated for different field strengths and displacement amplitudes. In order to measure the *efficiency* of a controllable fluid damper, it is important to know the amount of damping achieved for a unit volume of active fluid. In an ER fluid damper, the active fluid volume is the volume of fluid between the two electrodes. Thus for comparison purposes, it is more useful to calculate the dissipated energy per unit active fluid volume. These values were calculated and are plotted in Fig. 5.

The dissipated energy increases as a quadratic function of the electric field. In order to compare the damping performance of a controllable fluid damper with that of a conventional viscous dashpot damper, an equivalent damping coefficient can be determined for the former by equating the energies dissipated in the two cases. Thus

$$C_{eqv} = \frac{U}{\pi\omega X_0^2} \tag{2}$$

where ω is the excitation frequency and X_0 is the displacement amplitude. The equivalent damping coefficients for different sets of data are plotted in Fig. 6. It can be seen that for low amplitudes, where the fluid is in the pre-yield phase, the value of C_{eqv} rises more rapidly with increase in electric field than for high amplitudes, where the fluid is in the post-yield phase. Thus in order to exploit the adaptivity of the controllable fluid damper, the dampers have to operated close to the yield point. For high amplitudes, the C_{eqv} curve tends to flatten to a horizontal line (zero adaptivity) with the C_{eqv} value equal to that of the zero field case which is the Newtonian behavior. The dotted line represents the C_{eqv} value calculated for the zero field case using a simple Newtonian model as explained in Reference [10].

The Augmented Nonlinear Damper Model

The experimental results discussed in the previous section offer a good understanding of the phenomenology of an ER damper. There are two distinct rheological domains over which the dampers operate: the pre-yield and the post-yield regions. The pre-yield region is characterized by a strong viscoelastic nature and also exhibits some

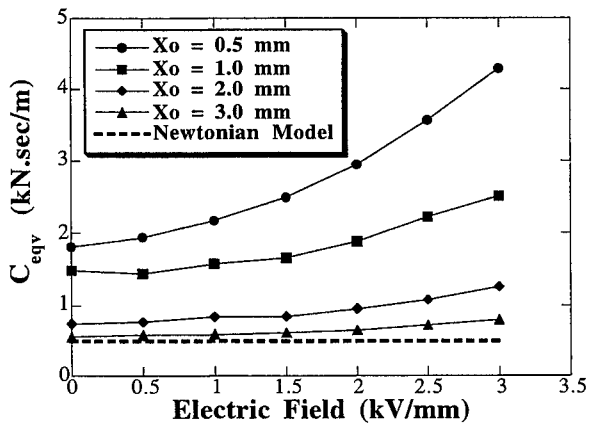

Figure 6: Variation of equivalent damping coefficient C_{eqv} with electric field for different displacement amplitudes with the Newtonian model as the baseline value.

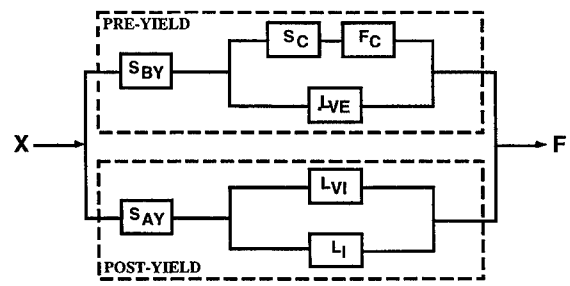

Figure 7: The schematic of the Augmented Nonlinear Model network for ER fluid dampers.

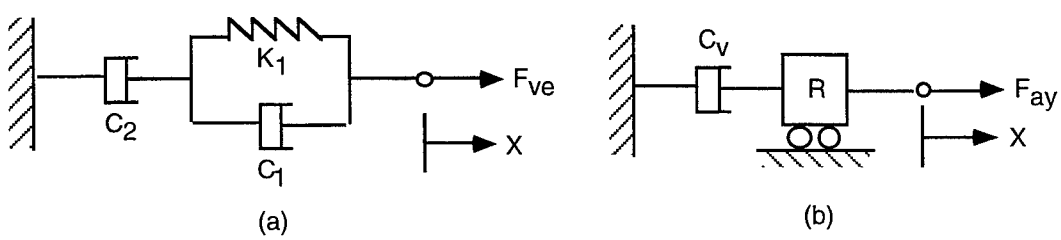

Figure 8: Mechanisms used in the model:(a) the viscoelastic mechanism L_{ve} in the pre-yield branch of the model (b) the viscous mechanism L_{vi} and the inertial mechanism L_i in the post-yield branch of the model.

sticktion properties. The Coulomb-like sticktion effects are contributed in different measures by the ER fluid and the damper components such as the dynamic rod seals. As the amplitude increases, the sticktion effects appear to be less significant. The post-yield region shows a dominant viscous behavior where the fluid inertia effects come into play. The yield point separating the two rheological domains varies as a function of the electric field and the displacement amplitude. The overall behavior of the ER damper can then be simulated by choosing the appropriate linear shear mechanisms for the two regions and then combining them to capture the transition between the two regions. A schematic of the network that accomplishes this is shown in Fig. 7. One branch of the network comprises of the pre-yield components while the other branch contains the post-yield components.

Pre-yield Mechanisms

The 3-parameter fluid model shown in Fig. 8(a) is used as the mehanical analog for the viscoelastic behavior in the pre-yield region. This is represented by the linear operator L_{ve} in the model network. The force-displacement differential equation in the time domain is given by

$$F + p_1\dot{F} = q_1\dot{X} + q_2\ddot{X} \tag{3}$$

where

$$p_1 = \frac{C_1 + C_2}{K_1} \tag{4}$$

$$q_1 = C_2 \tag{5}$$

$$q_2 = \frac{C_1 C_2}{K_1} \tag{6}$$

If a sinusoidal excitation is assumed, then the above differential equation can be written in the frequency domain as

$$F = G^* X \tag{7}$$

where G^* is the complex shear coefficient.

$$G^* = G' + jG'', \quad j = \sqrt{-1}$$

and

$$G' = \frac{K_1 C_2^2 \Omega^2}{K_1^2 + (C_1 + C_2)^2 \Omega^2} \tag{8}$$

$$G'' = \frac{(C_1 + C_2) C_1 C_2 \Omega^3 + K_1^2 C_2 \Omega}{K_1^2 + (C_1 + C_2)^2 \Omega^2} \tag{9}$$

where Ω is the excitation frequency. The sticktion effects seen in the damper behavior at low velocities is described using the parameter F_c and the shape function S_c given by the equation

$$S_c = \frac{1}{2}\left\{\tanh\left(\frac{\dot{X}}{4\epsilon_c}\right)\right\} \tag{10}$$

where $\dot{X}$ is the velocity amplitude and ϵ_c is the smoothening factor that ensures smooth transition from the negative to postive velocities and vice versa. Thus the pre-yield force component is given by

$$F_{by} = F_{ve} + S_c F_c \tag{11}$$

where F_{ve} is given by Eqn. 7.

The nonlinear shape function S_{by} is the pre-yield switching function which along with S_{ay} effects the smooth transition from the pre-yield phase to the post-yield phase. The function S_{by} is dependent on a yield parameter α_y that is chosen during the estimation process. S_{by} is given by

$$S_{by} = \frac{1}{2}\left\{1 - \tanh\left(\frac{\alpha - \alpha_y}{4\epsilon_y}\right)\right\} \tag{12}$$

where α_y is the yield parameter, α is the velocity nondimensionalized with respect to the velocity amplitude and ϵ_y is a smoothening parameter.

Post-yield Mechanisms

The post-yield branch of the network consists of L_{vi}, the viscous mechanism and L_i, the inertial component. These components can be combined and represented as shown in Fig. 8(b). Thus the post-yield force component is given by

$$F_{ay} = C_v \dot{X} + R\ddot{X} \tag{13}$$

S_{ay} is similar to the shape function S_{by} where S_{ay} acts as a switching function to turn on the post-yield mechanism when the damper crosses the yield point. It is given by

$$S_{ay} = \frac{1}{2}\left\{1 + \tanh\left(\frac{\alpha - \alpha_y}{4\epsilon_y}\right)\right\} \tag{14}$$

Augmented Model

For a sinusoidal displacement input the force output as given by the augmented nonlinear damper model is written as

$$F = S_{by} F_{by} + S_{ay} F_{ay} \tag{15}$$

where F_{by}, S_{by}, F_{ay} and S_{ay} are given by Eqns. 11, 12, 13, and 14 respectively.

Thus rather than using nonlinear elements, the augmented model takes the novel approach of using linear mechanisms in conjunction with nonlinear shape functions. Moreover, the mechanisms chosen, the type of shape functions and the structure of the model network are based heavily on the observed phenomenology of the damper behavior.

System Identification

Having established the model structure and the model components, the parameters in the model need to be identified. The unknown parameters are the viscoelastic parameters C_1, C_2 and K_1, the viscous parameter C_v, the inertial parameter R and the sticktion parameter F_c. The model uses the displacement as an input and then calculates the velocities and accelerations needed for the model and then gives the total force, given by Eqn. 15, as the output. Thus the parameters are estimated on the basis of minimizing the error between this force output F, and the actual force F_m obtained from experimental measurements. The error in the model is represented by the objective function J given by,

$$J = \sum_{i=1}^{N} (F_i - F_{m_i})^2 \tag{16}$$

where N is the number of data points for each hysteresis cycle, F is the force predicted by the model and F_m is the experimentally measured force. To obtain physically meaningful results, the parameters are constrained to have positive values. The constrained optimization was done using Design Optimization Tools (DOT) [23]. The parameter α_y was manually chosen such that the objective function reached a minimum.

Results

Using the parameters estimated from the system identification process, the force vs. displacement and the force vs. velocity hysteresis cycles were reconstructed and compared with the experimental data. For the sample data set shown in Fig. 3, the reconstructed hysteresis cycles are shown in Fig. 9 and Fig. 10. As it can be seen from the figures, the model accurately captures every nuance of the experimental data. The model has been significantly improved from the nonlinear viscoelastic-plastic model presented in References [20] and [21] with the inclusion of the inertial and the sticktion parameters.

To illustrate the importance of the parameters F_c and R in modeling ER fluid dampers, the force vs. velocity hysteresis cycles are reconstructed first without one or more of these parameters and then with the fully augmented model and each compared with the experimental data for two data sets. These plots are shown in Figs. 11 and 12. Figs. 11(a) and 12(a) compare the prediction of the model without the inertial or the sticktion parameter. The model predictions without these parameters show many discrepancies in correlation. The loops at the extremities of the hysteresis cycles are absent and the correlation is very poor close to zero velocities. On adding the inertial parameter, the loops appear in the hysteresis cycles, but the sticktion effect at low velocities is absent (Fig. 11(b) and Fig. 12(b)). On adding the sticktion parameter, the correlation is improved at low velocities (Fig. 11(c) and Fig. 12(c)).

The additional parameters minimally affect the correlation of the model with the experimental force vs. displacement hysteresis data. The viscoelastic-plastic model without the additional inertial and sticktion parameters is sufficient to accurately capture the force vs. displacement hysteresis cycles. Hence, if the amount of damping is the important criterion, then the model without the additional parameters should give a good estimate. But if the force vs. velocity hysteresis behavior is important for predicting system behavior, then the augmented model should be used.

Conclusions

A detailed experimental study of a moving electrode ER damper is presented. The hysteresis data gives a clear picture of the phenomenology of the damper behavior. The two rheological domains in the ER fluid are distinctly observed and are manifested in the hysteresis behavior. An augmented nonlinear model for the ER damper is proposed that derives its structure solely from the phenomenology of the force vs. displacement and force vs. velocity hysteresis characteristics as observed from experiments. The model faithfully captures the damper behavior for different field strengths and displacement amplitudes. The sticktion effects are important for low amplitudes when the fluid is in the pre-yield phase. For large amplitudes, the fluid is in the post-yield phase and the inertial factors become important here. More experiments are underway to determine the effects of frequency on the damper behavior.

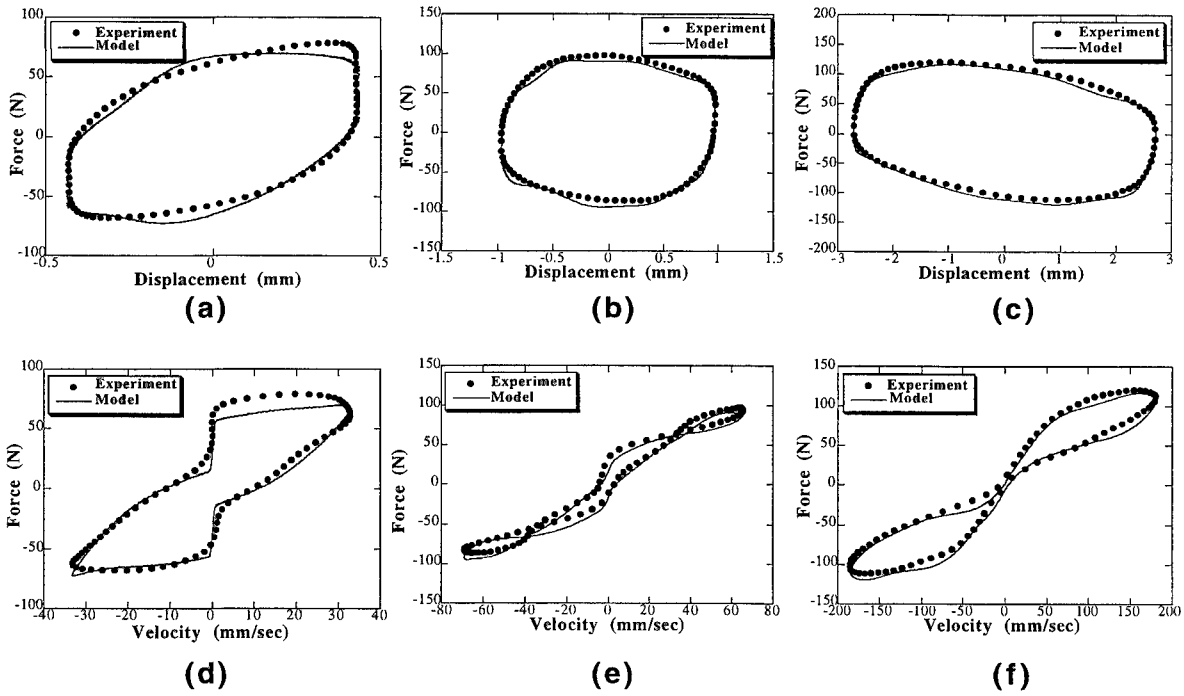

Figure 9: A comparison of hysteresis cycles from estimated parameters with experimental hysteresis data for E = 0 kV/mm: (a) F vs. X plots for 0.5 mm amplitude (b) F vs. X plots for 1.0 mm amplitude (c) F vs. X plots for 3.0 mm amplitude (d) F vs. V plots for 0.5 mm amplitude (e) F vs. V plots for 1.0 mm amplitude (f) F vs. V plots for 3.0 mm amplitude.

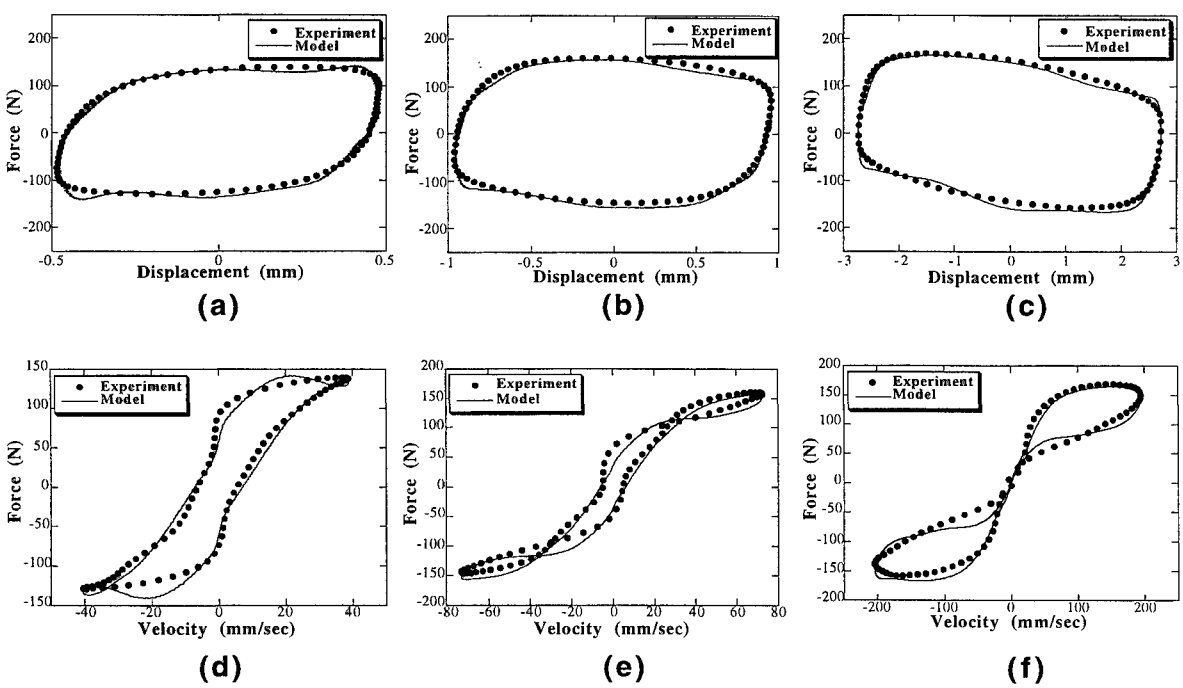

Figure 10: A comparison of hysteresis cycles from estimated parameters with experiments for E = 3 kV/mm: (a) F vs. X plots for 0.5 mm amplitude (b) F vs. X plots for 1.0 mm amplitude (c) F vs. X plots for 3.0 mm amplitude (d) F vs. V plots for 0.5 mm amplitude (e) F vs. V plots for 1.0 mm amplitude (f) F vs. V plots for 3.0 mm amplitude.

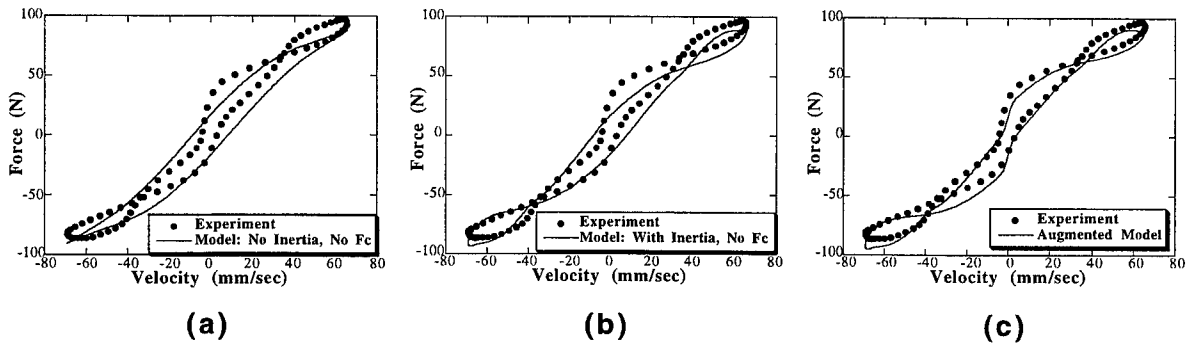

Figure 11: A comparison of experimental hysteresis data for $E = 0$ kV/mm, $X_0 = 1.0$ mm with the hysteresis plots obtained using (a) the model without the inertial or sticktion parameters (b) the model with the inertial parameter but without the sticktion parameter (c) the fully augmented model.

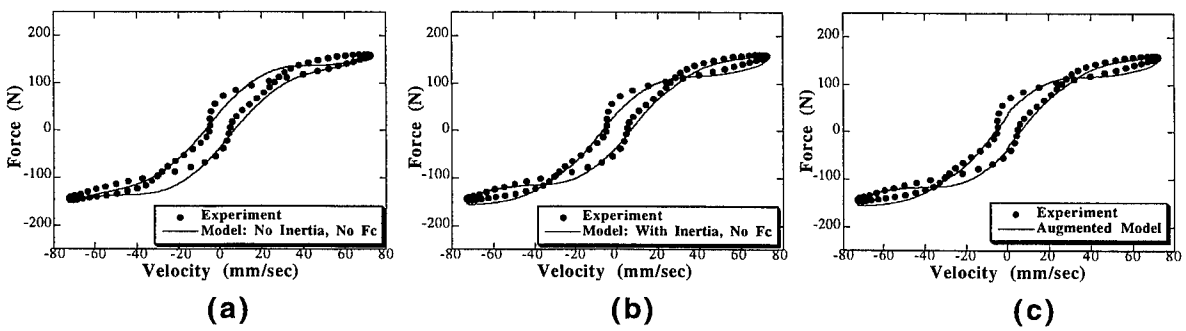

Figure 12: A comparison of experimental hysteresis data for $E = 3$ kV/mm, $X_0 = 1.0$ mm with the hysteresis plots obtained using (a) the model without the inertial or sticktion parameters (b) the model with the inertial parameter but without the sticktion parameter (c) the fully augmented model.

Acknowledgment

This work is supported by the U.S. Army Research Office under the Smart Structures University Research Initiative, contract no. DAAL03-92-G-0121, with Dr. Gary Anderson serving as contract monitor.

References

[1] Chopra, I., "Perspectives in Aeromechanical Stability of Helicopter Rotors," *Vertica*, Vol. 14, No. 4, 1990, pp. 457-508.

[2] Felker, F.F., Lau, B.H., McLaughlin, S., and Johnson, W., "Nonlinear Behavior of an Elastomeric Lag Damper Undergoing Dual-Frequency Motion and its Effect on Rotor Dynamics," *J. American Helicopter Society*, Vol. 34, No. 4, 1987, pp. 45-53.

[3] McGuire, D.P., "Fluidlastic Dampers and Isolators for Vibration Control in Helicopters," Presented at the 50th *Annual Forum of American Helicopter Society*, Washington D.C., May 1994.

[4] Panda B., and Mychalowycz, E., "Aeroelastic Stability Wind Tunnel Testing with Analytical Correlation of the Comanche Bearingless Main Rotor," Presented at the 52nd *Annual Forum of American Helicopter Society*, Washington D.C., June 1996.

[5] Stanway, R., Sproston, J.L., and El-Wahed, A.K., "Application of Electro-Rheological Fluids in Vibration Control: a Survey," *Smart Mater. Struct*, In Press.

[6] Brooks, D.A., "Design and Development of Flow Based Electro-Rheological Devices," *Int. J. Modern Physics* B, Vol. 6, 1992, pp. 2705-30.

[7] Duclos, T.G., "Design of Devices using Electrorheological Fluids," *Automotive Engineering*, Paper No. 881134, pp. 2.532-2.536.

[8] Carlson, J.D., Catanzarite, D.M., and St.Clair, K.A., "Commercial Magneto-Rheological Fluid Devices," Presented at the 5th *Int. Conf. on Electro-Rheological, Magneto-Rheological Suspensions and Associated Technology*, Sheffield, U.K., July 1995.

[9] Weiss, K.D., Carlson, J.D., and Nixon, D.A., "Viscoelastic Properties of Magneto- and Electro-Rheological Fluids," *J. Intelligent Material Systems and Structures*, Vol. 5, 1994, pp. 772-775.

[10] Kamath, G.M., Hurt, M.K., and Wereley, N.M., "Analysis and Testing of Bingham Plastic Behavior in Semi-Active Electrorheological Fluid Dampers," *Smart Mater. Struct*, Vol. 5, October 1996.

[11] Gamota, D.R., Wineman, A.S., and Filisko, F.E., "Fourier Transform Analysis: Nonlinear Dynamic Response of an Electrorheological Material," *J. Rheology*, Vol. 37, No. 5, 1993, pp. 919-33.

[12] Gamota, D.R., and Filisko, F.E., "Dynamic Mechanical Studies of Electro-Rheological Materials: Moderate Frequencies," *J. Rheology*, Vol. 35, No. 3, 1991, pp. 399-425.

[13] Gamota, D.R., and Filisko, F.E., "High Frequency Dynamic Mechanical Study of an Aluminosilicate Electro-rheological Material," *J. Rheology*, Vol. 35, No. 7, 1991, pp. 1411-26.

[14] Kamath, G.M., and Wereley, N.M., "Distributed Damping of Rotorcraft Flexbeams Using Electrorheological Fluids," *AIAA Adaptive Structures Forum*, New Orleans, April, 1995, pp. 300-325.

[15] Kamath, G.M., and Wereley, N.M., "A Nonlinear Viscoelastic-Plastic Model for Electrorheological Fluids," Presented at the *Second Workshop on Smart Structures and Materials* sponsored by the US Army Research Office, Sept 5-7, 1995, College Park, MD.

[16] Stanway, R., Sproston, J., and Stevens, N.G., "Non-Linear Modelling of an Electro-rheological Vibration Damper," *Journal of Electrostatics* , Vol. 20, 1987, pp. 167-184.

[17] Ehrgott, R.C., and Masri, S.F., "Modelling the Oscillatory Dynamic Behavior of Electrorheological Materials," *Smart Mater. Struct*, Vol. 1, 1992, pp. 275-85.

[18] Lou, Z., Ervin, R.D., and Filisko, F.E., "A Preliminary Parametric Study of Electrorheological Dampers," *Electro-Rheological Flows, ASME*, FED-Vol . 164, 1993, pp. 143-156.

[19] Spencer, B.F., Dyke, S.J., Sain, M.K., and Carlson, J.D., "Phenomenological Model of a Magnetorheological Damper," *J. Engineering Mechanics*, ASCE, in press.

[20] Kamath, G.M., and Wereley, N.M., "System Identification of ER Fluid Dampers Using a Nonlinear Mechanisms-Based Model," Proceedings of the 1996 SPIE *Conference on Smart Structures and Materials*, San Diego, 26-29 Feb, 1996.

[21] Kamath, G.M., and Wereley, N.M., "Modeling the Damping Mechanism in ER Fluid Based Dampers," M3DIII: *Mechanics and Mechanisms of Material Damping*, Ed. V.K. Kinra and A. Wolfenden (ASTM) **STP 1304** In Press.

[22] Makris N., Burton, S.A., Hill, D., and Jordan, M., "Analysis and Design of ER Damper for Seismic Protection of Structures," *J. Engineering Mechanics*, ASCE, October 1996.

[23] DOT Users Manual, Version 2.04B, VMA Engineering.

Experimental Study of a Multi-Electrode Cylindrical ER Fluid Damper for In-plane Motions

Faramarz Gordaninejad[1], M. Saiid Saiidi[2] and Sivakumar Uthiram[3]

University of Nevada, Reno, Nevada 89557

ABSTRACT

Electro-rheological fluid (ERF) shock absorbers are semi-active vibration control devices that utilize ERF to control the damping capacity of the dampers. The focus of this work is on the experimental study of a multi-electrode, cylindrical ERF damper designed for in-plane motion. Several three-electrode ERF dampers are built and tested specifically for vibration damping of in-plane motions. The force-velocity loops were obtained and examined for different voltage levels and electrode lengths.

Keywords: ER fluid, semi-active, dampers, cylindrical, multi-electrode, in-plane motion.

1. INTRODUCTION

Electro-rheological fluids are those whose rheology changes with the application of an electric field. These fluids consist of solid particles dispersed in a nonconductive liquid of organic origin. The suspended particles change their random configuration to an aligned and relatively regular chain-like pattern in the presence of an electric field. The dispersion media (liquid) is usually a low viscosity hydrocarbon fluid with a high electrical resistivity [1]. The dispersed phase should posses high adsorptivity and a highly hydroxylated developed surface. Another substance, an activator, is applied to the surface of the solid phase to maximize viscosity changes in the presence of an electric field. Surfactants are added to allow a greater particle volume fraction to be utilized in a high concentration ERF and reduce sedimentation in a low concentration one.

Winslow [2] was the first to report the electro-rheological (Winslow's) effect. The rheology of ERF can be changed significantly in a very short period of time (10^{-4} to 10^{-3} sec) in the presence of an electric field. The resistance of these fluids to flow increases with the increase in the applied electric field strength, and at relatively high field strengths the fluid is reported to behave as a jell-like solid [3-9]. The rapid response of ERF to the applied electric field provides many design possibilities in different engineering disciplines wherein controlled suppression of undesirable vibrations is necessary. ERF may be used for semi-active control of undesirable vibration [10] such as in automotive suspension system, automatic valves [11], dampers, clutches, and robotics devices [12-15].

In addition to these applications, ERF dampers can potentially be used for the suppression of vibration in civil structures, such as bridges and buildings, that undergo seismic or strong wind excitations [16]. Currently employed techniques of vibration control in civil structures are based primarily on passive measures. Some examples include base isolations, friction and viscoelastic dampers and bracing systems. They offer limited capability to suppress the vibration of structures, while lacking in controlling motion under severe dynamic loading. The feasibility of active control systems for large structures has been demonstrated for certain cases by using variable stiffness devices such as hydraulic and electromagnetic actuators [17], active bracing [18,19] in

[1] Professor, Mechanical Engineering Department.
[2] Professor, Civil Engineering Department.
[3] Graduate Student, Mechanical Engineering Department.

laboratory testing and full-scale implementations [20,21]. The use of hybrid systems [22,23] is attractive because the passive system provides a steady dissipation capability while the active system can control the transient dynamic motion.

Several control schemes have been developed in recent years that utilize ER fluids [24-33]. Analytical and numerical simulations have been done by Leitmann et al. using Lyapunov stability theory as well as fuzzy logic control concept [29,30]. Control schemes were also developed on the basis of minimizing the rate of change of the energy of the system. Due to the nonlinear characteristic of ERF, Gavin et al. [28] modeled the control scheme assuming that a near resonance force is impressed upon the damper and that the excitation amplitude and the damping are small. Stanway et al. [31] used a sequential filtering technique to identify the damping law of an ERF. An attempt has also been made at nonlinear modeling of telescopic ERF dampers [32]. Bang-bang control and instantaneous optimal control algorithms were developed for hybrid dampers having an active and a passive damping component [33]. Ehrgott et al. [34,35] used a dynamic test device that consists of ERF between two coaxial cylinders. Dynamic properties of ERF were evaluated by subjecting them to oscillating shear strain. Hysteresis plots for a constant electric field and different frequencies were evaluated and were used to determine the equivalent viscous damping coefficient [34]. To reduce the vibration of the structure, pulse control was implemented wherein an out-of-phase force pulse was applied to the ERF damper [35].

In this study the performance of cylindrical, multi-electrode ERF dampers under in-plane vibrations is examined. Design modifications are made to allow for the flexibility of the electrodes under their own and the fluid's weights. The experimental set up provides the force and velocity measurements for different frequencies, lengths of the damper, and applied voltages.

2. EXPERIMENTAL STUDY

The goal of this study is to examine small ERF damper prototypes by generating the force-velocity loops. A brief description of the experimental study is as follows:

The damper is designed for an in-plane motion. A rod is placed at the center of the cylinder to transmit the force to a pair of moving electrodes inside the Plexiglas casing of the damper. This is illustrated in Figure 1. The rod, which is rigidly fixed to the inner moving electrodes, is connected to the loadcell. In order to balance (for the combined weights of the electrodes and the rod and the ERF) the inner moving electrodes to prevent arching between the fixed and moving electrodes, two Teflon bushings were considered as shown in Figure 1. The bushings were made of Teflon to minimize friction. The voltage is applied to the stationary electrode pairs which are fixed tightly inside the cylindrical casing of the damper. The damper is filled with LORD's Versa Flow ER-100 electro-rheological fluid. The fluid between the electrodes is electrically stressed by the voltage applied to the damper using a 408B Fluke High Voltage Power Supply.

The schematic of the experimental setup is illustrated in Figure 2. The damper is placed on a small shake table that provides horizontal motions, as shown in Figure 3. The table consists of a platform, supported at four corners by vertical bases. The platform is connected rigidly to a rod that is connected to a motor shaft. The connecting rod has an eccentricity (of 0.125″), so that the rotary motion of the motor is converted to a horizontal motion of the table. The speed of rotation the of the motor can be adjusted by the use of a variable rheostat. The motor is a Boston Gear with frequency range of 0-30 Hz. The force exerted by the damper (at different frequencies and voltage levels) is measured by EATON LEBOW 3397-25 loadcell. The loadcell is excited by a Hewlett Packard Harrison 6200B dc power supply. The output of the loadcell is amplified by a Tektronix TM503 AM502 differential amplifier. The velocity transducer used in the experiments is a Patriot Sensors PV-15A. The acceleration of the shake table is measured by using a piezoelectric PZ23 Bruel & Kjaer 4370 accelerometer. The signal from the accelerometer is amplified using a Kistler 504D charge amplifier. The force,

velocity and acceleration signals are collected by a KEITHLEY METRABYTE DAS 1602 data acquisition board and the LabTech software is used to process the collected data. A low-pass digital filtering is performed using LabTech software to reduce the noise in both force and velocity signals.

Using this experimental setup, results were obtained for different applied voltage and length of the electrodes. It should be noted that, for all tests conducted, the gap between the electrodes (2 mm), the number of electrodes (3), and the diameter (50 mm) of the dampers, were kept constant. In Figure 4 force-velocity loops for different electric field strengths are presented for the case where the length of the electrodes were 32 mm and the frequency of the motion was 8 Hz. As can be seen, the damping force increases nonlinearly as the voltage increases. In Figure 5, the results for a electrode length of 78 mm at 8 Hz is presented for different electric field strength levels. A comparison between Figures 4 and 5 shows that the length of the electrode has a significant effect on the damping force, and that the damping force varies almost linearly. Figure 6 demonstrates that by increasing the voltage and the length of the electrode the rate of the dissipated energy increases linearly.

3. CONCLUSIONS

Small prototypes of a multi-electrode, cylindrical ERF damper was designed, built and tested. The design was specifically intended for an in-plane motion. The experiments were conducted to obtain force-velocity loops. The effects of the applied voltage and the length of the electrodes was examined. It was shown that while the damping force varies nonlinearly with the change in the electric field strength and the length of the damper, the variation of the rate of dissipated energy remains linear for a wide rage of electric field strength and the electrode lengths.

4. ACKNOWLEDGMENTS

This project is funded by the National Science Foundation Grant Number CMS-9402535. The authors are thankful for the constant encouragement by Dr. S. C. Liu, the Program Director. Special Thank is due to Dr. Eric Wang for his help in the experimental set up.

5. REFERENCES

1. Korobko, E. V., "Some Aspects of Electrorheology," *Journal of Intelligent Material Systems and Structures*, Vol. 3, pp. 269-295, 1992.

2. Winslow, W. M., "Induced Fibration of Suspensions," *Journal of Applied Physics*, Vol. 20, pp. 1137-1140, 1949.

3. Klass, D. and Martinek, T. W., "Electroviscous Fluids. II. Electrical Properties," *Journal of Applied Physics*, Vol. 38, No. 1, pp. 75-80, 1967.

4. Mokeev, A. A., Korobko, E. V., and Vedernikova L. G., "Structural Viscosity of Electrorheological Fluids," *Journal of Non-Newtonian Fluid Mechanics*, Vol. 42, pp. 213-230, 1992.

5. Zukoski, C. F., and Goodwin, J. W., "Toward The electrical Control of Viscosity: Optimization of Electrorheological Fluids," *International Conference on Industrial Electronics, Control and Instrumentation*, Published by IEEE, pp. 9-13, 1986.

6. Weiss, K. D., Coulter, J. P., and Carlson, J. D., "Materials Aspect of Electrorheological Systems," *J. Intelligent Material Systems and Structures*, Vol. 4, No. 1, pp. 13-34, 1993.

7. Gast, A., and Ukoski, C., "Electrorheological Fluids As Colloidal Suspensions," *Advances in Colloid and Interface Science*, Vol. 30, pp. 153-202, 1989.

8. Block, H. and Kelly, P., "Electro-rheology," *Journal of Physics*, Vol. 21, No. 12, pp. 1661-1677, 1988.

9. Bares, J. E, and Carlson, J. D., "Electrorheological Fluid Design: An overview," *Proc. of the Second International Conference on ER Fluids*, Edited by J.D. Carlson, A.F. Sprecher, and H. Conrad, pp. 93-113, 1989.

10. Coulter, J. P., Weiss, K. D., and Carlson, J. D., "Engineering Applications of Electrorheological Materials," *J. Intelligent Material Systems and Structures*, Vol. 4, pp. 248-259, 1993.

11. Duclos, T. G., "Design of Devices using Electrorheological fluids," SAE Technical Paper Series No. 881134, *Future Transportation Technology Conference and Exposition*, San Francisco, California, August 8-11, 1988.

12. Coulter, J. P., and Duclos, T. G., "Application of Electrorheological Materials in Vibration Control," *Proc. of the Second International Conference on ER Fluids*, Edited by J.D. Carlson, A.F. Sprecher, and H. Conrad, pp. 300-324, 1989.

13. Brooks, D. A., "Devices Using Electro-Rheological Fluids," *Proc. of the Second International Conference on ER Fluids*, Edited by J.D. Carlson, A.F. Sprecher, and H. Conrad, pp. 371-401, 1989.

14. Duclos, T. G., "Electrorheological Fluids and Devices," *Automotive Engineering*, pp. 45-48, December 1988.

15. Coulter, J. P., and Miller, L. R., "Application for Smart Materials in the Field of Vibration Control," *Proc. of the Second International Conference on ER Fluids*, Edited by J.D. Carlson, A.F. Sprecher, and H. Conrad, pp. 132-146, 1989.

16. Makris, N. Burton, S. A., Hill, D, and Jordan, M., "Analysis and Design of ER Damper for Seismic Protection of Structures," ASCE *J. Engineering Mechanics*, Vol. 122, No. 10, October, 1996.

17. Kobori, T., et al., "Experimental Study on Active Variable Stiffness System," *Proc. Fourth World Congress of Tall Building and Urban Habitat*, Hong Kong, 1990.

18. Chung, L. L., Reinhorn A. M., and Soong T. T., "Experiments on Active Control of Seismic Structures," ASCE *J.Eng. Mech.*, Vol. 114, pp. 241-256, 1988.

19. Chung, L. L., Lin R. C., Soong T. T., and Reinhorn A.M., "Experimental Study of Active Control of MDOF Seismic Structures," ASCE *J.Eng. Mech.*, Vol. 115, pp. 1609-1627, 1989.

20. Soong, T. T. Marsi S.F., and Housner G. W., "An Overview of Active Structural Control under Seismic Loads," *Earthquake Spectra*, Vol. 7, No. 3, pp. 483-505, 1991.

21. Kobori, T., "State-of-the-Art of Seismic Response Control Research in Japan," *Proc. of the U.S. National Workshop on Structural Control Research*, Edited by G.W. Housner and S.F. Marsi, pp. 1-12, 1990.

22. Reinhorn, A. M., Soong T. T., and Wen C. Y., "Base Isolated Structures with Active Control," *Proc. ASME PVD Conf.*, PVP-127, pp. 413-420, San Diego, CA., 1987.

23. Kelly, J.M., Leitmann G., and Soldatos A.G., "Robust Control of Base-Isolated Structures Under Earthquake Excitations," *J. Optim. Th. Appl.*, Vol. 53, pp. 159-180, 1987.

24. Gordaninejad, F., A. Ray, and H. Wang, "Control of Forced Vibration Using Multi-Electrode Electro-Rheological Fluid Dampers," in press, to appear in the ASME *Journal of Vibration and Acoustics*, 1997.

25. Gordaninejad, F., and Bindu, R., "The Effect of Scale Factor on the Performance of Electro-Rheological Fluid Dampers," *Proceedings of the 5th International Conference on Electro-Rheological Fluids, Magneto-Rheological Suspensions and Associated Technology*, Sheffield, England, pp. 318-326, 1996.

26. Gordaninejad, F., Ray, A. and Bindu, R., "Vibration Control of Structures Using Hybrid ER/Viscous Dampers," *Proceedings of the First World Conference on Structural Control*, pp. TA2-41-49, 1994.

27. Gordaninejad, F., Ghazavi, A., Ray, A., Wang, H., and Saiidi, M., "Intelligent Electrorheological Fluids for Active Vibration Control: an Experimental Study," *Proc. of the 9th International Conference on Composite Materials*, Madrid, Spain, pp. 473-480, 1993.

28. Gavin, H. P., Ortiz, D. S., and Hanson, R. D., "Use of ER Fluid Dampers for Reduction of Seismic Structural Response," *UJNR Workshop on Smart and High Performance Materials and Systems*, Building Research Institute, Tsukuba, Japan, 1993.

29. Leitmann, G., and Reithmeier E., "Semiactive Control of a Vibrating System by Means of Electrorheological Fluid," *Dynamics and Control*, Vol. 3, pp. 7-33, 1993.

30. Leitmann, G., "Vibration Attenuation by Means of Semiactive Control Schemes", Submitted to Math. Modeling and Sci. Computing.

31. Stanway, R., Sproston, J. L., and Firoozian, R., "Identification of the Damping Law of an Electro-Rheological Fluid: A Sequential Filtering Approach," ASME *Journal of Dynamic Systems, Measurements and Control*, Vol. 111, pp. 91-96, 1989.

32. Stanway, R., Sproston, J. L., and Stevens, N. G., "Non-Linear Modeling of an Electro-Rheological Vibration Damper," *Journal of Electrostatics*, Vol. 20, pp. 167-184, 1987.

33. Feng, Q., and Shinozuka, M., "Control of Seismic Response of Bridge Structures Using Variable Dampers," *Journal of Intelligent Material Systems and Structures*, Vol. 4, pp. 117-122, 1993.

34. Ehrgott, R., and Masri, S.F., "Modeling the Oscillatory Dynamic Behavior of Electrorheological materials," *Smart Materials and Structures, Institute of Physics*, UK., Vol. 1, No. 4, pp. 275-285, 1992.

35. Ehrgott, R., and Masri, S.F., "Use of Electro Rheological materials in Intelligent Systems," *Proceedings of the U.S.- Italy - Japan Workshop on Structural Control and Intelligent Systems*, Sorrento, Italy, pp. 87-100, 1992.

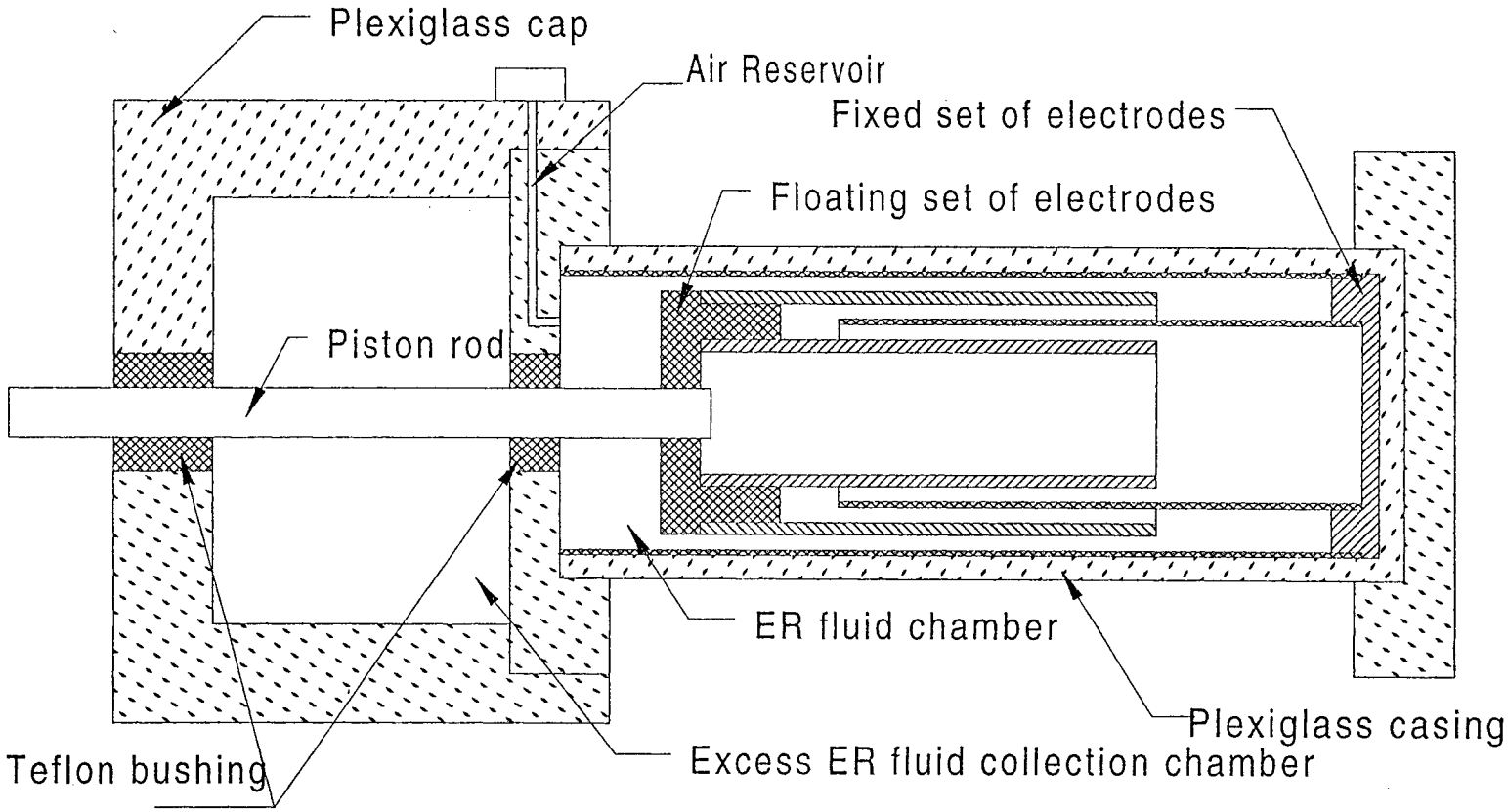

Figure 1. A section view of the multi-electrode ERF damper for in-plane motion.

1. Position-Velocity Transducer
2. Horizontal Shake Table platform
3. Accelerometer
4. ERF Damper
5. Vertical Blades for Platform Support
6. Loadcell
7. High Voltage Supply for ERF damper
8. DC Power Supply for Loadcell
9. Differential Amplifier for Loadcell
10. Computer
11. Dual Mode Charge Amplifier
12. DAS1602 Screw Terminal Accessory Board

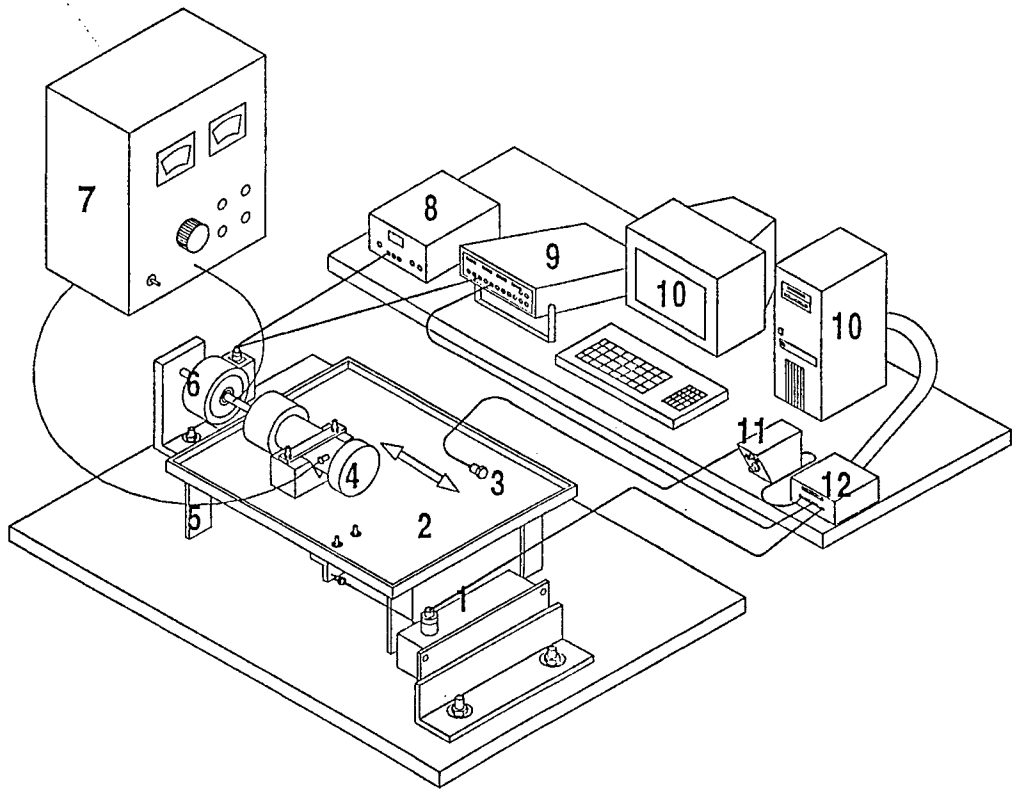

Figure 2. Schematic of the experimental setup.

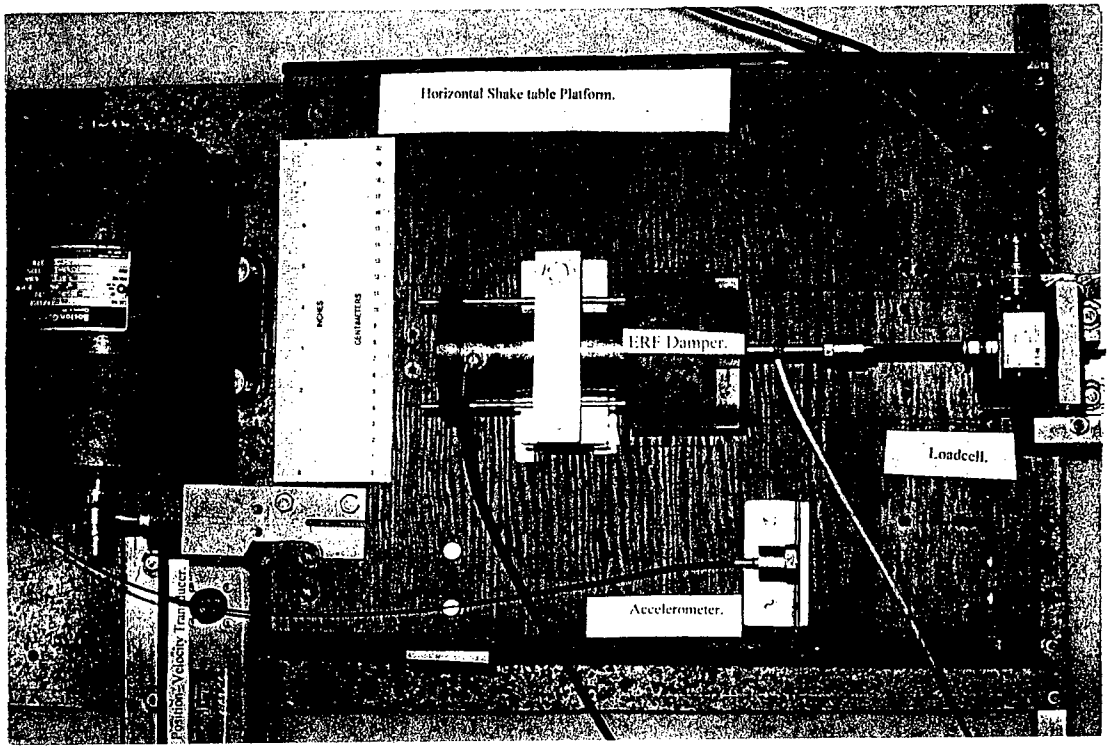

Figure 3. The photo of the ERF damper and the testing arrangement.

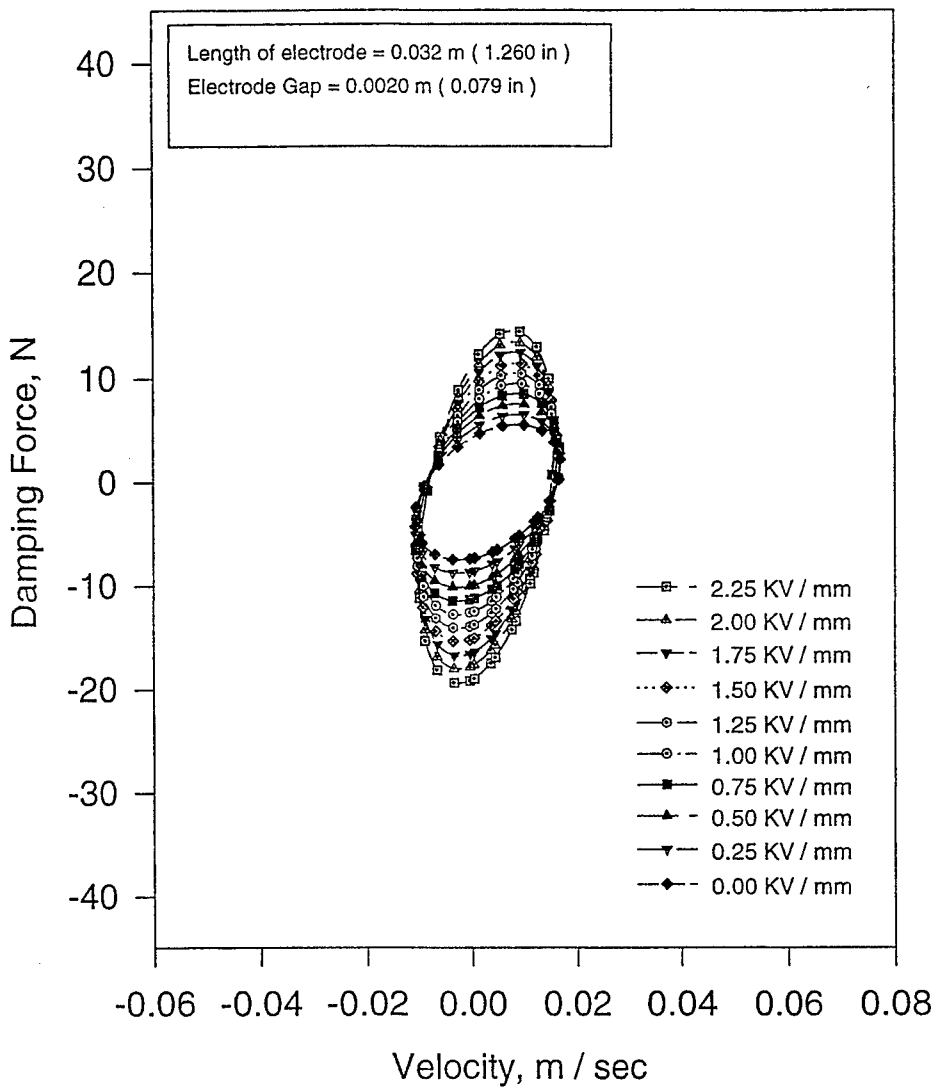

Figure 4. The effect of electric field strength on the damping force for a three-electrode ERF damper where the frequency of the motion is 8 Hz and the length of the electrodes are 32 mm.

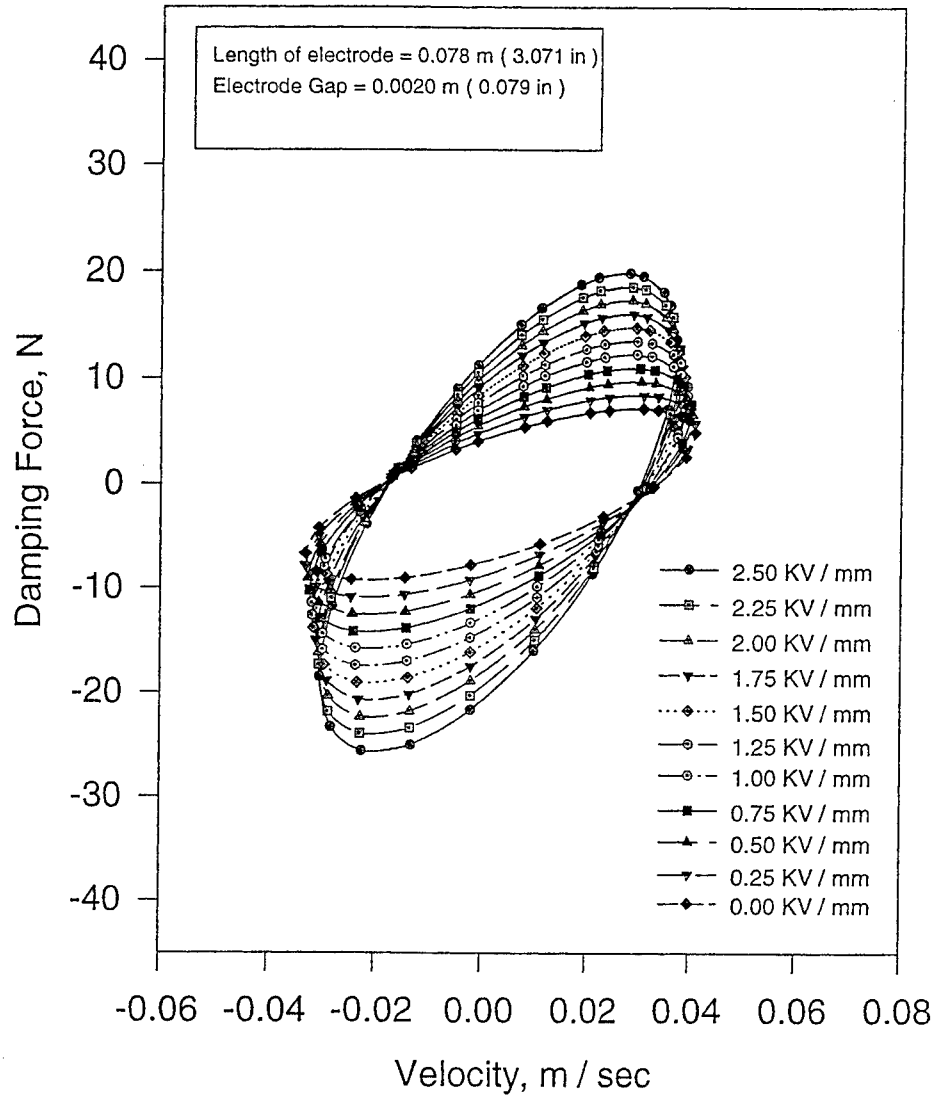

Figure 5. The effect of electric field strength on the damping force for a three-electrode ERF damper where the frequency of the motion is 8 Hz and the length of the electrodes are 78 mm.

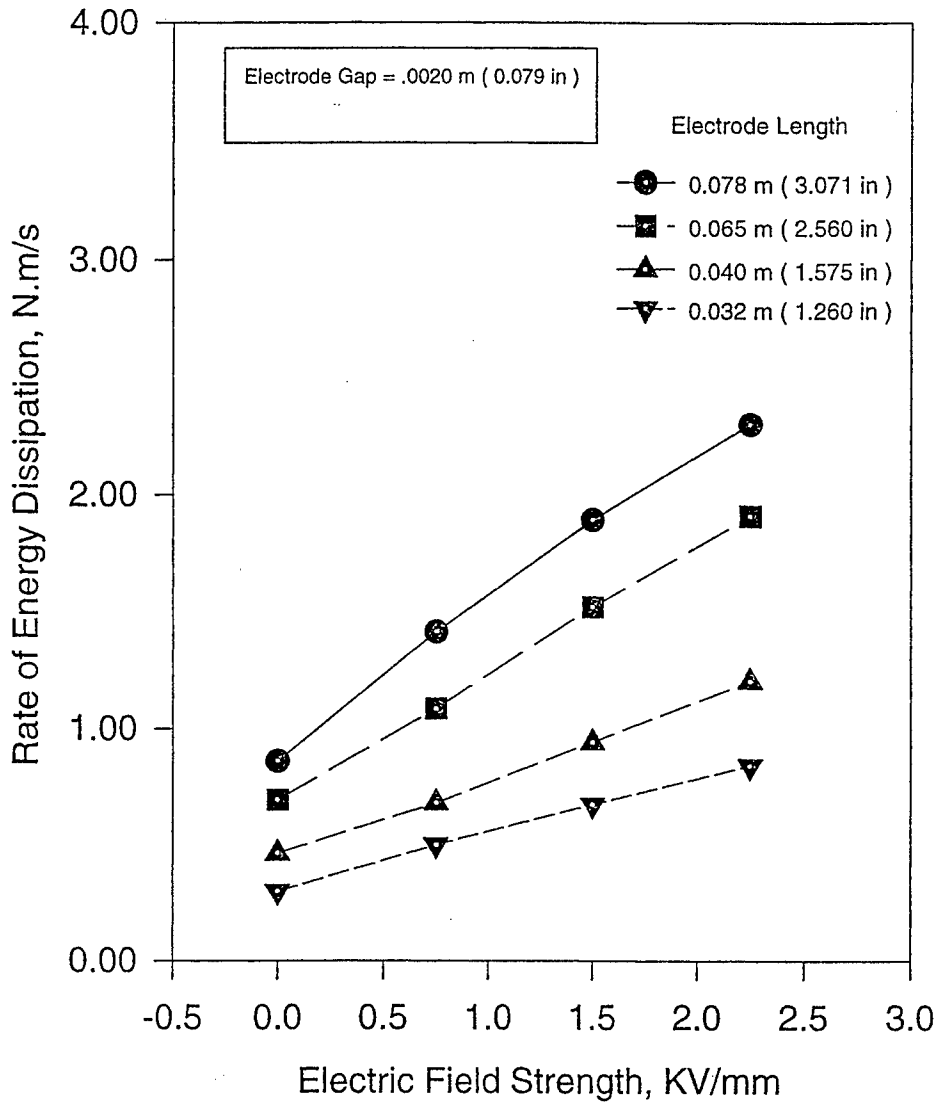

Figure 6. The effects of electric field strength and the electrode length on the rate of dissipated energy. The frequency of the motion is 8 Hz.

Experimental testing of a semi-active control scheme for vibration suppression

Wendy Taniwangsa[a] and James M. Kelly[b]

[a]Department of Civil Engineering, Santa Clara University, Santa Clara, CA 95053
[b]Earthquake Engineering Research Center, University of California at Berkeley, Richmond, CA 94804

1 ABSTRACT

An experimental investigation was performed on a semi-active control scheme that uses the rheological properties of electro-rheological fluids (ER-fluids) in squeeze-flow mode to control the dynamic behavior of Single-Degree-of-Freedom (SDOF) systems. The reversible and very rapid changes in the mechanical properties of the fluid under variable voltage are exploited by using a control scheme that automatically turns ***"on"*** and ***"off"*** the electrical field as loads are applied. This control scheme rapidly adapts to any changes in the mechanical properties of the system, reducing the response of the structure for a wide range of excitation frequencies. The ER-fluid used in this study, Zeolite in Silicone oil, was subjected to an electrical field range from one to five kV/mm. Tests were carried out for the ***"off"*** system, the ***"on"*** system, and the controlled system, and the experimental and analytical results were compared. The experimental results show that this control scheme is effective for reducing the vibration of the system. Other types of ER-fluid should be tested using this control scheme to investigate the most effective fluid for vibration suppression.

Keywords: bang-bang control, electro-rheological fluids, semi-active control, shock absorber, smart materials, vibration suppression.

2 INTRODUCTION

2.1 Control systems

Structures and mechanical systems should be designed to be functional under different types of loading, particularly dynamic and transient loads. to ensure a better performance of the system, the design process strives to reduce a system's response under these loads. There are three fundamental strategies to regulate or control the response of a system; through the use of passive control, active control, or semi-active control.

The first approach uses a passive control system where the properties of the system are modified by the addition of mechanical devices such as energy-dissipation devices or base isolators, which augment the dissipation capability or reduce the input energy to the system,thus improving its performance. Several applications of this method have been reported and implemented [1, 2]. In particular, rubber isolators have been used in a variety of structures to mitigate ground motion from earthquakes.

The second approach, called active control, involves the addition of "active" devices such as hydraulic or electromagnetic actuators that reduce vibrations by using an external energy source which responds to external input. These systems are slow, costly, and complicated and have been limited to a few civil engineering applications.

Further author information:

W.T (correspondence):

E-mail: WTaniwangsa@mailer.scu.edu; Telephone: (408) 554-6871; Fax: (408) 554-5474

J.M.K.: E-mail: jmkelly@eerc.berkeley.edu

SPIE Vol. 3045 • 0277-786X/97/$10.00

Semi-active control, the third and relatively new approach, involves modifying the mechanical properties of the system. One way to do this is to incorporate electro-rheological fluid (ER-fluid) into the system. The mechanical properties of ER-fluids [6]—in particular damping and stiffness—can be changed through the use of electrical fields. Because the change of rheological response is on the order of milliseconds, it has been suggested to use such fluids in the construction of controllers.

2.2 Semi-active control schemes using electro-rheological fluid

A semi-active control scheme that uses ER-fluid to modify the mechanical properties of a structure enables the response of the overall system to become tunable. There are no rules on how to incorporate ER-materials into structures, although two basic configurations have been studied. The first involves taking advantage of the behavior of the ER-suspensions in the shear-type configuration. The second approach uses extensional or squeeze-flow type configurations [8]. ER-effects change the damping and frequency of the system in both types of configuration. Some studies have shown, however, that under the same level of electrical field, ER-fluids in the squeeze-flow mode exhibited greater resistance than ER-fluids in shear mode [5,8]; thus, ER-effects are more effective when used in the squeeze-flow mode, especially in order to suppress higher frequency vibrations. This investigation used ER-fluid in a squeeze-flow mode.

Leitmann and Reithmeier [7] investigated an analytical model of a semi-active control scheme that suppresses the vibration of a system subjected to dynamic loads. The control scheme changes the stiffness and damping properties of a system through the rheological effects of the ER-fluid by automatically turning ***"on"*** or ***"off"*** the electrical field during the loading process. Because the changes are instantaneous, the delay problem associated with the typical active control scheme does not exist. This approach is called a "bang-bang scheme". A bang-bang scheme proposes to bound the response for a wide range of frequencies and that the bounded response values are smaller than those of the system when the maximum rheological effect is maintained for the total duration of response.

2.3 Bang-bang control scheme

A single-degree-of-freedom system (SDOF), shown in Fig. 1, demonstrates the applicability of the semi-active control system. A rigid body of mass, m, is mounted on a spring with a spring constant, k, and a damper with a damping coefficient, c. The spring constant, k, and the damping coefficient, c, are functions of the imposed voltage, u. If z is the relative displacement of the mass, m, relative to an inertial reference, the equation of motion of the system becomes

$$m\ddot{z} + c(u)\dot{z} + k(u)z = f(t) \tag{1}$$

The values of $k(u)$ and $c(u)$ vary due to the rheological effect of the ER-fluid, and the amount of the change is a function of the imposed voltage, u, as shown in Fig. 2. The imposed voltages, u, in the bang-bang control scheme are in an ***on*** or ***off*** position only, namely, $u=u_{max}$ or $u=0$, respectively. Thus, if the imposed voltage, u, is normalized with respect to its maximum value so that $\bar{u} = u/u_{max}$, then $\bar{u} = 0$ or 1, and the following values are defined:

$$\text{for } \bar{u} = 0 \rightarrow c(\bar{u}) = c_0,\ k(\bar{u}) = k_0 \tag{2}$$

$$\text{for } \bar{u} = 1 \rightarrow c(\bar{u}) = c_{max},\ k(\bar{u}) = k_{max} \tag{3}$$

$$\text{in general: } c(\bar{u}) = c_0 + (d_c)\bar{u}\ ,\ k(\bar{u}) = k_0 + (d_k)\bar{u} \tag{4}$$

where d_c and d_k are the damping and stiffness increments due to the rheological effect.

If the state of the system $[z(t), \dot{z}(t)]$ is represented by the vector x, then the state equation becomes

$$\dot{x} = [A_0(m, c_0, k_0) + B_g(m, dc, dk)\bar{u}]x + B_f(m)f(t) \tag{5}$$

where A_0, B_g, and B_f are defined as follows:

$$A_0 = \begin{bmatrix} 0 & 1 \\ (-k_0)/m & (-c_0)/m \end{bmatrix}$$

$$B_g = \begin{bmatrix} 0 & 0 \\ (-dk)/m & (-dc)/m \end{bmatrix} \text{ and } B_f = \begin{bmatrix} 0 \\ 1/m \end{bmatrix}$$

Furthermore, A_0 and B_g, can be associated as follows:

$$A_i = A_0 + B_g \bar{u} \tag{6}$$

in terms of which the state equation becomes

$$\dot{x} = A_i \cdot x + B_f \cdot f \tag{7}$$

The imposed voltage, $\bar{u}$, which is a function of z and $\dot{z}$, is chosen so that for all t positive, the state of the system should be as close as possible to the original state, independent of the disturbing force, $f(t)$. This condition can be achieved if the norm of the vector x on a given positive definite matrix, $\in \Re^2 : \|x_{(t)}\|_P = \sqrt{\left[x_{(t)}^T \cdot P \cdot x_{(t)}\right]}$, is as small as possible by switching $\bar{u}(t)$ to *on* and *off* for any perturbing force, $f(t)$.

To minimize $\|x_{(t)}\|_P$, let $V(x) = x^T P x$.

Hence, $L_{(x,t)}(\bar{u}) = \frac{d}{dt} V(x_{(t)}) = x^T P \dot{x} + \dot{x}^T P x$

The feedback control will minimize $L_{(x,t)}(\bar{u})$ for every (x,t) to guarantee that $x_{(t+1)} £ x_{(t)}$. Substituting $\dot{x}$, from Eq. 2 into Eq. 3 gives

$$L_{(x,t)}(\bar{u}) = a(x) + b(x)\bar{u} \tag{8}$$

where $a(x)$ and $b(x)$ are functions of x that can be computed using Eqs. 2 and 3. The $\bar{u}$ has a direct influence only on the term $b(x) = x^T R x$, where $R = (PB_g + B_g^T P)$. Since the bang-bang control scheme turns $\bar{u}$ to 0 or 1, only the sign of $b(x)$ is needed, that is, $\bar{u}$ should be *off* when $b(x) > 0$ and $\bar{u}$ should be *on* when $b(x) < 0$.

On the state plane, $\Re^2$, the *on* and *off* zones are bounded by two straight switching lines, g_1 and g_2, as shown in Fig. 3. These are the manifolds where the value of $b(x) = 0$ and are defined as follows:

$$g_1 = \{x \in \Re^2 | B_g \cdot x = 0\} = \{x \in \Re^2 | (dk)z + (dc)\dot{z} = 0\} \tag{9}$$

$$g_2 = \{x \in \Re^2 | \left[B_g^T \cdot P - J\right] \cdot x = 0\} = \{x \in \Re^2 | p_3 z + p_2 \dot{z} = 0\} \tag{10}$$

where $Jx = x^{\perp} = \begin{bmatrix} 0 & -1 \\ 1 & 0 \end{bmatrix} x$, and p_2 and p_3 are elements of the matrix P.

To guarantee the stability of this control scheme, let $P = \begin{bmatrix} p_1 & p_3 \\ p_3 & p_2 \end{bmatrix} = p_3 \begin{bmatrix} \xi & 1 \\ 1 & \eta \end{bmatrix}$ be a Lyapunov matrix so that the matrix

$Q_i = -(PA_i + A_i^T P)$ will be always definite negative for any matrix A_i. Thus the values of ξ and η have to satisfy the following conditions:

$$[\xi - \eta k(\bar{u}) - c(\bar{u})]^2 < 4k(\bar{u})(\eta c(\bar{u}) - 1) \tag{11}$$

$$min\{\eta c(\bar{u}), \xi\eta\} > 1 \tag{12}$$

$$\xi, \eta, p_3 > 0 \tag{13}$$

3 EXPERIMENTAL MODEL AND TEST FACILITIES

3.1 Test facilities

The experimental work was carried out using the Material Testing System (MTS) machine at the Davis Hall Structural Laboratory, University of California at Berkeley. The testing machine is equipped with an adjustable load frame to set the test specimen. A hydraulic system provides the energy source to bring the 35-kips hydraulic actuator to the desired position. A five gallon-per-minute servo-valve regulates the fluid flow rate into the actuator cylinder in direct proportion to the magnitude of the control signal. The polarity of the control signal determines the direction of the piston strokes. The direction and magnitude of the piston strokes are captured by two types of transducers: a load cell or a linear variable displacement transducer (LVDT). The signal captured by the transducers is filtered through a conditioner module so that the output signal is in a suitable range. A feedback selector module selects the output of the particular conditioner that is used to control the hydraulic actuator.

A displacement control mode was used in this experiment. The signal selected by the feedback selector was applied to the servo-controller (servac). This compares a command signal representing the desired stroke and feedbacks the signal representing the actual stroke. If the command and feedback signals are not equal, the servac adjusts the servo-valve so that the difference is reduced to zero and the close-loop becomes balanced.

Harmonic and white-noise displacement signals were used as input commands and were generated by external signal generators. The harmonic signals were generated using a Beckman 9010 function generator, and the white-noise signals were generated using another signal generator.

3.2 SDOF model and properties

The test specimen was an electro-rheological squeeze-flow cell previously tested as a simple and compact damping device [8]. The specimen consisted of two electrodes, each one made out of copper discs, 50 mm in diameter. The lower electrode was connected to the high-voltage power supply and located inside a chamber constructed of insulating materials with an outside diameter of 80 mm and a height of 76 mm. This chamber held the ER-fluid and was attached to the head of the hydraulic actuator of the testing machine. The upper electrode was grounded and attached to the bottom surface of an upper cylinder that could be lowered into the chamber. The upper cylinder—constructed of insulating materials—supported a mass of 61.60 kg. This mass was free to vibrate vertically while guided by a linear bearing located on a vertical shaft that was hung to the top of the load frame of the testing machine. Fig. 4 shows a photograph of the test set-up.

A coil spring with a spring constant of ***275 lb/in*** was used to maintain separation of the electrodes. The ER-fluid used in this experiment was a suspension of zeolite in silicone oil [5] and was subjected to tension and compression as the mass on the top of the cylinder vibrated due to the input at the bottom of the chamber.

3.3 Instrumentation of the model

Each test used a pair of linear variable displacement transducers (LVDT's) of sprung armature type to measure the displacements at the base of the model and at the moveable mass, so that the deformation of the moveable mass could be determined. A linear velocity transducer from Trans-Tek Inc. was used to measure the relative velocity between the moveable mass and the base of the specimen. These three transducers were connected to CD19A MC1 system amplifiers before the signals were sent to the data acquisition board.

To perform the experiments using the bang-bang control scheme, it was necessary to implement a control program to compute the sign of $b(x)$ for all time t. Once the sign of $b(x)$ was obtained, a multifunction analog input/output board RTI-815 was used to send a command of "contact" or "release" to the vacuum relay to control the transmission of the high voltage to the test specimen. The time history of the high voltage sequence used during the bang-bang configuration was recorded during the test. A thermometer was inserted into the ER-fluid chamber to measure the temperature change in the ER-fluid during the test.

3.4 High-voltage supply scheme

To produce the rheological effect on the ER-fluid, a power supply unit, with a 5 kiloVolt DC capacity and variable electric current of 1 to 10 milliampere DC, was used to induce high voltage into the lower electrode . With the exception of the 0-Volt experiments, the power supply switch was turned ***on*** all the time. The flow of the electric current to the mechanical system was controlled through the contact and separation of a high-voltage vacuum relay RF53A from Jenning Corp. The high voltage in the lower electrode changes the properties of the ER-fluid instantaneously. The relay has a maximum operating time of 15 millisecond between opening and closing with an operating voltage of 12 kiloVolts DC between terminals. A block diagram of the close-loop of the high-voltage control system used for the bang-bang control scheme is shown in Fig. 5.

3.5 Data acquisition

This test series used Labtech Notebook for Windows for data acquisition. The signals were digitized by a digital analog system, DAS-1600, which has a 100 k-samples/sec capacity. A sampling rate of 200samples/sec was used in these test series. The data acquisition system could monitor simultaneously two channels during the test.

4 Test program

4.1 General

In addition to the identification tests to determine the properties of the ER-fluid, the specimen was tested under four different configurations: zero voltage, maximum voltage, bang-bang 1 control scheme, and bang-bang 2 control scheme. The bang-bang 1 configuration used $-p_2$ as the slope of the switching line g_2, and the bang-bang 2 configuration used the horizontal axis as the switching line g_2. The maximum voltage applied in this experiment was 5 kiloVolt DC, so that during the bang-bang control configurations the high-voltage supply was switched to 0 or 5 kiloVolt. Each configuration was subjected to a set of harmonic waves, sweep harmonic waves, and white-noise signals.

The rheological effect is obtained by adjusting the distance between the two electrodes using spacers below the coil spring. In this experiment, a 25mm spacer was inserted producing an initial 5mm gap between the upper and lower electrodes. The relative displacement amplitudes were limited to ±4 mm.

4.2 Electro-rheological fluid properties-identification tests

Three parameters were needed to perform the bang-bang control tests; d_k and d_c represented the stiffness and damping increases due to the rheological effect, and p_2 was used to guarantee the stability of the process. The identification tests consisted of a set of ten tests using random-noise input motions. A total of ten tests were conducted. The first five tests were conducted using a configuration of the system without imposed voltage, and the remaining five tests were carried out for a configuration of the system with maximum imposed voltage. The Fourier spectra of the displacement of the vibrating mass were calculated, smoothed,and averaged for each case. The natural frequency and fraction of critical damping for each configuration were obtained from these spectra.

The stiffness, k_0, and the damping value, c_0, were obtained from the system without imposed voltage, and the stiffness, k_{max}, and the damping value, c_{max}, were obtained from the tests results of the system with maximum imposed voltage. The different stiffness and damping values of the two configurations represent the changes of the mechanical properties of the ER-fluid due to the imposed voltage, parameters d_k and d_c, respectively. Once d_k and d_c were obtained, the matrix P was calculated using Eqs. 7, 8, and 9. The range of the values from which the normalized element of matrix P, ξ, η can be chosen is shown in Fig. 6. The mechanical properties of the system used for the bang-bang control tests, k_0, c_0, k_{max}, and c_{max}, is shown in Table 1.

4.3 Harmonic tests

Two types of harmonic tests were carried out, the simple harmonic tests and the sweep harmonic tests. The objective of the simple harmonic test was to observe the sensitivity of each configuration, 0kV, 5kV, bang-bang 1, and bang-bang 2, to a single frequency component. The model was subjected to sinusoidal input motions at selected frequencies around the estimated resonance frequency of the various configurations. The selected frequencies were 3.5 Hz, 4.0 Hz, 4.5 Hz, 5.0 Hz, and 5.5 Hz, with a maximum input displacement set to 0.51mm. Table 2 compares the maximum relative displacement and velocity of the mass for the different configurations for various input frequencies.

A sweep of sinusoidal waves across a frequency range of 1.0 Hz to 10 Hz was applied to each of the four configurations to verify if the mass displacement remained bounded within this range of frequencies. In order to observe the dominant frequency, the Fourier amplitude spectra of the mass displacement had to be normalized with respect to the Fourier amplitude spectra of the input displacement. This normalization was necessary because the servo-valve capacity of the testing machine was constant, 5 gallon per minute, and it was unable to produce a constant amplitude input displacement.

5 TEST RESULTS

The results of the simple harmonic tests show that for the same frequency of harmonic support motions, the response of the system with maximum imposed voltage is smaller than the response of the system without imposed voltage. The displacement response of the system with maximum imposed voltage is reduced by 60%, compared to the system without imposed voltage for forcing frequencies close to resonant frequency. The reduction in response is smaller for frequencies far from the resonant frequency.

The test results for the system using the bang-bang 1 configuration show no significant reduction in response compared with the results from the system with maximum imposed voltage. Because of the electro-rheological effect, the stiffness increment, ***dk,*** is small (10%), whereas the increment on damping value, ***dc,*** is very large (250%). Therefore, the switching lines, g_1 and g_2, are very close and the voltage ***off*** zone becomes very small and the voltage remains ***on*** most of the time. The system with the bang-bang configuration, however, is more advantageous than the system with maximum imposed voltage configuration because it needs less electric current to operate. This is important because it was observed that after long-term use, the ER-fluid can be damaged (burned) and its rheological effect is thus reduced. Fig. 7 show the comparison of the responses of the systems without imposed voltage, with maximum voltage, and with bang-bang 1 controller.

The switching line in the bang-bang 2 configuration is horizontal, therefore, the ***off*** zone in bang-bang 2 is off longer than the ***off*** zone in the bang-bang 1 configuration. Because the response is larger than the response of the system with the maximum imposed voltage, the test results for the system with the bang-bang 2 configuration are not significant improved.

A comparison of the amplification factors for the system with three configurations without imposed voltage, with maximum imposed voltage, and with the bang-bang 1 configuration is shown in Fig. 8. The results show that the amplification factors of bang-bang 1 and maximum imposed voltage are almost the same in the frequency range considered.

The system for the four configurations (without imposed voltage, with maximum imposed voltage, with the bang-bang 1 control, and with the bang-bang 2 control) were subjected to the sweep harmonic input in the frequency range of 1 to 10 Hz. The results show that the Fourier spectra are similar for the maximum imposed voltage configuration and the bang-bang 1 control. For the wider range of frequencies, the responses of these two configurations are smaller than the responses of 0-voltage and the bang-bang 2 configurations.

The mass displacement Fourier spectrum—normalized with respect to its input Fourier spectrum and shown in Fig. 9are comparable to the spectrum of the pure harmonic tests shown in Fig. 8. The small shift of the frequencies at the peak values of the spectra represents the shift of predominant frequency or change on the value of stiffness for the system with and without imposed voltage.

6 COMPARISON with THEORETICAL SIMULATION

A theoretical simulation of the response was performed using the values of c_0, k_0 and c_{max} , k_{max} obtained from the analysis of the experimental data (Table 1). The c values obtained were the values corresponding to the predominant frequency of the systems. The theoretical response was not always in good agreement with the test results.

This disagreement prompts the question of whether or not c and k are frequency dependent. Fig. 10 shows the plot of c values obtained from pure harmonic tests for the system without imposed voltage and for the system with maximum imposed voltage. The c values are not constant for each configuration, rather they change for every excitation frequency. Using these specific values of c for its corresponding excitation frequency, theoretical steady-state responses were in very good agreement with the responses obtained in the experiments, shown in Fig. 11.

According to Leitmann & Reithmeier's [7] analytical simulation, the bang-bang 1 control configuration should reduce the response more effectively than the configuration with maximum imposed voltage. This was not achievable in this experiment using this particular type of ER-fluid and the maximum voltage supply of 5kV. The bang-bang control configuration should yield better results if the properties of the ER-fluid were in a certain range so that the ER-effect was optimum, while the algorithm remained stable, as shown in Fig. 12. If the variation in damping, d_c, is large and the variation in stiffness, d_k, is small—as in the ER-fluid used in this experiment—the parabolic function of Eq. 7 for both systems is almost concentric and the bang-bang control is not effective; however, even if d_c is large, d_k cannot be too large, because, as shown in Fig. 12, the parabolic function will drift apart negating a stable solution. To obtain the most efficient bang-bang control scheme for this algorithm, d_k should be in the range of 20-30%, while d_c should be about 100-150%, thus enabling the system to experience significant change on its predominant period and its damping values.

7 SUMMARY and CONCLUSION

The electro-rheological effect changed the mechanical properties of a mechanical system under dynamic load.

The bang-bang control configuration is an effective and stable method to reduce the dynamic response of a mechanical system, although the response reduction level is not large. A comparable reduction in response was obtained for the control configuration that maintained maximum imposed voltage for the total duration of response. The bang-bang control configuration, however, needed less electric current than the configuration with constant maximum imposed voltage. This is an advantage because the use of high levels of electric current over a long period of time can deteriorate the properties of ER-fluids.

Additional tests using different electro-rheological fluids and higher levels of voltage are suggested. An ER-fluid that produces larger changes in stiffness, more than the 10% achieved with the fluid used in these tests, may improve the behavior of the system. The fluid must also provide changes in damping of greater than 100%. Future studies should be performed to investigate a damping model that includes the frequency and voltage dependency, $c(\bar{u}, \omega)$, instead of voltage dependency, $c(\bar{u})$, alone. This is an important parameter affecting the controlled response of the system.

8 ACKNOWLEDGEMENTS

The research reported here was funded by the National Center for Earthquake Engineering Research of The State University of New York at Buffalo under the grant NCEER/R07385. We would like to thank Professor George Leitmann for his support.

We thank Dr. C.E. Wilne from ICI Chemical & Polymers Ltd., England, for lending the test specimen and providing the ER-fluid used in this test series. The staff of the Structural Laboratory at Davis Hall, Dr. M. Blondet and Mr. T. Merport, offered invaluable assistance in the setting up and conduct of the experiment. Dr. J. Abrefah from Nuclear Engineering generously provided the high-voltage power supply used in the experiment.

9 REFERENCES

1. Tarics, A.G, Way, D. and Kelly J.M., "The Implementation of Base Isolation for the Foothill Communities Law & Justice Center", *Technical Report*, RTA, San Francisco (1984).
2. The Salt Lake City Corp., *Proceedings of International Seismic Isolation/Historic Preservation Symposium* (May 1988).
3. Choy, Y., Sprecher, A.F. and Conrad, H., "Vibration Characteristics of Composite Beam Containing an Electrorheological Fluid", *Journal of Intelligent Material Systems and Structures*, **1**:91-104 (January 1990).
4. Coulter, J.P., Weiss, K.P. and Carlson, D., "Engineering Applications of Electrorheological Materials", *Journal of Intelligent Material Systems and Structures*, **4**:248-259 (April 1993).
5. European Patent Application, "Apparatus Capable of Containing an Electro-rheological Fluid", Application no. 91304019.2 (1991).
6. Halsey, J. and Martin, J., "Electrorheological Fluids", *Journal of Scientific American*, pp. 58-64 (October 1993).
7. Leitmann, G. and Reithmeier, E., "Semiactive Control of a Vibrating System by Means of Electrorheological Fluids", *Journal of Dynamic and Control*, **3**:7-33 (1993).
8. Stanway, R., Sproston, J.L., Prendergast, M.J., Case, J.R and Wilne C.E., "ER Fluids in the Squeeze-flow Mode: An Application to Vibration Isolation", *Short Communication*, RS-004.

Table 1: : Mechanical properties of the system

	Without Imp. Voltage	With Max. Voltage	Increment - ER-fluid properties
Stiffness (lb/in)	275	295	20 (10%)
Damping (lb-sec/in)	1.18	4.07	2.89 (245%)
Damping Ratio (%)	6	20	

Table 2: : Maximum Values of Mass Displacement and Velocity Subjected to Harmonic Inputs.

	Without Imp. Voltage		With Max. Voltage		Bang-bang 1		Bang-bang 2	
Input Signal	Disp.	Vel.	Disp.	Vel.	Disp.	Vel.	Disp.	Vel.
Harmonic 3.5 Hz	0.0253	0.5387	0.0159	0.3215	0.0160	0.3373	0.0229	0.4701
Harmonic 4.0 Hz	0.0517	1.2000	0.0321	0.7163	0.0318	0.7227	0.0461	1.0411
Harmonic 4.5 Hz	0.1185	3.1143	0.0799	2.1620	0.0683	1.7940	0.0772	2.0754
Harmonic 5.0 Hz	0.0615	1.8285	0.0482	1.4129	0.0503	1.4939	0.0435	1.3046
Harmonic 5.5 Hz	0.0369	1.2270	0.0294	0.9654	0.0332	1.0989	0.0288	0.9633

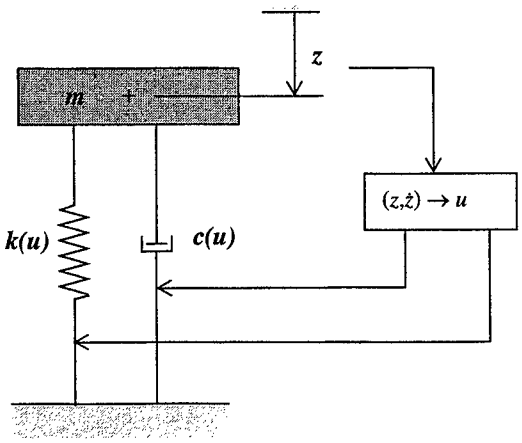

Figure 1: Analytical model of the SDOF system.

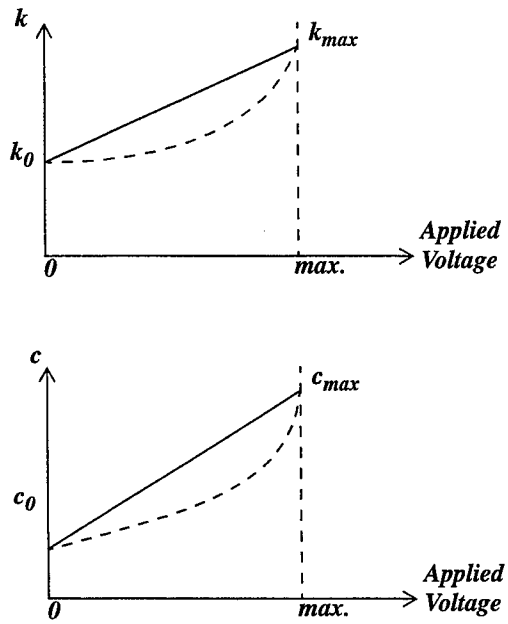

Figure 2: Variation of stiffness and damping with imposed voltage.

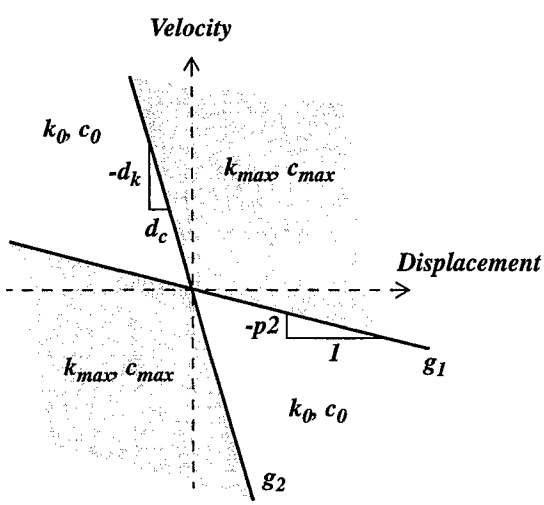

Figure 3: Switching lines g_1 and g_2 on the state plane.

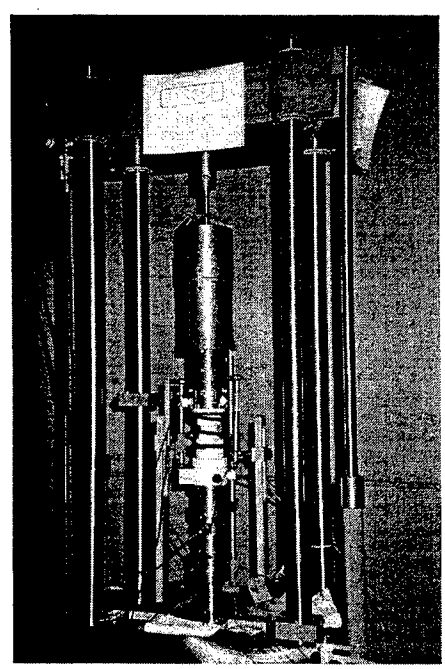

Figure 4: Photograph of the test set-up.

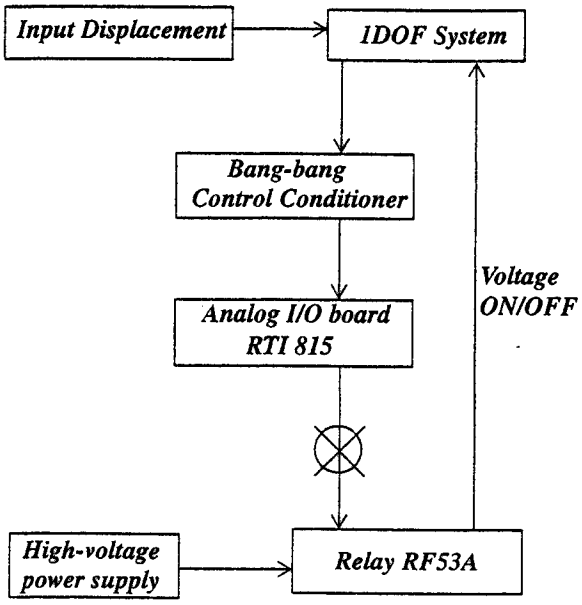

Figure 5: Close-loop of the high voltage control system for the bang-bang scheme

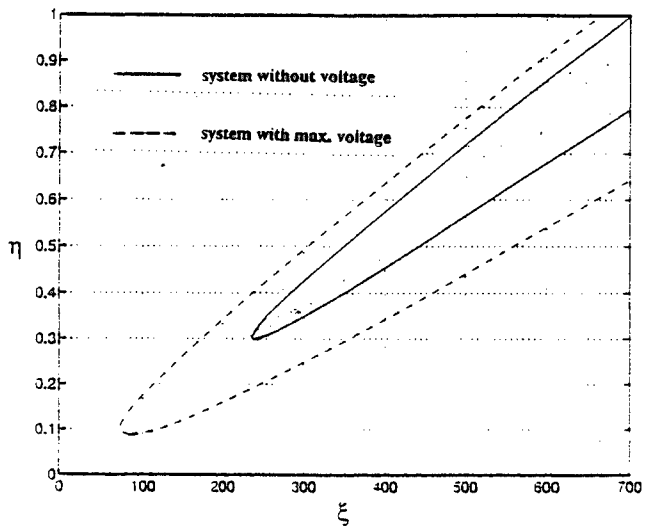

Figure 6: Range for ξ and η values

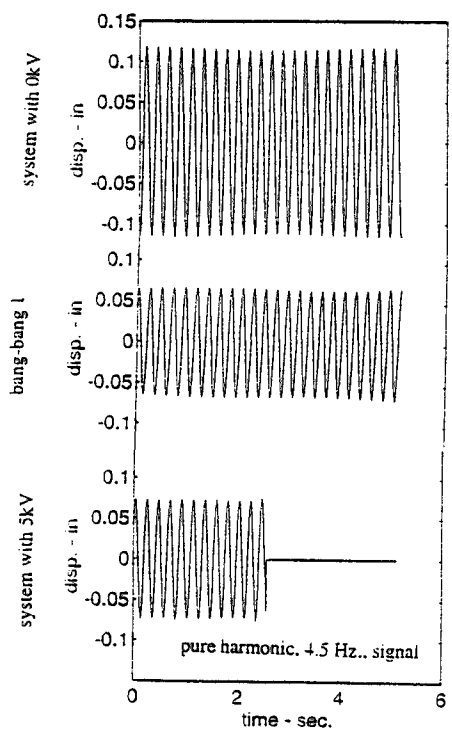

Figure 7: Responses for the three systems.

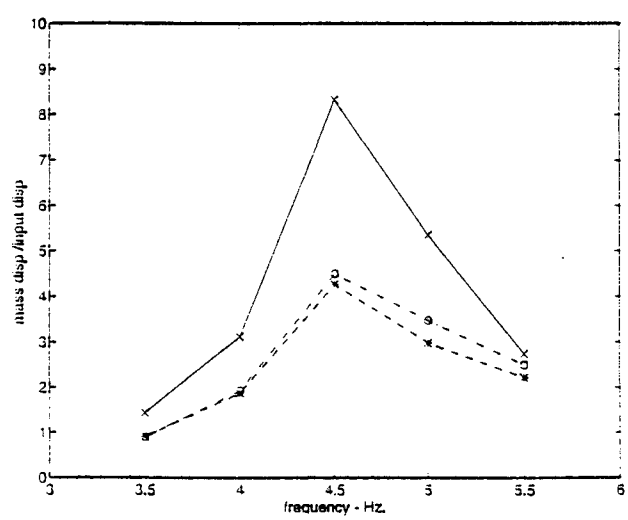

Figure 8: Amplification factor of the system subjected to pure harmonic motions.

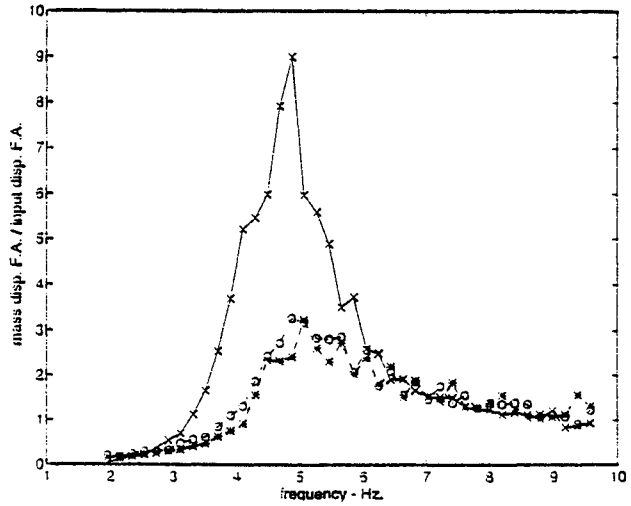

Figure 9: Amplification factor of the system subjected to pure harmonic motions.

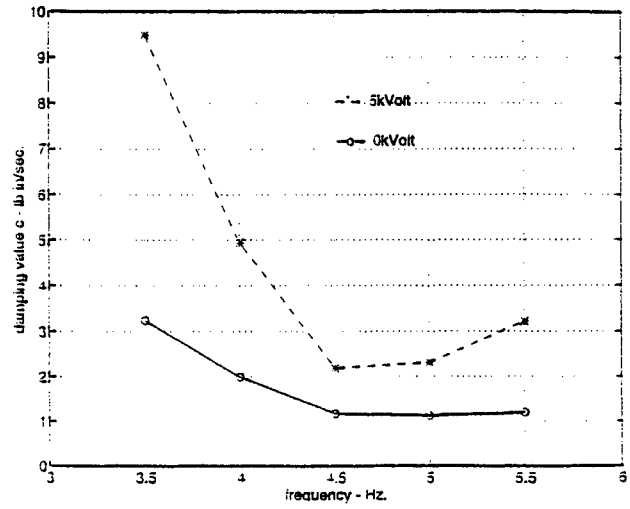

Figure 10: Damping versus frequency of the system subjected to the pure harmonic input.

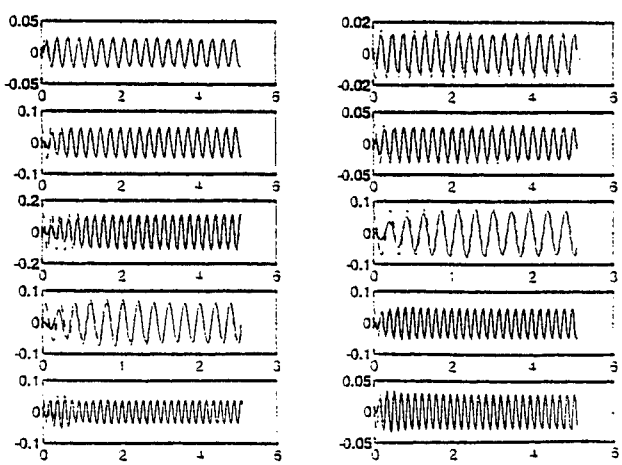

Figure 11: Comparison of theoretical and experimental responses of system subjected to pure harmonic input.

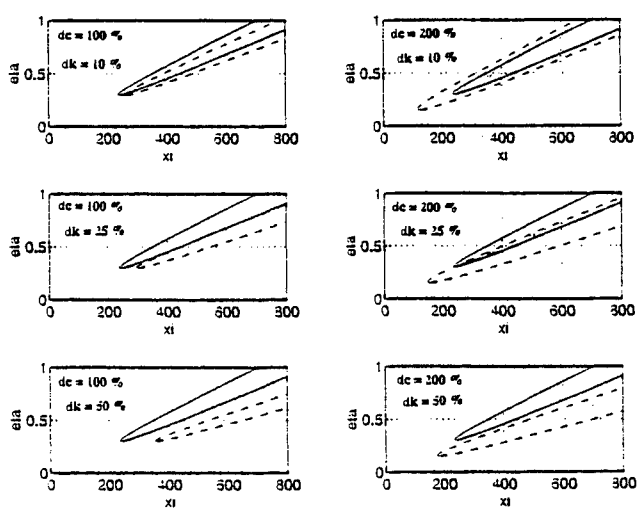

Figure 12: Range of ξ and η values for several combination of d_k and d_c..

Large-scale ER-damper for seismic protection

Scott McMahon[a] & Nicos Makris[b]

[a]Dept. of Civil Engrg. and Geological Sciences, Univ. of Notre Dame, IN 46556
[b]Dept. of Civil and Env. Engrg., 711 Davis Hall, Univ. of California, Berkeley, CA 94720

ABSTRACT

A large scale electrorheological (ER) damper has been designed, constructed, and tested. The damper consists of a main cylinder and a piston rod that pushes an ER-fluid through a number of stationary annular ducts. This damper is a scaled-up version of a prototype ER-damper which has been developed and extensively studied in the past[3,7]. In this paper, results from comprehensive testing of the large-scale damper are presented, and the proposed theory developed for predicting the damper response is validated.

Keywords: electrorheological damper, seismic protection

1. INTRODUCTION

Semi-active devices combine the benefits of active structural control with the benefits of passive damping. While the semi-active control device cannot add to the energy of the system as in active control, its mechanical properties can be varied in order to optimally dissipate energy and control vibrations. Several advantages of semi-active devices over active devices include: smaller power requirement, improved reliability, and reversion to a passive device in the event of a power failure[3]. Different types of semi-active dampers have been proposed and investigated to dissipate vibratory energy. Two of these are controllable fluid dampers[3,7] and variable orifice dampers[6,9]. Controllable fluid dampers utilize electrorheological (ER) or magnetorheological (MR) fluids to modify mechanical properties through the application of electric or magnetic fields. In this way, damping characteristics of the devices can be controlled to provide an optimal structural response.

Recently, a prototype ER damper with a damping constant of $C \approx 700$ lb-s/in at $E = 0$ kV/mm was constructed and tested at the University of Notre Dame[3,7]. In this paper, the development and testing of a large-scale ER damper with $C \approx 18{,}600$ lb-s/in (two bypasses) and $C \approx 12{,}400$ lb-s/in (three bypasses) is presented along with the validation of existing methodologies to predict the damper response using the developed theory of flow of viscoplastic materials. Of particular interest is the scalability of these methodologies from small to large-scale devices. In order to validate existing theories that predict ER damper response, dynamic testing was conducted using the arrangement shown in Figure 1.

2. ELECTRORHEOLOGICAL FLUID

The ER fluid used within the test damper is a suspension of crystalline alumino-silicate powder, or zeolite, in a silicone oil carrier with a specific gravity of 0.970 and kinematic viscosity of 1000 cSt. Particle concentration in the fluid is 46.8% by weight. Results from oscillatory and steady shear viscometric tests of the ER-fluid used have been presented in Makris et al. (1996), Jordan et al. (1997) and Burton (1996). Figure 2 shows the dependence of the yield stress, τ_y, of the material on the electric field. This indicates that this ER fluid is approximately proportional to E^2.

SPIE Vol. 3045 • 0277-786X/97/$10.00

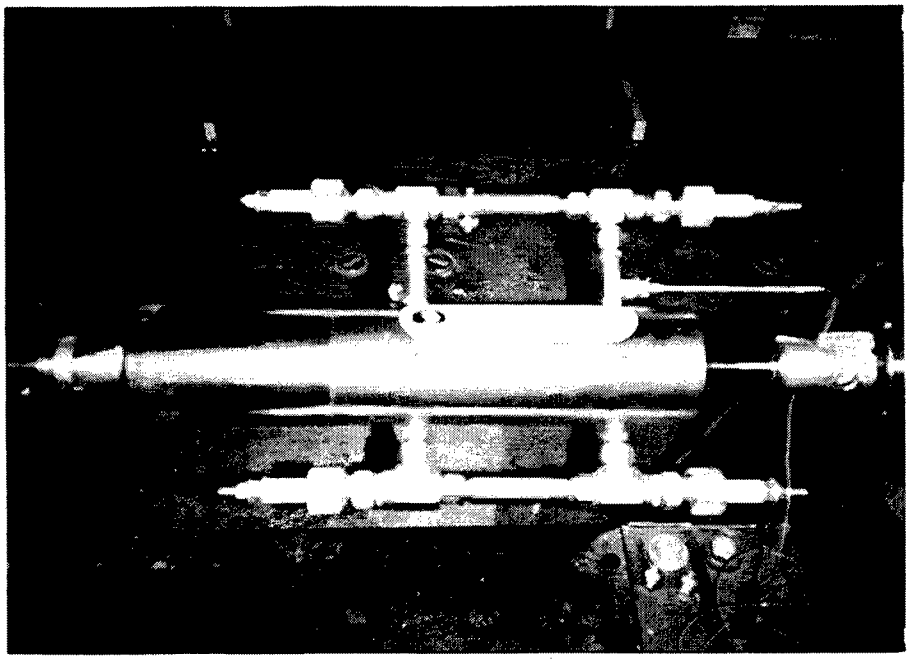

Figure 1. Large-Scale ER Damper and Testing Arrangement.

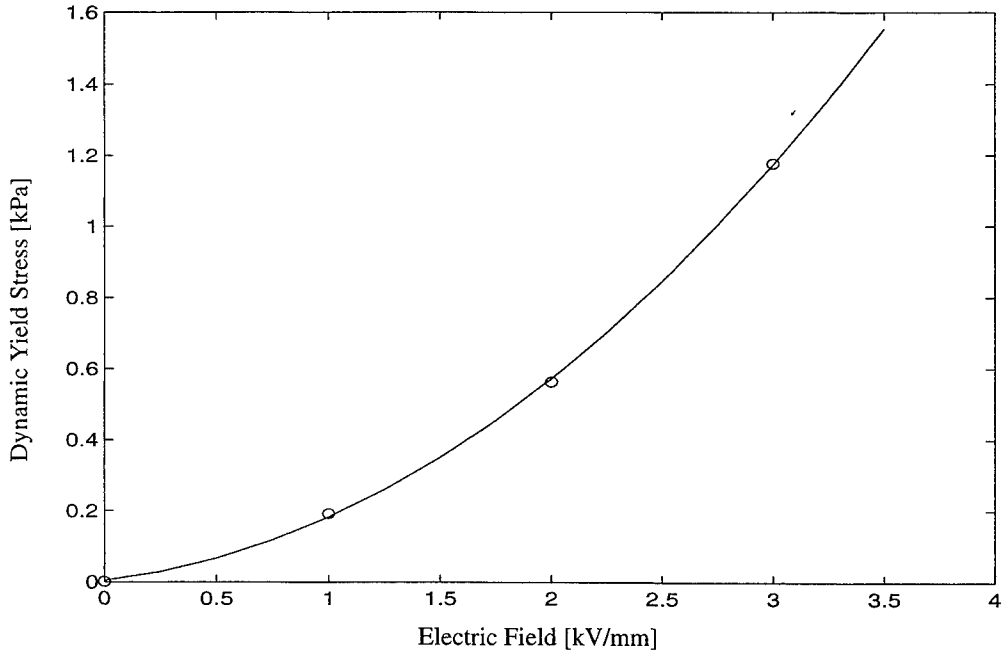

Figure 2. Yield stress of ER-fluid used as a function of electric field.

3. EXPERIMENTAL PROGRAM

3.1 Test setup

A hydraulic actuator, with a load rating of 250 kN (55 kips) and a 152.4 mm (6 in) stroke length induces a specified uniaxial displacement to the test damper. Actuator piston rod displacement is measured by a linear variable differential transformer (LVDT) mounted within the actuator. Damper force measurements are made through a stationary load cell mounted between the damper and the reaction frame.

The large-scale damper consists of an outer cylinder and a double-ended piston rod that pushes ER fluid through a number of stationary annular ducts. The damper can accommodate four bypass attachments to the main cylinder. The configuration shown in Figure 1 depicts the ER damper with two bypasses. A 12.7 mm (0.5 in) diameter stainless steel rod runs through the center of the bypass and is isolated from the system by teflon supports at each end.

Voltage for testing the ER effect is supplied to the system through a variable power supply and a high-voltage amplifier with a gain of 1000 V/V and output voltage of 0 to ±10 kV at a current of 0 to ±2.0 mA. The voltage is applied to a cathode which is a rod concentric to the bypass, and linked in parallel to the rods of the other bypasses. Ground wire is attached to the outside of all bypass cylinders.

Temperature measurements are made in two locations. The first is made by a surface thermocouple attached to a bypass cylinder. The second is made by a thermocouple probe which reads the temperature of the fluid at the core of the main cylinder. Both thermocouples are connected to panel meters for digital display. The recorded temperature should not exceed 240°C (450°F) to prevent damage to the insulators.

3.2 Experimental testing

Harmonic displacement histories were induced on the damper for the two and three bypass setups. The bypasses have gap width, h, of 1 mm and length, L, of 15 cm. The setups are tested with an applied electric field, E, of 0 and 3 kV/mm. Force response data is recorded and compared to the predicted response.

Figure 3 shows a recorded force-displacement loop at very small piston velocities with E = 0 kV/mm. At reversal of motion, there is a net force drop of approximately 900 N (200 lbs) which is due to the friction at the damper seal. The friction force, P_f is present in all experiments and is approximately 450 N (100 lbs).

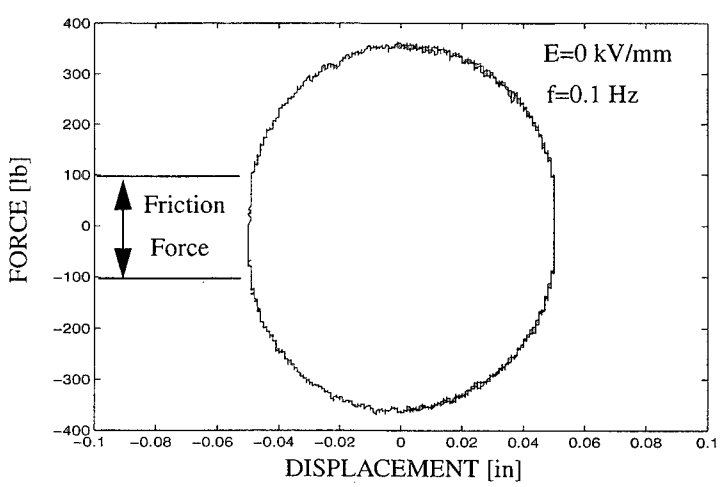

Figure 3. Recorded Force-Displacement loop at small piston velocities

Temperature dependence is in general an important design consideration for ER dampers in that it has been shown that temperature has an effect on the mechanical and electrical properties of ER fluids. The problem of estimating temperature increase due to viscous heating in passive and semi-active dampers has been addressed elsewhere[8]. One consequence of this temperature dependence is an increased current requirement for an increased fluid temperature[1]. Herein, the current investigation was conducted at a nearly constant outer surface temperature of 26.5°C (80°F).

One of the goals in ER damper design is to maximize the controllable force of the damper. This is accomplished by maximizing the yield force compared to viscous forces. At larger flow rates, the damping forces from viscous stresses dominate over damping forces from yield stresses, rendering the ER-effect less significant. In order to make the ER damper more effective at higher piston velocities, either a fluid with a lower viscosity and/or higher yield stress must be used or the flow rate must by maintained small across the bypass. Flow rate can be reduced by either increasing the gap width in the duct or by increasing the number of bypasses. The damper has been designed to accommodate four bypasses. This investigation analyzes the response results from the damper with two and three bypasses. Because the flow velocities in the bypasses are decreased, another benefit of the addition of bypasses is that temperature effects from viscous heating are reduced.

4. PREDICTION OF DAMPER RESPONSE

Prior investigation has indicated that for small piston velocities, the pressure drop across a piston for an ER damper can be adequately modeled by[7]

$$\Delta P = \frac{12Q\eta_0 L}{\pi d h^3}\frac{1}{1-\frac{3\tau_y L}{\Delta P h}+4\left(\frac{\tau_y}{\Delta P}\right)^3\left(\frac{L}{h}\right)^3} \tag{1}$$

where Q is the flow through the bypass and is given by

$$Q(t) = \dot{u}(t)\frac{\pi(d_p^2-d_r^2)}{4n} \tag{2}$$

Equation (1) was derived for a rigid-visco-plastic material[7] and is a nonlinear cubic equation in ΔP, which can be expressed as

$$\Delta P^3-\left(3\tau_y \mathrm{sgn}(\dot{\gamma}_{xr})\frac{L}{h}+\frac{12\eta_0 LQ}{\pi d h^3}\right)\Delta P^2+4(\tau_y \mathrm{sgn}(\dot{\gamma}_{xr}))^3\left(\frac{L}{h}\right)^3 = 0 \tag{3}$$

The solution of (3) is available in standard mathematical handbooks[11]. In the limiting case of a purely viscous material (τ_y=0), Equation (3) collapses to

$$\Delta P_v = \frac{12\eta_0 LQ}{\pi d h^3} \tag{4}$$

Predictions of damper response using Equation (3) are shown in Figure 4 for two bypasses and Figure 5 for three bypasses next to recorded data at E = 0 kV/mm and E = 3 kV/mm. For the model used, τ_y = 1.7 kPa and η_0 = 6 Pa-sec and 6 Pa-sec for E=0 and 3 kV/mm respectively. As these figures show, the proposed model adequately predicts damper response for small piston velocities (up to 0.2 in/sec) but does not capture satisfactorily the damper behavior at higher velocities. This is because at higher piston velocities, leakage through the piston head increases, thereby reducing the pressure drop. In addition, Equation (1) assumes that flow does not depend on end effects. Nevertheless, it is interesting to note that if t is the width of the small gap between the piston head and the damper cylinder, the area through which leakage occurs is: $A_l = 2\pi r_p t$. On the other hand, the area of the piston cylinder is $A_p = \pi r_p^2$, so the ratio of the volume rate of fluid that leaks to the fluid that advances is

$2tr_p$. Accordingly, the bigger the piston diameter the smaller the fraction of the fluid that leaks. This is probably the reason that in the small damper an average viscosity value of 7 Pa-sec resulted in a good prediction of the force, whereas in the large damper, a value of 6 Pa-sec is enough to predict the measured forces.

Figure 6 shows that the addition of bypasses gives greater control over the damping force caused by yield stresses as predicted by the above equations.

5. CONCLUSIONS

In this paper the issue of scalability of ER dampers has been addressed. A large-scale ER-damper has been designed and tested. The recorded response was used to validate a proposed theory that predicted successfully the response of a smaller prototype ER-damper. It was found that the existing theory is capable to predict satisfactorily the large damper response at small velocities. It was observed that since the volume fraction of the fluid that leaks to the fluid that advances is smaller as the diameter of the damper increases, a slightly smaller value of fluid viscosity was needed to predict the force-displacement loops of the large damper.

ACKNOWLEDGEMENTS

This work is supported by the National Science Foundation Grants BCS-9300827 and CMS-9623811, Dr. S.C. Liu, Program Director. The main cylinder of the damper was manufactured and donated by Taylor Devices, Inc., N. Tonawanda, NY.

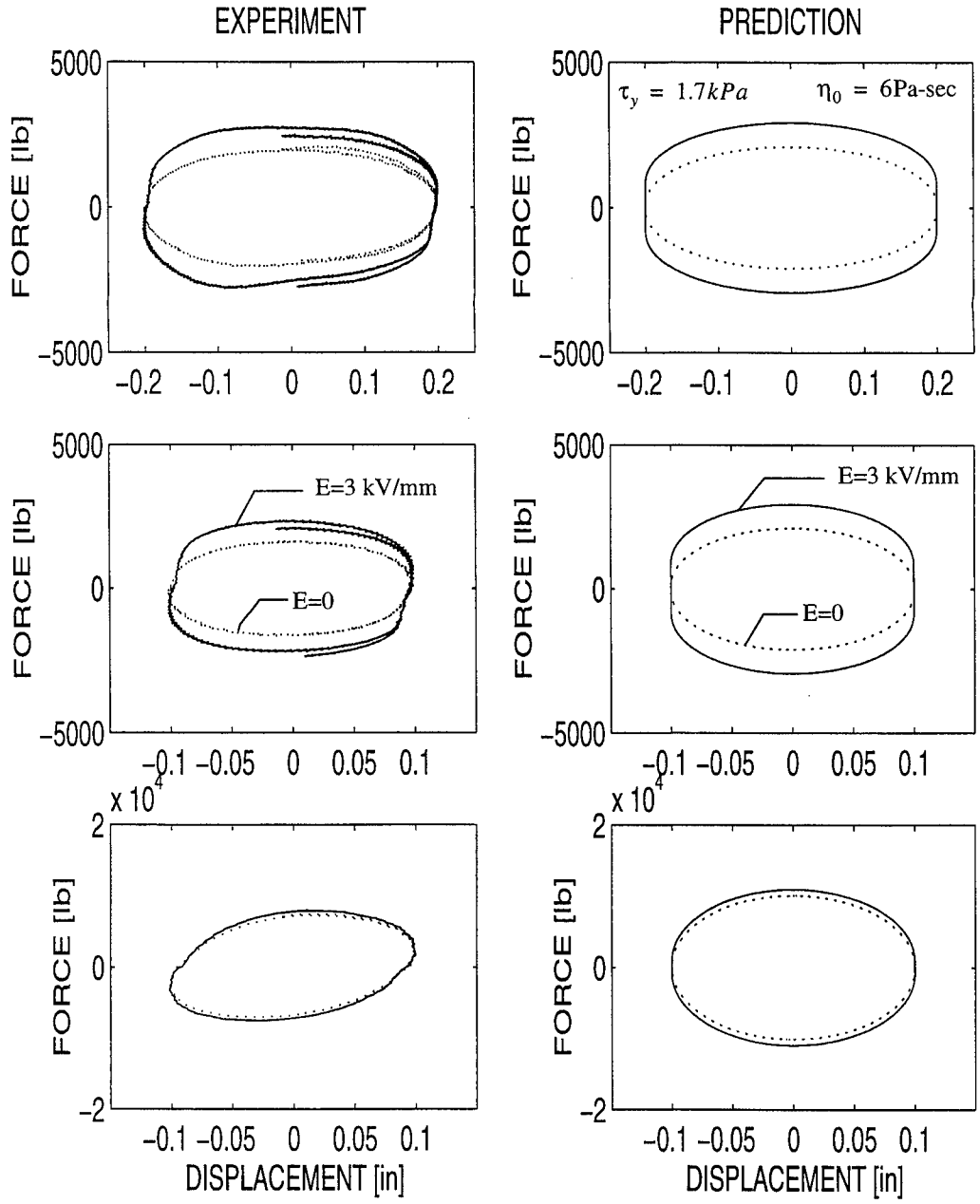

Figure 4. Comparison of Experimental Results to Predicted Response for E=0 kV/mm and E=3 kV/mm with Two Bypasses. From Top to Bottom (frequency/amplitude): 0.1 Hz/0.2 in; 0.2 Hz/0.1 in; 1.0 Hz/0.1 in.

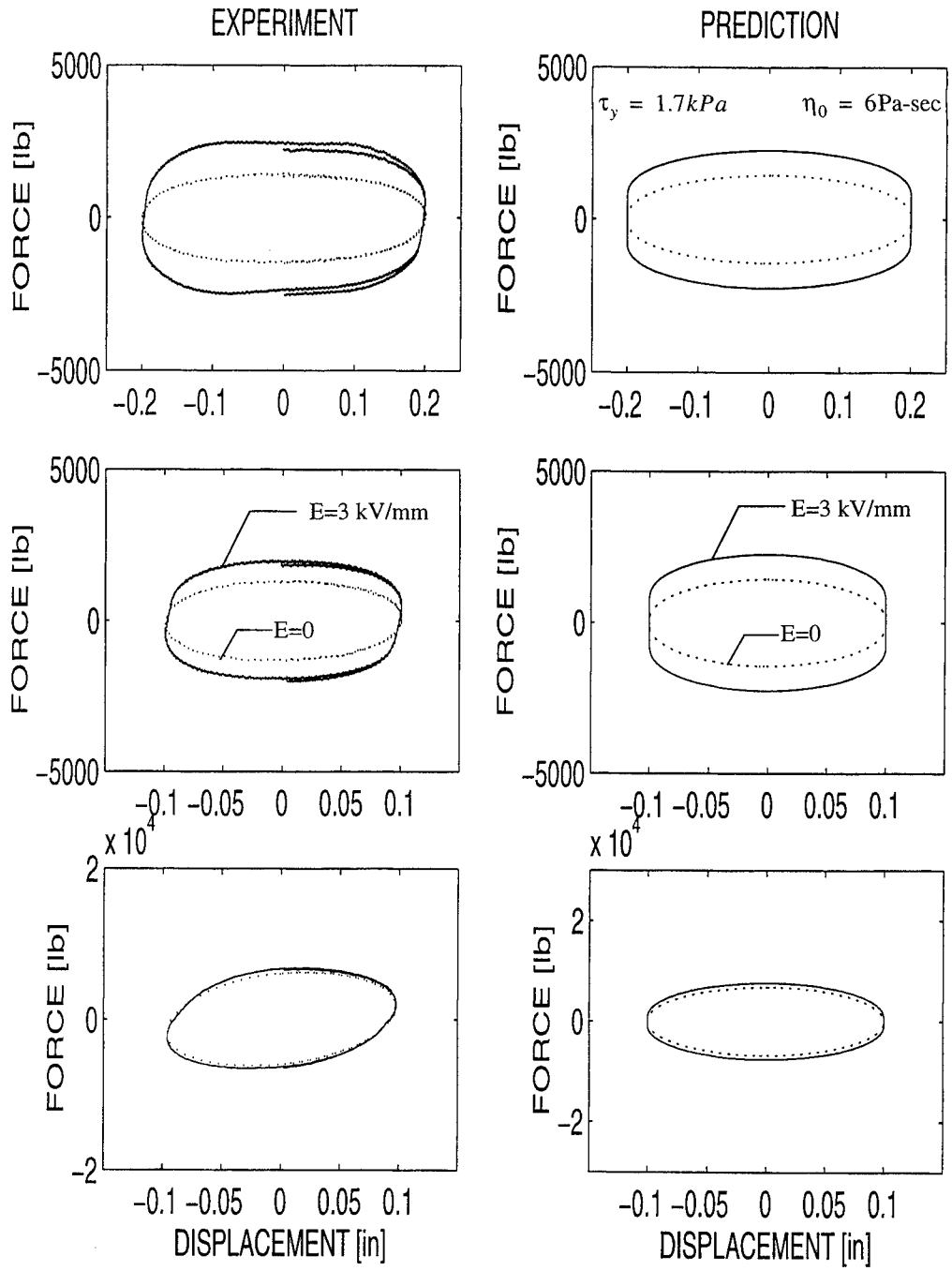

Figure 5. Comparison of Experimental Results to Predicted Response for E=0 kV/mm and E=3 kV/mm with Three Bypasses. From Top to Bottom (frequency/amplitude): 0.1 Hz/ 0.2 in; 0.2 Hz/0.1 in; 1.0 Hz/0.1 in.

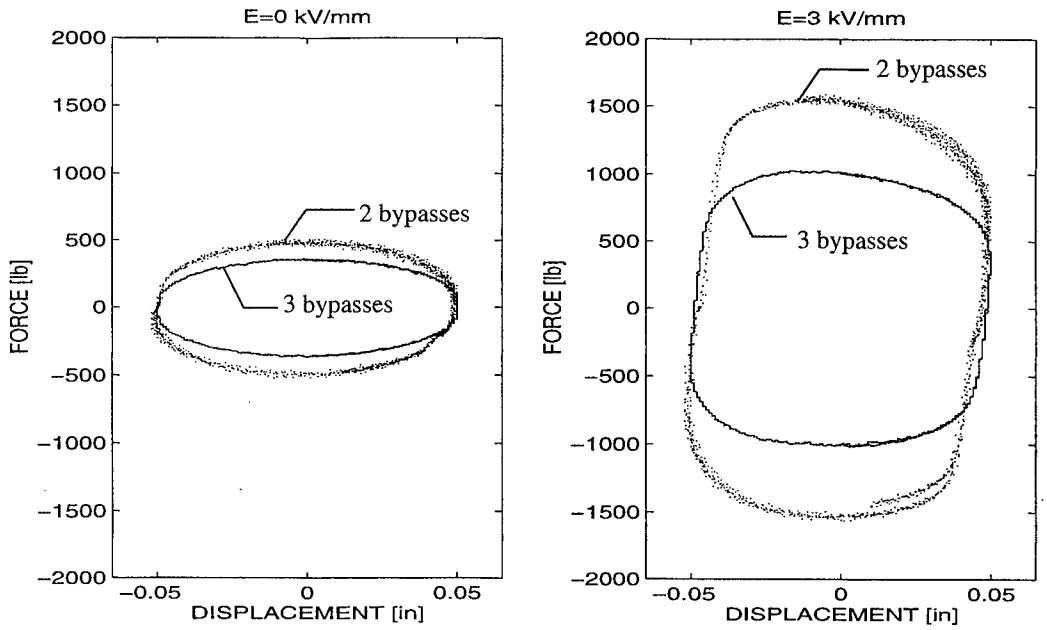

Figure 6. Comparison of Experimental Results for E=0 kV/mm and E=3 kV/mm with Two and Three Bypasses at 0.1 Hz/0.05 in.

REFERENCES

1. Brooks, D., "Applicability of Simplified Expressions for Design with Electro-Rheological Fluids", *J.Intelligent Material Systems and Structures*, **4**, pp. 409-414, 1993.
2. Buckle, I.G., "Earthquake protective systems for civil structures", *Proc. 10th European Conference on Earthquake Engineering*, Vienna, Austria, pp. 641-650, 1994.
3. Burton, S. A., Makris, N., Konstantopoulos, I., & Antsaklis, P. J. "Modeling the response of ER Damper: Phenomenology and Emulation", *J. Engrg. Mech.*, ASCE, **122**, pp. 897-906, 1996.
4. Fujino, Y., Soong, T.T. and Spencer Jr., B.F., "Structural Control: Basic Concepts and Applications", *Proc ASCE Struct. Congress*, Chicago, Illinois, Vol. 2, pp. 1277-1287, 1996.
5. Jordan, M., Schwendt, A., Hill, A.D., Burton, S. and Makris, N. "Zeolite-based electro-rheological fluids: Testing, modeling and intrumental artifacts", *J. of Rheology* **41(1)**, pp. 75-91, 1997.
6. Kawashima, K. and Unjoh, S., "Seismic Response Control of Bridges by Variable Dampers", *J. of Structural Engineering*, **120(9)**, pp. 2583-2601, 1994.
7. Makris, N., Burton, S., Hill, D., & Jordan, M. "Electrorheological fluid damper for seismic protection of structures", *J. Engrg. Mech.*, ASCE **122(10)**, pp. 1003-1011,1996.
8. Makris, N. and McMahon, S. "Seismic protection of bridges with fluid damper and the Issue of Viscous Heating", *Proc. Fourth U.S.-Japan Workshop on Earthquake Protective Systems for Bridges*, Osaka, Japan, 1996.
9. Patten, W.N., Sack, R.L. and He, Q., "Controlled Semiactive Hydraulic Vibration Absorber for Bridges", *J. of Structural Engineering*, **122(2)**, pp. 187-192, 1996.
10. Rosenbaum, D.B., "Seismic dampers gaining ground (inset, p.9)", *ENR*, **236(19)**, pp. 8-9, 1996.
11. Spiegel, M. R., *Mathematical Handbook of Formulas and Tables, Schaum's Outline Series*. McGraw-Hill, N.Y., 1968.

Design Rules for MR Fluid Actuators in Different Working Modes

Ralf Bölter and Hartmut Janocha

University of Saarland, Laboratory for Process Automation (LPA)
PO Box 15 11 50, 66041 Saarbrücken, Germany

ABSTRACT

The behaviour of actuators based on magnetorheological fluids is determined by a variety of parameters. The magnetorheological properties of the MR suspension, the working mode (shear mode, flow mode, squeeze mode) and the design of the magnetic circuit consisting of MR fluid, flux guide and coil all considerably influence the properties of the actuator. This paper presents design rules for MR fluid actuators in different working modes. The behaviour of MR fluids in the three working modes was investigated by using a rotational viscometer, a flow mode damper and a new measuring technique working in the squeeze mode. The measurement results for various magnetic flux densities are reported and the results of the different working modes are compared. High dynamic damping forces dependent on the magnetic field can be achieved especially in the squeeze mode . The design of the magnetic circuit of an MR fluid actuator is analysed by using finite–element–methods. The advantages of integrating permanent magnets into the magnetic circuit of an MR fluid actuator are pointed out. The working point of the actuator can be adjusted by permanent magnets without consuming any power and the maximum power required to drive the actuator can be reduced. From these results design rules for MR fluid actuators are developed.

Keywords: magnetorheological fluid, damper, clutch, squeeze mode, actuator

1 INTRODUCTION

Under the influence of an magnetic field magnetorheological fluids (MR fluids) show a continuous increase in the flow resistance of several dimensions within some milliseconds.[1] The first reports on suspensions that react on a magnetic field with a reversible change of their flow properties can be dated back to the 1940s.[2] The magnetic particles of the MR fluid suspended in a low–permeable base fluid form under the influence of a direct or alternating magnetic field magnetic dipoles which align according to the magnetic field and form chains and agglomerates along the magnetic field lines. These structures can be mechanically loaded and lead to the formation of a yield stress dependent on the magnetic flux density and a flow resistance continuously variable by the field amplitude.

The behaviour of actuators based on magnetorheological fluids is determined by a variety of parameters. The rheological and magnetic properties of the MR fluid, the working mode and the magnetic circuit (flux guide, coil) all considerably influence the design and properties of the actuator.

SPIE Vol. 3045 • 0277-786X/97/$10.00

2 MR SUSPENSIONS

There are different types of MR fluids. The micro MR suspensions consist of ferromagnetic particles (e.g. carbony iron alloy) in mineral or silicon oil. The percental share of particles lies between 20% and 60% by weight, and the diameter of the particles is $d > 1\,\mu$m. Shear stresses of up to 100 kPa can be transmitted with micro MR suspensions.[3] But some of these systems show a strong tendency towards sedimentation and abrasion.

High sedimentation stability and an abrasion which can be neglected in practical application can be attained by employing nano-sized particles ($d < 30$ nm).[4] Nano–sized magnetic particles are soft ferrites prepared by a wet chemical technique. The dispersing layer consists of molecules carrying on average more than five charges. All components are stable at high temperatures in air and are non–toxic. The total solids content is about 60 % weight.

Another type of MR suspensions can be realised by injection of nonmagnetic particles in a magnetic colloid fluid (ferrofluid). Under the influence of a magnetic field, the nonmagnetic particles form structures and the flow resistance increases.[1]

MR suspensions are superparamagnetic, their magnetic behaviour (magnetization vs. magnetic field strength) is hysteresis–free, they have a saturation magnetization and a permeability that depends on the magnetic field strength. The maximum yield stress is particularly determined by the concentration and magnetic saturation of the suspended particles.[5] As the magnetic saturation of carbony iron alloy is much higher than the magnetic saturation of ferrite, the maximum of shear stresses transferable by MR fluids based on carbony iron particles is much higher than that of MR fluids with ferrite particles. The saturation magnetization determines the maximum of transmittable shear stresses.[5]

3 WORKING MODES

Actuators with MR fluids operate in three working modes depending on the type of deformation employed (cf. Fig. 1): shear mode, flow mode or squeeze mode. In the case of the shear mode, the MR fluid is located between surfaces moving in relation to each other with the magnetic field flowing perpendicularly to the direction of motion of these shear surfaces. The shear stress can be controlled by the magnetic field. Clutches based on MR fluids work in the shear mode. In the flow mode the MR fluid flows directly between static pole pieces. The flow resistance and thus the pressure drop $\Delta p = p_1 - p_2$ can be controlled by the magnetic field which runs normal to the flow direction (valve principle). Electrically controlled vibration dampers and shock absorbers can be realized by integrating an

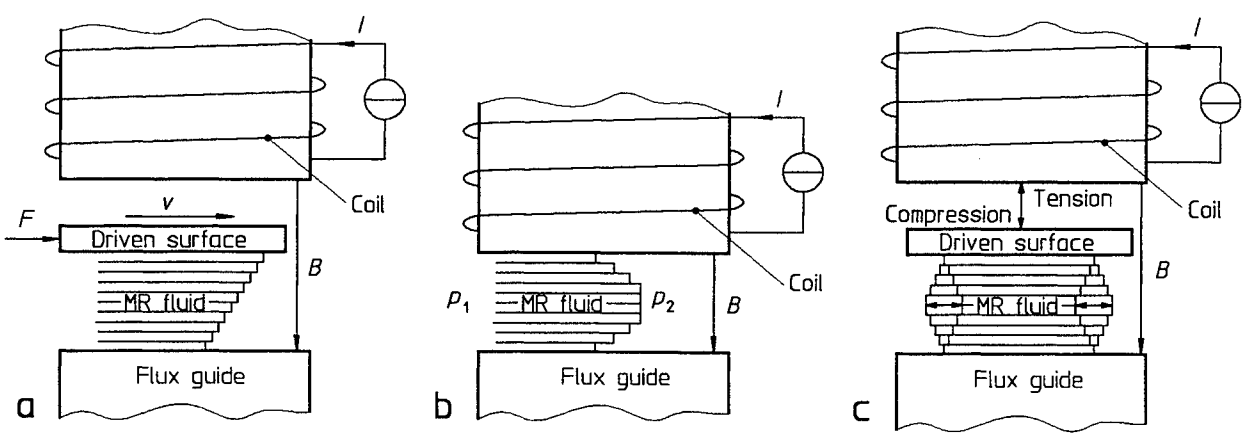

Figure 1: Working modes of MR fluid actuators. **a** shear mode, **b** flow mode, **c** squeeze mode

MR fluid valve. In the squeeze mode the MR fluid is squeezed by a normal pressure (cf. Fig. 1 c). A squeeze flow develops. The normal force required for the movement of the surface can be adjusted by varying the magnetic flux density. Using the squeeze mode, vibrations with high forces and low amplitudes, e.g. at machine tools, can be damped.

4 Shear Mode

4.1 Rotational Viscometer

The characterization of MR fluids in the shear mode can be achieved by using commercially available rotational viscometers modified for the measurement of MR fluids.[6] The behaviour of MR fluids in the shear mode was investigated by the use of a double gap system. Both pole pieces form two 90°–segments of the outer cylinder. The cylinder is completed by two 90°–segments made of low–permeability material. The inner cylinder also consists of high–permeability material to guide the magnetic flux and of low–permeability material to complete the cylindrical form.[6]

4.2 Measurement Results

Figure 2b shows an increase of the shear stress τ with a growing magnetic flux density B for the nano MR fluid 132 of the BASF AG. For low magnetic flux densities $B < 50\,\mathrm{mT}$, the increase of the shear stress corresponds to a power function. The rise of the curve is nearly constant in the range $50\,\mathrm{mT} < B < 100\,\mathrm{mT}$. The saturation magnetization of the nano MR fluid amounts to $M_S = 130\,\mathrm{mT}$. This results in a slight increase of the shear stress for $B > 150\,\mathrm{mT}$. The basic viscosity of the nano MR fluid is $\eta_0 = 1.4\,\mathrm{Pas}$ at a temperature $\vartheta = 50°\mathrm{C}$ and a shear rate $D = 1000\,\mathrm{s}^{-1}$. Figure 2a shows the flow curves recorded in the rotational viscometer. A yield stress which depends on the magnetic flux density is formed. The shear stress increases continuously with a growing shear rate for shear rates $D \leq 500\,\mathrm{s}^{-1}$. Under the influence of a magnetic field the shear stress is nearly independent of the shear rate

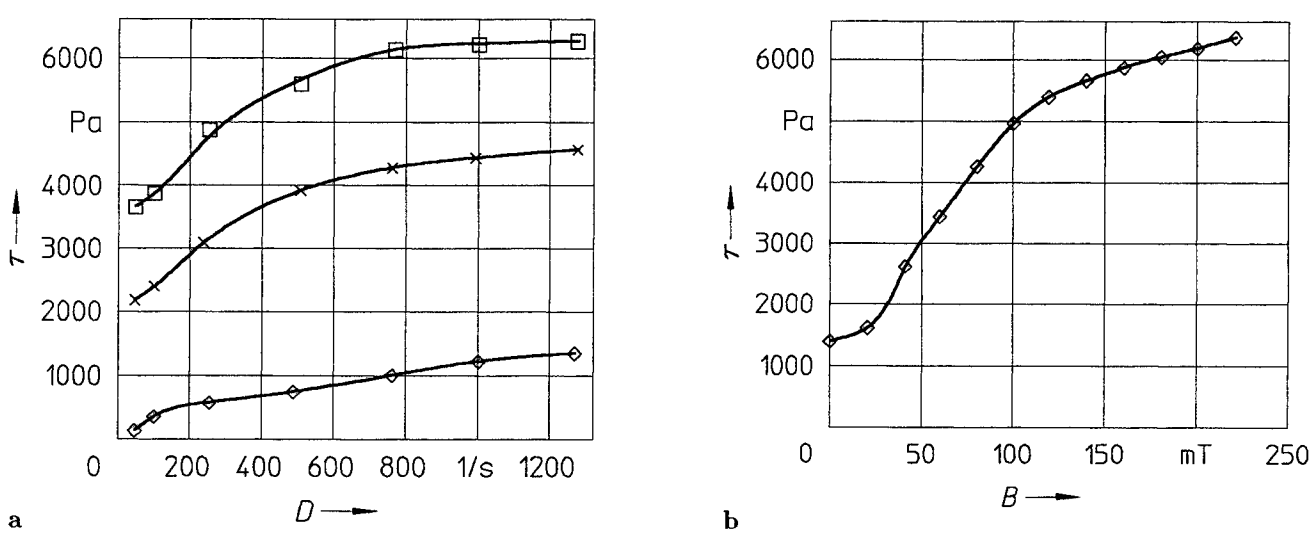

Figure 2: Shear stress vs. shear rate for magnetic flux densities $B = 0\,\mathrm{mT}$ (◇), $B = 100\,\mathrm{mT}$ (×) and $B = 200\,\mathrm{mT}$ (□) **(a)** and shear stress vs. magnetic flux density at a shear rate $D = 1000\,\mathrm{s}^{-1}$ **(b)** at a temperature $\vartheta = 50°\mathrm{C}$ for the nano MR fluid 132 of BASF AG

for shear rates $D > 750\,\mathrm{s}^{-1}$. Without a magnetic control field, the nano MR fluid shows a shear–thinning behaviour. Figures 3a and 3b show the shear stress in dependence of the shear rate and the magnetic flux density for an MR fluid of Bayer AG. As this sample has a relatively low particle content the basic viscosity is with $\eta_0 = 0.11\,\mathrm{Pas}$ at a temperature $\vartheta = 25°\mathrm{C}$ and a shear rate $D = 1000\,\mathrm{s}^{-1}$ much lower compared to a nano MR fluid. As the magnetic saturation of this suspension is higher than the magnetic saturation of the nano MR fluid, the shear stress of MR fluids of Bayer AG continuously increases with a growing flux density also for magnetic flux densities $B > 150\,\mathrm{mT}$. Much higher shear stresses than those displayed in Figure 3 can be achieved by increasing the particle content. Even the shear stress of the MR fluids of Bayer AG is for shear rates $D > 750\,\mathrm{s}^{-1}$ nearly independent of the shear rate (cf. Fig. 3a).

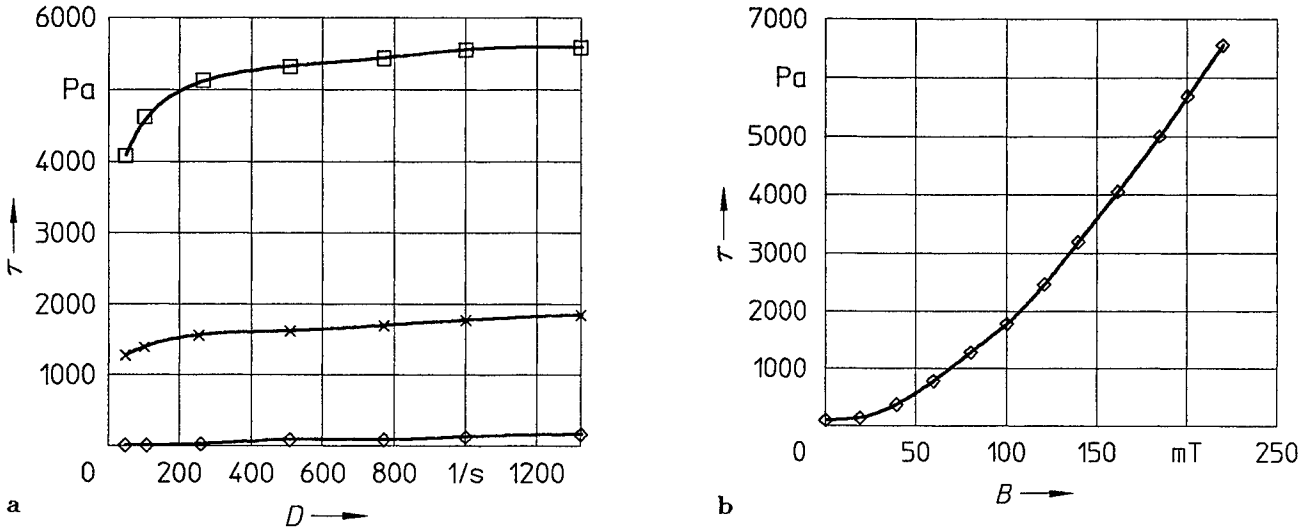

Figure 3: Shear stress vs. shear rate for magnetic flux densities $B = 0\,\mathrm{mT}$ (◇), $B = 100\,\mathrm{mT}$ (×) and $B = 200\,\mathrm{mT}$ (□) **(a)** and shear stress vs. magnetic flux density at a shear rate $D = 1000\,\mathrm{s}^{-1}$ **(b)** at a temperature $\vartheta = 25°\mathrm{C}$ for an MR fluid of Bayer AG

4.3 Clutches

Clutches based on MR fluids usually work in the shear mode. Figures 4 and 5 show two different coupling principles. Disc clutches are already installed as brakes in home trainers in series.[7] However, for high revolution frequencies of the disc clutch the particles of the suspensions will be segregated by centrifugation, the suspended particles move to the edge of the clutch plate. This can be avoided by a cylindrical location similar to the double

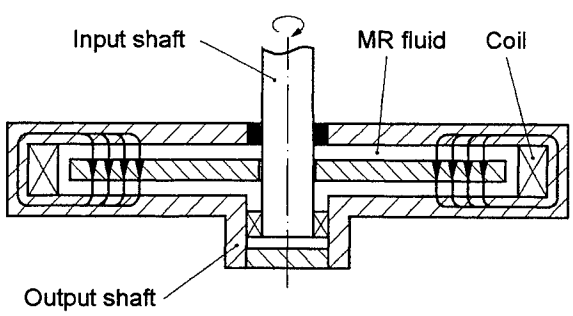

Figure 4: MR fluid disc clutch

gap configuration in the rotatinal viscometer. Fig. 5 shows the magnetic field configuration in the clutch. With a control current $I = 2\,\mathrm{A}$ a magnetic flux density $B = 0.3\,\mathrm{T}$ in the inner shear gap and $B = 0.23\,\mathrm{T}$ in the outer shear gap is generated. At a total length of the clutch $L_{\mathrm{cl}} = 42\,\mathrm{mm}$ and a diameter $d_{\mathrm{cl}} = 116\,\mathrm{mm}$ a torque $M = 3.85\,\mathrm{Nm}$ at a shear rate $D = 1000\,\mathrm{s}^{-1}$ can be transmitted with the MR suspension of Bayer AG shown in Figure 3.

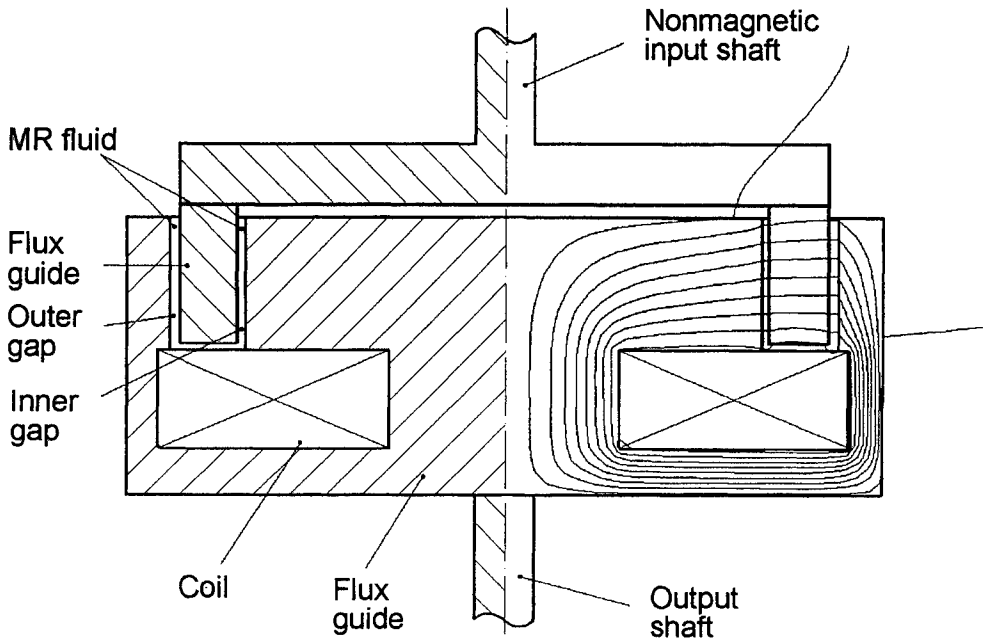

Figure 5: Cylindrical MR fluid clutch, on the right half the symmetric distribution of magnetic field lines is displayed

5 Flow Mode

5.1 Measurement technique

The behaviour of an MR fluid working in the flow mode can be examined with a damper with bypass. Two MR fluid valves are integrated in the bypass (Fig. 6), each of which has a length $L_{\mathrm{v}} = 50\,\mathrm{mm}$. The gap width of the valves is $w_{\mathrm{v}} = 201\,\mathrm{mm}$ and the separation of the pole pieces is $h_{\mathrm{v}} = 3\,\mathrm{mm}$. The piston has a diameter of $d_{\mathrm{p}} = 38\,\mathrm{mm}$ and the piston rod of $d_{\mathrm{r}} = 10\,\mathrm{mm}$. A magnetic field $B = 220\,\mathrm{mT}$ is generated in the MR fluid valves with a control current of $I = 2\,\mathrm{A}$ in the coil. The magnetic flux density within the valves is homogeneous over the whole valve length and the field lines run perpendicular to the flow direction of the MR fluid.[6] In a damper test assembly the damper makes an oscillating triangular movement, i.e. the piston speed is constant between both stationary points. The dynamic damper force and the distance at a given oscillation frequency is measured. As the damper force is caused almost exceptionally by the flow resistance of the MR fluid in the valves (the frictional forces of the damper can be neglected), the pressure drop above the valves and the volume flow can be calculated out of the damping force, the piston speed and the dimensions of the damper.

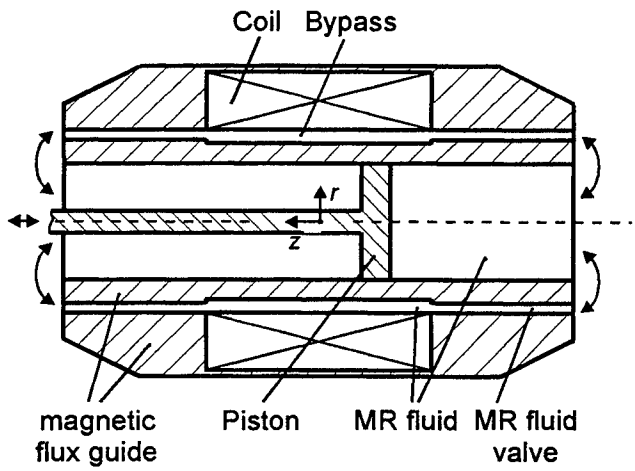

Figure 6: MR fluid damper

5.2 Measurement results

The damper was filled with the nano fluid of BASF AG. Figure 7a shows the dynamic force of the damper which has been measured and as a result the pressure difference which has been calculated above the two MR fluid valves as a function of the magnetic flux density for different piston speeds. Like the shear mode, the pressure drop at low magnetic flux densities $B < 50\,\mathrm{mT}$ increases according to a power function and reaches a limit value just above the magnetic saturation of the nano MR fluid. The saturation magnetization determines the maximum adjustable pressure drop at the valves. Without a magnetic control field the piston speed $v_\mathrm{p} = 0.27\,\frac{\mathrm{m}}{\mathrm{s}}$ corresponds to a shear rate $D = 1000\,\mathrm{s}^{-1}$ and at this shear rate the dynamic viscosity is, like in the shear mode, $\eta_0 = 1.4\,\mathrm{Pas}$. The dependence of the pressure drop on the volume flow Q is shown in figure 7b. The pressure differences at the valves increase with

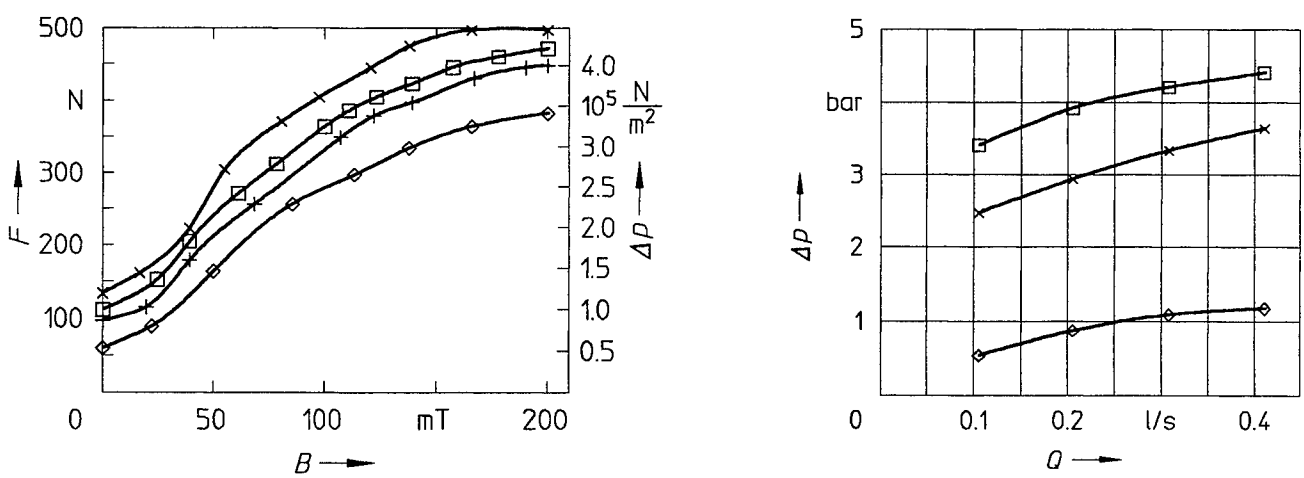

a b

Figure 7: Dynamic damping force and pressure drop at the MR fluid valves vs. magnetic fux density at a piston speed $v_\mathrm{p} = 0.09\,\frac{\mathrm{m}}{\mathrm{s}}$ (◇), $v_\mathrm{p} = 0.18\,\frac{\mathrm{m}}{\mathrm{s}}$ (+), $v_\mathrm{p} = 0.27\,\frac{\mathrm{m}}{\mathrm{s}}$ (□) und $v_\mathrm{p} = 0.36\,\frac{\mathrm{m}}{\mathrm{s}}$ (×) **(a)** and pressure drop vs. volume flow for magnetic flux densities $B = 0\,\mathrm{mT}$ (◇), $B = 100\,\mathrm{mT}$ (×) and $B = 200\,\mathrm{mT}$ (□) **(b)** at a temperature $\vartheta = 58°\mathrm{C}$ for the nano MR fluid 132 of BASF AG

growing volume flow, but the rise of the curve decreases with increasing volume flow. In the flow mode the pressure drop Δp is also generated by a shear stress τ caused by the sheared fluid, for newtonian fluids it is $\Delta p \sim \tau$. For an MR fluid follows

$$\Delta p(B,D) = 2\,\tau(B,D)\,\frac{L_\mathrm{v}}{h_\mathrm{v}} \tag{1}$$

$$D = D_\mathrm{shear} = D_\mathrm{flow} = \frac{6\,Q}{w_\mathrm{v} h_\mathrm{v}^2} \tag{2}$$

Figure 8 shows the pressure differences measured in the flow mode at a piston speed $v_\mathrm{p} = 0.27\,\frac{\mathrm{m}}{\mathrm{s}}$, this corresponds to a volume flow $Q = 0.31\,\frac{\mathrm{l}}{\mathrm{s}}$ and a shear rate $D_\mathrm{flow} = 1000\,\mathrm{s}^{-1}$. The pressure differences, which are calculated according to equation 1 from the results displayed in Figure 2b, are also shown. The results from the shear mode and the flow mode fit very well. The pressure differences occuring in the flow mode can be calculated from measurement results in the shear mode by equation 1.

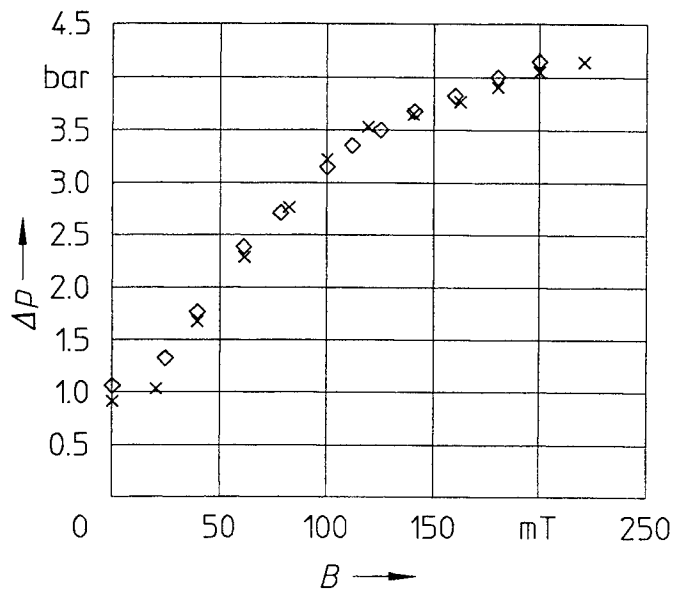

Figure 8: Pressure drop vs. magnetic flux density at a shear rate $D = 1000\,\mathrm{s}^{-1}$ and at temperature $\vartheta = 58°\mathrm{C}$ calculated from the flow mode (◇) and from the shear mode (×)

5.3 Damper

MR fluid dampers are usually built up in the flow mode. Apart from the configuration shown in Figure 6, where the valves, which control the dynamic damping force of the damper, are arranged in the bypass, the magnet circuit (including coil and MR fluid valves) can also be integrated in the piston.[8] The bypass is not needed any longer. This compact construction, however, requires high power density of the MR fluid.

6 Squeeze Mode

6.1 Measurement technique

In order to investigate the behaviour of MR fluids working in the squeeze mode, the measuring arrangement was used as shown in Fig. 9. The MR fluid is located in two gaps between the static pole pieces of the magnetic flux guide and the disc moved by the oscillation generator (Fig. 9). The generation of oscillation $z(t)$ is carried out by a piezostack. The MR fluid is pressed out of one gap into the other according to the direction of motion of the disc. The basic distance $z_0 = z(t = 0)$ between the disc and the pole pieces of the flux guide is adjustable. Furthermore, the test assembly is equipped with a displacement sensor to measure the time-dependent movement of the disc and a force sensor to determine the time-dependent normal force. The coil generates a magnetic field whose field lines are led through the MR fluid by the flux guide parallel to the direction of motion of the disc.

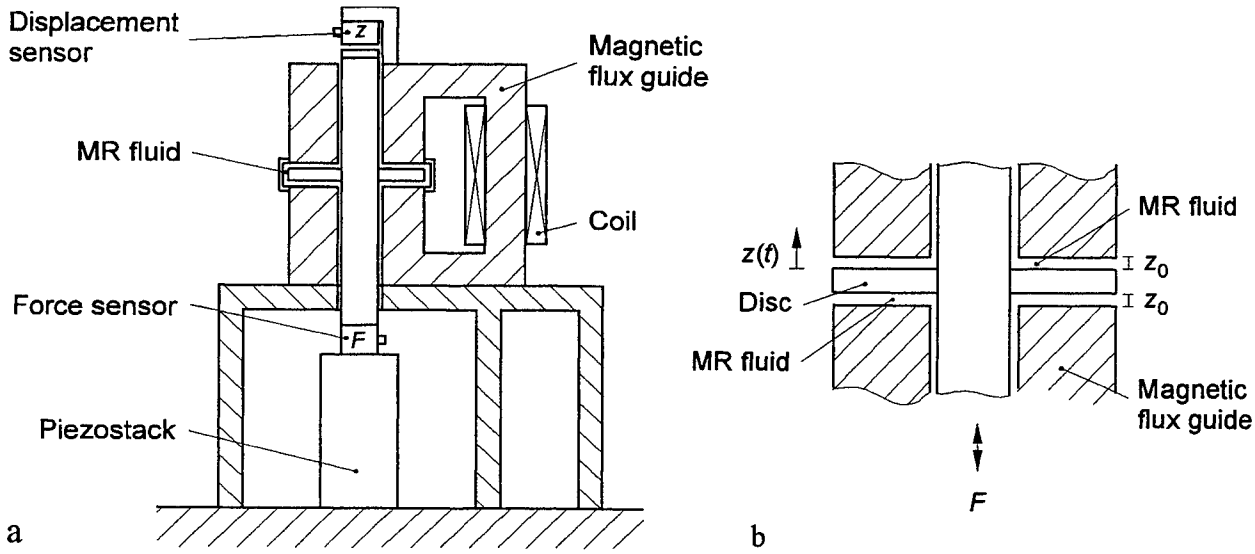

Figure 9: Measurement stand for squeeze mode

6.2 Measurement results

The basic distance between disc and flux guide was adjusted to $z_0 = 900\,\mu$m. The disc was driven by a piezostack with a sinusoidal oscillation of a frequency of $f = 2$ Hz and an maximum amplitude $\hat{z} = 80\,\mu$m. The results in Figure 10 show, that the normal stresses in the squeeze mode are considerably higher than the shear stresses in the shear mode. The rise of the curve decreases continuously with growing magnetic flux density.

6.3 Squeeze mode damper

A two-dimensional distribution of velocity of the squeeze flow, which interacts with the distribution of compression stresses and shear stresses, develops between the driven disc and the fixed pole pieces in the squeeze mode. If the shear stress falls below the yield stress of the MR fluid, the MR fluid 'solidifies' within this range. In this case the damper has viscose force components as well as elastic ones. The elastic components increase with increasing magnetic flux density.

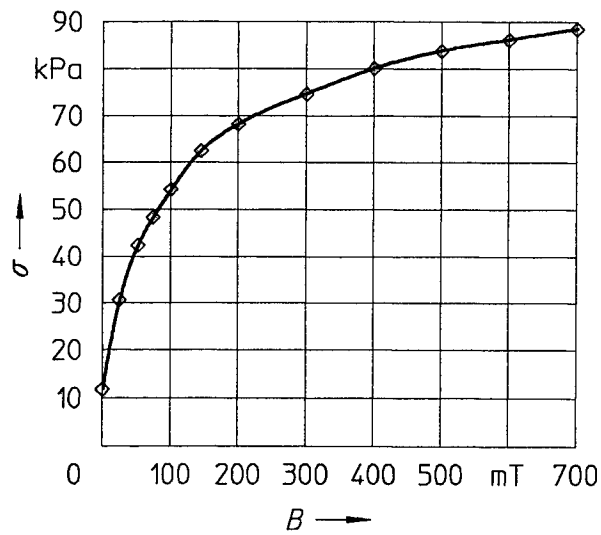

Figure 10: Normal stress σ vs. magnetic flux density B for the nano MR fluid 132 of BASF AG

In order to avoid cavitation effects the squeeze mode damper should have a design similar to Figure 9b. Two gaps, which exchange the MR fluid in dependence of the moving direction of the disc, prevent the generation of gas or vacuum bubbles in the fluid.

Squeeze mode dampers can damp vibrations of low amplitudes and high dynamic forces, as e.g. in machine tools. The squeeze mode damper can damp the high vibration amplitudes which occur in resonance.

7 DEPENDENCE ON TEMPERATURE

Figure 11 shows the dependence of the shear stress on the temperature for various magnetic flux densities for the nano MR fluid 98 of BASF AG. Especially within the temperature range $0°C < \vartheta < 30°C$, the zero–field viscosity of the nano MR fluid decreases considerably with increasing temperature. The largest MR effect $\tau(B > 0) - \tau(0)$ can

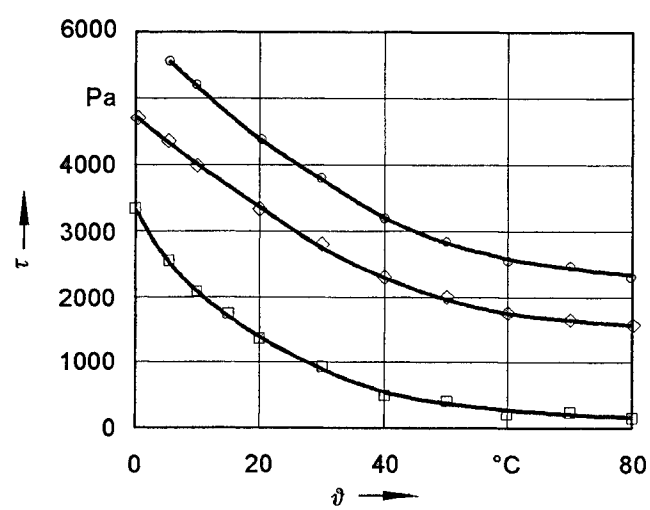

Figure 11: Shear stress vs. temperature for magnetic flux densities $B = 0\,\mathrm{mT}$ (□), $B = 100\,\mathrm{mT}$ (◇) and $B = 200\,\mathrm{mT}$ (○) at shear rate $D = 1000\,\mathrm{s}^{-1}$ for the nano MR fluid 98 of BASF AG[6]

be achieved at a temperature of $\vartheta = 25°\mathrm{C}$. As a general observation the shear stress of the Nano MR fluid decreases with increasing temperature.

8 DESIGN OF MAGNETIC CIRCUIT

The magnetic resistance of MR fluid actuators is determined by the gap with the MR fluid. The guidance of the magnetic field should guarantee that the magnetic field lines concentrate within the MR fluid volume between the pole pieces, especially if the MR fluid is in magnetic saturation. When designing and dimensioning the magnetic circuit, the flux guide should occupy as little constructional volume as possible and should not be operated in magnetic saturation. A low magnetic resistance of the magnetic circuit allows the application of coils with a low number of ampere turns. The distribution of the magnetic field within an MR fluid actuator can be determined precisely using a finite–element calculation. In the MR fluid gap the field lines are to run perpendicularly to the flow direction of the MR fluid in the shear mode and the flow mode ($\overline{B}_\perp \rightarrow$ max.), because the field components parallel to the flow direction of the MR fluid only give a slight contribution to the MR effect ($\overline{B}_\parallel \rightarrow 0$). Moreover the magnetic control field should be homogeneous over the total MR fluid gap ($\Delta B \rightarrow 0$). From these demands the following design criteria for the orientation of the magnetic field in the MR fluid gap can be developed.

$$\overline{B}_\perp = V_{\mathrm{MR}}^{-1} \iiint_{V_{\mathrm{MR}}} B_\perp \mathrm{d}V \rightarrow \max. \tag{3}$$

$$\Delta B_\perp = V_{\mathrm{MR}}^{-1} \iiint_{V_{\mathrm{MR}}} |B_\perp - \overline{B}_\perp| \, \mathrm{d}V \rightarrow 0 \tag{4}$$

$$\overline{B}_\parallel = V_{\mathrm{MR}}^{-1} \iiint_{V_{\mathrm{MR}}} B_\parallel \mathrm{d}V \rightarrow 0 \tag{5}$$

$$\Delta B_\parallel = V_{\mathrm{MR}}^{-1} \iiint_{V_{\mathrm{MR}}} |B_\parallel| \, \mathrm{d}V \rightarrow 0 \tag{6}$$

In the squeeze mode the magnetic field lines have to run parallel to the orientation of the vibration to be damped (see Fig. 9).

The use of permanent magnets for MR fluid actuators allows adjustment of the operating point without demanding electrical energy. A time–dependent alteration of this operating point can be attained with electromagnets amplifying or attenuating the field of the permanent magnet. Additionally, the electric control power can be reduced drastically. Using the damper explained in Figure 6 a magnetic field $\overline{B}_\perp = (0.226 \pm 0.006)\,\mathrm{T}$ and $\overline{B}_\parallel = (0 \pm 0.005)\,\mathrm{T}$ is generated in the MR fluid valves by a control current $I = 2\,\mathrm{A}$. Figure 12 shows the damper after the integration of two cylindrical NdFeB magnets. Without an electric control current, the magnetic field in the valves is $\overline{B}_\perp = (0.190 \pm 0.018)\,\mathrm{T}$ and $\overline{B}_\parallel = (0 \pm 0.022)\,\mathrm{T}$. With a control current of $I = \pm 1\,\mathrm{A}$ the magnetic flux density can be reduced to $\overline{B}_\perp = 0\,\mathrm{T}$ or raised to $\overline{B}_\perp = 0.256\,\mathrm{T}$. By integrating of the permanent magnets into the magnetic circuit the maximum electric control power could be reduced by more than 50%.

A small basic viscosity of the MR fluids results in a small power transmission without magnetic control field and a higher MR effect

$$\Delta\tau_{\mathrm{MR}}(B, D) = \tau(B, D) - \tau(0, D). \tag{7}$$

The gap with the MR fluid in the magnetic flux guide can be tightened without changing the low power transmission without control field. This reduces the magnetic resistance of the magnetic circuit. The coil generating the magnetic control field can be equipped with a lower number of ampere turns, which makes it possible to use a compact construction with a low driving power.

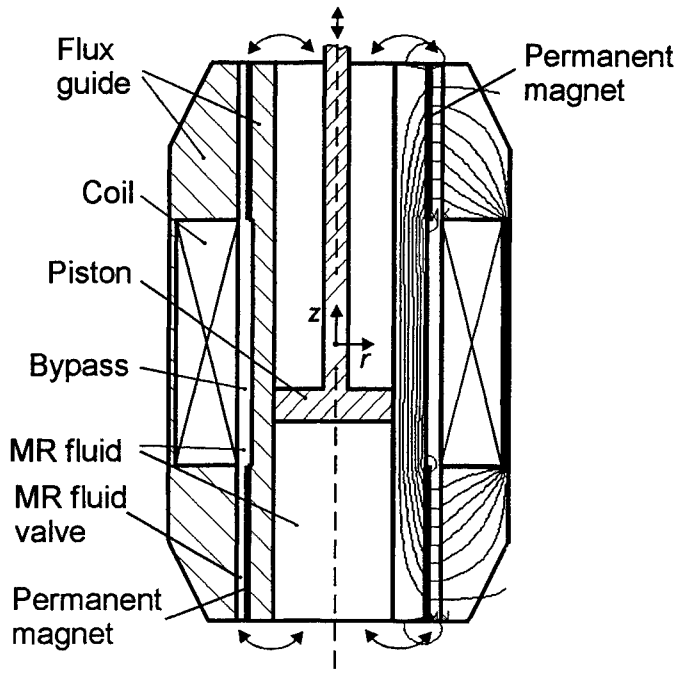

Figure 12: MR fluid damper with permanent magnets, on the right half the symmetric distribution of magnetic field lines is displayed

9 SUMMARY AND CONCLUSIONS

The behaviour of an MR fluid actuator is particularly determined, beside the properties of the MR fluid and the design of the magnetic circuit, by the choice of the working mode. A cylindrical construction can avoid the segregation of suspensions in electrically adjustable clutches. Especially in clutches, MR fluids have the advantage of a magnetic resistance that is nearly independent on temperature, whereas the electrical conductivity of an electrorheological fluid increases with rising temperature and therefore also the electric driving power increases. Electrically adjustable dampers for high vibration amplitudes can be realized in the flow mode. The MR fluid valve to control the dynamic damping force can be integrated in the bypass or in the piston of the damper, including the entire magnetic circuit. The behaviour of an MR fluid in the flow mode can be calculated from measurement results in the shear mode. The squeeze mode damper is built in a very compact way and can generate high damping forces. It is a high force, low stroke device.

In the three working modes the properties of the MR fluids, especially the maximum transferable forces, are determined by the saturation magnetization of the suspension, which again depends on the magnetic properties of the suspended particles. Also the basic viscosity plays an important role. A low basic viscosity causes a small gap, so that the magnetic resistance of the magnetic circuit and therefore also the number of ampere turns of the coil can be reduced drastically.

Many technical applications are possible for MR fluid actuators such as clutches, (hydraulic) valves and vibration dampers for automobiles and machine tools. Known elements with improved properties or entirely new applications can be realized with the help of MR fluids. The advantage of MR fluid actuators is that they can be constructed simply and compactly in comparison to conventional solutions as MR fluid actuators normally require few mechanical parts. The electrical control signal can be converted directly without the use of additional mechanical positioning components.

ACKNOWLEDGEMENTS

The authors are grateful to the BASF AG and the Bayer AG for the support with MR fluid samples. The authors thank the BASF AG for providing a damper test assembly.

REFERENCES

[1] V.I. Kordonsky, Z. P. Shulman, S. R. Gorodkin, S. A. Demchuk, I. V. Prokhorov, E. A. Zaltsgendler, B. M. Khusid: *Physical Properties of Magnetizable Structure–Reversible Media*; Journal of Magnetism and Magnetic Materials 85, pp. 114–120, 1990

[2] J. Rabinow: *The Magnetic Fluid Clutch*, AIEE Transactions 67, pp. 1308–1315, 1948

[3] K. D. Weiss, T. G. Duclos, J. D. Carlson, M. J. Chrzan, J. D. Margida: *High Strength Magneto– and Electro–rheological Fluids*, Society of Automotive Engineers, SAE Paper 932451, 1993

[4] Cl. Kormann, M. Laun, G. Klett: *Magnetorheological Fluids with Nano–sized Particles for Fast Damping Systems*; Proceedings of 4th International Conference on New Actuators, (15.–17. Juni 1994, Bremen); H. Borgmann, K. Lenz (ed.); pp. 271–274

[5] J. M. Ginder, L. C. Davis: *Shear Stresses in Magnetorheological Fluids: Role of Magnetic Saturation*; Applied Physics Letters 65 (26), pp. 3410–3412; 1994

[6] R. Bölter, H. Janocha, St. Hellbrück, Cl. Kormann: *Design of Magnetorheological Fluid Actuators*; Proceedings of 5th International Conference on New Actuators (26.–28. Juni 1996, Bremen); H. Borgmann (ed.); pp. 329–332

[7] LORD Corp.: *Product information*; 1996

[8] J. D. Carlson; M. J. Chrzan: *Magnetorheological Fluid Dampers*, United States Patent 5,277,281; 1994

SESSION 5

Passive Constrained Layer Damping (CLD)

Fluid Surface Damping Versus Constrained Layer Damping for Vibration Suppression of Simply Supported Beams

Hany Ghoneim
Rochester Institute of Technology
Department of Mechanical Engineering
Rochester, NY 14623

ABSTRACT

A fluid surface damping (FSD) technique proposed for vibration suppression of beam-like structures is applied to a generic simply supported aluminum beam. The steady-state frequency response of the FSD-treated beam at the vicinity of one end, due to an applied white noise displacement excitation at the other end, is determined using the finite element method. The response is found over a range of frequency covering the first four resonant frequencies and over a wide temperature range. Comparison of the results with the corresponding ones of a beam treated with the constrained layer damping method indicates that the FSD technique has a much greater potential for the vibration suppression of beam-like structures. Results also indicate that the FSD technique can provide a good vibration suppression over a wider temperature range.
Keywords: vibration suppression, beams, frequency response, viscous fluid damping, viscoelasticity.

2. INTRODUCTION

Vibration control of thin structures is of great importance to automobile, aircraft and space industries. Both active and passive techniques have been utilized for vibration suppression of such structures. Because of their simplicity and reliability the passive techniques are probably still more attractive and widely applied. Constrained layer damping (CLD)[1], viscous fluid layer[2], shunted piezoelectrics[3], electromechanical surface damping[4], particle damper[5], and fluid surface damping (FSD)[6] are some of the passive techniques used for the vibration suppression of beam-like and plate-like structures. This paper provides further analytical investigation of the FSD technique. The technique is applied for the vibration suppression of a simply-supported generic aluminum beam over a wide range of frequencies and temperatures. The steady-state frequency response of the beam at the vicinity of one end, due to an applied white noise displacement excitation at the other end, is determine using the finite element method. The responses of the FSD-treated beam are compared with the corresponding ones of the CLD-treated beam. Results are analyzed and discussed, and an assessment of the advantages of the FSD technique is presented.

A schematic of a FSD element applied to a beam-like structure is illustrated in Figure 1, and the corresponding physical and hydraulic models that illustrate the fundamental working principal of the FSD element are presented in Figure 2. Two viscoelastic surface layers containing fluid-filled cavities are attached symmetrically to the opposite surfaces of the beam. The cavities on one side of the beam's neutral axis are connected to the corresponding cavities on the opposite side via narrow passages. When the beam bends, the layer attached to one side of the beam contracts and the opposite layer stretches, causing the respective cavities to contract and expand and the fluid to be pumped from the contracting to the expanding cavities through the connecting passages as illustrated in Figure 2. As the beam vibrates, the fluid is pumped back and forth through the connecting passages dissipating part of the excessive energy of vibration. Therefore, in addition to the viscoelastic damping provided by the surface layers, the technique offers viscous damping due to the fluid flow through the passages.

SPIE Vol. 3045 • 0277-786X/97/$10.00

3. MATHEMATICAL MODEL

3.1 Basic assumptions:

Development of the governing equations for the FSD-treated portion of the beam is based on the following assumptions:

- small displacements and strains;
- perfect bonding between the surface viscoelastic layers and the beam;
- plane cross-sections remain plane;
- no transverse normal strains;
- axial loading and mid-plane axial displacements of the beam are negligible;
- rotary inertia and shear deformation are negligible (Euler-Bernoulli beam);
- linear, isotropic, elastic material-behavior for the beam and viscoelastic material-behavior for the surface layer;
- incompressible, laminar flow;
- the pressure inside the cavities is uniform, that is, the pressure drop along the axes of the cavities due to the fluid flow inside the cavities is negligible; and
- viscous damping due to the fluid flow through the passage is the dominant source of hydraulic damping.

3.2 Governing equation:

Using the differential element shown in Fig. 3, the governing equation of the FSD-treaded portion of the beam can be determined:[6]

$$\frac{\partial^2}{\partial x^2}\left\{EI(\omega i)\frac{\partial^2 w_0}{\partial x^2}\right\} - \rho A\omega^2 w_0 = 0, \qquad (1_a)$$

subject to $M(x_a) = -M_v$ and $M(x_b) = M_v$, where $M_v(\omega i) = Q^2 K^*(\omega i)\Delta\Theta$. (1_b)

In (1), w_0 is the amplitude of the transverse displacement ($w = w_0 e^{i\omega t}$), Θ is the amplitude of the angular displacement ($\theta = \Theta e^{i\omega t}$), ω is the excitation frequency, and $EI(\omega i)=E_1I_1+E^*_2(\omega i)I_2$ where E^*_2 is the complex Young's modulus of the surface layers' viscoelastic material and E_1I_1 is the flexure rigidity of the aluminum beam. Based on the assumptions stated earlier and the hydraulic model shown in Figure 2b, the hydraulic complex bulk modulus, $K^*(\omega i)$, of the FSD element is

$$K^*(\omega i) = \frac{\Delta p}{q} = \frac{1}{nC_e}\left\{\frac{-I_f\omega^2 + R\omega i}{-I_f\omega^2 + R\omega i + 1/C_e}\right\} = \frac{R}{n}\frac{-\frac{1}{\tau}\left(\frac{\omega}{\omega_n}\right)^2 + \omega i}{1-\left(\frac{\omega}{\omega_n}\right)^2 + \tau\omega i} \qquad (2)$$

In the above equation, R is the hydraulic resistance of the connecting passage, C the hydraulic capacitance of the upper and lower cavities, I_f the fluid inertia or hydraulic inertance ($I_f = 128\mu l/\pi d^4$, where μ is the fluid dynamic viscosity), τ the hydraulic time constant ($\tau=RC_e$), ω_n the hydraulic natural frequency ($\omega_n = 1/\sqrt{I_f C_e}$), C_e the equivalent hydraulic capacitance of the connected cavities ($C_e=C/2$, for identical cavities), and n is the number of parallel fluid circuits per element (in the case shown in Figure 1, n=3). For simplicity, the following non-dimensional variables and parameters are adopted:

X the non-dimensional axial coordinate, $X=x/L$,

W the non-dimensional transverse displacement, w_0/L,

$\tilde{M}$ the non-dimensional bending moment, $\tilde{M} = ML/E_1I_1$,

α the non-dimensional complex flexure rigidity, $\alpha = EI/E_1I_1$,

m the non-dimensional mass per unit length, $m = \rho A/\rho_1 A_1$,

Ω the non-dimensional frequency, $\Omega = \omega/\omega_0$,

where L is the length of the beam and $\omega_0 = \sqrt{E_1 I_1/\rho_1 A_1 L^4}$. Notice that for the untreated portions of the beam, α=m=1. Upon normalization of the governing equations (1_a) and (1_b), we get

$$\alpha \frac{\partial^4 W}{\partial X^4} - m\Omega^2 W = 0 \qquad (3_a)$$

subject to $\tilde{M}(X_a) = -\tilde{M}_v$ and $\tilde{M}(X_b) = \tilde{M}_v$, where $\tilde{M}_v = \tilde{K}(\Omega i)\Delta\Theta$. ($3_b$)

The non-dimensional complex modulus, $\tilde{K}(\Omega i)$, is expressed as

$$\tilde{K}(\Omega i) = \tilde{R}\left\{\frac{-\frac{1}{T}\left(\frac{\Omega}{\Omega_n}\right)^2 + \Omega i}{1-\left(\frac{\Omega}{\Omega_n}\right)^2 + T\Omega i}\right\} \qquad (4)$$

where $\tilde{R}$ is the non-dimensional hydraulic resistance of the connecting passage ($\tilde{R} = RQ^2/n\rho_1 A_1 L^3 \omega_0$), T is the non-dimensional time constant ($T = \tau\omega_0$) and Ω_n is the non-dimensional natural frequency ($\Omega_n = \omega_n/\omega_0$).

4. RESULTS AND DISCUSSION

In order to assess the potential of the FSD treatment for vibration suppression of beam-like structures, the frequency response of a partially FSD-treated simply supported beam is investigated. The response is compared with a corresponding partially CLD-treated beam in order to provide a reference for vibration-suppression assessment. A schematic of the treated beam is shown in Figure 4. A 2x0.05x0.02 m^3 aluminum beam is chosen for the investigation. The beam is subjected to a white noise displacement excitation at one end (X=1) and the response is determined at the vicinity of the other end (X=0.1). The response is determined over a range of frequencies that covers the first four resonant frequencies. This location for the output signal (X=0.1) is chosen because it does not coincide with any of the four modal nodes. A FSD as well as a CLD patch of length $L_b = 0.2$ L is attached at the middle of the beam.

Two cases are studied. The first case compares the optimum responses of both treatments and indicates their maximum potential for the vibration suppression of the beam. The second case investigates the effect of temperature on the vibration-suppression efficacy of both treatments. In this case, practical material parameters, pertaining to Soundcoat DYAD 600 series, are adopted for the viscoelastic layers' material. In both cases the frequency response is determined using the finite element method with twenty cubic Hermit beam elements.

4.1 Optimum responses:

The frequency responses of the beam treated with optimum FSD and CLD patches, together with the response of the untreated beam, are shown in Figure 5. To simplify the optimization procedure, design variables are limited to the most effective three. They are $\tilde{R}$, T and b_n ($b=\Omega^{0.5}$) for the FSD treatment; and the shear storage modulus of the constrained layer, G_2', the thickness of the constrained layer, h_2, and the thickness of the constraining layer, h_3, for the CLD treatment. The optimization objective is to minimize the sum of all four peak-displacement amplitudes. Pertained dimensions and material parameters for the FSD and CLD patches are given in Table 1. The optimum design variables are marked by the superscript "*". Figure 5 clearly demonstrates the superior vibration-suppression ability of the FSD treatment over the CLD one particularly at higher frequencies.

4.2 Temperature effect:

For the second case a Soundcoat DYAD 606 viscoelastic material is adopted for the CLD treatment and DYAD 609 for the FSD treatment. Material properties at different temperatures and the corresponding non-dimensional parameters of the fluid circuit are shown in Table 2. The diameters of the fluid cavity and the connecting passage, a and d, are 10 and 1 mm, respectively. These values ensure that the hydraulic resistance of the fluid cavities is negligible compared to that of the connecting passages rendering the last two assumptions stated earlier valid.

The frequency responses of the CLD- and FSD-treated beams at three different temperatures (20, 40 and 60 ^{0}C) are displayed in Figures 6a and 6b, respectively. Only the frequency responses at the vicinity of the third and fourth resonant frequencies are shown. The temperature effect on the frequency responses at the vicinity of the first and second resonant frequencies is similar, but much smaller, to that at the vicinity of the third and fourth. As the temperature increases, Figure 6a indicates that the vibration-suppression capability of the CLD treatment significantly deteriorates. The FSD treatment, on the other hand, preserves its vibration-suppression ability with increasing temperature, as demonstrated in Figure 6b. It should be pointed out that some new special viscoelastic materials with effective damping over a wider temperature range are being developed. However, the deterioration of the damping effectiveness with changing temperature is still, in general, a major problem of the CLD treatment. This problem as demonstrated by the results in Fig. 6 can be controlled using the proposed FSD technique.

5. CONCLUSION

Comparison of the frequency responses of a simply supported beam treated with the FSD technique and a beam treated with the CLD one indicates:

1. The FSD treatment has a much higher potential for the vibration suppression of the beam, particularly at higher frequencies.
2. The FSD treatment preserves its effective vibration-suppression ability over a wide temperature range.

More analytical investigation and experimental work, however, are needed before the technique is brought into practical applications.

6. REFERENCES

1. D. Nashif, D. I. G. Jones, and J. P. Henderson, J. P., *Vibration Damping*, John Wiley & Sons, New York, 1985.
2. T. Onsay, "Dynamic interaction between the bending vibrations of a plate and a fluid attenuator", *Journal of Sound and Vibration*, Vol. 178, pp. 289-313, 1994.
3. N. W. Hagood, and A. Von Flotow, "Damping of structural vibrations with piezoelectric materials and passive electrical networks", *Journal of Sound and Vibration,* Vol. 146, pp. 243-268, 1991.
4. H. Ghoneim,"Application of the electromechanical surface damping to the vibration control of a cantilever plate", *ASME Journal of Vibration and Acoustics,* Vol. 118, 1996.
5. S. S. Simon, "Particle beam damper", *SPIE Proceedings: Smart Materials and Structures*, Vol. 2445, pp 149-160, 1995.
6. H. Ghoneim, "Fluid surface damping: a technique for vibration suppression of beams", *Shock and Vibration,* accepted for publication.

Aluminum beam		CLD element		FSD element	
E_1 (GPa)	70	$(G_2')^*$ (GPa)	0.27	E_2' (GPa)	0.7
η_1	0.001	E_3 (GPa)	70	η_2	1
ρ_1 (kg/m^3)	2700	η_2^G	1	ρ_2 (kg/m^3)	1000
L (m)	2	η_3	0.001	ρ_3 (kg/m^3)	1000
b (m)	0.05	ρ_2 (kg/m^3)	1000	h_2/h_1	1
h_1 (m)	0.02	ρ_3 (kg/m^3)	2700	$(\tilde{R})^*$	0.1
L_b (m)	0.4	h_2^*/h_1	0.1	T^*	0.001
		h_3^*/h_1	0.2	b_n^*	20

Table 1. Material parameters and dimensions used for the numerical examples of the optimum case

Temperature (^{0}C)	20	40	60
E_2' (GPa)	0.7	0.5	0.25
η_2	0.15	0.4	0.68
μ (kg/m-s)	1	0.3	0.08
$\tilde{R}$	0.04	0.012	0.0032
T	0.023	0.01	0.005
b_n	20.8	19.1	15.5
G_2' (MPa)	100	20	4
η_2^G	0.8	1	1

Table 2. Material parameters and design variables used for the numerical examples studing the temperature effect

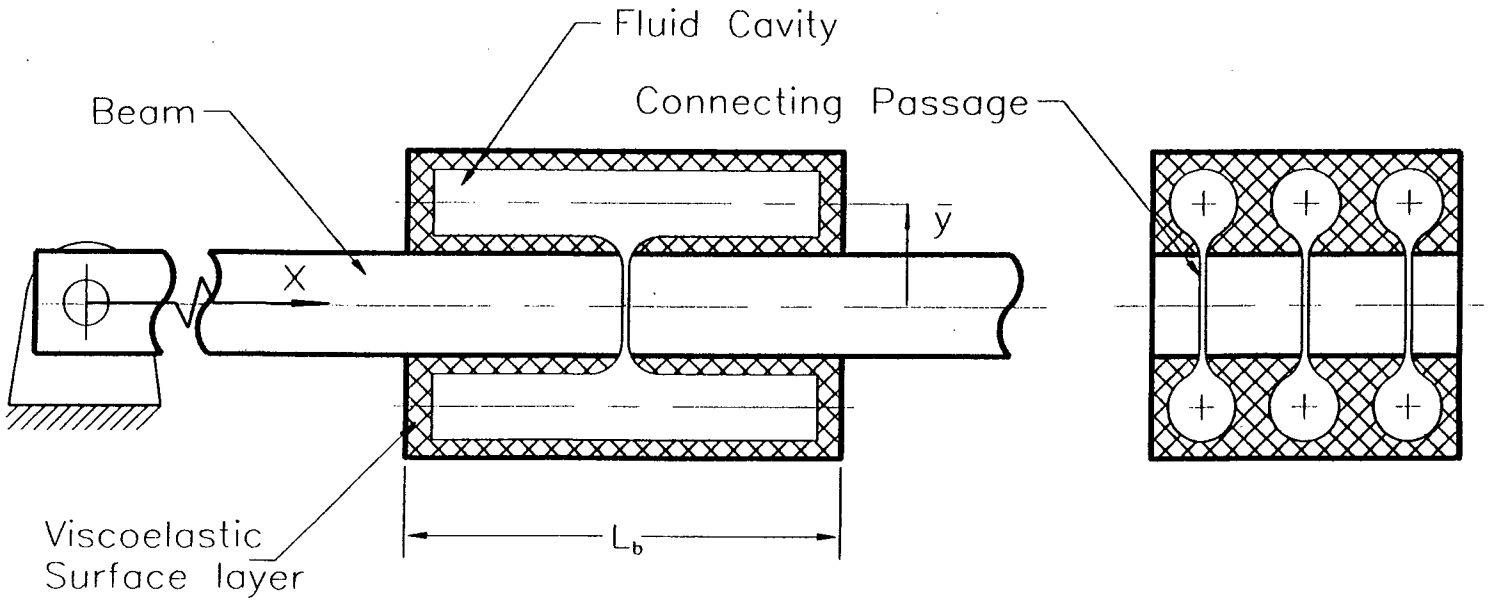

Fig. 1 Schematic of a beam-like-structure treated with a Fluid Surface Damping (FSD) element.

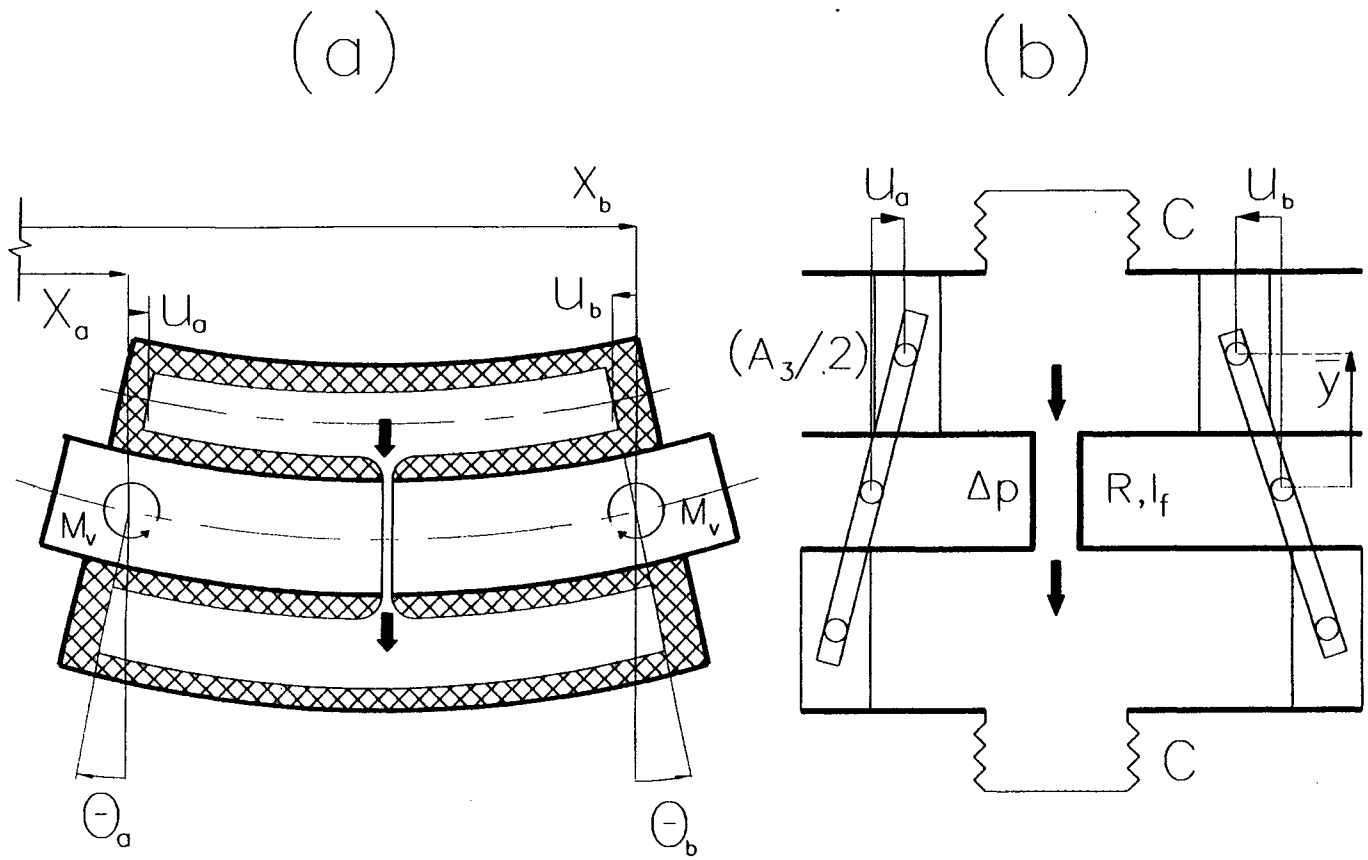

Fig. 2 Physical (a) and hydraulic (b) models of the FSD element.

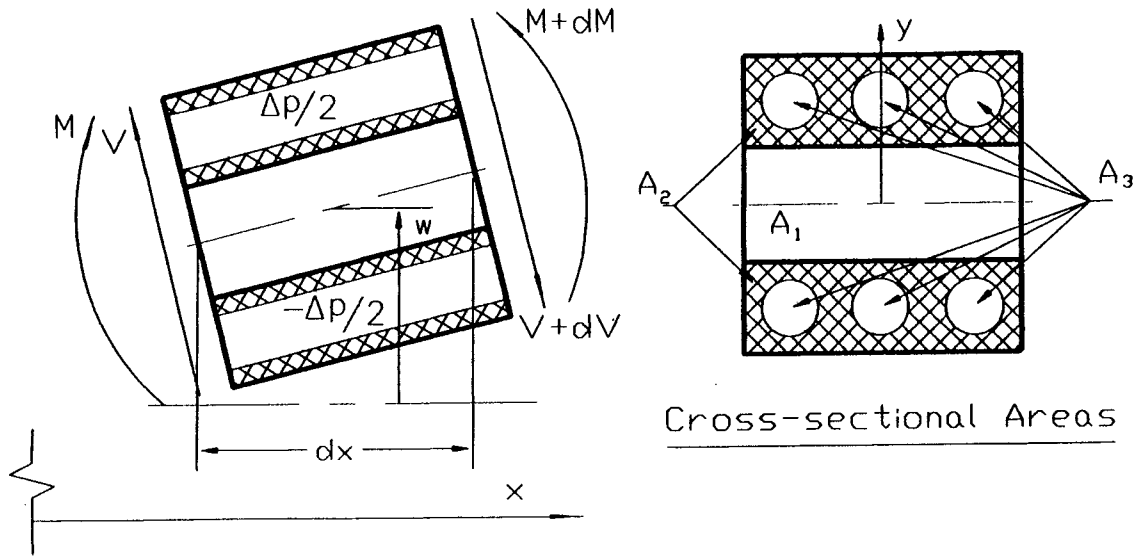

Fig. 3 A Differential element of the FSD-treated beam with an illustration of the different cross-sectional areas.

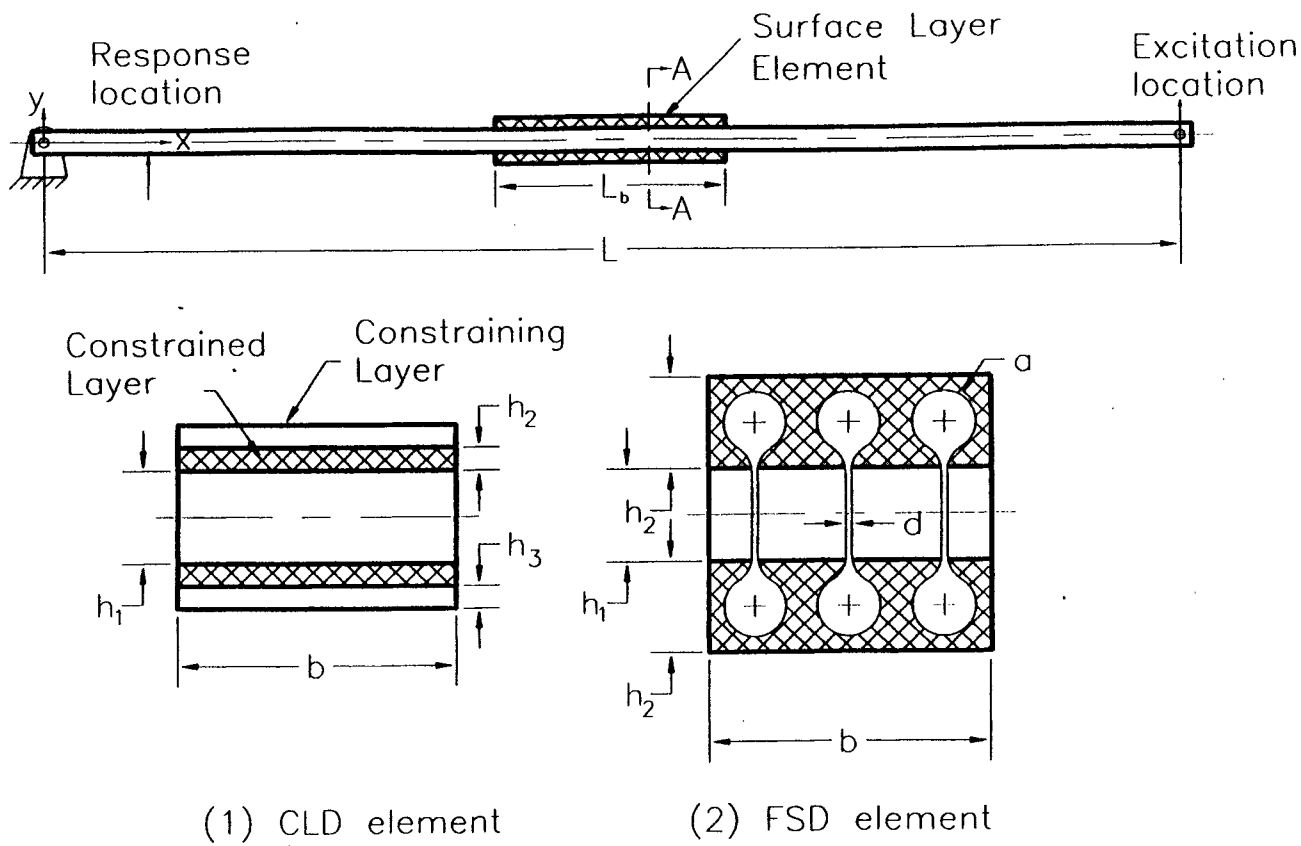

Fig. 4 Schematic of a simply supported beam treated with (1) a CLD patch and (2) a FSD patch, with illustration of relevant dimensions.

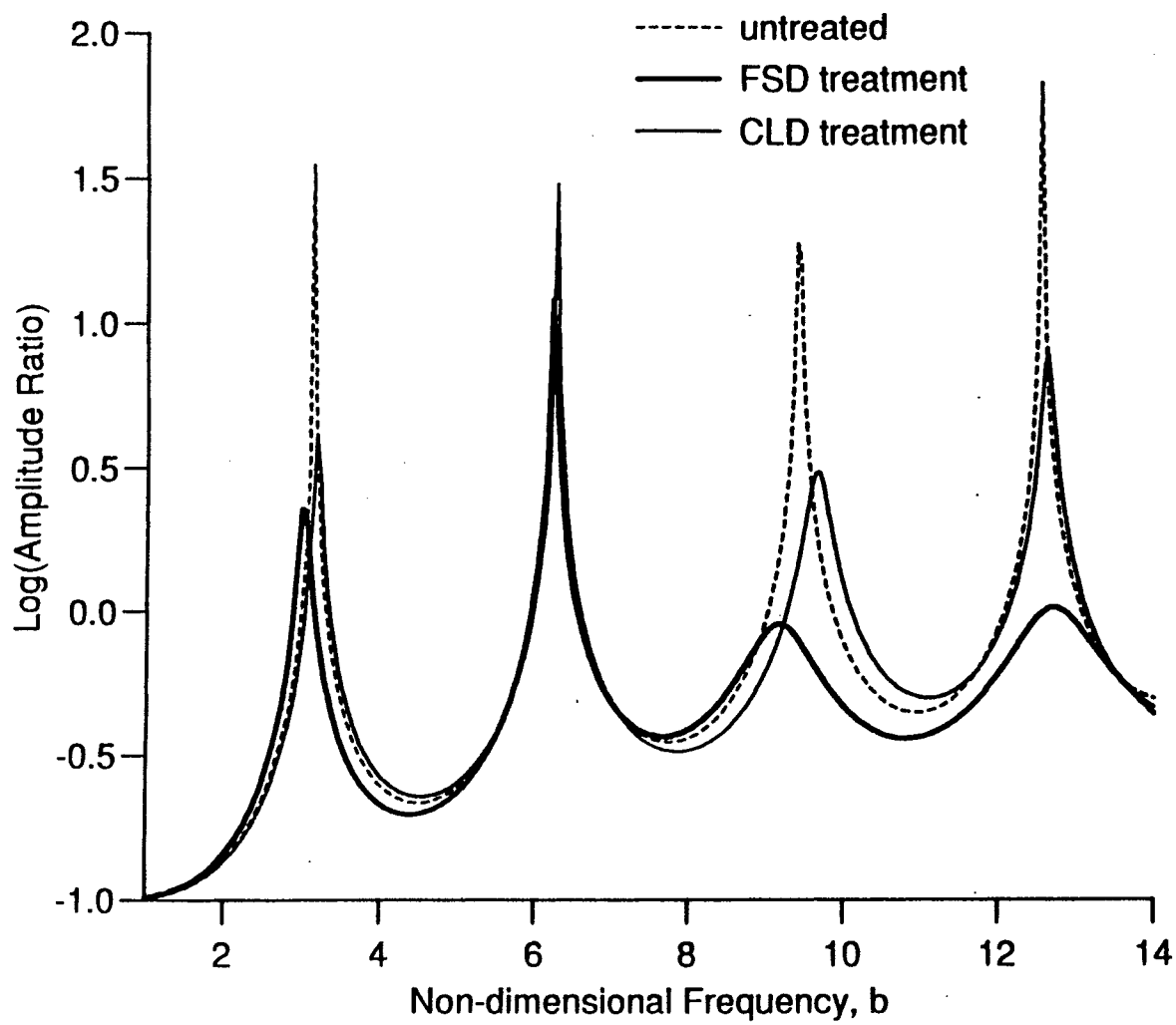

Fig. 5 Comparison of the frequency responses of the optimum FSD-treated and CLD-treated beams.

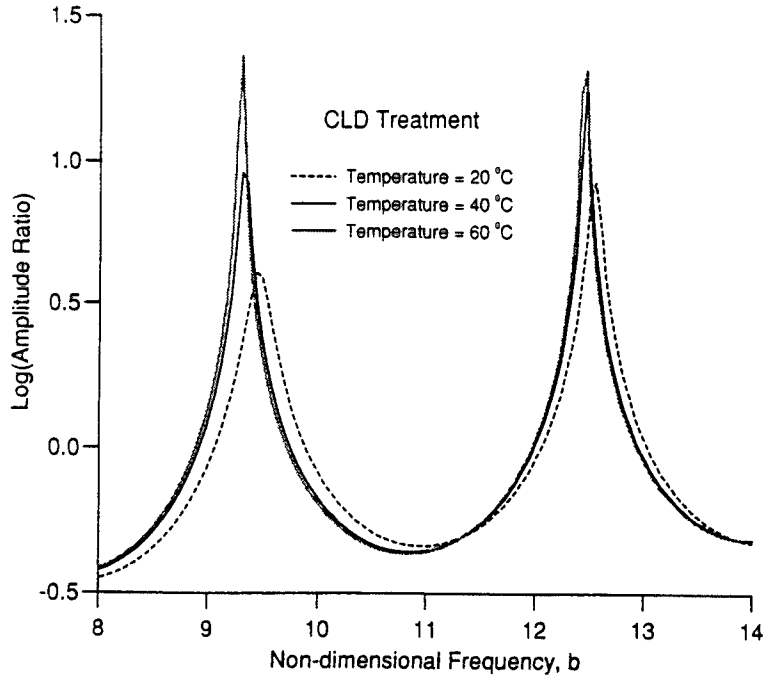

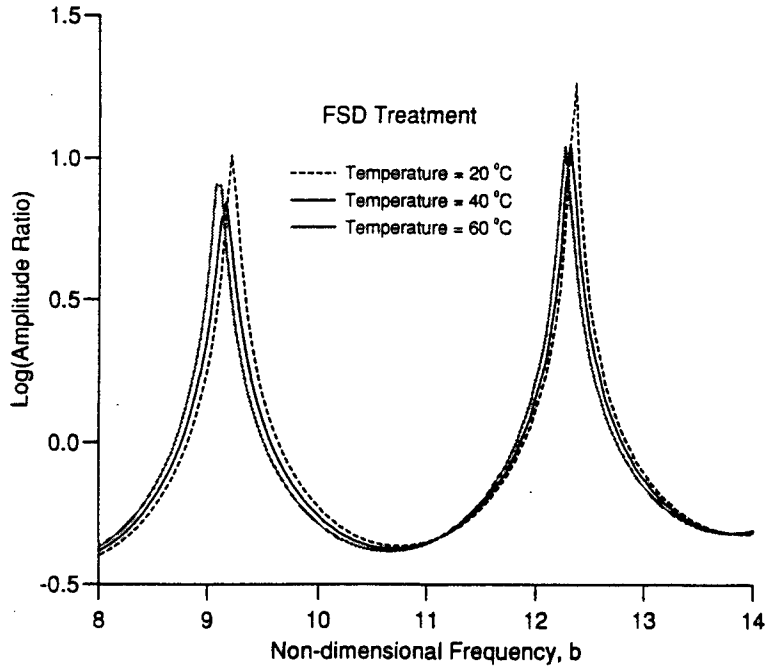

Fig. 6 Frequency responses of (a) a CLD-treated beam and (b) a FSD-treated beam at different temperatures.

Studies on the kinematic assumptions for sandwich beams

Eric M. Austin and Daniel J. Inman

Virginia Polytechnic Institute & State University
Engineering Science and Mechanics
Blacksburg, VA 24061-0219 USA

ABSTRACT

Much of the work done on active and passive constrained-layer beams is done with models using kinematic assumptions proposed by Kerwin, Mead and Markus, and others. The key assumption is that the base and constraining layers undergo identical transverse displacements, which is a reasonable assumption when the middle layer (here a viscoelastic material) is thin and the constraining layer is relatively weak. There are, however, many practical cases where an effective passive damping design requires the stiffness of the constraining layer to be on the order of that of the base layer. If the base structure is stiff to begin with, a constraining layer that will produce good damping is likely to violate the above stated assumption by refusing to follow the base layer exactly. The question arises as to how this affects predictions of damping.

In this work the facesheets are treated as independently deforming Timoshenko beams, which results in a more general state of strain in the core material. Expressions for the potential and kinetic energies are developed from basic principles of continuum mechanics, and the assumed modes method is used to predict how levels of strain energy in the core are affected by the assumptions on the relative motions of the facesheets.

Keywords: passive, damping, energy, viscoelastic, beam, sandwich, Timoshenko

1. INTRODUCTION

The concept of enhancing energy dissipation by integrating damping materials into a structure dates back to Liénard[1] and Oberst[2] in the early 1950's. Kerwin[3] in 1959 was perhaps first to analyze a viscoelastic material (VEM) constrained with another metal layer. Presumably, the concept of constrained layer damping already existed, since Kerwin stated that "damping tapes are available from several manufacturers in the United States." Kerwin's analyzed bars in bending covered with a VEM and a relatively thin constraining layer. His key assumptions were the VEM core was soft relative to the facesheets but stiff enough to maintain a constant spacing between the facesheets and the bending stiffness of the constraining layer is small compared to that of the base layer. The first point results in only shear in the VEM, and the latter point means the constraining layer carries only axial strains.

Many of the models used in research on sandwich beams with viscoelastic cores can be traced to DiTaranto[4] and Mead and Markus[5] for the axial and bending vibrations of beams, respectively. Most authors seem to reference Mead and Markus, who similar to Kerwin assumed 1) the constraining layer bends in the transverse direction exactly as the base layer, 2) the viscoelastic layer undergoes pure shear, and 3) the viscoelastic layer does not change its thickness during deformation. These assumptions are valid if the core material is relatively thin and the stiffnesses of the two surface layers are not too high. Many subsequent authors have reported formulations and techniques adopted to study the damping mechanism of the viscoelastic layer, e.g., Douglas and Yang[6] and Rao,[7] and some authors modified or extended the model for different applications, e.g., Yan and Dowell[8] and Rao and He.[9] Applications of constrained layer damping treatments are reviewed by Johnson,[10] and the mechanics is presented in book form by Sun and Lu.[11] Since 1992 active constrained layer damping (ACLD) has gained much attention, as summarized by Baz and Ro.[12]

Damping problems in industry include, but certainly are not limited to, thin beams and plates. When designing a damping treatment, there are five main design options:

Other author information: (Send correspondence to EMA.)
Email: austine@vt.edu and dinman@vt.edu; Telephone: EMA 540-231-9366, DJI 540-231-4709; Fax: both 540-231-4574; This research is supported by the Army Research Office.

1. the thickness of the VEM,
2. the modulus of the VEM (frequency and temperature dependent!),
3. the location of the VEM,
4. the thickness of the constraining layer, and
5. the modulus of the constraining layer, i.e., the type of material.

The design process consists of finding the combination of the above options that results in the most damping in the vibration modes of interest. An effective damping treatment is one that "coaxes" strain energy into the VEM, and a good VEM is one that dissipates this energy efficiently. In situations where the substrate is very stiff and significant (5%+) damping is needed, a thick soft VEM and thin constraining layer will be ineffective. For simple beams, the optimum damping treatment occurs when the stiffness of the constraining layer is close to that of the base structure,[13,7] and intuitively the engineer will recognize that the trend is similar for more complicated structures. Constraints on the the weigh and/or thickness of the damping treatment often limit the amount of damping achievable, so the design process is one of getting the most out of the least. Often times extruded C- or I-sections are used as constraining elements to increase specific stiffness. At some point the question of whether the constraining layer is still "following" the substrate must be addressed. This is the basis of this work.

The fundamental properties of viscoelastic materials, shear modulus and loss factor, are frequency and temperature dependent, and accurate predictions of damping require this to be accounted for. The present work seeks only to demonstrate possible limitations on the assumption that the facesheets move together, and this will occur with a real-valued core material as well as a complex one. Consequently, the core material, even though it is referred to as a VEM throughout the paper, has real properties. The well-known modal strain energy method[14] relates the modal damping to the VEM loss factor times the fraction of modal strain energy in the VEM. Even with it's limitations on high levels of damping and high loss factors, this is a reasonable indicator for the present study.

2. MATHEMATICAL MODEL

An analytical model is an engineering tool for exploring new designs and trying untested concepts. For complicated systems, there is always a tradeoff between the complexity and engineering utility of the model. For this particular model, some assumptions are made and some aspects of strict 3-D elasticity are violated, though no worse than those made in Euler or Timoshenko beams. The model is checked for reasonableness through "sanity checks."

The model of the sandwich beam is developed via energy methods and some very basic principles of continuum mechanics. The primary assumptions are 1) plane stress, 2) no slipping at the interfaces, and 3) displacements linear within the core. The generalized coordinates used to locate particles within the structure are given in Table 1, and Fig. 1 shows schematically this sandwich beam in a displaced configuration. Note that $h_v\hat{\epsilon}$ represents the transverse

	transverse	axial	shear
Base layer	w	u_b	ψ
Constraining layer	$w + h_v\hat{\epsilon}$	u_c	α

Table 1. Displacement variables for the sandwich beam with independent facesheets.

displacement of the constraining layer *relative* to the base layer. Doing this makes $\hat{\epsilon}$ the 3–3 strain in the VEM, so generalized coordinate $\hat{\epsilon}$ is essentially just a scaled displacement.

2.1. Potential energy

The expression for strain energy (same as potential energy) density in a continuum is $\frac{1}{2}\epsilon_{ij}\tau_{ij}$. If the continuum is linear elastic isotropic, plugging the constitutive relationship $\tau_{ij} = \lambda\vartheta\delta_{ij} + 2\mu\epsilon_{ij}$ yields the strain energy density in terms of the six unique strain components:

$$W = \frac{1}{2}\epsilon_{ij}\tau_{ij} = \frac{1}{2}\lambda\vartheta^2 + \mu\left(\epsilon_{11}^2 + \epsilon_{22}^2 + \epsilon_{33}^2 + 2\epsilon_{12}^2 + 2\epsilon_{23}^2 + 2\epsilon_{13}^2\right), \tag{1}$$

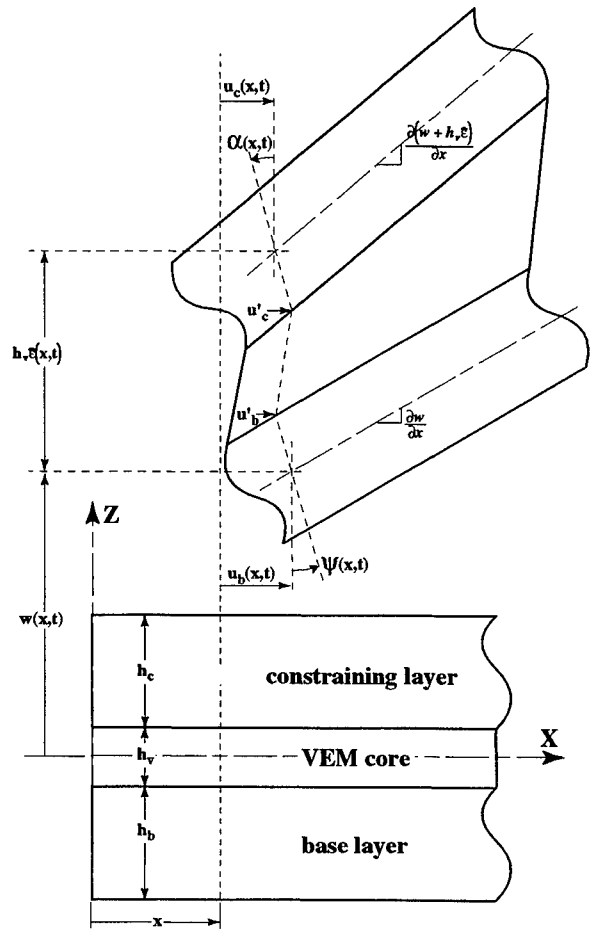

Figure 1. Sandwich model with independent facesheets.

where $\vartheta = \epsilon_{ii}$ and λ and μ are Lame's constants. The subscripts 1, 2, and 3 refer to the X, Y, and Z directions respectively in Fig. 1. Rewritten in terms of the more familiar shear modulus G and Poisson's ratio ν, this is

$$W = \frac{G\nu}{1-2\nu}\vartheta^2 + G\left(\epsilon_{11}^2 + \epsilon_{22}^2 + \epsilon_{33}^2 + 2\epsilon_{12}^2 + 2\epsilon_{23}^2 + 2\epsilon_{13}^2\right), \tag{2}$$

Since plane stress is assumed τ_{22}, τ_{21}, and τ_{23} are neglected, so the implied strain in the 2–2 direction is $\epsilon_{22} = \frac{-\nu(\epsilon_{11}+\epsilon_{33})}{1-\nu}$. Plugging this into equation 2 leads to the strain energy density

$$W = \frac{G}{1-\nu}\left(\epsilon_{11}^2 + \epsilon_{33}^2 + 2\nu\epsilon_{11}\epsilon_{33}\right) + 2G\epsilon_{13}^2. \tag{3}$$

This is the proper expression for the VEM core in this work since ϵ_{33} is assumed nonzero. If in addition the 3–3 faces of the VEM are assumed stress free, $\epsilon_{33} = \epsilon_{22} = -\nu\epsilon_{11}$ and equation 3 reduces further to the familiar

$$W = G\left(1+\nu\right)\epsilon_{11}^2 + 2G\epsilon_{13}^2 = \frac{1}{2}E\epsilon_{11}^2 + 2G\epsilon_{13}^2. \tag{4}$$

This is the expression commonly found in the literature that assumes equal displacements of the base and constraining layers, but is should at least be noted that this expression is a result of assuming a relative displacement of $-h_v\nu\epsilon_{11}$ between the facesheets, not zero. However, it is common and reasonable to neglect this quantity based on axial strains in the VEM compared with transverse displacements of the beam.

In any subsequent discussions concerning the VEM core, strain energies will be expressed only in terms of the shear modulus G and Poisson's ratio ν. While it is familiar for engineers to substitute Young's modulus E into expressions such as Eq. 4, it desensitizes them to the fact only the shear modulus is relatively easy to obtain for viscoelastic materials. Poisson's ratio is needed to calculate E, or vice versa, and neither is easy to measure for VEMs.

2.1.1. Facesheets

Defining the strain energy density in the facesheets is again a matter of finding strains from the displacement field and using Eq. 4. If z_b is a local coordinate with origin at the center of the base layer, the displacements are written

$$\begin{aligned} u_1(x, z_b) &= u_b - z_b\psi \\ u_3(x, z_b) &= w. \end{aligned} \tag{5}$$

With the strains defined as $\epsilon_{ij} = \frac{1}{2}(u_{i,j} + u_{j,i})$, the relevant strains (plane stress assumption) are $\epsilon_{11} = \frac{\partial u_b}{\partial x} - z_b\frac{\partial \psi}{\partial x}$ and $\epsilon_{13} = \frac{\partial w}{\partial x} - \psi$. Plugging these into Eq. 4 yields the strain energy density

$$W_b = G_b(1+\nu_b)\left(\frac{\partial u_b}{\partial x} - z_b\frac{\partial \psi}{\partial x}\right)^2 + \frac{1}{2}G_b\left(\frac{\partial w}{\partial x} - \psi\right)^2.$$

Integration over some width b and through the thickness h_b yields the strain energy for the base layer:

$$U_b = G_bA_b(1+\nu_b)\int_0^L \left\{\left(\frac{\partial u_b}{\partial x}\right)^2 + \frac{h_b^2}{12}\left(\frac{\partial \psi}{\partial x}\right)^2\right\} dx + \frac{G_bA_b}{2}\int_0^L \left\{\left(\frac{\partial w}{\partial x}\right)^2 - 2\frac{\partial w}{\partial x}\psi + \psi^2\right\} dx \tag{6}$$

where $A_b = bh_b$ is the cross-sectional area of the base layer.

The displacement field for the constraining layer is analogous to that given in Eq. 5 for the base layer with u_b replaced by u_c, ψ replaced by α, and w replaced by $w + h_v\hat{\epsilon}$. Following the same procedure as for the base layer yields a similar expression for the strain energy.

$$\begin{aligned} U_c = {} & G_cA_c(1+\nu_c)\int_0^L \left\{\left(\frac{\partial u_c}{\partial x}\right)^2 + \frac{h_c^2}{12}\left(\frac{\partial \alpha}{\partial x}\right)^2\right\} dx \\ & + \frac{G_cA_c}{2}\int_0^L \left\{\left(\frac{\partial w}{\partial x}\right)^2 + 2h_v\frac{\partial w}{\partial x}\frac{\partial \hat{\epsilon}}{\partial x} + h_v^2\left(\frac{\partial \hat{\epsilon}}{\partial x}\right)^2 - 2\frac{\partial w}{\partial x}\alpha - 2h_v\frac{\partial \hat{\epsilon}}{\partial x}\alpha + \alpha^2\right\} dx \end{aligned} \tag{7}$$

2.1.2. Viscoelastic material

The strain energy in the VEM is developed exactly as for the facesheets, with the exception that now Eq. 3 applies instead of Eq. 4 since ϵ_{33} is nonzero. The analogy is even more clear defining u_v as the axial deformation of the center of the VEM and ϕ as the angle of shear (reference Fig. 1).

$$u_v = \frac{1}{2}(u_b' + u_c') = \frac{1}{2}\left(u_b + u_c - \frac{h_b}{2}\psi + \frac{h_c}{2}\alpha\right) \tag{8a}$$

$$\phi = \frac{u_b' - u_c'}{h_v} = \frac{1}{h_v}\left(u_b - u_c - \frac{h_b}{2}\psi - \frac{h_c}{2}\alpha\right) \tag{8b}$$

The displacement field becomes

$$\begin{aligned} u_1(x, z) &= u_v - z\phi \\ u_3(x, z) &= \frac{1}{2}(h_v\hat{\epsilon} + 2w) + z\hat{\epsilon}, \end{aligned} \tag{9}$$

and the relevant strains are

$$\left\{ \begin{array}{c} \epsilon_{11} \\ \epsilon_{33} \\ 2\epsilon_{13} \end{array} \right\} = \left\{ \begin{array}{c} \frac{\partial u_1}{\partial x} \\ \frac{\partial u_3}{\partial z} \\ \frac{\partial u_3}{\partial x} + \frac{\partial u_1}{\partial z} \end{array} \right\} = \left\{ \begin{array}{c} \frac{\partial u_v}{\partial x} - z\frac{\partial \phi}{\partial x} \\ \hat{\epsilon} \\ \frac{\partial w}{\partial x} + \frac{h_v}{2}\frac{\partial \hat{\epsilon}}{\partial x} + z\frac{\partial \hat{\epsilon}}{\partial x} - \phi \end{array} \right\}. \tag{10}$$

Plugging the strains from Eq. 10 into Eq. 3 and integrating over the width y and thickness z yields strain energy

$$\begin{aligned} U_v = & \frac{G_v A_v}{1-\nu_v} \int_0^L \left\{ \left(\frac{\partial u_v}{\partial x}\right)^2 + \frac{h_v^2}{12}\left(\frac{\partial \phi}{\partial x}\right)^2 + \hat{\epsilon}^2 + 2\nu_v \frac{\partial u_v}{\partial x}\hat{\epsilon} \right\} dx \\ & + \frac{G_v A_v}{2} \int_0^L \left\{ \frac{h_v^2}{3}\left(\frac{\partial \hat{\epsilon}}{\partial x}\right)^2 + \left(\frac{\partial w}{\partial x}\right)^2 + \phi^2 - h_v \frac{\partial \hat{\epsilon}}{\partial x}\phi - 2\frac{\partial w}{\partial x}\phi + h_v \frac{\partial w}{\partial x}\frac{\partial \hat{\epsilon}}{\partial x} \right\} dx \end{aligned} \tag{11}$$

where $A_v = bh_v$ is the cross-sectional area of the VEM.

2.2. Kinetic energy

The expressions for kinetic energy is relatively straightforward given the displacement fields in equations 9 and 5. The kinetic energy for any layer is the integral over the volume of the velocity field squared:

$$T = \frac{1}{2} \int_{\forall} \rho\, \dot{\mathbf{q}} \cdot \dot{\mathbf{q}}\, d\forall. \tag{12}$$

The displacement fields given by equations 5 and 9 are referenced to an inertial coordinate system, so the velocity field comes from differentiating each term with respect to time and plugging into Eq. 12. After integration over the width and through the appropriate thicknesses, the kinetic energies are

$$T_b = \frac{\rho_b A_b}{2} \int_0^L \left\{ \left(\frac{\partial u_b}{\partial t}\right)^2 + \frac{h_b^2}{12}\left(\frac{\partial \psi}{\partial t}\right)^2 + \left(\frac{\partial w}{\partial t}\right)^2 \right\} dx \tag{13}$$

$$T_v = \frac{\rho_v A_v}{2} \int_0^L \left\{ \left(\frac{\partial u_v}{\partial t}\right)^2 + \frac{h_v^2}{12}\left(\frac{\partial \phi}{\partial t}\right)^2 + \left(\frac{\partial w}{\partial t}\right)^2 + \frac{h_v^2}{3}\left(\frac{\partial \hat{\epsilon}}{\partial t}\right)^2 + h_v \frac{\partial w}{\partial t}\frac{\partial \hat{\epsilon}}{\partial t} \right\} dx \tag{14}$$

$$T_c = \frac{\rho_c A_c}{2} \int_0^L \left\{ \left(\frac{\partial u_c}{\partial t}\right)^2 + \frac{h_c^2}{12}\left(\frac{\partial \alpha}{\partial t}\right)^2 + \left(\frac{\partial w}{\partial t}\right)^2 + h_v^2 \left(\frac{\partial \hat{\epsilon}}{\partial t}\right)^2 + 2h_v \frac{\partial w}{\partial t}\frac{\partial \hat{\epsilon}}{\partial t} \right\} dx \tag{15}$$

2.3. Constraints between layers

As long as there is no slipping between layers, tractions and displacement should be continuous at the interfaces. Displacement continuity is built in to the definitions of the displacement fields, but stress continuity is not. Consistent with the assumptions stated above, only the 1–3 stress can be matched at the interfaces between the VEM and facesheets. This yields two constraint equations, so two of the generalized coordinates can be removed from the problem. Enforcement of stress continuity is not an option if simple Euler beams are used for the facesheets since the 1–3 shear stress is zero by formulation. Some authors neglect the axial inertia and write equilibrium ($\tau_{ji,j} = \rho \dot{V}_i$) for an element at the interface. For example, equilibrium in the 1-direction for an element on the constraining layer at the interface with the VEM would be

$$\frac{\partial \tau_{11}}{\partial x} + \overbrace{\frac{\partial \tau_{21}}{\partial y}}^{negl.} + \overbrace{\frac{\partial \tau_{31}}{\partial z}}^{0\, since\, const.} = \rho\, \dot{V}_1 \Big|_{\hat{z}_c = -\frac{h_c}{2}} = \rho \ddot{u}_c', \tag{16}$$

A constraint equation follows by neglecting the right-hand side, defining $\tau_{11} = E_c \frac{\partial u_c'}{\partial x}$, and using τ_{13} from the VEM (it doesn't exist in the constraining layer).

Since the current model allows shear in both all the layers, continuity if τ_{13} at the two interfaces provides two constraint equations. The VEM/base layer interface yields

$$\begin{aligned} \tau_{13_b}\big|_{\frac{h_b}{2}} &= G_b \left(\frac{\partial w}{\partial x} - \psi \right) \\ \tau_{13_v}\big|_{-\frac{h_v}{2}} &= G_v \left(\frac{\partial w}{\partial x} - \phi \right) \end{aligned} \tag{17}$$

Equating the right-hand sides, the shear angle ϕ in the VEM is

$$\phi = \frac{\partial w}{\partial x} \left(1 - \frac{G_b}{G_v} \right) + \frac{G_b}{G_v} \psi. \tag{18}$$

Similarly for the VEM/constraining layer interface,

$$\begin{aligned} \tau_{13_c}\big|_{-\frac{h_c}{2}} &= G_c \left(\frac{\partial w}{\partial x} + h_v \frac{\partial \hat{\epsilon}}{\partial x} - \alpha \right) \\ \tau_{13_v}\big|_{\frac{h_v}{2}} &= G_v \left(\frac{\partial w}{\partial x} + h_v \frac{\partial \hat{\epsilon}}{\partial x} - \phi \right) \end{aligned} \tag{19}$$

Equating the left-hand sides, and substituting ϕ from Eq. 18 yields

$$\alpha = \frac{\partial w}{\partial x} \left(1 - \frac{G_b}{G_c} \right) + \frac{G_b}{G_c} \psi + h_v \frac{\partial \hat{\epsilon}}{\partial x} \left(1 - \frac{G_v}{G_c} \right) \tag{20}$$

Equations 18 and 20 predict $\alpha = \phi = \psi$ in the case where $G_b = G_v = G_c$, and this serves as one check on the model and the constraints. Combining Eqs. 8b, 18, and 20 yields the following expression for u_c:

$$u_c = u_b - \frac{\partial w}{\partial x} \left[h_v \left(1 - \frac{G_b}{G_v} \right) + \frac{h_c}{2} \left(1 - \frac{G_b}{G_c} \right) \right] - \psi \left[\frac{h_c}{2} \frac{G_b}{G_c} + h_v \frac{G_b}{G_v} + \frac{h_b}{2} \right] - \frac{h_v h_c}{2} \frac{\partial \hat{\epsilon}}{\partial x} \left(1 - \frac{G_v}{G_c} \right) \tag{21}$$

Finally, variable u_v comes from Eqs. 8a, 20, and 21:

$$u_v = u_b + \frac{h_v}{2} \left(\frac{G_b}{G_v} - 1 \right) \frac{\partial w}{\partial x} - \left(\frac{h_b}{2} + \frac{h_v}{2} \frac{G_b}{G_v} \right) \psi \tag{22}$$

For the case of equal moduli for all layers, Eq. 21 predicts $u_c = u_b - d\psi$, where $d = \frac{h_b}{2} + h_v + \frac{h_c}{2}$, the distance between the centers of the facesheets. This also is a physical result of the constrain equations.

2.4. Final energy expressions

The constraints chosen for this model allow the potential and kinetic energies of Eqs. 11, 7, 14, and 15 to be expressed in terms of generalized coordinates u_b, w, ψ, and $\hat{\epsilon}$. Equations 6 and 13 are inherently in terms of these coordinates. Intermediate coordinates u_v and ϕ are removed by their definitions, Eqs. 8a and 8b, and constraining layer coordinates u_c and α are removed via Eqs. 21 and 20. The resulting expression are messy, and U_b and T_b are repeated for completeness.

$$T_b = \frac{\rho_b A_b}{2} \int_0^L \left\{ \left(\frac{\partial u_b}{\partial t} \right)^2 + \frac{h_b^2}{12} \left(\frac{\partial \psi}{\partial t} \right)^2 + \left(\frac{\partial w}{\partial t} \right)^2 \right\} dx \tag{23}$$

$$\begin{aligned} T_v = \frac{\rho_v A_v}{2} \int_0^L \Bigg\{ & \left(\frac{\partial u_b}{\partial t} \right)^2 + V_{21} \frac{\partial u_b}{\partial t} \frac{\partial^2 w}{\partial x \partial t} + V_{22} \frac{\partial u_b}{\partial t} \frac{\partial \psi}{\partial t} + \left(\frac{\partial w}{\partial t} \right)^2 + h_v \frac{\partial w}{\partial t} \frac{\partial \hat{\epsilon}}{\partial t} + V_{23} \left(\frac{\partial^2 w}{\partial x \partial t} \right)^2 \\ & + V_{24} \frac{\partial^2 w}{\partial x \partial t} \frac{\partial \psi}{\partial t} + \frac{h_v^2}{3} \left(\frac{\partial \hat{\epsilon}}{\partial t} \right)^2 + V_{25} \left(\frac{\partial \psi}{\partial t} \right)^2 \Bigg\} dx \end{aligned} \tag{24}$$

$$T_c = \frac{\rho_c A_c}{2} \int_0^L \left\{ \left(\frac{\partial u_b}{\partial t}\right)^2 + +C_{21}\frac{\partial u_b}{\partial t}\frac{\partial w}{\partial t} + C_{22}\frac{\partial u_b}{\partial t}\frac{\partial^2 \hat{\epsilon}}{\partial x \partial t} + C_{23}\frac{\partial u_b}{\partial t}\frac{\partial \psi}{\partial t} + \left(\frac{\partial w}{\partial t}\right)^2 + 2h_v \frac{\partial w}{\partial t}\frac{\partial \hat{\epsilon}}{\partial t} + C_{24}\left(\frac{\partial^2 w}{\partial x \partial t}\right)^2 \right.$$
$$\left. + C_{25}\frac{\partial^2 w}{\partial x \partial t}\frac{\partial^2 \hat{\epsilon}}{\partial x \partial t} + C_{25}\frac{\partial^2 w}{\partial x \partial t}\frac{\partial \psi}{\partial t} + h_v^2 \left(\frac{\partial \hat{\epsilon}}{\partial t}\right)^2 + C_{28}\frac{\partial^2 \hat{\epsilon}}{\partial x \partial t}\frac{\partial \psi}{\partial t} + C_{29}\left(\frac{\partial \phi}{\partial t}\right)^2 \right\} dx \tag{25}$$

$$U_b = G_b A_b (1+\nu_b) \int_0^L \left\{ \left(\frac{\partial u_b}{\partial x}\right)^2 + \frac{h_b^2}{12}\left(\frac{\partial \psi}{\partial x}\right)^2 \right\} dx + G_b A_b \int_0^L \left\{ \left(\frac{\partial w}{\partial x}\right)^2 - 2\frac{\partial w}{\partial x}\psi + \psi^2 \right\} dx \tag{26}$$

$$U_v = G_v A_v \int_0^L \left\{ V_1 \left(\frac{\partial u_b}{\partial x}\right)^2 + V_2 \frac{\partial u_b}{\partial x}\frac{\partial^2 w}{\partial x^2} + V_3 \frac{\partial u_b}{\partial x}\hat{\epsilon} + V_4 \frac{\partial u_b}{\partial x}\frac{\partial \psi}{\partial x} + V_5 \left(\frac{\partial w}{\partial x}\right)^2 + V_6 \frac{\partial w}{\partial x}\frac{\partial \hat{\epsilon}}{\partial x} \right.$$
$$+ V_7 \frac{\partial w}{\partial x}\psi + V_8 \left(\frac{\partial^2 w}{\partial x^2}\right)^2 + V_9 \frac{\partial^2 w}{\partial x^2}\hat{\epsilon} + V_{10}\frac{\partial^2 w}{\partial x^2}\frac{\partial \psi}{\partial x} + V_{11}(\hat{\epsilon})^2 + V_{12}\hat{\epsilon}\frac{\partial \psi}{\partial x} + V_{13}\left(\frac{\partial \hat{\epsilon}}{\partial x}\right)^2$$
$$\left. + V_{14}\frac{\partial \hat{\epsilon}}{\partial x}\psi + V_{15}(\psi)^2 + V_{16}\left(\frac{\partial \psi}{\partial x}\right)^2 \right\} dx \tag{27}$$

$$U_c = G_c A_c \int_0^L \left\{ (1+\nu_c)\left(\frac{\partial u_b}{\partial x}\right)^2 + C_1 \frac{\partial u_b}{\partial x}\frac{\partial^2 w}{\partial x^2} + C_2 \frac{\partial u_b}{\partial x}\frac{\partial^2 \hat{\epsilon}}{\partial x^2} + C_3 \frac{\partial u_b}{\partial x}\frac{\partial \psi}{\partial x} + C_4 \left(\frac{\partial w}{\partial x}\right)^2 + C_5 \frac{\partial w}{\partial x}\frac{\partial \hat{\epsilon}}{\partial x} \right.$$
$$+ C_6 \frac{\partial w}{\partial x}\psi + C_7 \left(\frac{\partial^2 w}{\partial x^2}\right)^2 + C_8 \frac{\partial^2 w}{\partial x^2}\frac{\partial^2 \hat{\epsilon}}{\partial x^2} + C_9 \frac{\partial^2 w}{\partial x^2}\frac{\partial \psi}{\partial x} + C_{10}\left(\frac{\partial \hat{\epsilon}}{\partial x}\right)^2 + C_{11}\frac{\partial \hat{\epsilon}}{\partial x}\frac{\partial \psi}{\partial x} + C_{12}\left(\frac{\partial^2 \hat{\epsilon}}{\partial x^2}\right)^2$$
$$\left. + C_{13}\frac{\partial^2 \hat{\epsilon}}{\partial x^2}\frac{\partial \psi}{\partial x} + C_{14}(\psi)^2 + C_{15}\left(\frac{\partial \psi}{\partial x}\right)^2 \right\} dx \tag{28}$$

The constants C_i and V_i above are messy combinations of the basic material and geometric properties. Their derivation is straightforward bookkeeping, and they are not presented here due to space. Finally, a shear factor is generally added to the shear stress of a Timoshenko beam to account for approximating the shear across the cross-section as linear. Reference 15 has a good table of values. The shear factors for rectangular sections are are based only of Poisson's ratio. With the way the constraints are enforced in these studies, these shear factors are nearly equal and tend to cancel each other. Thus, they are not included in the equations.

2.5. Equations of motion

The assumed modes method (see Ref. 16) is used to derive the equations of motion. Prior to invoking Lagrange's equations, expand the generalized coordinates as follows:

$$\begin{aligned} u_b(x,t) &= U(x)\,\xi(t) \\ w(x,t) &= W(x)\,\eta(t) \\ \hat{\epsilon}(x,t) &= V(x)\,\sigma(t) \\ \psi(x,t) &= \Psi(x)\,\theta(t) \end{aligned} \tag{29}$$

Plugging Eqs. 29 into, for example, Eq. 23 results in

$$T_b = \dot{\xi}^T M_1^b \dot{\xi} + \dot{\eta}^T M_2^b \dot{\eta} + \dot{\theta}^T M_3^b \dot{\theta}.$$

Using the notation

$$(\alpha, \beta)_{mb} \equiv \frac{\rho_b A_b}{2} \int_0^L \alpha\, \beta^T\, dx, \tag{30}$$

the components of the mass matrix are defined as

$$
\begin{aligned}
M_1^b &= (U, U)_{mb} \\
M_2^b &= (W, W)_{mb} \\
M_3^b &= \frac{h_b^2}{12} (\Psi, \Psi)_{mb}
\end{aligned}
\tag{31}
$$

Similar algebra follows for the other energy terms of Eqs. 24–28. The kinetic and potential energies are next summed and the Lagrangian is formed via $\mathcal{L} = T - U$. Finally, the coupled equations of motion come from

$$
\frac{d}{dt}\left(\frac{\partial \mathcal{L}}{\partial \dot{q}_i}\right) - \frac{\partial \mathcal{L}}{\partial q_i} = Q_i \qquad (i = \xi, \eta, \sigma, \theta), \tag{32}
$$

where the Q_i are generalize loads. This is expressed in matrix form as

$$
\begin{bmatrix} M_{\xi\xi} & M_{\xi\eta} & M_{\xi\sigma} & M_{\xi\theta} \\ M_{\eta\xi} & M_{\eta\eta} & M_{\eta\sigma} & M_{\eta\theta} \\ M_{\sigma\xi} & M_{\sigma\eta} & M_{\sigma\sigma} & M_{\sigma\theta} \\ M_{\theta\xi} & M_{\theta\eta} & M_{\theta\sigma} & M_{\theta\theta} \end{bmatrix} \begin{Bmatrix} \ddot{\xi} \\ \ddot{\eta} \\ \ddot{\sigma} \\ \ddot{\theta} \end{Bmatrix} + \begin{bmatrix} K_{\xi\xi} & K_{\xi\eta} & K_{\xi\sigma} & K_{\xi\theta} \\ K_{\eta\xi} & K_{\eta\eta} & K_{\eta\sigma} & K_{\eta\theta} \\ K_{\sigma\xi} & K_{\sigma\eta} & K_{\sigma\sigma} & K_{\sigma\theta} \\ K_{\theta\xi} & K_{\theta\eta} & K_{\theta\sigma} & K_{\theta\theta} \end{bmatrix} \begin{Bmatrix} \xi \\ \eta \\ \sigma \\ \theta \end{Bmatrix} = \begin{Bmatrix} Q_\xi \\ Q_\eta \\ Q_\sigma \\ Q_\theta \end{Bmatrix}, \tag{33}
$$

where again straightforward bookkeeping produces the above matrices. If synchronous motion is assumed, the eigenproblem performed on Eq. 33 provides the system's natural frequencies and mode shapes.

A set of admissible functions will be chosen for each of the trial functions $U, W, V,$ and Ψ in Eq. 29. If the VEM and constraining layer thicknesses go to zero, Eq. 33 degenerates to the two second-order coupled equation of a Timoshenko beam. Modeling the sandwich beam as cantilevered at $x = 0$, the geometric boundary conditions are just $W(0) = 0$ and $\Psi(0) = 0$, and as such axial modes of a fixed-end rod are admissible functions. However legitimate these functions are, their convergence extremely poor since they are unable to represent the natural boundary condition $\frac{\partial w}{\partial x} - \psi = 0$ at the free end. One option is to augment the set of functions with some designed to help meet the natural boundary conditions. Meirovitch presents a discussion of this in Ref. 17. However, if the solution is not well represented by a relatively small number (fewer than about ten) of the original trial functions, any functions added are likely to be linearly dependent on these original basis functions. Consequently, the choices are poor convergence or a singular matrix.

If the problem were just a Timoshenko beam, an obvious choice for comparison functions would be the eigenfunctions themselves. While the results were predictably good for the case of the base layer only, the results were poor for the sandwich beam. One reason for this surprising result might be the constraints used to represent the axial and shear deformation of the constraining layer with those of the base layer. The resulting functions $W(x)$ and $\Psi(x)$ are apparently quite different than the eigenfunctions for a Timoshenko beam.

After trying many combinations of trial functions, the best results came from using polynomials. Shames[18] in a discussion of the Rayleigh-Ritz method for beams introduces a set of polynomials that happened to provide good convergence for this problem. Figure 2a shows the first five functions used to expand $u_b, w,$ and ψ, while $\hat{\epsilon}$ was expanded with the function in Fig. 2b. The first set reflects the geometric boundary condition at x=0 for the functions $u_b, w,$ and ψ, but note that their derivatives are nonzero. The same set is used for $\hat{\epsilon}$ except a rigid-body mode is added to allow $\hat{\epsilon}$ to be nonzero even at x=0.

For most cases, the inertia terms associated with the axial and relative transverse displacements of the facesheets are negligible compared to those of the transverse and shear displacements. In such cases, the rows and columns are dropped from the mass matrix in Eq. 33 and the stiffness matrix is condensed accordingly (see Ref. 19).

The final step was to do the eigenproblem on the mass and stiffness matrices of Eq. 33. MATLAB's standard eigenvalue routine was used during checkout, but a power method[17] was used to increase speed of the analyses where only the first eigenpair were sought.

The modal strain energy comes from the eigenvectors and the expressions for the potential energy. It is simple matter to calculate the strain energy in each layer for each mode, thus providing and indication of damping effectiveness for each treatment.

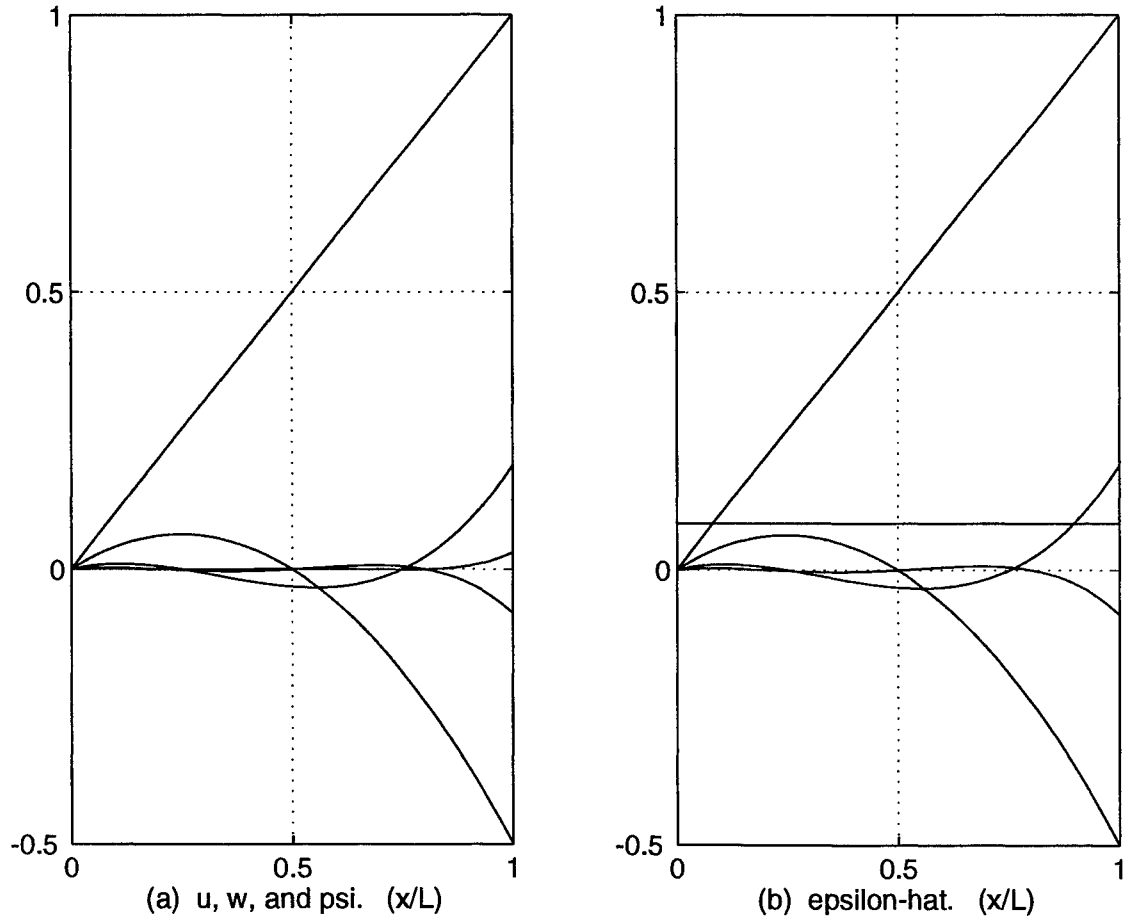

Figure 2. Admissible functions used in the assumed modes analysis.

The above model was easily modified to simulate the constraining layer having the same transverse displacement the base layer. Strictly speaking, the relative displacement $h_v\hat{\epsilon}$ does not go to zero; rather it becomes $-h_v\nu_v\epsilon_{11}$ assuming the y and z surfaces are stress free. However, consistent with other assumptions made in this model, this is considered negligible compared to transverse displacement w, so all terms containing any mention of $\hat{\epsilon}$ or its derivatives are dropped from Eqs. 23–28. Another difference is that the strain energy in the VEM is calculated via Eq. 4 rather than Eq. 3 since both the y and z surfaces are now assumed stress free.

3. RESULTS

In sandwich beams where high damping is the goal, there will most likely be a large mismatch the moduli of adjoining layers. Another way to look at this is even though the 1-3 stress is forced to be continuous, there is a large jump in the 1-3 strain. One of the side effects of enforcing this stress continuity the way done here is terms containing the large number $\frac{G_b}{G_v}$ as well as the dominating multiplier $\left(\frac{G_b}{G_v}\right)^2$. If all but these $\left(\frac{G_b}{G_v}\right)^2$ terms are discarded, all trace of the axial and relative transverse displacement are lost. The conditioning of the matrices was more a function of how $\frac{G_b}{h_b}$ related to $\frac{G_v}{h_v}$. Note that G_b and G_c where on the same order for this study. At some point the VEM gets so soft compared to the facesheets that an ill-conditioned stiffness matrix results. Reposing the problem would no doubt help this, but simple scaling would not.

The beam simulated is a unit-width, 12-inch-long aluminum cantilever with only the base layer fixed. Again, the viscoelastic core is approximated here by *real* properties since the effects demonstrated are due to a soft core, not a

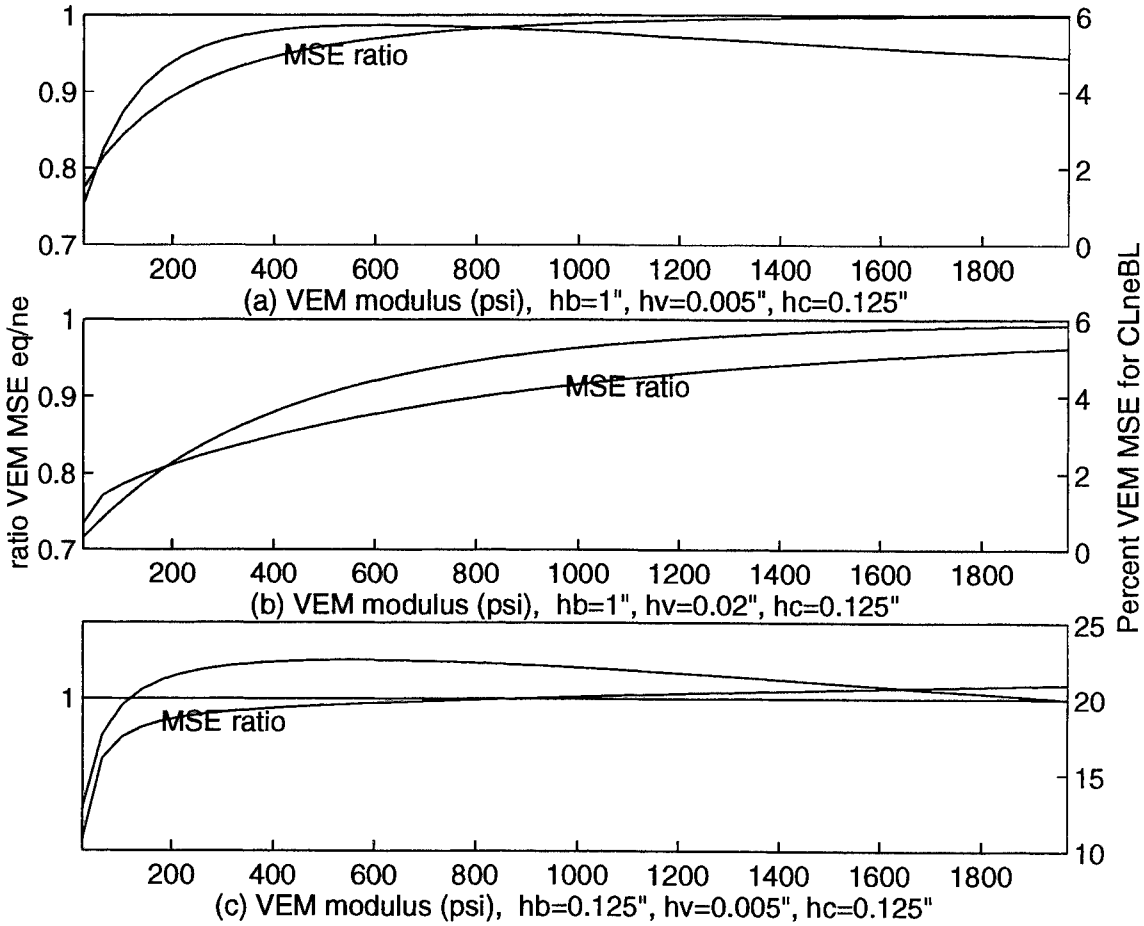

Figure 3. MSE in VEM for CL≠BL and ratio VEM MSE CL=BL/CL≠BL versus VEM shear modulus.

soft complex core.

The most important measure of the effect of facesheet kinematic assumptions is the fraction modal strain energy (MSE) in the VEM. In fact, beams analyzed with the two sets of assumptions produce very similar natural frequencies, but the difference in VEM MSE is very noticeable, particularly for unfortunate choices of VEM thickness and shear modulus. The premise of this work is that a soft VEM layer will not always result in the constraining layer following a stiff base structure. The stiffness of the VEM is some combination of shear modulus and thickness. In this case, "soft" is related to $\frac{G_v}{h_v}$, so it could mean low modulus, high thickness, or both. Figure 3 shows three situations where the VEM shear modulus is varied over a wide range. In the titles, h_b, h_v, and h_c refer respectively to the thicknesses of the base, VEM, and constraining layers. The first five of the trial functions shown in Fig. 2 where used to expand each of the generalized coordinates. The curve labeled "MSE ratio" is the ratio of the VEM MSE predicted by assuming the facesheets move together (CL=BL) to that assuming they move independently (CL≠BL). The other curve is simply the percent strain energy in the VEM predicted by CL≠BL. For values of shear modulus less that 250 psi, the CL=BL model predicts between %70–%95 of what the CL≠BL does. As one would expect, the two predictions converge as the VEM modulus increases and is better able to "pull" the constraining layer along. The VEM in case (b) is softer than that in case (a) since it is thicker, and accordingly the predictions for low shear modulus values are worse. Case (c) follows the same trend, except the ratio of VEM modal strain energies goes to 1.0 and keeps going. A possible explanation for this may be revealed by the level of VEM MSE, which is most likely caused by the inability of the high strains in the VEM to be expressed in terms of the base-layer generalized coordinates. This is a point of continuing research.

The two MSE predictions tend to approach each other at higher modulus values, but many materials commonly used have moduli near the low end of those in Figure 3. For instance, 3M's ISD 112 has a shear modulus of approximately 125 psi at room temperature and 100 Hz.[13]

4. FUTURE WORK

The implementation of the current model in MATLAB is too sensitive to the large stiffness mismatch between the facesheets and VEM. Enforcing continuity of the 1–3 stress (3–3 was ignored) between layers, however correct and physical, aggravated the problem, and simple nondimensionalization will not entirely solve the problem. The current plan is to recognize that this sandwich beam is some perturbation of a simpler structure, and small parameters must be assigned to the variations from this simpler structure. Simple perturbation analysis then provides the tools for ensuring that the important terms are retained and negligible ones are dropped in the formulation.

ACKNOWLEDGEMENTS

The authors wish to thank the Army Research Office for their support of this work.

REFERENCES

1. P. Liénard, "Étude d'une méthode de mesure du prottement intérieur de revetements plastiques travaillant en flexion," *La Recherche Aéronautique* **20**, pp. 11–22, 1951.
2. H. Oberst, "Ueber die dämpfung der biegeschwingungen dünner bleche durch fest haftende beläge," *Acustica* **2**, pp. 181–194, 1952.
3. E. M. Kerwin, "Damping of flexural waves by a constrained visco-elastic layer," *Journal of the Acoustical Society of America* **31**, pp. 952–962, 1959.
4. R. A. DiTaranto, "Theory of vibratory bending for elastic and viscoelastic layered finite-length beams," *Journal of Applied Mechanics* **32**, pp. 881–886, 1965.
5. D. J. Mead and S. Markus, "The forced vibration of a three-layer, damped sandwich beam with arbitrary boundary conditions," *Journal of Sound and Vibration* **10**(2), pp. 163–175, 1969.
6. B. E. Douglas and J. C. S. Yang, "Transverse compressional damping in the vibratory response of elastic-viscoelastic-elastic beams," *AIAA Journal* **16**(9), pp. 925–930, 1978.
7. D. K. Rao, "Frequency and loss factors of sandwich beams under various boundary conditions," *J. Mech. Engr. Science* **20**(5), pp. 271–282, 1978.
8. M. J. Yan and E. H. Dowell, "Governing equations of vibrating constrained-layer damping sandwich plates and beams," *ASME Journal of Applied Mechanics* **39**, pp. 1041–1046, 1972.
9. M. D. Rao and S. He, "Dyanmic analysis and design of laminated composite beams with multiple damping layers," *AIAA Journal* **31**(4), pp. 736–745, 1993.
10. C. D. Johnson, "Design of passive damping systems," *Journal of Mechanical Design and Journal of Vibration and Acoustics* **117 (B)**, pp. 171–177, 1995. ASME 50th Anniversary Design Engineering Division.
11. C. T. Sun and Y. P. Lu, *Vibration Damping of Structural Elements*, Prentice Hall, first ed., 1995.
12. A. Baz and J. Ro, "Optimum design and control of active constrained layer damping," *Journal of Mechanical Design and Journal of Vibration and Acoustics* **117 (B)**, pp. 135–144, 1995. ASME 50th Anniversary Design Engineering Division.
13. A. D. Nashif, D. I. G. Jones, and J. P. Henderson, *Vibration Damping*, Wiley-Interscience, first ed., 1985.
14. C. D. Johnson and D. A. Kienholz, "Finite element prediction of damping in structures with constrained viscoelastic layers," *AIAA Journal* **20**(9), pp. 1284–1290, 1982.
15. R. D. Blevins, *Formulas for Natural Frequency and Mode Shape*, Krieger, 1984.
16. L. Meirovitch, *Elements of Vibration Analysis*, McGraw-Hill, second ed., 1986.
17. L. Meirovitch, *Principles and Techniques of Vibrations*, Prentice Hall, first ed., 1997.
18. I. H. Shames and C. L. Dym, *Energy and Finite Element Methods in Structural Mechanics*, Taylor and Francis, first ed., 1985.
19. R. R. Craig, *Structural Dynamics*, Wiley, first ed., 1981.

Passive damping of beams with constrained viscoelastic material

Alessandro Fasana, Luigi Garibaldi, Ermanno Giorcelli, Massimo Ruzzene

Dipartimento di Meccanica, Politecnico di Torino
Corso Duca degli Abruzzi 24, 10129 Torino, Italy

ABSTRACT

Even in this period of large expansion of active control for noise and vibration suppression, passive damping technology is widely accepted and used because of its low cost and high reliability in many common applications. Viscoelastic materials play an important role in vibration reduction both in their free and constrained layer forms. This paper addresses the problem of calculating the modal frequencies and loss factors of beams containing a constrained viscoelastic layer. The problem is approached from an analytical point of view and an approximation is proposed on the mode shapes to simply take into account different boundary conditions. Calculations are performed on the basis of the energy method and compared with the results of the classical RKU theory and a finite elements model. A similar approach is also adapted to the study of partially covered beams; in this situation the RKU theory doesn't fit and only the FE model has been used as reference.

Keywords: beams, constrained viscoelastic material, partial coverage

1. BASIC HYPOTHESES

The hypotheses at the basis of this work (see [1], for example) are briefly summarized hereafter (see also Fig.1).

1. Plane transverse sections remain plane and normal to the longitudinal direction after bending.
2. The transverse displacement $w(x,t)$ doesn't vary through the thickness of the beam.
3. The longitudinal displacements $u(x,t)$ vary linearly in each layer; $u_1(x,t)$ and $u_3(x,t)$ are the displacements of the mean line of layers 1 and 3.
4. All displacements are small and there is perfect continuity at the interfaces.
5. Shear and extension of the core can both be included.

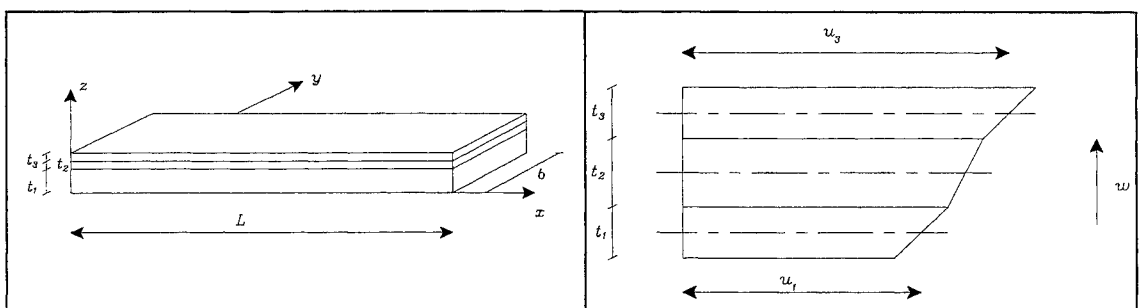

Figure 1. Scheme of the sandwich beam and its displacements.

With these assumptions it is possible to express the kinetic and strain energies of the sandwich beam in terms of $u_1(x,t)$, $u_3(x,t)$, $w(x,t)$ and their space and time derivatives.

Applying the Hamilton's principle and performing the variation term by term, the following equations for the flexural vibrations of the sandwich beam are obtained [1,2]:

SPIE Vol. 3045 • 0277-786X/97/$10.00

$$(D_1+D_3)w^{iv}-\frac{\gamma_2\, c}{t_2^2}\left(c\,w''-u_1'+u_3'\right)-\frac{\rho_1 t_1^3+\rho_3 t_3^3}{12}\ddot{w}''+\rho\ddot{w}-\rho_2 t_2\left[\varepsilon_3\ddot{u}_1'+\varepsilon_4\ddot{u}_3'+\left(\varepsilon_1^2+\frac{\varepsilon_3^2}{12}\right)\ddot{w}''\right]+$$

$$+E_2 t_2\left(\varepsilon_3 u_1'''+\varepsilon_4 u_3'''+\frac{t_1^2+t_2^2-t_1 t_3}{12}w^{iv}\right)=0$$

$$\gamma_2\left(\frac{c}{t_2^2}w'-\frac{u_1-u_3}{t_2^2}\right)+\gamma_1 u_1''-\left[\rho_1 t_1\ddot{u}_1+\rho_2 t_2\left(\frac{\ddot{u}_1}{3}+\frac{\ddot{u}_3}{6}+\varepsilon_3\ddot{w}'\right)\right]+E_2 t_2\left(\frac{u_1''}{3}+\frac{u_3''}{6}+\varepsilon_3 w'''\right)=0$$

$$-\gamma_2\left(\frac{c}{t_2^2}w'-\frac{u_1-u_3}{t_2^2}\right)+\gamma_3 u_3''-\left[\rho_3 t_3\ddot{u}_3+\rho_2 t_2\left(\frac{\ddot{u}_1}{6}+\frac{\ddot{u}_3}{3}+\varepsilon_4\ddot{w}'\right)\right]+E_2 t_2\left(\frac{u_1''}{6}+\frac{u_3''}{3}+\varepsilon_4 w'''\right)=0 \qquad (1)$$

where:

$$D_1=\frac{E_1 t_1^3}{12},\qquad D_3=\frac{E_3 t_3^3}{12},\qquad \gamma_1=E_1 t_1,\qquad \gamma_2=G_2 t_2,\qquad \gamma_3=E_3 t_3,$$

$$c=t_2+\frac{t_1+t_3}{2},\qquad \rho=\rho_1 t_1+\rho_2 t_2+\rho_3 t_3,$$

$$\varepsilon_1=\frac{t_3-t_1}{4},\qquad \varepsilon_2=\frac{t_3+t_1}{2},\qquad \varepsilon_3=\frac{t_3-2t_1}{12},\qquad \varepsilon_4=\frac{2t_3-2t_1}{12}.$$

The solution of these differential equations can be sought in the form:

$w(x,t)=f_w(x)\,\sin(\omega t)$
$u_1(x,t)=f_1(x)\,\sin(\omega t)$
$u_3(x,t)=f_3(x)\,\sin(\omega t)$

where ω is the circular frequency of the oscillation and $f_w(x), f_1(x), f_3(x)$ define the displacements of the layers.
To determine the three functions, $f_w(x), f_1(x)$ and $f_3(x)$, appropriate boundary conditions should be applied to both the ends of the beam and Eqs. (1) contemporaneously fulfilled, which is a not always simple task to accomplish.

2. AN APPROXIMATE SOLUTION

In order to find a simple solution of the problem, we decided to assume flexural mode shapes of the sandwich beam equal to the mode shapes of a single layer beam. This of course can be a very coarse approximation but is very helpful for quickly defining the deformations of the system.
For a simply supported beam we then have [3]:

$f_w(x)=\sin(n\pi x/L)$

with L=length of the beam and n=number of the mode, which is, by the way, the exact solution.

For a clamped-free beam we have:

$$f_w(x)=a\,\sin(\lambda_n x/L)+b\,\cos(\lambda_n x/L)+d\,sh(\lambda_n x/L)+e\,ch(\lambda_n x/L) \qquad (2)$$

$\sigma_n=\dfrac{sh\lambda_n-\sin\lambda_n}{ch\lambda_n+\cos\lambda_n}$, λ_n are the solution of the equation $ch\lambda\,\cos\lambda+1=0$ and $a=\sigma_n$, $b=-1$, $d=-\sigma_n$, $e=1$.

Different boundary conditions generate different values for a, b, d, e, σ and λ but the structure of $f_w(x)$ doesn't change.

Assuming Eq. (2) as expression of the flexural mode shapes, it's also possible to define $f_1(x)$ and $f_3(x)$ in a similar way:

$$f_1(x) = A_1 \cos(\lambda_n x/L) + B_1 \sin(\lambda_n x/L) + D_1 ch(\lambda_n x/L) + E_1 sh(\lambda_n x/L)$$

$$f_3(x) = A_3 \cos(\lambda_n x/L) + B_3 \sin(\lambda_n x/L) + D_3 ch(\lambda_n x/L) + E_3 sh(\lambda_n x/L). \quad (3)$$

The substitution of Eqs.(2) and (3) in Eq. (1), let us build up four separate systems, each containing three equations in the unknown ω and, respectively, the couples A_1 - A_3, B_1 - B_3, D_1 - D_3, E_1 - E_3., whose solution can be found iteratively.
Starting with a given value ω_i, the linear systems are solved and the expressions of $f_w(x)$, $f_1(x)$, $f_3(x)$ are used to compute the strain and kinetic energies of the sandwich beam. Their ratio gives a new frequency value ω_{i+1} which can be compared with the previous one. The procedure can be halted when the difference on the frequencies is considered negligible.
The direct consequence of this assumption is that the mode shape doesn't change even if the mode frequency does.

3. PARTIALLY COVERED BEAMS

Also the problem of partially covered beams has been approached in a similar way to bypass a number of analytical difficulties that arise in this situation.
In such a case even the basic equations describing the motion of the sandwich differ from Eqs. (1). Those equations were defined, through the Hamilton's principle, taking start from the expressions of the kinetic and strain energies but these expressions now have to vary because only a part of layer 1 is topped with the viscoelastic material and the constraining layer.
What we did is to assume that Eqs. (1) still hold [4] and, again, that the mode shapes of the partially covered beam don't change with respect to the mode shapes of the bare beam. The procedure is then as described in the previous paragraph but, because of the new assumptions, the approximation is even larger than in the case of the full sandwich beam.

4. FE MODEL

The comparison of the results obtained with the described method has been carried out on the basis of a simple FE model.
The first layer of the sandwich beam has been modelled with 99 eight-nodes solid elements along its length (x direction), two elements along its depth (y direction) and just one element along the thickness (z direction). Also layers 2 and 3 were meshed in the same way (99-2-1) for the fully covered beam whilst, in the partially covered model, the number of elements has been reduced in order to select the same nodes of the first layer and keep a constant length of the elements. Various tests on a clamped-free beam and a three-layer beam showed that this mesh is sufficient to guarantee reliable results on the FE model and don't generate too large aspect ratios in the elements (the dimensions of the beam are reported in paragraph 5).
Since the FE package doesn't allow to use viscoelastic materials, the Young modulus of the three layers remained unchanged with frequency (temperature was considered fixed).
The loss factor of structure η_{st} has been defined, for each mode, according to [5]:

$$\eta_{st} = \eta_2 U_2/U_{st} \quad (4)$$

where η_2 is the loss factor of the damping material, U_2 and U_{st} are the strain energies of the damping layer and of the sandwich beam.
Also for the loss factor of the damping material no variation with frequency and temperature has been taken into account.

5. NUMERICAL EXAMPLES

For all the numerical examples we used the following constant values:

$E_1 = 2.07\ 10^{11}$ N/m^2	$E_2 = 5.00\ 10^7$ N/m^2	$E_3 = 2.07\ 10^{11}$ N/m^2
$\rho_1 = 7800$ kg/m^3	$\rho_2 = 1500$ kg/m^3	$\rho_3 = 7800$ kg/m^3
$\nu_2 = 0.49$	L = 0.20 m	b = 4 mm
$t_1 = 1$ mm	$t_3 = 0.1$ mm	

The thickness t_2 of the viscoelastic layer is specified in each example.

The percentage values reported in each example, expressing the variation of the mode shapes computed with the FE model (w_{FE}) and compared with the theoretical deformations (w_{Th}), are defined as:

$$error = 100 \cdot \frac{\|w_{Th} - w_{FE}\|}{\|w_{Th}\|}$$

Simply supported sandwich beam

In order to verify the behaviour of the procedure we took start from a simply supported beam. With these boundary conditions also the classical Ross-Kerwin-Ungar theory [6] can be used for a comparison of the results and the assumption that the mode shapes don't change should be verified.

With t_2 = 0.2 mm the percentage errors on the mode shapes are in fact very small:

Mode	1	2	3	4
Error [%]	0.003	0.043	0.162	0.397

The modal frequencies and loss factors of the FE model, of the approximate method (AP) and of the RKU theory are (with η_2=0.1):

Mode	f_{FE} [Hz]	η_{FE}/η_2 [%]	f_{AP} [Hz]	η_{AP}/η_2 [%]	f_{RKU} [Hz]	η_{RKU}/η_2 [%]
1	68.9	1.94	68.9	1.94	68.9	1.92
2	268	6.07	268	6.06	269	6.02
3	585	9.65	585	9.66	585	9.62
4	1009	11.5	1008	11.5	1009	11.5

The values of η_{FE}/η_2 and η_{AP}/η_2 are both computed as in Eq. (4) and are independent from η_2; η_2 is instead part of the computational process in the RKU method and its increment results in a less accurate evaluation of the ratio η_{RKU}/η_2. For example, with η_2=0.5 we got:

Mode	1	2	3	4
f_{RKU} [Hz]	68.9	270	589	1016
η_{RKU}/η_2 [%]	1.58	5.14	8.57	10.6

Also with t_2 = 0.4 mm the situation doesn't change and the results of the approximate method are as accurate as these.

Clamped-free sandwich beam

In this second example, the results obtained with clamped-free boundary conditions are presented.

With t_2=0.2 mm the errors on the mode shapes are:

Mode	1	2	3	4
Error [%]	0.21	1.42	2.69	3.57

It is easy to note that these values, although small, are at least one order of magnitude greater than those of the simply supported beam.

The calculation of the frequencies and loss factors gave:

Mode	f_{FE} [Hz]	η_{FE}/η_2 [%]	f_{AP} [Hz]	η_{AP}/η_2 [%]	f_{RKU} [Hz]	η_{RKU}/η_2 [%]
1	24.7	0.85	24.7	0.78	24.7	0.73
2	151	4.51	153	4.61	152	3.86
3	412	7.96	417	8.37	413	8.01
4	784	10.4	791	11.0	784	10.8

It is worth noting that the results obtained with the RKU method (η_2 = 0.1), that is strictly valid only for simply supported beams, are not too far from the reality.

We also have to mention that the results of the approximate method are relative to a value of γ_2 defined as:

$$\gamma_2 = G_2 t_2 \sqrt{1+\eta_2^2} \quad \text{with} \quad \eta_2 = 0.5.$$

This means that γ_2 has been defined using the modulus of G_2 and not only its real part; assuming $\eta_2 = 0.1$ the frequencies don't change but the loss factor estimates increase.

With t_2=0.4 mm the errors on the mode shapes are:

Mode	1	2	3	4
Error [%]	0.61	3.06	4.86	5.60

Frequencies and loss factors, evaluated as above, are:

Mode	f_{FE} [Hz]	η_{FE}/η_2 [%]	f_{AP} [Hz]	η_{AP}/η_2 [%]	f_{RKU} [Hz]	η_{RKU}/η_2 [%]
1	26.8	2.06	26.8	1.98	26.7	1.85
2	159	9.49	164	10.4	161	8.70
3	422	14.2	431	15.9	424	15.0
4	787	16.1	797	17.7	786	16.9

The difference among the values are becoming larger even if the errors on the mode shapes are still limited. This happens because most of the discrepancies among the theoretical and actual mode shapes are concentrated in the regions of maximum curvature, which are the most important in the definition of the strain energy associated to the viscoelastic layer.

Clamped-free partially covered beam.

When only part of the beam is covered with the viscoelastic and the constraining layers, assuming the same physical and geometrical properties of the previous examples (with t_2=0.2 mm), the situation becomes more critic. The variations between the assumed and the actual mode shapes are larger thus causing errors in the definition of the deformations and the loss factors.

As a matter of example Fig.3 represents the 1st and 3rd mode shape of the clamped-free partially covered beam sketched in Fig.2 (solid line: theoretical mode shapes - grey circles: FE mode shapes).

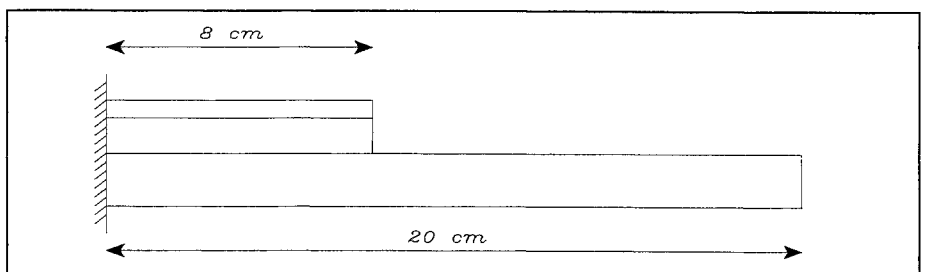

Figure 2. Sketch of the partially covered beam

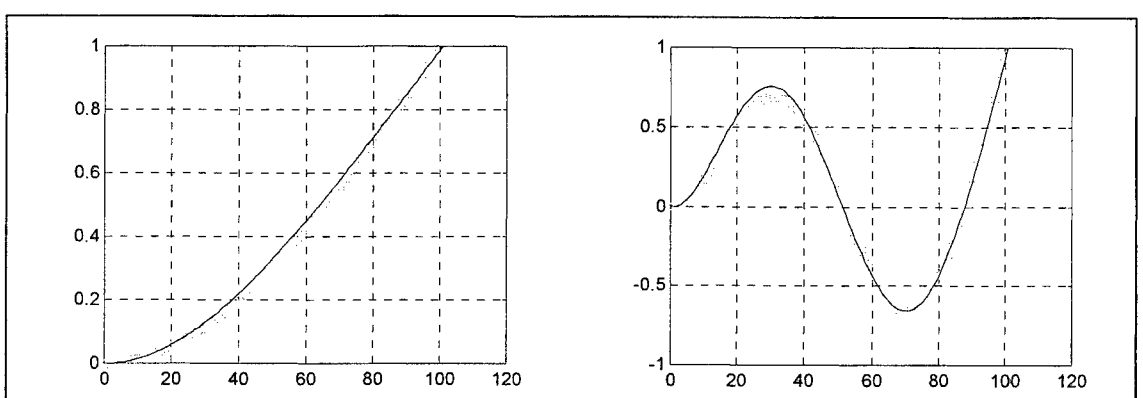

Figure 3. 1st and 3rd mode shape of the partially covered beam

The resulting frequencies and loss factors, evaluated as above, are:

Mode	f_{FE} [Hz]	η_{FE}/η_2 [%]	f_{AP} [Hz]	η_{AP}/η_2 [%]
1	25.0	2.73	25.7	0.12
2	137	2.44	142	0.96
3	378	4.71	388	1.61
4	737	4.18	746	3.84

As usual the discrepancies on the loss factors are much more evident than those on the frequencies and it's also quite surprising that the loss factor of the 1st mode is larger than the corresponding value on the fully covered beam. We think this may be due to the different relative motion of the 1st and 3rd layer in the two damped configurations.

6. CONCLUSION

The method described in this paper, with its assumptions and approximations, showed some good characteristics but also some evident drawbacks. The basic hypotheses lead to a model of the sandwich beam which may simply be solved if mode shapes are assumed to remain unchanged. In this situation the solution is quickly determined, with a good accuracy also for boundary conditions different from the double support. Of course the errors increase when the thickness of the supporting beam (layer 1) is insufficient to ensure the validity of the postulates.

The limitations are well stressed by the example regarding the partially covered beam. The lack of definition in the deformations results in large errors in the loss factors; also small differences on the mode shapes degenerate in damping estimations far from those of the FE model, that are assumed as reference values. Anyway both for the full and partial coverage the estimation of the modal frequencies is quite accurate. We then consider appropriate to apply the described approximations only when the rigidity of the basic layer is so high to assure insignificant changes of the mode shapes.

REFERENCES

1. Y.V.K. Sadasiva Rao, B.C. Nakra, "Vibration of unsymmetrical sandwich beams and plates with viscoelastic core", J. of Sound and Vibration, 34(3), pp. 309-326, 1974.
2. Y.P. Lu, J.C. Clemens, A.J. Roscoe, "Vibration of composite plate structures consisting of a constrained-layer damping sandwich with viscoelastic core", J. of Sound and Vibration, 158(3), pp. 552-558, 1992
3. R.D. Blevins, *Formulas for natural frequency and mode shape*, pp. 108-109, Van Nostrand Reinhold Company, New York, 1979.
4. A.K. Lall, N.T. Asnani, B.C. Nakra, "Vibration and damping analysis of rectangular plate with partially covered constrained viscoelastic layer", J. of Vibration, Acoustics, Stress, and Reliability in Design, Vol. 109, pp. 241-247, July 1987.
5. C.D. Johnson, D.A. Kienholz, "Finite element prediction of damping in structures with constrained viscoelastic layers", AIAA Journal, Vol. 20, No. 9, pp. 1284-1290, Sept. 1982.
6. D. Ross, E.E. Ungar, E.M. Kerwin Jr., "Damping of plate flexural vibrations by means of viscoelastic laminae", Structural Damping, ASME, pp. 49-87, Dec. 1959

Multilaminated plates with thin, compliant adhesive layers

S. W. Hansen

Department of Mathematics, Iowa State University
Ames, Iowa 50011 USA

ABSTRACT

A dynamic model for a multilayered laminated plate is developed. The laminated plate consists of $2n$ plate layers and $2n-1$ adhesive layers. The layers (both plate and adhesive layers) are assumed to be homogeneous, transversely isotropic and perfectly bonded to one another. In the initial modeling, the Reissner-Mindlin theory of shear deformable plates is applied to each layer, resulting in a high-order plate theory in which the shear motions of the layers are completely independent. Simpler, lower-order models can then be obtained from this initial model from asymptotic limits based upon the assumptions that (i) the adhesive layers are very thin,(ii) the elastic modulii of the adhesive layers are small compared to those of the plate layers, (iii) the shear stiffnesses of the plate layers are very large, (iv) the rotatonal moments of inertia of the individual plate layers are very small.

Keywords: laminated plate, multilayer plate, constrained-layer plate, laminated beam, constrained-layer beam, laminated beam

1. INTRODUCTION

Since the pioneering work on shear deformable beams and plates of Reissner[1] and later Mindlin,[2] numerous models have been developed to predict the dynamic behavior of thin multilayered plates. In particular many of the constrained layer models (see Sun and Lu[3] for a survey and many references) have been valuable in analyzing the dynamical properties of these plates. However the range of applicability of these models is often assessed only through experiment and there is a lack of theoretical foundation from which to to evaluate the accuracy of these models.

One problem is that all of these models are developed by making restrictive *a-priori* kinematic assumptions upon the class of possible motions through the thickness of the plate. In particular, a common assumption is that the shear stresses or strains are assumed to be continuous across the interfaces of the adjacent layers. Although this sounds like a natural assumption, when this assumption is coupled with continuity of displacement across the interfaces, one is left with two conditions at each interface. This effectively forces a *direct coupling* between the motion of all the layers in the sense that a motion in one layer uniquely determines the motion in all other layers. Thus, unless one knows the extent to which these kinematic assumptions are valid, and for what applications, it is difficult to make any valid assesments concerning the accuracy the model.

The approach described here overcomes part of this problem by starting with a high-order plate model in which no interface conditions, other than continuity of displacement, are assumed. By applying natural asymptotic assumptions, this initial high-order model can be used to obtain lower-order models with limited degrees of freedom. One then has a basis of comparison with which to assess the validity of the lower-order models.

We apply in our initial modeling a multilayer version[4] of the Reissner-Mindlin theory of shear deformable plates. This is a high-order plate theory in which the shear motions of each layer are completely independent. Simpler, lower-order models are then be obtained from this initial model from asymptotic limits based upon the assumptions that (i) the adhesive layers are very thin, (ii) the elastic modulii of the adhesive layers are small compared to those of the plate layers, (iii) the shear stiffnesses of the plate layers are very large, (iv) the rotatonal moments of inertia of the individual plate layers are very small. The resulting laminated plate model is a generalization of the model described in Hansen,[5] in which only one adhesive layer is present.

Our general approach is valid for general (nonsymmetric) laminated plates, however for simplicity of exposition we consider in this article the symmetric case in which all the material parameters are symmetric with respect to the geometric midsheet of the plate.

Email: shansen@iastate.edu; Supported in part by the National Science Foundation under Grant DMS9623144

This article is organized as follows. In Section 2 we review the basic assumptions used in the derivation of the multilayer plate model of Hansen.[4] In Section 3 we obtain the lower order models by taking asymptotic limits of the initial model. Some asymptotic and spectral properties of these resulting models are investigated, such as the dependence of the plate stiffness upon the glue stiffness and frequency of vibration. Some conclusions are given in Section 4.

2. MULTILAYER PLATES

The laminated plate models we will consider are all based upon the multilayer plate model in Hansen.[4] This multilayer plate model is derived under the assumptions that no slip occurs along the interfaces and each of the layers satisfy the assumptions of Reissner-Mindlin plate theory,[1,2] namely, within each layer the in-plane displacements vary linearly with respect to the transverse coordinate and the transverse displacements are constant with respect to the transverse coordinate. A possible deformation is indicated in Fig. 1.

Although we are mainly interested in the case of a symmetric multilayer plate, our approach is valid for nonsymmetric plates. In the following subsection we briefly describe the general n-layer model of Hansen[4] before specializing to the symmetric case.

2.1. General n-layer plate

The plate is assumed to consist of n plate layers which occupy the region $\Omega \times (-h/2, h/2)$ at equilibrium, where Ω is an open bounded domain in $\mathbf{R}^2$ with boundary Γ. Let

$$-h/2 = z_0 < z_1 < \ldots < z_{n-1} < z_n = h/2, \qquad h_i = z_i - z_{i-1},\ i = 1, 2, \ldots, n$$

We use the rectangular coordinates $\underline{x} = \{x_1, x_2\}$ to denote points in Ω and $x = \{\underline{x}, x_3\} = \{x_1, x_2, x_3\}$ to denote points in $Q = \cup_{i=1}^n Q_i$, where

$$Q_i = \Omega \times (z_{i-1}, z_i), \qquad i = 1, 2, \ldots, n.$$

For $x \in Q$ let $U(x) = \{U_1, U_2, U_3\}(x)$ denote the displacement vector of the point which, when the plate in equilibrium has coordinates $x = \{x_1, x_2, x_3\}$. In addition define $u^i = \{u_1^i, u_2^i\}$ and u_3^i, $i = 0, 1, 2, \ldots n$ by

$$u_j^i(\underline{x}) = U_j(\underline{x}, z_i) \quad j = 1, 2, 3, \quad \forall \underline{x} \in \Omega.$$

Throughout this paper the index i will refer to a particular layer or interface within the composite plate. For *vector* quantities whose components vary from layer to layer, the index i will be *superscripted*, while for *scalar* quantities the i will be *subscripted*.

Let $\sigma_{jk}, \epsilon_{jk}$ $(j, k = 1, 2, 3)$ denote the stress and strain tensors, respectively. For a small displacement theory we assume

$$\epsilon_{jk}(x) = \frac{1}{2}\left(\frac{\partial U_j(x)}{\partial x_k} + \frac{\partial U_k(x)}{\partial x_j}\right), \quad \forall\, x \in Q. \tag{1}$$

Each layer is assumed to be homogeneous and transversely isotropic, however the material properties can vary from layer to layer. Following Mindlin's approach,[2] the constitutive equations for 3-dimensional transversely isotropic elasticity are reduced to following constitutive equations by assuming σ_{33} to be negligible.

$$\begin{aligned} \sigma_{11} &= \tfrac{E_i}{1-\nu_i^2}(\epsilon_{11} + \nu_i \epsilon_{22}) & \sigma_{12} &= \tfrac{E_i}{1+\nu_i}\epsilon_{12} \\ \sigma_{22} &= \tfrac{E_i}{1-\nu_i^2}(\nu_i \epsilon_{11} + \epsilon_{22}) & \sigma_{13} &= 2G_i\epsilon_{13} \\ \sigma_{33} &= 0 & \sigma_{23} &= 2G_i\epsilon_{23}, \end{aligned} \tag{2}$$

where E_i denotes the in-plane Young's modulus, G_i denotes the transverse shear modulus (with shear correction[2] included), and ν_i denotes the in-plane Poisson's ratio, all for the ith layer.

Due to the assumption that the transverse displacements are constant in the transverse direction, we may simply define the scalar function w as the transverse displacement. Thus

$$w(\underline{x}) \equiv u_3^0(\underline{x}) = u_3^1(\underline{x}) = \ldots = u_3^n(\underline{x}) \quad \forall\, \underline{x} \in \Omega.$$

Due to the assumption that the surfaces are perfectly bonded we find that each filament that is originally orthogonal to the surfaces has $2n+3$ degrees of freedom: w, $u^0, \ldots, u^n$.

For $i = 1, 2, \ldots, n$ define $\psi^i = \{\psi_1^i, \psi_2^i\}$, $\varphi^i = \{\varphi_1^i, \varphi_2^i\}$, and $v^i = \{v_1^i, v_2^1\}$ by

$$\psi^i = \frac{u^i - u^{i-1}}{h_i}, \quad \varphi^i = \psi^i + (\nabla w)^T, \quad v^i = \frac{u^{i-1} + u^i}{2}. \tag{3}$$

In addition, let u, ψ, v, φ denote the matrices whose ith row is u^i, ψ^i, v^i, φ^i, respectively. Furthermore let $\vec{\nabla} w$ denote the $n \times 2$ matrix whose ith row is $(\nabla w)^T$. The components ψ_j^i of ψ^i can be viewed as the *total rotation angles* of filament within the i-th layer in the x_j-x_3 plane (with negative orientation). The components of φ represent the (small angle approximation for the) *shear angles* within each layer. (See Figure 1.) The components of v^i represent the in-plane displacements of the midplanes of the i-th layer.

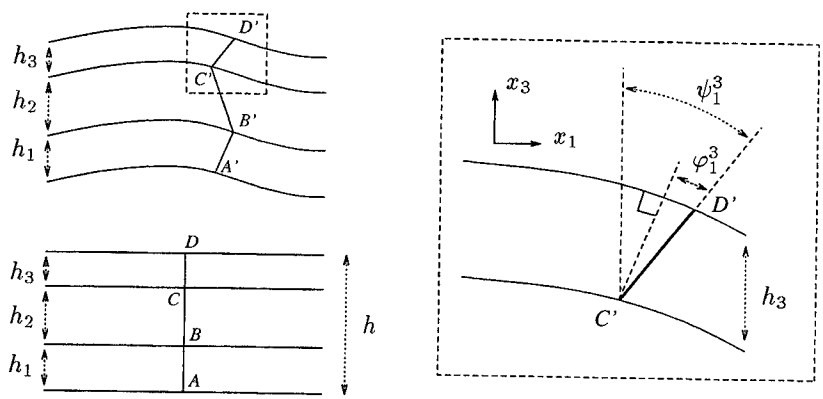

Fig. 1. A projection onto the x_1-x_3 axis of the deformation of the straight filament A-B-C-D at equilibrium (bottom left) into the deformed filament A'-B'-C'-D'. If C and D have coordinates $\{\underline{x}, z_2\}$ and $\{\underline{x}, z_3\}$ then C' and D' have coordinates $\{\underline{x} + u^2(\underline{x}), z_2 + w(\underline{x})\}$ and $\{\underline{x} + u^3(\underline{x}), z_3 + w(\underline{x})\}$, respectively.

Define $\hat{z}_i = (z_{i-1} + z_i)/2$. The displacements within the ith layer can be written in terms of the translations v^i and total rotation angles ψ^i as

$$\begin{aligned} U_1(\underline{x}, x_3) &= v_1^i(\underline{x}) + (x_3 - \hat{z}_i)\psi_1^i(\underline{x}) \quad && z_{i-1} < x_3 < z_i \\ U_2(\underline{x}, x_3) &= v_2^i(\underline{x}) + (x_3 - \hat{z}_i)\psi_2^i(\underline{x}) \quad && z_{i-1} < x_3 < z_i \\ U_3(\underline{x}, x_3) &= w(\underline{x}) && z_{i-1} < x_3 < z_i. \end{aligned} \tag{4}$$

The displacement equations (4) should be interpreted in terms of the state variables $\{u, w\}$; that is, v and ψ are actually functions of the state $\{u, w\}$ by (3). In particular, continuity of displacements along the interfaces is automatic.

Substituting (4) into (1) gives an expression for the strain within the i-th layer:

$$\begin{aligned} \epsilon_{11} &= \tfrac{\partial v_1^i}{\partial x_1} + (x_3 - \hat{z}_i)\tfrac{\partial \psi_1^i}{\partial x_1} \quad \epsilon_{22} = \tfrac{\partial v_2^i}{\partial x_2} + (x_3 - \hat{z}_i)\tfrac{\partial \psi_2^i}{\partial x_2} \\ \epsilon_{12} &= \tfrac{1}{2}\left[\tfrac{\partial v_1^i}{\partial x_2} + \tfrac{\partial v_2^i}{\partial x_1} + (x_3 - \hat{z}_i)\left(\tfrac{\partial \psi_1^i}{\partial x_2} + \tfrac{\partial \psi_2^i}{\partial x_1}\right)\right] \\ \epsilon_{13} &= \tfrac{1}{2}(\varphi_1^i) \qquad \epsilon_{23} = \tfrac{1}{2}(\varphi_2^i). \end{aligned} \tag{5}$$

Since σ_{33} is assumed to be negligible we may assume (for the purpose of calculating the energy) that $\epsilon_{33} = 0$.

The strain energy $\mathcal{P} = \sum_{i=1}^{n} \mathcal{P}_i$ and kinetic energy $\mathcal{K} = \sum_{i=1}^{n} \mathcal{K}_i$ for the composite plate are given by

$$\mathcal{P}_i = \frac{1}{2}\int_{Q_i} \sum_{j,k=1}^{3} \epsilon_{jk}\sigma_{jk} d\underline{x} dx_3, \qquad \mathcal{K}_i = \frac{1}{2}\int_{Q_i} \rho_i(\dot{U}_1^2 + \dot{U}_2^2 + \dot{U}_3^2) d\underline{x} dx_3,$$

where $\dot{} = d/dt$ and $\rho_i > 0$ denotes the mass density per unit volume within the i-th layer. From (2) and (5) the strain energy of the ith layer can be written as

$$\begin{aligned}
\mathcal{P}_i &= \tfrac{h_i^3}{2}\textstyle\int_\Omega D_i \left[\left(\frac{\partial\psi_1^i}{\partial x_1}\right)^2 + \left(\frac{\partial\psi_2^i}{\partial x_2}\right)^2 + 2\nu_i\left(\frac{\partial\psi_2^i}{\partial x_2}\frac{\partial\psi_1^i}{\partial x_1}\right)\right. \\
&\quad \left. + \left(\tfrac{1-\nu_i}{2}\right)\left(\frac{\partial\psi_1^i}{\partial x_2} + \frac{\partial\psi_2^i}{\partial x_1}\right)^2\right] d\underline{x} \\
&\quad + \tfrac{h_i}{2}\textstyle\int_\Omega 12 D_i \left[\left(\frac{\partial v_1^i}{\partial x_1}\right)^2 + \left(\frac{\partial v_2^i}{\partial x_2}\right)^2 + 2\nu_i\left(\frac{\partial v_1^i}{\partial x_1}\frac{\partial v_2^i}{\partial x_2}\right)\right. \\
&\quad \left. + \left(\tfrac{1-\nu_i}{2}\right)\left(\frac{\partial v_1^i}{\partial x_2} + \frac{\partial v_2^i}{\partial x_1}\right)^2\right] + G_i((\varphi_1^i)^2 + (\varphi_2^i)^2) d\underline{x}
\end{aligned} \tag{6}$$

where $D_i = E_i/12(1-\nu_i^2)$. $D_i h_i^3$ is the *modulus of flexural rigidity* for the ith layer and $h_i G_i$ is the *modulus of elasticity in shear* for the ith layer. Likewise the kinetic energy of the ith layer is

$$\mathcal{K}_i = \frac{1}{2}\int_\Omega \rho_i h_i (\dot{w})^2 + \frac{\rho_i h_i^3}{12}\left(\dot{\psi}^i \cdot \dot{\psi}^i\right) + \rho_i h_i \left(\dot{v}^i \cdot \dot{v}^i\right) d\underline{x}, \tag{7}$$

where the "dot product" denotes the usual scalar product on $\mathbf{R}^2$.

Define the following n by n matrices:

$$\begin{aligned}
\mathbf{h} &= \operatorname{diag}(h_1, h_2, \ldots, h_n) & \mathbf{D} &= \operatorname{diag}(D_1, D_2, \ldots, D_n) \\
\mathbf{p} &= \operatorname{diag}(\rho_1, \rho_2, \ldots, \rho_n) & \mathbf{G} &= \operatorname{diag}(G_1, G_2, \ldots, G_n).
\end{aligned}$$

If θ and ξ are matrices in $\mathbf{R}^{lm}$, by $\theta \cdot \xi$ we mean the scalar product in $\mathbf{R}^{lm}$. We will also denote

$$(\theta, \xi)_\Omega = \int_\Omega \theta \cdot \xi \, d\underline{x}, \qquad (\theta, \xi)_\Gamma = \int_\Gamma \theta \cdot \xi \, d\Gamma.$$

The expressions for the kinetic and potential energy can be rewritten as

$$\mathcal{K}(t) = c(\dot{v}, \dot{\psi}, \dot{w}; \dot{v}, \dot{\psi}, \dot{w})/2 \qquad \mathcal{P}(t) = a(v, \psi, \varphi; v, \psi, \varphi)/2$$

where $c(\cdot\,;\cdot)$ and $a(\cdot\,;\cdot)$ denote the bilinear forms

$$\begin{aligned}
c(\psi, v, w; \hat{\psi}, \hat{v}, \hat{w}) &= ((\mathbf{h}\cdot\mathbf{p})w, \hat{w})_\Omega + ((\mathbf{p}\mathbf{h}^3/12)\psi, \hat{\psi})_\Omega + (\mathbf{h}\mathbf{p}v, \hat{v})_\Omega \\
a(\psi, v, \varphi; \hat{\psi}, \hat{v}, \hat{\varphi}) &= a_0(\mathbf{h}^3\psi; \hat{\psi}) + 12 a_0(\mathbf{h}v; \hat{v}) + a_1(\varphi; \hat{\varphi}) \\
a_0(\psi, \hat{\psi}) &= \textstyle\sum_{i=1}^{n} a_0^i(\psi^i; \hat{\psi}^i) \\
a_0^i(\psi^i; \hat{\psi}^i) &= \left(D_i \frac{\partial\psi_1^i}{\partial x_1}, \frac{\partial\hat{\psi}_1^i}{\partial x_1}\right)_\Omega + \left(D_i \frac{\partial\psi_2^i}{\partial x_2}, \frac{\partial\hat{\psi}_2^i}{\partial x_2}\right)_\Omega \\
&\quad + \left(\nu_i D_i \frac{\partial\psi_2^i}{\partial x_2}, \frac{\partial\hat{\psi}_1^i}{\partial x_1}\right)_\Omega + \left(\nu_i D_i \frac{\partial\psi_1^i}{\partial x_1}, \frac{\partial\hat{\psi}_2^i}{\partial x_2}\right)_\Omega \\
&\quad + \left(\left(\tfrac{1-\nu_i}{2}\right) D_i \left(\frac{\partial\psi_1^i}{\partial x_2} + \frac{\partial\psi_2^i}{\partial x_1}\right), \left(\frac{\partial\hat{\psi}_1^i}{\partial x_2} + \frac{\partial\hat{\psi}_2^i}{\partial x_1}\right)\right)_\Omega \\
a_1(\varphi; \hat{\varphi}) &= (\mathbf{G}\mathbf{h}\varphi, \hat{\varphi})_\Omega.
\end{aligned} \tag{8}$$

For simplicity, we will assume there are no external forces acting on the plate and no damping is included. To obtain the equations of motion, one first expresses v, ψ and φ in terms of the state variables $\{u, w\}$, then forms the Lagrangian from the expressions for the potential and kinetic energy, and finally applies Hamilton's principle.

For example, if the plate is clampted on the boundary we let $\{\hat{u}, \hat{w}\} = \{\hat{u}^0, \hat{u}^1, \ldots, \hat{u}^n, \hat{w}\}$ denote a test function on $\Omega \times (0, T)$ (with dimensionality matching that of $\{u, w\}$) for which

$$\{\hat{u}, \hat{w}\} = \{\frac{\partial \hat{u}}{\partial n}, \frac{\partial \hat{w}}{\partial n}\} = 0 \quad \text{on } \Gamma \times (0, T),$$

$$\{\hat{u}, \hat{w}\}|_{t=0} = \frac{\partial}{\partial t}\{\hat{u}, \hat{w}\}|_{t=0} = \{\hat{u}, \hat{w}\}|_{t=T} = \frac{\partial}{\partial t}\{\hat{u}, \hat{w}\}|_{t=T} = 0 \quad \text{in } \Omega$$

where n is the outward unit normal to Γ. An application of Hamilton's principle leads to the equations of motion in weak form:

$$\int_0^T c\left(\dot{\psi}, \dot{v}, \dot{w}; \dot{\hat{\psi}}, \dot{\hat{v}}, \dot{\hat{w}}\right) - a\left(\psi, v, \varphi; \hat{\psi}, \hat{v}, \hat{\varphi}\right) = 0\, dt \tag{9}$$

where $\hat{v}$, $\hat{\psi}$ and $\hat{\varphi}$ are given in terms of $\{\hat{u}, \hat{w}\}$ by (3) (but with hats on u, v, w, φ, ψ).

An explicit form of the equations of motion (and corresponding boundary conditions) can be obtained from (9) by a procedure involving an integration by parts in time, and Green's theorem in the spatial variables. The resulting boundary value problem involves a system of $2n + 3$ coupled PDE's whose explicit form is given in Hansen.[4] It is important to note that neither ψ nor v may be used in place of u for a state variable due to the fact that u has $2n+2$ coordinates while v and ψ each have $2n$ coordinates. This situation improves, however in the symmetric case.

2.2. Symmetric multilayer plates

In the case where the material properties of the multilayer plate are symmetric with respect to the centersheet, all solutions $\{u, w\}$ of the multilayer plate system decouple into the sum of a *symmetric solution* $\{u_s, 0\}$ and an *antisymmetric solution* $\{u_a, w\}$, where u_s (resp., u_a) denotes a displacement that is symmetric (resp., antisymmetric) with respect to the centersheet of the multilayer plate. (See Hansen[4] for a precise statement about this decoupling.) Since the symmetric part is independent of the transverse displacement, for what concerns bending it is enough to consider only the antisymmetric part. Although this antisymmetric part still satisfies the equations of motion (9), many of these equations become redundant, due to this decoupling.

To obtain a minimal set of equations, one needs to make use of the symmetry.

First consider the case in which there are an even number of layers, so that the centersheet of the multilayer plate coincides with the middle interface. Assume that the multilayer plate consists of $2n$ layers, indexed $i = \pm 1, \pm 2, \ldots, \pm n$, and $2n + 1$ interfaces (this includes the outer faces), indexed $i = 0, \pm 1, \ldots \pm n$, where the $i = 0$ interface represents the centersheet of the multilayer plate, and the $i = \pm 1$ layers are adjacent, and so forth, with the outer layers indexed $\pm n$. Since $u_i = -u_{-i}$ (for antisymmetric motions), the motion below the centersheet is exactly opposite that of the top half, and furthermore the potential and kinetic energies of the top and bottom halfs are the same. Consequently it is enough to consider only the energy corresponding to the *top half* of the composite plate, i.e., those layers indexed from $i = 1$ to $i = n$ and those interfaces indexed from $i = 0$ to $i = n$. Except for the factor of two, the same Lagrangian is obtained, and consequently (9) remains valid for representing the equations of motion (provided that once a solution is obtained, the motions from the bottom half of the plate are determined by antisymmetry).

In the case of an odd number of layers, we artificially divide the center layer into two layers with an interface through the centersheet of the middle layer. This effectively creates an even number of layers, reducing the problem to the previously descussed case. Note that we have not changed the problem since no additional degrees of freedom are created in dividing the middle layer. (Additional degrees of freedom only contribute to the in-plane solution and do not change the form of the antisymmetric component.)

Therefore, when considering the antisymmetric motions, we only need to consider the case of an even number of layers, with the $i = 0$ interface representing the center interface. Note that in this case, by the antisymmetry of motions we have that $u_0 \equiv 0$. As a consequence, only $2n + 1$ state variables are needed (instead of $2n + 3$) and hence

$\{\psi, w\}$ (or $\{v, w\}$) may be used as state variables. Thus, to obtain the strong form of the equations of motion from (9), one can choose $\{\psi, w\}$ as the state variables, then express v in terms of ψ and integrate by parts, as mentioned earlier, to obtain a system of PDEs and boundary conditions.

Before writing down the boundary value problem associated with (9) we first need to develop some notation.

2.2.1. Notation

Define

$$L^i\phi = \{L_1^i\phi, L_2^i\phi\}$$

by

$$\begin{aligned} L_j^i\phi = \tfrac{\partial}{\partial x_j}\left(D_i\tfrac{\partial\phi_j}{\partial x_j}\right) &+\tfrac{\partial}{\partial x_k}\left(\tfrac{(1-\nu_i)}{2}D_i\tfrac{\partial\phi_j}{\partial x_k}\right)+\tfrac{\partial}{\partial x_k}\left(\tfrac{(1-\nu_i)}{2}D_i\tfrac{\partial\phi_k}{\partial x_j}\right)\\ &+\tfrac{\partial}{\partial x_j}\left(\nu_i D_i\tfrac{\partial\phi_k}{\partial x_k}\right), \quad (j,k)=(1,2),\,(2,1). \end{aligned}$$

Also define the boundary operators $\mathcal{B}^i\phi = \{\mathcal{B}_1^i(\phi_1,\phi_2), (\mathcal{B}_2^i(\phi_1,\phi_2)\}$ by

$$\begin{aligned} \mathcal{B}_1^i(\phi_1,\phi_2) &= D_i\left[\left(\tfrac{\partial\phi_1}{\partial x_1}n_1+\nu_i\tfrac{\partial\phi_2}{\partial x_2}n_1\right)+\left(\tfrac{1-\nu_i}{2}\right)\left(\tfrac{\partial\phi_1}{\partial x_2}+\tfrac{\partial\phi_2}{\partial x_1}\right)n_2\right]\\ \mathcal{B}_2^i(\phi_1,\phi_2) &= D_i\left[\left(\tfrac{\partial\phi_2}{\partial x_2}n_2+\nu_i\tfrac{\partial\phi_1}{\partial x_1}n_2\right)+\left(\tfrac{1-\nu_i}{2}\right)\left(\tfrac{\partial\phi_2}{\partial x_1}+\tfrac{\partial\phi_1}{\partial x_2}\right)n_1\right]. \end{aligned}$$

In the above, (n_1, n_2) denotes the outward unit normal vector to Γ. The following Green's formula is valid for all sufficiently smooth $\hat{\phi}$, ϕ:

$$a_0^i(\phi,\hat{\phi}) = (\mathcal{B}^i\phi,\hat{\phi})_\Gamma - (L^i\phi,\hat{\phi})_\Omega. \tag{10}$$

For $\xi = (\xi_j^i)$ $(i = 1, 2, \ldots, n,\ j = 1, 2)$ define the matrices $L\xi$ and $\mathcal{B}\xi$ by

$$(L\xi)_{ij} = (L_j^i\xi^i), \qquad (\mathcal{B}\xi)_{ij} = (\mathcal{B}_j^i\xi^i), \qquad i = 1, 2, \ldots, n,\ j = 1, 2.$$

As we have mentioned, if we choose $\{\psi, w\}$ for state variables, we need to express v in terms of ψ. Let M denote the matrix relating ψ to v:

$$v = M\psi.$$

2.2.2. Boundary value problem

An integration by parts in t of (9) followed by an application of (10) leads to the following:

$$\begin{aligned} &\mathbf{h}\cdot\mathbf{p}\ddot{w} - \operatorname{div}\textstyle\sum_{i=1}^n(G_ih_i\varphi^i) = 0, && \underline{x}\in\Omega,\ t>0\\ &M^T\mathbf{hp}\ddot{v} - M^T\mathbf{h}Lv + \mathbf{ph}^3\ddot{\psi}/12 - \mathbf{h}^3L\psi + \mathbf{Gh}\phi = 0, && \underline{x}\in\Omega, t>0 \end{aligned} \tag{11}$$

where $v = M\psi$, $\varphi = \psi + \vec{\nabla}w$.

In the case of simply supported boundary conditions (the no applied moments on the boundary, zero transverse displacement) the appropriate boundary conditions are:

$$w = 0, \qquad \mathbf{h}^3\mathcal{B}\psi + 12M^T\mathbf{h}\mathcal{B}v = 0, \qquad \text{on } \Gamma. \tag{12}$$

The reader is referred to Hansen[4] for a more detailed discussion of the system (11), and other possible sets of boundary conditions.

3. LAMINATED PLATE MODELS

We describe four models for laminated plates in this section. The first is the initial model based upon the symmetric multilayer model descrbibed in section 2. The second is obtained from the first as an asymptotic limit, using the assumption that the adhesive layers are thin and compliant. The third is obtained from the second as an asymptotic limit under the assumption that the shear stiffnesses of the plate layers are very large. Our final model is an approximation of the third in which the rotational moments of inertia of the individual plate layers are assumed to be negligible.

3.1. Initial model

We consider a laminated plate with laminates that are symmetric with respect to the centersheet of the laminated plate. We assume that the laminated plate consists of $2n$ plate layers and $2n-1$ adhesive layers. (The case of $2n+1$ plate layers is similar.) Thus the middle layer is an adhesive layer.

As discussed in the previous subsection, we artificially divide the middle layer into two layers, so that the top and bottom half both consist of n adhesive layers and n adhesive layers. As discussed in Section 2, we only need to consider the top half of the laminated plate. Therefore assume that the bottom (of the top half) is the $i = 0$ interface and the top surface is the $i = 2n$ interface. The layers are indexed from $i = 1$ to $i = 2n$, with higher layers corresponding to higher indices. Thus adhesive layers are indexed odd and plate layers are indexed even.

To calculate the potential and kinetic energies of the top half, we use the same expressions for the energies of each layer (6), (7), but with $2n$ instead of n layers. Consequently our initial model for a symmetric laminated plate with $2n$ plate layers and $2n$ glue layers is given by (11) but with n replaced by $2n$.

3.2. Limit model for thin, compliant adhesive layers

We now assume that the adhesive layers are thin in comparison to the plate layers and the shear moduli of the adhesive layers are small in comparison to the those of the plate layers. Therefore we treat $\mathbf{h}_a$ and $\mathbf{G}_a$ as small parameters and would like to obtain a limiting model as these parameters tend to zero. However to retain the potential energy in shear of the adhesive layers we need to retain the ratio $\gamma_i := G_i/h_i$ fixed for the adhesive layers. We therefore would like to determine the limiting form of the system (11) as $G_i \to 0$, $h_i \to 0$, with $\gamma_i := G_i/h_i$ fixed for odd i (adhesive layers).

Before we get to this however we will need some notation to distinguish quantities relating to plate layers from from those of adhesive layers.

Let P_a be the projection (a $2n$ by n matrix) that maps $(a_1, a_2, \ldots, a_{2n})^T \to (a_1, a_3, \ldots, a_{2n-1})^T$ and define P_p to be the corresponding projection that maps to the even-indexed coordinates. For each vector that is indexed by the layers, like ψ, for example, we define $\psi_a = P_a\psi$ and $\psi_p = P_p\psi$. (We will not need to refer to directional components, so there should be no confusion.) For matrix quantities, $\mathbf{h}$, for example, we define $\mathbf{h}_a$ to be the n by n diagonal matrix whose diagonal elements are the thicknesses of the adhesive layers (in symbols: $\mathbf{h}_a = P_a\mathbf{h}P_a^T$). Likewise $\mathbf{h}_p$ denotes the diagonal matrix of plate layer thicknesses.

We are interested in finding the limiting form of (11) as

$$\mathbf{h}_a \to 0, \quad \mathbf{G}_a \to 0 \quad \text{with } \gamma = \mathbf{h}_a^{-1}\mathbf{G}_a \quad \text{fixed.} \tag{13}$$

Due the possibility of large shears in the adhesive layers we define a new state variable for these layers:

$$\delta_a = \mathbf{h}_a\psi_a.$$

By (3) we see that $\delta_a^i = u^i - u^{i-1}$ (i odd) and hence represents a differential in displacement of the adhesive layers.

We will wish to use $\{w, \psi_p, \delta_a\}$ as state variables. Therefore we need to express the potential and kinetic energies in terms of these quantities. Furthermore, to obtain the equations of motion explicitly, we will need to express v in terms of δ_a and ψ. Using that $u^0 \equiv 0$ (since this is the middle and we are considering only antisymmetric motions) we obtain the following.

$$\begin{pmatrix} v_a \\ v_p \end{pmatrix} = \begin{pmatrix} (N+I/2) & N \\ (N+I) & (N+I/2) \end{pmatrix} \begin{pmatrix} \delta_a \\ \mathbf{h}_p\psi_p \end{pmatrix} =: \begin{pmatrix} A & B \\ C & A \end{pmatrix} \begin{pmatrix} \delta_a \\ \mathbf{h}_p\psi_p \end{pmatrix}, \tag{14}$$

where N denotes the nilpotent matrix with $1's$ below the main diagonal and 0's everywhere else.

The bilinear forms c and a can be rewritten:

$$\begin{aligned} c(\psi, v, w; \hat{\psi}, \hat{v}, \hat{w}) &= ((\mathbf{h}_a \cdot \mathbf{p}_a + \mathbf{h}_p \cdot \mathbf{p}_p)w, \hat{w})_\Omega + c_a(\delta_a, \psi_p; \hat{\delta}_a, \hat{\psi}_p) + c_p(\delta_a, \psi_p; \hat{\delta}_a, \hat{\psi}_p), \\ a(\psi, v, \varphi; \hat{\psi}, \hat{v}, \hat{\varphi}) &= a_a(\delta_a, \psi_p; \hat{\delta}_a, \hat{\psi}_p) + a_p(\delta_a, \psi_p; \hat{\delta}_a, \hat{\psi}_p) \end{aligned} \tag{15}$$

where c_a and c_p are the bilinear forms corresponding to the in-plane kinetic energy of the adhesive layers, and plate layers, respectively, and a_a and a_p correspond to the strain energies of the adhesive and plate layers, respectively. For example,

$$\begin{aligned} c_a(\delta_a, \psi_p; \hat{\delta}_a, \hat{\psi}_p) &= \tfrac{1}{12}(\rho_a \mathbf{h}_a \delta_a, \hat{\delta}_a)_\Omega + (\mathbf{h}_a \rho_a v_a, A\hat{\delta}_a + B\mathbf{h}_p \hat{\psi}_p)_\Omega, \\ c_p(\delta_a, \psi_p; \hat{\delta}_a, \psi_p) &= \tfrac{1}{12}((\rho_p \mathbf{h}^3)\psi_p, \hat{\psi}_p)_\Omega + (\mathbf{h}_p \rho_p v_p, C\hat{\delta}_a + A\mathbf{h}_p \hat{\psi}_p)_\Omega, \end{aligned}$$

where v_p and v_a are defined in terms of the state variables by (14).

Taking the limit in (13) we find that c_p and a_p are unchanged, while

$$c_a \to 0, \qquad a_a \to (\gamma\delta_a, \hat{\delta}_a)_\Omega.$$

We remark that it will be clear how to include the mass of the adhesive layers in the model at a later stage, if this is signicant.

The equations of motion can now be calculated in the same way as before. We obtain

$$\begin{aligned} &\mathbf{h} \cdot \mathbf{p}\ddot{w} - \operatorname{div} \textstyle\sum_{i=1}^{n} (G_{2i} h_{2i} \varphi^{2i}) = 0, && \underline{x} \in \Omega,\ t > 0 \\ &C^T(\mathbf{h}_p \mathbf{p}_p \ddot{v}_p - 12\mathbf{h}_p L_p v_p) + \gamma\delta_g = 0, && \underline{x} \in \Omega, t > 0 \\ &\mathbf{h}_p A^T(\mathbf{h}_p \mathbf{p}_p \ddot{v}_p - 12\mathbf{h}_p L_p v_p) + \tfrac{1}{12}\mathbf{h}_p^3 \mathbf{p}_p \ddot{\psi}_p - \mathbf{h}_p^3 L_p \psi_p) = 0, && \underline{x} \in \Omega, t > 0 \end{aligned} \tag{16}$$

where v_p is given by (14), and $\varphi = \psi + \vec{\nabla} w$, as before.

The simply supported boundary conditions are

$$w = 0, \qquad \mathcal{B}_p v_p = 0, \qquad \mathcal{B}_p \psi_p = 0.$$

For other sets of boundary conditions and comparisons with other plate theories, see Hansen[5]).

The system of equations (16) is a generalization of the *interfacial slip* model in Hansen[5] in which only one adhesive layer is present. The "interfacial slip" refers to the variables δ_a, which can be viewed as small interfacial slips between the *plate layers* once the limit (13) has been passed. Alternatively, δ_a can be viewed as a measure of the shear in the adhesive layers, if one considers those layers to have positive thickness.

An important property is that the limit in (13) is in fact a *regular perturbation*, that is, the perturbation does not greatly change the solution, provided that these parameters were sufficiently small to begin with. (The proof of this will appear in a later paper.) As a consequence of this, the regularity properties, spectral properties, wave speeds, etc., of the the model (16) are the nearly the same as that of the original model (11).

3.3. Limit model for stiff plate layers

Due to the fact that the adhesive layers have a small shear modulus in comparison to the plate layers, most of the shear motions will occur within the adhesive layers. This suggests that the solutions would not be greatly different if the shear stiffnesses of the plate layers were taken to be infinite.

However, unlike the previous limit, letting the shear stiffness tend to infinity results in a *singular perturbation* and it is not obvious that limiting solutions (if any) are close to (in some sense) solutions of the original system. Furthermore, it is not obvious how one formally obtains a limiting form of the system (16).

However, this problem has been carefully analyzed in Hansen[5] for the case of one adhesive layer and the same basic reasoning applies for this case. One begins by considering a sequence of solutions to the previous system corresponding to increasingly large values of shear stiffness in each layer. The initial data are fixed and such that no energy is stored in shear. By energy estimates one can prove that the sequence of solutions converges in a certain weak sense to a unique limit, which is itself the solution of a certain limiting problem. A detailed discussion of this is impossible here, so we simply indicate the steps one takes to obtain this limiting problem.

Step 1: First, drop the term in a_a involving $\mathbf{G}_p$. (See (8).) This is due to the fact that in the limit, the amount of energy in shear motions of the plate can be shown to go to zero.

Step 2: Second, set $\delta_p = -\mathbf{h}_a \vec{\nabla} w$ in the bilinear forms a_a, a_p, c_p. (Recall that $\vec{\nabla} w$ is the matrix with $(\nabla w)^T$ in each row.) This corresponds to the fact that in the limit all shear motions are eliminated in the plate layers.

Before writing down the limiting form of the bilinear forms, note that the only material property remaining from the adhesive layers is γ. All other material parameters are from plate layers. Therefore we will henceforth omit the subscript b as it is understood. Likewise we will refer to δ_a simply as δ. One finds that

$$\begin{aligned} c &\to (\mathbf{h}\cdot\mathbf{p}w, \hat{w})_\Omega + \tfrac{1}{12}(\mathbf{p}\mathbf{h}^3\vec{\nabla} w, \vec{\nabla}\hat{w})_\Omega - (\mathbf{h}A^T\mathbf{h}\mathbf{p}v_p, \vec{\nabla}\hat{w})_\Omega + (C^T\mathbf{h}\mathbf{p}v_p, \hat{\delta})_\Omega \\ a &\to a_{0,b}(\mathbf{h}^3\vec{\nabla} w, \vec{\nabla}\hat{w})_\Omega + 12a_{0,b}(\mathbf{h}v_p; C\hat{\delta} - a\mathbf{h}\vec{\nabla}\hat{w}) + (\gamma\delta, \hat{\delta})_\Omega. \end{aligned}$$

Step 3: Let us denote by $\vec{1}$ the column vector consisting of n 1's, so that $\vec{\nabla} w = \vec{1}\nabla w$. An integration by parts in t of (9) followed by an application of the Green's formula (10) leads to the following:

$$\mathbf{h}\cdot\mathbf{p}\ddot{w} - \operatorname{div}\vec{1}^T\frac{\rho\mathbf{h}^3}{12}\vec{1}\nabla\ddot{w} + \operatorname{div}\vec{1}^T\mathbf{h}A^T\mathbf{h}\rho\ddot{v}_p + \operatorname{div}\vec{1}^T L\mathbf{h}^3\vec{1}\nabla w - 12\operatorname{div}\vec{1}^T L\mathbf{h}A^T\mathbf{h}v_p = 0 \tag{17}$$

$$C^T\mathbf{h}\rho\ddot{v}_p - 12LC^T\mathbf{h}v_p + \gamma\delta = 0. \tag{18}$$

where $v_p = C\delta - A\mathbf{h}\vec{1}\nabla w$.

In the case of simply supported boundary conditions with no applied moments acting on the adhesives on Γ (the boundary), the boundary conditions are

$$w = 0, \qquad \mathcal{B}C^T\mathbf{h}v_p = 0, \qquad \vec{1}^T\mathbf{h}^3\mathcal{B}\vec{1}\nabla w\cdot n - (12)\vec{1}^T\mathbf{h}\mathcal{B}A^T\mathbf{h}v_p = 0, \qquad \text{on } \Gamma.$$

In the case of a single adhesive layer, the system (17), (18) reduces to one obtained by similar means in Hansen.[5] System (17), (18) is also related to the Kirchhoff plate model in some limiting cases we discuss below.

First let us examine the limiting behavior as the adhesive stiffness of each adhesive layer tends to ∞.

3.3.1. Limit as $\gamma \to \infty$

As $\gamma \to \infty$ the shear motions in the adhesive layers become increasingly penalized and in the limit such motions would imply infinite energy. This suggest simply putting $\delta = 0$ in (17) to obtain the limiting system. However, again, this limit results in a singular perturbation and consequently it is not obvious that limiting solutions (if any) are close in any sense to those of the initial system. Nevertheless, by an analysis similar to one in Hansen[5] it can be shown that one obtains convergence of solutions in a certain weak star topology. Roughly speaking, solutions will not converge in any pointwise sense, but only in the sense of averaging.

Putting $\delta = 0$ in (17) and simplifying, we obtain

$$m\ddot{w} - \alpha_\infty\Delta\ddot{w} + K_\infty\Delta^2 w = 0 \tag{19}$$

where

$$m = \sum_{i=1}^{n} h_i\rho_i, \quad \alpha_\infty = \vec{1}^T(\frac{\rho\mathbf{h}^3}{12} + \mathbf{h}A^T\mathbf{h}\rho A\mathbf{h})\vec{1}, \quad K_\infty = \vec{1}^T(\mathbf{D}\mathbf{h}^3 + 12\mathbf{D}\mathbf{h}A^T\mathbf{h}A\mathbf{h})\vec{1}. \tag{20}$$

In the case where $\rho_i = \rho_0$, all i, (same density of each beam layer) $m = \rho_0\tau/2$, where $\tau = 2\sum_{i=1}^n h_i$ is the total thickness of the beam, and $\alpha_\infty = (1/2)\rho_0\tau^3/12$ is the half of the mass moment of inertia of the beam. If $D_i = D_0$, all i, then $K = D_0\tau^3/2$ is half the stiffness of the beam. (Our factor of 1/2 appearing in all terms is due to calculating the energy of the upper half of the plate.)

Thus as the adhesive becomes increasingly stiff, if the densities and Young's moduli of each layer are the same, the system (17), (18) reduces to the usual Kirchhoff plate. In more general cases where the densities or Youngs' moduli of the layers are not constant the expressions for m, α_∞ and K_∞ give the effective constants for (half of) the longitudinal inertia, rotational inertia and stiffness, respectively, for a layered plate in which the layers are perfectly bonded to one another.

3.3.2. Limit as $\gamma \to 0$

Let us now consider the limiting behavior as $\gamma \to 0$. Physically, when there is no (or very little) adhesive bonding the layers, the moment of inertias of the layers are no longer coupled and the stiffness the entire beam should reduce to the sum of the stiffnesses of each layer. Indeed this is what one finds.

If $\gamma = 0$ there is no resistance to shear in the adhesive layers, and hence the term due to shear potential energy in (8) will vanish. In this case (18) reduces to a hyperbolic PDE with (assuming simply supported boundary conditions) homogeneous boundary conditions. Assuming initial conditions such that v and $\dot{v}$ are zero at time zero, the unique solution of this system is the zero function. Putting $v_p = 0$ into (17) results in

$$\frac{1}{2}(m_0\ddot{w} - \alpha_0\Delta\ddot{w} + K_0\Delta^2 w) = 0 \tag{21}$$

where

$$m_0 = \sum_{i=1}^{n} h_i\rho_i, \quad \alpha_0 = \frac{1}{12}\sum_{i=1}^{n}\rho_i h_i^3, \quad K = \sum_{i=1}^{n} D_i h_i^3. \tag{22}$$

Thus term m_0 remains the same, the moment of inertia term α_0 reduces to the sum of the moments of inertia of each layer, while K_0 becomes the linear sum of the stiffnesses of each layer.

In the case where $\rho_i = \rho_0$, all i, (same density of each beam layer) $m = \rho_0\tau$, where $\tau = 2\sum_{i=1}^{n} h_i$ is the total thickness of the beam, and $\alpha_0 = \rho_0\tau^3/12$ is the mass moment of inertia of the beam. If $D_i = D_0$, all i, then $K = D_0\tau^3$ is the stiffness of the plate.

3.4. Long wave approximation

If the plate layers are very thin, or if the frequencies of vibration are not too high, then the rotational inertia of the individual plate layers becomes negligible. Neglecting those inertial terms in (18) gives

$$\mathbf{h}\cdot\mathbf{p}\ddot{w} - \frac{1}{12}\operatorname{div}\vec{1}^T\rho\mathbf{h}^3\vec{1}\nabla\ddot{w} + \operatorname{div}\vec{1}^T\mathbf{h}A^T\mathbf{h}\rho\ddot{v}_p + \operatorname{div}\vec{1}^T L\mathbf{h}^3\vec{1}\nabla w - 12\operatorname{div}\vec{1}^T L\mathbf{h}A^T\mathbf{h}v_p = 0, \tag{23}$$

$$-12LC^T\mathbf{h}v_p + \gamma\delta = 0 \tag{24}$$

where $v_p = C\delta - A\mathbf{h}\vec{1}\nabla w$.

We have retained the rotational inertia term in (23) since this reflects the net rotational energy of the entire laminated plate.

With the inertial terms gone, (24) is an eliptic system in which δ may be determined in terms of $\vec{\nabla}w$, and consequently $\operatorname{div}\delta$ can be determined in terms of Δw. Once this is substituted back in (23), a scalar equation results.

3.4.1. Plate layers made out of the same material

The system (23), (24) is simplest to analyze in the case where the plate layers are made out of the same material. It does not matter if the adhesive stiffnesses or thickenesses vary from layer to layer. So assume that

$$D_i = D_0, \qquad \rho_i = \rho_0, \qquad i = 1, 2, \ldots n$$

Under these assumptions one obtains

$$\operatorname{div}\delta = C^{-1}(\Delta I - \Gamma)^{-1}A\mathbf{h}\vec{1}\Delta w \qquad \text{where } \Gamma = (12DC^T)^{-1}\gamma C^{-1}$$

Thus

$$\begin{aligned}\operatorname{div} v_p &= C\operatorname{div}\delta - A\mathbf{h}\vec{1}\Delta w \\ &= (\Delta I - \Gamma)^{-1}\Delta A\mathbf{h}\vec{1}w - A\mathbf{h}\vec{1}w = [(\Delta I - \Gamma)^{-1}\Delta - I]A\mathbf{h}\vec{1}w \\ &= [(\Delta I - \Gamma)^{-1}A\mathbf{h}\vec{1}]\Delta w =: -PA\mathbf{h}\vec{1}\Delta w.\end{aligned}$$

Therefore the plate system (23, (24) becomes

$$m\ddot{w} - \alpha\triangle\ddot{w} + K\triangle^2 w = 0, \tag{25}$$

where

$$\begin{aligned} m &= \mathbf{p}\cdot\mathbf{h} = \textstyle\sum_{i=1}^{n} \rho_i h_i = \rho_0 h/2 \\ \alpha &= \vec{1}^T \tfrac{1}{12}\mathbf{p}\mathbf{h}^3\vec{1} + \vec{1}^T\mathbf{h}A^T\mathbf{h}\mathbf{p}PA\mathbf{h}\vec{1} \\ K &= \vec{1}^T\mathbf{D}h^3\vec{1} + 12\vec{1}^T\mathbf{D}\mathbf{h}A^T\mathbf{h}PA\mathbf{h}\vec{1}. \end{aligned}$$

Thus for the case in which all the plate materials are the same, the system reduces to one which resembles a standard Euler-Bernoulli beam, although the coefficients α and K contain the operator P.

Let us examine the operator P more closely. Suppose (λ_k), $k = 1, 2, \ldots$ are the eigenvalues of $\triangle$, arranged in nondecreasing order and let ϕ_k denote the corresponding eigenfunctions. In one dimension, $\lambda_k = -k^2\pi^2/(L^2)$ and $\phi_k = \sin(k\pi x/L)$, where L is the length of the interval. If $|\lambda_k|$ is small (low frequencies) then

$$P\phi_k = -(\triangle I - \Gamma)^{-1}\Gamma\phi_k \approx I\phi_k = \phi_k \qquad \text{(low frequency approximation)}.$$

That is, at a low enough frequency Γ is more dominant that $-\triangle I$ and hence $P \approx I$. On the other hand, as λ_k gets large, $\triangle I$ must dominate and

$$P \to 0 \qquad \text{(high frequency approximation)}.$$

Thus, we can make the following observations.

At very low frequencies, the rotational inertia parameter α and the stiffness parameter K tend to the values in (20), which correspond to the case in which the adhesive is infinitely strong. Of course, the degree of similarity is limited, due to the fact that the lowest eigenvalue may still be quite large.

As the frequency increases, P tends to zero, and hence α and K tend to the values in (22), which is simply the linear sum of the rotational inertias and stiffnesses of each layer. Thus at higher frequencies the multilayer plate (23), (24) becomes increasingly flimsy. However, it should be kept in mind that P was obtained by throwing out the dynamics in (18) (i.e., a long wave approximation) and (23), (24) should underpredict the stiffness, as compared to (17), (18).

4. Conclusions

In this preliminary report we have derived several models for laminated plates that are related by asymptotic limits. The value of this approach is that one can then compare solutions of the original high-order model (11) to the solutions of the low order model (21) and obtain useful estimates on range of validity of the low order model. Indeed, this has been carried out for the case of a beam with one adhesive layer.[7] We hope to examine the same problem for the case of multiple adhesive layers in the near future.

The adjustments necessary to include external forces and damping in the laminated plates are fairly minor. For the case of one adhesive layer see.[5,7]

For the free motion of the laminated plates we found that the system can be represented in the form

$$m\ddot{w} + -\alpha\ddot{\triangle}w + K\triangle^2 w$$

where the coefficients α and K depend upon the frequency. The expression we obtain for α and K predict that at low frequencies the effect of the adhesive is minor, and the plate vibrates almost as if the plate layers are perfectly bonded together. However as the frequency increases, the amount of shearing in the adhesive layers increases until at very high frequencies, the laminated plate (23), (24) vibrates almost as if the plate layers are moving independently. Of course the assumptions used to obtain (23), (24) break down at a high enough frequency and and the model 17 should be used instead.

REFERENCES

1. E. Reissner, "The effect of transverse shear deformations on the bending of elastic plates," *J. Appl. Mech.* **12**, pp. A69–A77, 1945.
2. R. Mindlin, "Influence of rotary inertia and shear on flexural motions of isotropic elastic plates," *J. Appl. Mech.* **18**, pp. 31–38, 1951.
3. C. T. Sun and Y. P. Lu, *Vibration Damping fo Structural Elements,* Prentice Hall, Englewood Cliffs, New Jersey, 1995.
4. S. W. Hansen, "A dynamical model form multilayered plates with independent shear deformations," *Q. Appl. Math., (to appear)* .
5. S. W. Hansen, "A model for a two-layered plate with interfacial slip," in *Estimation and Control of Distributed Parameter Systems: Nonlinear Phenomena*, F. K. W. Desch and K. Kunisch, eds., *Inter. Ser. Num. Math.* **118**, pp. 143–170, Birkhauser-Verlag, (Basel), 1994.
6. S. W. Hansen, "Models for structural damping due to interfacial slip," *J. Sound Vib. (to appear)* .

SESSION 6

Characterization of Damping Materials

Time Domain Characterisation of the Dynamic Properties of Viscoelastic Materials

S.O. Oyadiji and L. Chu
Dynamics and Control Research Group,
Division of Mechanical Engineering,
Manchester School of Engineering,
University of Manchester,
Manchester, M13 9PL, U.K.

ABSTRACT

By means of the split Hopkinson pressure bar (SHPB) technique, the time domain dynamic mechanical properties of a polyisoprene elastomer were characterised over a range of temperatures. These properties include the dynamic stress-strain and compressional relaxation modulus characteristics of the elastomer. In the SHPB technique employed in the measurements, two identical long steel bars, which are known as the incident and transmitter pressure bars, were used as wave guides. Solid disc specimens of 10 mm diameter by 3 mm and 6 mm thickness of the polyisoprene rubber were sandwiched, in turn, between the bars. Strain pulses were generated in the incident pressure bar by the collinear impact of a hardened steel spherical ball, which was fired from a mechanical launcher, with the plane free end of the incident pressure bar via a small cylindrical anvil which was attached to the impacted end of the incident pressure bar. The strain pulses generated and propagated down the pressure bar were incident on, reflected from and transmitted through the polyisoprene specimen. These pulses were monitored by PZT sensors of dimensions 5 mm x 3 mm, which were bonded to the middle locations of the pressure bars, and were used to derive the dynamic properties of the specimens. It is shown that the stress and compressional relaxation modulus characteristics of this elastomer undergo larger variations and attain higher values at low temperatures than at high temperatures.

Keywords : dynamic properties, viscoelastic materials, split Hopkinson pressure bar, relaxation modulus, stress relaxation technique

1. INTRODUCTION

Several methods have been developed for the characterisation of the dynamic mechanical properties of viscoelastic and polymeric materials[1,2,3]. Because most of the analytical/numerical computations associated with the applications of the dynamic mechanical properties of viscoelastic materials for vibration damping, vibration isolation and noise insulation are based in the frequency domain, most of the characterisation methods are also based in the frequency domain. However, for the computation of the transient shock isolation/response characteristics of viscoelastically-damped structures, the time domain relaxation moduli of the materials are required.

The time domain characterisation of the dynamic properties of a viscoelastic material can be done by one of two approaches. One approach involves the indirect determination of the time domain relaxation moduli from the frequency domain complex moduli of a viscoelastic material via the use of the Fourier transform procedure. Although this approach is rather cumbersome and involves magnification of errors, it is commonly used[4,5]. Another approach involves the direct determination of the dynamic properties of the viscoelastic material in the time domain via the use of a creep or a stress relaxation technique such as the split Hopkinson pressure bar (SHPB) technique.

The SHPB technique is a fast transient stress relaxation method of characterisation of the dynamic mechanical properties of materials[6-10]. It involves the use of a small solid disc of the material being characterised. This specimen of the material is sandwiched between two long metal bars as shown schematically in Figure 1. The bars are known as the incident and transmitter pressure bars and serve, essentially, as wave guides. They are usually made of high-strength steel. The specimen is often held in

SPIE Vol. 3045 • 0277-786X/97/$10.00

place between the bars by means of petroleum jelly whose primary function is that of a lubricant for minimising the interfacial frictional forces generated between the plane faces of the pressure bars and the specimen during the passage of a stress wave.

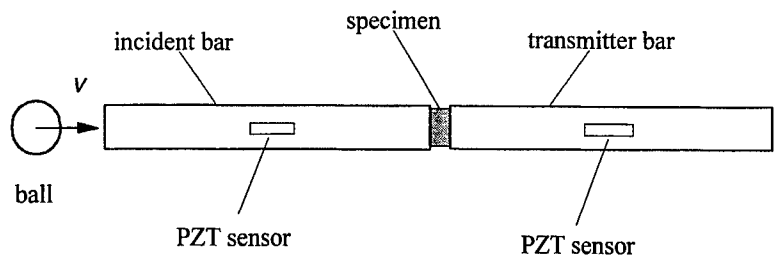

Figure 1 : Schematic representation of the compressive SHPB test set-up

By means of the collinear impact of a projectile with the plane free end of the incident pressure bar, a stress pulse is generated and propagated down the pressure bar. When the stress pulse reaches the interface of the incident pressure bar with the specimen, part of the pulse is reflected due to the difference between the mechanical impedances of the pressure bar and the specimen. The remaining part of the incident pulse is transmitted through the specimen and into the transmitter pressure bar. By means of strain sensors, which are mounted on each pressure bar at equidistant locations from the specimen, the incident, reflected and transmitted strains are monitored. Assuming that stress equilibrium exists throughout the specimen during the loading and unloading cycles, the dynamic stress-strain properties of the material of the specimen are derived from the measured strains.

In this paper, the SHPB method is used to characterise the dynamic stress-strain and relaxation modulus properties of two sets of specimens of polyisoprene rubber at different temperatures. In the application of the SHPB method by other workers[6-10], cylindrical projectiles were used. In the present work, a spherical steel ball was used as the projectile. The spherical ball projectile was fired from a launcher which impacted the desired impact velocity to the spherical ball. The ball impacted the free plane end of the incident pressure bar via a steel anvil. The strain pulses incident on, reflected from and transmitted through the rubber specimens were measured by means of small PZT sensors which were bonded to the middle locations of the incident and transmitter pressure bars. By means of a polynomial function, the measured dynamic stress-strain data is curve-fitted and differentiated to yield the compressional relaxation modulus of the polymeric material at several test temperatures.

2. SHPB THEORY

Figure 2 shows the vectorial representation of the strain pulses incident on, reflected from and transmitted through a specimen. The figure also shows the state variables and the associated geometry. The SHPB theory relates the stress σ_s and strain ε_s in the specimen to the measured reflected strain ε_R and strain rate $\dot{\varepsilon}_R$, and the measured transmitted strain ε_T. By the one-dimensional theory of elastic wave propagation,

$$u(t) = C_b \int_0^t \varepsilon(t)dt \tag{1}$$

where

$u(t)$ = displacements in the bar,

$\varepsilon(t)$ = measured strains,

C_b = elastic wave velocity of the bar

Displacement, $u_1(t)$, of the specimen face of the input bar is made up of both the incident strain pulse, $\varepsilon_I(t)$, travelling in the positive x direction and the reflected strain pulse, $\varepsilon_R(t)$, travelling in the negative x direction. Hence,

$$u_1(t) = C_b \int_0^t \varepsilon_I(t)dt + (-C_b) \int_0^t \varepsilon_R(t)dt$$

$$u_1(t) = C_b \int_0^t \{\varepsilon_I(t) - \varepsilon_R(t)\}dt \tag{2}$$

Similarly, the displacement, $u_2(t)$, of the specimen face of the output bar is obtained from the transmitted strain pulse, $\varepsilon_T(t)$, as :

$$u_2(t) = C_b \int_0^t \varepsilon_T(t)dt \tag{3}$$

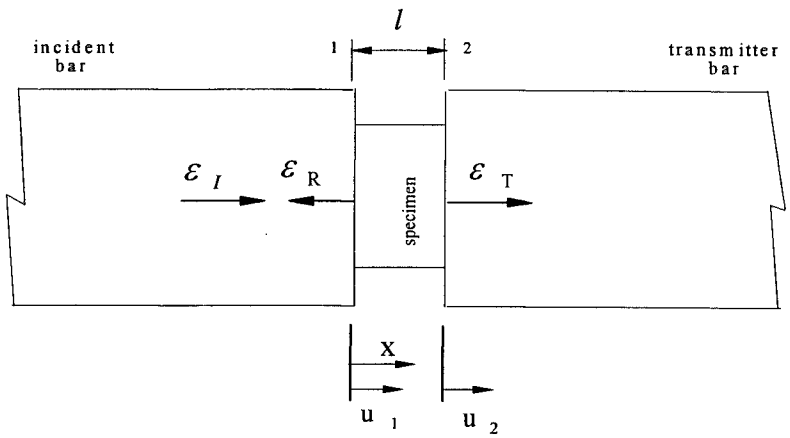

Figure 2 : Illustration of Strain Pulses in the SHPB System

The nominal strain in the specimen, $\varepsilon_S(t)$, is then given by:

$$\varepsilon_S(t) = \frac{u_1 - u_2}{l} = \frac{C_b}{l} \int_0^t (\varepsilon_I(t) - \varepsilon_R(t) - \varepsilon_T(t))dt \tag{4}$$

where l is the initial length of the specimen.

Assuming that the stress across the specimen is constant (an approximation which becomes exact as l approaches zero), then the net strain at the left and right end faces of the specimen will be equal. Thus,

$$\varepsilon_I(t) + \varepsilon_R(t) = \varepsilon_T(t) \tag{5}$$

Substituting in Eq. (4) gives

$$\varepsilon_S(t) = -\frac{2C_b}{l} \int_0^t \varepsilon_R(t)dt \tag{6}$$

Thus, the strain rate is obtained as

$$\dot{\varepsilon}_S(t) = -\frac{2C_b}{l} \varepsilon_R(t) \tag{7}$$

The applied forces $F_1(t)$ and $F_2(t)$ on each face of the specimen are

$$F_1(t) = EA[\varepsilon_I(t) + \varepsilon_R(t)] \tag{8}$$

$$F_2(t) = EA[\varepsilon_T(t)] \tag{9}$$

where E and A are the Young's modulus of elasticity and cross-sectional area of the pressure bars respectively. Thus, average stress in the specimen, $\sigma_S(t)$, is

$$\sigma_S(t) = E[\frac{A}{A_s}]\varepsilon_T(t) \tag{10}$$

where A_s is the cross-sectional area of the specimen.

It should be noted that in applying these equations, the measured strain pulses $\varepsilon_I(t)$, $\varepsilon_R(t)$ and $\varepsilon_T(t)$ are shifted in time such that they coincide at the specimen.

3. EXPERIMENTAL MEASUREMENTS

Solid disc specimens of dimensions 10 mm diameter by 3 mm and 6 mm thick were machined from a block of polyisoprene vulcanised rubber of international rubber hardness degree of 55. Each specimen was placed, in turn, between an incident and a transmitter steel pressure bars of 16 mm diameter of 1 m length as shown schematically in Figure 1. The ends of the pressure bars in contact with the specimen were polished so as minimise interfacial friction between the contacting faces of the specimen and the bars. In order to further reduce the interfacial friction, the interfaces between the plane surfaces of the specimen and the plane surfaces of the pressure bars in contact with the specimen were lubricated using petroleum jelly which has been shown to be very effective in minimising friction in SHPB tests[7].

Stress pulses were induced in the incident pressure bar by means of the collinear impact of a spherical steel ball on a polished steel anvil which was attached to the plane free end of the incident bar using petroleum jelly. The steel anvil was used in order to preserve the end of the incident pressure bar from local plastic deformation. Also, in order to ensure that plane waves are induced in the incident pressure bar and to ensure repeatability of tests, a newly polished steel anvil was used for each test. Each anvil was fixed to the plane free end of the incident pressure bar by means of petroleum jelly in order to minimise the interfacial frictional forces generated and, hence, to minimise the distortions of the incident stress pulse. The stress pulse induced in the incident pressure bar propagated to the other end of the bar where it was incident on, reflected from and transmitted through the specimen into the transmitter pressure bar.

A pair of small PZT sensors, of dimensions 5 mm x 3 mm, were bonded to the middle locations of each of the pressure bars. The pair of sensors on a bar were arranged in diametrically opposite positions and were used to monitor the incident, reflected and transmitted strain pulses. These pulses were sampled and recorded using a fast transient recorder card mounted in a PC. In order to cancel or minimise the effects of bending waves, the measured pulses from the pair of sensors on each pressure bar were averaged. The specimen and the portions of the pressure bars adjacent to the specimen were enclosed within a temperature-controlled environmental chamber which enabled the variation of the specimen temperature from -60 C to 100 C. The experimental procedure described above was repeated at each of the selected test temperatures within this range. Using the measured strain pulses, the stress-strain and compressional modulus relaxation properties of the elastomer were determined.

4. DISCUSSION OF RESULTS

A typical set of averaged pulses measured by the pair of PZT sensors on each of the pressure bars is shown in Figure 3. The top figure, Figure 3(a), shows the average of the pulses measured by the sensors on the incident pressure bar. The first pulse in Figure 3(a) is the compressive pulse incident (I) on the specimen while the second pulse is the tensile pulse reflected (R) from the specimen. Similarly, Figure 3(b) shows the compressive pulse transmitted (T) through the specimen. It is obvious that the compressive pulse transmitted through the specimen is less than the compressive pulse incident on the specimen. In Figure 3(c),

the reflected and transmitted pulses are compared. The time data of these two pulses were used in the equations above for the determination of the time domain dynamic properties of the specimen.

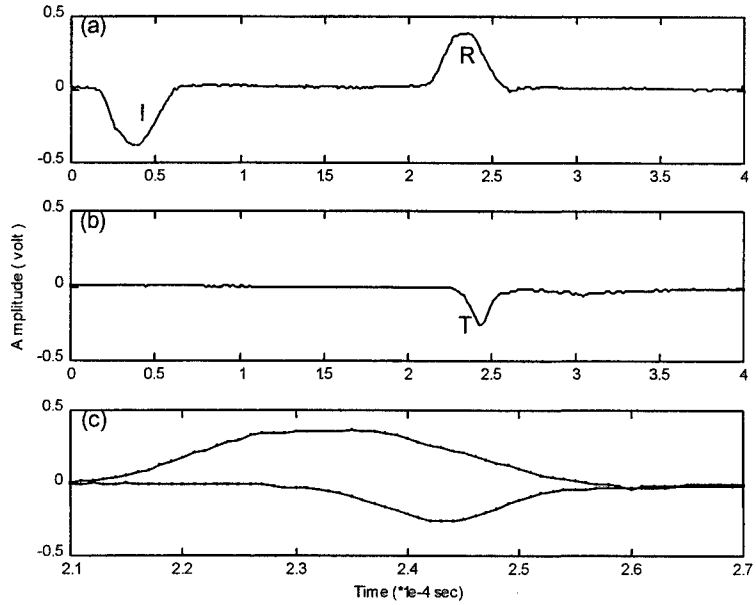

Figure 3 : Typical Measured Pulses, (a) Incident (I) and Reflected (R) Pulses Measured by the Incident Pressure Bar, (b) Transmitted (T) Pulse Measured by the Transmitter Pressure Bar, (c) Comparison of Measured and Curve-fitted Reflected and Transmitted Pulses (dotted line: measured, solid line: fitted).

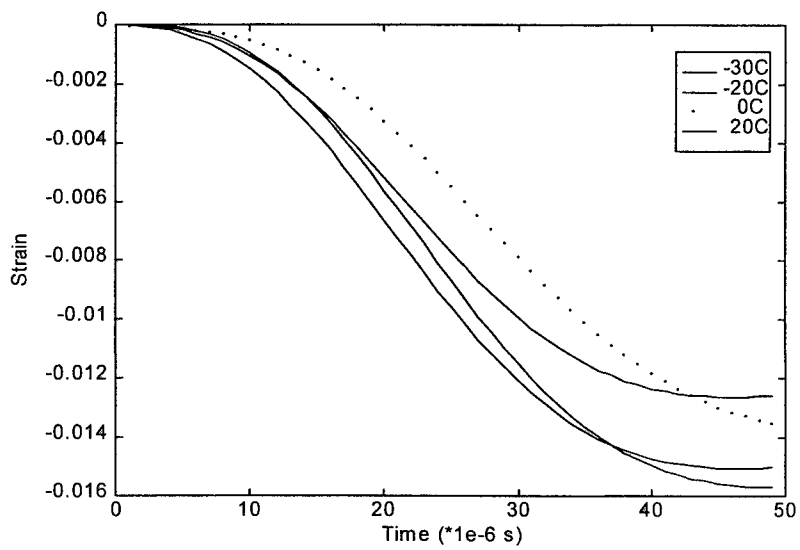

Figure 4 : Strain History for 6 mm Thick Polyisoprene Specimen at Various Temperatures (short dashes: -30 C, solid: -20 C, dotted: 0 C, chain: 20C).

Figure 4 shows a comparison of the initial portions of the induced strain histories of the 6 mm thick specimen at test temperatures of -30 C, -20 C, 0 C and 20 C. These strain histories were derived from the reflected strain pulses measured by the PZT sensors

on the incident pressure bar according to Eq.(6). It is obvious that the strain induced in the specimen is higher at the lower temperatures of -30 C and -20 C, at which the specimen is relatively stiffer, than at the higher temperatures of 0 C and 20 C. The figure also shows that the strain histories at -30 C and -20 C are quite similar. However, there is a slight difference between the strain histories at 0 C and 20 C which is probably due to the slight difference of the impact velocity of the spherical steel ball which was used to induce strain pulses in the incident pressure bar. It is also probable that the slight difference is partly due to the slight differences in the surface finish of the steel anvils used for converting the spherical waves induced at the impact point to a plane wave at the interface of the anvil with the incident pressure bar. During the tests, each of the steel anvils suffered permanent local plastic deformation at the point of impact. Thus, used anvils needed to be re-machined and re-polished for subsequent tests.

The corresponding stress histories of the 6 mm thick specimen, which were derived by using the transmitted strain pulses in Eq.(10), are shown in Figure 5. It is seen that the stresses induced in the specimen are much higher at the lower temperatures of -30 C and -20 C than at the higher temperatures of 0 C and 20 C. Furthermore, the figure shows that the stress induced in the specimen at -30 C and -20 C reaches maximum values of 600 kPa and 430 kPa, respectively, after the elapse of about 25 μs from the incidence of the pressure wave on the specimen. The corresponding values of stress induced in the specimen at 0 C and 20 C and at the same time instant are 80 kPa and 60 kPa, respectively. Thus, the specimen is much stiffer at the lower temperatures than at the higher temperatures as expected.

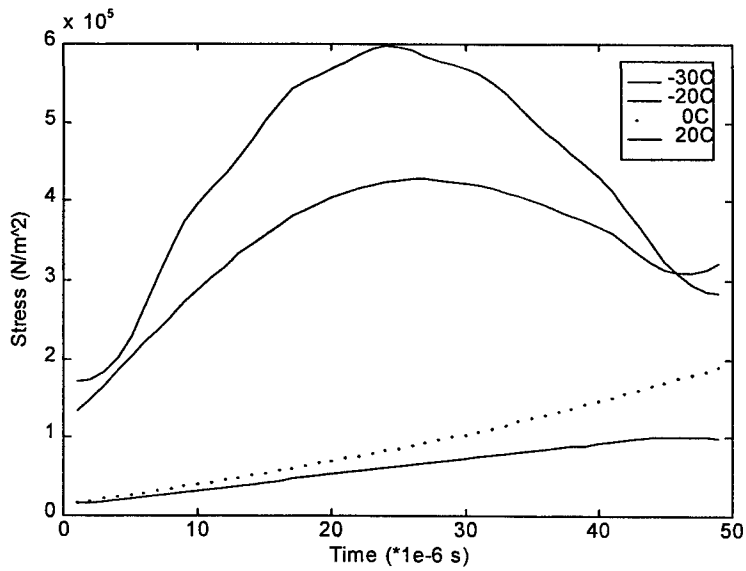

Figure 5 : Stress History for 6 mm Thick Polyisoprene Specimen at Various Temperatures.
(short dashes: -30 C, solid: -20 C, dotted: 0 C, chain: 20C).

The strain and stress histories shown in Figures 4 and 5 were combined to produce the dynamic stress-strain properties of the specimen at the four test temperatures as shown in Figure 6. From this figure, it is estimated that the stress induced in the specimen reached a maximum value of 600 kPa at -30 C and a compressional strain of 0.8 %, whereas the maximum stress induced at -20 C is 400 kPa and at a compressional strain of about 1.1 %. At 0 C and 20 C, it is seen that the values of the maximum stress induced in the specimen are lower. For the mean strain value of 0.8% used in these measurements, the stresses induced in the specimen are 600 kPa, 420 kPa, 105 kPa and 70 kPa at temperatures of -30 C, -20 C, 0 C and 20 C respectively. This implies that the specimen becomes progressively stiffer as the temperature decreases.

Since Figures 4 and 5 show the strain and stress relaxation behaviour of the specimen during the loading and unloading cycles, then Figure 6 which is derived from Figures 4 and 5 depicts the stress-strain relaxation characteristics of the specimen. By differentiating the stress-strain characteristics with respect to the strain, the compressional relaxation modulus properties of the

specimen are obtained. Figure 7 shows the resulting compressional relaxation modulus characteristics of the specimen which were derived at the four test temperatures. The figure shows that for these four temperatures, the specimen has the largest variation of its relaxation modulus at -30 C but the least variation at 20 C. The instantaneous moduli, that is the moduli at zero time, of the specimen at -30 C, -20 C, 0 C and 20 C are 550 MPa, 400 MPa, 100 MPa and 50 MPa respectively. Thus the instantaneous moduli at -30 C, -20 C and 0 C are factors of 11, 8 and 2 greater than the instantaneous modulus at 20 C.

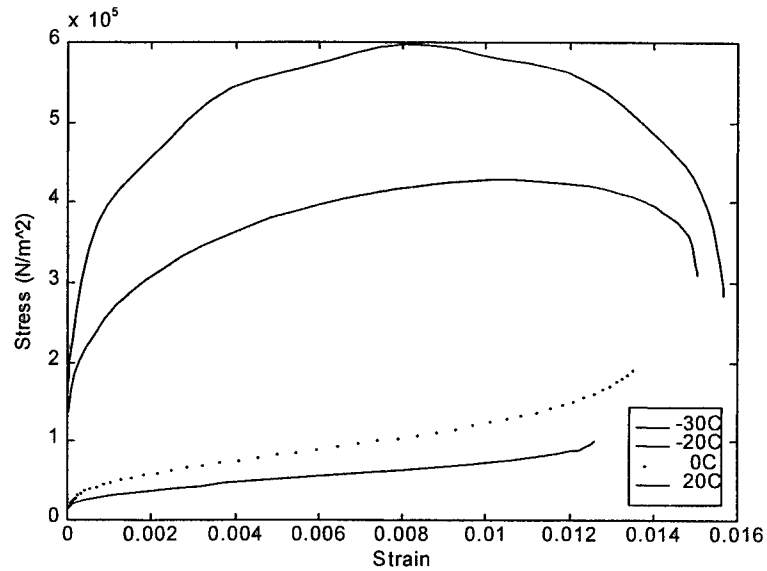

Figure 6 : Stress versus Strain for 6 mm Thick Polyisoprene Specimen at Various Temperatures. (short dashes: -30 C, solid: -20 C, dotted: 0 C, chain: 20C).

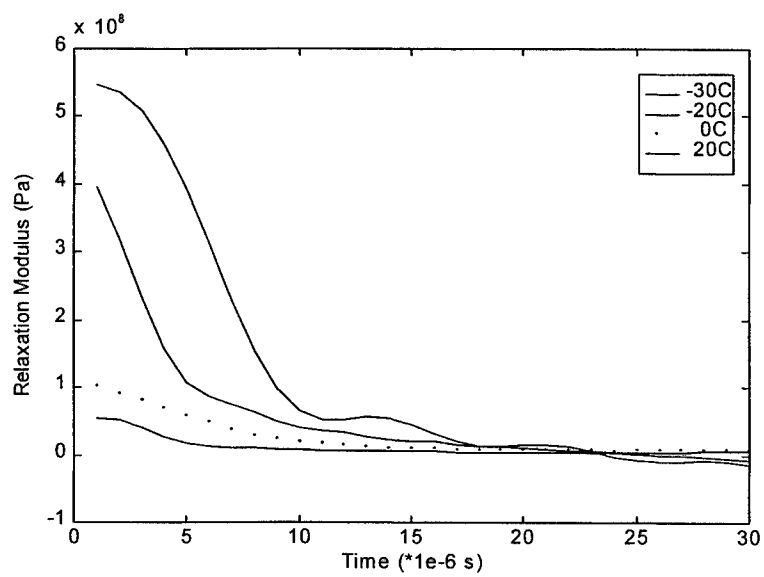

Figure 7 : Relaxation Modulus of 6 mm Thick Polyisoprene Specimen at Various Temperatures. (short dashes: -30 C, solid: -20 C, dotted: 0 C, chain: 20C).

From the relaxation modulus properties of the 6 mm thick specimen, which were derived at other temperatures within the range of -60 C to 100 C, the instantaneous compression modulus values were determined. The variation of these instantaneous compression modulus of the specimen with temperature is shown in Figure 8. It is seen that between -60 C and -50 C, the instantaneous modulus of the specimen decreases very slightly from a value of 5650 MPa at -60 C to a value of 5600 MPa at -50 C. However, as the temperature increases from -50 C to -40 C, the instantaneous modulus decreases sharply to a value of 1200 MPa at -40 C. This is due to the transition of the material behaviour of the specimen from a glassy to a rubbery behaviour. Thus, the glass-to-rubber transition temperature of the specimen is within the range -50 C to -40 C.

As the temperature of the specimen is increased further beyond -40 C, the instantaneous modulus decreases further but at a slower rate. The numerical values of the instantaneous compression modulus of the specimen are approximately 150 MPa, 70 MPa, 50 MPa and 10 MPa at 0 C, 20 C, 40 C and 100 C respectively. Thus, it is seen that the instantaneous modulus of the elastomer decreases by a factor of more than 500 as the specimen temperature is increased from -60 C to 100 C. Also, it can be inferred that the polyisoprene elastomer exhibits glassy behaviour at temperatures below -50 C, whereas it exhibits rubbery behaviour at temperatures greater than -40 C. At temperatures between -50 C and -40 C, the characteristics of the elastomer are intermediate between glassy and rubbery behaviour.

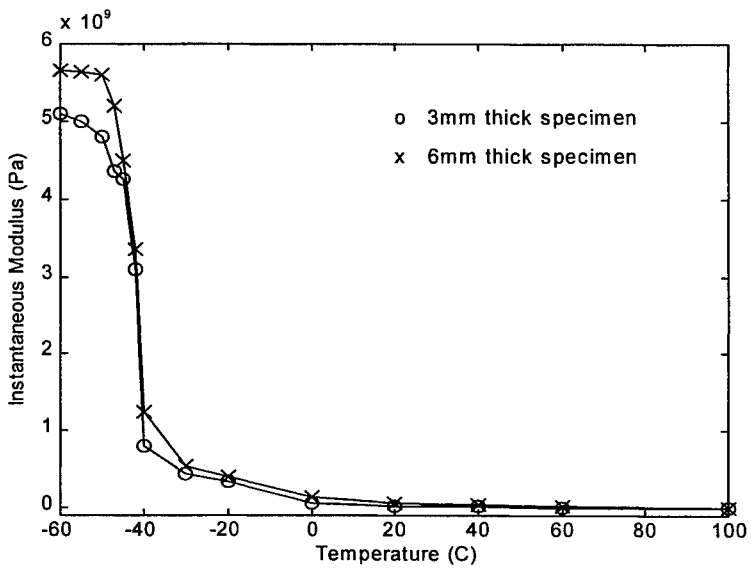

Figure 8 : Instantaneous Compression Modulus variation with Temperature for the 3 mm and 6 mm Thick Polyisoprene Specimens.

The variation of the instantaneous compression modulus of the 3 mm thick specimen with temperature is also depicted in Figure 8. It is seen that as the temperature increases from -60 C to -50 C, the instantaneous modulus obtained for this specimen decreases moderately from 5100 MPa to 4800 MPa. As the temperature increases to -40 C, the instantaneous modulus decreases sharply to 800 MPa indicating, again, that the material is undergoing a transition from glassy to rubbery behaviour within the temperature range of -50 C to -40 C. Increasing temperature leads to further reduction in the value of the instantaneous modulus.

Comparing the characteristics of the two specimens, it is seen that the instantaneous modulus of the 6 mm thick specimen is generally greater than that the instantaneous modulus of the 3 mm thick specimen at the various test temperatures. However, the instantaneous modulus of the two specimens should be identical at all temperatures. The discrepancy is due to the differences in the effects of interfacial friction and of, especially, differences in internal wave effects which are caused by differences in the inertia and geometry of the specimens.

5. CONCLUSIONS

The dynamic mechanical properties of two cylindrical specimens of polyisoprene rubber have been characterised by means of the split Hopkinson pressure bar (SHPB) method. It was shown that the stress and compressional relaxation modulus characteristics of this elastomer show larger variations and attain higher values at low temperatures than at high temperatures. The results show that the elastomer has its glass-to-rubber transition temperature within the range -50 C to -40 C. Also, the results show that the elastomer exhibits glassy behaviour at temperatures below -50 C, whereas it exhibits rubbery behaviour at temperatures greater than -40 C. At temperatures between -50 C and -40 C, the characteristics of the elastomer are intermediate between glassy and rubbery behaviour. Furthermore, the instantaneous modulus of the elastomer at -60 C is greater than the instantaneous modulus at 100 C by a factor of more than 500. In general, the accuracy of the dynamic properties of a sample of a material measured by the SHPB method depends on the elimination/minimisation of interfacial frictional effects and minimisation/correction of the effects of internal waves in the sample.

REFERENCES

1. J.D. Ferry, Viscoelastic Properties of Polymers, John Wiley & Sons, New York, 3rd Edition, 1980.
2. B.E. Read and G.D. Dean, The Determination of Dynamic Properties of Polymers and Composites, Adam Hilger Ltd, Bristol, 1978.
3. A.D. Nashif, D.I.G. Jones and J.P. Henderson, Vibration Damping, John Wiley & Sons, New York, 1985.
4. N .W. Tschoegl, The Phenomenological Theory of Linear Viscoelastic Behaviour: An Introduction, Springer-Verlag, Berlin, 1989.
5. S.O. Oyadiji, K.T. Feroz and G.R. Tomlinson, "Design of Polymer-Based Mechanical Filters for Shock Measurement Accelerometers", in Smart Structures and Materials 1996: Passive Damping and Isolation, C. D. Johnson, Editor, Proc. SPIE 2720, pp 305-316, 1996.
6. H. Kolsky, An Investigation of the Mechanical Properties of Materials at very High Strain Rates of Loading, Proc. Phys. Soc. 62B, pp 676-700
7. S. M. Walley, J.E. Field, P.H. Pope and N.A. Safford, The Rapid Deformation Behaviour of Various Polymers, Journal de Physique III France 1, pp 1889-1925, 1991.
8. N .N. Dioh, P.S. Leevers and J.G. Williams, Thickness Effects in Split Hopkinson Pressure Bar Tests, Polymer, 34(20), pp 4230-4234, 1993.
9. D. J. Parry, P.R. Dixon, S. Hodson and N. Al-Maliky, Stress Equilibrium Effects within Hopkinson Bar Specimens, Journal de Physique IV, pp C8:107-C8:112, 1994.
10. A.M. Bragov and A.K. Lomunov, Methodological aspects of Studying Dynamic Material Properties using the Kolsky Method, Int. J. Impact Engng, 14(2), pp321-330, 1995.

SESSION 7

System Applications of Passive Damping and Isolation

Durability patch: application of passive damping to high cycle fatigue cracking on aircraft

Lynn Rogers(1), I.R. Searle(2), R. Ikegami(2), R.W. Gordon(3), and D. Conley(3)

(1) CSA Engineering, Inc.; 2850 West Bayshore Road; Palo Alto, CA 94303
(2) Boeing Defense & Space Group
(3) US Air Force/Wright Lab/FIB; WPAFB, OH 45433

ABSTRACT

Although high-cycle fatigue cracks in secondary structure are often termed "nuisance cracks", they are costly to repair. Often the repairs do not last long because the repaired part still responds in a resonant fashion to the environment. Although the use of visco-elastic materials for passive damping applications is well understood, there have been few applications to high-cycle fatigue problems because the design information: temperature, resonant response frequency, and strain levels are difficult to determine. The Damage Dosimeter, and the Durability Patch are an effort to resolve these problems with the application of compact, off-the-shelf electronics, and a damped bonded repair patch. This paper will present the electronics, and patch design concepts as well as damping performance test data from a laboratory patch demonstration experiment.

Key words: Passive Damping, High-Cycle Fatigue, Bonded Repair, Cocuring, co-curing, viscoelastic material, composite material, finite element analysis, damping, modal strain energy.

1 SUMMARY

The Durability Patch Program addresses the restoration of structural integrity of cracked secondary structure induced by resonant high cycle fatigue. The program is based on adapting technology from three basic areas:

- bonded structural repair,
- vibration damping, and
- avionics.

These three areas each possess a large technology base and have achieved a threshold of maturity sufficient to support this program. A typical repair would be for a crack less than four inches long in 0.050 inch thick skin of the upper trailing edge of a wing. Nuisance cracking is a high maintenance and repair cost item. Typical sources of excitation are: pressure pulses from engine 1st stage compressor, jet engine exhaust, disturbed air flow behind stores, separated flow on upper wing, air flow around open cavities, propeller tip vortices, etc. Typical locations of nuisance cracking are: flap skins, spoiler skins, rudder skins, aileron skins, weapon bay doors, wing trailing edges, etc. Of course there are other possible causes of cracking in secondary or lightly loaded structure besides resonant high cycle fatigue.

Acknowledgement: Support of the US Air Force is gratefully acknowledged.

2 HIGH CYCLE FATIGUE

High cycle fatigue life and crack growth rates are key disciplines in evaluating the longevity of structural repair. Methodology for calculation of resonant high cycle fatigue (HCF, sometimes called sonic fatigue or acoustic fatigue) life and associated crack growth rates used here is well established and consistent with standard industry practice.[12345] It has been found that, in most cases, the HCF damage is due to linear resonant response in a single vibration mode; this implies that the vibratory stress is a narrow band random process. The threshold for number of cycles for high cycle fatigue is 10e6 (1,000,000) cycles. Fatigue consists of crack initiation, propagation and final rupture. The termination of the crack initiation phase is somewhat arbitrary since it depends on what is detectable and on what is acceptable in service. The basis for fatigue calculations is the S-N curve

$$S_{RMS} = S_{UHCF} N^b; N = (S_{RMS}/S_{UHCF})^{1/b} \tag{1}$$

where S_{RMS} is the rms stress, the coefficient S_{UHCF} may be considered to be a hypothetical ultimate rms high cycle fatigue stress which would cause failure at the first cycle, N is the fatigue life in number of cycles, and b is the Basquin parameter or exponent. This equation is a straight line when log-log scales are used for stress as a function of life. For 2024 aluminum the value of the exponent (Basquin parameter) is 0.1772 and the value of the coefficient is (98.26 ksi); for these values, a stress improvement factor (SIF) of 2 results in a life improvement factor (LIF) of 50, and fatigue strengths of (8.5 and 2.5 ksi) at 10e6 and 10e9 cycles respectively. Other aluminum alloys are not much different. Since HCF begins at 10e6 cycles, the upper threshold of interest for most aluminums is (8.5 ksi) rms, or a strain of 850 micro strain rms. This corresponds to approximately 3000 micro strain peak. Because of stress concentrations, uncertainties in locating strain gages, and averaging effects, measured strains are somewhat less.

It is envisioned that because of the existence of a crack, the life is known and the baseline or unrepaired stress level may be calculated; one objective is to reduce the stress level such that life is enhanced. Stress levels will be reduced through beef-up and through vibration damping using viscoelastic materials(vem's). The rms stress level is approximately proportional to the square root of modal damping; consequently, damping is a very useful approach for significant vibratory stress reduction. It happens that modal damping is dependent on the dynamic mechanical properties of the vem's, which in turn are dependent on service temperature and vibration frequency. It is therefore necessary to determine the vibration frequency and temperature at which damage accumulates in service. It is assumed that the temperature and stress time histories are available at the location of chronic nuisance cracking.

The analysis is performed for the i-th frequency band, the j-th temperature band, and the k-th time increment. If Φ is the Power Spectral Density (PSD) of stress, the rms stress is given by the square root of the area under the PSD curve.

$$S_{RMS} = \left[\int_{f_l}^{f_h} \Phi(f)\, df \right]^{1/2} \tag{2}$$

It may be desirable to calculate the contribution of one third octave (or other) bands

$$\varphi_{ik} = \left[\int_{f_{li}}^{f_{hi}} \Phi(f)\, df \right]^{1/2} \tag{3}$$

In this case, the rms is the square root of the sum of squares, but, because the response is dominated by only one

vibration mode, it may be represented by any of the following, including the sum or a single term

$$S_{RMS} = \left[\sum_{i=1}^{N_i} \varphi_{ik}^2\right]^{1/2} \cong \sum_{i=1}^{N_i} \varphi_{ik} \cong \varphi_{ik\max} \tag{4}$$

By substituting this expression for rms stress into the S-N curve, the fatigue life corresponding to that stress level may be found

$$N_{ijk} \cong (\varphi_{ik}/S_{UHCF})^{1/b} \tag{5}$$

Cumulative damage from different stress levels or time increments may be calculated by using the Palmgren-Miner rule (see Rudder[1] p. 195)

$$d = \sum n/N \tag{6}$$

where N is the number of cycles to failure at the stress level S; n is the number of cycles actually experienced at stress level S, (n/N) is the damage due to the n cycles; and d is the cumulative damage; when $d = 1$ a fatigue failure is indicated.

Time histories of the temperature and the one third octave bands are recorded

$$T_k, \varphi_{i,k}; i = 1, \ldots, N_i; k = 1, \ldots, N_k \tag{7}$$

A function may be defined as unity or zero based on whether or not the temperature for the k-th time increment is within the j-th temperature band

$$\delta_{T_k,T_j} = \{ \begin{matrix} 1; \text{if } T_k \text{ in } T_j \text{ band} \\ 0; \text{otherwise} \end{matrix} \tag{8}$$

The cumulative damage is given by

$$d_{ij} = \sum_{k=1}^{N_k} n_{ijk}/N_{ijk} \tag{9}$$

The number of cycles is

$$n_{ijk} = f_i \Delta t_k \tag{10}$$

The fatigue life at this stress level would be

$$N_{ijk} = (\varphi_{ik}/S_{UHCF})^{1/b} \delta_{T_k,T_j} \tag{11}$$

with appropriate substitution the cumulative damage may be calculated as a function of vibrational frequency and temperature

$$d_{ij} = \sum_{k=1}^{N_k} f_i \Delta t_k (\varphi_{ik}/S_{UHCF})^{1/b} \delta_{T_k,T_j} = d_{ij}\left(f_i, \Delta T_j\right) \tag{12}$$

and the capability to obtain this from service is crucial to the success of this program. The Dosimeter described below addresses this requirement. The above is the cumulative fatigue damage algorithm; it is adapted from standard industry practice and is judged sufficiently accurate for present purposes.

The acoustic noise excitation is typically represented by a broad band random uniform pressure field having a spectral density

$$G_p\left(f_1\right) \tag{13}$$

at the fundamental resonance frequency of the skin panel. The spectral density of the response is integrated over the frequency domain to obtain the expression for the mean square stress (see Rudder[1] p194)

$$\overline{\sigma^2\left(t\right)} = \frac{\pi f_1 G_p\left(f_1\right)}{2\eta}\left(\frac{\sigma_0}{P_0}\right)^2 \tag{14}$$

where σ_0 is the static stress at the appropriate location produced by the uniformly distributed pressure P_0 and and η is the modal damping. (Some investigators use the fraction of critical viscous damping ratio.)

Substitution leads to an expression for the ratio of repaired and unrepaired (ie, baseline) fatigue lives

$$\left[\frac{N_R}{N_U}\right] = \left[\left(\frac{\eta_U}{\eta_R}\right) * \left(\frac{f_R}{f_U}\right) * \left(\frac{\sigma_{OR}}{\sigma_{OU}}\right)^2\right]^{1/2b} \tag{15}$$

The above apply to total fatigue life; it is also desired to quantify unrepaired and repaired crack growth rates of existing cracks. The quantity of primary importance which influences the growth rate in typical aircraft skin structural materials of a fatigue crack is the variation of the crack tip stress intensity factor and the Paris equation is used

$$\frac{da}{dN} = C\Delta K_{RMS}^n \tag{16}$$

The parameters C and n are material properties. Most of the work has been done for centrally cracked thin sheets subjected to cyclically varying inplane loads, whereas here the interest is in edge cracked panels subjected to flexural loading or bending. Byrne[2] has arrived at the expression

$$K = 0.8\sigma_\infty a^{1/2} \tag{17}$$

for an edge cracked semi-infinite plate deformed into a cylindrical shape(ie, cylindrically bent). Different methods to calculate stress intensity, including FEA, will be considered.

3 SURVEY

In the interests of determining the nature and extent of maintenance and repair costs as a result of nuisance cracking, 126 copies of a survey letter were sent to structural sheet metal shops on flight lines. Additionally, expert personnel visited four flight lines to further assess available facilities, equipment, and personnel skills. It was concluded that this type of maintenance and repair is not accurately and completely documented. Also, typically, the logistics structures engineers are not fully aware of the nature and extent of nuisance cracking.

It was learned that almost all cracks are discovered and repaired before they reach a length of 4 inches. Also, scheduled flying and alert status dominates maintenance and repair techniques. A wing commander would be reluctant to accept a new repair technique if it required significantly more manhours or clock time to implement. A typical small non-flush mechanically fastened sheet metal patch requires two manhours to complete. This is accepted as a target for the present Durability Patch effort.

4 DOSIMETER

The Dosimeter has been conceived to gather service environmental data with regard to suspected resonant hcf cracks as economically as practical. Dosimeter requirements are that service data be gathered, processed and stored to permit

1. the design of a damping treatment (which requires the knowledge of the vibration frequency and temperature at which damage is being accumulated iin service)
2. a valid quantative comparison of structural life before and after Dpatch installation, and
3. any convenient additional diagnostic information.

The Dosimeter is a key component of the process to design and install the most effective patch possible. In order to provide this function the dosimeter must meet several goals:

- The dosimeter should be simple to install/dis-install on a widest practical variety of aircraft and locations.
- The dosimeter should measure high frequency strain and temperature while the aircraft is operational.
- The dosimeter should operate autonomously.
- The dosimeter should be "affordable".

To meet these goals the approach includes:

- Building the dosimeter from commercial off-the-shelf parts. This enables the construction of a dosimeter that is low-cost yet small enough that it can be installed on most aircraft for most hcf locations.
- Packaging the sensors, processor, and battery separately. The dosimeter design allows for a generous cable run (up to 50 feet) between the sensors (dynamic strain and temperature) and the processing/storage unit. The dosimeter power source is a battery, so that the dosimeter can operate autonomously. The battery will be packaged separately so that each package (battery and processor/storage unit) can be as small as possible, allowing more latitude in dosimeter installation. Additionally, this allows the battery size to be adjusted in the future as requirements (operational times) changes.

- Utilizing state of the art programmable digital signal processor (DSP) computer chips. This allows the dosimeter to function autonomously, by waking up at regular intervals, and statusing the sensors for significant activity. Similarly, the dosimeter puts itself into a sleep-mode when sensor activity has been insignificant for some predetermined period of time. A C-programmable DSP also offers the advantage of configurability by downloading new programs via the dosimeter's serial port.

These concepts have been used for the preliminary design of a prototype dosimeter processing/storage unit.

This design has enough processing and memory capacity (a minimum of 1 mega-byte) to provide sufficient flexibility in computing the necessary design information for patch design. At present the procedure for using the dosimeter can be outlined as follows:

- **Installation** of the dosimeter. The sensors are bonded to the damage prone area. The dosimeter can be installed on an aircraft with, or without an existing HCF crack. Without is preferred since the patch can be most effective as a preventive measure.

  Once the sensors, dosimeter processor/storage unit, and battery are installed, the dosimeter is powered on. There will be status LEDs to indicate that the dosimeter is in a powered standby state, ready to begin data collection.

- **Data-Collection** is performed autonomously as the aircraft is operated throughout a 3-10 day period. The dosimeter takes a single sample of strain data from the sensor. If the sensor RMS levels are significant, the dosimeter powers up, and records data until sensor activity reduces to insignificant levels.

  The dosimeter records a time-history of strain each second, and processes the time-history for the remainder of each second. This method is valid as long as peak value strain detection is not important, which is the case with HCF cracking problems. Typically the structure is responding in a steady-state fashion. From each time-history, the RMS strain in certain 1/3 octave bands is computed, along with minimum, and maximum strain values and temperature. These data are saved in memory, along with "typical" and worst-case sample strain time-histories. If the dosimeter's memory should ever become full the dosimeter will power itself down so that the gathered data can be downloaded.

- **Data-Removal** is performed over a serial-port with a laptop computer. At this point the dosimeter can be removed from the aircraft, or left installed to verify that the newly designed durability patch meets its performance goals.

The maximum overall level is not expected to exceed 3000 micro strain peak. The frequency range of interest is from 44.7 Hz (the lower limit of the 50 Hz band) to 2239Hz (the upper limit of the 2000 Hz band). It is required that the dosimeter be mounted on the aircraft so as to remain in place after high g loading; damage to dosimeter and to aircraft is acceptable as a result of any high g loading. The dosimeter is designed such that it will not be intrusive on operations.

5 BONDED REPAIR

The technology base for application of bonded repairs to aircraft structure has achieved a threshold of maturity sufficient to support this effort. Structural repair materials, structural adhesives, surface preparation techniques, design methods, and installation processing and procedures are well established. There are many applications performing satisfactorily in service, many of which are for primary structure. Bonded repair technology is well documented.[6,7,8] One recommended design practice is that the patch match the extensional membrane stiffness of the baseline structure in order to avoid load attraction or shedding. Single sided repair results in eccentricity of load which induces bending stresses which must be accommodated.

The design concepts for patches used in bonded repair of primary structure are monolithic and laminated. Structural patch materials are aluminum, fiber metal laminate (FML, eg, GLARE, an aluminum and FG laminate), graphite fiber/epoxy prepreg, and boron fiber/epoxy prepreg.

Applications of bonded repair to primary structure is far more demanding than applications to secondary structure, where there are no significant safety of flight concerns. However, some aspects of bonding are exacting.

6 DAMPING

Viscoelastic vibration damping technology has achieved a level of maturity sufficient to support this effort.[3] The stand off damping treatment configuration has been established as possessing very high modal damping performance, high weight efficiency, and significantly less dependent on temperature. Conventional constrained layer damping is flying in service in air flow on external surfaces, some with an edge sealant and some with their perimeter adhesively bonded. The highest practical levels of damping will be used; this will enhance the life of the repaired skin, and will also enhance the life of adjacent bays of skin and substructure. This approach is judged to be appropriate in the context of demonstrated opportunity for improvement in durability with respect to nuisance cracking. Often the intrinsic damping is low; this fact makes the structure more susceptible to resonant high cycle fatigue cracking. This fact also increases the benefits of damping because rms stress levels are highly dependent on modal damping. The dynamic magnification factor is inversely proportional to the square root of modal damping. The modal strain energy (MSE) has been established as the proper approach to calculate modal damping.[9,10,11]

7 CONCEPTS

The presumption here is that the Durability Patch will be a bonded repair; advantages and disadvantages of bonded and mechanically fastened repair are well established and documented[6,8] and will not be repeated here. A further presumption is that the installation of the bonded repair will be on the flight line at an operational base; this is considered to be somewhere between very challenging and unrealistic/impossible by many experts in bonded repair of primary structure. It is noted that the direct economic and technical consequences of extensive disbonding of a Durability Patch is minor and that this type of repair is a very low profile application. This situation may be used to good advantage in order to maximize benefits.

The fundamental purpose of the Durability Patch Program is to establish a repair technique for secondary structure (or other lightly loaded structure) which has been cracked due to sonic fatigue. The repair consists of restoration of structural integrity, which implies both static load carrying ability and life considerations. Very importantly, the Dpatch must offer an attractive option (relative to conventional techniques) to the potential user, or it will not be accepted. This means that it must be simple to install, require no more manhours than conventional repair, require no more clock time, no more requirements for aircraft environment, environmentally safe, etc. It must result in net cost savings with no adverse effects.

The following design philosophy points summarizes these factors:

- RESTORE STATIC CAPABILITY
- ENHANCE LIFE
- MINIMUM QUALITY ASSURANCE/INSPECTION
- COST SAVINGS
- EASE OF INSTALLATION

- AERODYNAMICALLY SMOOTH

To amplify on each of these points, the static capability of the structure must be restored. It is well known in bonded repair that the extensional membrane stiffness of the original skin should be closely matched to avoid load attraction and load shedding. Of course this is true only if the structure carries significant stress. Regardless, the repaired structure must be capable of carrying any applied loads. Since the existence of nuisance cracking demonstrates the opportunity for improvement in durability, the local flexural stiffness should be enhanced in order to better withstand loads.

The life of a properly designed and installed bonded repair will exceed the life of the undamaged baseline structure, although that is known to offer opportunities for improvement. The Dpatch must withstand moisture for decades, must reduce stress intensity and consequent crack growth rate, should reduce static stresses, and must reduce dynamic stresses. These points suggest no stress concentrations or hard points, vibration damping, and high tolerance of large disbonds/porosity.

In order to minimize costs, there should be a minimum of quality assurance and in service inspection. Measurement and recording of temperatures during cure, and a visual and coin tap afterward are probably the only requirements. No scheduled in service inspection is being considered.

In the interests of aerodynamic smoothness, the maximum thickness will be 1/8 inch, which is negligible with respect to the boundary layer on the aft 80 percent of any surface; also, a beveled edge with a en to one slope will be incorporated.

The context may be summarized by the following list of points:

- Need for restoration of structural integrity of cracked secondary structure
- Demonstrated opportunity for improvement in durability
- Bonding installation on flight line by inexperienced personnel
- Minor direct consequences of large disbonds
- Opportunity for developing bonding personnel/service experience

Concepts for different aspects of the Durability Patch are listed:

- Prep of crack: stop drill, scarf, seal
- Design: 1-, 2-sided, monolithic, laminated, sandwich (edge: beveled, square, etc)
- Planform: oval, rectangular, fingered
- Perimeter: sealant, integrally tapered core, beveled
- Structural materials: aluminum (2024, 1100, etc; sheet; foil, ribbon, wire), FML, GLARE, fiberglass/epoxy (E or S glass), graphite/epoxy, boron/epoxy, quartz/epoxy, etc.
- Sandwich Core materials: syntactic foam, structural adhesive, etc
- Life enhancement: reduce crack growth rate (choice of structural material, laminations, etc), beef-up(ie, reduce static stresses), damping, etc.(ie, reduce vibratory stresses)
- Damping: stand off (spaced) constrained layer; structural adhesive perimeter

- Damping Stand Off Layer (grooved): syntactic foam, structural adhesive, etc
- Structural Adhesives: film: FM73; paste: etc.
- VEM: PSA, bonded, co-cured,

There are many advantages to a sandwich repair configuration: increased flexural stiffness reduces the eccentricity of the load path due to in-plane loading; reduced patch bending; reduced bending of the original skin, reduced peel stresses, reduced stress intensity at the crack tip - increased flexural stiffness reduces the curvature of the original skin at the crack due to vibration, reduced stresses skin, patch, adhesive, reduced stress intensity factor for vibration.

A sandwich Durability Patch design concept has been selected for further study as well as others. It will be further evaluated for all criteria and parameters. Near the center, there is an elliptical sandwich region which functions as a repair; the outer face sheet and the core of the sandwich is extended in all directions to form a rectangular overlay of standoff damping.

Layer 6 is a structural adhesive film next to the original, cracked skin. Layers 5A, 5B, 5C,...., are graduated ellipses; collectively they serve as one face sheet of a sandwich repair area. Successive layers are slightly smaller to provide a gradual taper in thickness for aerodynamic smoothness and also for a consequent gradual change in stiffness. The total thickness provides one half or slightly more of the extensional stiffness of the original skin. Layer 3 is a rectangle of standoff layer having a beveled perimeter; it is stiff in shear and soft in flexure. Layer 2 consists of a rectangle of viscoelastic damping material with an elliptical insert of structural adhesive. The external layer (1A) is a prepreg and is rectangular with a generous radius in the corners; it extends beyond all other layers of the patch where its perimeter is adhesively bonded to the original skin. Successive graduated layers of prepreg (1B, 1C,....) contact only vem at their perimeter. The elliptical region of layer 1 (face sheet) and 3 (core) which shadows layer 5 (face sheet) serves as a symmetric sandwich static repair. The remaining region of layer 1 and 3 serves as the constraining layer and stand off layer respectively of a damping treatment. Substantial material and installation cost savings result from this highly integrated, multifunctional design concept.

The prepreg layers have the advantages of conformability, ease of installation, and aerodynamic smoothness. It also avoids a secondary operation of sealing the edges and installing an aerodynamic ramp. At this juncture, the only advantage of aluminum appears to be the possible residual compressive stress from cure and the consequent very low crack growth rates. A disadvantage of aluminum is the lack of conformability for significant thicknesses and compound curvatures. These aspects will be evaluated in the near future.

The area to be covered by a Dpatch installation would be two bays of skin covering the fastener row between the bays and almost to the perimeter fastener row, leaving room for the sealant line of a vacuum bag. Procedures will be investigated to accommodate fasteners which must be removed.

8 DESIGN

A sandwich design concept is described above. Finite element analysis will be performed to arrive at values for stresses for various parts of the repaired structure including in the original skin at the edge of the patch, the patch, the adhesive, etc., for a variety of loading conditions. The major design considerations are static stresses, vibratory stresses, and stress intensity and their effect on static strength, low cycle fatigue life, high cycle fatigue life, and crack growth rate. FEA stresses will be compared with the strength and fatigue allowables for the various materials constituting the Durability Patch. Stress intensity factors will also be investigated using finite elements for input to calculations to crack growth rates. The modal strain energy[9][10][11]will be used for calculations of modal damping. Viscoelastic damping materials will be selected to provide the highest practical damping in the

fundamental mode at the service temperature. The maximum damping will protect adjoining bays of structure somewhat.

9 DISCUSSION

The Durability Patch program has major payoff in cost avoidance savings in maintenance and repair of sonic fatigue cracking. Extensive annoyance cracking of secondary structure occurs in service. The consequences of this cracking are large cost of repair and maintenance and reduced operational readiness; there are no ramifications with respect to safety of flight. When annoyance cracking occurs at the same structural location on a substantial portion of the fleet at a small fraction of the intended service life, an opportunity for improvement in durability has been amply demonstrated. Aging aircraft are subject to even more annoyance cracking.

A major benefit of the Dpatch is the minimal potential for additional damage because repairs are made in-situ which minimizes handling damage. The DPP has additional payoff beyond the program and repair in that service experience for bonded repair and a pool of personnel skills will be developed. Furthermore, experience is provided for future applications of micro data collectors analyzers loggers, eg, health monitoring.

10 REFERENCES

[1] Rudder, F.F., Jr. and Plumblee, H.E., Jr., "Sonic Fatigue Design Guide for Military Aircraft," USAF AFFDL-TR-74-112, May 1975 (Available from Defense Technical Information Center as AD B 004600). ASIAC 6915

[2] Byrne, K.P., "On the Growth Rate of Bending Induced Edge Cracks in Panels Excited by Convected Random Pressure Fields," J. Sound Vib. (1980) 68(2), pp 161-171.

[3] Soovere, J., and M.L. Drake, "Aerospace Structures Technology Damping Design Guide," USAF-AFWAL-TR-84-3089, 3 Vols., Dec. 1985.

[4] Clarkson, B.L. , "Review of Sonic Fatigue Technology," NASA Contractor Report 4587, NASA Langley Research Center, Hampton, VA, April 1994.

[5] Wolfe, H.F., Shroyer, C.A. , Brown, D.L. , and Simmons, L.W. , "An Experimental Investigation of Nonlinear Behavior of Beams and Plates Excited to High Levels of Dynamic Response," USAF-WL-TR-96-3057, October 1995.

[6] Baker, A.A., and R. Jones, eds., *Bonded Repair of Aircraft Structures*, Martinus Nijhoff Publishers, 1988.

[7] Fredell, Robert S., USAF/DFEM, Academy Department of Engineering Mechanics, "Damage Tolerant Repair Techniques for Pressureized Aircraft Fuselages" 2E WL-TR-94-3134, 1994.

[8] anon, Composite Repair of Military Aircraft Structures, AGARD CP 550, Oct. 1994.

[9] Rogers, L. C., R.W. Gordon, and C.D.Johnson "Seminar.on Damped Laminated Beams," unpublished, WPAFB OH, 19 March 1980.

[10] Johnson, C. D., Kienholz, D. A. ,Rogers, L. C. "Finite Element Prediction of Damping in Beams with Constrained Viscoelastic Layers," *Shock and Vibration Bulletin*, No. 51, pp. 71-81, May 1981.

[11] Johnson, C. D., Kienholz, D. A., "Finite Element Prediction of Damping in Structures with Constrained Viscoelastic Layers," *AIAA Journal*, Vol. 20, No. 9, September 1982.

[12] Rogers, L. C.and Fowler, B. L., "Smoothing, Interpolating and Modelling Complex Modulus Data," CSA RPT, to be published.

Compensation for Passive Damping in a Large Amplitude Microgravity Suspension System

Mark C. Anderson[a], Timothy K. Hasselman[a], and Thomas C. Pollock[b]

[a]ACTA Inc., 23430 Hawthorne Blvd., Suite 300, Torrance, CA 90505
[b]Dept. of Aerospace Engineering, Texas A&M University, College Station, TX 77843

ABSTRACT

ACTA has developed and demonstrated a three-dimensional, large amplitude, actively-controlled, multi-cable suspension system for dynamically testing large space structures in a simulated microgravity environment. Tension in the cables is actively controlled by large amplitude rotary actuators designed and built at Texas A&M University. The actuators passively support the weight of the test article on soft spiral springs. Spring stiffness in each actuator is compensated by a torque-controlled direct current motor. Bearing and brush friction and damping are actively compensated as well as the algorithmic damping induced by the control law. Actuator stiffness properties were determined by measuring the torque-deflection characteristics of the actuator. Hysteresis loops are compared for the different spring materials. Actuator friction and damping properties (velocity-dependent resistance) are determined by measuring the torque-speed characteristics of the actuator with the spring disconnected. Multiple tests were conducted to establish the degree of randomness in these characteristics for robust control design. This paper describes the characterization of actuator stiffness, kinetic friction, and damping, and describes how these characteristics are used to negate the resulting resistance torques in the suspension system. Conclusions regarding the effectiveness of the system and possible enhancements are discussed.

Keywords: passive damping, active compensation, suspension system, microgravity, space structures, dynamic testing

1. SYSTEM DESCRIPTION

The Microgravity Suspension System (MSS) is designed primarily to provide gravity offload for ground-based testing of flexible space structures, or scale models of such structures, while providing minimal resistance to motion in the three translational degrees of freedom at each attachment point.[1-6] To accomplish this the system uses a triangular arrangement of single degree of freedom actuators attached to the test article at a given point by an inverted triangular pyramid of relatively rigid cables. Such a tetrahedral arrangement of actuators and cables is referred to as tripod and is depicted for a compact test article in Figure 1. Collinear and non-collinear attachment of multiple tripods facilitates limited motion of the test article in up to six degrees of freedom.

The basic unit of the MSS is the actuator. Each actuator is a single degree of freedom mechanical system providing active control of the forces applied to the suspended test article. The basic concept is centered around the simple mechanical oscillator as illustrated in Figure 2. The mass M, representing the test article, is supported by a spring which is characterized (idealized) by a linear spring constant k. Of course, in addition to supporting the weight of the test article, the spring also imparts a force which opposes any motion under the action of the external force F. The objective of the active control system is to minimize any forces which oppose motion due to the external force while supporting the weight of the test article.

An obvious way of accomplishing this objective compensates for the spring force by generating a force, f, which acts in the direction opposite the spring force and thus facilitates motion. Clearly, f cannot be greater in magnitude than the spring force or the system will be unstable. The case of "perfect" compensation is only marginally stable. Any nonlinearities or

Author contact information—
M.C.A. and T.K.H.: Email: actainc@cerf.net; Telephone: 310-378-6254; Fax: 310-375-0663
T.C.P.: Telephone: 409-845-1686; Fax: 409-845-6051

uncertainties in the spring force will preclude such compensation. Hence, practical considerations limit the degree of compensation to that for which the system remains stable throughout the range of motion.

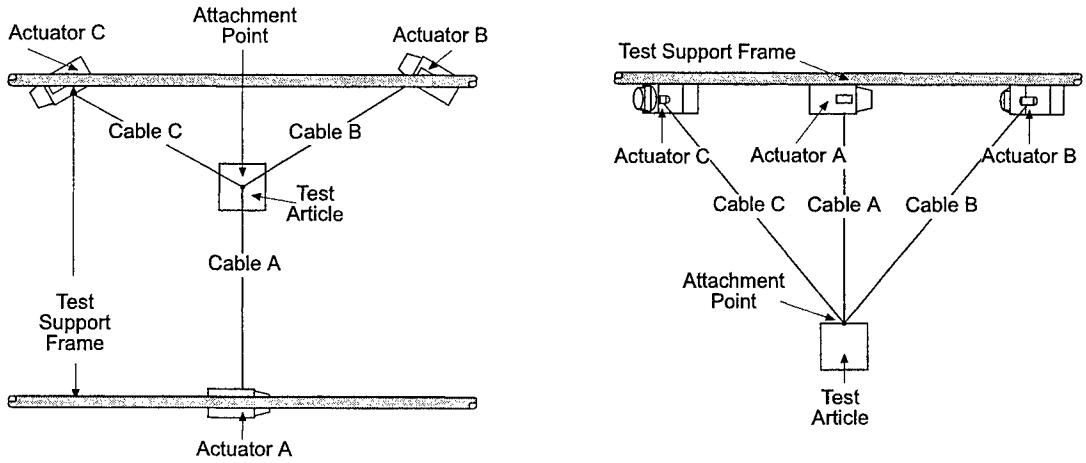

(a) Top view (b) Front view

Figure 1. Suspension system tripod.

The displacements possible using only the force f for compensation are limited by the deflection capability of the spring and the ability of the system to provide adequate force to overcome the restoring force due to the spring. For these reasons, providing all compensation via the force f is practical only for relatively small displacements and is referred to as the small amplitude concept. The large amplitude concept overcomes these limitations by moving the ground point of the spring to follow the motion. This reduces the force in the spring, from kx to $kx - ky$, and reduces the magnitude of the force f required to achieve a given level of compensation. The large amplitude concept is subject to the same limitations with regard to the maximum practical compensation as the small amplitude concept.

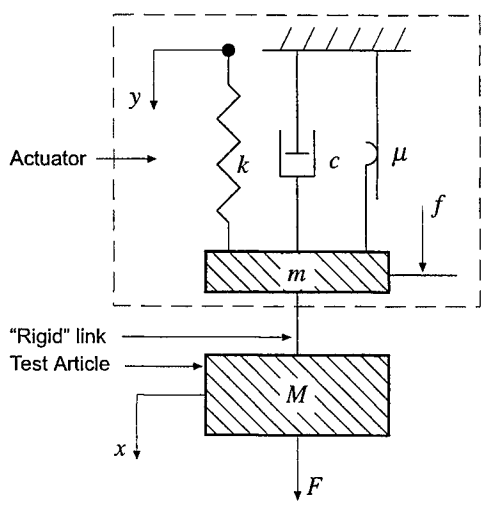

Figure 2. Actuator concept.

A translational actuator such as that illustrated in Figure 2 requires linear actuators to provide the compensating force and to follow the spring. Implementation of such a system has inherent problems, including the requirement of a long stroke for the spring-following actuator and complicated inertia properties which are difficult to offset when the actuators are connected to form a tripod. To preclude these issues and to facilitate a compact design, the MSS employs rotary actuators. The equation of motion for a rotary actuator corresponding to the model in Figure 2 is

$$\left(I+Mr^2\right)\ddot{\phi}+\mu\,\mathrm{sgn}\left(\dot{\phi}\right)+c\dot{\phi}+k\left(\phi-\varphi\right)=Fr+T \tag{1}$$

where r is the spool radius and the residual force, $mr\ddot{\phi}-F$, here denoted by F_{res}, is represented by

$$F_{res}=-\frac{1}{r}\left[I\ddot{\phi}+\mu\,\mathrm{sgn}\left(\dot{\phi}\right)+c\dot{\phi}+k\left(\phi-\varphi\right)-T\right] \tag{2}$$

The analogy is completed by noting that $x=r\phi$, $y=r\varphi$, $m=I/r^2$ and $fr=T$, and defining μ, c, and k in consistent units.

The equation of motion (1) and residual force representation (2) constitute an idealized model. The damping and spring force models are linear and the (kinetic) friction model is piecewise linear. Nonlinearities, other than the kinetic friction, and uncertainties in the physical implementation of the model are not represented.

In any practical implementation of these concepts, physical hardware is required to generate the compensating force f and to move the ground point of the spring. This equipment will possess a certain amount of inertia and will give rise to various non-conservative (dissipative) forces which will inhibit the motion of the test article. Minimization of the residual forces in a practical actuator necessitates reduction of these inertial and dissipative forces by design and/or active compensation via the force f. A hybrid approach was taken with the MSS. Inertia effects, represented by I in (1) and (2), are minimized by design only. Dissipative forces are reduced by design, but are also offset by active compensation.

2. CONTROL STRATEGY

The control system design for the MSS is based on a three-tiered approach.[6] The first tier, called Level 1, is concerned with single degree-of-freedom control of a single actuator. The middle tier, denoted Level 2, groups three actuators into a tripod and compensates for the tripod geometry as the test article attachment point moves in space. Both Level 1 and 2 are independent of the specific application. Coordination of multiple tripods, Level 3 control, is application-dependent.

2.1 Level 1(actuator) control

Given the system model and the ability to provide a compensating torque and to move the ground point of the spring, the question of the optimum control strategy arises. Two basic approaches are possible. The most straightforward approach is to accurately determine the physical characteristics of the system (μ, c, k, etc. and their generalizations) and use the compensating torque and ground point motion to offset them. Only the displacement and ground point angles, ϕ and φ, respectively, need be monitored during operation to implement this approach. A second strategy is to use an "abstract" controller, i.e., one that does not attempt to directly model the physics of the actuator, to minimize the difference between the system response and the "desired" response. Since the external force and the motion under its action are arbitrary, the only practical definition of "desired" response is that the residual force be as small as possible, necessitating accurate measurement of the cable tension. Therefore, the direct approach was used.

Equation (2) suggests the torque compensation command,

$$\hat{T}=k_p\phi+c_p\dot{\phi}+\mu_p\,\mathrm{sgn}\left(\dot{\phi}\right) \tag{3}$$

For present purposes, the output torque of the motor may be expressed via the formal differential equation

$$\tau_p\dot{T}+T=\hat{T} \tag{4}$$

where τ_p is the time constant of the motor. Using (2), (3), and (4) yields a residual force for the small amplitude concept of the form

$$\begin{aligned}F_{res}=&-\frac{1}{r}\left[I\ddot{\phi}+\left(\mu-\mu_p\right)\mathrm{sgn}\left(\dot{\phi}\right)+\left(c-c_p\right)\dot{\phi}+\left(k-k_p\right)\phi\right]\\&-\frac{\tau_p}{r}\frac{d}{dt}\left[\left(I+mr^2\right)\ddot{\phi}+\mu\,\mathrm{sgn}\left(\dot{\phi}\right)+c\dot{\phi}+k\phi-Fr\right]\end{aligned} \tag{5}$$

Note that the first term on the right hand side of (5) is the residual force for an actuator with an ideal motor, i.e., one that has a zero response time. The second term, which accounts for the finite motor response, is merely the time derivative of the equation of motion for a passive actuator.

The large amplitude case includes high and low pass filters to separate the torque and ground point spring compensations so that the ground point follows slow, quasi-rigid body motions while the torque compensates for oscillations about the quasi-rigid motion. Both filters are simple first-order filters with a common cutoff frequency of $2\pi/\tau$, chosen to be below the lowest frequency of interest for the test article. For the large amplitude concept, the torque compensation command is

$$\hat{T} = \hat{T}_k + c_p\dot{\phi} + \mu_p \operatorname{sgn}(\dot{\phi}) \tag{6}$$

where $\hat{T}_k$ is the spring compensation torque command. The filters formally introduce the differential equations

$$\tau\dot{\hat{T}}_k + \hat{T}_k = \tau k_p(\dot{\phi} - \dot{\varphi}) \tag{7}$$

$$\tau\dot{\hat{\varphi}} + \hat{\varphi} = k_s(\phi - \varphi) \tag{8}$$

where $\hat{\varphi}$ is the ground point position command. Analogous to (4), the response of the positioning motor can be expressed by the differential equation,

$$\tau_s\dot{\varphi} + \varphi = \hat{\varphi} \tag{9}$$

where τ_s is the positioning motor response time constant. The residual force may be deduced from (2) and (6)-(9) and is given by

$$\begin{aligned}
F_{res} = & -\frac{1}{r}\left[I\ddot{\phi} + (c - c_p - \tau k_p)\dot{\phi} + (\mu - \mu_p)\operatorname{sgn}(\dot{\phi}) + \left(\frac{k}{1+k_s}\right)\phi\right] \\
& + \left(\frac{1}{1+k_s}\right)\left[\tau\tau_p\tau_s\frac{d^3}{dt^3} + (\tau\tau_p + \tau\tau_s + \tau_p\tau_s)\frac{d^2}{dt^2} + (\tau + \tau_p + \tau_s)\frac{d}{dt}\right]\left\{F - \frac{1}{r}\left[(I + Mr^2)\ddot{\phi} + c\dot{\phi} + \mu\operatorname{sgn}(\dot{\phi}) + k\phi\right]\right\} \\
& + \left(\frac{\tau_p k_s}{1+k_s}\right)\left(\frac{d}{dt}\right)\left\{F - \frac{1}{r}\left[(I + Mr^2)\ddot{\phi} + c\dot{\phi} + \mu\operatorname{sgn}(\dot{\phi})\right]\right\} \\
& + \left(\frac{1}{1+k_s}\right)\left[\tau\tau_s\frac{d^2}{dt^2} + (\tau + \tau_s)\frac{d}{dt}\right]\left\{\frac{1}{r}\left[c_p\dot{\phi} + \mu_p\operatorname{sgn}(\dot{\phi})\right]\right\} \\
& + \left(\frac{\tau\tau_s}{1+k_s}\right)\left(\frac{d}{dt}\right)\left(\frac{1}{r}k_p\dot{\phi}\right)
\end{aligned} \tag{10}$$

Note that the right hand side of the residual force equation (10) has several distinct terms. The first term represents the residual force that would be obtained with an actuator with ideal motors which performed all of the spring compensation with the positioning motor and used the torque motor for damping and friction compensation. This term represents the bulk of the residual force. The presence of the spring compensation torque term multiplying the velocity represents the effect of the high pass filtering of the spring compensation torque command. The second term exhibits the effects of the motor responses and the low pass filtering of the ground point positioning command on the uncompensated system. The third term illustrates the interaction of the ground point positioning with the torque motor response. The interaction of the unfiltered friction and damping compensations with the low pass filter and positioning motor response is shown by the fourth term. The final term represents the interplay between the high pass-filtered spring compensation torque command and the response of the ground point positioning motor.

2.2 Level 2 (tripod) control

The tripod, or Level 2, control algorithm is a conceptually simple extension of the Level 1 algorithm. To facilitate motion in three-dimensional space, three actuators are connected to a common point providing determinate control of the residual forces in all three dimensions. For a given actuator the only differences between the Level 1 and Level 2 configurations are that the effective test article mass and static equilibrium position will change as the attachment point moves in space and some of the cable tension will be reacted by axial forces on the spool as the attachment point moves parallel to the spool axis.

An idealized model of the tripod can be constructed similar to that for a single actuator. The equation of motion for actuators connected in a tripod is then

$$I_\alpha \ddot{\phi}_\alpha + c_\alpha \dot{\phi}_\alpha + \mu_\alpha \operatorname{sgn}(\dot{\phi}_\alpha) + k_\alpha(\phi_\alpha - \varphi_\alpha) = \frac{r_\alpha}{{}^0\ell_\alpha - r_\alpha \phi_\alpha}(f_\alpha - {}^0 f_\alpha)\gamma_\alpha(x_1, x_2, x_3) \tag{11}$$

where the subscript α denotes the actuator, ${}^0\ell_\alpha$ is the initial cable length, f_α and ${}^0 f_\alpha$ are the instantaneous and initial cable tensions, respectively, and γ_α is a geometric function of the attachment point coordinates which accounts for the proportion of the cable tension which is normal to the spool axis of revolution. There are three such equations, one for each actuator. There are also three equations of motion for the attachment point. If the test article is considered as a point mass, these equations are represented by

$$M\ddot{x}_\beta = F_\beta + \sum_\alpha \left(\frac{{}^0 x_{\alpha\beta} - x_\beta}{{}^0\ell_\alpha - r_\alpha \phi_\alpha} \right)(f_\alpha - {}^0 f_\alpha) - \delta_{\beta 3} Mg \tag{12}$$

where the subscript β denotes the Cartesian coordinate, ${}^0 x_{\alpha\beta}$ is the initial position of actuator α in the β direction with respect to the attachment point, and $\delta_{\beta 3}$ is the Kronecker delta with "3" denoting the local vertical direction.

Note that (11) and (12) for the coordinates ϕ_α and x_β define a six-dimensional configuration space for the tripod. There are also three holonomic constraint equations which define the geometry of the tripod,

$$\left({}^0\ell_\alpha - r_\alpha \phi_\alpha\right)^2 = \sum_\beta \left({}^0 x_{\alpha\beta} - x_\beta\right)^2 \tag{13}$$

Equations (11)-(13) indicate that the system has three degrees of freedom. While it is possible to use (13) to reduce the number of equations of motion to three; this is not useful since the resulting equations are implicit, highly nonlinear, strongly coupled, and not linearizable via the assumption of small amplitudes.

The control strategy, i.e., minimization of residual forces, is carried out via the compensation commands given by (3) and (6) for the small and large amplitude cases, respectively, with a correction term added to account for the changing cable tension due to gravity offload as the test article moves in space. The geometry correction command, $\hat{T}_g$, is of the form

$$\left(\hat{T}_g\right)_\alpha = -\frac{Mgr_\alpha}{\lambda}\left[\frac{\lambda_\alpha + \rho_\alpha x_1 + \sigma_\alpha x_2}{{}^0 x_{\alpha 3} - x_3} - \frac{\lambda_\alpha {}^0\ell_\alpha}{{}^0 x_{\alpha 3}\left({}^0\ell_\alpha - r_\alpha \phi_\alpha\right)}\right]\gamma_\alpha(x_1, x_2, x_3) \tag{14}$$

where λ, λ_α, ρ_α, and σ_α are terms which depend on the initial tripod geometry. Assuming an accurate characterization of this geometry, gravity compensation provided by (14) can be assumed to be essentially exact. The residual force components are then

$$(F_{res})_\beta = \sum_\alpha \left(\frac{{}^0 x_{\alpha\beta} - x_\beta}{{}^0\ell_\alpha - r_\alpha \phi_\alpha} \right)(F_{res})_\alpha \tag{15}$$

where the residual forces on the right hand side of (15) are given, with some modifications due to the torque motor responses to the geometry compensation commands, by expressions of the form (5) and (10), respectively, for the small and large amplitude actuators. Equation (15) represents a change of coordinates from the actuator frame to the test article frame.

The Level 2 implementation is merely an extension of the Level 1 strategy with the geometry correction torques added after the Level 1 compensations are determined. Optimization of performance is accomplished by accurately measuring/calculating the initial tripod geometry and optimizing the Level 1 performance of the actuators. The same comments regarding limitations on the levels of compensation for Level 1 control are applicable for the tripod. Nonlinearities and uncertainties in the physical characteristics of the individual actuators preclude perfect compensation and determine the stability limits for the tripod.

2.3 Multiple tripod considerations

The discussions of control models and strategies for Level 1 (single actuator) and Level 2 (single tripod) considered the test article as either a point mass or a rigid body supported at its center of gravity and free to rotate about this point. Most applications of the MSS will be for testing larger structures which may consist of multiple, linked (relatively) rigid and flexible bodies. Many of these will require multiple tripods to provide the requisite gravity offload. In general, attaching

tripods at the centers of gravity of each body will not be possible. In this event, the mass moments of inertia of these bodies, the boundary conditions between the bodies, and the types and magnitudes of externally imposed forces and displacements become relevant to the suspension system design.

Coordination of multiple tripods for such a test article is referred to as Level 3 control. Obviously, implementation of this control is application-dependent. Examples of Level 3 coordination for specific programs include modification of the gravity offload compensation to account for mass moments of inertia and/or modal mass effects from the oscillations of a flexible body, pre-programmed relative motion of the tripods to accommodate very large amplitude slewing maneuvers, and use of the actuators to excite modes of the test article.

3. DISSIPATIVE FORCES

Restricting attention to a single actuator (Level 1), there are four distinct sources of dissipative (non-conservative) forces which inhibit motion of the test article under the action of external forces. The types of dissipative forces encountered include classical velocity-dependent damping and friction (both static and kinetic), hysteretic damping induced by large deflections of the spring material, and forces which arise from the temporally finite motor responses and, in the large amplitude case, the filtering of the spring compensation commands. The latter is referred to as algorithmic damping within the present context and is not a "passive" force in the usual sense. However, sense it comes about as a byproduct of compensating for other forces, it must be dealt with in order to optimize system performance. The origins, characterization, and minimization of each of these dissipative forces are discussed in the paragraphs to follow.

3.1 Classical damping and Coulomb friction

Perhaps the simplest dissipative forces to characterize are the classical damping and Coulomb friction which accompany any real motor. Classical damping arises due to bearing lubrication, if it exists, and to the effects of the back electromotive force generated in the motor as it rotates in the driving magnetic field. Static and kinetic Coulomb friction are the result of dry friction in the four bearings which retain the motor/spool shaft. The motors which provide compensating torque for the MSS are directly attached to the spool, opposite the spring, and are the source of the classical non-conservative forces for the system.

Linear damping and friction were characterized by performing torque-speed tests of each of the torque compensating motors.[7,8] Tests were repeated numerous (at least six) times and the results averaged to verify repeatability, or the lack thereof, and obtain reliable parameter estimates. A typical torque-speed curve is shown in Figure 3. Note that the positive and negative zero offsets are different. This is due to the directionality of the brushes in the torque compensating motors. The linear damping was very consistent for a given motor and varied between 0.0051 and 0.0084 in-lb-sec/rad among the different motors, with a positive-negative variation of less than 0.0011 in-lb-sec/rad.. The kinetic friction, however, was not repeatable. The measured values ranged from less than 0.1 in-lb to more than 1.0 in-lb, with positive-negative differences of up to 0.5 in-lb. Static friction was not systematically determined, but informal tests showed that it was close to the zero offset values calculated from the torque-speed tests.

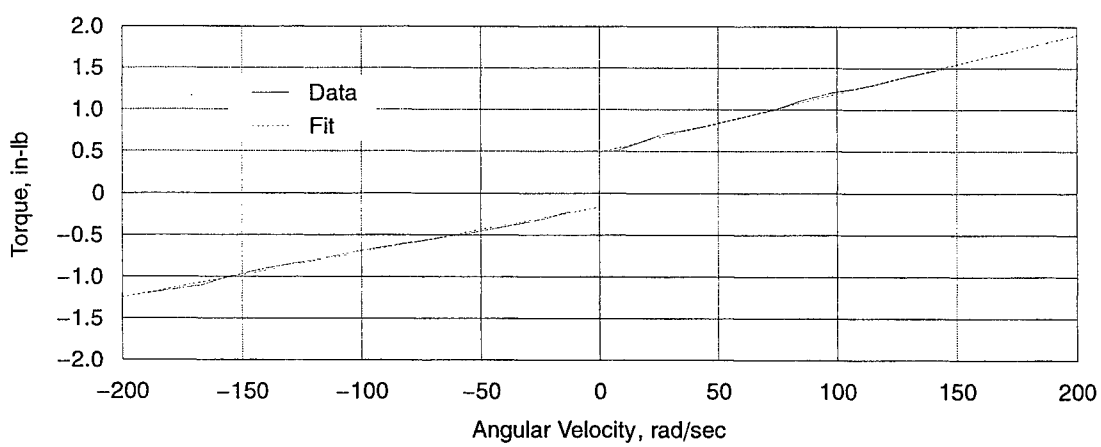

Figure 3. Classical damping and Coulomb friction for a typical actuator.

The compensation strategy for classical dissipative forces was straightforward. Part of the velocity proportional compensation was taken as λc, where a λ value of 0.95 to 0.99 was typical. The kinetic friction compensation was only slightly more complicated. Due to the observed variability of the friction, the mean low value was compensated for completely and a random dither was applied which ranged from the mean low value to the mean high value. Different values were used for positive and negative velocities. This provided a robust control algorithm and helped offset the effects of static friction, but was sub-optimal in the sense that some residual friction was inevitable.

3.2 Material hysteresis

One source of dissipative forces which was not anticipated at the outset was significant hysteresis in the spring material under strain induced by the compensated motion of a supported test article.[6,8] The MSS employs spiral springs to support the static weight of the test article. Each spring is wound from a 1 in. wide by 0.063 in. thick by 72 in. long strip of steel, which is heat treated after winding to increase strength and reduce residual stresses induced by cold working. The maximum tip deflection to which the springs are subjected during use is about 6 in. Assuming uniform heat treatment, this deflection should not (theoretically) produce any local yielding or even any nonlinear behavior with the original material (AISI 4140). However, as a result of the seven-turn spring geometry, it proved very difficult to get a uniform heat treatment. Thus, local regions of the spring were left in the essentially annealed condition and the springs became nonlinear or even yielded slightly at higher deflections.

The hysteretic behavior of the original spring material is illustrated in the torque-deflection plots of Figures 4 through 6. A static weight of 30 lb. was used for these tests. At small deflections on the order of ±1 in. (Figure 4), the springs do not exhibit noticeable hysteresis other than the apparent hysteresis due to friction. At moderate deflections of about ±2 in. (Figure 5), hysteresis beyond the friction effect is apparent. As Figure 6 depicts, large deflections of ±3 in. produce significant hysteresis. Thus, the hysteresis exhibited by the AISI 4140 material generates an effective damping which can be quite large for large deflections.

The hysteretic behavior of the springs was not compensated for by the control system. Rather, a stronger spring material (AISI 1095) was substituted for the original material. The hysteresis loops generated by the original and replacement materials are compared in Figure 7 for a static load of 30 lb. and a ±2 in. dynamic deflection. As the figure shows, the replacement material exhibits less hysteresis at this deflection. Larger deflections with the replacement material proved inadvisable because the material was quite brittle in the heat treated state. Therefore, operation of actuators outfitted with the replacement springs was limited to test article attachment point movements which produced ±2 in. deflections or less.

To avoid these issues in the future, two avenues of attack are currently being investigated. One, development of better spring fabrication processes, is likely to be a long term effort. The springs are currently manufactured at Texas A&M University, the original developer, because quantity requirements are too low to offset tooling costs for commercial spring manufacturers. The second approach is the investigation of alternate spring materials which are less sensitive to non-uniform heat treatment and/or exhibit superior heat transfer and other material properties which obviate the problem and which are less brittle in the heat treated state. The current candidate is Hitachi ATS34, similar to AISI 440C, which has a higher yield stress and greater ductility than AISI 1095.

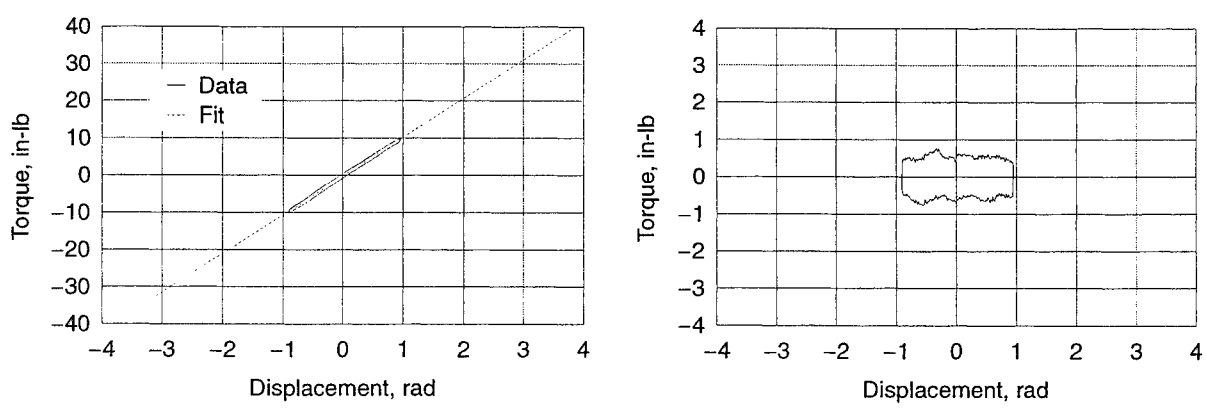

(a) Quasi-static torque-deflection curve (b) Hysteresis loop including friction

Figure 4. Force-deflection curve and hysteresis loop for AISI 4140 at ±1 in. deflection with 30 lb. static load.

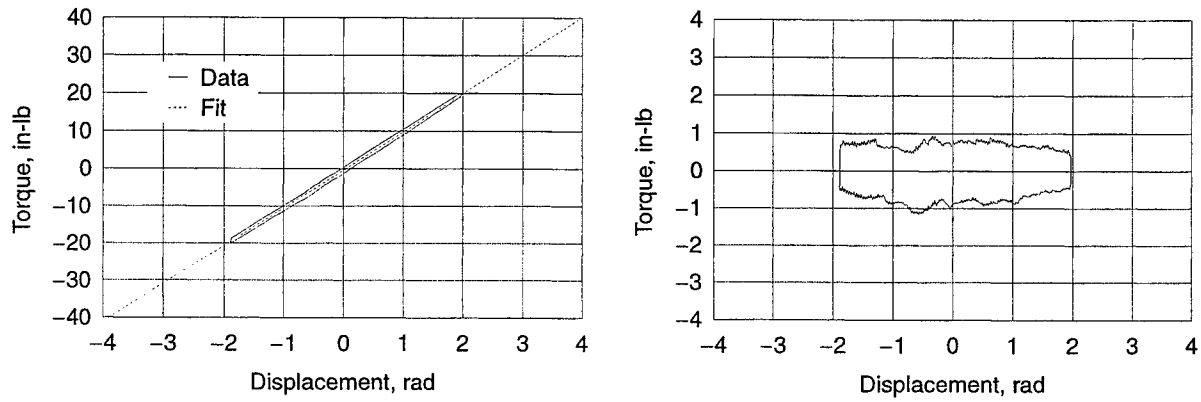

(a) Quasi-static torque-deflection curve (b) Hysteresis loop including friction

Figure 5. Force-deflection curve and hysteresis loop for AISI 4140 at ±2 in. deflection with 30 lb. static load.

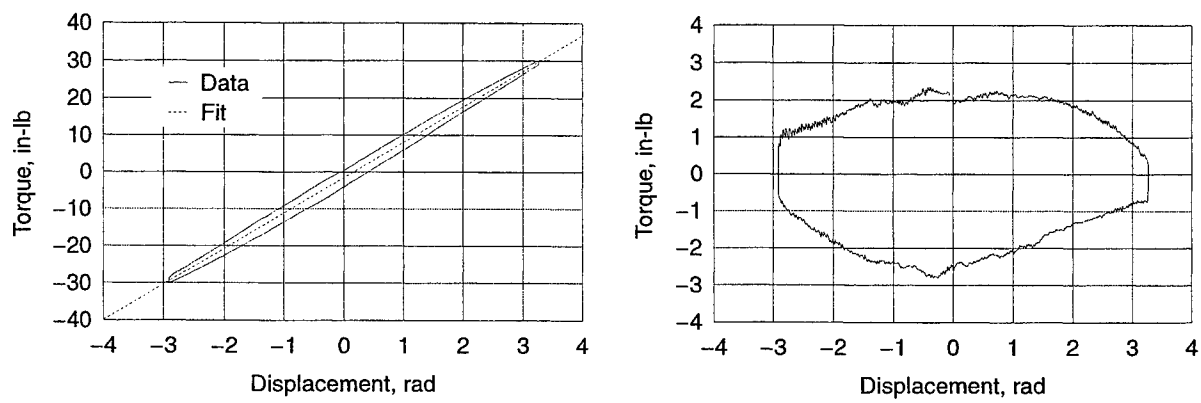

(a) Quasi-static torque-deflection curve (b) Hysteresis loop including friction

Figure 6. Force-deflection curve and hysteresis loop for AISI 4140 at ±3 in. deflection with 30 lb. static load.

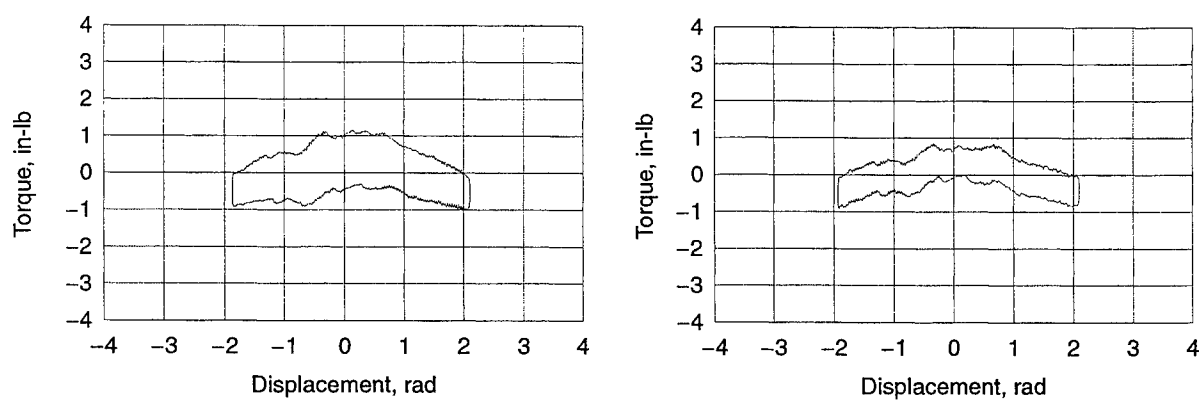

(a) Original material (AISI 4140) (b) Replacement material (AISI 1095)

Figure 7. Comparison of the hysteresis loops for original and replacement materials.

3.3 Algorithmic damping

The final source of non-conservative forces for the MSS is the dynamic response effects of finite motor and control system lag times and the effective global frequency response of the system as a whole, including the control algorithm. The

dynamic response effects of the motors and amplifiers were minimized by choosing equipment with low enough time constants (0.005 sec and 0.060 sec, respectively, for the torque and positioning motors) to exclude most of these effects from the frequency range of interest (0.5-5.0 Hz) and by compensating for some of the effects of finite response time. The global frequency response effects which arise from the filters used by the large amplitude control algorithm were also partially offset via direct compensation.

These dynamic response effects may be seen by studying the frequency response function of the (single actuator) system without friction. Dissipative terms are those which are real multiples of $i\omega$, where ω is the frequency in rad/sec. For the small amplitude case an effective damping may be defined as

$$c_{eff}(\omega) = \frac{1}{r^2}\left(c - \frac{c_p - k_p\tau_p}{1+\omega^2\tau_p^{\,2}}\right) \tag{16}$$

Typically, $k_p\tau_p$ is about seven times the nominal linear damping for an average actuator. Note, from Equation (16), that

$$c_{eff}(0) = \frac{1}{r^2}\left(c - c_p + k_p\tau_p\right) \tag{17}$$

Thus, by Equation (17), in the critical low frequency range an optimal choice of damping compensation is

$$c_p = \lambda c + k_p\tau_p \tag{19}$$

where λ is close to unity. Since all the constants are positive, Equations (16) and (19) show that the residual damping will always be positive and will be approximately $(1-\lambda)c$ for low frequencies. The effective frequency response magnitude and frequency-dependent damping for a small amplitude actuator without friction are depicted in Figure 8. These curves were generated with 80% spring torque compensation and 95% linear damping compensation, using average actuator properties and assuming a static test article weight of 20 lb. The effective residual damping is 0.05% at the actuator fundamental frequency of 0.94 Hz. Figure 8(b) indicates that the damping compensation given by (19) results in an effective residual damping that is constant from 0.01 to 1 Hz and is less than the nominal linear damping across the entire operating range.

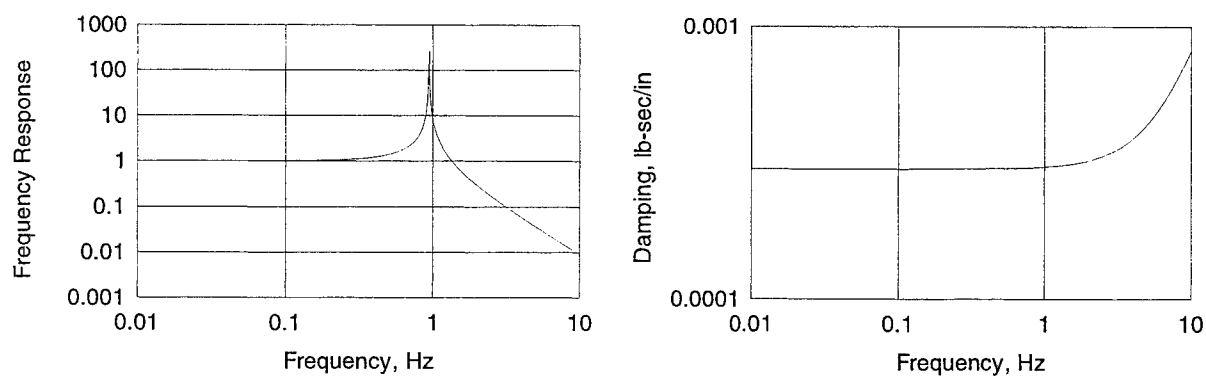

(a) Frequency response magnitude (b) Frequency-dependent damping

Figure 8. Frequency response of the small amplitude actuator.

The large amplitude case is somewhat more involved due to the presence of the positioning motor and the filters which separate the torque and ground point compensations for the spring. As mentioned previously, these filters are included to separate the torque and ground point spring compensations so that the ground point follows slow, quasi-rigid body motions while the torque compensates for small, higher frequency oscillations about the quasi-rigid motion. This is not necessary in general, but was implemented in the MSS because of velocity limitations of the positioning motors and the disparate response time constants of the torque and positioning motors (0.005 and 0.060 sec, respectively).

As with the small amplitude case, the frequency response function of the (friction-less) large amplitude actuator produces an effective damping term proportional to $i\omega$. In this case, the frequency-dependent damping explicitly shows the effects of the filters used to separate the two types of spring compensation. The effective damping is of the form

$$c_{eff}(\omega)=\frac{1}{r^2}\left(c-\frac{c_p-k_p\tau_p}{1+\omega^2\tau_p^{\,2}}\right)+\frac{1}{r^2}\left(\frac{kk_s(\tau+\tau_s)}{\left(1+k_s-\omega^2\tau\tau_s\right)^2+\omega^2(\tau+\tau_s)^2}\right)$$
$$-\frac{1}{r^2}\left\{\frac{k_p\left[\tau(1+k_s)-\omega^2\tau\left(\tau\tau_p-k_s\tau_p\tau_s-\tau_s^{\,2}\right)-\omega^4\tau^2\tau_p\tau_s\right]}{\left[1+k_s-\omega^2\left(\tau\tau_p+\tau\tau_s+\tau_p\tau_s\right)\right]^2+\left[\tau+\tau_p\left(1+k_s-\omega^2\tau\tau_s\right)+\tau_s\right]}\right\} \tag{20}$$

where the first term is the same as the effective damping for the small amplitude case, the second term represents the effect of the filtered ground point spring compensation, and the last term models the dissipative contribution of the filtered torque spring compensation. From Equation (20),

$$c_{eff}(0)=\frac{1}{r^2}\left(c-c_p+\frac{kk_s(\tau+\tau_s)}{(1+k_s)^2}-\frac{k_p\tau}{1+k_s}\right) \tag{21}$$

The effect of the third and fourth terms in (21) is about twenty-one times the nominal linear damping for the typical actuator at low frequencies. Equation (21) suggests that choosing

$$c_p=\lambda c+\frac{kk_s(\tau+\tau_s)}{(1+k_s)^2}-\frac{k_p\tau}{1+k_s} \tag{23}$$

generates optimal compensation in the low frequency range. Figure 9 illustrates the frequency response magnitude and effective frequency-dependent damping for the large amplitude case. These figures were calculated using 80% spring torque compensation, 95% spring ground point compensation, and 95% linear damping compensation. As before, average actuator properties were used along with a static test article weight of 20 lb. The effective natural frequency and residual damping at that frequency are 0.48 Hz and 1.4%, respectively. Here, however, as shown in Figure 9(b), the effective residual damping is only below the nominal linear damping for frequencies below about 0.5 Hz. Above that frequency the residual damping climbs rapidly to about one hundred times the nominal. The rapid increase is primarily due to the frequency dependent terms in the numerator of Equation (20).

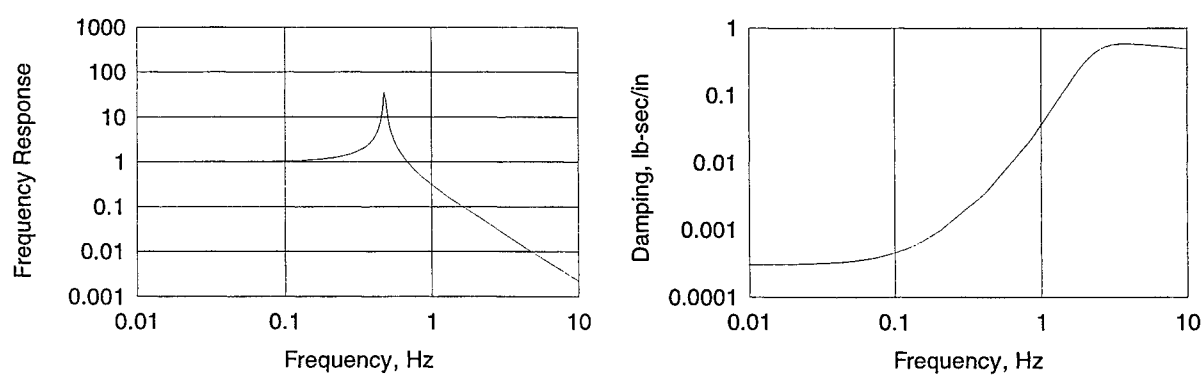

(a) Frequency response magnitude (b) Frequency-dependent damping

Figure 9. Frequency response of the large amplitude actuator.

The behavior of the effective damping for the large amplitude case is an inevitable byproduct of the filters used to separate the two types of spring compensation and the use of a constant, i.e., non-frequency-dependent, damping compensation such as that given by (23). One possible solution is to use an adaptive control algorithm which monitors the near instantaneous frequency content of the system response and adjusts the damping compensation according to (20). Such an approach was not taken for the subject project, but could be implemented for future applications.

3.4 Test results

Each actuator of the MSS was individually tested to verify the stability and repeatability of the control algorithm and to optimize the compensations.[6-8] A compact test article was attached to the actuator, slowly displaced a given distance, held for

a short time, and released. Tests were performed with both 20 and 40 lb. static weights and repeated a number of times. Typical test results are shown in Figure 10. The responses shown are for a static load of 20 lb. And relatively small deflections across the spring to preclude the appearance of hysteretic effects. Figure 10(a) depicts the response of an uncompensated test article, illustrating the nominal spring stiffness, linear damping, and Coulomb friction. The response of the small control algorithm is illustrated in Figure 10(b). The large amplitude response is shown in Figure 10(c). Test results verify the analytical results. Since they include the effect of Coulomb friction, the number of response cycles is less and the rate of decay is greater than predicted by a linear analysis which is to be expected.

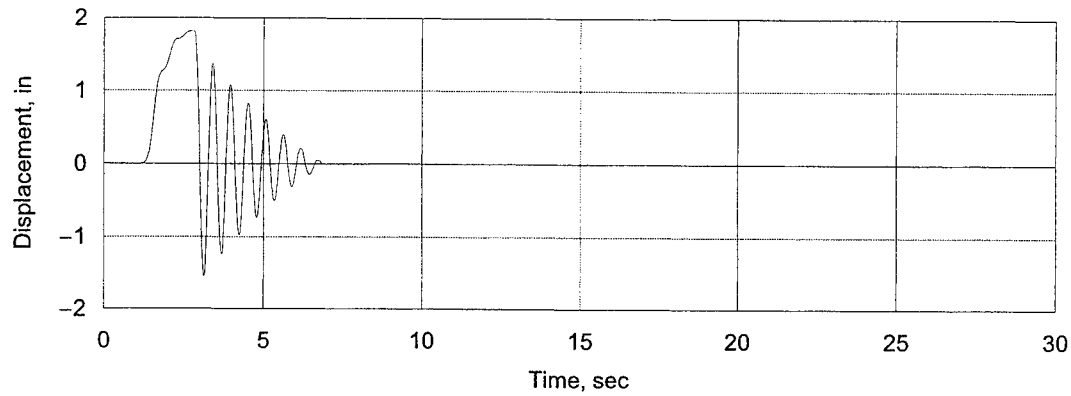

(a) No compensation

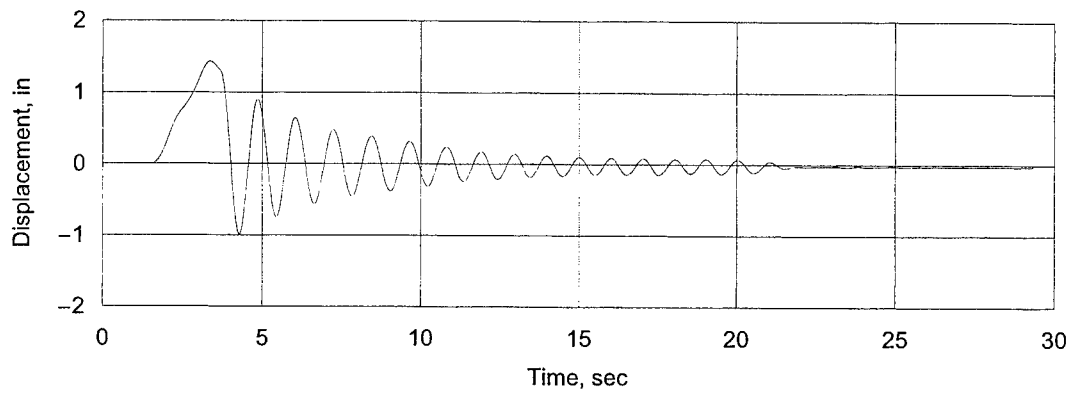

(b) Small amplitude response with 80% spring torque compensation

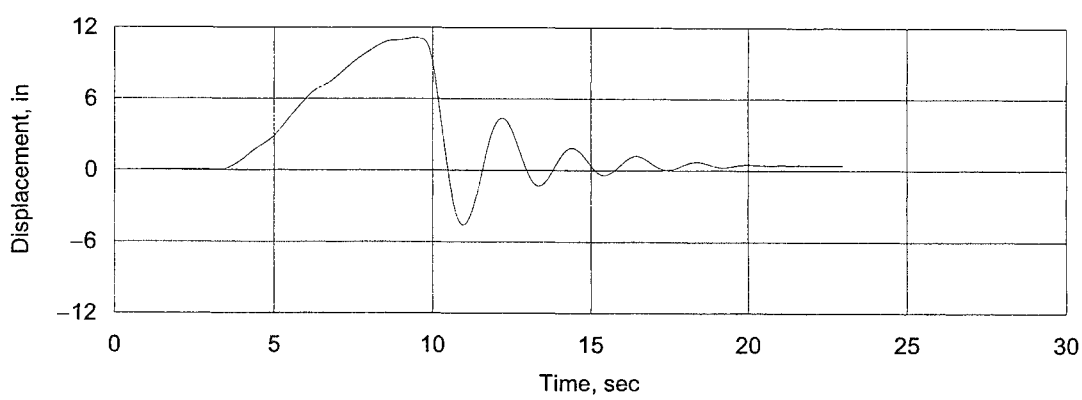

(c) Large amplitude response with 80% spring torque compensation and 95% ground point compensation

Figure 10. Typical actuator response with a 20 lb. test article.

4. CONCLUDING REMARKS

The direct control approach taken for Level 1 control of the MSS actuators has proven to be stable and to produce repeatable responses within the variability of system parameters. The approach compensates for three of the four non-conservative force types which arise during system operation. Classical damping compensations of 95 to 99% are easily attained. Coulomb friction compensation is limited by the variability of the static and kinetic friction parameters. Further reduction of friction forces requires either the use of more sophisticated components, such as air or magnetic bearings, or an auxiliary compensation approach. Energy dissipation due to material hysteresis in the spring is not actively compensated for, but may be minimized or eliminated by restricting the possible deflections across the spring and/or using a spring material which does not exhibit these effects. Finally the "pseudo-passive" dissipative force resulting from the motor responses and control algorithm filters is adequately compensated for at low frequencies, but requires a more sophisticated control approach at higher frequencies of interest, especially for the large amplitude case.

ACKNOWLEDGEMENT

This work was supported by the U.S. Air Force under SBIR Phase II Contract No. F29601-93-C-0170.

REFERENCES

1. A. K. Amos, et al, "Microgravity Simulation in Ground Validation Testing of Large Space Structures," Air Force Office of Scientific Research, November 1988.
2. T. K. Hasselman, ed., *Proceedings of the AIAA/AFSOR Workshop on Microgravity Simulation in Ground Validation Testing of Large Space Structures*, AIAA Conference Publication No. CP-8913, Denver, CO, November 1-2, 1989.
3. T. K. Hasselman, J. D. Chrostowski, and R. Quartararo, "Global Control of Suspension Forces for Microgravity Simulation," Technical Report No. PL-TR-91-3021, prepared for the Air Force Phillips Laboratory by Engineering Mechanics Associates, Inc., June 1991.
4. T. K. Hasselman and J. D. Chrostowski, "Optimum Distribution of Static Suspension Forces for Modal Testing in a Simulated Weightless Environment," Paper No. AIAA-95-1165, *Proceedings of the 36th AIAA/ASME/ASCE/AHS/ASC Structures, Structural Dynamics, and Materials Conference*, New Orleans, LA, April 10-12, 1995.
5. T. K. Hasselman and R. Quartararo, "A Suspension System for Large Amplitude Dynamic Testing in a Simulated Weightless Environment," *Proceedings of the SPIE Smart Structures and Materials Conference*, Albuquerque, NM, February 1-4, 1993.
6. T. K. Hasselman, et al, "Global Control of Suspension System Forces for Microgravity Simulation," Technical Report No. PL-TR-96-1141, prepared for the Air Force Phillips Laboratory by ACTA Inc., Torrance, CA, August 1996.
7. M. C. Anderson and T. K. Hasselman, "Test Report: Unit and Tripod Tests of a Three Dimensional Medium Amplitude Microgravity Suspension System," Technical Report No. 95-294-1, prepared for the Air Force Phillips Laboratory by ACTA Inc., Torrance, CA, January 1995.
8. M. C. Anderson and T. K. Hasselman, "Test Report: Component Test of the Microgravity Suspension System," Technical Report No. 96-294-1, prepared for the Air Force Phillips Laboratory by ACTA Inc., Torrance, CA, August 1996.

Performance prediction of D-Strut™ isolation systems

George W. Wilson[a] and Patrick J. Wolke[a]

[a]Honeywell Inc., Satellite Systems Operation, Glendale, Arizona, 85308

ABSTRACT

Dynamic models and simulation results are presented for D-Strut™ isolators. The D-Strut is a passive spring-damper device with space flight heritage used for vibration isolation. Detailed models will be presented for both hydraulically and pneumatically damped D-Struts and the performance achieved by each will be compared. All of the models presented are single degree-of-freedom with a mass isolated from base motion by one isolator element. A simulation program was used to investigate the frequency domain and time domain dynamic response of the D-Strut models. The results are presented.

Keywords: isolator, hydraulic, pneumatic, dynamic models, performance prediction, simulation, vibration

SYMBOLOGY

Hydraulic D-Strut Dynamic Models

M_{PL} ..... Mass of payload
K_A ..... Bellows spring constant without fluid
K_B ..... Bellows spring constant due to fluid compression
C_A ..... Equivalent fluid damping in orifice $=C/(N_o)^2$
M_f ..... Mass of fluid in orifice
M_{eq} ..... Equivalent mass of fluid in orifice $=M_f/(N_o)^2$
C ..... Fluid damping in orifice
A_p ..... Cross-sectional area of bellows
A_o ..... Cross-sectional area of orifice
N_o ..... A_o/A_p

Pneumatic D-Strut Dynamic Model

M_{PL} ..... Mass of payload
mdem ..... Mass of damper end mass
ms ..... Mass of gas in the spring bellows
md ..... Mass of gas in the damper bellows
morf ..... Mass of gas in the orifice
kas ..... Spring constant of spring bellows without gas
kad ..... Spring constant of damper bellows without gas
kpldem ..... Spring constant of compliance between payload and damper end mass
corf ..... Damping in the orifice
asb ..... Cross-sectional area of spring bellows
adb ..... Cross-sectional area of damper bellows
vs ..... Volume of spring bellows
vd ..... Volume of damper bellows

SPIE Vol. 3045 • 0277-786X/97/$10.00

nds ..... $\upsilon d/\upsilon s$
aorf ..... Cross-sectional area of the orifice
lorf ..... Length of the orifice
P_0 ..... Nominal gas pressure
ps ..... Gas pressure in the spring bellows
pd ..... Gas pressure in the damper bellows
γ ..... Gas law constant

1. BACKGROUND

Passive isolation with viscous fluid damping had its first application of isolating precision optical structures from disturbance sources within the Hubble Space Telescope in 1985.[1] These isolators were the first to implement Honeywell's patented D-Strut isolation and damping technology. Since that time, the D-Strut isolators have been employed in several aerospace applications where jitter-sensitive optical systems have required isolation from disturbance sources.[2,3,4]

Several attributes of the D-Strut isolator make it ideal for use in optical systems. They behave linearly over a wide dynamic range of displacement and force inputs, and have been shown to continue to damp in the nanometer level of operation. They have predictable behavior over environmental extremes and have been qualified for use near optics in the vacuum of space. Their isolation characteristic has discriminatingly superior performance with low in-band amplification, 40 dB/decade roll-off, and recent designs with isolation floors below *70 dB*. More recently, applications have arisen where the benefits of pneumatic isolation have proven merit. That is, a compressible damping medium is used rather than incompressible media.

New applications of D-Strut technology have required tighter control of in-band amplification while maintaining the 40db/decade roll-off characteristic and achieving lower isolation floors. These conditions have demanded the development of refined models of the isolator to capture and control higher-order effects as well as changing the damping media from hydraulic to pneumatic. The paper addresses how the isolators are modeled, and the performance predicted for various implementations.

2. HYDRAULIC D-STRUT DYNAMIC MODELS

Previous isolator element dynamic models have generally been either two- or three-lumped parameter models. The two-parameter model is simply a spring and damper in parallel. The D-Strut three-parameter model[3] places a second spring, K_B, in series with the damper. Figure 2-1 shows a mechanical schematic of a D-Strut isolator element, and Figure 2-2 compares a simple two-parameter spring-damper with a three-parameter D-Strut isolator element.

The spring K_A is due to the normal DC compliance of the D-Strut bellows and spring system without any fluid restriction. The spring K_B is due to the compliance of the fluid and the bellows in the axial direction; as the gap (Z_B - Z_{PL}) decreases, with a fixed fluid mass, it causes the bellows to "bulge". The damping term, C_A, is generated by the shear force on the fluid as it passes through the orifice. The three-parameter D-Strut dynamic model is shown in Figure 2-3.

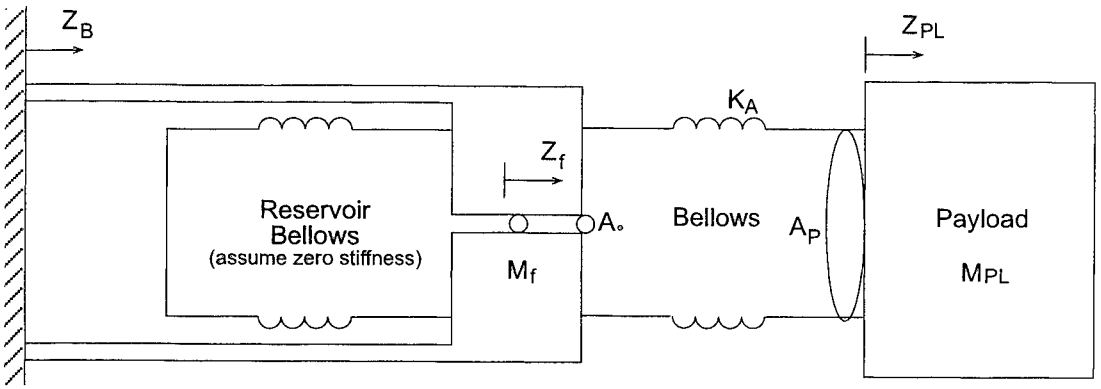

Figure 2-1. D-Strut Isolator Element Mechanical Schematic

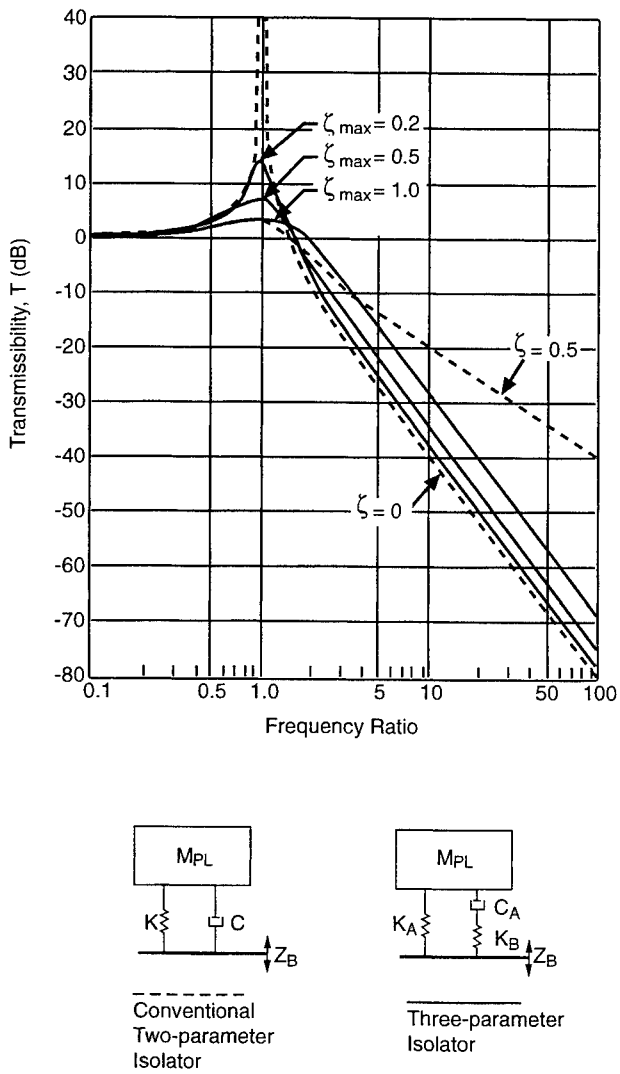

Figure 2-2. A Three-parameter Isolator Compared to a Simple Spring-Damper

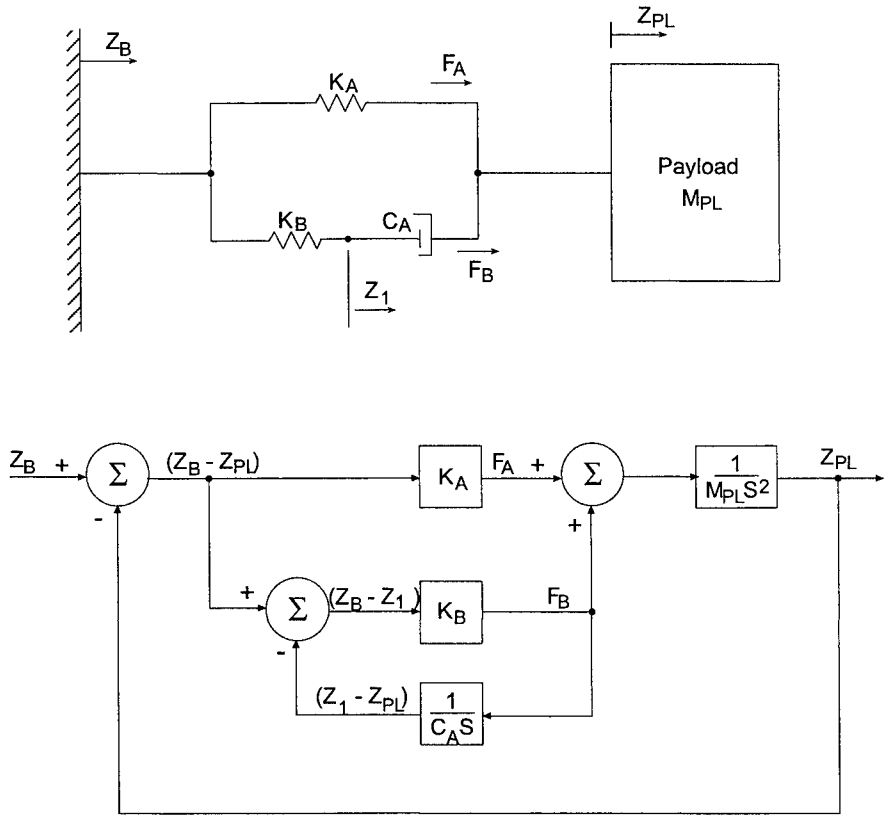

$$\frac{Z_{PL}}{Z_B} = \frac{\left[\frac{(K_A+K_B)\,C_A}{K_A K_B}\,S + 1\right]}{\left[\frac{M_{PL}C_A}{K_A K_B}\,S^3 + \frac{M_{PL}}{K_A}\,S^2 + \frac{(K_A+K_B)\,C_A}{K_A K_B}\,S + 1\right]}$$

Figure 2-3. Three-parameter D-Strut Dynamic Model Block Diagram

A four-parameter D-Strut dynamic model, which accounts for the fluid mass flow in the orifice, will now be developed. The equations-of-motion for the isolator element, shown in Figure 2-1, are as follows:

$$M_{PL}\,\ddot{Z}_{PL} = K_A\,(Z_B - Z_{PL}) + K_B\left[\left(\frac{A_o}{A_p}\right)Z_f - Z_{PL} + \left(\frac{A_p - A_o}{A_p}\right)Z_B\right] \tag{1}$$

$$M_f\,\ddot{Z}_f = -\left(\frac{A_o}{A_p}\right)K_B\left[\left(\frac{A_o}{A_p}\right)Z_f - Z_{PL} + \left(\frac{A_p - A_o}{A_p}\right)Z_B\right] + C\left(\dot{Z}_B - \dot{Z}_f\right) \tag{2}$$

Where A_p = cross-sectional area of the bellows

A_o = cross-sectional area of the orifice

Equations 8) and 9) are presented in block diagram form in the upper block diagram shown in Figure 2-4. Defining

$$N_o \triangleq A_o / A_p \tag{3}$$

$$C_A \triangleq C / (N_o)^2 \tag{4}$$

$$M_{eq} \triangleq M_f / (N_o)^2 \tag{5}$$

and rearranging produces the equivalent dynamic model shown in the lower block diagram of Figure 2-4.

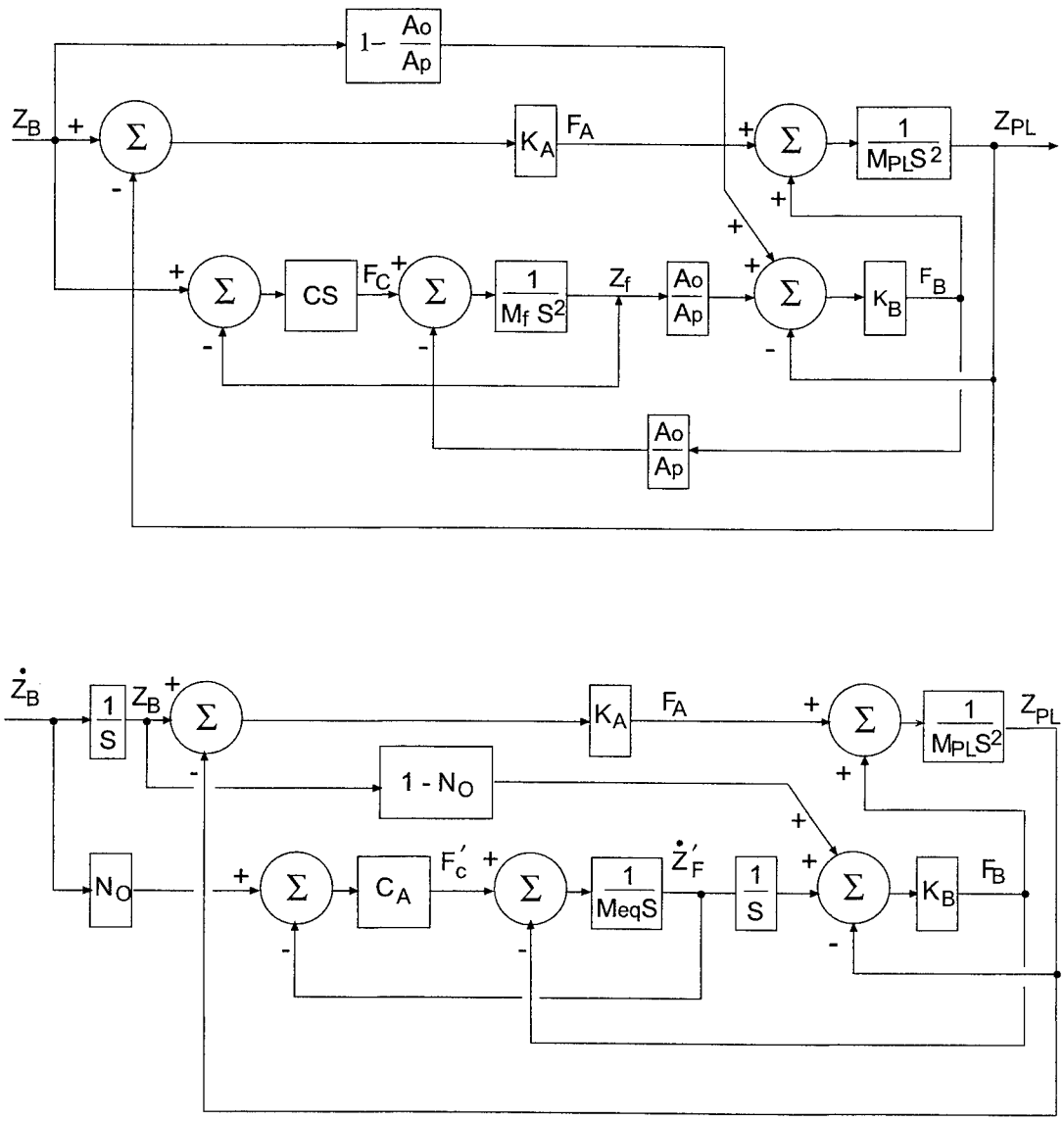

Figure 2-4. Four-parameter D-Strut Dynamic Model Block Diagram

The transmissibility transfer function for this dynamic model is

$$\frac{\ddot{Z}_{PL}}{\ddot{Z}_B}(S) = \frac{\left[\frac{M_{eq}\left[K_A + K_B(1 - N_o)\right]}{K_A K_B} S^2 + \frac{(K_A + K_B)}{K_A K_B} C_A S + 1\right]}{\left[\frac{M_{PL}\, M_{eq}}{K_A K_B} S^4 + \frac{M_{PL}\, C_A}{K_A K_B} S^3 + \left(\frac{M_{PL}}{K_A} + \frac{(K_A + K_B) M_{eq}}{K_A K_B}\right) S^2 + \frac{(K_A + K_B)}{K_A K_B} C_A S + 1\right]} \tag{6}$$

Note that, if $M_{eq} = \left(\frac{A_p}{A_o}\right)^2 M_f = 0$, this transmissibility transfer function becomes identical to the three-parameter dynamic model transmissibility transfer function shown in Figure 2-3.

3.0 PNEUMATIC D-STRUT DYNAMIC MODEL

A simplified mechanical schematic of a pneumatic D-Strut isolator is shown in Figure 3-1. It is similar to the hydraulic D-Strut isolator, with two major exceptions:

- The hydraulic fluid is replaced with a gas.
- The orifice through which the gas flows is much longer, with a smaller cross-sectional area, to generate sufficient damping.

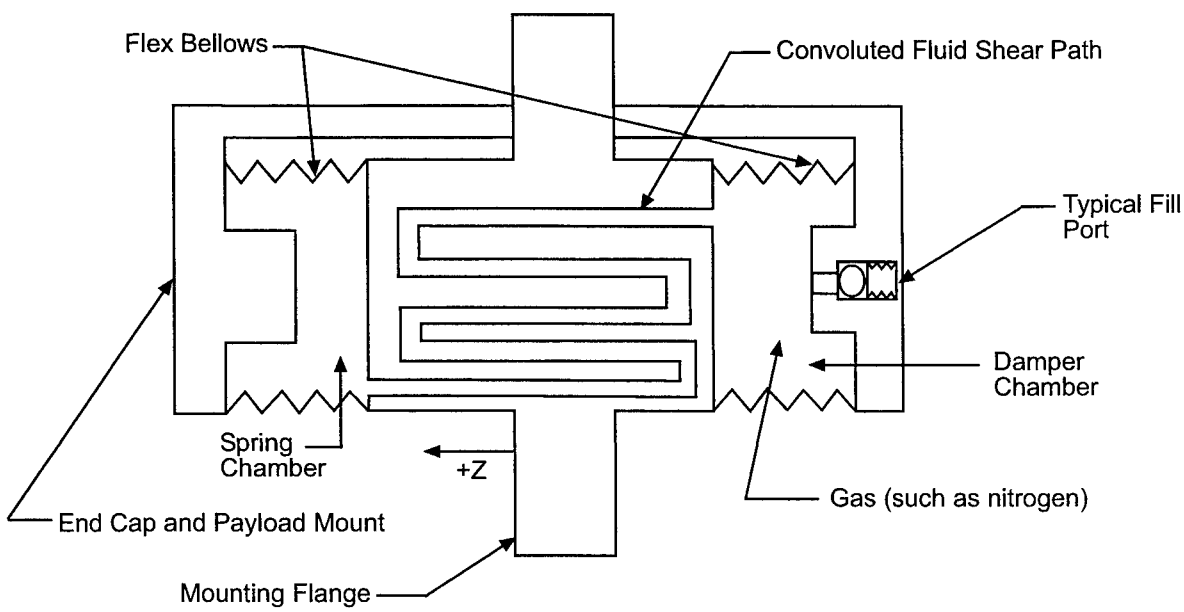

Figure 3-1. Simplified Pneumatic D-Strut Mechanical Schematic

The equations which define the operation of the pneumatic D-Strut are divided into five groups, as follows:

Spring chamber gas law:

$$\frac{p(\upsilon)^{\gamma}}{m} = RT = \text{constant} \tag{7}$$

$$ps = P_o \left[\frac{\left(1 + \Delta ms / ms\right)}{\left(1 + \Delta \upsilon s / \upsilon s\right)^{\gamma}} \right] \tag{8}$$

Damper chamber gas law: Similar to spring chamber gas law,

$$pd = P_o \left[\frac{\left(1 + \Delta md / md\right)}{\left(1 + \Delta \upsilon d / \upsilon d\right)^{\gamma}} \right] \tag{9}$$

Mass flow in the orifice:

$$morf \ S^2 \Delta Z_{orf} = aorf\,(pd - ps) + corf \ S(Z_B - Z_{orf}) \tag{10}$$

$$\Delta ms = -\Delta md = \Delta morf = \left(morf / lorf\right) \Delta Z_{orf} \tag{11}$$

Payload motion:

$$M_{PL} S^2 Z_{PL} = (ps - P_o) asb - kas(Z_{PL} - Z_B) - kpldem(Z_{PL} - Z_{dem}) \tag{12}$$

$$\left(1 + \Delta \upsilon s / \upsilon s\right) = 1.0 + (Z_{PL} - Z_B) asb / \upsilon s \tag{13}$$

Damper chamber end mass motion:

$$mdem \ S^2 Z_{dem} = (P_o - pd)(adb) - kad \ (Z_{dem} - Z_B) + kplem \ (Z_{PL} - Z_{dem}) \tag{14}$$

$$\left(1 + \Delta \upsilon d / \upsilon d\right) = 1.0 - (Z_{dem} - Z_B) asb / \upsilon d \tag{15}$$

The preceding five groups of equations describe the single degree-of-freedom dynamic model of a payload supported by a nonlinear pneumatic D-Strut. These equations are combined to produce the block diagram of the entire model which is shown in Figure 3-2.

The pneumatic D-Strut nonlinear dynamic model can be linearized for small perturbations about an operating point. This requires that the spring chamber and damper chamber gas law equations be linearized as follows:

Spring chamber:

$$\frac{(P_o + \Delta ps)(\upsilon\, s + \Delta\upsilon\, s)^{\gamma}}{(ms + \Delta ms)} = \frac{P_o(\upsilon s)^{\gamma}}{ms} = \text{constant} \tag{16}$$

$$(P_o + \Delta ps)(\upsilon\, s)^{\gamma}\left(1 + \frac{\Delta\upsilon\, s}{\upsilon\, s}\right)^{\gamma} = P_o(\upsilon s)^{\gamma}\left(1 + \frac{\Delta ms}{ms}\right) \tag{17}$$

Noting that

$$\left(1 + \frac{\Delta\upsilon s}{\upsilon s}\right)^{\gamma} \approx \left[1 + (\gamma)\left(\frac{\Delta\upsilon s}{\upsilon s}\right)\right] \text{ for } \frac{\Delta\upsilon s}{\upsilon s} << 1 \tag{18}$$

and neglecting the product of two Δ's gives

$$\Delta ps \cong P_o\left[\frac{\Delta ms}{ms} - (\gamma)\left(\frac{\Delta\upsilon s}{\upsilon s}\right)\right] \tag{19}$$

Similarly, the damper chamber gas law linearization gives

$$\Delta pd \cong P_o\left[\frac{\Delta md}{md} - (\gamma)\left(\frac{\Delta\upsilon d}{\upsilon d}\right)\right] \tag{20}$$

Replacing the nonlinear gas law equations in Figure 3-2 with these linearized versions yields a linearized pneumatic D-Strut dynamic model.

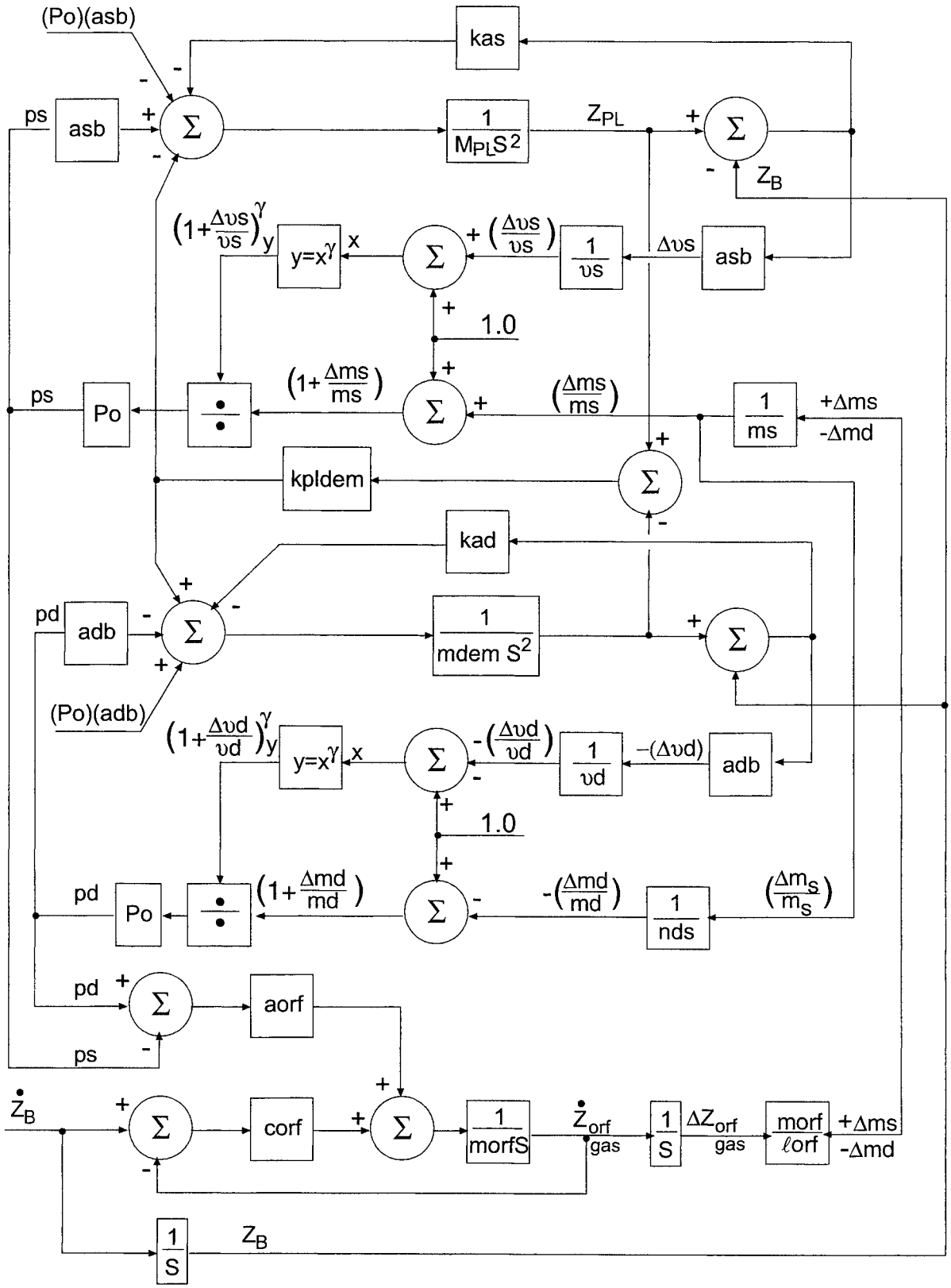

Figure 3-2. Nonlinear Pneumatic D-Strut Dynamic Model Block Diagram

4.0 DYNAMIC MODELS PERFORMANCE PREDICTIONS

4.1 Frequency responses of linear models

The three-parameter and four-parameter D-Strut isolator dynamic models presented in Section 2 are both linear models. The pneumatic D-Strut dynamic model shown in Figure 3-2 is a nonlinear model. However, it was shown how the model could be linearized for small perturbations about an operating point by linearizing the spring chamber and damper chamber gas law equations.

The frequency responses (transmissibilities) of these three linear D-Strut dynamic models are shown in Figure 4-1. The model parameter values are as shown in Table 4-1. The parameter values used for the three-parameter and four-parameter hydraulic D-Strut models correspond to an actual D-Strut developed for the Vibration Isolation and Steering System (VISS), which is scheduled to fly as part of the Ballistic Missile Defense Organization's (BMDO) Space Technology Research Vehicle (STRV-2) in 1998.[4] The parameters of the pneumatic D-Strut isolator dynamic model were selected to make it have a dynamic response similar to the VISS hydraulic isolator. An additional case is included for an hydraulic D-Strut with an equivalent fluid mass which is a factor of ten greater than the nominal mass.

The results show that an equivalent high frequency performance is achieved by all of the isolators. At lower isolation frequencies, a small variation ($\simeq$3dB) between the approaches can be noted for the isolators with the nominal parameter values. The results also show that, for an hydraulic isolator, the fluid mass effect can cause a resonant peak in the transmissibility if the fluid mass is too large.

The maximum allowable equivalent fluid mass to preclude peaking in the transmissibility can be determined by investigating the isolator mechanical impedance transfer function. Consider the four parameter hydraulic D-Strut dynamic model shown in the lower portion of Figure 2.4. Letting $Z_{PL} = 0$, the isolator mechanical impedance is

$$\frac{F_I}{Z_B} = \left(\frac{F_A + F_B}{Z_B}\right) = \frac{K_A\left[\frac{M_{eq}\left[K_A + (1 - N_o)K_B\right]}{K_A K_B}S^2 + \frac{(K_A + K_B)C_A}{K_A K_B}S + 1\right]}{\left[\frac{M_{eq}}{K_B}S^2 + \frac{C_A}{K_B}S + 1\right]} \tag{21}$$

$$\text{Let } \frac{F_I}{Z_B} = \frac{KA\left[\frac{S^2}{W_1^2} + \frac{2\zeta_1}{W_1}S + 1\right]}{\left[\frac{S^2}{W_2^2} + \frac{2\zeta_2}{W_2}S + 1\right]} \tag{22}$$

It can be shown that

$$\zeta_2 < \zeta_1 \tag{23}$$

$$\zeta_2 = C_A \Big/ 2\sqrt{K_B M_{eq}} \tag{24}$$

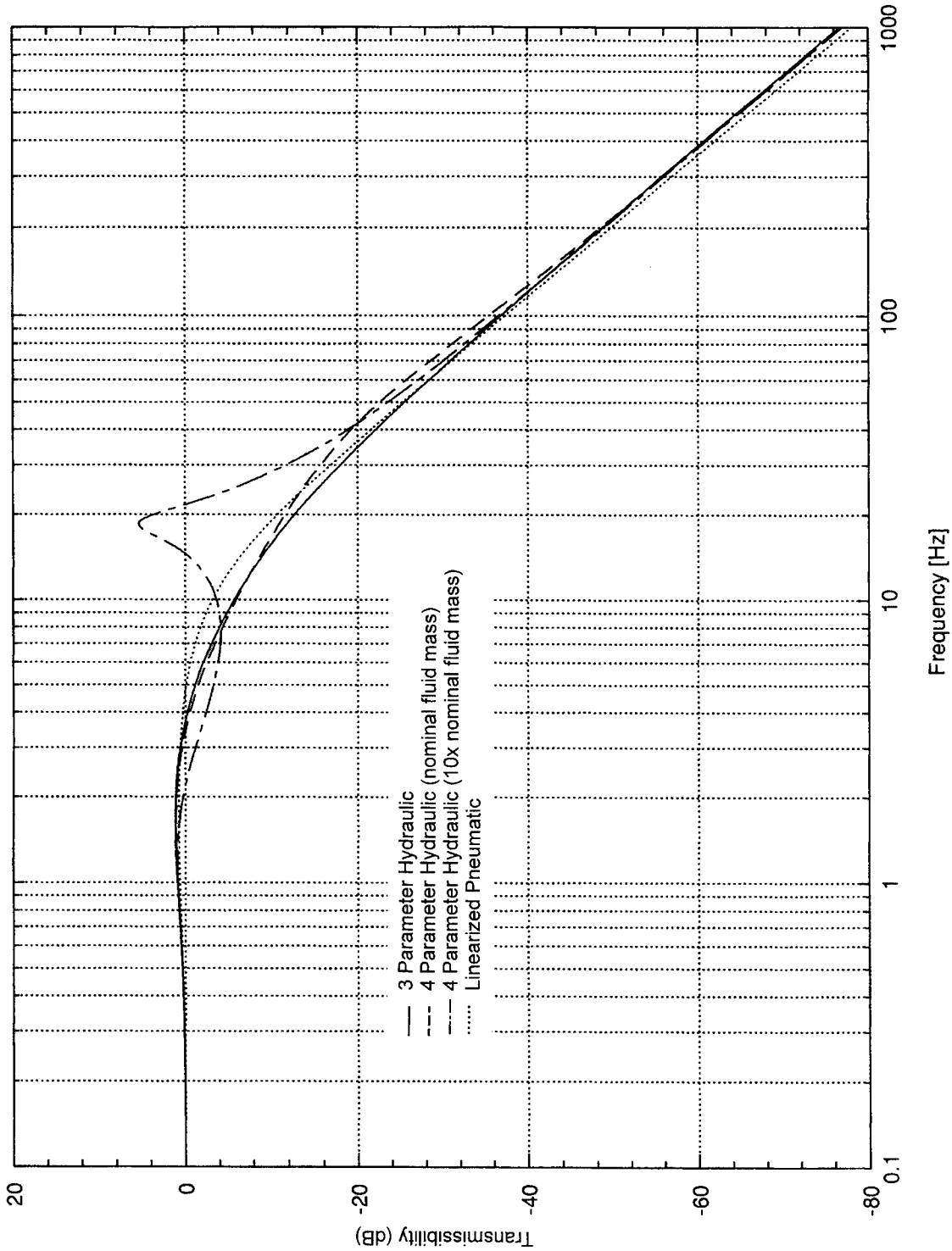

Figure 4-1. Frequency Response of Three Linear D-Strut Isolation Systems

The fluid mass effect can be kept negligible by requiring that $\zeta_1>0.7$ and $\zeta_2>0.7$. Since $\zeta_1>\zeta_2$, it is only necessary to require that $\zeta_2>0.7$. Therefore, the condition to ensure that the fluid mass effect be negligible is

$$\zeta_2 = \frac{C_A}{2\sqrt{K_B M_{eq}}} > 0.7 \tag{25}$$

Note that the parameter values shown in Table 4-1 give ζ_2=0.787 and ζ_2=0.249 for the nominal value of Meq and ten times the nominal value of Meq, respectively. This accounts for the resonance peak in the transmissibility for the four-parameter model with ten times the nominal value of Meq. Also note that, for a given hydraulic fluid, reducing the orifice cross-sectional area will both increase C_A and reduce Meq, thus increasing ζ_2. Therefore, it is concluded that small orifices are required to avoid the fluid mass effect.

Table 4-1
D-Strut Dynamic Models Parameter Values

Three-Parameter and Four-Parameter Hydraulic D-Struts		
Parameter	Value	Units
M_{PL}	0.02015	lb-s^2/in.
M_{eq}	0.0013033	lb-s^2/in.
K_A	3.79	lb/in.
K_B	113.65	lb/in.
C_A	0.606	lb-s/in.
N_o	0.037445	----

Nitrogen Pneumatic D-Strut		
Parameter	Value	Units
M_{PL}	0.02015	lb-s^2/in.
mdem	6.992×10^{-5}	lb-s^2/in.
morf	8.42×10^{-10}	lb-s^2/in.
ms	1.0462×10^{-8}	lb-s^2/in.
nds	1.0	----
lorf	13.1	in.
aorf	0.00057255	(in.)^2
corf	8.806×10^{-7}	lb-s/in.
vs=vd	0.0964	(in.)^3
asb=adb	0.474	(in.)^2
kas=kad	1.894	lb/in.
γ	1.4	----
P_o	14.7	lb/(in.)^2

4.2 Time domain transient responses

The unit amplitude step responses of the three linear dynamic models (three- and four-parameter hydraulic isolator and linearized pneumatic isolator) are shown in Figure 4-2. The model parameter values are the same as shown in Table 4-1.

The results indicate that the step response of the three-parameter and four-parameter hydraulic isolators with nominal parameter values are nearly identical. However, the step response of the four-parameter model, with the fluid mass increased by a factor of ten, shows a damped oscillation at approximately 19 Hz. This is consistent with the frequency response peaking (shown in Figure 4-1) for this isolator. The step response of the linearized pneumatic isolator model has a slightly faster rise time and less overshoot than the hydraulic isolator models.

The step responses of the linearized and nonlinear pneumatic isolator dynamic models are presented in Figure 4-3 for the following three base acceleration step commands:

$$\ddot{Z}_B = 10,\ 25,\ \text{and}\ 35\ \text{in./s}^2$$

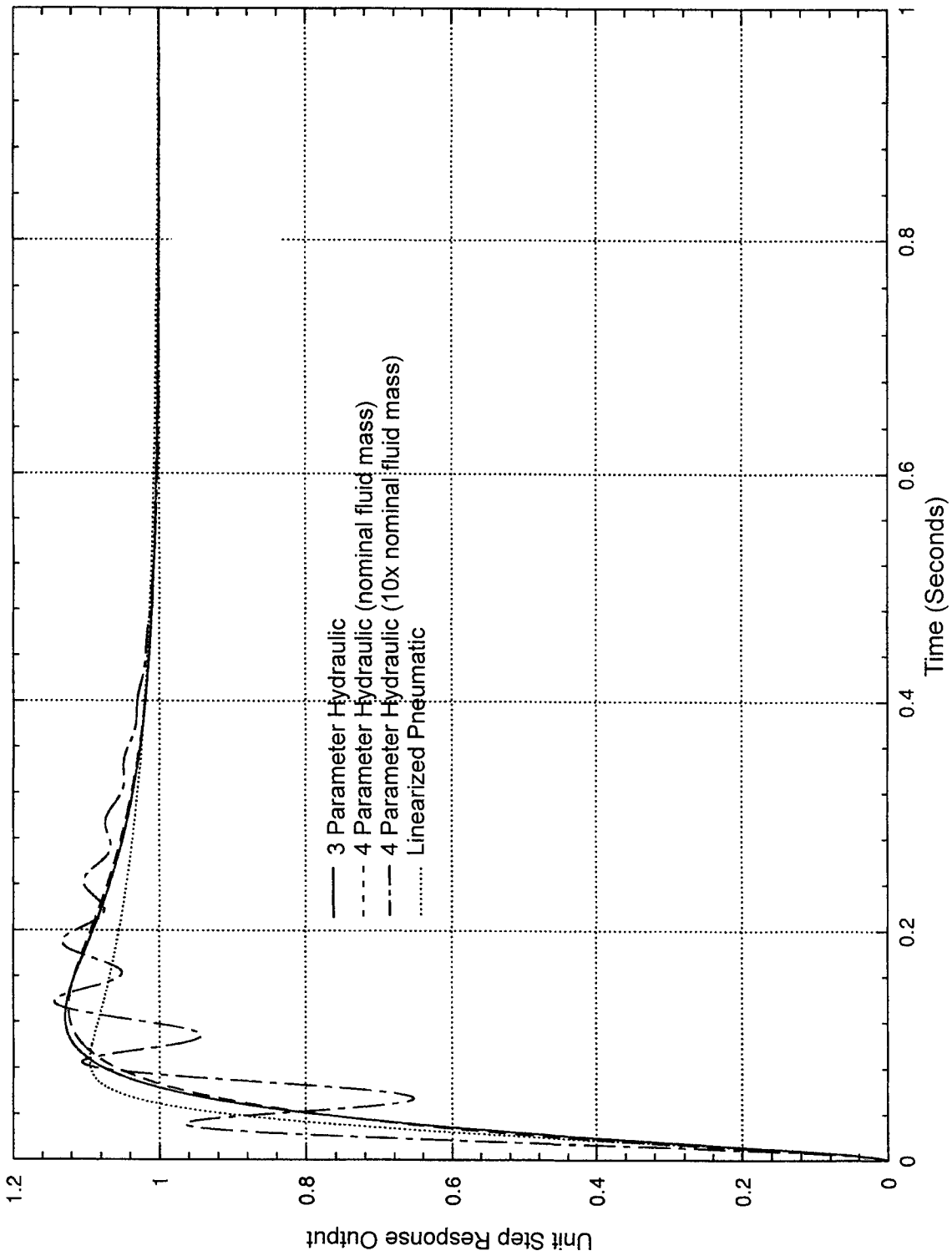

Figure 4-2. Step Responses of Three Linear D-Strut Isolation Systems

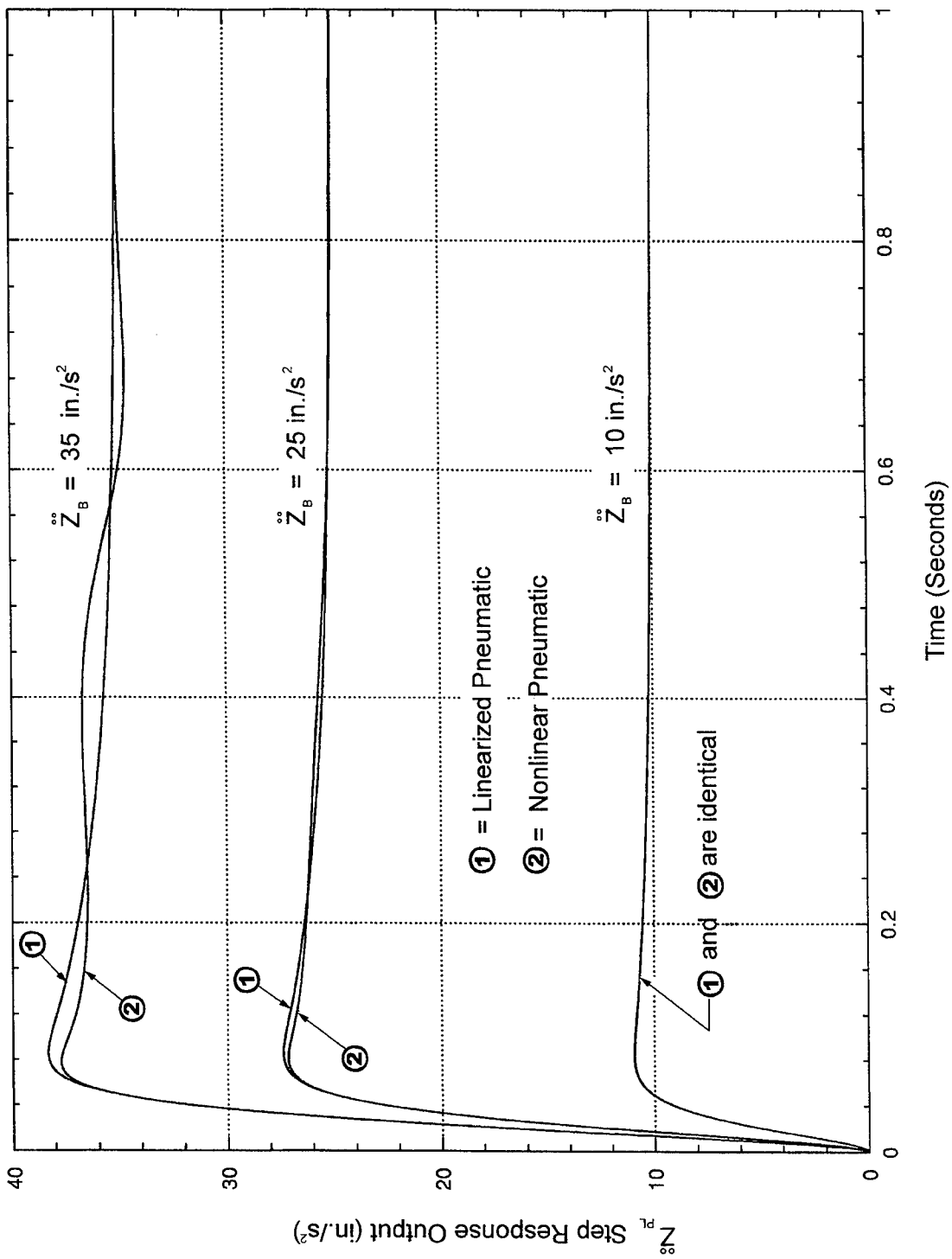

Figure 4-3. Step Response Comparison of Linearized and Nonlinear Pneumatic D-Strut Isolation Systems

The step responses are identical for $\ddot{Z}_B$ =10 in./s2. The step responses of the two models diverge as the amplitude of the input step command increases. The maximum allowable base acceleration step amplitude is limited to 36 in./s^2 by the maximum allowable gap transient, which is:

max gap = vs/asb = vd/adb = 0.0964 (in.)^3/0.474 (in.)^2 = 0.2034 in.

The peak gap transient and steady-state gap are 0.198 inches and 0.186 inches, respectively, for $\ddot{Z}_B$ = 36 in./s^2. The step response of the linearized isolator dynamic model only deviates by a maximum of approximately 6% from the nonlinear model over the entire operating range of the pneumatic isolator.

5.0 CONCLUSIONS

The hydraulic D-Strut three-parameter dynamic model [3] was expanded to a four-parameter model by including the effect of the fluid mass flow. The frequency responses and step responses of the two models are compared in Figures 4-1 and 4-2, respectively, for a typical D-Strut. These results indicate that the fluid mass flow is a predictable second-order effect. If $\frac{C_A}{2\sqrt{K_B M_{eq}}} > 0.7$, the three-parameter model of the hydraulic D-Strut is adequate.

A dynamic model was presented for a pneumatic D-Strut. This model is inherently nonlinear due to the compressibility of the gas. The nonlinear model was also linearized for small motion about an operating point. The pneumatic D-Strut parameters were intentionally selected such that its performance is comparable to the hydraulic D-Strut. The frequency responses and step responses of the hydraulic D-Strut and the linearized pneumatic D-Strut were compared. The results indicate that a pneumatic D-Strut can be designed to perform similar to a hydraulic D-Strut.

The step response of the nonlinear pneumatic D-Strut dynamic model was compared to the linear pneumatic D-Strut model. The linear and nonlinear model step responses are identical for a 10 in./s^2 step of base acceleration. This shows that the linear model is accurate for small motion. As the amplitude of the base acceleration is increased the nonlinear model step response begins to deviate from linear model step response. The largest base acceleration step input creates a gap transient which is nearly the maximum allowable by the length of the bellows.

REFERENCES

1. J. Rodden, H. Dougherty, L. Reschke, M. Hasha, and P. Davis, "Line-of-Sight Performance Improvement with Reaction Wheel Isolation," AAS Paper 86-005, AAS Guidance and Control Conference, February 1986.

2. D. Cunningham and P. Davis, "A Multiaxis Passive Isolation System for a Magnetic Bearing Reaction Wheel," AAS Paper 93-006, AAS Guidance and Control Conference, February 1993.

3. P. Davis, D. Cunningham, and J. Harrell, "Advanced 1.5 Hz Passive Viscous Isolation System," AIAA SDM Conference, Hilton Head, South Carolina, April 1994.

4. P. Davis, D. Carter, J. Sullivan, T. Hoffman, and A. Das, "Vibration Isolation System Using Hybrid D-Strut™ Technology for Precision Payloads," 19th Annual AAS Guidance and Control Conference, Paper No. AAS96-062, 1996.

Trade Study on Damping Curved Airfoil Shaped Plates

Michael L. Drake
Geoffrey J. Frank
David M. Hopkins

University of Dayton Research Institute
Aerospace Mechanics Division
300 College Park
Dayton, OH 45469-0110

ABSTRACT

This paper discusses the results of a project which focused on the development and evaluation of internal damping concepts applicable to damping curved airfoil shaped plates. Thirteen damping concepts were analyzed. The analysis was completed using an FEA. The initial analysis computed modal damping for the first four modes of the structure. As the study progressed, the final analysis on the best two damping concepts calculated the modal damping for the first thirty modes.

The system damping results were obtained using various damping materials, Young's moduli, and an assumed damping material loss factor of 1.0. The modal damping was calculated as the ratio of the strain energy in the damping elements (SED) divided by the total strain energy (TSE) in the structure times the assumed material loss factor. The damping goal was set at 0.04 loss factor. The final designs developed had an average modal damping value which exceeded 0.1. This paper details the damping concepts evaluated, the thought process which led from one design to the next, the analysis used to evaluate the damping concepts, and the results of the trade study.

KEY WORDS: damping, curved plates, finite element analysis,

1. INTRODUCTION

The damping of curved airfoil shaped structures has been, and will continue to be, of interest to the engineering community. Adding passive damping, in the form of externally applied constrained layer damping systems (CLD), to stationary vanes in a jet engine has been demonstrated successfully and implemented into standard production procedure on several engines. **(1,2,3)** The effectiveness of externally applied CLD on blades has been demonstrated on several projects, along with initial evaluation in the rotating environment. **(4,5,6)** However, in these programs, the durability of the CLD in the centrifugal force environment was very poor. The durability of external CLD on rotating blades, as well as the need to damp stationary vanes where external damping concepts are not aerodynamically acceptable, has lead to interest in developing internal damping systems for airfoil shaped structures. The current trend to hollow blades and the results of **reference 5**, demonstrate that there is room for damping systems inside the blades. The following paragraphs describe a design study which evaluated various concepts for incorporating viscoelastic damping materials inside an airfoil shaped structure.

2. STUDY STRUCTURE AND DESIGN GOALS

A cross section of the structure used in this study is shown in **Figure 1**. The airfoil cross section had a leading to trailing edge length of about 32 inches and a maximum thickness around 3 inches. **Figure 2** shows a 3-D view of the structure, which was about 84 inches long with an 8 foot radius curvature. The structural material was brass. The damping design goal was to obtain a modal loss factor of 0.04 or greater. The structural requirements placed on the damping design were:

Further author information -

E-mail: drake@udri.udayton.edu; WWW: http://www.udri.udayton.edu/conf/vdsc; Telephone: (937) 229-2654; Fax: (937) 229-4251

- the pocket could not be symmetric through the cross section;
- the minimum wall thickness on one side would be 1.0 inches; and,
- the minimum wall thickness on the other side would be 0.25 inches.

This study evaluated various pocket sizes and locations. The pockets were filled either with a damping material or with a three layer sandwich consisting of a damping material, a floating constraining layer (FCL), and another damping layer. These two basic concepts are illustrated in **Figures 3** and **4** respectively. In all but one case, the FCL was modeled as brass.

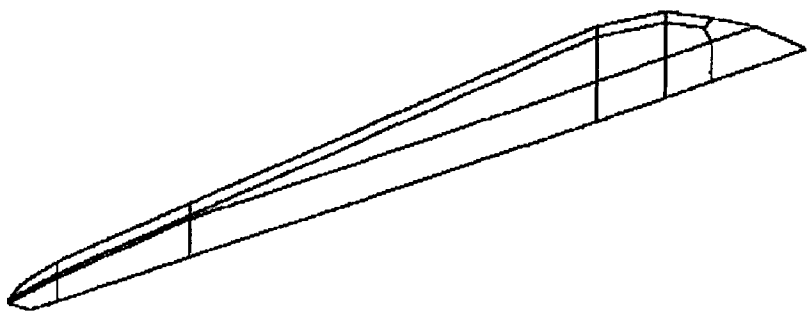

Figure 1. Cross Section of Structure Studied

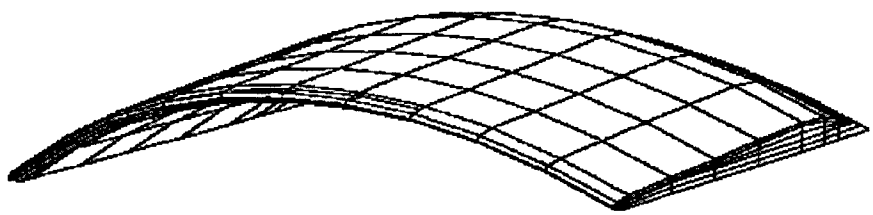

Figure 2. Structure Evaluated During The Study

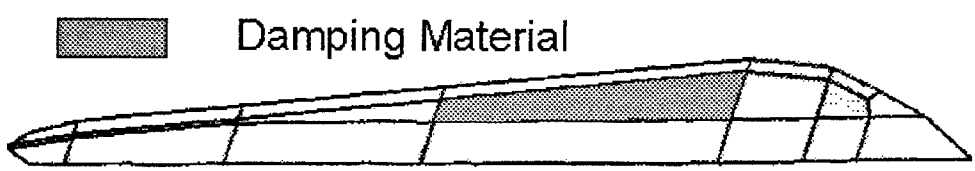

Figure 3. Damping Material Filled Pocket

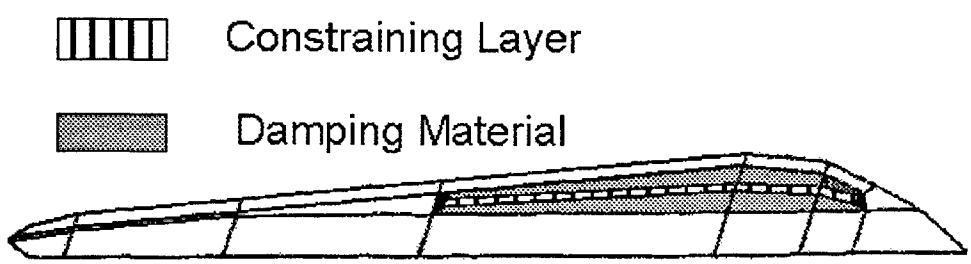

Figure 4. Floating Constraining Layer Concept

3. ANALYSIS APPROACH AND BASIC MODEL

The analysis approach used for this study was based on finite element analysis. Initial analysis (analysis of the low frequency modes) was completed using a PC based version of COSMOS/M (7); while analysis of the higher frequency modes was completed on a work station based version of ABAQUS (8). The modal damping was calculated using the modal strain energy method (9).

A cross section of the basic FE model used during this study is shown in **Figure 5**. Twenty node solid brick elements were used for the structure and damping systems. For the low mode analysis, the modal range of interest was the first four modes. To obtain accurate analysis with quick run times, 10 number of elements were used along the length of the structure. In the case of the high-frequency mode analysis, the first 30 modes were investigated and a total of 20 number of elements were used along the length of the structure.

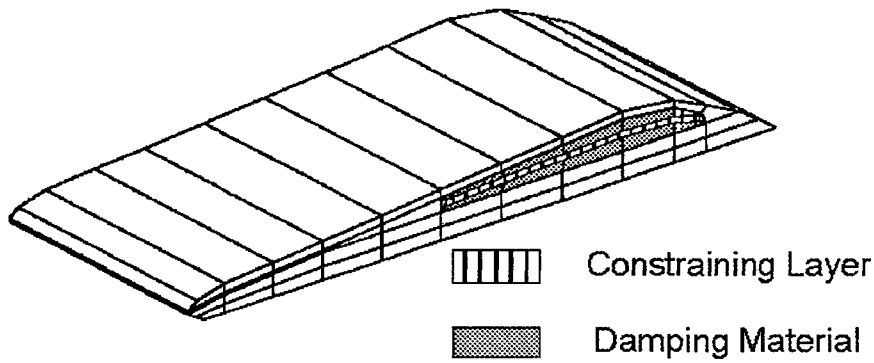

Figure 5. Basic FEA Model

To accomplish the goal of this study, it was necessary to determine the maximum level of damping attainable for various damping concepts. Therefore, the damping material was modeled with a material loss factor of 1.0. The damping material modulus was varied to identify the modulus value, for each damping concept evaluated, which stored the maximum strain energy for each resonant mode analyzed. This method of damping design analysis is detailed in **reference 10**. The process results in the definition of damping material properties required to obtain the maximum level of damping for a given damping configuration. This approach allows damping concept evaluation to occur on a "level playing field," and helps identify the appropriate damping material for the best damping concept for the system under study. This design process does not initially consider the variation damping material properties with temperature. The temperature variation must be considered as the design progresses for establishment of optimal parameters to production design specifications.

Table 1 shows the wall thickness combinations evaluated. **Figure 6** illustrates the six variations of damping concepts evaluated. A total of 19 damping design and structure combinations were identified with 13 of these combinations analyzed in detail. Six combinations were not analyzed because the results from similar concepts indicated that these concepts would not meet the requirements.

Table 1
Wall Thickness Combinations Evaluated

Structural Configuration	Base Thickness (in.)	Cover Thickness (in.)
A (Thickest/Thickest)	1-3/8	3/8
B (Thinnest/Thinnest)	1	1/4
C (Thickest/Thinnest)	1-3/8	1/4
D (Thinnest/Thickest)	1	3/8

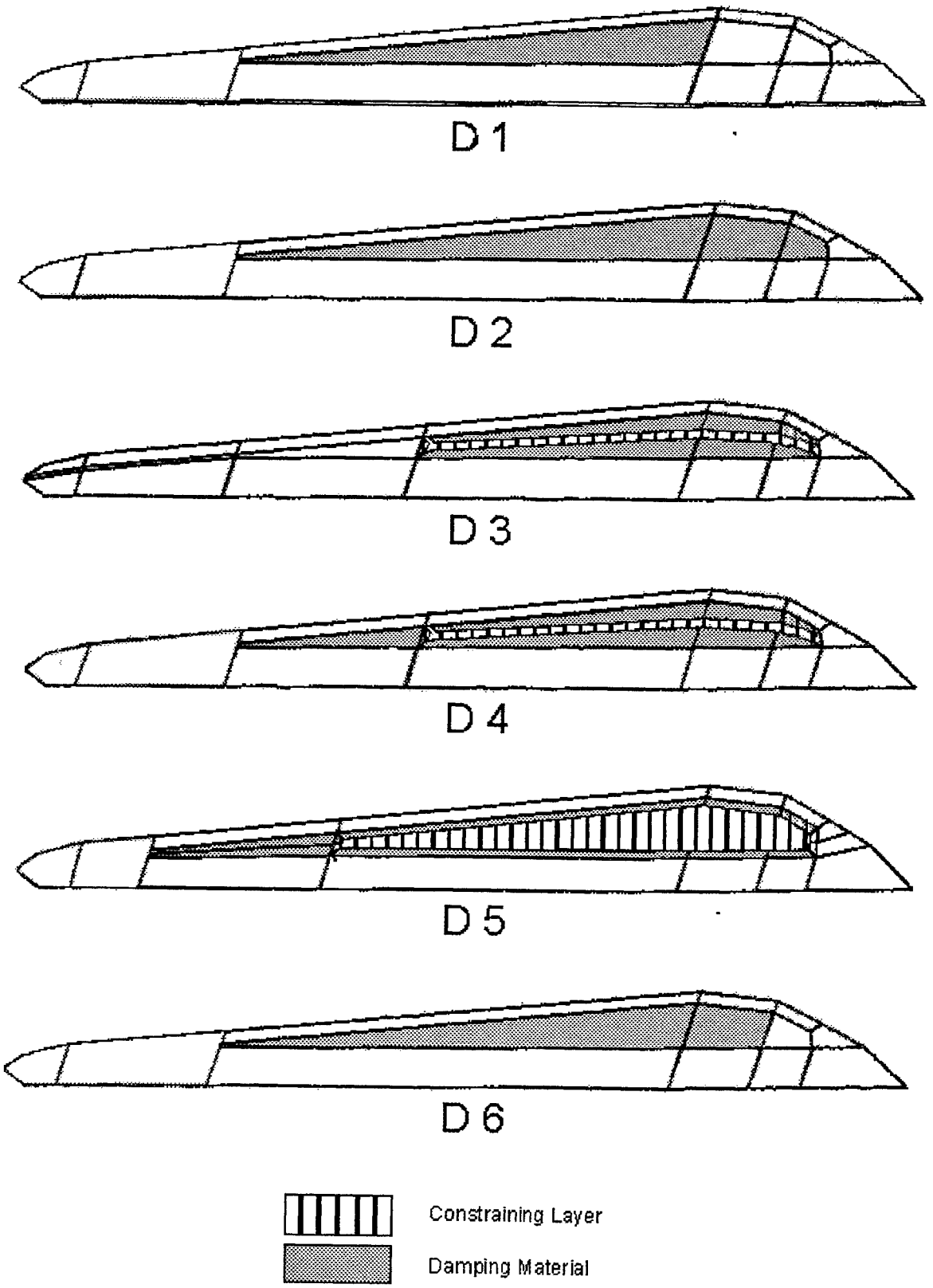

Figure 6. Specific Damping Concept Variations Evaluated

Table 2
Low Mode Analysis Results

Model #	Structural Configuration	Damping Configuration	Modal Damping	Required Modulus
1	A	D1	M1 - 0.035 M2 - 0.049 M3 - 0.016 M4 - 0.036	120,000 psi
2	A	D2	M1 - 0.071 M2 - 0.077 M3 - 0.039 M4 - 0.047	120,000 psi
3	D	D2	M1 - 0.083 M2 - 0.094 M3 - 0.051 M4 - 0.070	120,000 psi
4	D	D1	M1 - 0.042 M2 - 0.065 M3 - 0.021 M4 - 0.053	120,000 psi
5	C	D1	M1 - 0.034 M2 - 0.048 M3 - 0.017 M4 - 0.034	180,000 psi
6	A	D3	M1 - 0.036 M2 - 0.040 M3 - 0.044 M4 - 0.037	180,000 psi
7	A	D3*	M1 - 0.044 M2 - 0.043 M3 - 0.051 M4 - 0.045	120,000 psi
8	A	D3+	M1 - 0.036 M2 - 0.034 M3 - 0.039 M4 - 0.035	60,000 psi
9	A	D4	M1 - 0.078 M2 - 0.089 M3 - 0.055 M4 - 0.089	60,000 psi
10	D	D5	M1 - 0.115 M2 - 0.132 M3 - 0.087 M4 - 0.147	60,000 psi
11	A	D6	M1 - 0.057 M2 - 0.067 M3 - 0.028 M4 - 0.042	120,000 psi
12	A	D4 ^	M1 - 0.064 M2 - 0.076 M3 - 0.047 M4 - 0.082	60,000 psi
13	C	D5#	M1 - 0.105 M2 - 0.133 M3 - 0.073 M4 - 0.166	30,000 psi

* 50% stiffer constraining layer
+ constraining layer with Poison's ratio = 0.3
^ damping material between FCL and thin wall very soft
# constraining layer modulus $1 \cdot 10^7$ Psi

4. LOW-FREQUENCY MODE ANALYSIS RESULTS

Table 2 shows the results of the low-frequency mode analysis. Table 2 shows that even with the "perfect" damping material, models numbered 1, 2, 4, 5, 6, 7, and 10 would not achieve the required damping goal of 0.04 modal damping for all the modes. Several of the configurations have borderline compliance with the goal. For these configurations, using a damping material with the required modulus and a loss factor greater than 1.0 would probably result in compliance with the modal damping requirement. However, one should keep in mind that the greater the margin by which the design exceeds the goal, the better the design will perform over a wide temperature and frequency range. Also, the designer will have more overall latitude in the implementation of a more robust design.

The highest modal damping is achieved in models numbered 9 and 10. The difference in these two models is whether the damping layer or FCL is maintained at a constant thickness over the length of the design. In model 9, the FCL is constant thickness; while in model 10, the damping layer is constant thickness. The results of this study indicate that a constant damping layer thickness results in a higher modal damping.

The material modulus values required for maximum modal damping are highly dependent on the base structure, the constraining layer, and the geometry of the design. The modulus values shown in Table 2 may appear to be very high to someone who is used to damping thin sheet metal structures. **Table 3** presents modulus data for several damping materials which illustrate that the required damping material modulus is feasible.

Table 3
Damping Material Modulus Values

Material	Maximum Material Loss Factor (MMLF)	Young's Modulus @ MMLF (PSI)
Filled Butyl 1066	1.2	40,500
Class II Type 2.5	1.6	39,000
Class II Type 2	1.1	120,000
3M ISD-112	1.2	1,800

5. HIGHER FREQUENCY ANALYSIS RESULTS

Model 9 and 10 were refined and analyzed further. The analysis was completed for the first 30 modes of the structure. The results are given in **Tables 4** and **5. Figure 7** presents mode number 4 and **Figure 8** presents mode Number 26. The data in **Tables 4** and **5** and in Figures 7 and 8 indicate that the modal density and modal complexity were quite high. However, the damping systems performed very well with the modal damping for model 9 ranging from 0.031 to 0.229. Model 10 damping ranged from 0.069 to 0.323. Note that, with the analysis extended to a higher number of modes, only model 10 met the design goal of 0.04 modal damping for all the modes.

Table 4
Model 9 Modal Damping

Mode Number	Frequency (Hz)	Modal Damping	Mode Number	Frequency (Hz)	Modal Damping
1	63.11	0.076751	16	564.20	0.125025
2	106.94	0.089009	17	566.22	0.111795
3	158.06	0.056695	18	582.01	0.103819
4	202.39	0.093488	19	612.58	0.096638
5	215.93	0.069041	20	671.31	0.034618
6	221.76	0.100960	21	675.00	0.124544
7	274.38	0.031447	22	725.55	0.093083
8	325.26	0.052748	23	737.41	0.229064
9	345.09	0.119127	24	768.33	0.140488
10	368.86	0.084794	25	776.30	0.168338
11	408.50	0.133756	26	803.19	0.095386
12	414.56	0.108591	27	833.37	0.181937
13	443.92	0.130978	28	849.52	0.109556
14	486.31	0.098110	29	873.64	0.088070
15	497.29	0.141058	30	914.48	0.153358

Table 5
Model 10 Modal Damping

Mode Number	Frequency (Hz)	Modal Damping	Mode Number	Frequency (Hz)	Modal Damping
1	70.67	0.114249	16	540.79	0.183841
2	115.99	0.134114	17	575.72	0.176148
3	171.75	0.090922	18	607.91	0.172477
4	210.28	0.152440	19	638.40	0.188961
5	228.95	0.120847	20	703.87	0.177167
6	238.66	0.149971	21	709.05	0.073094
7	300.86	0.068775	22	737.85	0.323070
8	340.94	0.139644	23	739.72	0.151647
9	354.08	0.147808	24	767.95	0.191787
10	379.78	0.158813	25	777.37	0.292453
11	419.18	0.192787	26	788.70	0.169028
12	439.35	0.138469	27	840.42	0.252791
13	466.73	0.182845	28	841.10	0.144064
14	516.58	0.197399	29	918.22	0.188567
15	522.05	0.197229	30	924.48	0.210199

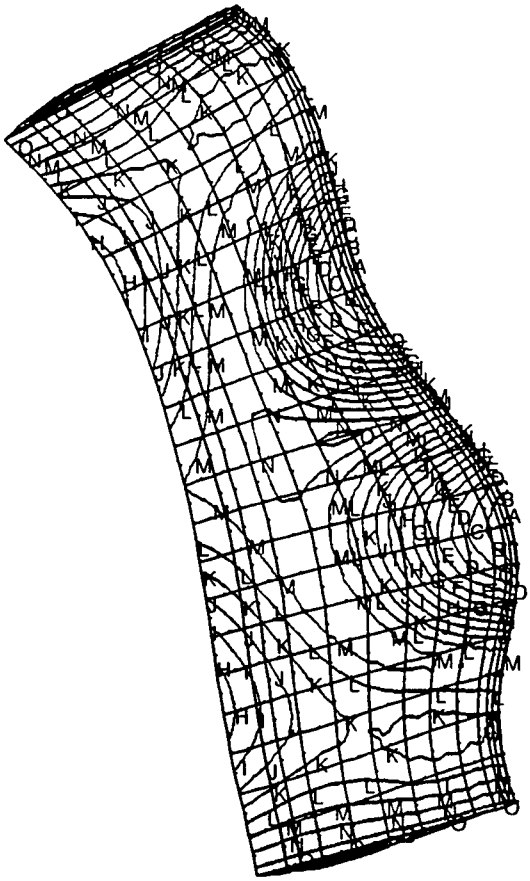

Figure 7. Calculated Mode Shape for Mode 4

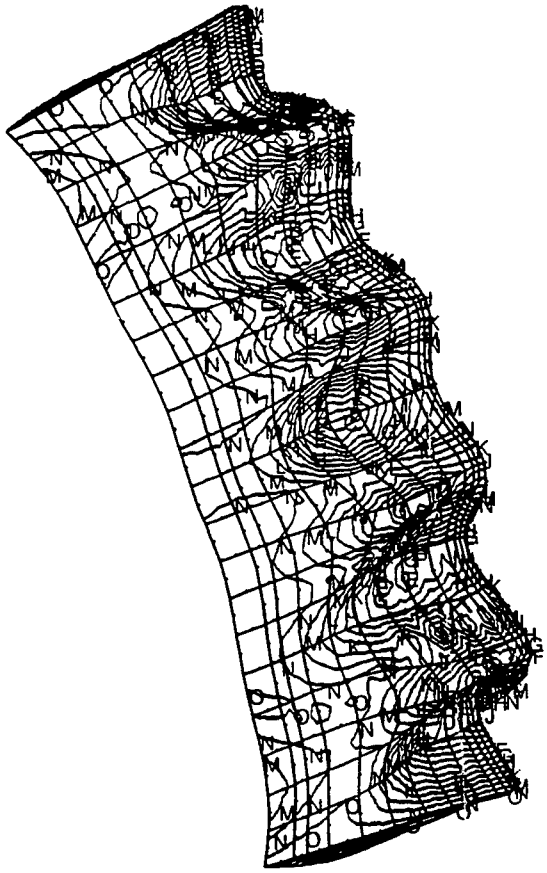

Figure 8. Calculated Mode Shape for Mode 26

6. CONCLUSIONS

The results of this effort demonstrated that significant damping can be added to an airfoil shaped structure through the use of internal damping concepts. The concept of an internal floating constrained layer damping system produced the maximum level of modal damping. The modal damping achieved extended over a large frequency range, provided that the proper damping material modulus was used. The location of the internal damping system and the damping material modulus are the controlling factors in the level of modal damping.

REFERENCES

1. Drake, M. L., "15th Annual Short Course on Damping Design for Vibration Control," University of Dayton, Dayton, OH, July 1992.

2. Rogers, L.C., and Parin, M. L., "Additive Damping for Vibratory Stress Reduction of Jet Engine Inlet Guide Vanes," presented at the 47th Shock and Vibration Symposium, Albuquerque, NM, 1976, published in the 47th S&V Bulletin.

3. Drake, M. L. and Sharp, J. D., "An Example of Additive Damping as a Cost Savings Alternative to Redesign," presented at the ASME Winter Annual Meeting, Atlanta, GA, Nov. 27 - Dec. 2, 1977, published in ASME Paper No. 77-WAGT-2.

4. Drake, M. L., Dominic, R. J., and Kumar, B., "Evaluation of High Temperature Damping Applications to Increase Fatigue Life in Rotating Jet Engine Components," AFWAL-TR-80-4174, Materials Laboratory WPAFB, December 1980.

5. Kluesener, M. F., "Dynamic Behavior of Advanced Fan Materials," AFWAL-TR-85-4105, Materials Laboratory WPAFB, October 1985.

6. Woehr, D. A. and Manwaring, S. R., "Augmented Damping of Low Aspect Ratio Fans (ADLARF)," WL-TR-95-2008, October 1994.

7. COSMOS/M Finite Element Analysis System, version 1.71, Structural Research and Analysis Corporation, Los Angeles, CA, 1994.

8. ABAQUS, version 5.4, Hibbitt, Karlsson, & Sorensen, Inc. Pawtucket, RI, 1994.

9. Johnson, C. D., Kienholz, D. A., and Rogers, L. C., "Finite Element Prediction of Damping in Beams with Constrained Viscoelastic Layers," The Shock and Vibration Bulletin, Vol 51, part 1 pp. 71-82, May 1981.

10. Drake, M. L., "A Different Approach to 'Designed In' Passive Damping," presented at the 55th Shock and Vibration Symposium, October 23-25, 1984, WPAFB.

A passive damper exhibiting the ideal dashpot characteristic, F = CV

Stephen Bennett[a] , Torey Davis[a], Paul Wilke[b], Gene Fosness[c]

[a]Honeywell Inc., Satellite Systems Operation, Glendale, Arizona
[b]CSA Engineering
[c]USAF Phillips Laboratory, Kirtland AFB, New Mexico

ABSTRACT

One of the most difficult tasks in the structural control industry is providing linear, predictable, passive damping over a wide frequency range. This challenge has been worked around successfully in the past, but rarely has it been performed ideally. The subject matter of this paper takes a radical step toward attaining the goal of linear damping performance, while adding very low static stiffness to the system being damped.

INTRODUCTION

This paper focuses on a passive damper that has been developed for a Payload Isolation Platform (PIP), a launch vibration isolation system. This passive damper closely exhibits the ideal relationship between force and velocity ($F = C \cdot V$, where C is a damping constant), over a wide frequency range. This unique damper utilizes viscous fluid, a *rigid* piston, and housing to achieve this highly linear performance (refer to Figure 1). The damper is also hermetically sealed, as required for almost all space flight hardware.

Constant Volume Damper Performance Parameters
Damping Coefficient: 25 lb-sec/in.
Operating Freq: 2 to >300 Hz
Damping Force: >500 lb
Stroke: ± 0.210 in.
Damper: Envelope: 1.8 in. dia x 5 in. long
Weight: 8.8 oz

Figure 1. ***Constant Volume Damper. One of eight constant volume dampers shown with rod ends for implementation into the CSA Payload Isolation Platform.***

The content herein will cover the design constraints and highlight some of the equations utilized to predict the operation of the constant volume damper. Details of the build and test will also be discussed. A prototype damper was designed and built as Honeywell Internal Research and Development (IR&D) project. This was the first opportunity to develop a working model of the theory on which the design is based. A contract for ten of the PIP dampers was awarded soon after, though the delivery schedule was too aggressive to allow extensive investigation of the IR&D damper. Customer testing was done with the prototype damper and aspects that could be improved with a redesign were revealed. Any areas to be improved compared to the prototype damper would require resolution with the first deliverable articles, without adverse effects to other features of the prototype design.

DESIGN CONSIDERATIONS

It is not possible to discuss the design details of the constant volume damper in depth, as the damper has been submitted for patent. Two important characteristics of fluid flow were needed to accurately predict the operation of the damper. The first is the damping coefficient realized when moving fluid from a chamber (bellows etc) through a hollow shaft. For an equation derivation, see below (also see references 2 and 3).

Description of the volume change in a fluid cavity:

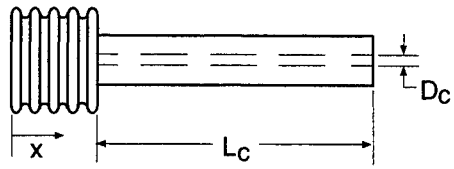

$$dV = \frac{\pi \cdot D^2}{4} x \text{ , D = effective diameter of bellows, x = displacement of cartridge body} \quad (1)$$

The flow rate is then:

$$\frac{dV}{dt} = \frac{\pi \cdot D^2}{4} \frac{dx}{dt} \text{ or } Q = \frac{\pi \cdot D^2}{4} U, \text{ where U = fluid velocity and Q = volumetric flow rate.} \quad (2)$$

Equating this flow rate to the flow through the orifice tube and solving for the differential pressure with respect to velocity yields:

$$\frac{dP_c}{U} = \frac{32 D^2 L_c \mu}{D_c^4}, \text{ : } D_c \text{ = tube inner diameter, } L_c \text{ = tube length, and } dP_c \text{ = differential pressure across tube.}$$

Utilizing the pressure drop and the equation for the damping constant, C=F/U, the equation for the damping constant can be determined:

$$C = \frac{8\pi \cdot D^4 L_c \mu}{D_c^4}, \text{ where D = effective diameter of bellows, } L_c \text{ = length of orifice, } \mu \text{ = fluid viscosity, and } D_c \text{ = orifice diameter.}$$

The second damping constant to be determined is the damping realized when moving a piston through a cylinder with an annulus for fluid passage between the two, see also reference 2.

The volume change due to motion of the piston is:

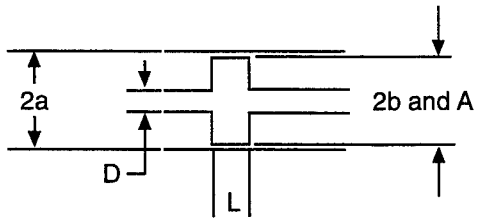

$$dV = \pi \cdot x \cdot \frac{A^2 - D^2}{4} \tag{9}$$

Where x is the piston displacement, A is the diameter of the piston, and D is the diameter of the shaft on which the piston travels.

The flow rate is then:

$$Q = \pi \cdot U \cdot \frac{A^2 - D^2}{4} \tag{10}$$

Where U is piston velocity.

This must be equal to the flow through the annulus formed by the piston and the cylinder in which it travels.

The flow rate though the annulus is developed for the case where the inside wall of the annulus (the piston) is moving opposite the flow (see references 1 and 2). Equating the flow rates:

$$\frac{\pi}{4} \cdot U \cdot \left[A^2 - D^2\right] = \frac{\pi \cdot dP}{8 \cdot \mu \cdot L}\left[a^4 - b^4 - \frac{\left[a^2 - b^2\right]^2}{\ln\left[\frac{a}{b}\right]}\right] - \pi \cdot U \cdot \left[a^2 - \frac{a^2 - b^2}{2 \cdot \ln\left[\frac{a}{b}\right]}\right] \tag{11}$$

Solving for dP/U:

$$\frac{dP}{U} = 8 \cdot \mu \cdot L \cdot \frac{\frac{A^2 - D^2}{4} + a^2 - \frac{a^2 - b^2}{2 \cdot \ln\left[\frac{a}{b}\right]}}{a^4 - b^4 - \frac{\left[a^2 - b^2\right]^2}{\ln\left[\frac{a}{b}\right]}}$$

The force required to balance the pressure drop is:

$$F = \frac{\pi}{4} \cdot \left[A^2 - D^2\right] \cdot dP \tag{13}$$

The coefficient of damping is C = F/U. Letting A = 2b, and combining:

$$C = \frac{2 \cdot \pi \cdot L \cdot \left[A^2 - D^2\right] \cdot \left[\frac{A^2 - D^2}{4} + a^2 + \frac{a^2 - b^2}{2 \cdot \ln\left[\frac{a}{b}\right]}\right]}{a^4 - b^4 - \frac{\left[a^2 - b^2\right]^2}{\ln\left[\frac{a}{b}\right]}} \tag{14}$$

Where D = diameter of piston shaft, A = diameter of piston, a = outer radius of annulus, b = inner radius of annulus, and L = length of annulus (piston).

Using the above design principles, the prototype rigid volume damper was designed and parts fabricated. The prototype rigid volume damper build went without incident. Filling the damper, however, was not completely straightforward.

The prototype damper tested well for short strokes, but an extended duration with longer strokes created a small dead band in the damper. It is believed the high shear forces and the high temperatures worked in conjunction to outgas the fill fluid, hence releasing an air bubble from solution.

The deliverable dampers would have to be filled with hydraulic fluid outgassed to alleviate the above anomaly, but fixes would not be tested due to schedule and equipment limitations. With this in mind, the fill fluid was processed to ensure it had been better outgassed before filling the damper. First a heater/agitator was ordered to better outgas the fill fluid. A glass flask is filled with silicone fill fluid, then put on a hot plate with a mechanical stirrer. This flask is evacuated using a high vacuum pump while being heated and stirred. Heating and stirring the fluid while applying vacuum outgasses the fill fluid. This outgassed fluid is more stable during rigorous damper movements, minimizing any air that may escape from solution under the elevated temperature and intense agitation of damper actuation. The damper, which is also under vacuum, is filled without the damper volume or the fluid being exposed to the atmosphere.

Build and test went smoothly for the deliverable dampers. Testing exhibited characteristics of a true linear damper (refer to Figures 2 through 5).

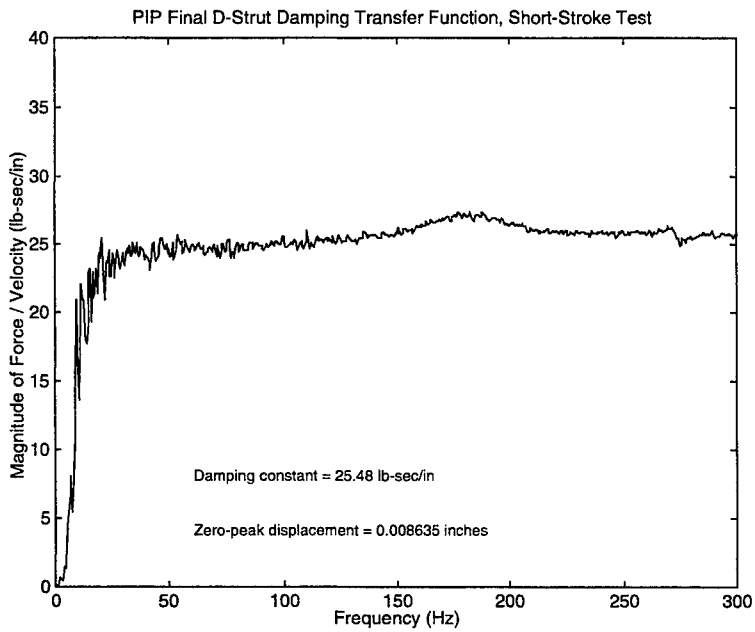

Figure 2. ***Transfer function for the short stroke testing of a PIP damper. The axes are Frequency vs. Damping constant.***

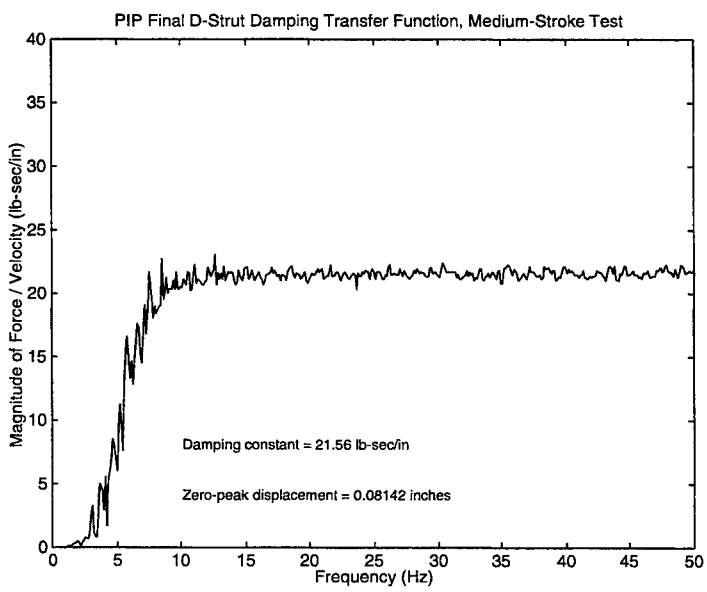

Figure 3. ***Transfer function for the medium stroke testing of a PIP damper. The axes are Frequency vs. Damping constant.***

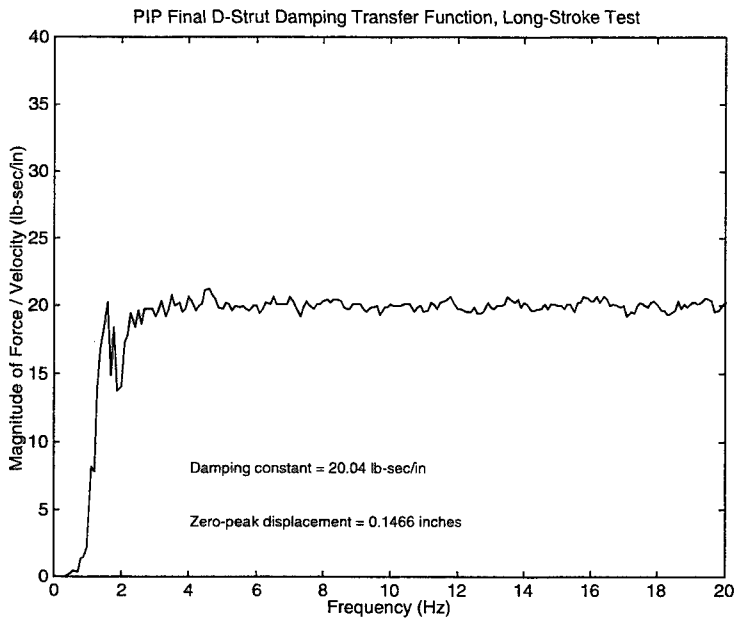

Figure 4. ***Transfer function for the long stroke testing of a PIP damper. The axes are Frequency vs. Damping constant.***

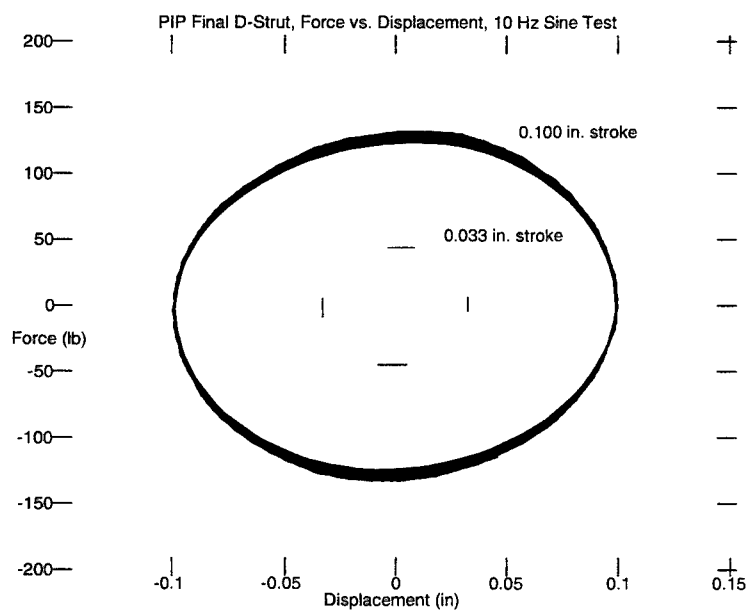

Figure 5. ***Orbit plot of Force vs. Displacement, exhibiting the circular nature of pure damping.***

As a practical matter, the rigid volume damper offers several distinct advantages. These include its relative simplicity, its complete analytical predictability, and its linear performance over a broad frequency spectrum.

This pure dashpot performance allows us to easily design a *typical* two parameter vibration isolation system, shown schematically in Figure 6. Designing a high performance three parameter system, also shown schematically in Figure 6, is straightforward with a frequency independent dashpot.

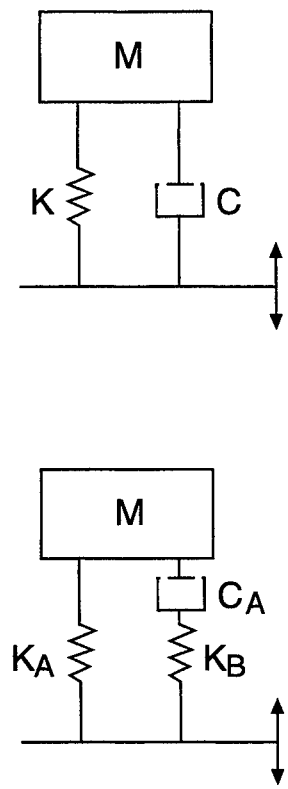

Figure 6. ***Schematics of a 2 and 3 parameter vibration isolation system. M is mass, K is a spring, and C is a dashpot.***

The two parameter system is a classical linear spring and dashpot isolation configuration, where the isolator softens the interface between the mass and its base structure. This softening reduces the dynamic loads transmitted to the mass from the base above the isolators natural frequency. A transmissibility plot for the two parameter system is shown in Figure 7. Note how the isolation system begins to reduce the dynamic loading after system resonance.

The three parameter system, by virtue of the tuning spring k_b, can dramatically improve vibration isolation performance at frequencies above the system resonance (refer to Figure 7). For an optimally tuned isolation system, this increased performance cost a small amount of damping at the isolator resonance frequency, also shown in the transmissibility plots in Figure 7.

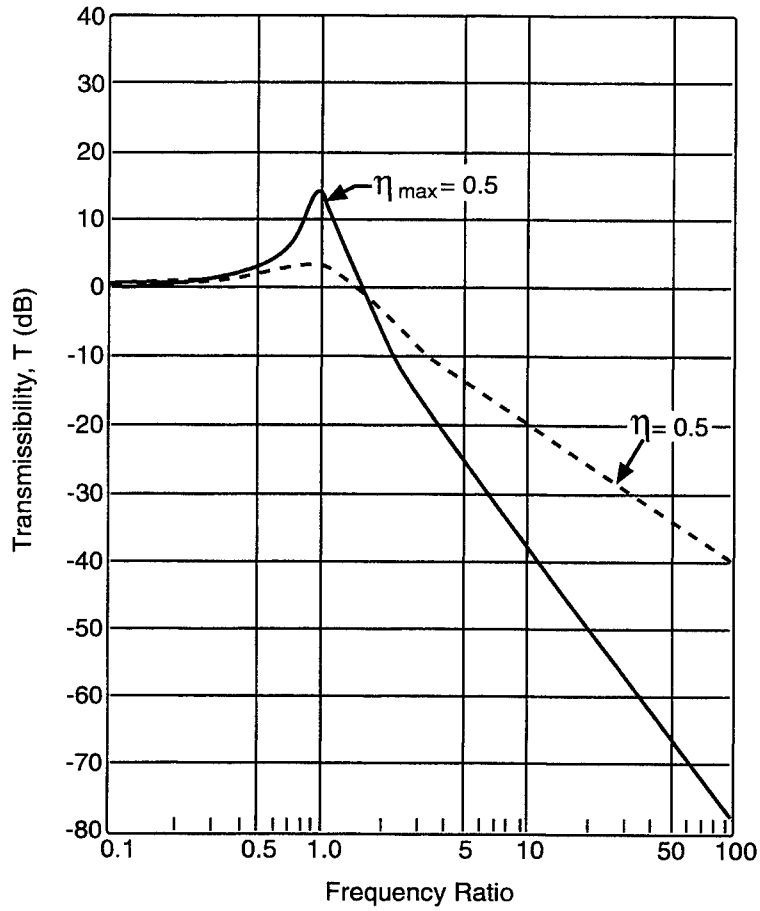

Figure 7. ***Example of transmissability curves for a two parameter system (dashed line) and the same system optimally tuned as a three parameter system (solid line).***

The decision to use a two or three parameter system is normally based on whether a high degree of isolation is required, necessitating a three parameter system; however, if a greater degree of energy removal through damping is required, a two parameter system is used. The two parameter system, in its purest form, is one of the most difficult to physically realize. Two of the most popular hardware implementations for vibration isolation systems are viscoelastic (rubber mounts) and viscous damped (automobile strut) isolation systems. For both of these vibration isolation mount technologies performance tradeoffs are almost always made to compensate for hardware shortcomings.

Viscoelastic isolators are difficult to design, in that stiffness and damping cannot be changed independently. Both characteristics, stiffness and damping, reside in the viscoelastic material. This makes it difficult to truly tune the two parameters to achieve the desired performance.

The viscous fluid damped two parameter isolation systems are also difficult to physically implement. Difficulties arise from stray structural compliances found in series with the dashpot. Stray compliances usually come in the form of flexible fluid containment chambers and housing flexibility. If not properly accounted for, these structural compliances, normally welcome in three parameter systems, can be the cause for less than ideal damping performance.

The rigid volume damper virtually erases both of these design limitations for isolation systems, giving the designer a piece of hardware that will perform as a pure dashpot over a large, useful frequency range (0 to > 300 Hz). The rigid volume damper also makes tuning a high performance, three parameter isolation system a less complicated and more predictable task. The stray compliances mentioned earlier no longer must be dealt with after testing, to optimally tune the isolation system. A simple tuning spring (K_b) placed in series with the rigid volume damper, early in the design phase, is all that is necessary to fine tune the system. In short, the rigid volume damper dramatically simplifies the steps necessary to design and build a truly optimum vibration isolation system.

Another practical use for the rigid volume damper is as a snubber for plumbing or equipment, subject to high vibration or impact loading. As a snubber, the rigid volume damper is perfectly suited to an adverse environment because it is hermetically sealed to prevent contamination to any of the precisely manufactured moving parts. It also has high load capacity in a small package. The damping constant is readily changed to accommodate most any application.

Finally the rigid volume damper has high stroke capacity for its size. Many similar designs are limited in their available stroke. As built the rigid volume damper has a stroke of ± 0.210 in. To increase this stroke even greater does not greatly increase the required envelope or weight of the rigid volume damper.

Follow on work is being done to incorporate the constant volume design into a hybrid, passive and active, isolator. The hydraulic section will be essentially the same in design with a pneumatic spring that can be controlled electronically to vary and tune isolator spring rates.

REFERENCES

1. Analysis: Axial Damping, David Cunningham, 1990.
2. Fluid Mechanics, Streeter, McGraw Hill, 1962.
3. Engineering Notebook, Brian Workman, 1991.

Passive damping in optical tables using highly distributed inertial dampers

Jeffrey. A. Zapfe

Kinetic Systems, Inc., 20 Arboretum Road, Boston, MA 02131

ABSTRACT

Optical tables are typically used in applications that require a very flat, rigid working surface. The grade of the optical table determines the amount of damping augmentation used to attenuate modal vibration. Discrete tuned mass dampers are a popular and effective damping method, however, their narrow effective bandwidth requires precise tuning to the table's resonant frequency. The present research deals with a damping method whereby a large number of small tuned dampers are distributed over the table's surface. In addition to the spatial distribution, the dampers are also distributed in frequency, providing energy dissipation over a wide frequency band. The wide effective bandwidth makes the distributed damping treatment extremely tolerant to variations in the table's dynamics. Test data is presented for a system of 349 dampers applied to a 243.8 cm x 121.9 cm x 20.3 cm optical table. The distributed damper attenuated both the first bending and the first torsion modes of the table, with a mass increase comparable to that realized with conventional discrete tuned dampers. The experimental results compared favorably to analytical predictions obtained using a full domain plate model.

Keywords: vibration control, passive damping, tuned mass dampers, optical table

1. INTRODUCTION

Optical tables are designed to provide a very flat, rigid working surface and are typically used for applications where even small deflections of the working surface (static and dynamic) can not be tolerated. The stiffness to weight ratio of the table is maximized through the use of a sandwich construction. The most common table configuration utilizes stainless steel facesheets with a steel honeycomb core. Optical tables range in size from 91 cm x 91 cm (3' x 3') to 183 cm x 488 cm (6' x 16') with thicknesses ranging from 20 cm (8") to 61 cm (24").

The optical table is usually supported by pneumatic mounts to isolate the working surface from the adverse effects of floor vibration. The standard pneumatic mount has a natural frequency of 1.75 Hz that provides approximately 90% isolation at 6 Hz and 99% at 20 Hz. At frequencies near the modal frequencies of the table, the floor input is very small, however the table may still experience excitation from installed equipment or even acoustic pressure.

Due to the metallic construction of the table, the inherent material damping is very low and the finished product can exhibit strong resonant peaks at its modal frequencies. The two lowest frequency modes are typically the first bending mode and the first torsion mode. The order of the two modes is dependent on the table's aspect ratio. Below a length to width ratio of 2:1, the torsion mode is usually the lowest in frequency, while the bending mode is typically lower for ratios above 2:1. For many applications, static deflection is the sole consideration, hence the table resonances are not a cause for concern. However, applications that require a stable dynamic surface do require some augmentation to attenuate the lowest frequency table modes. Damping methods for optical tables range from standard constrained layer treatments to inertial viscous dampers to tuned mass inertial dampers. Tuned mass dampers (TMDs) are popular because they provide lightweight, effective damping that can be targeted to address specific table resonances.

A TMD is a mass efficient damper that is very effective over a narrow bandwidth, however this local effectiveness also makes the TMD difficult to apply in practice. Because the modal frequencies of the undamped table fluctuate due to normal manufacturing variations, the TMDs must be specifically tuned for each table, requiring a time consuming step in the manufacturing process. The effective bandwidth of a TMD can be broadened somewhat through the introduction of

SPIE Vol. 3045 • 0277-786X/97/$10.00

dissipation. The effective band can be widened still further by combining a number of absorbers, each tuned to a slightly different frequency, into a distributed system.

Several authors have examined inertial dampers distributed either in space or in frequency. Nashif *et al.*[1] examined the effect of spatially distributed dampers on beams, while Smith, Rao and Dyer[2] analyzed the transverse vibration of flat plates with spatially distributed tuned absorbers. Igusa and Xu[3] showed, on a single degree of freedom base structure, how multiple TMDs, each tuned to a slightly different frequency, could provide broadband energy dissipation.

The analysis of tuned mass systems, distributed both spatially and in frequency is a more recent area of research. In the context of fuzzy structures, Pierce, Sparrow and Russell[4] used a distribution of spring/mass systems to model a plate with internal attachments. The authors showed how, as the number of absorbers became large, the effective mass of the absorbers could be approximated by a smoothly varying, complex function of the driving frequency.

The broadband effectiveness of highly distributed inertial dampers was demonstrated by Zapfe and Lesieutre[5] on simply supported beams. The authors showed how the distributed system could maintain its broadband damping effectiveness even when the beam was subjected to an in-plane tensile force, a loading condition that significantly reduced the effectiveness of a conventional strain based damping treatment.

The present research extends the work of Zapfe and Lesieutre to plates. Experimental results are presented for a highly distributed, broadband system of dampers applied to the surface of an optical table. The test data is compared to the analytical predictions of a full domain plate model. The highly distributed damping treatment is appealing because it surpasses the performance of a conventional discrete TMD treatment while eliminating the time consuming tuning step.

2. DISTRIBUTED TUNED MASS ABSORBERS

Consider a system of N discrete tuned mass dampers attached to a common rigid base. The individual damper natural frequencies are designed to fall within some frequency band. Motion of the base results in a dynamic reaction force produced by the collective TMDs. The magnitude and phase of the reaction force are related to the base motion by the effective dynamic mass of the combined system. In the frequency domain, the effective mass, $M_d(s)$, can be expressed by:

$$M_d(s) = \sum_{i=1}^{N} \frac{m_i}{\left(\frac{m_i}{k_i} s^2 + 1 \right)}, \tag{1}$$

where k_i and m_i are the stiffness and mass of the ith damper. For very low frequencies, the effective mass is simply the collective mass of the dampers. At very high frequencies, the masses are effectively motionless and the system behaves like N parallel springs. At intermediate frequencies, the effective mass has a magnitude and phase, meaning the damper has the ability to dissipate energy. As number of dampers becomes large and the frequency spacing becomes small, the dampers lose their individuality and the magnitude and phase of the effective mass can be accurately represented by smoothly varying functions of the driving frequency. The need for large numbers of dampers to achieve a smooth collective behavior can be alleviated through the introduction of dissipation into the spring material. In the present analysis, energy dissipation is modeled by a complex modulus formulation wherein the spring rate in Eq. (1) is replaced by the complex quantity,

$$k_i^* = k_i \left(1 + j \eta_i \right), \tag{2}$$

where η_i is the loss factor associated with the spring material.

Substitution of Eq. (2) into Eq. (1), along with the added substitution $s=j\omega$, yields the steady state effective mass for a collection of tuned mass dampers with dissipative springs,

$$M_d(j\omega) = \sum_{i=1}^{N} \frac{m_i \omega_i^2 \left(1 + j \eta_i \right)}{\omega_i^2 \left(1 + j \eta_i \right) - \omega^2}, \tag{3}$$

where $\omega_i^2 = k_i/m_i$, is the natural frequency of the ith damper. The spring rate does not appear explicitly in Eq. (3) since it is

determined once the mass and natural frequency of the damper are specified. Without dissipation, the magnitude of the effective mass is infinite at each of the damper resonant frequencies. With dissipation, the magnitude and phase of the effective mass are smoothly varying functions of the driving frequency.

2.1 Application of the distributed damper to a plate

For a plate application, the discrete dampers in Eq. (3) would be distributed over some coverage area. Assuming the dampers are evenly distributed within the area, the collective system can be described by an effective mass per unit area,

$$\rho_{eff}(\omega) = \frac{1}{A_d} \sum_{i=1}^{N} \frac{m_i\, \omega_i^2\, (\, 1 + j\, \eta_i\,)}{\omega_i^2\, (\, 1 + j\, \eta_i\,) - \omega^2}, \tag{4}$$

where A_d is the damper coverage area. The implicit assumption associated with Eq. (4) is that the effective mass of an elemental area ($dxdy$) is the same at all points within the coverage area. As an effective mass per unit area, the distributed damper can be readily incorporated into a plate (or shell) model as if it were a homogeneous material with a uniform area density, the only distinction being the area density has a magnitude and phase that are both frequency dependent. It should be noted that, at a specific driving frequency, the sum in Eq. (4) simply reduces to a complex number.

3. ANALYTICAL PLATE MODEL

The optical table utilizes a sandwich construction to produce a stiff, lightweight structure. The analytical plate model incorporates a Mindlin[6] displacement field through the thickness with full domain shape functions defined at the mid-plane, about which the table is assumed to be symmetric. The assumed displacement field in the plate is,

$$\begin{aligned} u(x,y,z,t) &= z\, \Psi_x(x,y)\, \Omega(t), \\ v(x,y,z,t) &= z\, \Psi_y(x,y)\, \Omega(t), \\ w(x,y,z,t) &= W_0(x,y)\, \Omega(t), \end{aligned} \tag{5}$$

where W_0 is the mid-plane deflection and Ψ_x and Ψ_y are the mid-plane rotations in the x and y directions respectively. Mid-plane extensions are not included in the model because the primary motion of interest is in the transverse direction. The mid-plane functions are interpolated spatially using the polynomial functions,

$$\begin{aligned} \{\, N_\Psi \,\} &= \{\, 1,\, x,\, x^2,\, \ldots\, x^N,\, y,\, yx,\, yx^2,\, \ldots\, yx^N,\, \ldots\, y^N,\, y^N x,\, y^N x^2,\, \ldots\, y^N x^N \,\}^T, \\ \{\, N_W \,\} &= \{\, 1,\, x,\, x^2,\, \ldots\, x^{N+1},\, y,\, yx,\, yx^2,\, \ldots\, yx^{N+1},\, \ldots\, y^{N+1},\, y^{N+1}x,\, y^{N+1}x^2,\, \ldots\, y^{N+1}x^{N+1} \,\}^T. \end{aligned} \tag{6}$$

The transverse polynomial field is one order higher than the in-plane polynomials to inhibit shear locking[7].

The interpolations functions are related to the nodal coordinates through transformation matrices. Figure 1 shows the nodal locations for a N=4 grid. In the figure, the common nodes are used both by $\{N_\Psi\}$ and $\{N_W\}$, while the nodes forming a cross in the center are only used by the higher order vector, $\{N_W\}$. The mid-plane deflections at any point in the plate can be expressed in terms of the nodal deflections by,

$$\begin{aligned} \Psi_x(x,y) &= \{\, N_\Psi \,\}^T\, [\, B \,]\, \{\, \Psi_A \,\}, \\ \Psi_y(x,y) &= \{\, N_\Psi \,\}^T\, [\, B \,]\, \{\, \Psi_B \,\}, \\ W_0(x,y) &= \{\, N_W \,\}^T\, [\, A \,]\, \{\, W \,\}, \end{aligned} \tag{7}$$

where $\{\Psi_A\}$, $\{\Psi_B\}$ and $\{W\}$ are the nodal rotations and transverse displacement, respectively. The $[A]$ and $[B]$ matrices are coefficient matrices used to generate Lagrangian shape functions from the polynomial field in Eq. (6). A Lagrangian shape function is unity at the node in question and zero at all others. The entries in the $[A]$ and $[B]$ matrices are determined by the (x,y) coordinates of the nodes in the mesh.

The displacement of a general point in the plate, in terms of the nodal displacements, is given by:

$$\{ U \} = [Z_1] [XY_1] [AB] \{ \delta \}, \tag{8}$$

where,

$$\{ U \} = \{ u, v, w \}^T, \qquad \{ \delta \} = \{ \{\Psi_A\}^T, \{\Psi_B\}^T, \{W\}^T \}^T,$$

$$[Z_1] = \begin{bmatrix} z & 0 & 0 \\ 0 & z & 0 \\ 0 & 0 & 1 \end{bmatrix}, \qquad [XY_1] = \begin{bmatrix} \{N_\Psi\}^T & \{0\}^T & \{0\}^T \\ \{0\}^T & \{N_\Psi\}^T & \{0\}^T \\ \{0\}^T & \{0\}^T & \{N_W\}^T \end{bmatrix}, \quad [AB] = \begin{bmatrix} [B] & [0] & [0] \\ [0] & [B] & [0] \\ [0] & [0] & [A] \end{bmatrix}.$$

The elemental strain-displacement relations, applied to the displacement field in Eq. (8), yield a relationship between the strain field and the nodal displacements,

$$\{ \epsilon \} = [Z_2] [XY_2] [AB] \{ \delta \}, \tag{9}$$

where,

$$\{ \epsilon \} = \{ \epsilon_x, \epsilon_y, \gamma_{xz}, \gamma_{yz}, \gamma_{xy} \}^T,$$

$$[Z_2] = \begin{bmatrix} z & 0 & 0 & 0 & 0 \\ 0 & z & 0 & 0 & 0 \\ 0 & 0 & 1 & 0 & 0 \\ 0 & 0 & 0 & 1 & 0 \\ 0 & 0 & 0 & 0 & z \end{bmatrix}, \quad [XY_2] = \begin{bmatrix} \{N_\Psi\}_x^T & \{0\}^T & \{0\}^T \\ \{0\}^T & \{N_\Psi\}_y^T & \{0\}^T \\ \{N_\Psi\}^T & \{0\}^T & \{N_W\}_x^T \\ \{0\}^T & \{N_\Psi\}^T & \{N_W\}_y^T \\ \{N_\Psi\}_y^T & \{N_\Psi\}_x^T & \{0\}^T \end{bmatrix},$$

and $\{\}_x$ and $\{\}_y$ represent partial differentiation with respect to x and y respectively.

The constitutive relationship between the stresses and strains is given by,

$$\{ \sigma \} = [E(z)] \{ \epsilon \}, \tag{10}$$

where, $[E(z)]$ is a 5 x 5 matrix whose entries depend on the thickness coordinate (facesheet or core material).

The mass and stiffness matrices are given by the following integrals,

$$\begin{aligned} [M] &= [AB]^T \int_{-a}^{a} \int_{-b}^{b} [XY_1]^T \int_{-h/2}^{h/2} [Z_1]^T \rho(z) [Z_1] \, dz \, [XY_1] \, dx \, dy \, [AB], \\ [K] &= [AB]^T \int_{-a}^{a} \int_{-b}^{b} [XY_2]^T \int_{-h/2}^{h/2} [Z_2]^T [E] [Z_2] \, dz \, [XY_2] \, dx \, dy \, [AB], \end{aligned} \tag{11}$$

where $\rho(z)$ is the material density distribution. The thickness integrations result in section stiffness and mass parameters analogous to the bending stiffness and area density in a Kirchoff isotropic plate model. In the present implementation, stiffness terms involving the transverse shear modulus are only integrated over the core. Further, a complex modulus formulation is used to model dissipation in the plate materials, hence the stiffness matrix is complex. The mass matrix includes both transverse and rotatory inertia. Because of the polynomial shape functions, the spatial integrals have closed form solutions.

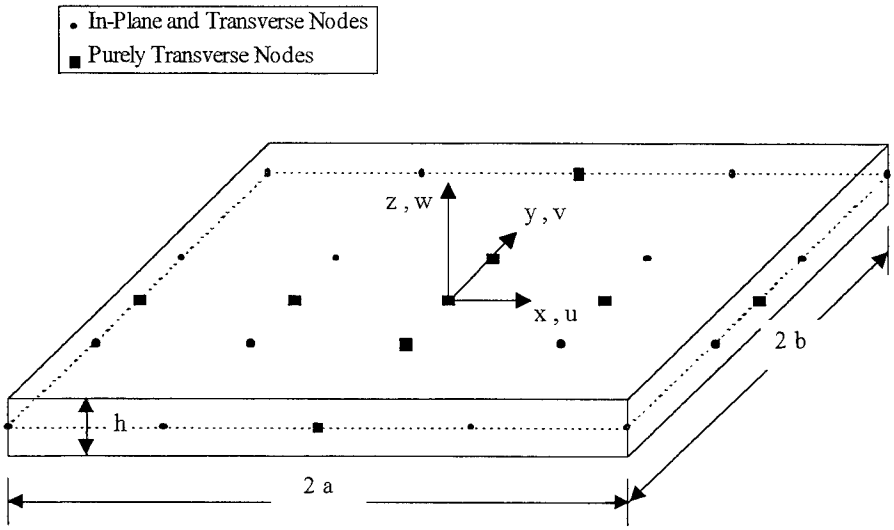

Figure 1. Plate model with N=4 mesh.

The stiffness and mass matrix can be partitioned into in-plane and transverse components, facilitating a condensation phase in the solution procedure. The partitioned mass and stiffness matrix are given by:

$$[\,K\,] = \begin{bmatrix} [K_{11}] & [K_{12}] & [K_{13}] \\ [K_{12}]^T & [K_{22}] & [K_{23}] \\ [K_{13}]^T & [K_{23}]^T & [K_{33}] \end{bmatrix}, \qquad [\,M\,] = \begin{bmatrix} [M_{11}] & [0] & [0] \\ [0] & [M_{22}] & [0] \\ [0] & [0] & [M_{33}] \end{bmatrix}. \tag{12}$$

The first row partition corresponds to the $\{\Psi_A\}$ nodal rotations, the second row to the $\{\Psi_B\}$ rotations and the third row to the transverse nodal deflections. The mid-plane rotations and transverse displacement are coupled only through the stiffness matrix. In the mass matrix, $[M_{11}]$ and $[M_{22}]$ arise because of rotatory inertia while $[M_{33}]$ corresponds to the transverse inertia.

3.1 Incorporation of the C channel

The C channel is a steel section that runs around the perimeter of the table. The C channel is welded to the top and bottom facesheets, thereby creating a torsion box that adds to the torsional stiffness of the table. The mass of the C channel is incorporated into the transverse portion of the mass matrix by the line integral,

$$[\,\Delta M_{33}^{C}] = \rho_C\,[\,A\,]^T \oint_L \{\,N_W\,\}^T\,\{\,N_W\,\}\,dl\,[\,A\,] = \rho_C\,[\,g^C\,], \tag{13}$$

where L is the path of integration, which in this case is a rectangular box, and ρ_C is the linear density of the C channel. The matrix $[g^C]$ is a geometric matrix that depends on the grid coordinates and the location of the channel. In the plate model, the plate's torsional stiffness is increased by an influence coefficient to account for the torsional stiffness of the C channel.

3.2 Incorporation of the distributed dampers

Because of the large number of dampers in the distributed system, the collective dampers can be accurately incorporated into the plate model as a frequency dependent mass per unit area. Further, the dampers are assumed to be applied in rectangular patches, which allows their placement in areas of maximum transverse motion. Using a frequency dependent effective mass per unit area, $\rho_{eff}(\omega)$, the contribution of the kth patch to the mass matrix is,

$$[\ \Delta M_{33}^{k}\ ] = \rho_{eff}(\omega)\ [\ A\ ]^T \int_{x_l}^{x_h} \int_{y_l}^{y_h} \{\ N_W\ \}^T\ \{\ N_W\ \}\ dx\ dy\ [\ A\ ] = \rho_{eff}(\omega)\ [\ g^k\ ], \tag{14}$$

where x_l, x_h, y_l, y_h define the physical dimensions of the rectangular patch. The matrix $[g^k]$ is a geometric matrix that depends on the grid and the patch size, while the multiplier, $\rho_{eff}(\omega)$ depends on the driving frequency. If the effective mass is the same for all patches, the total increment to the transverse mass matrix is,

$$[\ \Delta M_{33}\ ] = \rho_{eff}(\omega) \sum_{k=1}^{N_{patches}} [\ g^k\ ] = \rho_{eff}(\omega)\ [\ G\ ], \tag{15}$$

where, $[G]$ is the sum of the individual patch geometric matrices. It should be noted that, in this development, the distributed dampers only effect the transverse portion of the mass matrix, the rotatory inertia is not affected.

3.3 Forced response equations of motion

The steady state equations of motion for the plate subjected to a sinusoidally varying transverse load are,

$$\left[\begin{bmatrix} [K_{11}] & [K_{12}] & [K_{13}] \\ [K_{12}]^T & [K_{22}] & [K_{23}] \\ [K_{13}]^T & [K_{23}]^T & [K_{33}] \end{bmatrix} - \omega^2 \begin{bmatrix} [M_{11}] & [0] & [0] \\ [0] & [M_{22}] & [0] \\ [0] & [0] & [M_{33}] + [\Delta M_{33}{}^C] + \rho_{eff}[G] \end{bmatrix} \right] \begin{bmatrix} \{\Psi_A\} \\ \{\Psi_B\} \\ \{W\} \end{bmatrix} = \begin{bmatrix} \{0\} \\ \{0\} \\ \{F_W\} \end{bmatrix}, \tag{16}$$

where $\{F_W\}$ is the vector of consistent nodal forces. For the case of a single force applied to a specific node, $\{F_W\}$ contains zeros everywhere, except at the driving node. In the present study, the rotational nodal torques are zero, which allows the condensation of the equations of motion into an equivalent set involving only transverse degrees of freedom,

$$[\ MK(\omega)\ ]\ \{\ W\ \} = \{\ F_W\ \}, \tag{17}$$

where,

$$\begin{aligned}
[\ MK(\omega)\ ] &= [\ K_{13}\ ]^T [\ b_2\ ] + [\ K_{23}\ ]^T [\ b_1\ ] + [\ K_{33}\ ] - \omega^2 [\ M_{33}\ ] - \omega^2 [\ \Delta M_{33}^{C}\ ] - \omega^2 \rho_{eff}(\omega)\ [\ G\ ], \\
[\ b_2\ ] &= -\ [\ a_1\ ]^{-1} (\ [\ K_{12}\ ]\ [\ b_1\ ] + [\ K_{13}\ ]\ ), \\
[\ b_1\ ] &= -\ (\ [\ a_2\ ] - [\ K_{12}\ ]^T [\ a_1\ ]^{-1} [\ K_{12}\ ]\ )^{-1} (\ [\ K_{23}\ ] - [\ K_{12}\ ]^T [\ a_1\ ]^{-1} [\ K_{13}\ ]\ ), \\
[\ a_2\ ] &= [\ K_{22}\ ] - \omega^2 [\ M_{22}\ ], \\
[\ a_1\ ] &= [\ K_{11}\ ] - \omega^2 [\ M_{11}\ ].
\end{aligned}$$

The solution, $\{W\}$, to Eq. (17) is in general complex, giving the magnitude and phase of the nodal response vector. The present study is concerned with the driving point compliance of the table given by the ratio of the displacement to the applied force at the driving node.

4. EXPERIMENTAL RESULTS

A highly distributed damper was applied to the surface of an optical table measuring 243.8 cm (8 ft) long by 121.9 cm (4 ft) wide by 20.3 cm (8 in.) thick. The bare table mass, without dampers, was 330 Kg. The distributed damper consisted of 349 individual dampers that used rubber studmounts as the spring material. The studmounts measured 19 mm (0.75 in.) high by 25.4 mm (1 in.) in diameter. Steel wafers were used to load the springs, producing a range of natural frequencies within the design band. The mass and natural frequency of each spring/mass damper was measured and recorded.

4.1 Physical dimensions and material properties

The physical properties used in the plate model are summarized in Table 1. The steel properties were determined from static and dynamic tests on sample beams. The core shear modulus was obtained using a stiffness reduction factor (20%) applied to the theoretical shear stiffness of the honeycomb cell configuration. The reduction factor was chosen to match the plate model's first bending frequency to the experimental data. The core loss factor was chosen to reproduce the experimentally measured compliance at the first resonant frequency. The frequency dependent variations of the studmount loss factor and spring rate were determined from experimental tests on sample studmounts. The same loss factor and spring rate variation were assumed for all of the studmounts. The C channel was located 6.4 mm inside the table's perimeter. A 30% increase in the plate's torsional stiffness was used to account for the torsion box formed by the C channel. The 30% factor was determined based on the measured frequency of the first torsion mode.

4.2 Distributed damper properties

The distributed damping treatment consisted of 349 individual dampers whose natural frequencies fell within the design band of 150-300 Hz. Figure 2 shows the distribution of dampers within the design band, indicated by the number and total mass of the dampers within 10 Hz sub-bands. The total mass of the 349 dampers, M_{tot}, was 37.42 Kg. The damper coverage footprint, A_{tot}, was 1.4864 m^2, giving a real mass area density, ρ_A = 25.18 Kg/m^2. The frequency dependent effective mass per unit area of the distributed damper is shown in Figure 3. The effective mass takes into account the frequency dependent spring rate and loss factor in the studmount. As the figure shows, the effective mass at low frequency is simply equal to the real mass density of the damper. Within the design band, the effective mass exceeds its static magnitude by 2.5 times and has a non-zero phase. Above the design band, the effective mass decreases to zero. This particular damper was designed to provide a reasonably constant effective mass magnitude over the design band. The effective mass distribution can be readily tailored by adjusting the allocation of dampers within the band. In fact, recent research at KSI has shown that a damper with a low frequency weighted mass distribution can be more effective than the uniform distribution. For the present test, no attempt was made to optimize the damper design.

Material Type	thickness (cm)	Young's Modulus (GPa)	Poisson Ratio	Transverse Shear Modulus (MPa)	Material Loss Factor	Volume Density (Kg/m^3)	Linear Density (Kg/m)	Spring Rate (N/m)
Stainless Steel Facesheet	0.4656	219.8	0.29		0.002	7504		
Honeycomb Core	19.43	0	0	620	0.018	163.6		
C Channel	19.43						3.83	
Studmount					$\eta_i(\omega)$[a]			$K_i(\omega)$[b]

[a] $\eta_i(\omega) = 0.064 * \ln(\omega) - 0.2796$, ω=rad/s

[b] $K_i(\omega) = K_0 * (\omega/\omega_0)^{0.1355}$, K_0 = spring rate at damper design frequency ω_i

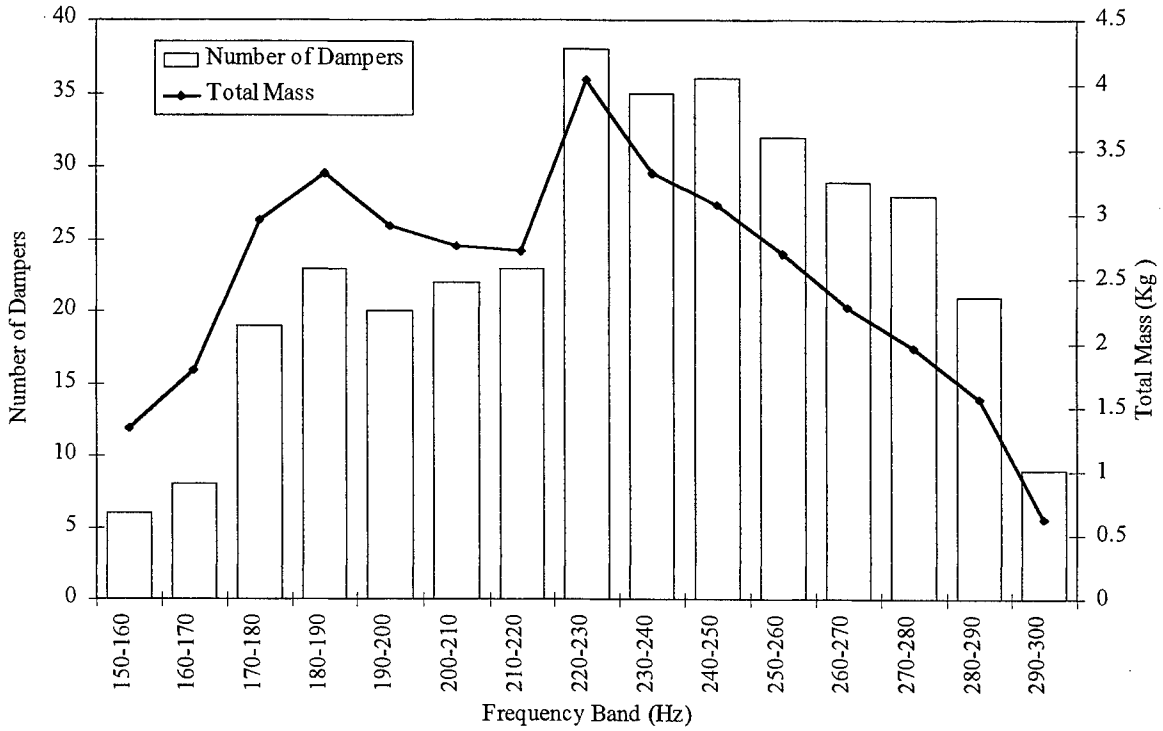

Figure 2. Distribution of dampers within the design band.

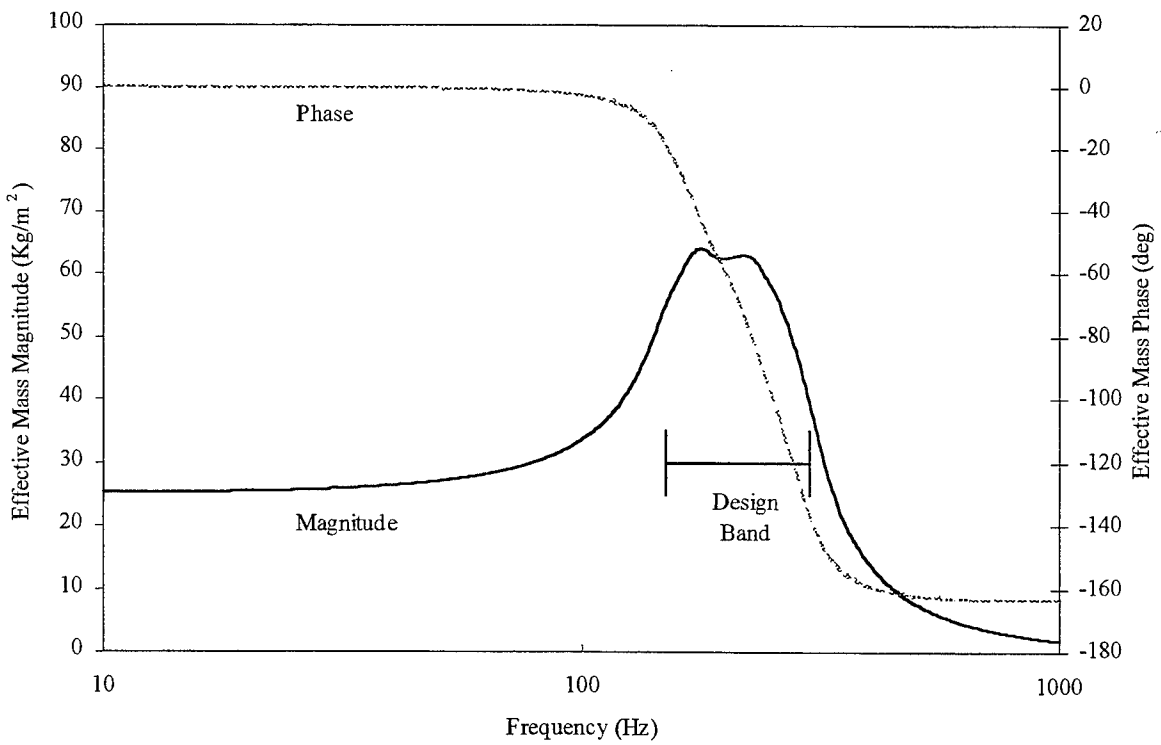

Figure 3. Effective mass of distributed damper.

4.3 Test Results

The distributed damper was applied to the surface of the optical table in five patches, one in each of the four corners and one in the center. The patch locations correspond to areas that experience large transverse motion in either the first bending or first torsion mode. An attempt was made to place the individual dampers randomly within each patch.

The experimental driving point compliance was measured in the corner of the table, at a point 12.7 cm from each edge. The corner driving point was used because it excited both the first bending mode and the first torsion mode. The compliance was measured using a PCB 308B accelerometer, PCB 086C05 impulse force hammer and Tektronix 2630 Fourier analyzer. 1600 lines of spectral data were collected between 0 Hz and 500 Hz.

Figure 4 shows the corner compliance measured on the undamped optical table. The resonant peak at 209 Hz corresponds to the first bending mode, while the peak at 232 Hz corresponds to the first torsion mode. The compliance of the first peak is 0.55 μm/N which exceeded the compliance limit for this size optical table (0.034 μm/N) by approximately 16 times. At low frequency, the compliance curve asymptotes to a diagonal "mass line" which corresponds to the compliance curve for a perfectly rigid body. The mass line can actually be calculated using the table's mass and principal moments of inertia. (For a center compliance measurement, the mass line corresponds to the actual mass of the table.) The analytical compliance predicted by the plate model is also shown on Figure 4. The agreement between the model and the experimental data was very good, in part because the core shear modulus and torsional stiffness were adjusted to reproduce the experimental frequencies. The roughness of the experimental compliance curve was a result of the input sensitivity on the Fourier analyzer that was required to capture the strong resonant peaks.

Figure 5 shows the corner compliance curve for a 243.8 cm x 121.9 cm x 20.3 cm optical table treated with a standard set of discrete dampers. The standard treatment consists of four 3.6 Kg dampers, located in each of the four corners of the table. The dampers, along with their supporting structure account for a 6.9% mass increase over the bare table. The additional peaks on the compliance curve were caused by the additional degrees of freedom introduced by the discrete dampers. For this particular table, the compliance limit was satisfied for the first two peaks (The limit is only mandatory for the first resonance.). The latter two peaks could be addressed with more dampers, however this would increase the complexity and cost of the damping operation.

Figure 6 shows the corner compliance for the optical table treated with 33% of the dampers. The damper mass of 12.5 Kg was equivalent to a mass increase of 3.8%. The distributed damper had two effects on the undamped response; first, it removed the distinction between the bending and torsional mode; and second, it significantly reduced the peak compliance. The peak compliance within the design band was 0.042 μm/N which only slightly exceeded the compliance limit. The damper addressed both modes within the design band, an improvement over the discrete tuned mass system. The predicted compliance from the plate model was in good agreement with the experimental data. The slight discrepancy in the peak compliance was most likely due to the assumptions in the plate model, namely that the damper distribution was purely random and that the frequency dependent properties were identical for all mounts. Figure 6 also illustrates how the distributed damper has very little influence on modes outside the design range, for example, the mode at 450 Hz was relatively unaffected by the damper. The corner compliance curve for a distributed system using 67% of the dampers (24.9 Kg, 7.6% mass increase) was very similar to Figure 6. The additional damper mass improved the effectiveness of the system, producing a peak compliance of .033 μm/N which fell below the allowable limit.

Figure 7 shows the corner compliance for the test table with all 349 dampers installed. The total damper mass of 37.4 Kg represented a 11.3% increase over the bare table. As the figure shows, the damper was very effective in attenuating both the bending and torsion modes. The peak compliance inside the design band was .03 μm/N, which was 10% below the compliance limit. The predicted compliance curve also appears on the figure and, as with the 33% coverage case, the plate model predicted the damper performance very well, capturing both the shape and magnitude of the compliance curve.

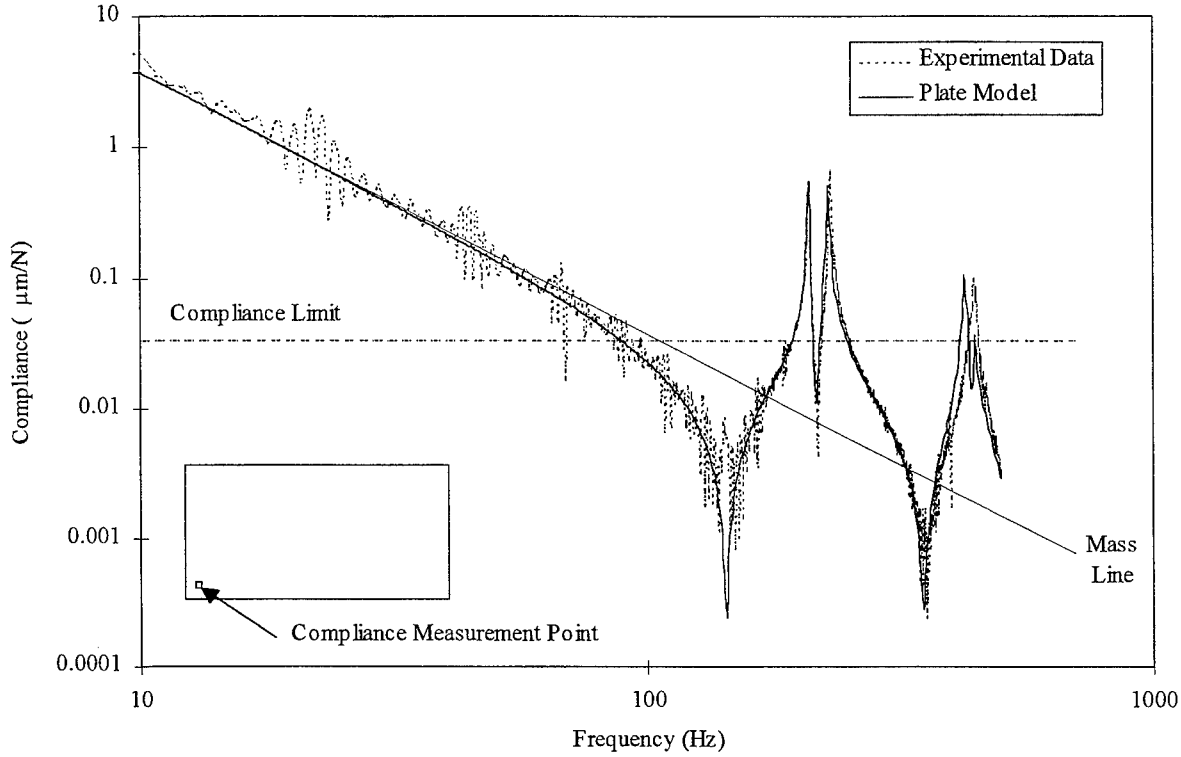

Figure 4. Undamped optical table corner compliance.

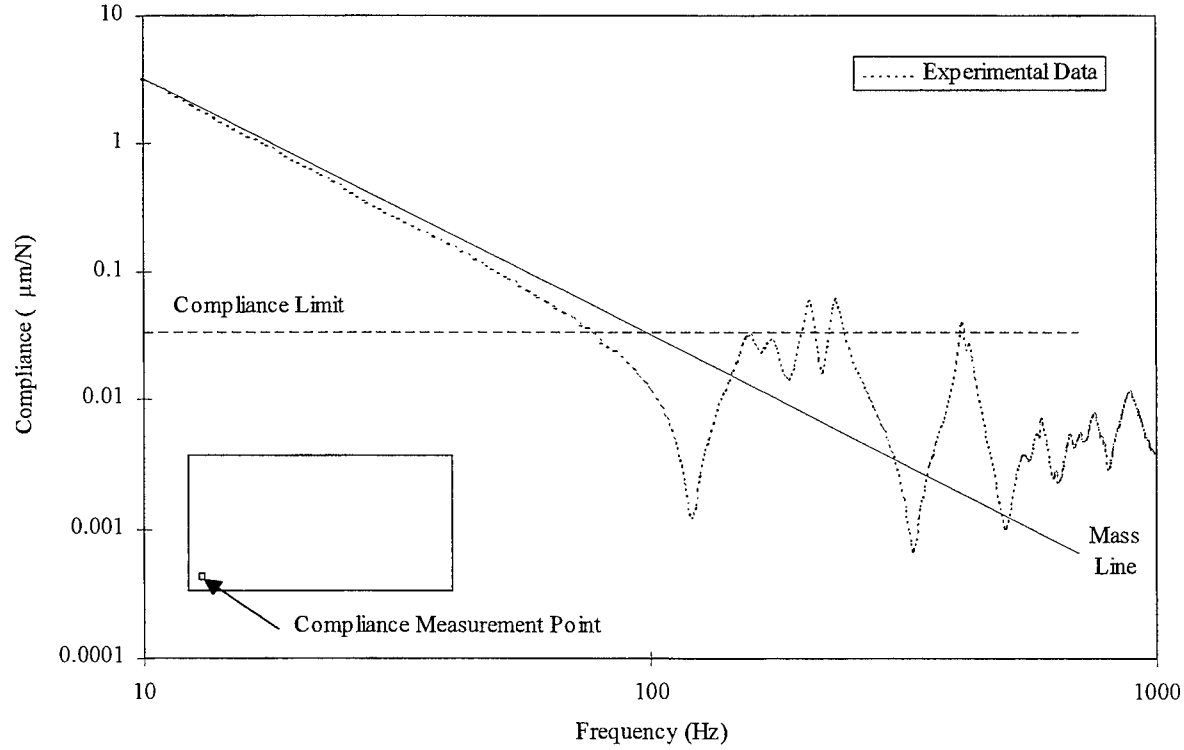

Figure 5. Optical table with standard discrete tuned mass dampers, 6.9% mass increase.

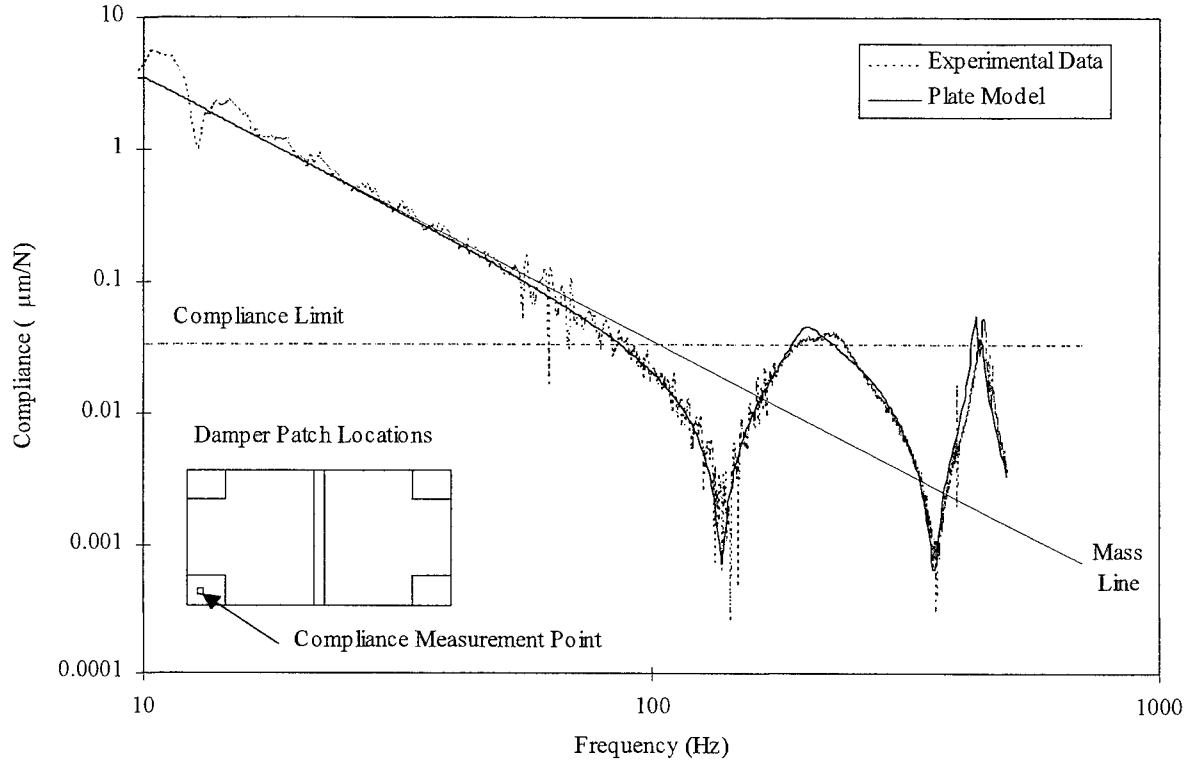

Figure 6. Optical table with distributed damper (33% coverage), 3.8% mass increase.

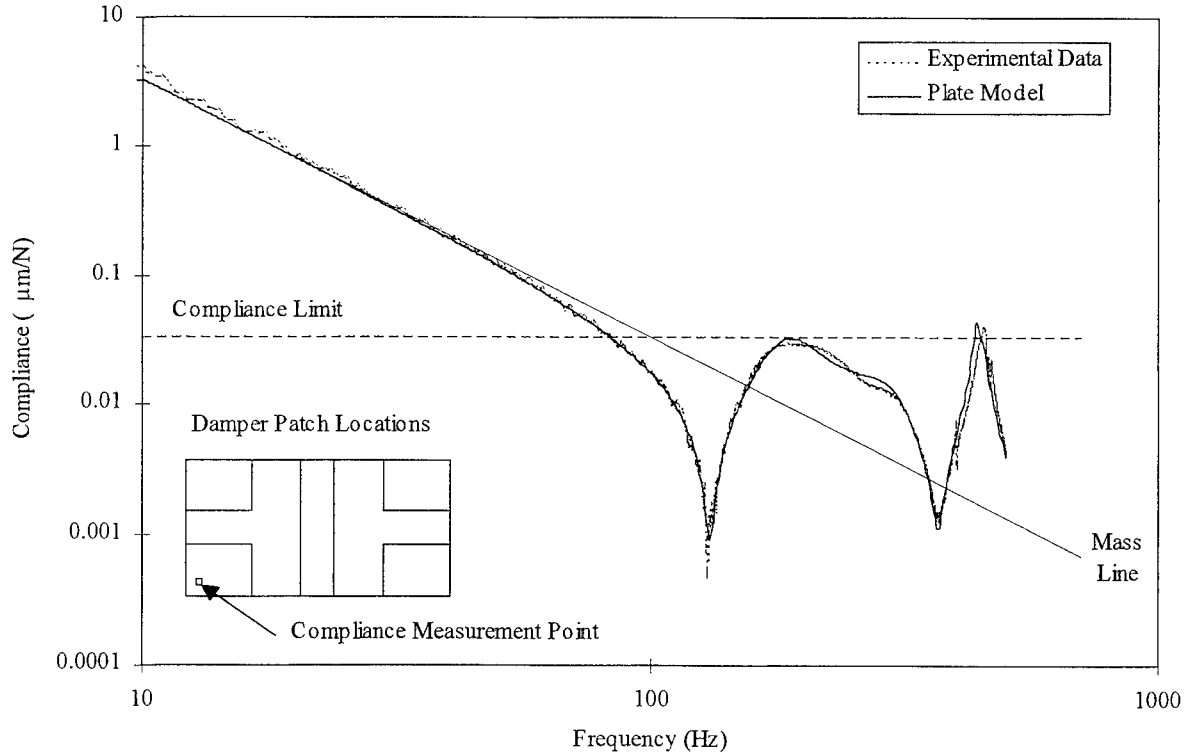

Figure 7. Optical table with distributed damper (100% coverage), 11.3% mass increase.

5. DISCUSSION

The primary intent of the present study was to experimentally verify the predicted performance of a highly distributed inertial damping treatment. The design goal of the damper was simplistic, namely to provide a relatively constant effective mass over a majority of the design band. No attempt was made to optimize the damper except for the specification of the smallest design band that would attenuate both the bending and torsion modes. KSI has recently determined that adequate attenuation can be achieved with effective mass distributions having less emphasis on the high end of the frequency band.

From a product performance standpoint, the distributed damper is attractive because it effectively attenuates both the bending and torsion modes, whereas discrete tuned dampers do not generally provide enough flexibility to address both modes. From a manufacturing standpoint, the distributed system has the potential to eliminate the tuning process altogether, allowing the dampers to be installed during the fabrication process.

It should be emphasized that the present study was intended as a demonstration of the theory of the distributed damper. In the study, the dampers were attached to the surface of the table because of convenience. In production, the dampers would be located inside the table where they would be transparent to the end user (as are the present discrete tuned dampers).

6. CONCLUSIONS

A highly distributed inertial damping treatment was successfully employed to attenuate vibration in optical tables. The damper consisted of a large number of small tuned mass absorbers tuned to different frequencies that were distributed over the surface of the table. The performance of the distributed damper surpassed that of a conventional discrete tuned mass system in its ability to damp all modes within the design range, with a comparable increase in the table's mass. An analytical plate model was presented that allowed the prediction of the damper's performance by modeling the collective dampers as a uniform covering with a dissipative, frequency dependent mass per unit area.

7. REFERENCES

1. A. D. Nashif, D. I. G. Jones, and J. P. Henderson, *Vibration Damping*, Ch. 5, John Wiley and Sons, New York, 1985.

2. T. L. Smith, K. Rao, and I. Dyer, "Attenuation of plate flexural waves by a layer of dynamic absorbers", *Noise Control Engineering Journal*, **26**, No. 2, pp. 56-60. 1986.

3. T. Igusa, and K. Xu, "Vibration control using multiple tuned mass dampers", *Journal of Sound and Vibration* **175**, No. 4, pp. 491-503. 1994.

4. A. D. Pierce, V. W. Sparrow, and D. A. Russell, "Fundamental structural-acoustic idealizations for structures with fuzzy internals", 93-WA/NCA-17, *ASME Winter Meeting*, November 28-December 3, 1993.

5. J. A. Zapfe, and G. A. Lesieutre, "Broadband vibration damping using highly distributed tuned mass absorbers", *AIAA Journal*, In Press.

6. R. D. Mindlin, "Influence of rotatory inertia and shear on flexural motions of isotropic, elastic plates", *Journal of Applied Mechanics*, March, pp. 31-38. 1951.

7. G. Prathap, and G. R. Bhashyam, "Reduced integration and the shear-flexible beam element", *International Journal for Numerical Methods in Engineering* **18**, pp. 195-210. 1982.

SESSION 8

Active CLD

Passive and active constrained layer damping of ring type structures

Jem A. Rongong and Geoffrey R. Tomlinson

Department of Mechanical Engineering, University of Sheffield, Sheffield S1 3JD, UK.

ABSTRACT

The performance of constrained layer damping treatments can be enhanced by optimising the segment length or through active control by inducing strains in the constraining layer. This paper investigates the effect of these methods on the flexural and extensional modes of a ring over a wide frequency range. Finite element models are first verified experimentally and then used in parametric studies. It is shown that segmentation of the constraining layer does not increase the maximum damping obtainable for a particular configuration but alters the mode number at which the maximum occurs. It is also shown that the optimum viscoelastic layer stiffness for active constrained layer damping is higher than that for the passive case.

Keywords: constrained layer damping, active constrained layer damping, viscoelastic materials, sandwich rings, finite element, vibration damping

1 INTRODUCTION

Surface treatments involving materials that display viscoelastic characteristics can be used to attenuate vibrations in many structures such as aircraft panels, car bodies and space vehicles. A constrained layer damping (CLD) treatment is formed by sandwiching a thin, compliant layer of viscoelastic material between a stiff constraining layer and the vibrating structure. Relative motion between the constraining layer and the structure deforms the viscoelastic material thereby dissipating energy.

The performance of CLD when used to suppress flexural vibrations in beams and plates has been extensively studied over the last forty years. Early work[1,2] identified shear deformation in the viscoelastic layer as being the principal mechanism for energy dissipation. The loss factor of a structure treated with CLD was shown to depend not only on the loss factor of the viscoelastic material but also on the thickness and elastic moduli of the viscoelastic and constraining layers. Subsequent work has found that when the viscoelastic layer is soft and thick, significant levels of damping can be obtained through transverse extensional deformations in the viscoelastic layer.[3,4]

Studies considering partially covered beams have shown that the total coverage does not always result in the highest loss factors.[5] Efforts have been made to identify the optimum length of a CLD treatment applied to a beam. The first analyses assumed a uniform strain distribution in the base structure to derive an expression for the optimum length.[6] It has recently been shown that if the strain in the base structure is non-uniform, this optimum length is significantly increased.[7]

In the last decade active constrained layer damping (ACLD) methods have received considerable attention.[8−13] An ACLD approach enhances the shear deformation in the viscoelastic layer by inducing appropriate strains in the constraining layer. This is usually achieved either by using a piezoelectric material to form the constraining layer or by bonding a piezoelectric actuator to an existing passive constraining layer.[10] The strain in the piezoelectric actuator

SPIE Vol. 3045 • 0277-786X/97/$10.00

and hence the deformation of the constraining layer can then be controlled by varying the electric potential across the piezoelectric material. Polyvinylidine fluoride (PVDF) film[8,9] and lead zirconate titanate (PZT) patches[11,12] have been used successfully as actuators to control vibrations in beams and plates. Significant improvements in performance over passive CLD have been demonstrated.

The passive damping supplied by the viscoelastic layer gives significant advantages over a purely active control approach, in which the actuators are bonded directly to the structure. In particular the effect of spillover,[14] where uncontrolled modes become unstable, is significantly reduced using ACLD. Theoretical and experimental comparisons have also been made between ACLD and active control of a structure with passive CLD.[11,13] These studies have shown that the stiffness of the viscoelastic layer is critical to the transfer of control effort from the actuator to the base structure.

Ring type structures are often found as components in rotating machinery. Vibrations developed can excite flexural modes of high nodal diameter. Recent studies[15] have shown that for a particular CLD treatment a graph of loss factor against damping shows two maxima as in figure 1. The first peak occurs when shear damping of the viscoelastic

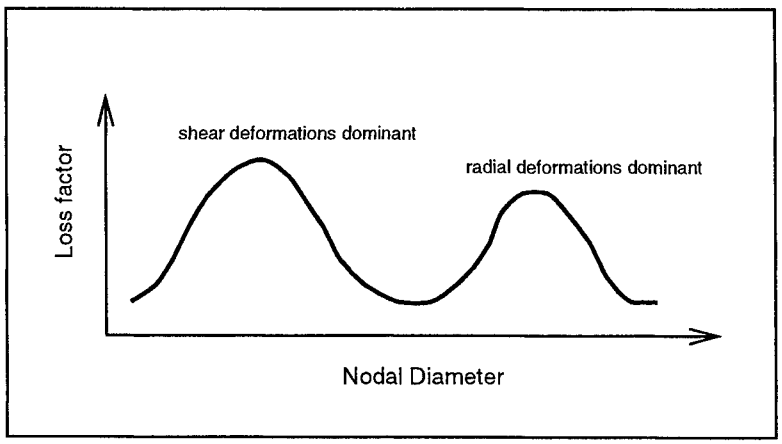

Figure 1: Typical plot of loss factor against nodal diameter for a ring with CLD

layer is optimised and the second when radial deformations become significant. The height of the peaks are affected mainly by the loss factor of the viscoelastic material and the flexural stiffness of the constraining layer. The modes at which these peaks occur depend mainly on the stiffness (in shear or extensional deformation) of the viscoelastic layer.

This paper examines the effect of methods used to enhance the performance of CLD, namely segmentation and ACLD, on the flexural (and extensional) modes of a ring. Frequency domain experimental and theoretical results are used to investigate the damping achieved over a large number of vibration modes. Numerical studies using finite element (FE) analysis are carried out to identify generic behaviour. The validity of the FE analysis methods used are then verified experimentally.

2 MODELLING VISCOELASTIC BEHAVIOUR

The mechanical properties of viscoelastic materials vary with both frequency and temperature. This behaviour can be modelled accurately in the frequency domain using the complex modulus obtained from the material master curve. Figure 2 shows the master curve or *international plot* for the shear modulus of 3M ISD112 - a popular damping material. The complex shear modulus $G^*(\omega)$ is defined as,

$$G^*(\omega) = G'(1 + j\eta) \qquad j = \sqrt{-1} \tag{1}$$

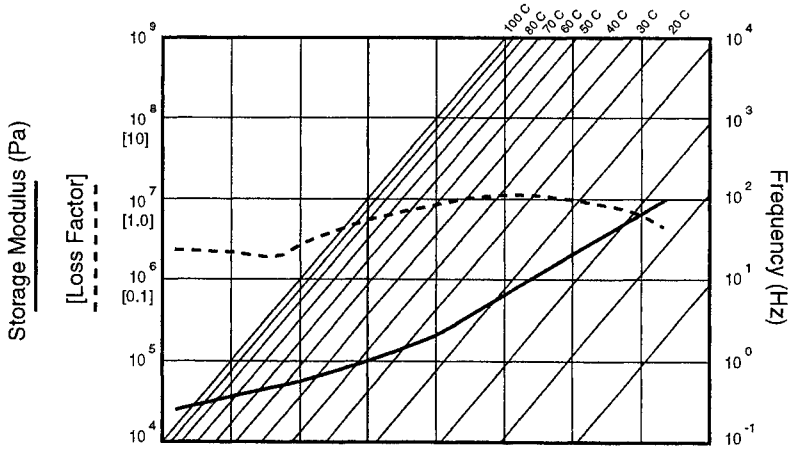

Figure 2: Shear modulus master curve for ISD 112

where G' and η are the storage modulus and loss factor respectively. These values can be used directly to carry out harmonic forced response calculations for viscoelastic structures.

Modal strain energy (MSE) analysis is an approximate method for obtaining loss factor and natural frequency data from a FE model.[16] It is based on an elastic analysis involving free eigenmodes and is therefore computationally inexpensive. Assuming low levels of damping in the base structure and constraining layer the loss factor of a ring with a CLD treatment can be estimated using,

$$\eta_{total} = \frac{\eta_r U_r + \eta_c U_c + \eta_v U_v}{U_{total}} \approx \eta_v \frac{U_v}{U_{total}} \tag{2}$$

where η is the loss factor, U is the modal strain energy and the subscripts r, c and v refer to the ring, constraining layer and viscoelastic layer respectively. It can be shown that the MSE method assumes proportional damping[17] and that it is the first order approximation to a full asymptotic solution.[18] It also does not allow for the frequency dependence of the viscoelastic material: to get correct values the eigenvalue calculation must be carried out for each mode using the material properties at that particular frequency. MSE analysis has been used successfully to predict the damping in the first thirty modes of steel-polyurethane-steel sandwich rings.[15]

3 SEGMENTED CLD

MSE analysis was used to estimate the loss factors of rings covered with CLD made up of 2, 4, 8 and 16 segments. The basic dimensions are presented in table 1. Two dimensional, eight noded biquadratic finite elements were used

Part	radius (mm)	thickness (mm)	width (mm)	density (kg/m^3)	Young's modulus (GPa)	Poisson's ratio
Ring	182.5	2.5	25	7860	205	0.3
Viscoelastic layer		0.127	25	1000	variable	0.499
Constraining layer		0.254	25	2700	70	0.33

Table 1: Dimensions and material properties

to model the CLD treated rings. Convergence studies found that the first thirty vibration modes could be calculated accurately using 240 elements around the circumference of the composite ring. The viscoelastic and constraining

layer were each one element Through the thickness, single elements were sufficient to model the viscoelastic and constraining layers and two were required for the ring.

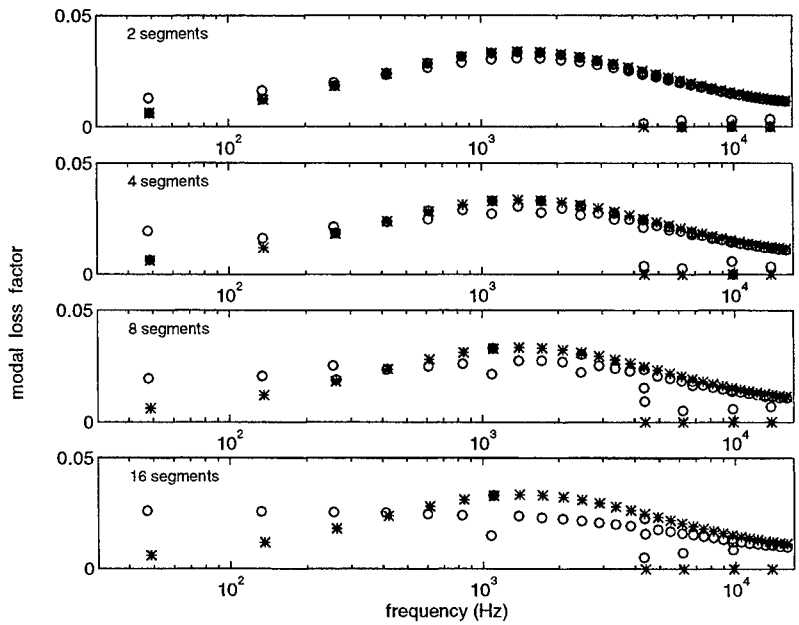

Figure 3: Loss factors of ring with segmented constraining layer E_v = 15 MPa (*** unsegmented, ooo segmented)

Figures 3, 4 and 5 show the modal loss factor against frequency of these rings for different values of viscoelastic layer Young's modulus (E_v). Results for segmented CLDs are marked with an 'o' and are compared with the unsegmented case marked with an asterisk.

The values of Young's modulus for the viscoelastic layer were chosen to illustrate the effect of segmentation on the double humped damping curve of figure 1. Figure 3 shows the first (shear) peak, figure 4 shows the start of the second (radial deformation) peak and figure 5 focuses on the area to the left of the first peak where the stiffness of the viscoelastic layer is higher than the optimum value. Note that the modes with very low loss factors near 4, 6, 10 and 15 kHz are extension modes.

In general, for flexural modes coinciding with the shear peak as in figure 3, segmentation offers no advantages as the configuration is optimised: in fact shorter segments lead to a lower peak. Figure 4 shows that in the trough between the peaks and on the second peak the segment length has very little effect. For modes to the left of the shear peak, where the loss factors achieved are suboptimal because the viscoelastic layer is either too thin or the shear modulus is too high, reducing the segment length improves the damping. This effect is most noticeable in figure 5. It is interesting to note that this improvement in damping achieved with segmentation never exceeds the height of the shear peak. This indicates that optimum performance can be achieved without segmenting the constraining layer, but by selecting the suitable values for the thickness and modulus of the viscoelastic layer. However in practice it is not always possible to do this - a designer is limited to real materials - and when this occurs segmentation can be used to shift the optimum peak to the required modes.

For extension modes, figures 3 and 5 show that increasing the number of segments, or alternatively reducing the segment length significantly improves the loss factor achieved.

From these graphs it can be seen that a pair of modes close in frequency but with significantly different damping levels often occur when a segmented CLD is used: for example, in figure 3 the ring with the 16 segment CLD has two modes near 1 kHz that have loss factors of 0.015 and 0.035 respectively.

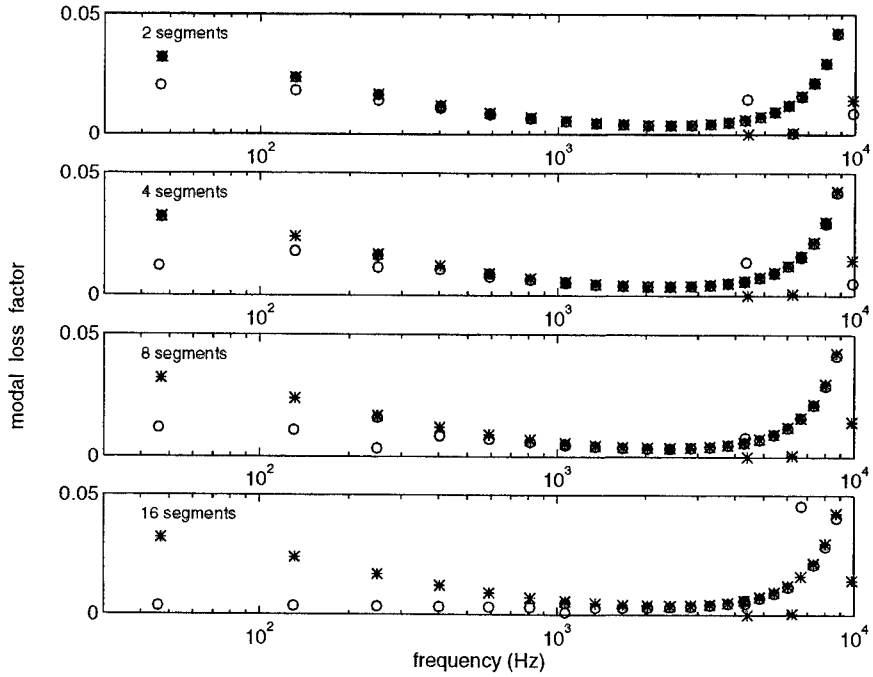

Figure 4: Loss factors of ring with segmented constraining layer $E_v = 0.5$ MPa (*** unsegmented, ooo segmented)

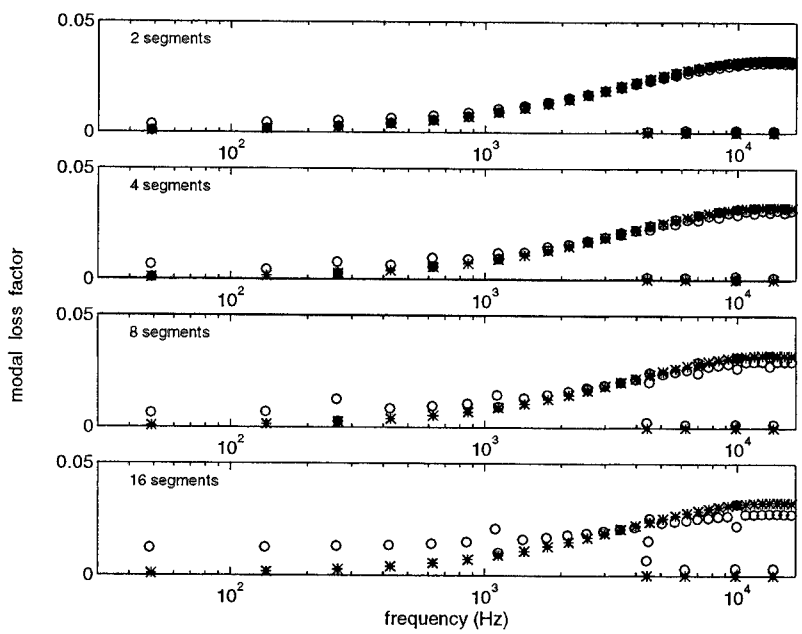

Figure 5: Loss factors of ring with segmented constraining layer $E_v = 150$ MPa (*** unsegmented, ooo segmented)

These are in fact modes with the *same* nodal diameter (8) but the positioning of the nodes with respect to the segments differs. The higher loss factor corresponds to the mode in which the nodes are aligned with the gaps between the CLD segments. Figure 6 shows the difference between these modes: mode 16 gives a significantly lower level of damping than mode 17. This behaviour only occurs when the nodal diameter of the vibration mode is a multiple of half the number of segments.

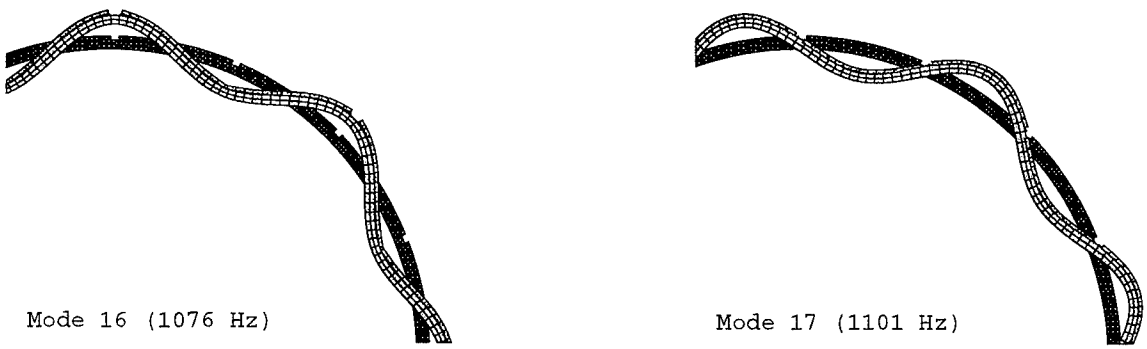

Figure 6: 8 nodal diameter mode shapes for ring with 16 segment CLD

4 VERIFICATION OF MSE METHOD FOR THE SEGMENTED CLD TREATMENT

To validate the numerical methods used in the previous section a comparison was made between the natural frequencies and loss factors obtained using MSE analysis to those obtained from direct forced response calculations and experimental results.

Four 250 mm length strips of aluminium backed ISD 112 damping tape were applied evenly to a steel ring. Dimensions and material properties are given in table 1 and figure 2. The ring was then suspended on soft elastic (free-free) supports and excited with an electrodynamic shaker using a 0-2 kHz band limited random noise source. The experimental layout is shown in figure 7. The response was measured using a minature accelerometer and frequency

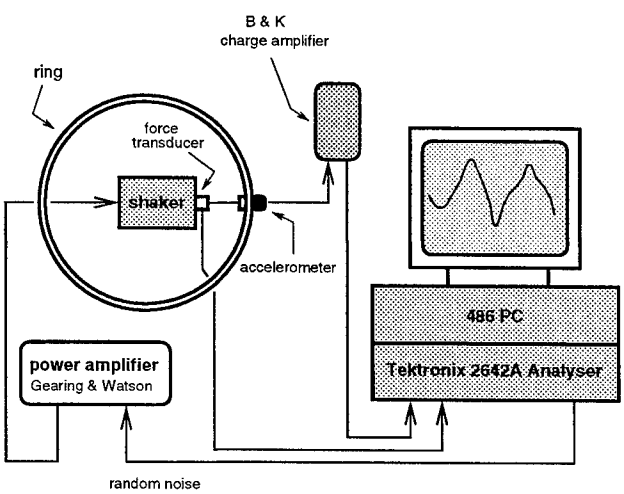

Figure 7: Schematic diagram of experimental set-up

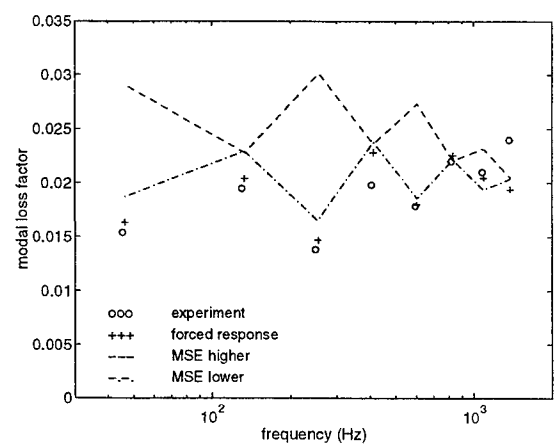

Figure 8: Modal loss factors with a 4 segment constraining layer: driving point opposite a gap between segments

response data was obtained using a PC based Fourier transform analyser. Estimates of natural frequency and modal loss factor for the first eight modes were made by fitting a single degree of freedom curve to the mobility plot. This

method gave good results as the resonances were well separated. Interactions with torsion modes and the support structure made measurements unreliable for higher modes (above 1.5 kHz). Three successive tests were made with the stinger rod of the shaker attached at different points on the ring. This was to investigate the pairs of modes of the same nodal diameter but different loss factors discussed in the previous section. With reference to figure 6 an excitation point opposite a gap between the segments was selected to drive modes with the lower loss factor. The second driving point was placed opposite a point half way along a segment (to excite the modes with higher damping) and a final point was fixed exactly between the first two points.

Theoretical predictions were made using both a direct forced response calculation (modal values obtained by curve fitting) and also using MSE analysis. Values for frequency dependent shear modulus of ISD 112 at 19° C were obtained from the international plot (figure 2). With the MSE method, the frequency dependent behaviour was included by following an iterative process calculating each eigenvalue in turn using the correct value for the elastic modulus of the viscoelastic material.

Comparisons of the results from the three different methods are presented in figures 8, 9 and 10. These figures show

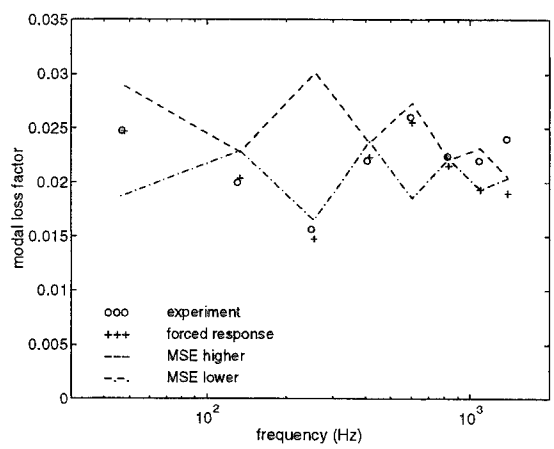

Figure 9: Modal loss factors with a 4 segment constraining layer: driving point opposite the centre of a segment

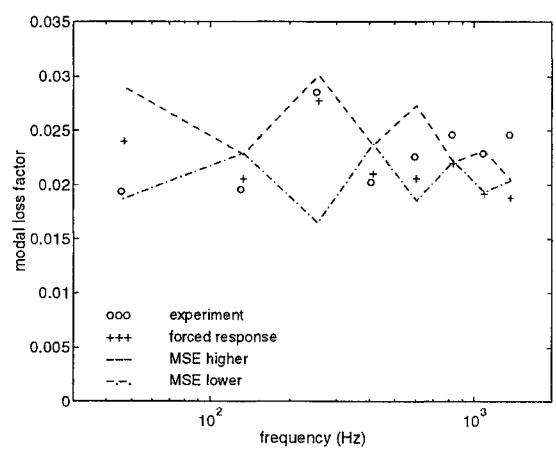

Figure 10: Modal loss factors with a 4 segment constraining layer: half way between previous points

good agreement between the experimental and theoretical forced response results. Figure 8 shows that when the excitation is at a gap between segments the behaviour follows the modes with lower damping obtained using MSE analysis. In figure 9 it can be seen that when the driving point is at the midpoint of a segment, the modes (apart from 4 nodal diameters at 250 Hz) excited correspond to the ones with higher damping. Finally figure 10 shows that for a driving point in a different position the loss factors obtained are between the limits indicated from an MSE analysis. In general it can be concluded that the results obtained using MSE analysis are valid and that for modes where the nodal diameter is a multiple of half the number of segments, the damping depends on the positioning of the exciting force.

5 ACTIVE CONSTRAINED LAYER DAMPING (ACLD) FOR A RING

The linear relationship linking stress, strain and electric field for piezoelectric materials can be written in tensor form as,

$$\epsilon = s^E \sigma + dE \tag{3}$$

where ϵ is the strain, s^E the compliance at constant electric field, σ the strain, d piezoelectric strain constants and E the applied electric field. For ACLD applications it is common to use a thin plate-like piezoelectric actuator poled in the thickness direction. Under these conditions the relationship can be simplified considerably. A voltage applied across the thickness of such an actuator bonded to a structure induces strains in the structure proportional to the d_{31} strain constant.

Various different control strategies have been employed in studies on ACLD. The work presented here is an initial study on the effect of activating the constraining layer on a wide range of modes of a ring. A voltage proportional to the radial velocity on the ring is used to control the strain deformation of a small piezoceramic (PZT) patch bonded to the constraining layer as shown in figure 11. A similar system has been used with considerable success to control first two modes of a cantilever beam.[10] Figure 12 shows a schematic diagram of the velocity feedback

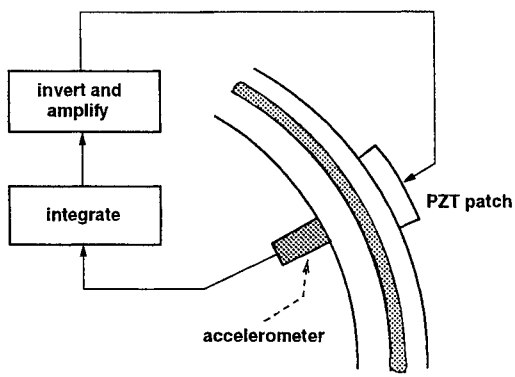

Figure 11: Velocity feedback control system

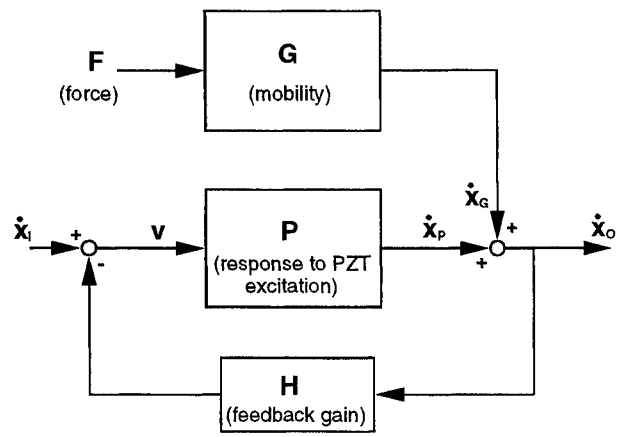

Figure 12: Schematic diagram of velocity feedback strategy

strategy employed. The object is to minimise the output velocity $\dot{x}_o$ with respect to the force F. As the set input $\dot{x}_i$ is zero, the model can be expressed mathematically as,

$$\frac{\dot{x}_o}{F} = \frac{G}{1+HP} \tag{4}$$

Note that this model assumes linear behaviour and ignores the effect of voltages generated *by* the actuator when it is deformed. Equation 4 indicates that it is possible to calculate the controlled response by measuring the mobility $G(=\frac{\dot{x}_G}{F})$ and the response to piezoelectric excitation $P(=\frac{\dot{x}_P}{v})$ separately.

To verify this model G and P were calculated numerically for the ring used in the previous section with a 5 mm PZT actuator bonded to the centre of one of the constraining layer segments. Measurements of these functions were made experimentally using a band limited 0-5 kHz random noise signal. As before, the velocity was obtained by using an accelerometer and integrating the signal, and the force F was measured using a force transducer. The piezoelectric drive voltage was amplified to approximately 100 V peak-to-peak. Dimensions and material properties of the PZT actuator are shown in table 2. The magnitude and phase of these responses predicted numerically are compared with

length (mm)	thickness (mm)	density (kg/m^3)	d_{31} (10^{-12} C/N)	Young's modulus (GPa)	Poisson's ratio
5	0.4	7700	-180	62.5	0.3

Table 2: Dimensions and material properties for Sonox P5 PZT actuator

the experimental values in figures 13 and 14. The figures show good agreement verifying the models used.

The methods developed were used to study the effect of viscoelastic layer stiffness on the performance of ACLD. Over the frequency range considered (10-5000 Hz) the elastic modului of a viscoelastic material can vary significantly: for example, the modulus of ISD112 increases by a factor of almost twenty. This can result in significantly different strain transfer behaviour between low and high modes. To investigate this effect the performance obtained using three different values of Young's modulus for the viscoelastic layer were compared.

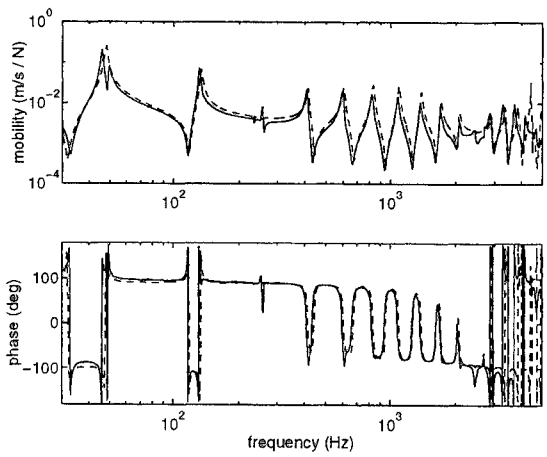

Figure 13: Mobility (G): full line for experimental and dashed line for simulated data

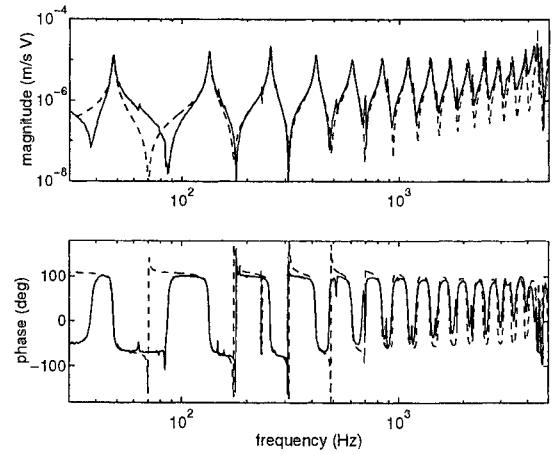

Figure 14: Response to PZT excitation (P): full line for experimental and dashed line for numerical data

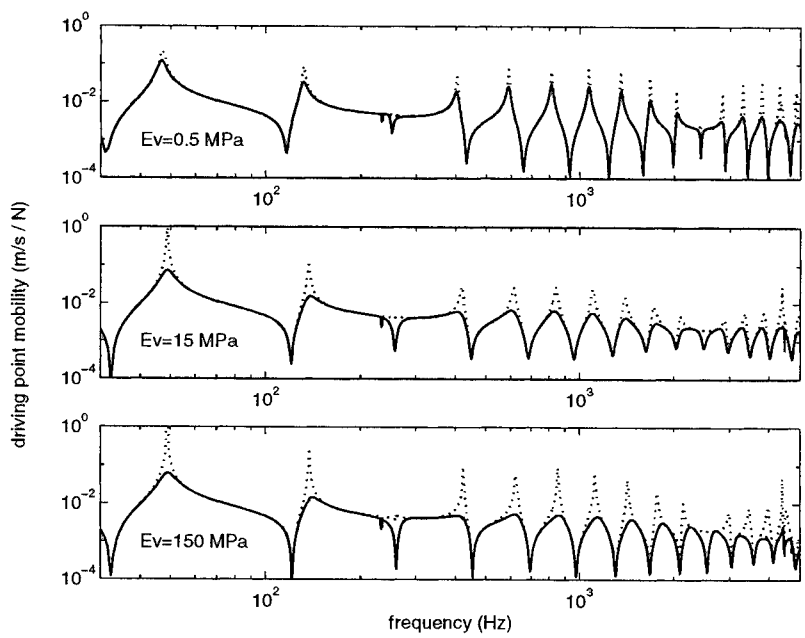

Figure 15: Simulated ACLD on a ring with different values of Young's modulus (dashed line for passive case)

Figure 15 shows the simulated results of ACLD applied to a ring with a full constraining layer. It can be seen that although the passive damping is optimised using a Young's modulus of 15 MPa, the 150 MPa case gives better performance when the constraining layer is activated. This result indicates that an ACLD treatment using a real viscoelastic material would show improved control performance in the high frequency modes.

6 CONCLUSIONS

In this paper the effect of segmenting the constraining layer on the overall value of damping for a CLD treated ring was studied. For flexural modes it was found that segmenting improved the damping only if the viscoelastic layer is stiffer than the optimum case. For extension modes however segmentation always improves the damping.

Active constrained layer damping was also considered. It has been shown that it is possible to enhance the damping of a large number of modes using a simple velocity feedback approach. It has also been shown that the optimal stiffness of the viscoelastic layer is higher for ACLD than for the passive case.

7 ACKNOWLEDGEMENTS

The authors are grateful to Rolls Royce plc for financial support provided for the work presented here.

8 REFERENCES

[1] Kerwin E M , 'Damping of flexural waves by a constrained viscoelastic layer', *J. Acoust. Soc. Am.*, **31**, pp 952-962, 1959.

[2] Mead D J and Markus S, 'Loss factors and resonant frequencies of encastre damped sandwich beams', *J. Sound Vibr.* **12**, pp 99-112, 1970.

[3] Douglas B E and Yang J C S, 'Transverse compressional damping in the vibratory response of elastic-viscoelastic-elastic beams', *AIAA J.*, **16**, pp 925-930, 1978.

[4] Miles N N and Reinhall P G, 'An analytical model for the vibration of laminated beams including the effects of both shear and thickness deformation in the adhesive layer', ASME J. Vibr. Acoust., **108**, pp 56-64, 1986.

[5] Nokes D S and Nelson F C, 'Constrained layer damping with partial coverage', *Shock Vibr. Bull.*, **38**, pp 5-12, 1968.

[6] Plunkett R and Lee C T, 'Length optimisation for constrained layer damping', *J. Acoust. Soc. Am.*, **48**, pp 150-161, 1970.

[7] Demoret K B and Torvik P J, 'Optimal length of constrained layers on a substrate with linearly varying strain', *ASME Design Eng. Tech. Conf.*, **84-3**(C), pp 719-726, 1995.

[8] Baz A and Ro J, 'Vibration of plates with active constrained layer damping', *Smart Mater. Struct.*, **5**, pp 272-280, 1996.

[9] Yellin J M and Shen I Y, 'A self-sensing active constrained layer damping treatment for an Euler-Bernoulli beam', *Smart Mater. Struct.*, **5**, pp 628-637, 1996.

[10] Azvine B, Tomlinson G R and Wynne R J, 'Use of active constrained layer damping for controlling resonant vibration', *Smart Mater. Struct.*, **4**, pp 1-6, 1995.

[11] Van Nostrand W C, Knowles G J and Inman D J, 'Active constrained layer damping for micro-satellites', *Dynamics and Control of Structures in Space II*, pp 667-681, 1993.

[12] Liao W H and Wang K W, 'Analysis and design of viscoelastic materials for active constrained layer damping treatments', *SPIE Proc. Conf. on Smart Struct. and Mater.*, **2720**, pp 212-223, 1996.

[13] Huang S C, Inman D J and Austin E M, 'Some design considerations for active and passive constrained layer damping treatments', *Smart Mater. Struct.*, **5**, pp 301-313, 1996.

[14] Balas M J, 'Trends in large space structure control theory: fondest hopes, wildest dreams', *IEEE Transact. Autom. Control*, **AC-27**, pp 522-535, 1982.

[15] Rongong J A and Tomlinson G R, 'Suppression of ring vibration modes of high nodal diameter using constrained layer damping methods', *Smart Mater. Struct.*, **5**, pp 672-684, 1996.

[16] Johnson C D and Kenholz D A, 'Finite element prediction of damping in structures with constrained viscoelastic layers', *AIAA J.*, 20, pp 1284-1290, 1982.

[17] Slater J C, Belvin W K and Inman D J, 'A survey of modern methods for modelling frequency dependent damping in finite element models', *Proc. 11^{t}h Modal Analysis Conf.*, pp 1508-1512, 1993.

[18] Ma B A and He J F, 'A Finite Element Analysis of Viscoelastically Damped Sandwich Plates', *J. Sound Vibr.*, **152**, pp 107-123, 1992.

VIBRATION CONTROL OF CYLINDRICAL SHELLS USING ACTIVE CONSTRAINED LAYER DAMPING

M. Ray, T. Chen and A. Baz

Mechanical Engineering Department
The Catholic University of America
Washington, DC 20064

ABSTRACT

The fundamentals of controlling the structural vibration of cylindrical shells treated with **A**ctive **C**onstrained **L**ayer **D**amping (**ACLD**) treatments are presented. The effectiveness of the **ACLD** treatments in enhancing the damping characteristics of thin cylindrical shells is demonstrated theoretically and experimentally.

A **F**inite **E**lement **M**odel (**FEM**) is developed to describe the dynamic interaction between the shells and the **ACLD** treatments. The **FEM** is used to predict the natural frequencies and the modal loss factors of shells which are partially treated with patches of the **ACLD** treatments. The predictions of the FEM are validated experimentally using stainless steel cylinders which are 20.32 cm in diameter, 30.4 cm in length and 0.05 cm in thickness. The cylinders are treated with **ACLD** patches of different configurations in order to target single or multi-modes of lobar vibrations. The **ACLD** patches used are made of DYAD 606 visco-elastic layer which is sandwiched between two layers of PVDF piezo-electric films. Vibration attenuations of 85% are obtained with maximum control voltage of 40 volts. Such attenuations are attributed to the effectiveness of the **ACLD** treatment in increasing the modal damping ratios by about a factor of four over those of conventional **P**assive **C**onstrained **L**ayer **D**amping (**PCLD**) treatments.

The obtained results suggest the potential of the **ACLD** treatments in controlling the vibration of cylindrical shells which constitute the major building block of many critical structures such as cabins of aircrafts, hulls of submarines and bodies of rockets and missiles.

1. INTRODUCTION

Considerable attention has been devoted to control the vibration of cylindrical shells using either passive or active control means. For example, Markus [1-2] used unconstrained passive damping layer treatments to suppress the axi-symmetric vibrations of thin cylindrical shells. However, for higher damping characteristics; the **P**assive

Constrained Layer Damping (**PCLD**) treatments have been successfully employed to various types of cylindrical shells [3-9]. Recently, several attempts have been made to actively control the vibration of shells using discrete piezo-electric actuators [10-15] bonded to the shell surfaces or distributed piezo-electric actuators embedded in the composite fabric of the shell [16].

In all the above studies, the emphasis is placed on using separately the passive or the active vibration control actions. In the present study, the passive and active control strategies are combined to operate in unison to achieve an optimal balance between the simplicity of the passive damping and the efficiency of the active control. A preferred configuration is the Active Constrained Layer Damping (**ACLD**) treatment which has been successfully used as an effective means for damping the vibration of beams and plates [17-25]. The **ACLD** treatment has also been used to control the axi-symmetric modes of vibration of cylindrical shells using a boundary control strategy [26].

In this paper, the focus is placed on extending the use of the **ACLD** treatments to control both the circumferential and longitudinal modes of vibration of thin cylindrical shells. Particular emphasis is placed on developing a finite element model to describe the vibrations of shells which are partially-treated with **ACLD** treatments. Experimental validation of the FEM model using various configurations of the **ACLD** patches is also one of the main purposes of this study.

This paper is organized in five sections. In Section **1** a brief introduction is given. In Section **2**, the concept of the active constrained layer damping is presented . The finite element model of the shell/ACLD system is developed in Section **3.** In Section **4** the performance of the shell/ACLD is presented for simple proportional and derivative controllers in comparison to that of conventional constrained layer damping. Section **5** gives a brief summary of the conclusions.

2. CONCEPT OF THE ACTIVE CONSTRAINED LAYER DAMPING

The **ACLD** treatment consists of a conventional passive constrained layer damping which is augmented with efficient active control means to control the strain of the constraining layer, in response to the shell vibrations as shown in Figure (1). The shear deformation of the visco-elastic damping layer is controlled by an active piezo-electric constraining layer which is energized by a control voltage V_c. In this manner, the **ACLD** when bonded to the shell acts as a smart constraining layer damping treatment with built-in actuation capabilities. With appropriate strain control, through proper manipulation of V_c, one or more of the structural modes of vibration can be targeted and damped out.

Also, the **ACLD** provides a practical means for controlling the vibration of massive structures with the currently available piezo-electric actuators without the need for excessively large actuation voltages. This is due to the fact that the **ACLD** properly utilizes the piezo-electric actuator to control the shear in the soft visco-elastic core which is a task compatible with the low control authority capabilities of the currently available piezo-electric materials.

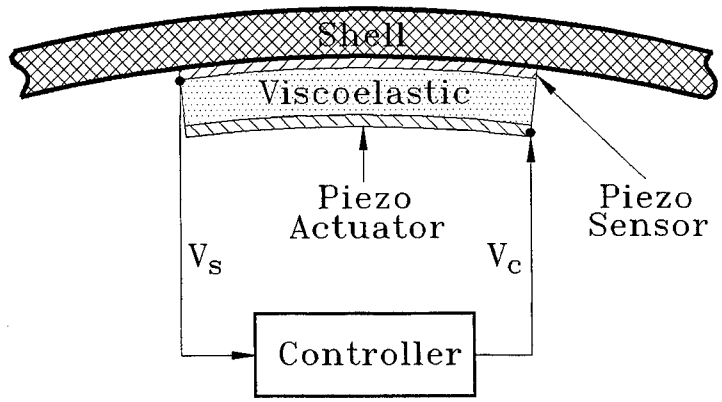

Figure (1) - The shell/ACLD system

3. FINITE ELEMENT MODELING

3.1. *Displacement Fields*

Figure (2) shows the cross section of a thin cylindrical shell treated partially with active constrained layer damping treatment. Also, Figure (3) shows the main geometric parameters of the shell/ACLD system in its undeflected and deflected states.

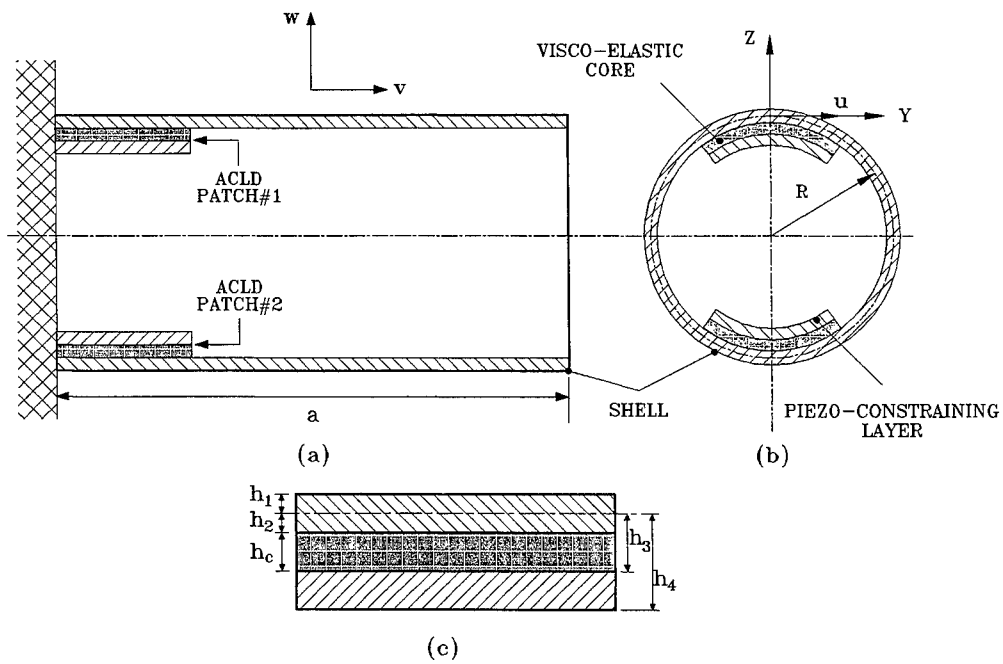

Figure (2) - Schematic drawing of the shell/ACLD system

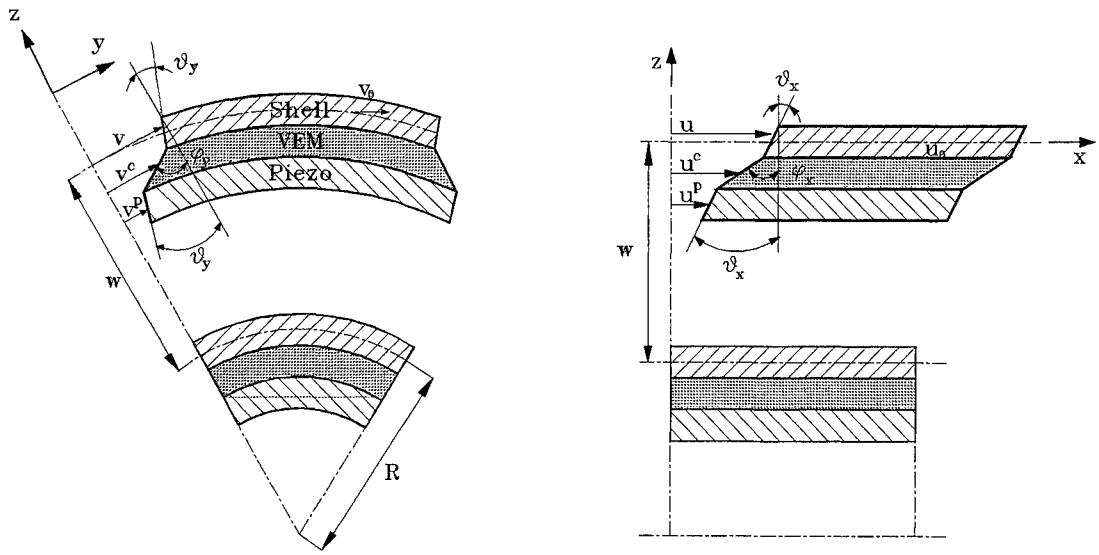

Figure (3) - Main geometric parameters of shell/ACLD system

The following displacement fields for the in-plane motions of the different layers of the system are used:

a. For cylinder

$$u = u_0 + z\theta_x, \quad v = v_0 + z\theta_y \tag{1-a}$$

b. For visco-elastic core

$$u^c = u_0 + (z - h_2)\psi_x + h_2\theta_x, \quad v^c = v_0 + (z - h_2)\psi_y + h_2\theta_y \tag{1-b}$$

c. For piezoelectric layer

$$u^p = u_0 + (z + h_c)\theta_x - h_c\psi_x, \quad v^p = v_0 + (z + h_c)\theta_y - h_c\psi_y \tag{1-c}$$

in which u, v are the in-plane displacements of any point in the cylinder along x and y axes, respectively; u^c, v^c and u^p, v^p are the corresponding displacements in the visco-elastic core and piezoelectric patch, respectively; u_0, θ_x and v_0, θ_y are the translational and rotational variables for the mid-plane deformation of the shell along x and y directions, respectively, ψ_x and ψ_y are the corresponding rotational variables for the mid-plane of the viscoelastic core. h_c is the thickness of the visco-elastic core. The radial displacement, w is assumed to be constant through the thickness.

The generalized displacement variables are divided into two parts as

$$\{d\} = [u_0 \quad v_0 \quad w \quad \theta_x \quad \theta_y]^T \ ; \ \{d_c\} = [\psi_x \quad \psi_y]^T \tag{2}$$

3.2. *Strain-displacement Relations*

Applying Donnell's theory for strain-displacement relations and using equations (1-a) - (1-c) the strain vectors at any point of the respective layers can be expressed as

$$\{\epsilon^1\} = [Z]\{\overline{\epsilon}\}; \ \{\epsilon^2\} = \{\overline{\epsilon}_1^c\} + [Z^c]\{\overline{\epsilon}_2^c\}; \ \{\epsilon^3\} = [Z_1^p]\{\overline{\epsilon}\} + [Z_2^p]\{\overline{\epsilon}_2^c\} \tag{3}$$

where the generalized strain vectors $\{\overline{\epsilon}\}$, $\{\overline{\epsilon}_1^c\}$ and $\{\overline{\epsilon}_2^c\}$ are given by

$$\{\overline{\epsilon}\} = \left[\frac{\partial u_0}{\partial x}, \ \frac{\partial v_0}{\partial y} + \frac{w}{R}, \ \frac{\partial \theta_x}{\partial x}, \ \frac{\partial \theta_y}{\partial y}, \ \frac{\partial w}{\partial x} + \theta_x, \ \frac{\partial w}{\partial y} - \frac{v_0}{R} + \theta_y, \right.$$
$$\left. \frac{\partial u_0}{\partial y} + \frac{\partial v_0}{\partial x}, \ \frac{\partial \theta_x}{\partial y} + \frac{\partial \theta_y}{\partial x}, \ \frac{\theta_y}{R}\right]^T,$$

$$\{\overline{\epsilon}_1^c\} = \left[\frac{\partial u_0}{\partial x} + h_2\frac{\partial \theta_x}{\partial x}, \ \frac{\partial v_0}{\partial y} + \frac{w}{R} + h_2\frac{\partial \theta_y}{\partial y}, \ \frac{\partial w}{\partial x}, \right.$$
$$\left. \frac{\partial w}{\partial y} - \frac{v_0}{R} - \frac{h_2}{R}\theta_y, \ \frac{\partial u_0}{\partial y} + \frac{\partial v_0}{\partial x} + h_2\left(\frac{\partial \theta_x}{\partial y} + \frac{\partial \theta_y}{\partial x}\right)\right]^T,$$

and $$\{\overline{\epsilon}_2^c\} = \left[\frac{\partial \psi_x}{\partial x}, \ \frac{\partial \psi_y}{\partial y}, \ \psi_x, \ \psi_y, \ \frac{\partial \psi_x}{\partial y} + \frac{\partial \psi_y}{\partial x}\right]^T$$

the transformation matrices $[Z]$, $[Z^c]$, $[Z_1^p]$ and $[Z_2^p]$ are given in Appendix A and the superscripts $1, 2$ and 3 represent the cylinder, visco-elastic core and the piezoelectric layer, respectively.

3.3. *Constitutive Equations*

The constitutive equation for the material of the piezoelectric constraining layer is

$$\{\sigma^3\} = [C^3]\,[\{\epsilon^3\} - \{\varepsilon_p\}] \tag{4}$$

where $\{\sigma\}$ and $\{\in\}$ represent the vectors of stress and strain, respectively $[C]$, the elastic constant matrix and the piezoelectrically induced-strain vector $\{\varepsilon_p\}$ for a biaxially polarized actuator layer is given by

$$\{\varepsilon_p\} = V\{\bar{\varepsilon}_p\} \tag{5}$$

with

$$\{\bar{\varepsilon}_p\} = \frac{1}{h_p}\begin{bmatrix} d_{31} & d_{32} & 0 & 0 & 0 \end{bmatrix}^T$$

d_{31}, d_{32} the piezoelectric strain constants, h_p the thickness of the actuator and V the applied voltage.

Also, the constitutive equations for the materials of the shell and the visco-elastic core are given by

$$\{\sigma^L\} = [C^L]\{\in^L\},\ (L = 1,\ \ 2) \tag{6}$$

3.4. *System Energies*

The potential energy T_p of the overall system is given by

$$T_p = \frac{1}{2}\sum_{L=1}^{3}\int_{h_{L+1}}^{h_L}\int_0^b\int_0^a \{\in^L\}^T\{\sigma^L\}dxdydz - \int_0^b\int_0^a \{\Delta\}^T{}_{z=h_1} f^s dxdy \tag{7}$$

and the kinetic energy T_k is given by

$$T_k = \frac{1}{2}\sum_{L=1}^{3}\int_{h_{L+1}}^{h_L}\int_0^b\int_0^a \rho^L\{\dot{\Delta}^L\}^T\{\Delta^L\}dxdydz \tag{8}$$

where b is the circumferencial length, a, the axial length, ρ , the mass density, $\{\Delta\}$, the vector of absolute displacements and $\{f^s\}$ is the vector of surface traction.

The continuum is discretized by an eight-noded two-dimensional isoparametric element. The generalized displacement vectors for the $i-$th $(i=1,2,\ldots,8)$ node of the element is then given by

$$\{d_i\} = [u_{0i} \quad v_{0i} \quad w_i \quad \theta_{xi} \quad \theta_{yi}]^T \ ;\ \{d_{ci}\} = [\psi_{xi} \quad \psi_{yi}]^T \tag{9}$$

and the generalized displacement vector at any point within the element is given by

$$\{d\} = [N]\{d^e\} \ ; \ \{d_c\} = [N_c]\{d_c^e\} \tag{10}$$

wherein

$$\{d^e\} = [\{d_1\}^T \quad \{d_2\}^T \quad . \ . \ . \quad \{d_8\}^T]^T, \ \{d_c^e\} = [\{d_{c1}\}^T \quad \{d_{c2}\}^T \quad . \ . \ . \quad \{d_{c8}\}^T]^T,$$

$$[N] = [N_1 \quad N_2 \quad . \ . \ . \quad N_8], \quad [N_c] = [N_{c1} \quad N_{c2} \quad . \ . \ . \quad N_{c8}],$$

$$[N_i] = n_i I \text{ and } [N_{ci}] = n_i I_c$$

with I and I_c being the identity matrices of appropriate dimension and n_i are the shape functions of natural coordinates.

The generalized strain vectors at any point within the element can be expressed as

$$\{\overline{\in}\} = [B]\{d^e\}, \ \{\overline{\in}_1^c\} = [B_1^c]\{d^e\} \ , \ \{\overline{\in}_2^c\} = [B_2^c]\{d_c^e\} \tag{11}$$

in which the nodal strain-displacement matrices are given by

$$[B] = [B_1 \quad B_2 \quad . \ . \ . \quad B_8], \quad [B_1^c] = [B_{11}^c \quad B_{12}^c \quad . \ . \ . \quad B_{18}^c],$$

$$\text{and} \quad [B_2^c] = [B_{21}^c \quad B_{22}^c \quad . \ . \ . \quad B_{28}^c]$$

The various submatrices $[B_i]$, $[B_{1i}^c]$ and $[B_{2i}^c]$ are given in Appendix A.

Using equations (2)-(6), (9)-(11) in (7) and (8) the strain energy of e th element can be expressed as:

$$T_p^e = \frac{1}{2}\int\Big[\{d^e\}^T[B]^T[D][B]\{d^e\} + \{d^e\}^T[B_1^c]^T[D_b][B_1^c]\{d^e\} + \{d^e\}^T[B_1^c]^T[D_{bc}][B_2^c]\{d_c^e\}$$

$$+ \{d_c^e\}^T[B_2^c]^T[D_{cb}][B_1^c]\{d^e\} + \{d_c^e\}^T[B_2^c]^T[D_{cc}][B_2^c]\{d_c^e\} + \{d^e\}^T[B]^T[D_p[B]\{d^e\}$$

$$+ \{d_c^e\}^T[B_2^c]^T[D_{cp}][B]\{d^e\} + \{d^e\}^T[B]^T[D_{pc}][B_2^c]\{d_c^e\} + \{d_c^e\}^T[B_2^c]^T[D_{cc}^p][B_2^c]\{d_c^e\}$$

$$-\frac{1}{2}\int_{h_4}^{h_3}\Big(\{d^e\}^T[B]^T[Z_1^p]^T[C^1]\{\varepsilon_p\} + \{d_c^e\}^T[B_2^p]^T[Z_2^p]^T[C^1]\{\varepsilon_p\}\Big)dz$$

$$-\{d^e\}^T[N]^T\{f^s\}\Big]dxdy \tag{12}$$

and the kinetic energy of the element can be obtained as

$$T_k^e = \frac{1}{2}\int \{\dot{d}^e\}^T[N]^T[\overline{m}][N]\{\dot{d}^e\}dxdy \tag{13}$$

in which the various rigidity matrices $[D_{ij}]$ and the matrix $[\overline{m}]$ are given in Appendix B.

3.5. *Equations of Motion*

Applying Hamilton's variational principle the following equations of motion for the element are obtained.

$$[M^e]\{\ddot{d}^e\} + [K_b^e]\{d^e\} + [K_{bc}^e]\{d_c^e\} = [K_{bp}^e]\{\overline{\varepsilon}_p\} + \{F^e\} \tag{14}$$

$$[K_{cb}^e]\{d^e\} + [K_{cc}^e]\{d_c^e\} = [K_{cp}^e]\{\overline{\varepsilon}_p\} \tag{15}$$

The various matrices stiffness and mass matrices and the load vector in eqns. (14) and (15) are given in Appendix B. Eliminating the rotational degrees of freedom $\{d_c^e\}$ for the viscoelastic core from the above equations one obtains the single equation of motion for an element of the ACLD system as

$$[M^e]\{\ddot{d}^e\} + [K^e]\{d^e\} = \{F^e\} + \{F_a^e\}V \tag{16}$$

where

$$[K^e] = [K_b^e] - [K_{bc}^e][K_{cc}^e]^{-1}[K_{cb}^e], \quad [F_a^e] = \left([K_{bp}^e] - [K_{bc}^e][K_{cc}^e]^{-1}[K_{cp}^e]\right)\{\overline{\varepsilon}_p\}$$

Note that the above modeling corresponds to the element with **ACLD** treatment. However, the equation of motion for an element without **ACLD** treatment can be easily obtained by suitably modifying the equation (14) only. The global equation of motion of the whole system can be obtained in the usual manner as

$$[M]\{\ddot{X}\} + [K]\{X\} = \{F\} + \{F_a\}V \tag{17}$$

where $[M]$, $[K]$ are the global mass and stiffness matrices, respectively, $\{X\}$, the global nodal generalized displacement coordinates, $\{F\}$, the global nodal force vector and $\{F_a\}$, the global nodal actuating force vector due to applied voltage.

3.6. *Control Law*

In the active control strategy, the voltage proportional to the normal displacement at a point of the cylinder where the actuator is placed is negatively fed back to the actuator. Care should be taken to choose the sensing point such that it is not a nodal point. Thus the applied voltage is given by

$$V = -K_g w \tag{18}$$

where K_g is the controller gain . This voltage can be expressed in terms of the nodal degrees of freedom of the element containing the sensing point in concern as

$$V = -K_g[0 \quad 0 \quad 1 \quad 0 \quad 0][N]\{d^e\} \tag{19}$$

which finally, can be expressed in terms of the global nodal degrees of freedom as

$$V = -K_g[\overline{F}]\{X\} \tag{20}$$

wherein $[\overline{F}]$ is a global row matrix.

Substitution of (20) into (17) yields the final equation of motion as

$$[M]\{\ddot{X}\} + [K^*]\{X\} = \{F\} \tag{21}$$

where the augmented stiffness matrix $[K^*]$ is given by

$$[K^*] = [K] + K_g\{F\}[\overline{F}]$$

Equation (21) can be formulated as the standard eigenvalue problem. The eigen solution gives the active/passive modal damping ratio of the system as the ratio between the imaginary and real parts of any eigen value. It can also be formulated to compute the **F**requency **R**esponse **F**unction (**FRF**) when the shell/ACLD system is subjected to sinusoidal excitations using the mechanical impedance approach of Douglas and Yang [27].

4. EXPERIMENTAL PERFORMANCE OF THE SHELL/ACLD SYSTEM

4.1. Overview

The effectiveness of Active Constrained Layer Damping (**ACLD**) treatments in controlling the vibration of flexible cylindrical shells is demonstrated experimentally. The experimental results are used also to validate the **FEM** presented in Section **3**. Experimental cylindrical shells are built and treated partially with patches of the **ACLD** treatment. The performance of these shells is monitored under various types of external excitations (tonal and random vibrations) to evaluate the effectiveness of the **ACLD** in attenuating the resulting vibrations when using **P**roportional and **D**erivative (**PD**) controllers. Comparisons are made with the performance of conventional **P**assive **C**onstrained **L**ayer **D**amping (**PCLD**). Particular emphasis is placed on controlling several radial (lobar) modes simultaneously because these modes are important

4.2 Experimental Materials, Facilities and Methods

4.2.1 *Materials*

Two prototypes of the cylindrical shells are made of thin stainless steel sheets. Each cylinder has outer diameter of 20.32 cm, wall thickness of 0.05 cm and length of 30.48 cm. Cylinder A is treated with two **ACLD** patches which are 15 cm long 8 cm wide. The patches are bonded to the inner wall of the cylinder and placed at the mid-span such that the lines between the centers of the patch and cylinder center are perpendicular to each other. Cylinder B is treated with two **ACLD** patches which are 11 cm in length and 7 cm in width. The patches are also bonded to the inner wall of the cylinder at its mid span. The centers of the two patch are placed on diametrically opposite to each other. All the **ACLD** patches are made of SOUNDCOAT (Dyad 606) visco-elastic layer sandwiched between two layers of AMP/polyvinylidene fluoride (PVDF) piezo-electric films. Figure (4) shows a schematic drawings of the experimental shells indicating the relative location of the **ACLD** patches.

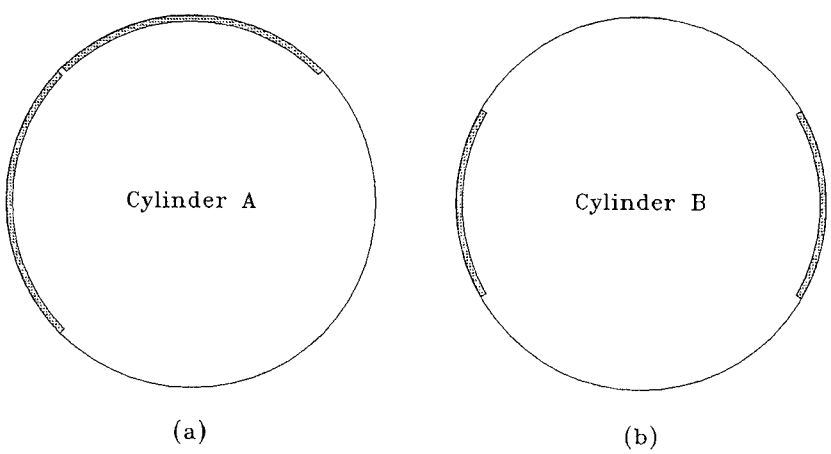

Figure (4) - Location of ACLD patches in the test cylinders

Tables (1), (2) and (3) list the main physical and geometrical parameters of the base cylindrical shell, the visco-elastic material and the piezo-electric films.

Table (1) - Physical and geometric properties of test cylinder

Length	O.D.	Thickness	Density	Young's Mod.
30.48 cm	20.32 cm	0.05 cm	7700 kg/m^3	195 GPa

Table (2) - Physical and geometric properties of the ACLD treatment

Layer	Thickness (mm)	Density (kg/m^3)	Modulus (MPa)
Visco-elastic	0.5	1140	20**
Piezo-electric	0.028	1800	2250*

*Young's Modulus **Shear Modulus

Table (3) - The main physical and geometric properties of the piezo-sensor and piezo-actuator layers

d_{31} (m/V)	d_{32} (m/V)	k_{31}	k_{32}	g_{31} (Vm/N)	g_{32} (Vm/N)	k_{3t}
23×10^{-12}	3×10^{-12}	0.12	0.01	216×10^{-3}	19×10^{-3}	12

4.2.2 *Experimental Set-up*

Figure (5) shows the experimental set-up used in testing the effectiveness of the Active Constrained Layer Damping in attenuating the vibration of the test cylinder as compared to conventional passive constrained layer damping. The cylindrical shell/ACLD system is suspended in air by light elastic bands and excited radially by an electro-mechanical speaker driven by sinusoidal or white noise sources through a power amplifier (Model 6020, JBL Corp.). The amplitude of vibration of the cylinder is monitored by an accelerometer (Model 303A03, PCB Piezotronics, Inc., NY), a non-contacting laser sensor (Model MQ, Aromat Corp., Providence, NJ) and the distributed piezo-sensors of the ACLD patches.

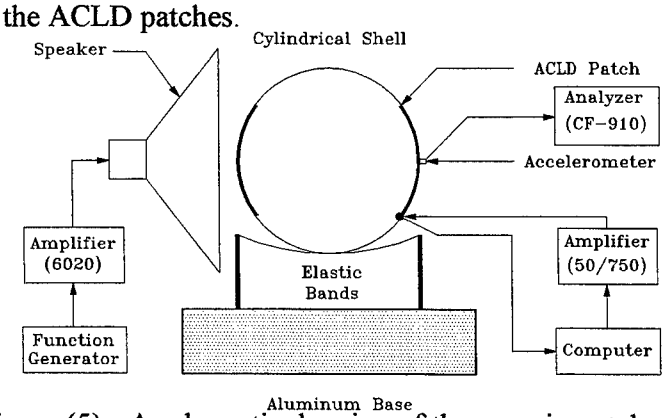

Figure (5) - A schematic drawing of the experimental set-up

4.2.3 *Experimental Procedures*

As the system is excited by the speaker by tonal or white noise signals, the output signal of the accelerometer is sent directly to a spectrum analyzer (Model CF-910, ONO SOKKI Co., MI) in order to determine the vibration characteristics both in the time and frequency domains. The signal from the piezo-sensor(s) is amplified using a charge amplifier (Model AM-5 from Wilcoxon Research, Rockville, MD). The amplified signal is manipulated, using analog or digital circuit to generate a proportional control law or a proportional and derivative control law. The resulting control action is then sent to the piezo-electric active constraining layer via analog power amplifiers (Model PA7C from Wilcoxon Research and Model 50/750 from TREK Co.).

4.3 Experimental Results

4.3.1 *Modes of Vibration*

Modal testing of the plain cylindrical shell gives three distict frequencies in the range 0-200 Hz. These modes are 27.5 Hz (Mode (0,2)), 32.5 Hz (mode (1,2)), 77. Hz (Mode (0,3)) and 84.5 Hz (Mode (1,3)) which represent the lowest three **lobar modes** of the cylinder. The corresponding numerical predictions are: 27.46, 32.48, 77.70 and 85.43 Hz.

4.3.2 *Vibration Control of the First Radial Mode (Mode (0,2))*

Cylinder A is treated with two patches of **ACLD** treatment in order to sense and control the vibration of the first radial mode. A switch is used to deliver the control voltage into either one or both of the patches. Figure (6) shows the results of single tone excitation through the speaker. The steady state control voltage is 40 volts. Lower vibration amplitude are observed by activating both patches. Comparisons are also shown in the figure between the amplitudes of vibration when the patches are unactivated (i.e., the patches act as a conventional **P**assive **C**onstrained **L**ayer **D**amping - **PCLD**).

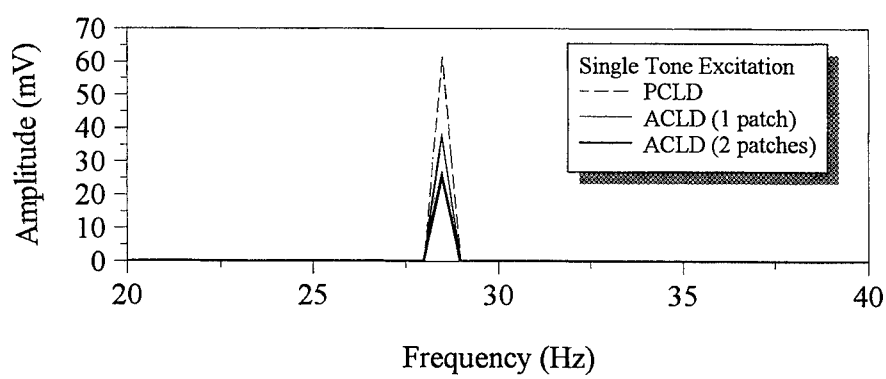

Figure (6) - Effect of control strategy on amplitude of vibration of shell A when excited at its first radial mode

Figure (7) shows the effect of varying the gain K_P of a proportional controller on amplitude of vibration when both **ACLD** patches are activated. It is very clear that vibration attenuations of 26%, 57% and 83% are achieved as the control voltages (steady-state) are set to 20, 40 and 60 volts, respectively.

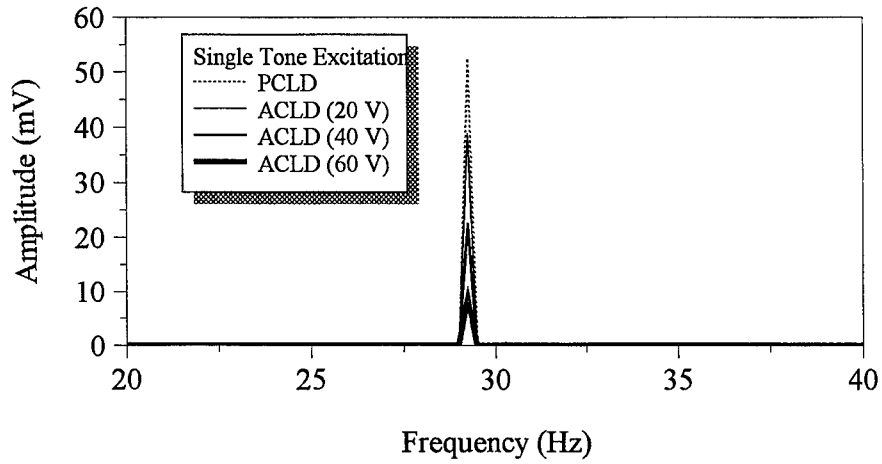

Figure (7) - Effect of control gain on amplitude of vibration of cylinder A when excited at its first radial mode.

Figure (8) shows the effect of varying the control voltage on the frequency spectrum of the amplitude of vibration when white noise excitation is used. Significant attenuation of the vibration is observed as the control voltage is increased. It is evident that the first resonant frequency (~ 28 Hz) of the shell increases with increased control voltage. Displayed also in Figure (8), for the sake of comparison, is the shell characteristics with unactivated patches which corresponds to the case of **PCLD**. The results obtained indicate that the **ACLD** treatment, with control voltage of 25 volt, reduces the amplitude of vibration to one fifth of that with the **PCLD** treatment.

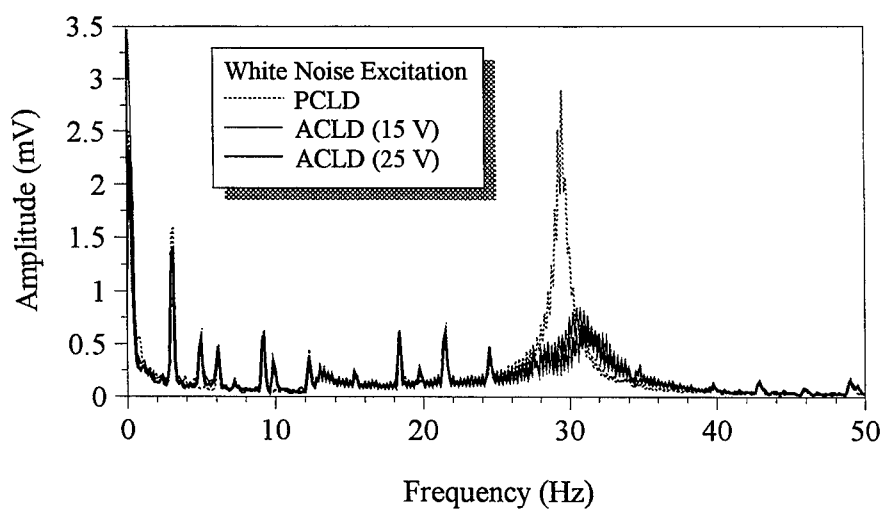

Figure (8) - Vibration control with different control gains for broad band excitation

4.3.3 *Vibration Control of two Radial Modes (Mode (0,2) and Mode (0,3))*

Cylinder B is treated with two patches of **ACLD** treatment in order to target both Mode (0,2) and Mode (0,3) simultaneously. White noise excitation is used. The output signal from the piezo-sensors of the two patches are sampled by a 486 micro-processor via an A/D board (Model DASH-16, METRABYTE, Tauton, MA). The board is capable of monitoring 16 inputs with a resolution of 12 bits and a conversion time of 15 μsec. The signal is manipulated to generate a proportional and derivative (**PD**) control law. The resulting control voltage is sent to the actuators of the two patches via a D/A board (Model DAC02, METRABYTE, Tauton, MA) and power amplifiers.

In this experiment, control gains K_P and K_d, are varied in order to achieve different control actions. Table (4) lists typical sets of gains considered in this study and the corresponding output voltages sent to both actuators. Figure (9) shows comparisons between the vibration amplitudes before and after applying the different control gains. The corresponding steady state control voltages sent to the controllers are 0 volt, 6 volts and 38 volts for the three gains displayed in Figure (9). It is obvious that higher control voltages result in better attenuation of the two modes of vibration simultaneously.

Table (4) - Control gains and corresponding output voltages

K_p	0.5	1.0	1.0	0.0	2.0	0.0	3.0
K_d	0.005	0.010	0.020	0.030	0.030	0.040	0.040
volt	4	6	13	16	19	35	38

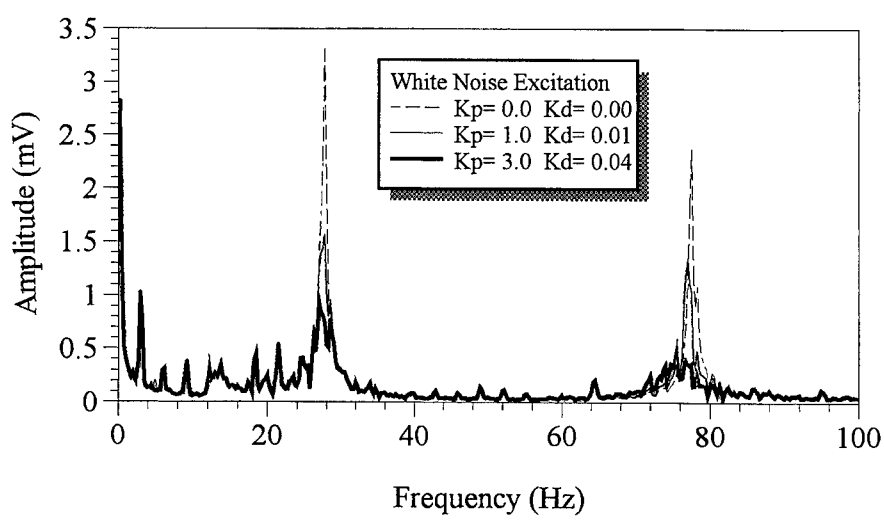

Figure (9) - Effect of control gain on simultaneous control of two vibration modes

In Figure (10), the vibration attenuation characteristics are displayed when the controller is a derivative controller i.e., $K_p = 0$.

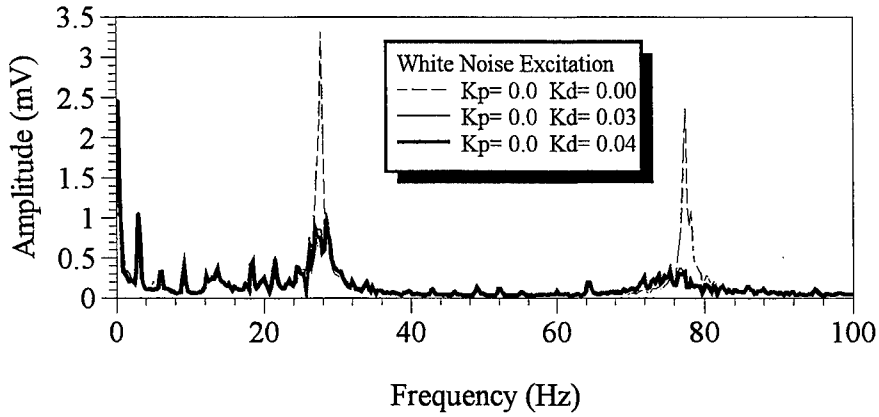

Figure (10) - Vibration control of two modes with derivative controller

4.4 Comparisons Between Theory and Experiments

Figure (11) shows comparisons between the theoretical and experimental resonant frequencies and damping ratios for cylinder A at the first radial mode for different control voltages.

Similar comparisons between the theoretical and experimental natural frequencies and damping ratios for cylinder B are displayed in Figures (12) and (13) for Modes (0,2) and (0,3) respectively. It is evident that there is excellent agreement between predicted and measured value of both natural frequencies and damping ratios.

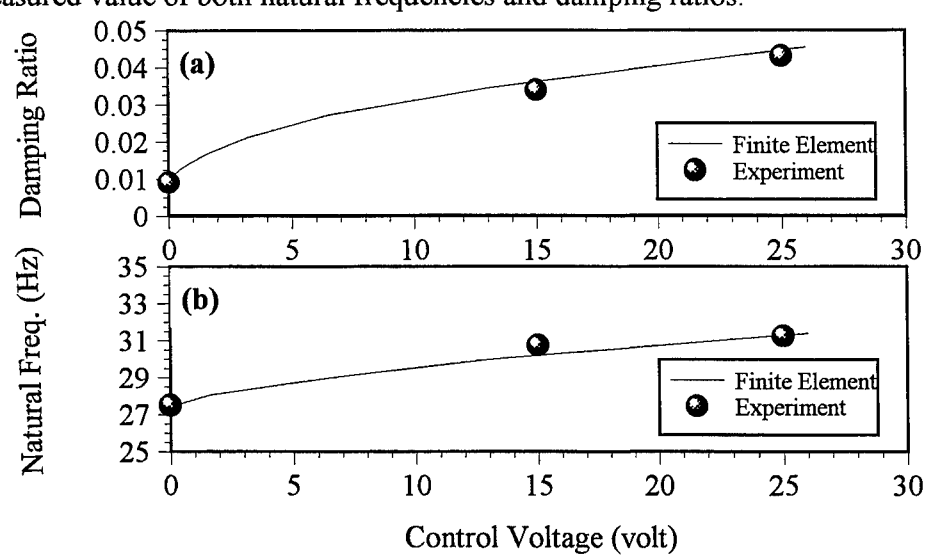

Figure (11) - Comparison between finite element calculation and experimental result
(a) - damping ratio (b) - natural frequency

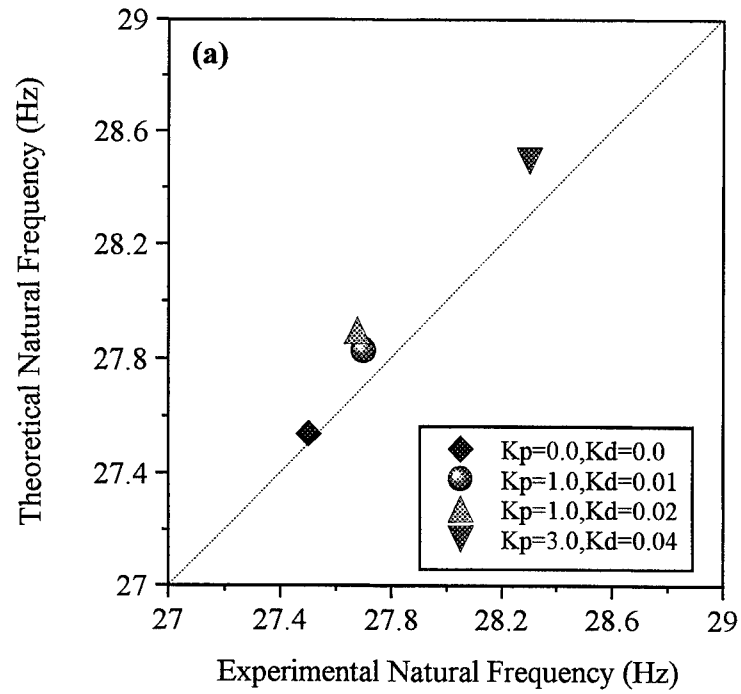

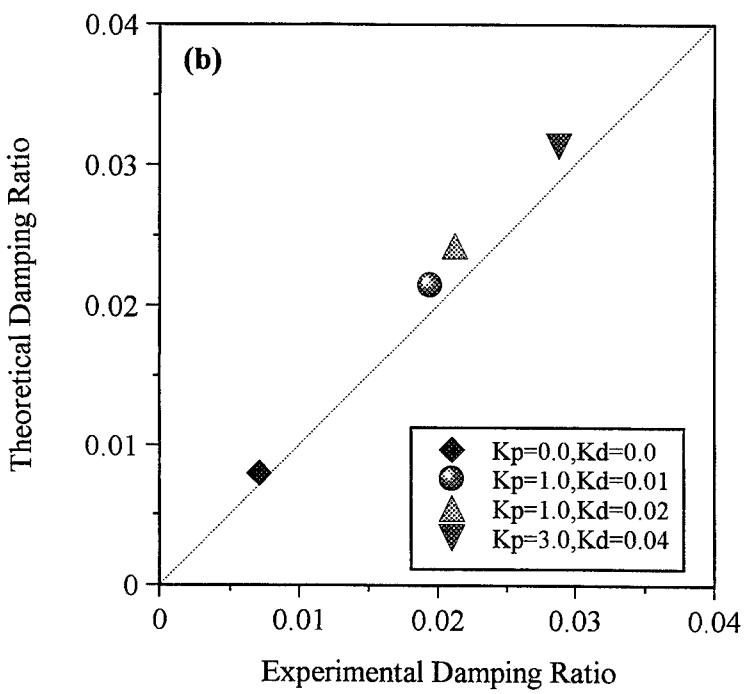

Figure (12) - Comparison for Mode (0,2) of cylinder B
(a) - natural frequency b. damping ratio

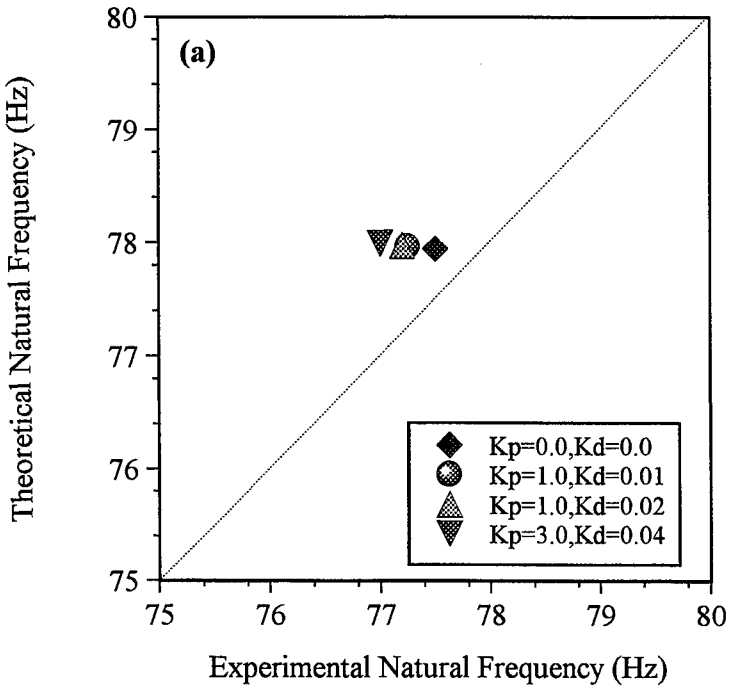

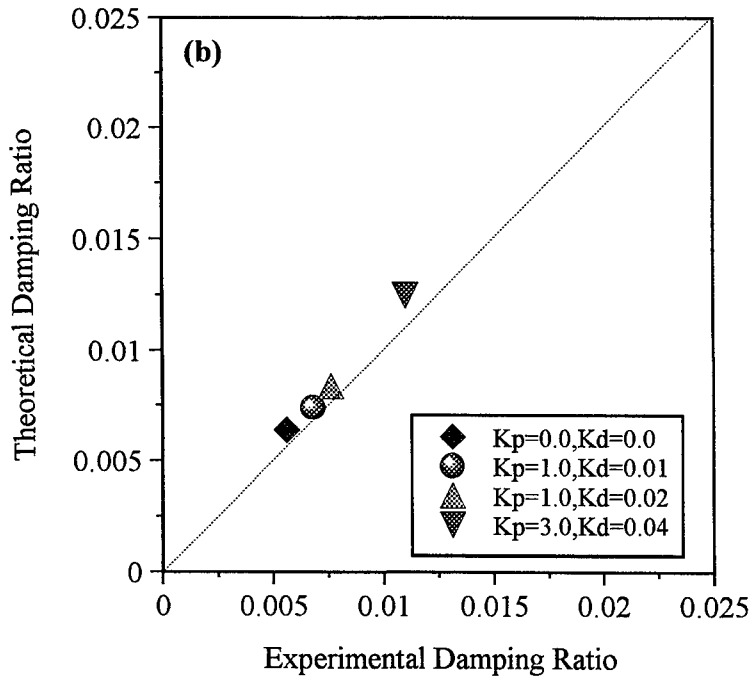

Figure (13) - Comparison for Mode (0,3) of cylinder B
a. natural frequency b. damping ratio

5. CONCLUSIONS

The effectiveness of the **A**ctive **C**onstrained **L**ayer **D**amping (**ACLD**) in controlling the vibration of thin cylindrical shells has been demonstrated theoretically and experimentally in this paper. A finite element model is developed to describe the dynamics and control phenomena associated with shell/ACLD systems. The model is based on Donnell's theory of shells and it discretizes the shell continuum into 8-noded two-dimensional iso-parameteric elements. The validity of the model is checked experimentally using simple proportional and derivative controllers applied to a stainless steel cylinder excited with tonal or random excitations. Several vibration modes have been controlled simultaneously. Attenuations of the structural vibrations of 85% are achieved with control voltages not exceeding 40 volts.

Work is now in progress to use the **ACLD** to control the sound radiation into the interior of the shell with appropriate modifications of the finite element model to account for the structure-fluid interactions. Also, work is also in progress to utilize the **ACLD** to control the sound radiation to the exterior of shells with fluid loading.

ACKNOWLEDGMENTS

This work is funded by the U.S. Army Research Office (AASERT Grant Number DAAH04-94-G-0163). Special thanks are due to Dr. Gary Anderson, the technical monitor of ARO, for his invaluable technical inputs.

REFERENCES

1 **S. Markus**, "Damping Properties of Layered Cylindrical Shells Vibrating in Axially Symmetric Modes", *Journal of Sound and Vibration*, **48**(4), 511-524, 1976.

2. **S. Markus**, "Refined Theory of Damped Axisymmetric Vibration of Double-Layered Cylindrical Shells", *Journal of Mechanical Engineering Science*, **21**(1), 33-37, 1979.

3. **I. W. Jones and V. L. Salerno**, "The Effect of Structural Damping on the Forced Vibration of Cylindrical Sandwich Shells", *Transactions of the American Society of Mechanical Engineers, Journal of Engineering for Industry*, **88**, 318-324, 1966.

4. **H. H. Pan**, "Axisymmetric Vibrations of a Circular Sandwich Shell with a Visco-elastic Core Layer", *Journal of Sound and Vibration*, **9**(2), 338-348, 1969.

5. **Y. P. Lu, B. E. Douglas, and E. V. Thomas**, "Mechanical Impedance of Damped Three-Layered Sandwich Rings", *AIAA Journal*, **11**(3), 1973.

6. **R. A. DiTaranto**, "Free and Forced Response of a Laminated Ring", *The Journal of the Acoustical Society of America*, **53**(3), 748-757, 1972.

7. **W. Leissa, and K. M. Iyer**, "Modal Response of Circular Cylindrical Shells with Structural Damping", *Journal of Sound and Vibration*, **77**(1), 1-10, 1981.

8. **Naiyer Alam, and N. T. Asnani**, "Vibration and Damping Analysis of a Multi-layered Cylindrical Shell, Part I: Theoretical Analysis", *AIAA journal*, **22**(6), 803-810, 1984.

9. **Naiyer Alam, and N. T. Asnani,** "Vibration and Damping Analysis of a Multi-layered Cylindrical Shell, Part II: Numerical Results", *AIAA journal*, **22**(7), 975-981, 1984.

10. **R. L. Forward**, "Electronic Damping of Orthogonal Bending Modes in a Cylindrical Mast Experiment", *Journal of Spacecraft*, **18**, 11-17, 1981.

11. **Harold C. Lester**, and Sylvie Lefebvre, "Piezoelectric Actuator Model for Active Sound and Vibration Control Cylinders", *Journal of Intelligent Material System and Structures*, **4**, 295-306, July, 1993.

12. **Suwei Zhou, C. Liang, and Craig A. Rogers**, "Impedance Modeling of Two-Dimensional Piezoelectric Actuators Bonded on A Cylinder", *Adaptive Structures and Material Systems ASME*, **35**, 247-255, 1993.

13. **H. T. Banks, R. C. Smith and Yun Wang**, "The Modeling of Piezoceramic Patch Interactions with Shells, Plates, and Beams", *Quarterly of Applied Mathematics*, **LIII**(2), 353-381, June, 1995.

14. **Z. Chaudhry, F. Lalande and C. A. Rogers**,. "Special Considerations in the Modeling of Induced Strain Actuator Patches Bonded to Shell Structures", *Proc. of SPIE Conference on Smart Structures*, **2190**, 563-570,1994.

15. **V. R. Sonti and J. D. Jones**, "Curved Piezo-actuator Model for Active Vibration Control of Cylindrical Shells", *AIAA Journal*, **34**(5), 1034-1040, 1996.

16. **H. S. Tzou**, *Piezoelectric Shells: Distributed Sensing and Control of Continua*, Kluwer Academic Publishers, Dordrecht, The Netherlands, 1993.

17. **A. Baz**, "Active Constrained Layer Damping", U.S. Patent 5,485,053, Jan. 1996.

18. **A. Baz and J. Ro**, "Vibration Control of Plates with Active Constrained Layer Damping", *Journal of Smart Materials and Structures*, **5**, 272-280,1996.

19. **A. Baz and J. Ro**, "Optimum Design and Control of Active Constrained Layer Damping", *ASME J. of Vibration and Acoustics*, **117B**, 135-145, 1995.

20. **G. S. Agnes and K. Napolitano**, "Active Constrained Layer Viscoelastic Damping", *Proc. of 34th SDM Conference*, 3499-3506, 1993

21. **B. Azvine., G. Tomlinson and R. Wynne**, "Initial Studies into the Use of Active Constrained-Layer Damping for Controlling Resonant Vibrations", *Proc. of Smart Structures and Materials Conference on Passive Damping*, **2193**, 138-149, Orlando, Florida, 1994.

22. **D. Edberg and A. Bicos**, "Design and Development of Passive and Active Damping Concept for Adaptive Structures", *Conference on Active Materials and Adaptive Structures, IOP Publishing Ltd.*, Bristol UK, 377-382, 1992.

23. **J. Plump and J. E. Hubbard**, "Modeling of an Active Constrained Layer Damper", *Twelve's Intl. Congress on Acoustics, Paper #401*, Toronto, Canada, 1986.

24. **I. Y. Shen**, "Hybrid Damping Through Intelligent Constrained Layer Treatments", *ASME Journal of Vibration and Acoustic*, **116**(3), 341-348, 1994.

25. **Van. Nostrand, W. G. Knowies and D. Inman**, "Finite Element Modeling for Active Constrained-Layer Damping", *Proc. of Smart Structures and Materials Conference on Passive Damping*, **2193**, 126-137, 1994.

26. **A. Baz and T. Chen**, "Boundary Control of Axi-Symmetric Vibrations of Cylindrical Shell Using Active Constrained Layer Damping", AIAA paper # 97-0360, *35th AIAA Aerospace Sciences Conf.*, Reno, Nevada, Jan. 1997.

27. **B. E. Douglas and J. C. Yang**, "Transverse Compressional Damping in the Vibratory Response of Elastic-Viscoelastic-Elastic Beams", *AIAA Journal*, **16**(9), 925-930, 1978.

APPENDIX - A

Transformation Matrices

$$[Z]=\begin{bmatrix} 1 & 0 & z & 0 & 0 & 0 & 0 & 0 & 0 \\ 0 & 1 & 0 & z & 0 & 0 & 0 & 0 & 0 \\ 0 & 0 & 0 & 0 & 1 & 0 & 0 & 0 & 0 \\ 0 & 0 & 0 & 0 & 0 & 1 & 0 & 0 & -z \\ 0 & 0 & 0 & 0 & 0 & 0 & 1 & z & 0 \end{bmatrix},$$

$$[Z_2^p]=-h_c\begin{bmatrix} 1 & 0 & 0 & 0 & 0 \\ 0 & 1 & 0 & 0 & 0 \\ 0 & 0 & 0 & 0 & 0 \\ 0 & 0 & 0 & -\frac{1}{R} & 0 \\ 0 & 0 & 0 & 0 & 1 \end{bmatrix},\quad [Z^c]=\begin{bmatrix} z-h_2 & 0 & 0 & 0 & 0 \\ 0 & z-h_2 & 0 & 0 & 0 \\ 0 & 0 & 1 & 0 & 0 \\ 0 & 0 & 0 & 1-\frac{z-h_2}{R} & 0 \\ 0 & 0 & 0 & 0 & z-h_2 \end{bmatrix},$$

$$[B_i]^T=\begin{bmatrix} n_{i,x} & 0 & 0 & 0 & 0 & 0 & n_{i,y} & 0 & 0 \\ 0 & n_{i,y} & 0 & 0 & 0 & -\frac{n_i}{R} & n_{i,x} & 0 & 0 \\ 0 & \frac{n_i}{R} & 0 & 0 & n_{i,x} & n_{i,y} & 0 & 0 & 0 \\ 0 & 0 & n_{i,x} & 0 & n_i & 0 & 0 & n_{i,y} & 0 \\ 0 & 0 & 0 & n_{i,y} & 0 & n_i & 0 & n_{i,x} & \frac{n_i}{R} \end{bmatrix},$$

$$[B_{1i}^c]=\begin{bmatrix} n_{i,x} & 0 & 0 & h_2 n_{i,x} & 0 \\ 0 & n_{i,y} & \frac{n_i}{R} & 0 & h_2 n_{i,y} \\ 0 & 0 & n_{i,x} & 0 & 0 \\ 0 & -\frac{n_i}{R} & n_{i,y} & 0 & \frac{h_2 n_i}{R} \\ n_{i,y} & n_{i,x} & 0 & h_2 n_{i,y} & h_2 n_{i,x} \end{bmatrix},\ [B_{2i}^c]=\begin{bmatrix} n_{i,x} & 0 \\ 0 & n_{i,y} \\ n_i & 0 \\ 0 & 1 \\ n_{i,y} & n_{i,x} \end{bmatrix},\ \mathrm{n}_{\mathrm{i,x}}=\frac{\partial \mathrm{n}_{\mathrm{i}}}{\partial \mathrm{x}} \text{ and } \mathrm{n}_{\mathrm{i,y}}=\frac{\partial \mathrm{n}_{\mathrm{i}}}{\partial \mathrm{y}}$$

APPENDIX - B

Stiffness and Mass Matrices

$$[D]=\int_{h_2}^{h_1}[Z]^T[C^1][Z]dz\,,\quad [D_b]=\int_{h_3}^{h_2}[C^2]dz\,,\quad [D_{bc}]=\int_{h_3}^{h_2}[C^2][Z^c]dz\,,\quad [D_{cb}]=[D_{bc}]^T$$

$$[D_{cc}]=\int_{h_3}^{h_2}[Z^c]^T[C^2][Z^c]dz\,,\quad [D_p]=\int_{h_4}^{h_3}[Z_1^p]^T[C^3][Z_1^p]dz\,,\quad [D_{pc}]=\int_{h_4}^{h_3}[Z_1^p]^T[C^3][Z_2^p]dz$$

$$[D_{cp}]=[D_{pc}]^T\,,\quad [D_{cc}^p]=\int_{h_4}^{h_3}[Z_2^p]^T[C^3][Z_2^p]dz$$

$$[K_b^e]=\int_A\Big([B]^T[D][B]\ +\ [B_1^c]^T[D_b][B_1^c]\ +\ [B]^T[D_p][B]\Big)dA$$

$$[K_{bc}^e]=\int_A\Big([B_1^c]^T[D_{bc}][B_2^c]\ +\ [B]^T[D_{pc}][B_2^c]\Big)dA\,,\quad [K_{cb}^e]=[K_{bc}^e]^T$$

$$[K_{cc}^e]=\int_A\Big([B_2^c]^T[D_{cc}][B_2^c]\ +\ [B_2^c]^T[D_{cc}^p][B_2^c]\Big)dA$$

$$[K_{cp}^e]=\frac{1}{2}\int_A\int_{h_{k+1}}^{h_k}[B_2^c]^T[Z_2^p]^T[C^3]dzdA\,,\quad [K_{bp}^e]=\frac{1}{2}\int_A\int_{h_{k+1}}^{h_k}[B]^T[Z_1^p]^T[C^3]dzdA$$

Where A indicates the elemental surface area.

$$[M^e]=\int_A\{N\}^T[\overline{m}][N]dA\,,\qquad [\overline{m}]=\begin{bmatrix} I_0 & 0 & 0 & I_1 & 0\\ 0 & I_0 & 0 & 0 & I_1\\ 0 & 0 & I_0 & 0 & 0\\ I_1 & 0 & 0 & I_2 & 0\\ 0 & I_1 & 0 & 0 & I_2\end{bmatrix}$$

$$\begin{bmatrix} I_0 & I_1 & I_2\end{bmatrix}=\sum_{L=1}^{3}\int_{h_{L+1}}^{h_L}\rho^L\begin{bmatrix}1 & z & z^2\end{bmatrix}dz$$

A finite element for beams having segmented active constrained layers with frequency-dependent viscoelastic material properties

George A. Lesieutre*, Usik Lee

The Pennsylvania State University, University Park, PA 16802

Inha University, Inchon 402-751, South Korea

ABSTRACT

A finite element for planar beams with active constrained layer damping treatments is presented. Features of this non-shear locking element include a time-domain viscoelastic material model, and the ability to readily accommodate segmented (*i.e.* non-continuous) constraining layers. These features are potentially important in active control applications: the frequency-dependent stiffness and damping of the viscoelastic material directly affects system modal frequencies and damping; the high local damping of the viscoelastic layer can result in complex vibration modes and differences in the relative phase of vibration between points; and segmentation, an effective means of increasing passive damping in long-wavelength vibration modes, affords multiple control inputs and improved performance in an active constrained layer application. The anelastic displacement fields (ADF) method is used to implement the viscoelastic material model, enabling the straightforward development of time-domain finite elements. The performance of the finite element is verified through several sample modal analyses, including proportional-derivative control based on discrete strain sensing. Because of phasing associated with mode shapes, control using a single continuous ACL can be destabilizing. A segmented ACL is more robust than the continuous treatment, in that the damping of modes at least up to the number of independent patches is increased by control action.

1. INTRODUCTION AND BACKGROUND

ACTIVE CONSTRAINED LAYER DAMPING TREATMENTS

A number of researchers have explored the potential effectiveness and optimization of active constrained layer (ACL) damping treatments. An ACL treatment parallels that of a conventional passive constrained layer treatment, consisting of a layer of high damping viscoelastic material (VEM) sandwiched between a base structure and a constraining layer. In the passive case, the constraining layer serves to develop high shear strain energy in the lossy viscoelastic layer. In the active case, the dimensions of the constraining layer can be actively modified to further enhance the shear in the viscoelastic layer.

Research efforts on active constrained layer damping treatments can be distinguished on the basis of several features, including the following:

1) the specific ACL configuration and materials considered;
2) assumptions underlying the governing equations (*e.g.*, shear, rotatory inertia);
3) method used to model viscoelastic material (damping) behavior;
4) control approach;
5) response solution method (*i.e.*, analytical, Galerkin, finite elements); and
6) optimization of ACL placement, number, and sizing.

Plump and Hubbard (1986) developed a 6th order governing PDE for an active constrained layer damper (PVDF constraining layer), using a complex modulus approach for the viscoelastic material. No analysis or experimental results were presented.

Baz and Poh (1988) investigated the effects of the bonding layer on active control effectiveness, without considering the damping properties of the bonding layer. In subsequent work, Baz (1993) and Baz and Ro (1994a) proposed an ACL with an additional piezoelectric sensor layer between the base structure and the VEM. A complex modulus approach was evidently used to model VEM behavior in this work. Using proportional control, the performance of the ACL was compared to that of a passive constrained layer (PCL) treatment. In later work, Baz and Ro (1994b) investigated, both theoretically and experimentally, combined proportional and derivative (PD) control along with a spatially-varying piezoelectric sensor, and

* G.A.L.: Email: g-lesieutre@psu.edu; Telephone: 814-863-0103. Associate Professor of Aerospace Engineering.
U.L.: Email: ulee@dragon.inha.ac.kr; Telephone: 32 860-7318. Associate Professor of Mechanical Engineering.

demonstrated good broadband vibration attenuation capability. Baz and Ro (1995a) also developed a beam finite element model, and selected PD control gains (full state feedback) based on a linear quadratic regulator (LQR) performance index. The thickness and shear modulus of the viscoelastic layer were optimized to maximize damping with minimum mass addition. A plate finite element model was developed by Baz and Ro (1995b) and theoretical and experimental results (natural frequencies and damping) were compared for PD-control and a single partial-coverage ACL treatment.

Leibowitz and Vinson (1993) presented a concept for an ACL configuration and developed the governing equations using an energy method. The viscoelastic material was modeled using a complex modulus approach. They proceeded to investigate the performance of an ACL on a beam using partial coverage, and reported the results of parametric studies, concluding that an ACL could outperform a purely passive constrained layer treatment.

Agnes and Napolitano (1993) suggested that an ACL could combine the advantages of both passive and active vibration control approaches. VanNostrand, Knowles, and Inman (1994) developed a beam finite element model, using the ATF time-domain modeling method (Lesieutre and Mingori, 1990; Lesieutre 1992) to capture the frequency-dependent behavior of the viscoelastic material. In subsequent research, VanNostrand, Knowles, and Inman (1993) experimentally investigated the effects of VEM stiffness on ACL effectiveness, as well as the implications of sensor type on control structure. Lam, Saunders, and Inman (1995) investigated the use of the GHM method (Golla and Hughes, 1985; McTavish and Hughes, 1993) to model VEM behavior.

In a series of paper, Shen (1994, 1995a, 1995b, 1996) investigated several aspects of ACL treatments, with emphasis on performance, controllability, and stability. In contrast to Baz, Shen considered the use of a point strain sensor rather than a sensing layer. Composite beam and plate models were developed, using a complex modulus approach to model VEM behavior. Numerical response results were obtained using a Galerkin discretization approach. From experiments, Shen reported that a single ACL treatment was ineffective in controlling bending and torsional vibration simultaneously, and that cracks in the PZT piezoelectric constraining layer resulted in noisy signals.

Azvine, Tomlinson, and Wynne (1995) considered an ACL concept in which the piezoelectric actuator is bonded to (not replacing) the constraining layer. They used a complex modulus approach to model the VEM, and investigated the effect of ACL location on modal damping of a cantilevered beam using a control signal proportional to the tip velocity. Veley and Rao (1995) developed a finite element model by combining a piezoelectric element and a constrained layer damping element, retaining both mechanical and electrical DOFs. They investigated optimal ACL placement using a PD control approach.

Nath and Wereley (1995) investigated the application of an ACL to rotorcraft flex beams, the goal being to enhance lag mode damping. They developed a differential equation model for a completely-treated beam, with special attention to the boundary conditions. Frequency response methods were used to study the steady-state performance of the ACL system, based on a frequency-dependent complex shear modulus model of the viscoelastic material.

Liao and Wang (1995, 1996a) considered the ACL approach in the context of active-passive hybrid structures, with the goal of preserving the advantages of fully passive (stable, fail-safe, no power) and fully active (high performance) systems. They developed a mathematical model of a beam with a partial-coverage ACL treatment, using the GHM method to model VEM behavior, Galerkin's method to discretize the governing equations, and an LQR optimal control law to obtain control gains for a specified performance index. They investigated the effects of the VEM on control authority and identified situations in which an ACL may perform better than purely passive or active systems. In recent research, Liao and Wang (1996b) suggested a way to increase active control transmissibility by using stiff "edge elements" on the perimeter of the ACL to provide a parallel load path to the base structure. Although this approach is likely to degrade passive performance, it may also increase reliability by preventing delamination.

In summary, numerous researchers are investigating the utility of active constrained layer damping treatments. Several of these researchers have used finite elements in their work, most commonly employing a complex modulus approach as a model of the behavior of the viscoelastic layer. Three research efforts report the use of time-domain methods (ATF, GHM) to model the characteristic frequency-dependent behavior of the viscoelastic damping layer; two of these used beam finite element discretizations, while the other used a Galerkin approach.

Researchers have generally addressed the use of a <u>single</u> active constraining layer in a particular application. Segmentation of the constraining layer is a well-known, effective means of increasing passive damping in long-wavelength vibration modes (by increasing the number of high-shear regions), but its use has not yet been explored in an ACL configuration. In addition to the potential passive benefits, segmentation provides the possibility of additional independent control inputs, a feature which is likely to improve achievable performance.

The objective of the present research was to develop an ACL beam finite element that would be useful for investigating active constrained layer treatments. To facilitate controls synthesis, this model was required to be formulated in the time-domain, preferably in state-space form, with the possibility of segmentation a desirable feature.

VISCOELASTIC DAMPING MATERIALS AND MODELS

The mechanical properties of the "damping materials" used in passive constrained layer damping treatments are often sensitive to frequency, temperature, type of deformation, and sometimes amplitude (Nashif, Jones, and Henderson, 1985). To ensure design adequacy, performance is usually analytically evaluated at a few temperatures that span the expected operating range of interest. Material properties appropriate to each temperature of interest are used in such analyses. For operation at a nearly-constant temperature, it is most important to consider the dependence of stiffness and damping properties on frequency; over a broad frequency range, damping can vary by an order of magnitude, and stiffness by several orders of magnitude.

While damping models currently available in commercial finite element software (e.g., viscous damping, proportional damping, hysteretic or structural damping, and viscous modal damping (via the modal strain energy (MSE) method (Johnson, Keinholz, and Rogers, 1981)) do provide energy dissipation, in general they are not physically motivated and suffer from various limitations. In particular, none of these captures, in a time-domain model, the frequency-dependent behavior characteristic of real materials. Furthermore, such issues of model fidelity are especially important in control applications.

Dissatisfaction with available damping modeling techniques has motivated considerable research on the subject of time-domain methods that capture the essential frequency dependence of viscoelastic material properties and that are compatible with current structural finite element analysis techniques. This research can be broadly classified into: 1) those that use fractional time derivatives to model material relaxation behavior; and 2) those that use integer time derivatives. Both kinds of approaches have advantages and disadvantages, and none is clearly superior to others in all cases.

In a series of papers, Bagley and Torvik and their collaborators (Bagley and Torvik, 1983, 1985; Bagley and Calico, 1991) developed a fractional derivative model of viscoelastic material behavior and applied it to a number of structural problems. An important feature of their approach is the ability to capture the relatively weak frequency dependence exhibited by many materials using just a few, typically four, model parameters. This feature makes the fractional derivative model especially useful in frequency-domain analyses. Frequency-domain finite elements were initially developed to obtain structural responses for load histories which have Laplace transforms, while a time-domain version with fractional state equations was developed later. In the time domain, the presence of fractional operators makes the solution of structural equations more complicated than it is for those involving ordinary differential operators. Enelund and Olsson (1995) proposed using a different form of the time-domain equations of motion, as well as a different method for time discretization. This solution approach requires that a truncated time history be retained for use, in effect adding coordinates to the model.

Structural equations with time domain damping models involving ordinary integer differential operators are easier to solve than those involving fractional derivative operators. Several of these kinds of models have been proposed in the literature, including the ATF/ADF model (Lesieutre and Mingori, 1990; Lesieutre, 1992; Lesieutre and Bianchini, 1995) the GHM model (Golla and Hughes, 1985; McTavish and Hughes, 1993), and Yiu's model (Yiu, 1993; Yiu, 1994).

The augmenting thermodynamic fields (ATF) method is a time-domain continuum model of material damping that preserves the characteristic frequency-dependent damping and modulus of real materials—a physically-motivated model compatible with current finite element structural analysis methods. In its initial development, the ATF method introduced a single augmenting field to model the behavior of materials and structures with light damping. In subsequent work, the ability to model high–damping materials having relatively weak frequency-dependence was developed, using multiple ATFs. However, this early work was effectively limited to structural members under uniaxial stress states, such as bars and beams. Subsequently, "anelastic displacement fields" (ADF), special kinds of ATF, were introduced. Instead of addressing physical damping mechanisms directly, their effects on the displacement field were considered. The ADF method has several advantages over the initial ATF method; in particular, it has been generalized to 3-D problems, to problems involving temperature dependence (Lesieutre and Govindswamy, 1995), and to problems involving non-linear strain dependence.

The GHM model and Yiu's model are similar in several ways to the ADF model. All yield time-domain viscoelastic finite elements, and use additional coordinates to more accurately model material behavior. The ADF method differs in that it involves a direct time-domain formulation—not transform–based, and yields finite elements using conventional methods. The "dissipation coordinates" of the GHM method are internal to individual elements, while the "anelastic displacement fields" of ADF are continuous from element to element, reflecting its basis as a field theory. The "internal unobservable degrees of freedom" of Yiu's model are introduced as nodal variables using an analogy with a generalized lumped-parameter Maxwell model. Because it was developed explicitly with second–order dynamics, the GHM method is quite compatible with current structural analysis methods, and has proven to be useful in practice. Both the ADF and Yiu's models may, however, also be readily expressed in second-order form. Although the second-order form of a GHM ("mini-oscillator") model can permit unrealistic material behavior, difficulty can be avoided by proper selection of material model parameters. Yiu's model also assumes a single loss factor for all material moduli (*e.g.*, shear and bulk for an isotropic material).

In many respects, however, finite element models yielded by the GHM method and especially Yiu's method are quite similar to those developed using ADF. In what follows, the ADF method is used as a representative time domain viscoelastic model.

2. FINITE ELEMENT DEVELOPMENT

ACTIVE CONSTRAINED LAYER CONFIGURATION AND KINEMATIC ASSUMPTIONS

ACL Configuration and Field Variables. Figure 1 illustrates the ACL beam configuration under consideration. There are three components: the base beam, the viscoelastic layer, and the piezoelectric (ceramic) constraining layer; quantities associated with each of these layers are denoted with subscripts "*b*," "*v*," and "*p*," respectively. Points in the cross-section are denoted using the independent coordinates "*x*" and "*z*," with the origin of the primary coordinate system located at the center of the left end of the base beam, and secondary coordinate systems located at the bottom of each of the layers.

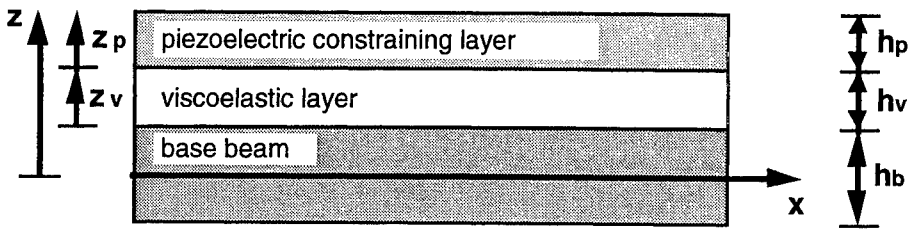

Figure 1: Active Constrained Layer Configuration

As shown in Figure 2, the motion of points in the system is described using the following dependent fields: the lateral deflection "*w*," the longitudinal displacement "*u*," the shear angle in the viscoelastic layer "β," and, when the time-domain viscoelastic model is included, the anelastic part of the shear angle in the viscoelastic layer "β^A".

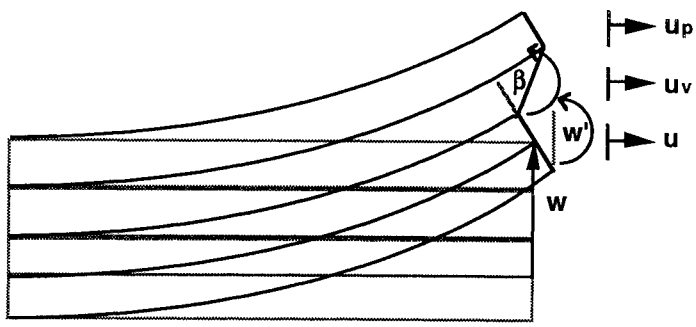

Figure 2: Displacements and Sign Conventions

Assumptions. The model is based on the following assumptions:

1) The base beam is elastic, and the Bernoulli-Euler bending assumptions are valid (transverse shear strain is negligible). The lateral displacement of the middle of the base beam, *w(x,t)*, is shared by all points in the cross section (transverse normal deformation is negligible, and rotations are small). The longitudinal displacement of the middle of the base beam is not required to be zero (bending extension coupling is included). Transverse and rotatory inertia are included.

2) The viscoelastic layer is lossy, and the Bernoulli-Euler assumptions are augmented with an additional shear angle associated with non-negligible transverse shear. An anelastic shear angle may be included to model frequency-dependent viscoelastic behavior. Longitudinal normal strain in the viscoelastic layer is included. Transverse and rotatory inertia are included.

3) The piezoelectric constraining layer is poled through the thickness, is elastic, and the Bernoulli-Euler bending assumptions are valid. The rotations of constraining layer cross-sections are the same as the rotations of the base beam at the same *x*-coordinate. The layer has both extensional and bending stiffness. Transverse and rotatory inertia are included.

Kinematics. Figure 3 illustrates the nodal degrees of freedom (DOF) of the finite element to be developed. The element has length "*L*." The lateral deflection, *w(x,t)* is interpolated using a cubic polynomial in *x*, allowing element-to-element continuity of deflection (*w*) and slope (*w'*, or longitudinal displacement *u*).

$$w = w(x,z,t) = w(x,t) = \left[N_w\right]\{\overline{w}\} \tag{1}$$

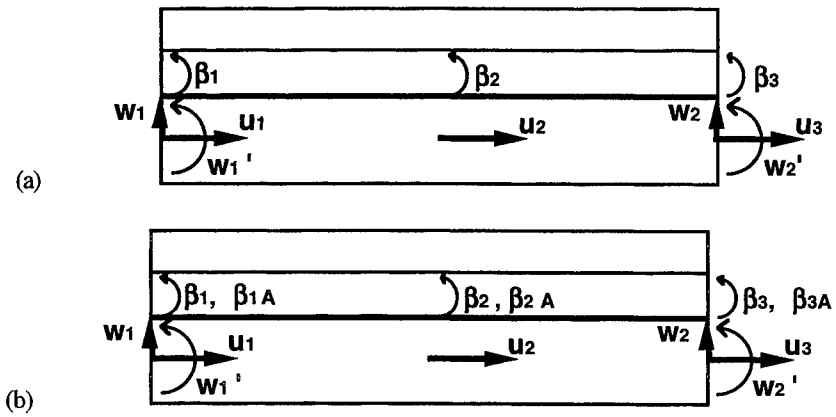

Figure 3: Nodal Degrees of Freedom of (a) Elastic and (b) Damped ACL Finite Element

where $[N_w]=[N_w(x)]=\left[\left(1-3\left(\frac{x}{L}\right)^2+2\left(\frac{x}{L}\right)^3\right)\ \left(\left(\frac{x}{L}\right)-2\left(\frac{x}{L}\right)^2+\left(\frac{x}{L}\right)^3\right)\ \left(3\left(\frac{x}{L}\right)^2-2\left(\frac{x}{L}\right)^3\right)\ \left(-\left(\frac{x}{L}\right)^2+\left(\frac{x}{L}\right)^3\right)\right]$

and $\{\overline{w}\}=\{\overline{w}(t)\}=\begin{Bmatrix} w_1(t) \\ w_1'(t) \\ w_2(t) \\ w_2'(t) \end{Bmatrix}$

The longitudinal displacement at the reference axis, $u_0(x,t)$ is interpolated with a quadratic polynomial, and an internal node.

$$u_0(x,t)=[N_u]\{\overline{u}\} \tag{2}$$

where $[N_u]=[N_u(x)]=\left[\left(1-3\left(\frac{x}{L}\right)+2\left(\frac{x}{L}\right)^2\right)\ \left(4\left(\frac{x}{L}\right)-4\left(\frac{x}{L}\right)^2\right)\ \left(-\left(\frac{x}{L}\right)+2\left(\frac{x}{L}\right)^2\right)\right]$

and $\{\overline{u}\}=\{\overline{u}(t)\}=\begin{Bmatrix} u_1(t) \\ u_2(t) \\ u_3(t) \end{Bmatrix}$

Because slope (w') and longitudinal displacement (u) are interpolated consistently, the element will not shear lock. The shear angle(s) in the viscoelastic (β, β^A) is/are interpolated consistent with u and w'.

$$\beta(x,t)=[N_u]\{\overline{\beta}\} \tag{3}$$

where $\{\overline{\beta}\}=\{\overline{\beta}(t)\}=\begin{Bmatrix} \beta_1(t) \\ \beta_2(t) \\ \beta_3(t) \end{Bmatrix}$

Now, the model displacements may be explicitly stated in terms of these nodal quantities and interpolation functions.

Base Beam. The lateral deflection of a point in the base beam, or anywhere on the cross-section, is given by:

$$w=w(x,z,t)=w(x,t)=[N_w]\{\overline{w}\} \tag{4}$$

The longitudinal displacement of a point in the base beam is given by:

$$u_b=u_b(x,z,t)=u_0(x,t)-z\,w'(x,t)=[N_u]\{\overline{u}\}-z\,[N_w']\{\overline{w}\} \tag{5}$$

Viscoelastic Layer. The longitudinal displacement of a point in the viscoelastic layer is given by the following (note that β is positive in the same direction as w').

$$u_v = u_v(x,z,t) = u_0(x,t) - z\,w'(x,t) - z_v\,\beta(x,t) = [N_u]\{\bar{u}\} - \left(\frac{h_b}{2} + z_v\right)[N'_w]\{\bar{w}\} - z_v\,[N_u]\{\bar{\beta}\} \tag{6}$$

Piezoelectric Constraining Layer. The longitudinal displacement of a point in the constraining layer is given as follows. Note that constraining layer may be segmented by not enforcing element-to-element continuity of β.

$$u_p = u_p(x,z,t) = u_0(x,t) - z\,w'(x,t) - h_v\,\beta(x,t) = [N_u]\{\bar{u}\} - \left(\frac{h_b}{2} + h_v + z_p\right)[N'_w]\{\bar{w}\} - h_v\,[N_u]\{\bar{\beta}\} \tag{7}$$

Strains. Now that the displacements of any point in the ACL system have been defined, the longitudinal normal and transverse shear strains may be determined. These are needed in strain energy expressions to develop the element stiffness matrix. Longitudinal normal strain is found from:

$$\varepsilon_{xx} = \frac{\partial u}{\partial x} \tag{8}$$

And transverse shear strain is found from:

$$\varepsilon_{xz} = \left(\frac{\partial u}{\partial z} + \frac{\partial w}{\partial x}\right) \tag{9}$$

Base Beam. The longitudinal normal strain at a point in the base beam is given by the following. The transverse shear strain in the base beam is negligible, by assumption.

$$(\varepsilon_{xx})_b = (\varepsilon_{xx}(x,z,t))_b = \left[[N'_u] \quad -z\,[N''_w] \quad [0]\right]\begin{Bmatrix}\{\bar{u}\}\\ \{\bar{w}\}\\ \{\bar{\beta}\}\end{Bmatrix} \tag{10}$$

Viscoelastic Layer. The longitudinal normal strain at a point in the viscoelastic layer is given by:

$$(\varepsilon_{xx})_v = (\varepsilon_{xx}(x,z,t))_v = \left[[N'_u] \quad -\left(\frac{h_b}{2} + z_v\right)[N''_w] \quad -z_v[N'_u]\right]\begin{Bmatrix}\{\bar{u}\}\\ \{\bar{w}\}\\ \{\bar{\beta}\}\end{Bmatrix} \tag{11}$$

The transverse shear strain in the viscoelastic layer is related to the shear angle:

$$(\varepsilon_{xz})_v = (\varepsilon_{xz}(x,z,t))_v = \left[[0] \quad [0] \quad -[N_u]\right]\begin{Bmatrix}\{\bar{u}\}\\ \{\bar{w}\}\\ \{\bar{\beta}\}\end{Bmatrix} \tag{12}$$

Piezoelectric Constraining Layer. The longitudinal normal strain at a point in the piezoelectric constraining layer is given by the following. The transverse shear strain is negligible, by assumption.

$$(\varepsilon_{xx})_p = (\varepsilon_{xx}(x,z,t))_p = \left[[N'_u] \quad -\left(\frac{h_b}{2} + h_v + z_p\right)[N''_w] \quad -h_v[N'_u]\right]\begin{Bmatrix}\{\bar{u}\}\\ \{\bar{w}\}\\ \{\bar{\beta}\}\end{Bmatrix} \tag{13}$$

STIFFNESS, MASS, AND DAMPING MATRICES; LOAD VECTOR

The stiffness and mass matrices are to be developed using energy methods, so expressions for strain and kinetic energy are required. The load vector associated with piezoelectric forcing is to be developed by considering virtual work. The damping matrix is to be developed using the ADF method. Note that the energy expressions developed could also be used to derive governing PDEs and boundary conditions using Hamilton's Principle.

Strain Energy, Stiffness Matrix. The strain energy stored in a deformed ACL beam of width "b" and length "L" is given by:

$$\begin{aligned} U = U(t) &= \tfrac{1}{2} b \int_0^L \int_z \left(E(x,z)\left(\varepsilon_{xx}(x,z,t)\right)^2 + G(x,z)\left(\varepsilon_{xz}(x,z,t)\right)^2 \right) dz\, dx \\ &= U_E + U_G \\ &= \left(U_{Eb} + U_{Ev} + U_{Ep}\right) + U_{Gv} \end{aligned} \tag{14}$$

noting that the energy can be divided into parts associated with longitudinal normal deformation (extension and bending) and shear deformation and, further, into parts associated with each component of the ACL system. The strain energy associated with longitudinal normal deformation of the base beam is given by:

$$U_{Eb} = \frac{1}{2} \begin{Bmatrix} \{\bar{u}\} \\ \{\bar{w}\} \\ \{\bar{\beta}\} \end{Bmatrix}^T b E_b \int_0^L \int_{-h_b/2}^{+h_b/2} \begin{bmatrix} [N_u']^T[N_u'] & -z[N_u']^T[N_w''] & [0] \\ -z[N_w'']^T[N_u'] & z^2[N_w'']^T[N_w''] & [0] \\ [0] & [0] & [0] \end{bmatrix} dz\, dx \begin{Bmatrix} \{\bar{u}\} \\ \{\bar{w}\} \\ \{\bar{\beta}\} \end{Bmatrix} \tag{15}$$

The strain energy associated with longitudinal normal deformation of the viscoelastic layer is given by the following. Note that this part of the strain energy is often neglected.

$$U_{Ev} = \frac{1}{2} \begin{Bmatrix} \{\bar{u}\} \\ \{\bar{w}\} \\ \{\bar{\beta}\} \end{Bmatrix}^T b E_v \int_0^L \int_0^{h_v} \begin{bmatrix} [N_u']^T[N_u'] & -\left(\frac{h_b}{2}+z_v\right)[N_u']^T[N_w''] & -z_v\,[N_u']^T[N_u'] \\ -\left(\frac{h_b}{2}+z_v\right)[N_w'']^T[N_u'] & \left(\frac{h_b}{2}+z_v\right)^2[N_w'']^T[N_w''] & \left(\frac{h_b}{2}+z_v\right) z_v\,[N_w'']^T[N_u'] \\ -z_v\,[N_u']^T[N_u'] & \left(\frac{h_b}{2}+z_v\right) z_v\,[N_u']^T[N_w''] & z_v^2\,[N_u']^T[N_u'] \end{bmatrix} dz_v\, dx \begin{Bmatrix} \{\bar{u}\} \\ \{\bar{w}\} \\ \{\bar{\beta}\} \end{Bmatrix} \tag{16}$$

The strain energy associated with longitudinal normal deformation of the piezoelectric constraining layer is given by:

$$U_{Ep} = \frac{1}{2} \begin{Bmatrix} \{\bar{u}\} \\ \{\bar{w}\} \\ \{\bar{\beta}\} \end{Bmatrix}^T b E_p \int_0^L \int_0^{h_p} \begin{bmatrix} [N_u']^T[N_u'] & -\left(\frac{h_b}{2}+h_v+z_p\right)[N_u']^T[N_w''] & -h_v\,[N_u']^T[N_u'] \\ -\left(\frac{h_b}{2}+h_v+z_p\right)[N_w'']^T[N_u'] & \left(\frac{h_b}{2}+h_v+z_p\right)^2[N_w'']^T[N_w''] & \left(\frac{h_b}{2}+h_v+z_p\right) h_v\,[N_w'']^T[N_u'] \\ -h_v\,[N_u']^T[N_u'] & \left(\frac{h_b}{2}+h_v+z_p\right) h_v\,[N_u']^T[N_w''] & h_v^2\,[N_u']^T[N_u'] \end{bmatrix} dz_p\, dx \begin{Bmatrix} \{\bar{u}\} \\ \{\bar{w}\} \\ \{\bar{\beta}\} \end{Bmatrix} \tag{17}$$

And, finally, the strain energy associated with shear deformation of the viscoelastic layer is given by:

$$U_{Gv} = \frac{1}{2} \begin{Bmatrix} \{\bar{u}\} \\ \{\bar{w}\} \\ \{\bar{\beta}\} \end{Bmatrix}^T b G_v \int_0^L \int_0^{h_v} \begin{bmatrix} [0] & [0] & [0] \\ [0] & [0] & [0] \\ [0] & [0] & [N_u']^T[N_u'] \end{bmatrix} dz_v\, dx \begin{Bmatrix} \{\bar{u}\} \\ \{\bar{w}\} \\ \{\bar{\beta}\} \end{Bmatrix} \tag{18}$$

Each of these strain energy expressions clearly shows the contributions of each to the elastic element stiffness matrix.

$$[K] = [K_E] + [K_G] = \left([K_{Eb}] + [K_{Ev}] + [K_{Ep}]\right) + [K_{Gv}] \tag{19}$$

Kinetic Energy, Mass Matrix. The kinetic energy of a moving ACL beam of width "b" and length "L" is given by:

$$\begin{aligned} T = T(t) &= \tfrac{1}{2} b \int_0^L \int_z \rho(x,z)\left(\left(\dot{w}(x,z,t)\right)^2 + \left(\dot{u}(x,z,t)\right)^2\right) dz\, dx \\ &= T_w + T_u \\ &= T_w + \left(T_{ub} + T_{uv} + T_{up}\right) \end{aligned} \tag{20}$$

noting that the energy can be divided into parts associated with transverse motion and longitudinal motion and, further, into parts associated with each component of the ACL system. Note that longitudinal motion includes motion often associated

with "rotatory inertia". The kinetic energy associated with transverse motion of the entire ACL system is given by the following, where the density and thickness have been assumed uniform over the length of the element.

$$T_w = \frac{1}{2}\begin{Bmatrix}\{\dot{\bar{u}}\}\\ \{\dot{\bar{w}}\}\\ \{\dot{\bar{\beta}}\}\end{Bmatrix}^T b\left(\rho_b h_b + \rho_v h_v + \rho_p h_p\right)\int_0^L \begin{bmatrix}[0] & [0] & [0]\\ [0] & [N_w]^T[N_w] & [0]\\ [0] & [0] & [0]\end{bmatrix} dx \begin{Bmatrix}\{\dot{\bar{u}}\}\\ \{\dot{\bar{w}}\}\\ \{\dot{\bar{\beta}}\}\end{Bmatrix} \tag{21}$$

The kinetic energy associated with longitudinal motion of the base beam is given by:

$$T_{ub} = \frac{1}{2}\begin{Bmatrix}\{\dot{\bar{u}}\}\\ \{\dot{\bar{w}}\}\\ \{\dot{\bar{\beta}}\}\end{Bmatrix}^T b\rho_b \int_0^L\int_{-h_b/2}^{+h_b/2} \begin{bmatrix}[N_u]^T[N_u] & -z[N'_w]^T[N_u] & [0]\\ -z[N'_w]^T[N_u] & z^2[N'_w]^T[N'_w] & [0]\\ [0] & [0] & [0]\end{bmatrix} dz\, dx \begin{Bmatrix}\{\dot{\bar{u}}\}\\ \{\dot{\bar{w}}\}\\ \{\dot{\bar{\beta}}\}\end{Bmatrix} \tag{22}$$

The kinetic energy associated with longitudinal motion of the viscoelastic layer is given by:

$$T_{uv} = \frac{1}{2}\begin{Bmatrix}\{\dot{\bar{u}}\}\\ \{\dot{\bar{w}}\}\\ \{\dot{\bar{\beta}}\}\end{Bmatrix}^T b\rho_v \int_0^L\int_0^{+h_v} \begin{bmatrix}[N_u]^T[N_u] & -\left(\frac{h_b}{2}+z_v\right)[N_u]^T[N'_w] & -z_v[N_u]^T[N_u]\\ -\left(\frac{h_b}{2}+z_v\right)[N'_w]^T[N_u] & \left(\frac{h_b}{2}+z_v\right)^2[N'_w]^T[N'_w] & \left(\frac{h_b}{2}+z_v\right)z_v[N'_w]^T[N_u]\\ -z_v[N_u]^T[N_u] & \left(\frac{h_b}{2}+z_v\right)z_v[N_u]^T[N'_w] & z_v^2[N_u]^T[N_u]\end{bmatrix} dz_v\, dx \begin{Bmatrix}\{\dot{\bar{u}}\}\\ \{\dot{\bar{w}}\}\\ \{\dot{\bar{\beta}}\}\end{Bmatrix} \tag{23}$$

And, finally, the kinetic energy associated with longitudinal motion of the piezoelectric constraining layer is given by:

$$T_{up} = \frac{1}{2}\begin{Bmatrix}\{\dot{\bar{u}}\}\\ \{\dot{\bar{w}}\}\\ \{\dot{\bar{\beta}}\}\end{Bmatrix}^T b\rho_p \int_0^L\int_0^{h_p} \begin{bmatrix}[N_u]^T[N_u] & -\left(\frac{h_b}{2}+h_v+z_p\right)[N_u]^T[N'_w] & -h_v[N_u]^T[N_u]\\ -\left(\frac{h_b}{2}+h_v+z_p\right)[N'_w]^T[N_u] & \left(\frac{h_b}{2}+h_v+z_p\right)^2[N'_w]^T[N'_w] & \left(\frac{h_b}{2}+h_v+z_p\right)h_v[N'_w]^T[N_u]\\ -h_v[N_u]^T[N_u] & \left(\frac{h_b}{2}+h_v+z_p\right)h_v[N_u]^T[N'_w] & h_v^2[N_u]^T[N_u]\end{bmatrix} dz_p\, dx \begin{Bmatrix}\{\dot{\bar{u}}\}\\ \{\dot{\bar{w}}\}\\ \{\dot{\bar{\beta}}\}\end{Bmatrix} \tag{24}$$

Each of these kinetic energy expressions clearly shows the contributions of each to the element mass matrix.

$$[M] = [M_w] + [M_u] = [M_w] + \left([M_{ub}] + [M_{uv}] + [M_{up}]\right) \tag{25}$$

Piezoelectric Forcing, Load Vector. The contributions of the piezoelectric forcing to the element load vector are found by considering the virtual work done by the blocked stresses moving through a virtual displacement of the ACL system. The blocked (zero strain) longitudinal normal stress in a piezoceramic, poled through the thickness, is given by:

$$\left(\sigma_{xx}\right)_p = \left(\sigma_{xx}(x,z,t)\right)_p = -e^t E_3 \tag{26}$$

where e^t is a piezoelectric coefficient, and E_3 is the electric field in the z-direction. Note that the electric field can be expressed in terms of the drive voltage and the thickness of the piezoelectric constraining layer as

$$E_3 = E_3(x,z,t) = E_3(t) = -\frac{V(t)}{h_p} \tag{27}$$

so that the blocked stresses may be expressed as:

$$\left(\sigma_{xx}\right)_p = +\frac{e^t}{h_p}V(t) \tag{28}$$

Finally, the virtual work of the blocked stress is given by:

$$\delta W_p = \delta W_p(t) = \tfrac{1}{2} b \int_0^L \int_0^{h_p} \left(\sigma_{xx}(x,z,t)\right)_p \left(\delta\varepsilon_{xx}(x,z,t)\right)_p \, dz_p \, dx$$

$$= \begin{Bmatrix} \{\delta \bar{u}\} \\ \{\delta \bar{w}\} \\ \{\delta \bar{\beta}\} \end{Bmatrix}^T b \frac{e^t}{h_p} \int_0^L \int_{-h_b/2}^{+h_b/2} \begin{bmatrix} [N_u']^T \\ -\left(\frac{h_b}{2} + h_v + z_p\right)[N_w'']^T \\ -h_v\,[N_u']^T \end{bmatrix} dz_p \, dx \quad V(t) \tag{29}$$

This work expression clearly shows the contribution of piezoelectric forcing to the element load vector.

$$\{f\} = \begin{Bmatrix} \{f_{pu}\} \\ \{f_{pw}\} \\ \{f_{p\beta}\} \end{Bmatrix} V(t) = \{F\}\, V(t) \tag{30}$$

Damping, Additional ADF DOF and ADF Evolution Equations. The frequency- or time-dependent behavior of the viscoelastic material can be captured by using a time-domain model such as the ADF method. In this approach, the total deformation (shear angle) of the material is considered to be the sum of two parts: 1) an elastic part, in which the strain is instantaneously proportional to the stress; and 2) an anelastic part, which captures the characteristic relaxation behavior.

$$\{\bar{\beta}\}_{Total} = \{\bar{\beta}\}_{Elastic} + \{\bar{\beta}\}_{Anelastic} \qquad \text{or} \qquad \{\bar{\beta}\} = \{\bar{\beta}^E\} + \{\bar{\beta}^A\} \tag{31}$$

Note that the entire anelastic displacement field itself may be comprised of several individual fields. This possibility is useful in modeling the behavior of materials that exhibit relatively weak frequency-dependence. In a finite element context, the total and anelastic fields are interpolated identically, introducing additional DOF for the anelastic displacements. Since the kinetic energy is expressed in terms of the total motion, it is unchanged. The elastic displacements that appear in strain energy expressions, however, are replaced by the difference between the total and anelastic displacements.

$$\{\bar{\beta}^E\} = \{\bar{\beta}\} - \{\bar{\beta}^A\} \tag{32}$$

Finally, an additional set of ordinary differential equations (ODE) that describe the time evolution of the anelastic displacement fields must be developed. They have the following general form:

$$\tfrac{c}{\Omega}[K_\beta]\{\dot{\bar{\beta}}^A\} - [K_\beta]\{\bar{\beta}\} + c[K_\beta]\{\bar{\beta}^A\} = \{0\} \tag{33}$$

where "$[K\beta]$" is a stiffness matrix that appears in the elastic equations, "c" is a material constitutive coupling parameter, and "Ω" is a characteristic relaxation time at constant strain.

Because the ADF cannot be directly affected through the action of external forces, but only through coupling with the total displacement field, they are effectively internal fields. Consequently, there are no geometric boundary conditions for the ADF analogous to those for the total displacement field. There are, however, force-type boundary conditions: the anelastic stress is proportional to the anelastic strain rate (Lesieutre, 1996).

Discretized Equations of Motion. The final discretized equations of motion for a single element may be expressed in the following standard second order form with evident mass, damping and stiffness matrices:

$$[M]\{\ddot{q}\} + [C]\{\dot{q}\} + [K]\{q\} = \{f\} \tag{34}$$

where the nodal DOF vector is ordered as:

$$\{q\} = \begin{Bmatrix} \{\bar{u}\} \\ \{\bar{w}\} \\ \{\bar{\beta}\} \\ \{\bar{\beta}^A\} \end{Bmatrix} = \left[u_1 \;\; u_2 \;\; u_3 \mid w_1 \;\; w_1' \;\; w_2 \;\; w_2' \mid \beta_1 \;\; \beta_2 \;\; \beta_3 \mid \beta_1^A \;\; \beta_2^A \;\; \beta_3^A\right]^T \tag{35}$$

Some details of the structure of this matrix equation are evident in the following form, particularly the presence of submatrices that are multiples of elastic stiffness submatrices. Once the mass and elastic stiffness matrices have been determined, the submatrices associated with ADF degrees of freedom may be readily determined without additional calculation.

$$\left[\begin{array}{ccc|c} M_{uu} & M_{uw} & M_{u\beta} & 0 \\ M_{uw}^T & M_{ww} & M_{w\beta} & 0 \\ M_{u\beta}^T & M_{w\beta}^T & M_{\beta\beta} & 0 \\ \hline 0 & 0 & 0 & 0 \end{array}\right] \left\{\begin{array}{c} \ddot{\bar{u}} \\ \ddot{\bar{w}} \\ \ddot{\bar{\beta}} \\ \hline \ddot{\bar{\beta}}^A \end{array}\right\} + \left[\begin{array}{ccc|c} 0 & 0 & 0 & 0 \\ 0 & 0 & 0 & 0 \\ 0 & 0 & 0 & 0 \\ \hline 0 & 0 & 0 & \frac{c}{\Omega} K_{\beta\beta} \end{array}\right] \left\{\begin{array}{c} \dot{\bar{u}} \\ \dot{\bar{w}} \\ \dot{\bar{\beta}} \\ \hline \dot{\bar{\beta}}^A \end{array}\right\} + \left[\begin{array}{ccc|c} K_{uu} & K_{uw} & K_{u\beta} & -K_{u\beta} \\ K_{uw}^T & K_{ww} & K_{w\beta} & -K_{w\beta} \\ K_{u\beta}^T & K_{w\beta}^T & K_{\beta\beta} & -K_{\beta\beta} \\ \hline -K_{u\beta}^T & -K_{w\beta}^T & -K_{\beta\beta} & c\,K_{\beta\beta} \end{array}\right] \left\{\begin{array}{c} \bar{u} \\ \bar{w} \\ \bar{\beta} \\ \hline \bar{\beta}^A \end{array}\right\} = \left\{\begin{array}{c} f_{pu} \\ f_{pw} \\ f_{pb} \\ \hline 0 \end{array}\right\} \tag{36}$$

Note that the matrix $[K_{\beta\beta}]$ is symmetric. If desired, these equations may be combined in first order form:

$$\begin{bmatrix} M_{uu} & M_{uw} & M_{u\beta} & 0 & 0 & 0 & 0 \\ M_{uw}^T & M_{ww} & M_{w\beta} & 0 & 0 & 0 & 0 \\ M_{u\beta}^T & M_{w\beta}^T & M_{\beta\beta} & 0 & 0 & 0 & 0 \\ 0 & 0 & 0 & I & 0 & 0 & 0 \\ 0 & 0 & 0 & 0 & I & 0 & 0 \\ 0 & 0 & 0 & 0 & 0 & I & 0 \\ 0 & 0 & 0 & 0 & 0 & 0 & \frac{c}{\Omega} K_{\beta\beta} \end{bmatrix} \begin{Bmatrix} \ddot{\bar{u}} \\ \ddot{\bar{w}} \\ \ddot{\bar{\beta}} \\ \dot{\bar{u}} \\ \dot{\bar{w}} \\ \dot{\bar{\beta}} \\ \dot{\bar{\beta}}^A \end{Bmatrix} + \begin{bmatrix} 0 & 0 & 0 & K_{uu} & K_{uw} & K_{u\beta} & -K_{u\beta} \\ 0 & 0 & 0 & K_{uw}^T & K_{ww} & K_{w\beta} & -K_{w\beta} \\ 0 & 0 & 0 & K_{u\beta}^T & K_{w\beta}^T & K_{\beta\beta} & -K_{\beta\beta} \\ -I & 0 & 0 & 0 & 0 & 0 & 0 \\ 0 & -I & 0 & 0 & 0 & 0 & 0 \\ 0 & 0 & -I & 0 & 0 & 0 & 0 \\ 0 & 0 & 0 & -K_{u\beta}^T & -K_{w\beta}^T & -K_{\beta\beta} & c\,K_{\beta\beta} \end{bmatrix} \begin{Bmatrix} \dot{\bar{u}} \\ \dot{\bar{w}} \\ \dot{\bar{\beta}} \\ \bar{u} \\ \bar{w} \\ \bar{\beta} \\ \bar{\beta}^A \end{Bmatrix} = \begin{Bmatrix} f_{pu} \\ f_{pw} \\ f_{pb} \\ 0 \\ 0 \\ 0 \\ 0 \end{Bmatrix} \tag{37}$$

The equations of motion for a complete ACL system or structure can be found using standard finite element assembly procedures. In such an approach, the total energy is just the sum of the energies of the individual elements, and common nodal DOF are eliminated when continuity is to be enforced.

3. ACL PERFORMANCE

To verify the correct performance of the subject ACL beam finite element, several numerical experiments were performed. First, passive performance was studied, for both continuous and segmented constrained layer treatments. Next, performance with a simple active proportional-derivative (PD) control law was investigated. The following subsections describe these numerical experiments and the results. In all cases, the ACL finite element and the modeled system performed as expected.

PASSIVE PERFORMANCE

The dynamic behavior of a cantilevered beam with ACL treatments were investigated. In the initial cases of interest, the ACL operated in a passive mode, *i.e.,* as a conventional constrained layer damping treatment. As shown in Figure 4, the first case of interest involved complete coverage with a continuous treatment, while the second case of interest involved complete coverage with a segmented treatment. Table 1 summarizes some of the parameter values used.

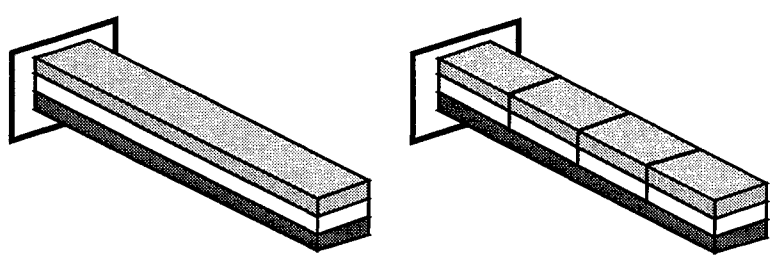

(a) (b)

Figure 4. Beam and ACL Configurations Considered

Initial calculations were made using an elastic version of the finite element (without ADF DOFs, $\bar{\beta}^A$) and verified that modal frequencies were calculated correctly. Figure 5 shows modal damping ratios and modal frequencies for the first 5 modes of a finite element model constructed using 5 equal-length elements. The apparent frequency-dependence of modal damping is

due to a combination of two effects: the inherent variation of viscoelastic material loss factor with frequency, and the effect of different mode shapes on the fraction of strain energy stored in the viscoelastic. In addition, segmentation evidently makes the damping treatment considerably more effective in the lower modes, as expected, but slightly worse in higher modes.

Table 1. Configuration Parameter Values

Beam length (m)	0.200	Number of elements (typical)	5-25
Beam width (m)	0.010		
Base beam		Viscoelastic Layer	
Thickness (m)	0.00100	Thickness (m)	0.00025
Young's modulus (GPa)	70	Young's modulus (MPa)	25
Density (kg/m^3)	2700	Shear modulus (MPa)	10
		Density (kg/m^3)	1600
Piezoelectric Constraining Layer		ADF 'c'	1.2
Thickness (m)	0.00025	ADF 'Ω' (rad/sec)	1500
Young's modulus (GPa)	50		
Density (kg/m^3)	7500		
Piezoelectric constant (N/m-V)	-5.40		

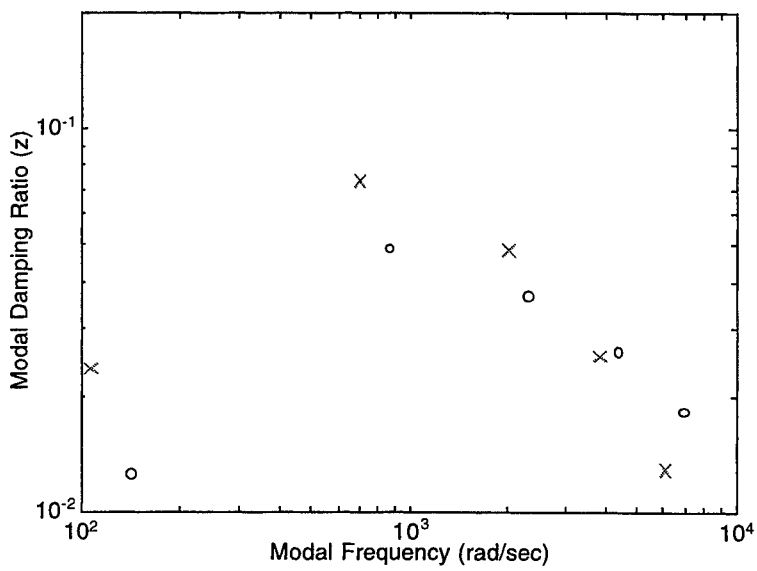

Figure 5. Passive Performance of ACL Treatments ('o' continuous; 'x' segmented)

ACTIVE PERFORMANCE

Performance of an ACL with a simple active proportional-derivative (PD) control law was subsequently investigated. In these cases, the control voltage for a particular ACL 'patch' was based on a discrete strain in the base beam, at the center of the patch, as shown in Figure 6.

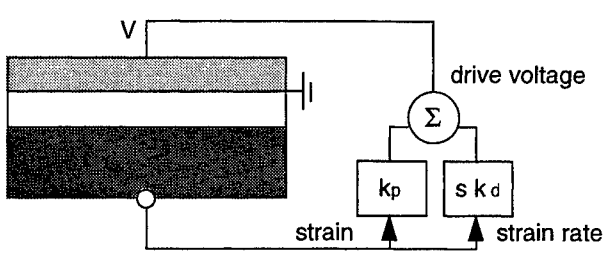

Figure 6. General Local Control Strategy for a Single ACL "Patch"

The drive voltage was taken as the sum of two terms, one proportional to strain, the other to the strain rate, as follows:

$$V_i = -k_p\,\varepsilon_{xx_i} - k_d\,\dot{\varepsilon}_{xx_i} \tag{38}$$

Eq. 10 may be used to obtain the strain at the desired location for element *"i"* as:

$$\left(\varepsilon_{xx}(x=\tfrac{L_i}{2}, z=-\tfrac{h_b}{2}, t)\right)_{b_i} = \left[\left[N_u'\left(\tfrac{L_i}{2}\right)\right] \quad \tfrac{h_b}{2}\left[N_w''\left(\tfrac{L_i}{2}\right)\right] \quad [0] \quad [0]\right]\begin{Bmatrix}\{\bar{u}\}\\ \{\bar{w}\}\\ \{\bar{\beta}\}\\ \{\bar{\beta}^A\}\end{Bmatrix}_i \tag{39}$$

$$= [E]_i\{q\}_i$$

The elemental piezoelectric forcing then may be expressed in terms of the nodal DOF as (Eq. 30):

$$\{f\}_i = -k_p\{F\}_i\,[E]_i\{q\}_i - k_d\{F\}_i\,[E]_i\{\dot{q}\}_i \tag{40}$$

In this form, the piezoelectric forcing terms may be moved to the left hand side of the governing equations and treated as modifications to the stiffness and damping matrices. Table 2 summarizes the control gains used for validation purposes.

Table 2. Control Gains

Proportional gain, k_p	3,000,000 V	Derivative gain, k_d	60 V-s

Figure 7 shows the modal damping ratios and modal frequencies for the first 5 modes of a finite element model constructed using 5 equal-length elements, with control active. Relative to passive operation (Fig. 5), active control clearly increases the damping of the fundamental mode in for both continuous and segmented ACLs. In the case of the single continuous ACL, control is less effective in the higher modes. In fact, because of phasing associated with mode shapes, control using a single continuous ACL can be destabilizing: the frequency and damping of mode 3 are both decreased. The segmented ACL is more robust than the continuous treatment, in that the damping of modes at least up to the number of independent patches is increased by control action.

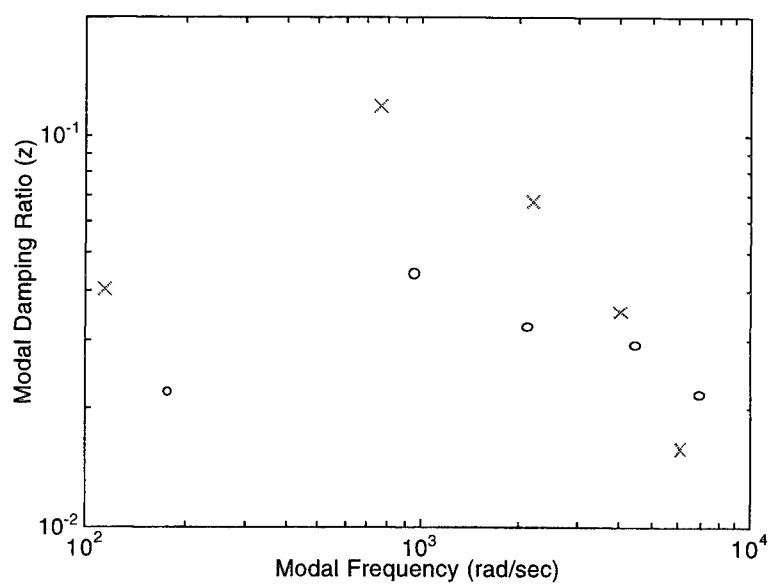

Figure 7. Active Performance of ACL Treatments ('o' continuous; 'x' segmented)

4. SUMMARY AND CONCLUSIONS

A finite element for planar beams with active constrained layer damping treatments was developed using an energy method in combination with the ADF viscoelastic modeling method. Features of this element that are potentially important in active control applications include the following: immunity to shear locking for accuracy; use of a time-domain viscoelastic material model to capture the frequency-dependent stiffness and damping of the viscoelastic material; and the ability to readily accommodate segmented constraining layers with partial coverage, permitting multiple control inputs. Future modifications could include the explicit addition of electrical degrees of freedom for current and power considerations.

The performance of the finite element was verified through several sample modal analyses, including purely passive performance in both continuous and segmented configurations, as well as corresponding active performance using a PD control strategy based on discrete strain sensing. Because of phasing associated with mode shapes, control using a single continuous ACL can be destabilizing. A segmented ACL is more robust than a continuous treatment, in that the damping of modes at least up to the number of independent patches is increased by control action.

REFERENCES

Agnes, G. and K. Napolitano, "Active Constrained Layer Viscoelastic Damping," *Proceedings of the 34th AIAA/ASME/ASCE/AHS/ASC Structures, Structural Dynamics, and Materials Conference*, LaJolla, CA, April 19-22, 1993, pp. 3499-3506.

Azvine, B., Tomlinson, G.R., and Wynne, R.J., "Use of Active Constrained-Layer Damping for Controlling Resonant Vibration," *Journal of Smart Materials and Structures*, Vol. 4, 1995, pp. 1-6.

Bagley, R.L., and P.J. Torvik, "Fractional Calculus - A Different Approach to Analysis of Viscoelastically Damped Structures," *AIAA Journal*, Vol. 21, No. 5, 1983, pp. 741-748.

Bagley, R.L., and P.J. Torvik, "Fractional Calculus in the Transient Analysis of Viscoelastically Damped Structures," *AIAA Journal*, Vol. 23, No. 3, 1985, pp. 201-210.

Bagley, R.L., and R.A. Calico, "Fractional Order State Equations for the Control of Viscoelastically Damped Structures," *Journal of Guidance, Control, and Dynamics*, Vol. 14, No. 2, 1991, pp. 304-311.

Baz, A. and Ro, J-J., "Optimum Design and Control of Active Constrained Layer Damping," *Transactions of the ASME*, Special 50th Anniversary Design Issue, Vol. 117, 1995, pp. 135-144.

Baz, A. and Ro, J-J., "Performance Characteristics of Active Constrained Layer Damping," *Proceedings of Conference on Smart Structures and Materials: Passive Damping*, ed. C.D. Johnson, Orlando, FL, Feb. 14-16, 1994, SPIE Vol. 2193, pp. 98-114.

Baz, A. and Ro, J-J., "The Concept and Performance of Active Constrained Layer Damping Treatments," *Journal of Sound and Vibration*, March, 1994, pp. 18-21.

Baz, A. and Ro, J-J., "Vibration Control of Plates with Active Constrained Layer Damping," *Proceedings of Conference on Smart Structures and Materials: Passive Damping*, ed. C.D. Johnson, San Diego, CA, March, 1995, SPIE Vol. 2445, pp. 393-409.

Baz, A., 1993, "Active Constrained Layer Damping," *Proceedings of Damping '93*," San Francisco, CA, November, 1993, pp. IBB 1-23.

Baz, A., and Poh, S., "Performance of an Active Control System with Piezoelectric Actuators," *Journal of Sound and Vibration*, Vol. 126, No. 2, 1988, pp. 327-343.

Enelund, M. and P. Olsson, "Damping Described by Fading Memory Models," *Proceedings of the 36th AIAA/ASME/ASCE/AHS Structures, Structural Dynamics & Materials Conference*, April 10-13, 1995, New Orleans, LA, Vol. 1, pp. 207-220.

Golla, D.F., and Hughes, P.C., "Dynamics of Viscoelastic Structures - A Time-Domain, Finite Element Formulation," *Journal of Applied Mechanics*, Vol. 52, 1985, pp. 897-906.

Johnson, C.D., Keinholz, D.A., and Rogers, L.C., "The Modal Strain Energy Finite Element Method and its Application to Damped Laminated Beams," *Shock and Vibration Bulletin*, Vol. 51, 1981, pp. 71-81.

Lam, M.J., Saunders, W.R. and Inman, D.J., "Modeling Active Constrained Layer Damping using Golla-Hughes-McTavish Approach," *Proceedings of Conference on Smart Structures and Materials: Passive Damping*, ed. C.D. Johnson, San Diego, CA, March, 1995, SPIE Vol. 2445, pp. 86-97.

Leibowitz, M.M., and Vinson, J.R., "On Active (Piezoelectric) Constrained Layer Damping in Composite Sandwich Structures," *Proceedings of the 4th International Conference on Adaptive Structures*, eds. Breitbach, E.J., Wada, B.K., and Natori, M.C., Cologne, Germany, November 2-4, 1993, pp. 530-541.

Lesieutre, G.A., and E. Bianchini, "Time-Domain Modeling of Linear Viscoelasticity using Anelastic Displacement Fields," *Journal of Vibration and Acoustics*, Vol. 117, No. 4, 1995, pp. 424-430.

Lesieutre, G.A., and Govindswamy, K.M., "Finite Element Modeling of Frequency–Dependent and Temperature–Dependent Dynamic Behavior of Viscoelastic Materials in Simple Shear," *International Journal of Solids and Structures*, Vol. 33, No. 3, 1995, pp. 419-432.

Lesieutre, G.A., and Mingori, D.L., "Finite Element Modeling of Frequency-Dependent Material Damping Using Augmenting Thermodynamic Fields", *Journal of Guidance Control and Dynamics*, Vol. 13, No. 6, 1990, pp. 1040-1050.

Lesieutre, G.A., "Finite Elements for Dynamic Modeling of Uniaxial Rods with Frequency Dependent Material Properties", *International Journal of Solids and Structures,* Vol. 29, 1992, pp. 1567-1579.

Liao, W.H. and K.W. Wang, "Analysis and Design of Viscoelastic Materials for Active Constrained Layer Damping Treatments," *Proceedings of Conference on Smart Structures and Materials: Passive Damping*, ed. C.D. Johnson, San Diego, CA, March, 1996, SPIE Vol. 2720, pp. 212-223.

Liao, W.H. and K.W. Wang, "On the Active-Passive Hybrid Vibration Control Actions of Structures with Active Constrained Layer Treatments," *Proceedings of the ASME 15th Biennial Conference on Mechanical Vibration and Noise*, ASME DE-Vol. 84-3, 1995, pp. 125-141.

Liao, W.H. and K.W. Wang, "Synthesis and Control of Active Constrained Layers with Enhanced Boundary Actions," *Proceedings of Conference on Smart Structures and Materials: Mathematics and Control in Smart Structures*, ed. V.V. Varadan, San Diego, CA, March, 1996, SPIE Vol. 2715, paper no. 27.

McTavish, D.J., and Hughes, P.C., "Modeling of Linear Viscoelastic Space Structures," *Journal of Vibration and Acoustics,* Vol. 115, No. 1, 1993, pp. 103-113.

Nashif, A. D., Jones, D. I.G., and Henderson, J. P., *Vibration Damping*, New York, Wiley, 1985, Chapter 1.

Nath, Subhobroto, and Wereley, N.M., "Active Constrained Layer Damping for Rotorcraft Flex Beams," *Proceedings of the 34th AIAA/ASME/ASCE/AHS/ASC Structures, Structural Dynamics, and Materials Conference*, New Orleans, LA, April 10-13, 1995, pp. 2867-2875.

Plump, J.M. and Hubbard, J.E. Jr., "Modeling of an Active Constrained Layer Damper," *Proceedings of the 12th International Congress on Acoustics*, Toronto, Canada, July 24-31, 1986, Paper No. D4-1.

Shen, I.Y., "Bending and Torsional Vibration Control of Composite Beams Through Intelligent Constrained Layer Treatments," *Proceedings of Conference on Smart Structures and Materials: Passive Damping*, ed. C.D. Johnson, San Diego, CA, March, 1995, SPIE Vol. 2445, pp. 110-122.

Shen, I.Y., "Bending-Vibration Control of Composite and Isotropic Plates Through Intelligent Constrained Layer Treatments," *Journal of Smart Materials and Structures*, Vol. 4, 1995, pp. 59-70.

Shen, I.Y., "Hybrid Damping Through Intelligent Constrained Layer Treatments," *Journal of Vibration and Acoustics*, Vol. 116, July, 1994, pp 341-349.

Shen, I.Y., "Stability and Controllability of Euler-Bernoulli Beams with Intelligent Constrained Layer Treatments," *Journal of Vibration and Acoustics*, Vol. 118, January, 1996, pp 70-77.

VanNostrand, W.C., Knowles, G., and Inman, D.J., "Active Constrained Layer Damping for Micro-Satellites," *Proceedings of the 2nd International Conference on Dynamics and Control of Structures in Space*, eds. Kirk, C.L. and Hughes, P.C., Cranfield Institute of Technology, OK, September 6-10, 1993, pp. 667-681.

VanNostrand, W.C., Knowles, G., and Inman, D.J., "Finite Element Model for Active Constrained-Layer Damping," *Proceedings of Conference on Smart Structures and Materials: Passive Damping*, Orlando, FL, February 14-16, 1994, SPIE Vol. 2193, pp. 126-137.

Veley, Duane E. and Rao, S.S., "Optimal Design of Structures with Active Constrained Layer Damping," *Proceedings of Conference on Smart Structures and Materials: Passive Damping*, ed. C.D. Johnson, San Diego, CA, March, 1995, SPIE Vol. 2445, pp. 98-109.

Yiu, Y.C., "Finite Element Analysis of Structures with Classical Viscoelastic Materials," *Proceedings of the 34th Structures, Structural Dynamics, and Materials Conference*, La Jolla, CA, April, 1993, pp. 2110-2119.

Yiu, Y.C., "Substructure and finite element formulation for linear viscoelastic materials," *Proceedings of the 35th AIAA/ASME/ASCE/AHS/ASC Structures, Structural Dynamics, and Materials Conference*, Hilton Head, SC, April, 1994, Vol. 3, pp. 1585-1594.

Modeling and Experimental Validation of a Sandwich Plate with Isotropic Face-Plates and Viscoelastic Core *

Sudha Veermani
Graduate Research Assistant

Norman M. Wereley †
Assistant Professor

Alfred Gessow Rotorcraft Center
Dept. of Aerospace Engineering
University of Maryland
College Park, MD 20742

Abstract

We analyze and experimentally validate an analysis of a sandwich plate structure, where anisotropic face plates sandwich a viscoelastic core. Existing analytical models have been modified to incorporate piezo-actuation in anisotropic and 3-layered thin plates, using the variational energy method. The 3-layered sandwich consists of anisotropic face-plates with surface bonded piezo-electric actuators, and a viscoelastic core. The analysis includes the membrane and transverse energies in the face plates, and shear in the viscoelastic core. A constant, complex shear modulus was used for the dissipative core, thus frequency and temperature dependence of viscoelastic propoerties is neglected in this model. Simplified forms of the equations are stated based on neglecting shear in face-plates. Experiments were conducted on sandwich plates with aluminum face-plates under clamped boundary conditions to validate the simplified model. Symmetric and asymmetric sandwiches were tested. The maximum error in the first eight natural frequency predictions obtained via the assumed modes solution is less than <10%. Analytical studies on the influence of the number of assumed modes in the Galerkin approximation, and the core storage modulus variation, were conducted. The importance of the in-plane extension modes in sandwich plate analysis was demonstrated. Error in the first natural frequency is nearly 100% when in-plane modes are ignored; error reduces and converges to 6.7% as number of modes is increased to 16 in each of the in-plane directions for each face plate.

Keywords: sandwich plate, viscoelastic core, anisotropic face-plates, piezo-actuation, experimental validation, clamped

1 Introduction

Our current research is motivated by the helicopter industry's goal of achieving a "jet-smooth quiet ride". Noise levels inside a helicopter cabin ranges between 100 and 120 dBA over a frequency range of 40-6000 Hz. The contribution of the main and tail rotors and the turbines is in the frequency range below 500 Hz. The transmission adds the higher frequency disturbance in the 500-6000 Hz range. These disturbances are borne through the air and via structural vibrations into the cabin. Damping of disturbance transmitted into enclosures may be achieved by different approaches. A hybrid method, utilizing piezo-actuation of damped plate to enhance stability robustness of the controller, was suggested in our earlier work [3]. The current research examines an actuated, damped sandwich plate which represents the vibrating wall of an enclosure.

Flexural vibration of viscoelastic sandwich structures has been investigated since the 1950s. Ross, Ungar and Kerwin [5] studied simply-supported plates, and assumed perfect interface and constant amount of transverse displacement in each layer. DiTaranto [6] extended this work to include arbitrary end conditions in beams. Mead and

Marcus [7] modeled the damping of three layered sandwiched beams with isotropic constraining layers sandwiching a viscoelastic core, using sixth order differential equations of motion. Rao and Nakra [8] included the inertia effects of transverse, longitudinal and rotary motion. Bai and Sun [9] eliminated the perfect interface and constant transverse deformation assumptions.

Rao and Nakra [15] developed the basic equations of vibratory bending of asymmetric sandwich plates with isotropic face-plates and viscoelastic core. Lu et. al. [16] developed a finite element model and presented experimental data for sandwich plates under free boundary conditions. Cupial and Niziol [17] used the variational method to model sandwich plates with anisotropic face-plates, and our model closely follows their approach. Additionally, piezo-patch actuators bonded to the two surfaces of the plate are also modeled.

In this paper, a general model for 3-layered plates with viscoelastic sandwiched between anisotropic/generally orthotropic plates has been derived. The development of equations, and notation used, follow the work of Cupial and Niziol [17] closely. The equations reduce to those of Cupial and Niziol when the piezo-actuators are absent, and further reduce to the equations of motion presented by Rao and Nakra [15], when the face-plates are isotropic.

2 Sandwich Plate Model

The equations of vibration of a piezo-actuated, 3-layered sandwich with anisotropic face-plates and a dissipative core are developed. The layers are numbered 1 through 3, as in Fig. 1. Layers 1 and 3 are the multilaminate anisotropic face-plates, whereas the core or the middle layer is the viscoelastic material (VEM) layer. The face-plates are assumed to have bending, shear and extensional stiffnesses. Their rotatory inertia has also been included in the model. The VEM layer is assumed to have shear stiffness alone.

The following assumptions are made in the sandwich plate model: a) in the individual layers, plane sections normal to the mid-plane before bending, remain plane and perpendicular after bending, b) there is no compressional damping, c) all displacements are small, d) there is no slip in the interfaces between the face-plates and the core, e) damping in the faces is small compared to that in the core, and, f) in-plane stresses in the core are small compared with those in the faces.

2.1 Contribution of Piezo-actuators

The piezo-actuators patches are surface-bonded to the exposed surfaces of the two face-plates in the sandwich. They are assumed to be orthotropic in nature, and the bonding is assumed to be infinitely thin and perfect. The actuator patches are integrated into each of the face-plates as one of its laminae.

The patch actuators cover a limited area of the plate surfaces. Hence, a function ϑ is introduced. ϑ is unity over the area of the face-plates where the piezo-actuator is present, and is zero over the rest of the area. The stiffness and mass in the area where the actuators are bonded differ from those in the surrounding area. Their contribution is modeled below.

The density of the complete sandwich now is:

$$\tilde{\bar{\rho}} = \frac{\sum_{i=1}^{3} \rho_i h_i + 2\vartheta \rho_c h_c}{\sum_{i=1}^{3} h_i + 2\vartheta h_c} \tag{1}$$

where h_c is the thickness of the actuator. The density of each of the faces is:

$$\tilde{\rho}^{(i)} = \frac{\rho_i h_i + \vartheta \rho_c h_c}{h_i + \vartheta h_c} \tag{2}$$

The new thickness of the face-layers is written as:

$$\tilde{h}^{(i)} = h_i + \vartheta h_c \tag{3}$$

The actuation moment induced by the piezo-actuators is:

$$\{M_\Lambda\} = \sum_{i=1}^{N_c} \left[\int_{h_c} Q_c \Lambda z \, dz \right]^{(i)} \tag{4}$$

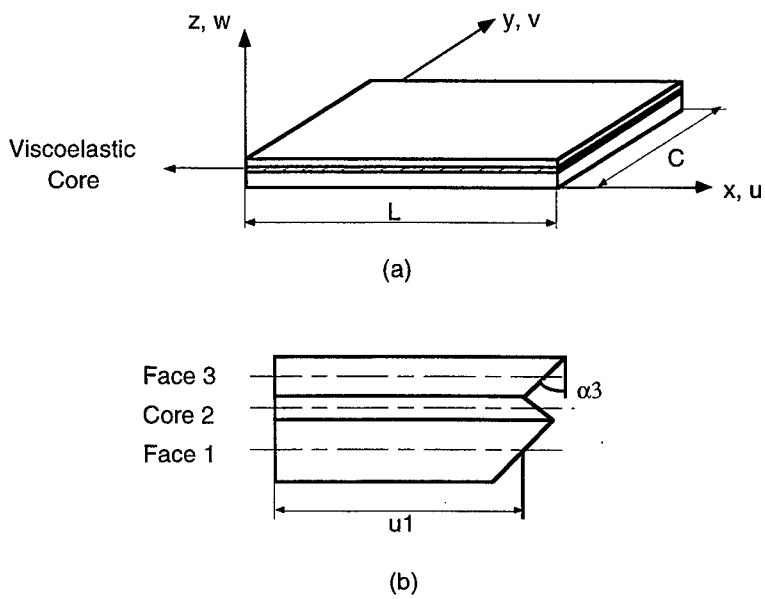

Figure 1: Sandwich plate and layer displacements: (a) Sandwich plate showing its co-ordinate axes and dimensions, and (b) Layers forming the sandwich, and the associated displacements.

where N_c is the number of actuators affixed to the plate, and Q_c is the reduced stiffness of the orthotropic piezo-ply. The external forcing caused by this moment can be written as:

$$\delta W = \int_{A_c} \{M_\Lambda\}'\{\delta\kappa\}\, dA \tag{5}$$

2.2 Plate Energies

The total kinetic energy including the transverse, translatory and rotatory inertias in all the layers may be written as:

$$\begin{aligned} T = \frac{1}{2}\int_V \tilde{\tilde{\rho}}\dot{w}^2 dV \quad &+ \quad \frac{1}{2}\sum_{i=1,3}\int_V \tilde{\rho}^{(i)}\left(f\dot{u}^{(i)} + gz\dot{\alpha}^{(i)}\right)^2 dV \\ &+ \quad \frac{1}{2}\sum_{i=1,3}\int_V \tilde{\rho}^{(i)}\left(f\dot{v}^{(i)} + gz\dot{\beta}^{(i)}\right)^2 dV \\ &+ \quad \text{core terms as in Cupial and Niziol [17]} \end{aligned} \tag{6}$$

The variational kinetic energy, therefore is:

$$\begin{aligned} \delta T \quad = \quad & (\rho h + 2\vartheta\rho_c h_c)\int_A \frac{\partial w}{\partial t}\frac{\partial \delta w}{\partial t} dA \\ & + f\sum_{i=1,3}(\rho_i h_i + \vartheta\rho_c h_c)\int_A \left(\frac{\partial u^{(i)}}{\partial t}\frac{\partial \delta u^{(i)}}{\partial t} + \frac{\partial v^{(i)}}{\partial t}\frac{\partial \delta v^{(i)}}{\partial t}\right) dA \\ & + g\sum_{i=1,3}\frac{1}{12}(\rho_i h_i + \vartheta\rho_c h_c)(h_i + \vartheta h_c)^2\int_A \left(\frac{\partial \alpha^{(i)}}{\partial t}\frac{\partial \delta\alpha^{(i)}}{\partial t} + \frac{\partial \beta^{(i)}}{\partial t}\frac{\partial \delta\beta^{(i)}}{\partial t}\right) dA \\ & + \text{core terms} \end{aligned} \tag{7}$$

The variational potential energy, on including the transverse, in-plane and shear energies in the faces, and the shear energy alone in the core is:

$$
\begin{aligned}
\delta U \;=\; \int_A \Bigg[& \sum_{i=1,3} \tilde{N}_x^{(i)} \frac{\partial \delta u^{(i)}}{\partial x} + \sum_{i=1,3} \tilde{M}_x^{(i)} \frac{\partial \delta \alpha^{(i)}}{\partial x} + \sum_{i=1,3} \tilde{N}_y^{(i)} \frac{\partial \delta v^{(i)}}{\partial y} + \sum_{i=1,3} \tilde{M}_y^{(i)} \frac{\partial \delta \beta^{(i)}}{\partial y} \\
& + \sum_{i=1,3} \tilde{N}_{xy}^{(i)} \left(\frac{\partial \delta u^{(i)}}{\partial y} + \frac{\partial \delta v^{(i)}}{\partial x} \right) + \sum_{i=1,3} \tilde{M}_{xy}^{(i)} \left(\frac{\partial \delta \alpha^{(i)}}{\partial y} + \frac{\partial \delta \beta^{(i)}}{\partial x} \right) \\
& + \sum_{i=1,3} \tilde{Q}_x^{(i)} \left(\delta \alpha^{(i)} + \frac{\partial \delta w}{\partial x} \right) + \sum_{i=1,3} \tilde{Q}_y^{(i)} \left(\delta \beta^{(i)} + \frac{\partial \delta w}{\partial y} \right) \Bigg] dA \\
& + \text{core terms}
\end{aligned}
\tag{8}
$$

N, M and Q are the resultant forces, moments and shears in the face-plates calculated over the face thicknesses given by eq. (3).

2.3 Governing Equations

Applying the Hamilton's principles to the energies and work done discussed above, yields the equations of motion. There are 9 equations corresponding to the 9 independent co-ordinates.

$$
\begin{aligned}
(\rho h + 2\vartheta \rho_c h_c)\ddot{w} &= \frac{\partial \tilde{Q}_x}{\partial x} + \frac{\partial \tilde{Q}_y}{\partial y} + \vartheta f_c \\
f\left[(\rho_1 h_1 + \vartheta \rho_c h_c)\ddot{u}_1 + \frac{1}{2}\rho_2 h_2 \ddot{u}_2\right] - \frac{1}{12} g \rho_2 h_2^2 \ddot{\alpha}_2 &= \frac{\partial \tilde{N}_x^{(1)}}{\partial x} + \frac{\partial \tilde{N}_{xy}^{(1)}}{\partial y} + \frac{Q_x^{(2)}}{h_2} \\
f\left[(\rho_3 h_3 + \vartheta \rho_c h_c)\ddot{u}_3 + \frac{1}{2}\rho_2 h_2 \ddot{u}_2\right] + \frac{1}{12} g \rho_2 h_2^2 \ddot{\alpha}_2 &= \frac{\partial \tilde{N}_x^{(3)}}{\partial x} + \frac{\partial \tilde{N}_{xy}^{(3)}}{\partial y} - \frac{Q_x^{(2)}}{h_2} \\
f\left[(\rho_1 h_1 + \vartheta \rho_c h_c)\ddot{v}_1 + \frac{1}{2}\rho_2 h_2 \ddot{v}_2\right] - \frac{1}{12} g \rho_2 h_2^2 \ddot{\beta}_2 &= \frac{\partial \tilde{N}_y^{(1)}}{\partial y} + \frac{\partial \tilde{N}_{xy}^{(1)}}{\partial x} + \frac{Q_y^{(2)}}{h_2} \\
f\left[(\rho_3 h_3 + \vartheta \rho_c h_c)\ddot{v}_3 + \frac{1}{2}\rho_2 h_2 \ddot{v}_2\right] + \frac{1}{12} g \rho_2 h_2^2 \ddot{\beta}_2 &= \frac{\partial \tilde{N}_y^{(3)}}{\partial y} + \frac{\partial \tilde{N}_{xy}^{(3)}}{\partial x} - \frac{Q_y^{(2)}}{h_2} \\
\frac{1}{4} f \rho_2 h_2 \tilde{h}_1 \ddot{u}_2 + \frac{1}{12} g \left[(\rho_1 h_1 + \vartheta \rho_c h_c)(h_1 + \vartheta h_c)^2 \ddot{\alpha}_1 - \frac{1}{2}\rho_2 h_2^2 \tilde{h}_1 \ddot{\alpha}_2\right] & \\
= \frac{\partial \tilde{M}_x^{(1)}}{\partial x} + \frac{\partial \tilde{M}_{xy}^{(1)}}{\partial y} - \tilde{Q}_x^{(1)} + \frac{\tilde{h}_1}{2h_2} Q_x^{(2)} & \\
-\frac{1}{4} f \rho_2 h_2 \tilde{h}_3 \ddot{u}_2 + \frac{1}{12} g \left[(\rho_3 h_3 + \vartheta \rho_c h_c)(h_3 + \vartheta h_c)^2 \ddot{\alpha}_3 - \frac{1}{2}\rho_2 h_2^2 \tilde{h}_3 \ddot{\alpha}_2\right] & \\
= \frac{\partial \tilde{M}_x^{(3)}}{\partial x} + \frac{\partial \tilde{M}_{xy}^{(3)}}{\partial y} - \tilde{Q}_x^{(3)} + \frac{\tilde{h}_3}{2h_2} Q_x^{(2)} & \\
\frac{1}{4} f \rho_2 h_2 \tilde{h}_1 \ddot{v}_2 + \frac{1}{12} g \left[(\rho_1 h_1 + \vartheta \rho_c h_c)(h_1 + \vartheta h_c)^2 \ddot{\beta}_1 - \frac{1}{2}\rho_2 h_2^2 \tilde{h}_1 \ddot{\beta}_2\right] & \\
= \frac{\partial \tilde{M}_y^{(1)}}{\partial y} + \frac{\partial \tilde{M}_{xy}^{(1)}}{\partial x} - \tilde{Q}_y^{(1)} + \frac{\tilde{h}_1}{2h_2} Q_y^{(2)} & \\
-\frac{1}{4} f \rho_2 h_2 \tilde{h}_3 \ddot{v}_2 + \frac{1}{12} g \left[(\rho_3 h_3 + \vartheta \rho_c h_c)(h_3 + \vartheta h_c)^2 \ddot{\beta}_3 - \frac{1}{2}\rho_2 h_2^2 \tilde{h}_3 \ddot{\beta}_2\right] & \\
= \frac{\partial \tilde{M}_y^{(3)}}{\partial y} + \frac{\partial \tilde{M}_{xy}^{(3)}}{\partial x} - \tilde{Q}_y^{(3)} + \frac{\tilde{h}_3}{2h_2} Q_y^{(2)} &
\end{aligned}
\tag{9}
$$

where

$$\tilde{Q}_x = \sum_{i=1,3} \tilde{Q}_x^{(i)} + Q_x^{(2)} \text{ and } \tilde{Q}_y = \sum_{i=1,3} \tilde{Q}_y^{(i)} + Q_y^{(2)} \tag{10}$$

and f_c is the actuation forcing obtained from eq. (5).

3 Analysis and Validation

3.1 Analytical Validation

This section compares the frequencies of free vibration of a simply-supported sandwich plate with symmetric isotropic face-plates, as predicted by the model, with an analytical solution of Abdulahadi as presented in [17]. For a simply-supported plate, the eigenfunctions are of the form:

$$\begin{aligned} u_i(x,y,t) &= U_i \cos\frac{m\pi x}{L} \sin\frac{n\pi y}{C} \\ v_i(x,y,t) &= V_i \sin\frac{m\pi x}{L} \cos\frac{n\pi y}{C} \\ w(x,y,t) &= W \sin\frac{m\pi x}{L} \sin\frac{n\pi y}{C} \end{aligned} \tag{11}$$

The mode shapes given by eq. (11) are used in the model. The predicted modes of free vibration, and the corresponding modal loss factors are tabulated against the exact solution in Table 1. The predicted values match the closed form analytical solution, and error is within 1.5% for both the natural frequencies and the loss factors.

3.2 Experimental Validation

This section presents experimental validation of the sandwich model with isotropic face-plates. Three different sandwich plates have been tested. The first of these is a symmetric sanwich, with aluminum face-plates of thickness 1/32", sandwiching a 2 mil thick viscoelastic layer. The other two plates are asymmetric, with face-plates of thickness 1/32" and 1/16". One of these asymmetric plates has a core thickness of 2 mil, while the other has 5 mil. The plates were clamped atop an aluminum stand using 28 bolts around the perimeter. The test area of the plates is 26.5" x 20.5". The viscoelastic material used is 3M Scotchdamp ISD-112.

The approximate mode shapes assumed for the case of a plate clamped on all sides are as follows:

$$\begin{aligned} u_i(x,y,t) &= U_i \sin\frac{m\pi x}{L} \sin\frac{n\pi y}{C} \\ v_i(x,y,t) &= V_i \sin\frac{m\pi x}{L} \sin\frac{n\pi y}{C} \end{aligned} \tag{12}$$

For the bending mode shapes, beam bending modes in x and y directions have been assumed. Polynomial approximations of the beam mode characteristic functions tabulated in Blevins [14] have been used. Note: The number of assumed modes used in the model are n=16 in the transverse directions, and m=16 in each of the in-plane directions, unless otherwise mentioned.

The storage modulus and loss factor of the VEM are functions of the frequency and temperature. The model, however, assumes the complex modulus to be a constant. The dimensions of the specimens used in the tests, and the actuation using a centrally mounted PZT, allow clear identification of modes below 200Hz. Hence, the value for the storage modulus used here, is chosen to be that at the mid-frequency of 100Hz. The modulus is picked from the product information chart provided by 3M to be G′=1.0MPa at this frequency, at 20°C. The loss factor of the VEM at the same frequency and temperature is η=1.

The results of the experiments conducted on the symmetric sandwich, have been tabulated against the frequencies predicted by the model in Table 2. Three different values of the storage modulus, G′, have been used in the analysis, to compare the accuracy of the model predictions under the constant modulus assumption.

At the 50 Hz value of G′=0.75MPa, the least error is seen to be at the mode closest to 50 Hz i.e. mode (2,1). The model overpredicts at frequencies below 50Hz, and underpredicts above the same. When the G′ value is chosen at 100 Hz, the errors are seen to shift. Once again, the change of sign of the error is noticed around the G′ frequency. The least error is seen to be at the modes (1,2) and (3,1). Finally, when the G′ value is picked at 200 Hz, the point of

Table 1: Comparison of natural frequencies and loss factors of a symmetric sandwich with isotropic face-plates: L = 0.3480 m, C = .3048 m, $h_1 = h_3 = 0.762$ mm, $h_2 = 0.254$ mm, $E_1 = E_3 = 68.9$ GPa, $\nu_1 = \nu_3 = 0.3$, $\rho_1 = \rho_3 = 2740$ kg/m^3, $\rho_2 = 999$ kg/m^3, $G_2 = 0.869$ MPa, $\eta_2 = 0.5$. The exact values are from the analytical solution by Abdulhadi from Cupial and Niziol (1995).

	Plate Frequencies			Loss Factor		
Mode No.	Exact [Hz]	Predicted [Hz]	Error [%]	Exact	Predicted	Error [%]
(1,1)	60.3	60.7	0.72	0.190	0.190	0.05
(1,2)	115.4	115.9	0.43	0.203	0.205	1.15
(2,1)	130.6	130.9	0.26	0.199	0.201	1.33
(2,2)	178.7	179.0	0.18	0.181	0.182	0.83
(1,3)	195.7	197.3	0.86	0.174	0.173	-0.59

Table 2: Experimental validation using using symmetric clamped sandwich of dimensions: 26.5" x 20.5" x (1/32" Al - 2 mil VEM - 1/32" Al). Effect of varying storage modulus, G_2'. Here, number of bending mode shapes, $n = 16$, and number of in-plane mode shapes, $m = 16$, for each

		$G_2' = 0.75$MPa @ 50Hz		$G_2' = 1.0$MPa @ 100Hz		$G_2' = 1.4$MPa @ 200Hz	
Mode No.	Expt [Hz]	Theory [Hz]	Error [%]	Theory [Hz]	Error [%]	Theory [Hz]	Error [%]
(1,1)	38.0	39.8	4.78	40.5	6.80	41.3	8.73
(2,1)	68.5	67.3	-1.78	69.2	1.07	71.0	3.76
(1,2)	90.3	87.7	-2.83	91.0	0.80	94.2	4.33
(3,1)	109.1	106.9	-2.03	110.9	1.60	115.1	5.52
(2,2)	120.0	110.2	-8.15	114.9	-4.2	119.7	-0.25
(3,2)	-	145.7	-	152.6	-	160.2	-
(1,3)	162.0	151.0	-6.78	158.1	-2.40	165.5	2.19
(4,1)	187.0	171.3	-8.40	179.9	-5.45	189.2	1.20

minimum error moves to the high modes near 200 Hz. The model overpredicts for all the frequencies below this value (except at mode (2,2) which may be attributed to experimental error). This table clearly elucidates the strong effect of G′ on the model predictions. Overall error in the frequency range under study (0-200 Hz) is below 10%. However, if the bandwidth is increased, the errors are likely to be unacceptably high. Therefore, including the frequency dependence of the shear layer storage modulus in the sandwich plate model will increase the accuracy of the model over the entire bandwidth. This can be accomplished via the modal strain energy [11], Golla-Hughes-McTavish [12] or anelastic displacement fields [13] models.

The experimental validation of the sandwich model in case of two of the asymmetric sandwiches is presented in Table 3. These plates have face-plates of thickness 1/16" and 1/32". One has a VEM core thickness of 2 mil, and the other, 5 mil. Also shown in this table are the frequencies and loss factors of a uniform aluminum plate with no damping layer, to study the effect of increasing shear layer thicknesses.

In case of the asymmetric sandwiches, an error of ≈13% is seen in the first mode. For the uniform plate of thickness 3/32", also, 16% error is noted. The uniform plate model is a well validated one. Material properties of the aluminum used are also well known. Therefore, the source of the error is probably the design of the aluminum stand. Experiments are currently ongoing to calibrate and improve the experimental set-up for testing of thicker plates.

In Table 3, a downward shift in the frequencies on increasing layer thicknesses of the VEM, is noticed. The trend is similar in case of the experiments and the model predictions.

3.3 Influence of In-plane Energies

The number of assumed modes used in the analysis is seen to have a considerable effect on the accuracy of the predictions. Table 4 tabulates the predicted frequencies for the symmetric sandwich using different number of assumed modes.

The number of in-plane modes, m, is varied while keeping the number of transverse vibration modes, n, constant.

Table 3: Experimental validation for 26.5" x 20.5" x (1/32" Al - VEM - 1/16" Al) asymmetric clamped sandwich plate; $G_2' = 1.0$MPa. Here, n = 16 is number of assumed plate modes in w; m = 16 is number of assumed plate modes in u, v in each of the face-plates.

	Uniform Plate			2 mil VEM			5 mil VEM		
Mode No.	Expt [Hz]	Thry [Hz]	Error [%]	Expt [Hz]	Thry [Hz]	Error [%]	Expt [Hz]	Thry [Hz]	Error [%]
(1,1)	53.5	62.0	15.88	53.0	59.4	12.16	49.7	56.3	13.33
(2,1)	93.2	105.8	13.52	91.7	100.3	9.43	89.9	92.0	2.38
(1,2)	125.9	142.4	13.10	118.0	131.4	11.40	107.0	118.2	10.46
(3,1)	156.0	180.8	15.89	141.4	161.1	13.96	138.0	144.9	5.03
(2,2)	167.0	185.1	10.84	162.0	165.7	2.30	161.5	147.7	-8.54
(3,2)	212.0	255.9	20.71	-	220.8	-	-	195.6	-
(1,3)	230.0	272.4	18.40	-	229.9	-	-	203.6	-
(4,1)	246.2	280.4	13.89	-	261.0	-	-	216.3	-

Table 4: Effect of the number of assumed modes on the clamped symmetric plate model predictions. Here, n = number of assumed plate modes in w; m = number of assumed plate modes in u, v in each of the face-plates.

		n = 16, m = 0		n = 16, m = 3		n = 16, m = 5	
Mode No.	Expt [Hz]	Anal [Hz]	Error [%]	Anal [Hz]	Error [%]	Anal [Hz]	Error [%]
(1,1)	38	76.3	100.9	41.7	9.7	41.7	9.7
(2,1)	68.5	112.6	64.4	108.0	57.7	69.7	1.8
(1,2)	90.3	133.3	47.67	127.0	40.6	121.0	34.0
(3,1)	109.1	157.2	44.1	150.2	37.7	150.2	37.6
(2,2)	120.0	158.6	32.2	150.6	25.5	150.6	25.5
(3,2)	-	196.7	-	191.1	-	187.8	-
(1,3)	162.0	199.6	23.2	196.7	21.4	191.2	18.0
		n = 16, m = 8		n = 16, m = 16		n = 8, m = 16	
Mode No.	Expt [Hz]	Anal [Hz]	Error [%]	Anal [Hz]	Error [%]	Anal [Hz]	Error [%]
(1,1)	38	41.4	9.0	40.5	6.8	40.6	6.87
(2,1)	68.5	69.8	1.8	69.2	1.07	69.2	1.1
(1,2)	90.3	91.4	1.2	91.0	0.8	91.2	1.0
(3,1)	109.1	114.6	5.1	110.9	1.6	111.5	2.2
(2,2)	120.0	143.6	19.6	114.9	-4.2	114.6	-4.4
(3,2)	-	187.51	-	152.6	-	152.96	-
(1,3)	162.0	188.2	16.2	158.1	-2.4	158.4	-2.2

When $m = 0$, that is, the in-plane energies are excluded altogether, error is extremely large. The first mode has 100% error. On increasing m the error in prediction is seen to fall. When $m = 3$, error in the first mode is down to 9.7%, although error in the second mode is still high at 57.7%. When the number of in-plane modes is increased to 5 in each direction, the error in the second mode reduces to 1.8%. Further increase in the value of m sees a convergence in results, with low error. The final column shows the change when the number of in-plane modes is maintained at 16, but the number of transverse modes is reduced to 8. The change in the frequencies predicted is small. Error increases by less than 1% in the modes.

From Table 4, it may be concluded that the inclusion of the in-plane strain energies is of significant import in the analysis of sandwich plates. In-plane extension adds to the shearing of the dissipative layer, and therefore affects the overall stiffness of the sandwich. Bending energy, on the other hand, only mildly affects the shearing of the core. Accounting for the coupling between the extensional and bending modes of the plate, hence, is crucial in sandwich structure analyses.

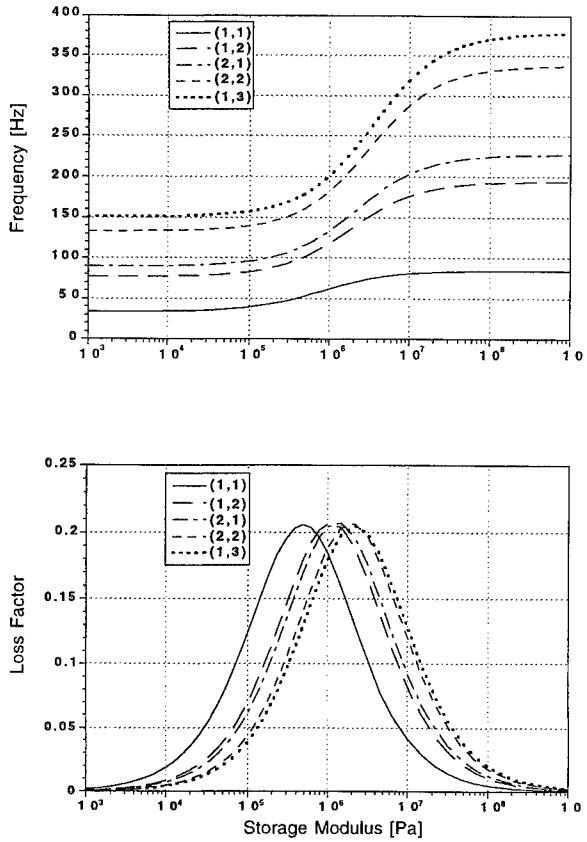

Figure 2: Natural frequencies and modal loss factors for simply-supported sandwich plate: L = 13.69", C = 12", $h_1 = h_3 = 0.03$", $h_2 = 10$ mil

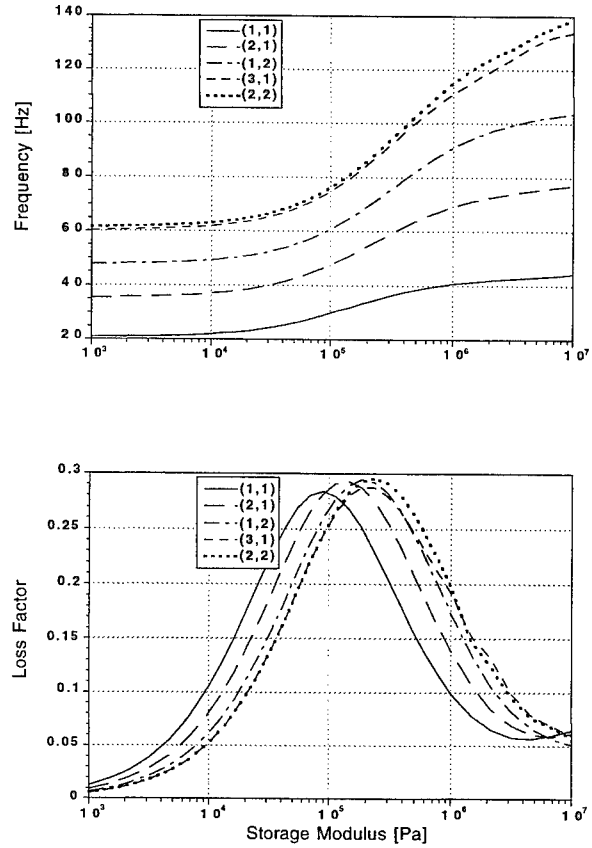

Figure 3: Natural frequencies and modal loss factors for clamped symmetric sandwich plate: L = 26.5", C = 20.5", $h_1 = h_3 = 1/32$", $h_2 = 2$mil

3.4 Influence of Core Storage Modulus

This section presents a parametric study on the influence of the storage modulus of the shear layer on the natural frequencies and the modal loss factors of the sandwich plate. All the four plates used in the validation in the previous section are subject to this study. The first of these plates is symmetric supported, the second, symmetric clamped, and the last two, asymmetric clamped. The results of this study are presented in Fig. 3.4 through Fig. 3.4. The curves have been plotted for the first five plate modes.

The behavior of the curves is seen to be similar irrespective of the boundary conditions, (simply-supported or clamped), of the symmetric or asymmetric nature of the sandwich, and also of the thickness of the VEM layer (2 mil or 5 mil). Storage modulus has significant influence on both the frequencies and the modal loss factors. The frequency increases rapidly from 10^5 to 10^7 Pa and is asymptotic outside this range. From the modal loss factors curves, it can be seen that for each of the plate modes, there is a range of values of shear modulus, G, for which there is high damping. This information may be used in designing the plate configuration to provide maximum modal damping at the operating frequency (and hence storage modulus). For instance, in case of the aysmmetric damped plate with 5 mil VEM layer (Fig. 3.4), the region of maximum modal damping is around $G' = 10^6$, which, incidentally, coincides with the value of storage modulus being used.

In case of the simply supported symmetric plate (13.69" x 12" x 0.06"), the VEM layer of 10mil results in a maximum modal loss factor of about 0.21, which is ≈40% of the VEM loss factor of 0.5. For the clamped symmetric plate (26.5" x 20.5" x 0.0625"), a 2 mil VEM of 1.0 loss factor results in maximum modal loss of 0.29. The asymmetric clamped plates (26.5" x 20.5" x 0.09375") with VEM layers of 2 and 5 mil have peak modal loss of 0.23 and 0.25 respectively. Increase in the viscoelastic layer thickness is thus seen to result in higher damping in the plate, as expected.

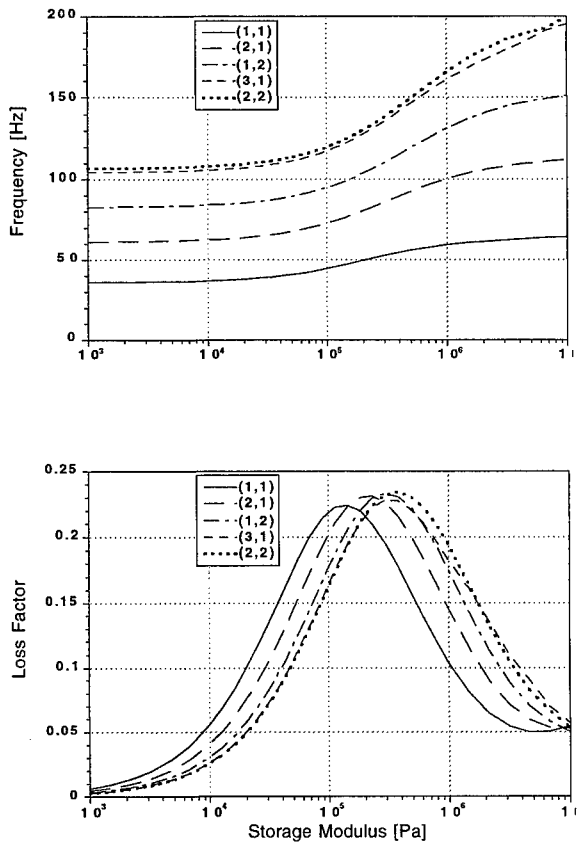

Figure 4: Natural frequencies and modal loss factors for asymmetric clamped sandwich plate: L = 26.5", C = 20.5", h_1 = 1/16", h_3 = 1/32", h_2 = 2mil

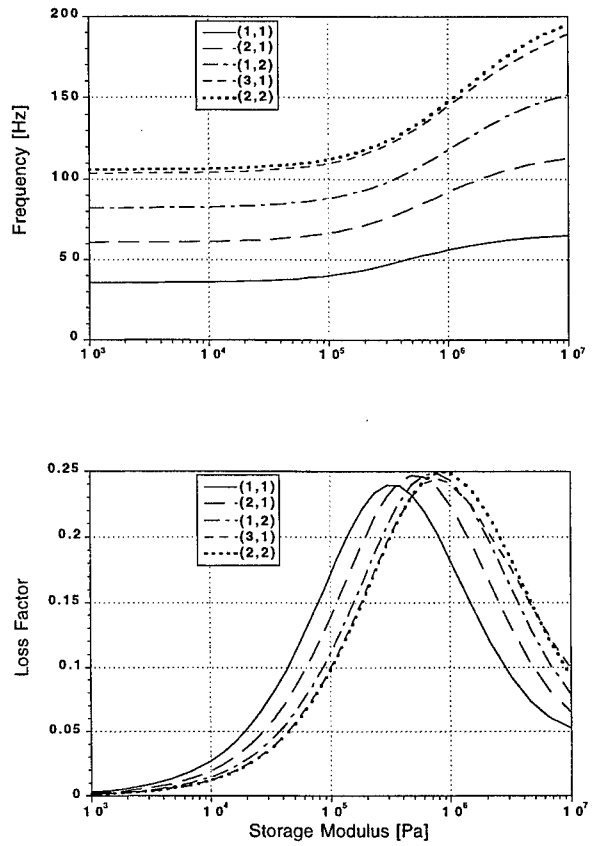

Figure 5: Natural frequencies and modal loss factors for asymmetric clamped sandwich plate: L = 26.5", C = 20.5", h_1 = 1/16", h_3 = 1/32", h_2 = 5mil

4 CONCLUSIONS

An analytical model for a piezo-actuated sandwich plate with a dissipative core and anisotropic face-plates has been developed and validated. Shear deformation of the face layers as well as the rotatory inertia are included. Flexural and membrane energies in the face-plates are accounted for, while the core is assumed to have shear stiffness alone. A first order shear deformation theory is used to describe the deformation in the layers. The core shear modulus is assumed to have a stationary complex value.

Validation of the model under simply-supported boundary conditions against a closed form solution shows an error of <1% in the prediction of natural frequencies. Also, experiments have been conducted on symmetric and asymmetric clamped sandwich plates. The measured frequencies and modal loss factors are used to further validate the model. The symmetric sandwich consists of 2 aluminum layers of thickness 1/32" sandwiching a 2 mil thick viscoelastic core. Very good correlation (6.8 % error in the first mode) between theory and experiments was observed in the symmetric sandwich plate. The error in the frequencies near 100Hz is low (<2%) when the value of G′ at 100Hz is used in the model, and similarly, the error in frequencies near 200Hz is minimal when G′ at 200Hz is used. Hence, the error in the predictions may be attributed to the assumption of a constant value of core storage modulus. For the thicker asymmetric sandwiches, the measured modal frequencies and loss factors did not correlate as well as for the symmetric plates, but the trend in natural frequencies matched that of the model, and was attributed to inadequate plate stand design. An immediate goal is to reduce the experimental error by redesigning the plate stand to increase its mass and stiffness, to improve results for these thicker asymmetric plates.

Analytical studies on the influence of the number of plate mode shapes assumed in the Galerkin approximation, and that of the shear modulus have been conducted. The in-plane mode shapes are seen to have a significant influence on the prediction of the vibratory modes. Error in the 1st mode is 100% when no in-plane modes are included, and converges to 6.8% when their number is increased to 16. Similarly, error in the 2nd mode starts at 64.5%, drops to

57.7% when the number of modes in each in-plane direction assumed is 3, and further reduces to 1% when 16 modes are used. Therefore, we conclude that in-plane modes must be included in sandwich structure analyses.

The value of G′ is also seen to have a large effect on the frequency and loss factor. For every mode, a region of G′ exists wherein the change of frequency with G′ is large, and where the modal loss factor attains a maximum. The damping layer may hence be tailored, by selecting the optimal thickness and material, to maximize damping in the structure. Modal loss factor is seen to be between 25 and 40% of the viscoelastic loss factor in the plates studied.

Future work includes experimentally validating the general model with anisotropic (composite) face-plates will be validated. as well as the actuation induced by single/multiple pairs of piezo-actuator. The frequency and temperature dependence of the viscoelastic core modulus was not modeled in this study, but will be accounted for using methods based on modal strain energy, Golla-Hughes-McTavish, or anisotropic displacement fields.

Acknowledgments

This work is supported by the U.S. Army Research Office under the Smart Structures University Research Initiative, contract no. DAAL03-92-G-0121, with Dr. Gary Anderson serving as contract monitor.

References

[1] Sun, C.T., and Lu, Y.P., *Vibration Damping of Structural Elements*, Prentice Hall PTR, 1995.

[2] Baz, A., and Ro, J., "Performance characteristics of active constrained layer damping," SPIE, Vol. 2193, 1994, pp. 98-114.

[3] Veeramani, S., and Wereley, N. M., "Hybrid Passive/Active Damping for Robust Multivariable Acoustic Control in Composite Plates," SPIE *Conference on Smart Structures and Integrated Systems*, San Diego, CA, SPIE Paper 2717-32, 1996.

[4] Flügge, W., *Viscoelasticity*, Blaisdell Publishing Co., 1967.

[5] Ross, D., Ungar, E.E., and Kerwin, J., "Damping of plate flexural vibrations by means of viscoelastic laminate," ASME *Structural Damping*, 1959, pp. 49-88.

[6] DiTaranto, R.A., "Theory of vibratory bending for elastic and viscoelastic layered finite length beams," *J. Applied Mechanics*, Vol. 87, 1965, pp. 881-886.

[7] Mead, D.J., and Markus, S.,"The forced vibration of a three-layer, damped sandwich beam with arbitrary boundary conditions," *J. Sound and Vibration*, Vol. 10, No. 2, 1969, pp. 163-175.

[8] Rao, Y.V.K.S., and Nakra, B.C., "Vibrations of unsymmetrical sandwich beams and plates with viscoelastic cores," *J. Sound and Vibration*, Vol. 34, No. 3, 1974, pp. 309-326.

[9] Bai, J.M., and Sun, C. T., "The effect of viscoelastic adhesive layers on structural damping of sandwich beams," *Mechanical Structures and Machines*, Vol. 23, No. 1, 1995, pp. 1-16.

[10] Nashif, A.D., Jones, D., and Henderson, J.P., *Vibration Damping*, John Wiley & Sons, 1985.

[11] Johnson, C.D., and Keinholz, D.A., "Finite element prediction of damping in structures with constrained viscoelastic layers," *AIAA Journal*, Vol. 20, No. 9, 1982, pp. 1284-1290.

[12] McTavish, D.J., and Hughes, P.C., "Finite Element Modeling of Linear Viscoelastic Structures: The GHM Method," Proceedings of the 33rd AIAA/ ASME/ASCE/AHS/ASC Structures, Structural Dynamics and Materials Conference, 1992, Paper No. AIAA-92-2380-CP.

[13] Lesieutre, G.A. and Lee, U., "A finite element for beams having segmented active constrained layers with frequency-dependent viscoelastics, " *J. Smart Materials and Structures*, Vol. , No. , 19, pp.

[14] Blevins, R.D., *Formulas for Natural Frequencies and Mode Shapes*, Van Nostrand Reinhold Company, 1979.

[15] Rao, Y.V.K.S., and Nakra, B.C., "Theory of vibratory bending of unsymmetrical sandwich plates," *Archives of Mechanics*, Vol. 25, No. 2, 1973, pp. 213-225.

[16] Lu, Y.P., Killian, J.W., and Everstine, G.C., "Vibrations of three layered damped sandwich plate composites," *J. Sound and Vibration*, Vol. 64, No. 1, 1979, pp. 63-71.

[17] Cupial, P., and Niziol, J., "Vibration and damping analysis of a three-layered composite plate with a viscoelastic mid-layer," *J. Sound and Vibration*, Vol. 183, No. 1, 1995, pp. 99-114.

Addendum

The following papers were announced for publication in this proceedings but have been withdrawn or are unavailable.

[3045-02] **Nonobstructive particle damping effectiveness under forced compaction**
H. V. Panossian, Rockwell International Corp./Rocketdyne Div.

[3045-04] **Hysteresis in active and passive damping devices**
H. T. Banks, North Carolina State Univ.

[3045-05] **Modeling and identification of nonlinear hysteretic vibration isolators**
Y. Q. Ni, J. M. Ko, C. W. Wong, Hong Kong Polytechnic Univ.

[3045-23] **Constrained layer damping treatment configurations**
D. E. Veley, Air Force Wright Lab.

[3045-34] **Comparison of experimental measurements and theoretical predictions of a self-sensing active constrained layer treatment**
J. M. Yellin, I. Y. Shen, Univ. of Washington

[3045-38] **Design and analysis of a passively damped instrument isolator for space structures**
T. Fronk, Utah State Univ.

[3045-40] **Test and analysis of stand-off damping treatments as applied to composite sandwich panels**
E. Haugse, R. Ikegami, Boeing Defense & Space Group; M. Parin, Damping Technologies, Inc.

Author Index

Anderson, Mark C., 224
Austin, Eric M., 173
Banks, H. Thomas, Addendum
Baz, Amr M., 293
Bennett, Stephen, 259
Bicos, Andrew S., 14, 40
Bölter, Ralf, 148
Bullough, William A., 96
Chen, T., 293
Chu, L., 204
Conley, Dave, 214
Davis, Christopher L., 51
Davis, L. Porter, 14, 31
Davis, Torey, 259
Dosch, Jeffrey, 51
Drake, Michael L., 251
Edberg, Donald L., 31
Esipov, Sergei E., 2
Fasana, Alessandro, 184
Fosness, Eugene R., 20, 31, 259
Frank, Geoffrey J., 251
Friend, R. D., Addendum
Fronk, Thomas, Addendum
Garibaldi, Luigi, 184
Ghoneim, Hany, 162
Giorcelli, Ermanno, 184
Gordaninejad, Faramarz, 119
Gordon, Robert W., 214
Hansen, Scott W., 190
Hasselman, Timothy K., 224
Haugse, Eric, Addendum
Hopkins, David M., 251
Ikegami, Roy, Addendum, 214
Inman, Daniel J., 60, 173
Janocha, Hartmut, 148
Johnson, Conor D., 14, 20, 31
Kamath, Gopalakrishna M., 108
Kelly, James M., 130
Kinra, Vikram K., Addendum
Ko, J. M., Addendum
Lam, Margaretha J., 60
Lee, Usik, 315
Lesieutre, George A., 51, 315
Liao, W. H., 70
Makris, Nicos, 140
McMahon, Scott, 140
Ni, Y. Q., Addendum
Oyadiji, S. O., 204
Panossian, Hagop V., Addendum
Parin, Mike, Addendum
Peel, David J., 96
Pöschel, Thorsten, 2
Pollock, Thomas C., 224
Rawal, Suraj P., Addendum
Ray, M., 293
Ray, Sourav, Addendum
Rogers, Lynn C., 214
Rongong, Jem A., 282
Ruzzene, Massimo, 184
Saiidi, M. Saiid, 119
Salueñya, Clara, 2
Saunders, William R., 60
Searle, Ian R., 214
Shen, I. Yeu, Addendum
Stanway, Roger, 96
Taniwangsa, Wendy, 130
Tomlinson, Geoffrey R., 282
Tsai, Meng Shiun, 82
Uthiram, Sivakumar, 119
Veermani, Sudha, 329
Veley, Duane E., Addendum
Wang, Kon Well, 70, 82
Wereley, Norman M., 108, 329
Wilke, Paul S., 20, 259
Wilson, George W., 236
Wolke, Patrick J., 236
Wong, C. W., Addendum
Wu, Shu-yau, 40
Yellin, Jessica M., Addendum
Zapfe, Jeffrey A., 268
Zhu, Changyi, Addendum